



**University of  
Nottingham**  
UK | CHINA | MALAYSIA

**MULTIPHASE FLOW DYNAMICS AND MASS  
TRANSFER IN DIFFERENT MULTIPHASE REACTOR  
FOR SHEAR CONTROLLABLE SYNTHESIS PROCESS**

by

**Yanqing GUO**

A thesis submitted to the University of Nottingham in partial fulfilment  
of the requirements for the degree of  
Doctor of Philosophy

Under the supervision of  
Prof. Xiaogang Yang  
Dr. Guang Li

**December 2020**

## ACKNOWLEDGEMENTS

On the very outset of this dissertation, I would like to extend my sincere obligation towards all the personages who have helped me in this endeavour, especially my supervisor Prof. Xiaogang Yang. Without his kindness, generosity, patience, support, encouragement and expertise, I would not have made headway in this journey. His constructive criticism, expertise guidance and brainstorming made my studies thoughtful and productive ever since he has provided me a first glance on fluid dynamics in my undergraduate. He is not only the best supervisor for academic studies but also acts as a mentor of life with his life experience, wisdom and passion for science. I would always remember his words and try to be a person with diligence and rigorous attitude in my research career. I appreciate all his contributions for comments and revisions on this thesis.

I would like to acknowledge the PhD scholarship granted by the International Doctoral Innovation Centre (IDIC) of the University of Nottingham Ningbo China. My sincerest thanks to Ms. Jessica Wang for her administrative support. This work was also financially supported by the National Natural Science Foundation of China (Grant Nos. 21576141, 21761132026).

I gratefully acknowledge all members in FAST team, Dr. Guang Li, Dr. Jie Yang, Dr. Lu Liu, Dr. Luming Chen, Dr. Chenyang Xue, Dr. Yiyi Wu, Dr. Collins Ezech, Dr. Bin Dong, Dr. Weibin Shi, Dr. Xiani Huang, Ms. Xinyue Cai, Mr. Bin Li, Ms. Shanshan Long, Ms. Lulu Wang, Ms. Jiaying Lu for their assistance and meaningful discussions. It has been a great pleasure to work with all of you. I am also glad to have the support of my fellow colleagues, especially Mr. Jie Dong and Mr. Jiarui Gao for your generous help and support.

I would especially like to thank my best friend Ms. Shuyao Wei. Thank you for sailing through this journey with me, loving me and always cheering me during the most difficult days. You have been my greatest support and companion. I am also grateful to the other best friend of mine, Mr. Yuhui Wang for always being there for me despite the distance.

I would also like to extend my gratitude to the technician team of Faculty of Science and Engineering of the University of Nottingham Ningbo China, Mr. Julian Zhu, Mrs. Helen Xu, Mrs. Jane Zhang, Mrs. Carey Tao, Ms. Kate Yuan, Mr. Jason Wang and Mr. John Zhu, for their technical support in lab experiment.

Finally yet importantly, I am extremely grateful to my lovely parents, Mr. Bin Guo and Mrs. Baoyun Liu for their love, prayers, caring and sacrifices for educating and preparing me for my future. You are my everything.

## SYNOPSIS

Multiphase flow dynamics in different multiphase reactors for shear controllable synthesis process is a multidisciplinary study intersecting reactor engineering, chemical reaction, molecular dynamics and micro-technology. The functional fine particle produced by shear controllable synthesis has broad applications in pharmaceutical engineering, energy field, electronic technology, environmental engineering and other fields, providing a foundation for modern high-tech industries. Considering the drawbacks of traditional multiphase reactors including high energy consumption, low conversion rate, poor mixing performance, thermo-runaway and long reaction time, novel multiphase reactors such as impinging jet reactors (IJR) and swirling vortex flow reactors (SVFR) are employed to prepare micro/nano particles. Its hydrodynamics effect on mixing, heat and mass transfer, chemical reaction and synthesised particle properties has been discussed in this PhD thesis. In order to improve the particle synthesis process in aforementioned aspects and enhance production efficiency for target particle characteristics, fine-particle synthesis process is prepared by approach of turbulence intensification. In this research, investigation on particle synthesis process in IJR and SVFR assist by ultrasound has been carried out on aspect of flow pattern, chemical reaction, mixing and mass transfer. Moreover, the laminar-regime hydrothermal post-treatment in hydrothermal autoclave has been attempted and analysed to further improve and modify the synthesised particle properties. It has been widely realised that controllable synthesis is a complex process with considerations of mass, momentum and energy transport as well as sophisticated chemical reaction and the deep understanding of such a process is still challengeable. Consequently, there is a necessity to build models and correlations on multiphase flow dynamics and particle synthesis to achieve the aim of shear controllable synthesis of micro/nano particles.

The principal work conducted and delivered outcomes from the research are summarised:

- (1) Chapter 2 presents a fast way of preparation of nano-sized  $\text{FePO}_4$  in the impinging jet reactor (IJR) with assist of ultrasound irradiation. Impinging jet reactor is a fast-mixer where the two linear liquid jets collide with high velocity to diminish the segregation. The collision in high speed creates a stagnant region where engulfment occurred breaking eddies into smaller ones in Kolmogorov scale. By imposing the ultrasound to the IJR, micro-scale turbulent eddies generated as the result of collapse of acoustic streaming which generates strong local shear. Both experimental and simulation work has been carried out and results show that turbulence is intensified by acoustic streaming and  $\text{FePO}_4$  particles are synthesised with higher crystallinity, better uniformity, higher porosity and smaller size. Such characteristics benefit  $\text{FePO}_4$  nano-particles as precursor materials for subsequent assembly, especially high porosity that is important for subsequent assembly for lithium ion batteries.
- (2) Chapter 3 mainly focuses on micromixing that takes place down to the molecular level. In this chapter, the chemical reaction has been considered and analysed not only experimentally but also in simulation work. This chapter investigates the micromixing performance in the impinging jet reactor by employing Villermaux-Dushman reaction with variables of acid concentration, inlet Reynolds number and ultrasound amplitude. It is found that higher acid concentration leads to higher likelihood of occurrence of side reactions, thus contributing to higher segregation index and poor mixing performance. Furthermore, both increasing inlet Reynolds number and ultrasound amplitude contribute to intensification of turbulence. To be specific, the micromixing time is significantly reduced up to 66.7% once ultrasound power increases to 840W. The simulation results show consistence with experimental results within the margin of error. The enhancement of micromixing

performance owing to turbulence intensification by the adoption of ultrasound is attributed to engulfment flow and generation of small-scale as the result of acoustic streaming.

- (3) Chapter 2 and 3 have discussed the multiphase flow dynamics on FePO<sub>4</sub> nano-particle synthesis and micromixing performance in the IJR. Chapter 4 concentrates on a totally different structured mixer that is firstly put forward in this thesis named ‘swirling vortex flow reactor (SVFR)’. The SVFR is able to generate a strong ‘Rankine vortex-like’ flow with a great velocity gradient in the radial direction, trapping the synthesised aggregated SiO<sub>2</sub> nano-particles into the vortex core to form aggregation. The mass transfer is studied by combination of simulation and experiment in the shear controllable synthesis of nano-sized aggregated particles in a swirling vortex flow reactor. It is found that the mass transfer can be significantly enhanced by engulfment between the slabs due to liquid streams tangentially entering the reactor. Local shear in the turbulent eddies with the length scales down to the Kolmogorov scale shape the aggregated SiO<sub>2</sub> nano-particles, yielding well spherical morphology and narrower size distribution. Furthermore, both numerical simulation and experimental results clearly indicate that assist of ultrasound is able to further enhance the mass transfer due to the intensified micro-turbulent streaming.
- (4) The properties of aggregated SiO<sub>2</sub> nanoparticles synthesised in SVFR can be further modified by hydrothermal post-treatment that is discussed in Chapter 5. Unlike IJR and SVFR, the shear force in hydrothermal autoclave driven by natural convection is steady and gentle in laminar flow regimes indicated by Rayleigh number. The natural convection acts as driven force on particle movement significantly affected by the temperature difference. A visual image of Rayleigh-Benard vortex pattern in the hydrothermal autoclave has been reproduced via Euler–Lagrange modelling with two-way coupling. The buoyance force is strengthened by increasing temperature difference between top-half region and bottom-half region. The buoyance-driven

convection greatly promotes heat transfer and in turn weakens the temperature gradient. Furthermore, particle trajectory shows that particle is tightly trapped in circulation flow but affected by disturbance. From experimental results, SiO<sub>2</sub> particles are synthesised with smaller size, higher tapped density with higher crystallinity under consistent and steady shear flow. The hydrothermal post-treatment for aggregated SiO<sub>2</sub> nano-particles makes it possible for one-step particle control without calcination.

In short, this thesis gives insight in detailed particle synthesis process modelling in two main multiphase reactors (IJR and SVFR) and experiments of synthesis of FePO<sub>4</sub> and SiO<sub>2</sub> aggregated particles are performed to analyse effect of hydrodynamics on particle properties. The attempt of combination of fast-mixer and external ultrasound field in micro/nano-particle synthesis has successfully intensified turbulence and such combination has positive effects on aspects of chemical reaction, mixing performance and mass transfer. Except for experimental work, the simulation work has been carried out to analyse flow patterns, turbulent intensity, chemical reaction as well as particle-fluid interaction in particle synthesis process in multiphase reactors. Such investigation makes it possible to build correlations on hydrodynamic parameters and particle characteristics and helps to predict the behaviour and properties of particles. This is meaningful for design, upgrade and scale-up of multiphase reactor in synthesis process.

# TABLE OF CONTENTS

ACKNOWLEDGEMENTS .....	i
SYNOPSIS .....	iii
TABLE OF CONTENTS .....	vii
LIST OF FIGURES AND GRAPHS .....	xii
LIST OF TABLES .....	xxiii
NOMENCLATURES .....	xxiv
LIST OF PUBLICATIONS .....	xxxvii

## **CHAPTER 1: CURRENT STATUS OF MODELLING OF HYDRODYNAMICS AND MASS TRANSFER IN NANO/MICRO PARTICLE SHEAR CONTROLLABLE SYNTHESIS PROCESSES**

SUMMARY .....	1-1
1.1 Fundamentals and turbulent-relevant-characteristics of multiphase reactors..	1-2
1.1.1 Types and characteristics of multiphase reactors.....	1-2
1.1.2 Fundamentals and relevance to turbulence .....	1-9
1.2 Process of mixing, chemical reaction and particle formation in the multiphase flow system .....	1-16
1.2.1 Mixing process in multiphase reactors.....	1-16
1.2.2 Intrinsic kinetics of multiphase reactions.....	1-23
1.2.3 Effect of hydrodynamics on particle formation in multiphase reactors.	1-27
1.3 Fluid dynamics effects in particle precipitation processes in multiphase flow system .....	1-35
1.3.1 Applicable numerical techniques to analyse multiphase system .....	1-35
1.3.2 Hydrodynamic interactions between particles and fluid/gas shear flows .....	1-44
1.4 Fundamental methodologies of controllable synthesis of nano- and micro-sized particles and process intensification (PI) for multiphase flows .....	1-53
1.4.1 Approaches to synthesise ultrafine particle synthesis.....	1-53

1.4.2 Process intensification (PI) for ultrafine particle synthesis in multiphase system .....	1-63
1.4.3 Controllable synthesis of micro/nano particles via hydrodynamic interaction.....	1-65
1.5 Scale-up of multiphase reactor on basis of similarity principle.....	1-67
1.5.1 Scale-up process.....	1-67
1.5.2 Scaling laws .....	1-68
1.5.3 Validation of scaling .....	1-72
1.6 Concluding remarks and recapitulation .....	1-75
References.....	1-78
Figures and Graphs .....	1-109
Tables.....	1-153

## **CHAPTER 2: EFFECT OF ULTRASONIC INTENSIFICATION ON SYNTHESIS OF NANO-SIZED PARTICLES WITH AN IMPINGING JET REACTOR**

SUMMARY .....	2-1
2.1 Introduction.....	2-2
2.2 Experimental Methods .....	2-4
2.2.1 Experimental setup and product characterization .....	2-4
2.2.2 LFP/C preparation.....	2-5
2.2.3 Description on synthesis reaction .....	2-6
2.3 Numerical simulation.....	2-7
2.3.1 Mathematical modelling .....	2-7
2.3.2 Numerical simulation.....	2-9
2.4 Results and discussion .....	2-11
2.4.1 Effect of ultrasound power intensity on crystallinity and morphology of FP precursors .....	2-11
2.4.2 Effect of ultrasound power on particle size and porosity of FP precursors .....	2-13
2.4.3 Effect of adoption of different ultrasound power intensities on the mixing .....	2-15
2.4.4 Effect of ultrasound power on electrochemical performance .....	2-17
2.5 Conclusions.....	2-19

References.....	2-22
Figures and graphs.....	2-26
Tables.....	2-36

**CHAPTER 3: TURBULENT MICROMIXING INTENSIFICATION IN THE IMPINGING JET REACTOR ASSISTED BY ULTRASOUND IRRADIATION AND CHARACTERISATION BY VILLERMAUX-DUSHMAN REACTION**

SUMMARY.....	3-1
3.1 Introduction.....	3-2
3.2 Experimental.....	3-4
3.2.1 Reaction descriptions.....	3-4
3.2.2 Calibration curve of UV spectrophotometer.....	3-8
3.2.3 Experimental setup and product characterisation.....	3-8
3.3 Numerical Modelling.....	3-9
3.3.1 Governing equations.....	3-9
3.3.2 Turbulence modelling.....	3-12
3.3.3 Modelling of ultrasound effect on the momentum equation and $k-\varepsilon$ turbulence model.....	3-12
3.3.4 Numerical Simulation.....	3-12
3.4 Results and discussion.....	3-14
3.4.1 Effect of $H^+$ concentration on micromixing performance in the IJR.....	3-14
3.4.2 Effect of local turbulence on mixing performance in the IJR.....	3-15
3.4.3 Effect of ultrasound amplitude on mixing performance in the IJR.....	3-17
3.4.4 The mixing time scale in the T-junction impinging jet reactor.....	3-21
3.5 Conclusions.....	3-24
References.....	3-27
Figures and Graphs.....	3-33
Tables.....	3-41
Appendix.....	3-43

## **CHAPTER 4: SHEAR TURBULENCE CONTROLLABLE SYNTHESIS OF AGGREGATED NANO-PARTICLES USING A SWIRLING VORTEX FLOW REACTOR ASSISTED BY ULTRASOUND IRRADIATION**

SUMMARY .....	4-1
4.1 Introduction.....	4-2
4.2 Experimental.....	4-5
4.2.1 Solution preparation.....	4-5
4.2.2 Experimental setup and product characterization .....	4-5
4.2.3 Description on synthesis reaction .....	4-7
4.3 Numerical simulation.....	4-8
4.3.1 Governing equations .....	4-8
4.3.2 Mass transfer models .....	4-11
4.3.3 Numerical Simulation .....	4-13
4.4 Results and discussions.....	4-14
4.4.1 Synthesised particle characterisation .....	4-14
4.4.2 Effect of turbulent intensity and vorticity strength on the synthesis.....	4-18
4.4.3 Effects of the interaction between turbulence induced shear and reaction characteristics on the synthesised particles.....	4-20
4.4.4 Effect of turbulence induced shear on mass transfer rates of the synthesised aggregate particles.....	4-22
4.5 Conclusions.....	4-26
References.....	4-29
Figures and Graphs .....	4-35
Tables.....	4-47

## **CHAPTER 5: SHEAR CONTROLLABLE SYNTHESIS OF MESOPOROUS SILICA SPHERICAL PARTICLES USING SWIRLING FLOW REACTORS AND POST-HYDROTHERMAL TREATMENT**

SUMMARY .....	5-1
5.1 Introduction.....	5-2
5.2 Experimental.....	5-6

5.2.1 Chemicals.....	5-6
5.2.2 Silica sources preparation .....	5-6
5.2.3 Hydrothermal post-treatment of the silica sources.....	5-6
5.3 Mathematical Modelling.....	5-7
5.3.1 Governing equations .....	5-7
5.3.2 Numerical modelling.....	5-11
5.4 Results and Discussion .....	5-13
5.4.1 Effects of Rayleigh convection in the hydrothermal autoclave on induced shear flow and temperature distribution.....	5-13
5.4.2 Effect of Rayleigh convection induced shear flow in hydrothermal autoclave on synthesised characteristics .....	5-15
5.4.3 SiO <sub>2</sub> particle dispersion in the hydrothermal autoclave.....	5-20
5.5 Conclusions.....	5-22
References.....	5-24
Figures and Graphs .....	5-29
Tables.....	5-40

## **CHAPTER 6: RECAPITULATION AND RECOMMENDATIONS**

6.1 Shear controllable synthesis of fine particles.....	6-1
6.2 Specific realisations .....	6-5
6.2.1 The hydrodynamic effect on synthesis of nano-sized FePO <sub>4</sub> in a impinging jet reactor.....	6-5
6.2.2 The hydrodynamic effect on synthesis of aggregated SiO <sub>2</sub> nanoparticles in a swirling vortex flow reactor and post-treatment in a hydrothermal autoclave .....	6-9
6.3 Recommendation of future work .....	6-14
References.....	6-19

# LIST OF FIGURES AND GRAPHS

## CHAPTER 1

- Figure 1.1** configuration of typical stirred tank reactor (Pangarkar, 2015). ..... 1-109
- Figure 1.2** 3D- and 2D-dimensional contour of solid volume fraction and the solid velocity-vector at impeller speed of 950rpm for (a) A310, (b) PBT, and (c) PF3 (Kazemzadeh *et al.*, 2019). ..... 1-109
- Figure 1.3** Homogeneity versus power consumption for different types of impellers (Kazemzadeh *et al.*, 2019). ..... 1-110
- Figure 1.4** Schematic diagram of Taylor-Couette reactor from side view and bottom view (Kim *et al.*, 2013). ..... 1-110
- Figure 1.5** SEM images of calcium carbonate synthesised in (a) CTR at CBO = 5 mol/m<sup>3</sup>; (b) STR at CBO = 5 mol/m<sup>3</sup>; (c) CTR at CBO = 48 mol/m<sup>3</sup>; (d) STR at CBO = 48 mol/m<sup>3</sup> (Jung *et al.*, 2010). ..... 1-111
- Figure 1.6** Particle distribution at stationary region (left: 200 rpm, 5 mL/min) and moving region (right: 200 rpm, 60 mL/min) (Kim *et al.*, 2013). ..... 1-111
- Figure 1.7** SEM images of copper sulfide nanoparticles with different morphology synthesized in CTR under different rotational speed. (a) 90 rpm; (b) 200 rpm; (c) 500 rpm; (d) 1000 rpm; (e) 85 rpm; (f) 80 rpm; (e) 50 rpm, and (h) 5 rpm respectively (Tang *et al.*, 2019). ..... 1-112
- Figure 1.8** Morphology of latex aggregates experiencing alternative steps of high-shear rate and the low-shear rate (Guérin *et al.*, 2017). ..... 1-112
- Figure 1.9** Cross-sectional of confined impinging jets reactor (Schwarzer and Peukert, 2004). ..... 1-113
- Figure 1.10** The yield of  $C_2$  ( $C_2H_2 + C_2H_4$ ) of different diameter in Jet-In-Cross-Flow (JICF) reactor and Forward-Impinging-Back (FIB) Reactor (Luo *et al.*, 2019). ..... 1-113
- Figure 1.11** Instantaneous flow field of confined impinging jet reactors on XZ planes with denote of vortex (the scale of arrow is 10 m/s) (Liu *et al.*, 2014). .. 1-114
- Figure 1.12** Contour of velocity magnitude and turbulent kinetic energy of micro-impinging stream reactor (MISR) at (a)  $Re_j = 395$ ; (b)  $Re_j = 1500$ ; (c)  $Re_j = 3161$  (Liu *et al.*, 2014). ..... 1-114
- Figure 1.13** 3D and 2D-dimensional particles trajectories without turbulent dispersion simulated by (a) RANS and (b) LES (Sadiki *et al.*, 2017). ..... 1-115
- Figure 1.14** Nusselt number  $Nu$  simulated from LES and RSM with experimental data (Zhou *et al.*, 2017a). ..... 1-115

<b>Figure 1.15</b> Iso-surface of pressure, visualizing the vortex rope simulated from models of (a) standard $k-\epsilon$ ; (b) RNG $k-\epsilon$ ; (c) DDES-SA; (d) LS (Javadi and Nilsson, 2015). .....	1-116
<b>Figure 1.16</b> Contours of vorticity magnitude at a horizontal plane simulated by (a) standard $k-\epsilon$ ; (b) RNG $k-\epsilon$ ; (c) DDES-SA; (d) LS (Javadi and Nilsson, 2015). ....	1-116
<b>Figure 1.17</b> Mechanistic model of a binary tree of masses and springs (Bak and Kalmár-Nagy, 2018). .....	1-117
<b>Figure 1.18</b> Qualitative graph of the Kolmogorov-spectrum for 3D homogeneous turbulence (Pope, 2000). .....	1-117
<b>Figure 1.19</b> Schematic representation of the path the drops following in the channel with a) $D=3\text{mm}$ ; b) $D=2\text{mm}$ at low jet velocities (Tsaoulidis and Angeli, 2017)...	1-118
<b>Figure 1.20</b> Photos of the liquid jet at (a) low and (b) high jet velocities (Tsaoulidis and Angeli, 2017).....	1-118
<b>Figure 1.21</b> Relationship between segregation index and micromixing time at various conditions (Rahimi <i>et al.</i> , 2014).....	1-111
<b>Figure 1.22</b> Configuration of streamlines inside a T-mixer at different mass flows (Engler <i>et al.</i> , 2004). .....	1-119
<b>Figure 1.23</b> Concentration field of a jet dyed with rhodamine in the confined impinging jet reactor under different Reynolds number (a) $Re=103$ , (b) $Re=111$ and (c) $Re=505$ (Brito <i>et al.</i> , 2020).....	1-120
<b>Figure 1.24</b> (a) Experimental flowchart for the iodide-iodate tests; (b) Schematic illustration of a single countercurrent-flow micro-channel reactor; (c) micromixing time $t_m$ versus Reynolds number $Re$ (Cheng <i>et al.</i> , 2019). .....	1-120
<b>Figure 1.25</b> Velocity magnitude vectors at horizontal intersecting face and various total flow rates (Rahimi <i>et al.</i> , 2014). .....	1-121
<b>Figure 1.26</b> Contour plots of $I_3^-$ mass fraction fields at horizontal intersecting face and various total flow rates (Rahimi <i>et al.</i> , 2014).....	1-121
<b>Figure 1.27</b> Schematic of the different-types of microchannel reactors (a) Y-shape; (b) T-shape; (c) Lambda shape (Faryadi <i>et al.</i> , 2014). .....	1-122
<b>Figure 1.28</b> (a) Pressure drop in microchannels of different geometry; (b) the performance ratio microchannels of different geometry (Faryadi <i>et al.</i> , 2014). .....	1-122
<b>Figure 1.29</b> The dimensionless mixing distance versus different thickness of injection ring and schematic diagram of moderated penetration model (Zhou <i>et al.</i> , 2019). .....	1-123

- Figure 1.30** Typical concentration profiles for a gas–liquid reaction (Pangarkar, 2015). ..... 1-123
- Figure 1.31** Typical concentration profiles for solid-catalyzed gas–liquid reaction (Pangarkar, 2015). ..... 1-124
- Figure 1.32** SEM images of  $\text{YPO}_4$  synthesized under hydrothermal treatment at  $180^\circ\text{C}$  with different additives for different reaction time: (a, b, c) citric acid for 2 h, 6 h, and 12 h, respectively; (d, e, f) oxalate for 2 h, 6 h, and 12 h, respectively; and (h, i, j) EDTA for 2 h, 6 h, 12 h, respectively (Lai *et al.*, 2014). ..... 1-124
- Figure 1.33** LaMer curve describing the three stages of metal nanocrystal formation in solution system. Stage I: atom producing, stage II: nucleation, and stage III: seed formation and growth (You and Fang, 2016). ..... 1-125
- Figure 1.34** (a) Schematic illustration of the effect of  $\text{Ag}^+$  ion concentration on the morphology of Ag mesoparticles. (b) Schematic diagram of 1D, 2D, and 3D morphologies have been prepared via particle-mediated growth (You and Fang, 2016). ..... 1-125
- Figure 1.35** Crystallisation of the  $\text{GdPO}_4$  into different morphology and size under different  $\text{PO}_4^{3-}/\text{Gd}^{3+}$  ratio in the reaction mixture. .... 1-126
- Figure 1.36** A) Experimental set-up for synthesis of ZnO particles in a CFI. Dashed arrows represent the change of direction of the secondary flow (Dean flow) due to  $90^\circ$  bends; B) Different CFIs used for carrying out the ZnO synthesis at different residence times (Delgado-Licona *et al.*, 2020). ..... 1-126
- Figure 1.37** Schematic representation of the ZnO formation mechanism by a change in hydrodynamics and reaction conditions: A)  $De \leq 20$  and  $[\text{OH}^-/\text{Zn}^{2+}] = 2$  where mass transfer controls the nucleation rate and B)  $De \geq 60$  and  $[\text{OH}^-/\text{Zn}^{2+}] = 10$ , where the growth of the particle is favored due to a formation of Dean flow. Colour contours represents the concentration of each reactants, whereas the green interface represents the concentration of the formed ZnO. Bold black lines represent the velocity profile in axial direction; C) SEM images of Spindle-like ZnO particles obtained at  $[\text{OH}^-/\text{Zn}^{2+}] = 2$ ; Flower-like ZnO particles obtained at  $[\text{OH}^-/\text{Zn}^{2+}] = 10$  (Delgado-Licona *et al.*, 2020). ..... 1-127
- Figure 1.38** Predicted contour graph of the relationship between  $[\text{OH}^-/\text{Zn}^{2+}]$  molar ratios, Dean numbers and residence time on the particle size (Delgado-Licona *et al.*, 2020). ..... 1-128
- Figure 1.39** Considerations for primary particles, aggregates and agglomerates. (A) synthesis approach of synthetic amorphous silica through a pyrogenic process; (B) aggregates and agglomerates of primary particles (Boverhof *et al.*, 2015). ..... 1-128
- Figure 1.40** (a) Schematic aggregation process with possible test methods; (b) Relative decrease in total particle concentration for perikinetic and orthokinetic aggregation (Gregory, 2009). ..... 1-129

<b>Figure 1.41</b> Schematic diagram of hybrid particle state and mass transfer between the gas-phase and the particle systems (Boje <i>et al.</i> , 2019). .....	1-129
<b>Figure 1.42</b> SEM images of aggregates with mobility diameters of (a) 30 nm, (b) 50 nm, and (c) 100 nm for (A) Original SEM images and (B) SEM images with sketched representative primary particle circles (Naseri and Thomson, 2019). 1-130	
<b>Figure 1.43</b> (a) Structured boundary-fitted mesh (b) Unstructured boundary-fitted mesh around a circular particle (Feng and Michaelides, 2009). .....	1-130
<b>Figure 1.44</b> Overview of gas-solid multiphase CFD models with an Eulerian-Eulerian and an Eulerian-Lagrangian approach (Hirche <i>et al.</i> , 2019). .....	1-131
<b>Figure 1.45</b> (a) Eulerian-Eulerian and Eulerian-Lagrangian treatment for a 2D geometry with finite volume method (FVM) method; (b) Coupling overview of Eulerian and Lagrangian treatment and introduction of transformed Eulerian particles as pseudo Lagrangian particles (Hirche <i>et al.</i> , 2019). .....	1-132
<b>Figure 1.46</b> (a) Numerical observations of a two-dimensional fluidised bed formulated with a Eulerian–Eulerian approach (time interval $\Delta t = 80$ ms); (b) Numerical observations of a two-dimensional fluidised bed formulated with an Eulerian-Lagrangian (EL) approach (Chiesa <i>et al.</i> , 2005). .....	1-133
<b>Figure 1.47</b> Position of bubbles in fluidised bed as a function of time for both Eulerian-Eulerian and Eulerian- Lagrangian approaches compared with experimental data (Chiesa <i>et al.</i> , 2005). .....	1-133
<b>Figure 1.48</b> Structural grids for ventilation ducts (Xu <i>et al.</i> , 2020b). .....	1-134
<b>Figure 1.49</b> Non-dimensional deposition velocity at different positions: (a) Lagrangian approach; (b) Eulerian approach (Xu <i>et al.</i> , 2020b). .....	1-134
<b>Figure 1.50</b> Variation of fouling mass on floor with time for $d_p = 5 \mu\text{m}$ : (a) Comparison of two approaches; (b) Eulerian approach (Xu <i>et al.</i> , 2020b). .....	1-135
<b>Figure 1.51</b> Instantaneous gas volume fraction and velocity vectors (color snapshots for gas volume fraction, white vector for gas phase, and black vector for discrete particles of (a) EL model; (b) solid phase of EE model; (c) Schematic of the internally circulating fluidized bed) (Zhang <i>et al.</i> , 2018). .....	1-135
<b>Figure 1.52</b> Schematic diagrams of the computational domain and boundary conditions for mass transfer simulation (Zhang <i>et al.</i> , 2015). .....	1-136
<b>Figure 1.53</b> (a) Effect of diffusivity on mass transfer coefficient at different residence times;(b) Dependence of concentrations of mass transfer species in aqueous phase on residence time for different types of reactions (Zhang <i>et al.</i> , 2015). .....	1-136
<b>Figure 1.54</b> Concentration distribution of the spherical cluster at different Reynolds number (Lu <i>et al.</i> , 2018). .....	1-137

- Figure 1.55** SEM images of (a) Ni-MOF; (b) CuO@NiO-400(1:2); (c) CuO@NiO-500 (1:2); (d) CuO@NiO-400 (1:1); (e) CuO@NiO-500 (2:1); (f) NiO nanoparticles; (g) TEM image of CuO@NiO-400 (1:2); (i) AP Pure(AP0) (h) and AP1 samples (Juibari and Tarighi, 2020). ..... 1-137
- Figure 1.56** Adsorption–desorption isotherms of N<sub>2</sub> on CuO@NiO-400(1:2) and CuO@NiO-500 (1:2) nanocomposites determined at 77.35 K (Juibari and Tarighi, 2020). ..... 1-138
- Figure 1.57** A typical hysteresis curve for co-precipitated cobalt ferrite nanoparticles at the three different calcination temperatures (600 °C, 800 °C and 1000 °C). The magnetisation step from the initial magnetised state (cobalt ferrite nano-magnetic particles) to saturated magnetisation, when a magnetic field of 5000 Oe is applied (Inset) (Purnama *et al.*, 2019). ..... 1-138
- Figure 1.58** Typical SEM images and particles size distribution analysis (inset) for cobalt ferrite after calcination for six hours under three different temperatures: (a) 600 °C, (b) 800 °C and (c) 1000 °C (Purnama *et al.*, 2019). ..... 1-1139
- Figure 1.59** (a) SEM micrographs of the Zn<sub>2</sub>Nb<sub>34</sub>O<sub>87</sub> powders calcined for 4 h with heating/cooling rates of 5 °C min<sup>-1</sup> at (a) 900 °C, (b) 1000 °C, (c) 1100 °C (d) 1200 °C and (e) 1300 °C; (b) Enlarged zone of XRD patterns showing peak broadening as a function of calcination temperature (Xiang *et al.*, 2019). ..... 1-139
- Figure 1.60** The schematic diagram of precursor growth process (Xiang *et al.*, 2019). ..... 1-140
- Figure 1.61** SEM images of products after calcining of precursors prepared at different hydrothermal reaction temperatures a) 120 °C; b) 140 °C; c) 160 °C; d) 180 °C (Xiang *et al.*, 2019). ..... 1-140
- Figure 1.62** Description of Type A and Type B crystallite size of two TiO<sub>2</sub> precursors and variation of BaTiO<sub>3</sub> obtained using type-A and type-B Ti precursors with temperature and time (Habib *et al.*, 2008). ..... 1-141
- Figure 1.63** TEM micrograph for BaTiO<sub>3</sub> sample obtained at 60, 90 and 150 °C for 48 h using type-B Ti precursor (Habib *et al.*, 2008). ..... 1-141
- Figure 1.64** SEM images of BT samples obtained at 90 °C for 48 h, 120 °C for 48 h and 150 °C for 24 h using type-A Ti precursor and BT samples obtained at 60 °C for 16 h, 90 °C for 24 h and 150 °C for 24 h using type-B Ti precursor (Habib *et al.*, 2008). ..... 1-142
- Figure 1.65** Fabrication of sol-gel metal oxide films. (a) Typical sol-gel metal oxide reaction products (i.e., sol, gel, and nanoparticles) (Park *et al.*, 2017). ..... 1-142
- Figure 1.66** Condensate rate-pH profile for an alkylsilanetriol and the average condensation rate for tetraethoxysilane (1/tgel) (Loy, 2003). ..... 1-143
- Figure 1.67** Contact angle of β-Bi<sub>2</sub>O<sub>3</sub> films with different concentration of the precursors (Baqiah *et al.*, 2020). ..... 1-143

- Figure 1.68** (a) XRD pattern for TiO<sub>2</sub> NPs prepared with different TIP: ethanol volume ratios of (f = 1:63, g = 1:21, h = 1:13, k = 1:9, m = 1:7). (b) XRD peak shift of the most intense peak (101) (Muthee and Dejene, 2020). ..... 1-144
- Figure 1.69** Schematic representation of the synthesis of MFe<sub>2</sub>O<sub>4</sub> MNPs by co-precipitation (Massart, 1981). ..... 1-144
- Figure 1.70** (a) XRD patterns of Na<sub>3</sub>GaF<sub>6</sub>:Mn<sup>4+</sup> synthesised with various Mn<sup>4+</sup> doping concentrations; (b) XRD patterns of amplified (110) diffraction peaks (Xu *et al.*, 2020a). ..... 1-145
- Figure 1.71** SEM images of Na<sub>3</sub>GaF<sub>6</sub>:Mn<sup>4+</sup> prepared with different (a) hydrofluoric acid concentrations; (b) solvents and (c) surfactants (Xu *et al.*, 2020a). ..... 1-145
- Figure 1.72** Development of the bubble cloud below the sonotrode in aluminium. Light grey contours represent volume fractions of 0.1% and darker contours represent volume fractions of 0.5% (Lebon *et al.*, 2017). ..... 1-146
- Figure 1.73** (a) Schematic of aluminium treatment setup; (b) Acoustic pressure predictions at selected points in aluminium domain (Lebon *et al.*, 2017). ..... 1-146
- Figure 1.74** Experimental setup used for ultrasound assisted transesterification (Sajjadi *et al.*, 2015). ..... 1-147
- Figure 1.75** Liquid flow pattern induced by ultrasound irradiation presented by (1) PIV and (2) CFD, under power amplitude of (a) 100 W, (b) 200 W, (c) 300 W and (d) 400 W (Sajjadi *et al.*, 2015). ..... 1-148
- Figure 1.76** Ink dispersion in the tank at circumstance of (a) activated ultrasound with  $f=1.7\text{MHz}$  and  $P_{\text{elec}} = 60\text{ W}$  and (b) non-activated ultrasound ( $T = 298\text{ K}$ ,  $P = 1\text{ atm}$ ) (Parvizian *et al.*, 2011). ..... 1-149
- Figure 1.77** (a) Photograph of continuous tubular sonoreactor; (b) Details of tubular sonoreactor design parameters; (c) The effect of feed flow rate on mean residence time ( $T = 298\text{ K}$ ,  $P = 1\text{ atm}$ ,  $f = 1.7\text{ MHz}$ ) (Parvizian *et al.*, 2012). ..... 1-149
- Figure 1.78** Possible combinations of microwave chemistry with well-established liquid-phase synthesis routes (Komarneni and Katsuki). ..... 1-150
- Figure 1.79** Hypothetical synthesis pathways of silica gels with (→) and without (--) microwave-assistance (Flores-López *et al.*, 2020). ..... 1-150
- Figure 1.80** (a) Predicted and measured characteristic micromixing times using Villermaux–Dushman test reaction; (b) Measurements and model predictions of macromixing time and film thickness (bottom) of film thickness in annular flow as a function of shear rate (Jose *et al.*, 2018). ..... 1-151
- Figure 1.81** Scale-up procedure to establish an industrial full-scale reactor (Kelkar and Ng, 2002). ..... 1-151
- Figure 1.82** Schematic illustration of scale-up methods for predicting the product distribution of competitive chemical reactions (CCRs) (Rehage *et al.*, 2020) .. 1-152

## CHAPTER 2

- Figure 2.1** Schematic diagram of the experimental setup of FePO<sub>4</sub> synthesis in the IJR. ....2-26
- Figure 2.2** Configuration of IJR with ultrasound transducer with scaled dimensions in millimetres. ....2-26
- Figure 2.3** 3D view of the computational domain and mesh structure of IJR. ...2-27
- Figure 2.4** TG-DTA curves of sample FP-600 before calcination at heating rate of 10 °C min<sup>-1</sup> in air. ....2-27
- Figure 2.5** XRD patterns of (a) FePO<sub>4</sub> and prepared (b) LiFePO<sub>4</sub> from FePO<sub>4</sub> in degree of from 10° to 90°. ....2-28
- Figure 2.6** The SEM images of FePO<sub>4</sub> synthesized under the conditions of applying different ultrasound powers and corresponding size distribution of FePO<sub>4</sub> samples synthesized under the conditions of applying different ultrasound powers. ....2-28
- Figure 2.7** (a) N<sub>2</sub> adsorption–desorption isotherm at 77 K and pore size distribution (the inset) calculated by the BJH method from the desorption branch of FePO<sub>4</sub>; (b) Average particles size and BET surface area of the sample prepared under different ultrasound power. ....2-29
- Figure 2.8** (a) Iso-surface distribution of turbulent kinetic energy (k) in IJR under the ultrasound power of 960W at 0.0023s. (i) 5 m<sup>2</sup>/s<sup>2</sup>, (ii) 20 m<sup>2</sup>/s<sup>2</sup>, (iii) 50 m<sup>2</sup>/s<sup>2</sup> and (iv) 80 m<sup>2</sup>/s<sup>2</sup>; (b) Turbulence Kinetic Energy (k) distribution of IJR under different power of ultrasound at 0.0023s. (i) 960W, (ii) 720W, (iii) 600w, (iv) 480W, (v) 360W and (vi) 0W. ....2-30
- Figure 2.9** Cross-section averaged shear stress at the transducer surface under the conditions of applying different ultrasound powers. ....2-31
- Figure 2.10** (a) Total pressure distribution (Pa) of x-z plane of IJR under different power of ultrasound at 0.0023s. (i) 960W, (ii) 720W, (iii) 600w, (iv) 480W, (v) 360W and (vi) 0W. (b) Dynamic pressure distribution (P) of x-z plane of IJR under different power of ultrasound at 0.0023s. (i) 960W, (ii) 600W, (iii) 360w, (iv) 0W. ....2-32
- Figure 2.11** Micromixing time *tm* as a function of ultrasound power P and velocity Magnitude (m/s) of x-z plane of IJR under different power of ultrasound at 0.0023s. ....2-33
- Figure 2.12** Spatial correlation  $R_{\epsilon,\Omega}$  along the reaction chamber from the tip of the ultrasound transducer (H=0) to the bottom of expansion (H=18mm) under different power of ultrasound at 0.0023s. ....2-33
- Figure 2.13** The streamline flow of the fluid in the peried from 44T to 45T (0.0022 s to 0.0023 s) in the IJR. ....2-34

**Figure 2.14** (a) Initial charge/discharge curves of the LFP/C composites at different ultrasound power at 0.1 C synthesized with anhydrous FePO<sub>4</sub>; (b) Cycle number of the LFP samples synthesized by different FP precursors. ....2-35

## CHAPTER 3

**Figure 3.1** Calibration curve of I<sub>3</sub> – concentration by a UV spectrophotometer at wavelength of 353 nm.....3-33

**Figure 3.2** Schematic diagram of experimental setup of micromixing in the impinging jet reactor with assist of ultrasound irradiation via Villermaux-Dushman reaction.....3-33

**Figure 3.3** 3D view and mesh of the computational domain and mesh structure of impinging jet obtained from ANSYS ICEM. ....3-34

**Figure 3.4** Experimental results of segregation index  $X_s$  under (a) different concentration  $C_H$  of acid under the Reynolds number  $Re = 2714$  and flowrate ratio  $R=1$ ; (b) different flowrate ratio  $R$  ( $R=1 \sim R=10$ ) with constant initial acid concentration  $C_H$ . ....3-35

**Figure 3.5** The 3D contour plot of turbulent kinetic energy (TKE) in the impinging jet reactor and the 2D plot of chamber downstream the impingement region the with different inlet flowrate without ultrasound irradiation.....3-35

**Figure 3.6** (a) The volumetric-averaged turbulent kinetic energy  $k$  ( $m^2/s^2$ ) and the turbulent Reynolds number  $Re_T$  versus inlet Reynolds number  $Re$ . ....3-36

**Figure 3.7** Experimental and simulation results of segregation index  $X_s$  versus turbulent Reynolds number without ultrasound (Exp ( $P_a = 0$ ) and Sim ( $P_a = 0$ )) and ultrasound amplitude of 50 % (Exp ( $P_a = 50\%$ ) and Sim ( $P_a = 50\%$ )) at constant acid concentration. ....3-36

**Figure 3.8** Experimental and simulated results of segregation index  $X_s$  versus turbulent Reynolds number under different ultrasound amplitude at turbulent Reynolds number  $Re_T = 14.0$  and constant acid concentration.....3-37

**Figure 3.9** (a) Contour of velocity magnitude and (b) streamlines under the ultrasound amplitude of 0%, 30%, 60% at downstream of impingement region at flow time  $t = 2.0$  s from simulation. ....3-37

**Figure 3.10** The volumetric-averaged concentration of I<sub>2</sub> and fluctuation degree  $\alpha$  in impinging jet reactor versus flow time  $t$  under the conditions of ultrasound amplitude of (a)  $P_a = 0\%$ ; (b)  $P_a = 30\%$ ; (c)  $P_a = 50\%$  and (d)  $P_a = 70\%$  at constant acid concentration at flow time  $t = 2.0$  s from simulation. ....3-39

**Figure 3.11** The correlation factor  $R_{\theta,\Omega}$  versus ultrasound amplitude  $P_a$  and iso-surface distribution of various vorticity magnitude of  $50 s^{-1}$ ,  $500 s^{-1}$ ,  $1000 s^{-1}$  and  $2000 s^{-1}$  in the imping jet reactor with constant inlet flowrate at flow time  $t = 2.0$  s from simulation. ....3-39

**Figure 3.12** (a) Relationship between micromixing time  $t_m$  and segregation index  $X_s$  based on Incorporation model; (b) Relationship between micromixing time  $t_m$  and segregation index  $X_s$  at various experimental conditions. ....3-40

## CHAPTER 4

**Figure 4.1** Schematic diagram of the experimental setup of SiO<sub>2</sub> synthesis using SVFR assist by ultrasound processor.....4-35

**Figure 4.2** The experimental rig and scaled dimensions of SVFR in millimetres. ....4-35

**Figure 4.3** SEM images and particle size distribution of sample SiO<sub>2</sub> synthesised under different condition of (a) Ultrasound power  $P$  at Reynolds number  $Re_V = 7859$ ; (b) Reynolds number  $Re_V$  under the ultrasound power of 240 W; (c) Volumetric flowrate ratio  $R$  under ultrasound power of 240 W. ....4-37

**Figure 4.4** (a) Schematic diagram of SiO<sub>2</sub> nanoparticles aggregation; TEM images of samples synthesised under the ultrasound power of 600 W at Reynolds number  $Re_V = 7859$  under the proportional scale of (b)100 nm; (c)50 nm; (d)20 nm. ....4-37

**Figure 4.5** (a) 2D-contour of characteristic particle length ratio  $d_p/\eta$  versus ultrasound amplitude  $P_A$  (W) and turbulent Reynolds number  $Re_V$ ; (b) 2D-contour of coefficient of variation (CV) versus ultrasound amplitude  $P_A$  (W) and turbulent Reynolds number  $Re_V$ .....4-38

**Figure 4.6** CFD Predicted tangential velocity distribution  $u_\theta$  (m/s) of continuous phase in the SVFR along radial direction at the surface of  $z = 5$  mm for the cases (a) Effect of variation of ultrasound power  $P$  at Reynolds number  $Re_V = 7859$ ; (b) Effect of Reynolds number  $Re_V$  at ultrasound power of 240 W; (c) Effect of variation of volumetric flowrate ratio  $R$  for the given ultrasound power of 240 W; (d) The tangential velocity distribution in radial direction in the Rankine vortex of the SVFR for Reynolds number  $Re_V = 7859$  and the applied ultrasound power of 240 W. 4-39

**Figure 4.7** Brunauer-Emmett-Teller (BET) surface area (m<sup>2</sup>/g) and Average pore width (nm) versus (a) Ultrasound power  $P$  at Reynolds number  $Re_V = 7859$ ; (b) Reynolds number  $Re_V$  under ultrasound power of 240 W; (c) Volumetric flowrate ratio  $R$  under ultrasound power of 240 W.....4-40

**Figure 4.8** Turbulence intensity versus (a) Ultrasound power  $P$  at Reynolds number  $Re_V = 7859$ ; (b) Reynolds number  $Re_V$  under ultrasound power of 240 W; (c) Volumetric flowrate ratio  $R$  under ultrasound power of 240 W. ....4-41

**Figure 4.9** Turbulent kinetic energy distribution in the reactor chamber under ultrasound power of (a) 0 W (b) 120 W (c) 240 W (d) 360W (e) 480 W (f) 600 W at Reynolds number  $Re_V = 7859$  at flow time  $t = 2.0$  s. ....4-42

**Figure 4.10** Iso-surface of vorticity at 100 s<sup>-1</sup> in the reactor chamber under ultrasound power of (a) 0 W (b) 120 W (c) 240 W (d) 360 W (e) 480 W (f) 600 W at Reynolds number  $Re_V = 7859$  at flow time  $t = 2.0$  s.....4-43

**Figure 4.11** Damköhler number and the mean turbulent energy dissipation rate  $\varepsilon$  versus (a) Ultrasound power  $P$  at Reynolds number  $Re_V = 7859$ ; (b) Reynolds number  $Re_V$  under the ultrasound power of 240 W; (c) Volumetric flowrate ratio  $R$  under the ultrasound power of 240 W.....4-44

**Figure 4.12** (a)  $(Sh - 2)Re_V^{0.5}\varphi^{0.5}Sc^{0.33}$  versus turbulence intensity  $I$  (%) by adoption of ultrasound power from 0W to 600W and (b) the plot of turbulence coefficient  $C(I)$  as a function of turbulence intensity  $I$  (%) with the error bar of turbulence coefficient.....4-45

**Figure 4.13** 3D-plot of Sherwood number  $Sh$  versus characteristic length ratio  $\varphi$  and turbulence intensity  $I$  (%).....4-45

**Figure 4.14** Correlation factor  $R_{G,Sh}$  between the predicted Sherwood number and local shear rate under (a) Ultrasound power  $P$  at Reynolds number  $Re_V = 7859$ ; (b) Reynolds number  $Re_V$ ; (c) Volumetric flowrate ratio  $R$  under ultrasound power of 240 W.....4-46

## CHAPTER 5

**Figure 5.1** Schematic diagram of experimental setup and post-hydrothermal treatment process of SiO<sub>2</sub> particles following a pre-swirling flow reactor synthesis. ....5-29

**Figure 5.2** 2-D CFD modelling of the temperature distribution surrounding the hydrothermal autoclave placed inside a muffle furnace under different operation conditions. (a) Case-1; (b) Case-2; (c) Case-3 (as shown Table 5.2); (d) Photos of placement of the hydrothermal autoclave in the muffle furnace. ....5-30

**Figure 5.3** (a) Numerical domain and thermal boundary conditions of 2D autoclave model; Temperature profile and boundary condition ( $T_1$  and  $T_2$ ) for autoclave obtained from simulation of muffle furnace for (a) Case-1; (b) Case-2; (c) Case-3 (as shown Table 5.2). ....5-31

**Figure 5.4** CFD modelling of time-dependant Rayleigh convection induced velocity and temperature distribution in a hydrothermal autoclave, obtained at the time  $t=10$  s, 30 s, 50 s, 100 s, 200 s for case-1. (a) Velocity distribution and (b) temperature profiles. ....5-32

**Figure 5.5** (a) Temperature and (b) velocity of specific points as a function of time under condition of case-1; (c) Temperature and (d) velocity at p2 as function of time under different conditions of case-1, case-2 and case-3. ....5-33

**Figure 5.6** Rayleigh number  $Ra$  versus hydrothermal treatment duration (min) under condition of case-1 at setup temperature of 373 K, 393 K and 413 K.....5-33

**Figure 5.7** (a) FTIR spectrograms and (b) XRD analysis of SiO<sub>2</sub> synthesized with hydrothermal post-treatment from primary particle a at different temperature a-373

at 240 min, a-393 at 240 min and a-413 at 240 min; (c) TEM images of primary particle of sample a-1 under scale of 20 nm and 50 nm. ....5-34

**Figure 5.8** SEM images and particle size distribution of sample SiO<sub>2</sub> samples synthesised after hydrothermal treatment under different condition with different primary particles from sample group (a) a-390, a-410 and a-430; (b) b-390 and (c) c-390. ....5-35

**Figure 5.9** 3D-contour of (a) product particle diameter  $d_p$  versus hydrothermal treatment duration and hydrothermal temperature; (b) product particle diameter  $d_p$  versus primary particle diameter and hydrothermal treatment duration. ....5-36

**Figure 5.10** N<sub>2</sub> adsorption–desorption isotherm at 77 K and pore size distribution (the inset) calculated by the BJH method from the desorption branch of presented SiO<sub>2</sub> samples at (a) 60 min and (b) 240 min; (c) Average particles size and BET surface area of the sample prepared at different hydrothermal temperature. ....5-37

**Figure 5.11** (a) Tapped density of samples under different conditions and (b) TG-DSC for samples of a-373. ....5-37

**Figure 5.12** Correlation factor  $RG, d$  and  $RG, Ra$  between the shear rate  $G$  and Rayleigh number  $Ra$  with the particle size  $d_{32}$  under different setup hydrothermal temperature. ....5-38

**Figure 5.13** Particle dispersion  $D_r(t)$  versus hydrothermal treatment duration (s) under condition of case-1 at setup temperature of 373 K, 393 K and 413 K. ....5-38

**Figure 5.14** (a) Particle distribution in the hydrothermal autoclave at different time with boundary conditions of case-1; Particle trajectory in the hydrothermal autoclave under different conditions of (b) case-1; (c) case-2; (d) case-3. ....5-39

# LIST OF TABLES

## CHAPTER 1

<b>Table 1.1</b> Theoretical model based on the N–S equations. ....	1-153
<b>Table 1.2</b> The comparison of Eulerian-Eulerian (EE) Lagrangian–Eulerian (EL) frameworks (Sardina <i>et al.</i> , 2019).....	1-154
<b>Table 1.3</b> The drag models and lift models of multiphase system (Zhou <i>et al.</i> , 2020). .....	1-154
<b>Table 1.4</b> Dimensionless groups relevant to multiphase systems .....	1-155

## CHAPTER 2

<b>Table 2.1</b> Samples with different ultrasound power and intensity.....	2-36
<b>Table 2.2</b> The average crystallite size of samples under different conditions .....	2-36

## CHAPTER 3

<b>Table 3.1</b> The concentration of reactants .....	3-41
<b>Table 3.2</b> Samples prepared under different conditions.....	3-41

## CHAPTER 4

<b>Table 4.1</b> Samples with different ultrasound power and intensity.....	4-47
<b>Table 4.2</b> Properties of dispersed phase. ....	4-48

## CHAPTER 5

<b>Table 5.1</b> Samples synthesized with different primary particles and post-hydrothermal treatment conditions .....	5-40
<b>Table 5.2</b> Boundary condition of the muffle furnace and hydrothermal autoclave .....	5-41
<b>Table 5.3</b> Physical properties of the fluid used in model .....	5-41
<b>Table 5.4</b> Grid independence test for the numerical model .....	5-42

# NOMENCLATURES

## CHPATER 1

$A_m$	[m <sup>2</sup> /s]	Molecular diffusivity
$A$	[-]	Pre-exponential factor
$A_p$	[m <sup>2</sup> ]	Surface area
AR	[-]	Active ratio
$A'$	[-]	Constant
$Ar_p$	[-]	Archimedes number
$C$	[-]	Kolmogorov constant
$C_b$	[mol/L]	Concentration of the bulk solution
$C_r$	[-]	Solubility of the particle
$C_i^*$	[mol/m <sup>3</sup> ]	Saturated state concentration
$C_l$	[mol/m <sup>3</sup> ]	Actual state concentration
$C_{11}$	[mol/m <sup>3</sup> ]	The concentrations of species 1 in phase 1
$C_{12}$	[mol/m <sup>3</sup> ]	The concentrations of species 1 in phase 2
$C_{2,sat}$	[mol/m <sup>3</sup> ]	Saturated concentration of the species A in phase 2
$C_{2,t=0}$	[mol/m <sup>3</sup> ]	Transient concentration at time $t$
$C_T$	[-]	Turbulent coefficient
$c_i$	[mol/m <sup>3</sup> ]	The concentration at the grid point
$\bar{c}_M$	[mol/m <sup>3</sup> ]	Optimal mixing concentration
$d$	[m]	Annulus width
$d_i$	[m]	Inlet diameter
$d_{imp}$	[m]	Impeller diameter
$d_b$	[m]	Bubble diameter
$d_p$	[m]	Particle radius
$D$	[m <sup>2</sup> /s]	Mass diffusivity

$D_L$	[m <sup>2</sup> /s]	Diffusion coefficient
$D_{th}$	[m <sup>2</sup> /s]	Thermal diffusivities
$D$	[m]	Bed diameter
$Da$	[-]	Damköhler number
$E$	[J]	Total kinetic energy
$f$	[Hz]	Measured frequency
$f^*$	[Hz]	Nondimensionalised frequency
$F^*$	[-]	Dimensionless drag coefficient
$F_D$	[N]	Drag force acting on the individual particles
$Fr_D$	[-]	Froude number
$g$	[m/s <sup>2</sup> ]	Gravity acceleration
$g$	[m/s <sup>2</sup> ]	Acceleration due to gravity
$\Delta G_v$	[J]	Bulk free energy
$\Delta G$	[J]	Total free energy
$H_o$	[-]	Suspension homogeneity
$Ha$	[-]	Hatta number
$H_s$	[m]	Settled bed height
$i$	[-]	Phase
$I$	[-]	Turbulent intensity
$J$	[1/s]	Rate of nucleation
$k$	[m <sup>2</sup> /s <sup>2</sup> ]	Turbulent kinetic energy
$k$	[mol/(L·s)]	Rate of surface reaction
$k_B$	[-]	Boltzmann's constant
$k_{p-q}$	[mol/(L·s)]	Intrinsic reaction rate constant
$K_{SL}$	[m <sup>2</sup> /s]	Solid–liquid mass transfer
$k_L a$	[m <sup>2</sup> /s]	Volumetric mass transfer coefficient
$k_l$	[m <sup>2</sup> /s]	Mass transfer coefficient
$L$	[m]	Outlet length

$m_p$	[kg]	Mass of single particle
$Nu$	[-]	Nusselt number
$N_{total}$	[-]	Total particle number
$N_{active}$	[-]	Active particles number
$n_p$	[-]	Particle number density
$Pr$	[-]	Prandtl number
$p$	[pa]	Pressure
$p^*$	[pa]	Nondimensionalised pressure
$r$	[m]	Radius of the particles
$R$	[m]	Mean radius of the inner cylinder and outer cylinder
$R'$	[-]	Ratio of two volumetric flow
$Re$	[-]	Reynolds number
$Re_j$	[-]	Reynolds number of inlet jet
$Re_p$	[-]	Reynolds number of particle
$S$	[-]	Supersaturation of the solution
$Sc$	[-]	Schmidt number
$Sh$	[-]	Sherwood number
$\overline{Sh}$	[-]	Average Sherwood number
$Sh_{mod}$	[-]	Modified Sherwood number
$Ta$	[-]	Taylor number
$t_r$	[s]	Reaction time
$t_m$	[s]	Micromixing time
$\bar{u}$	[m/s]	Axial velocity of fluid
$u_x$	[m/s]	Fluid velocity vector
$\overline{u_x}$	[m/s]	Time average velocity
$u_x'$	[m/s]	Instantaneous fluctuating velocity
$\mathbf{u}$	[m/s]	Velocity vector
$\mathbf{u}_l$	[m/s]	Liquid velocity field

$u$	[m/s]	Velocity field
$u_{mf}$	[m/s]	Minimum fluidisation velocity
$U_{f1}$	[m/s]	Superficial fluidisation velocity
$V$	[m <sup>3</sup> ]	Liquid volume
$v_{in}$	[m/s]	Inlet flowrate
$v$	[m <sup>3</sup> ]	Molar volume
$v_b$	[m/s]	Bubble slip velocity
$X_v$	[-]	Volume fraction of solid at each plane
$X_{av}$	[-]	Average volume fraction of solid at all planes
$X_s$	[-]	Segregation index

***Greek letters***

$\alpha$	[-]	Mixing quality
$\alpha_v$	[-]	Phase volume fraction
$a$	[m <sup>2</sup> ]	Interfacial area
$\epsilon$	[m <sup>2</sup> /s <sup>3</sup> ]	Energy dissipation rate
$\epsilon$	[-]	Bed voidage
$\epsilon_{mf}$	[-]	Bed voidage at minimum fluidisation
$\varepsilon$	[m <sup>2</sup> /s <sup>3</sup> ]	Local turbulent energy dissipation rate
$\eta$	[m]	Kolmogorov's length scale
$\eta_k$	[m]	Kolmogorov scale
$\eta_B$	[m]	Batchelor scale
$\kappa$	[1/m]	Wavenumber
$\kappa_{th}$	[m/s]	Heat transfer rate
$\hat{E}(\kappa)$	[-]	Energy spectrum
$\psi$	[-]	Stoichiometric factor
$\phi$	[-]	Sphericity of particles

$\rho$	[Kg/m <sup>3</sup> ]	Density
$\rho_l$	[Kg/m <sup>3</sup> ]	Liquid density
$\rho_p$	[Kg/m <sup>3</sup> ]	Particle density
$\rho_0$	[Kg/m <sup>3</sup> ]	Packed bed bulk density
$\rho_g$	[Kg/m <sup>3</sup> ]	Gas density
$\rho_p$	[Kg/m <sup>3</sup> ]	Particle density
$\tau_c$	[s]	Macro-mixing time
$\tau_s$	[s]	Meso-mixing time
$\tau_E$	[s]	Engulfment time constant
$\tau_G$	[s]	Characteristic time for molecular diffusion
$\tau_R$	[s]	Reaction time
$\tau_D$	[s]	Characteristic diffusion time
$\tau_i$	[pa]	Viscous stress tensor
$\tau_L$	[s]	Typical turbulent time scales
$\tau_c$	[s]	Chemical time scales
$\mu_i$	[pa·s]	Dynamic viscosity
$\mu_g$	[pa·s]	Dynamic viscosity of gas
$\nu$	[m <sup>2</sup> /s]	Kinematic viscosity of fluid
$\nu_l$	[m <sup>2</sup> /s]	Kinematic viscosity of fluid
$\delta$	[m]	Thickness of the gas film and liquid film
$\sigma_{max}^2$	[-]	Maximum variance of the mixture

## CHPATER 2

A	[m <sup>2</sup> ]	Cross section area of the reactor chamber
C	[m/s]	The sound speed in the water
$c_1$	[-]	Empirical constant
$c_2$	[-]	Empirical constant

$c_i$	[mol/L]	The concentration of species i
$c_e$	[C]	The concentration of lithium ion inside electrolyte
$C_\phi$	[-]	A function of the local turbulent Reynolds number
$G_k$	[J]	The generation of turbulence kinetic energy
$K$	[-]	Crystallite shape factor or Scherrer's constant
$L$	[nm]	Average crystallite size L
$P$	[Pa]	Pressure drop
$Q$	[m <sup>3</sup> /s]	Volumetric flow rate
$V$	[m <sup>3</sup> ]	Volume
$f$	[Hz]	Frequency of the ultrasound wave
$h$	[m]	Distance from the bottom the IJR
$k$	[m <sup>2</sup> /s <sup>2</sup> ]	Turbulent kinetic energy
$i$	[-]	Continuous or dispersed phase
$I$	[W/m <sup>2</sup> ]	Sound intensity
$\rho$	[kg/m <sup>3</sup> ]	Average density of liquid bulk
$p_{us}$	[W]	Ultrasonic power
$p$	[pa]	Pressure
$p_u$	[pa]	Pressure induced by sound field
$p_a$	[pa]	Amplitude of the sound pressure
$R$	[-]	Space correlation factor
$Re_t$	[-]	Local turbulent Reynolds number
$t$	[s]	Time
$u$	[m/s]	Liquid velocity
$v$	[m/s]	Inlet velocity

### ***Greek letters***

$\beta$	[rad]	Peak width of the diffraction peak profile at half maximum height
---------	-------	---

$\varepsilon$	$[\text{m}^2/\text{s}^3]$	Turbulence dissipation rate
$\sigma_k$	$[-]$	Empirical constant
$\sigma_\varepsilon$	$[-]$	Empirical constant
$\theta$	$[\text{degree}]$	Degree in XRD diffraction
$\mu_t$	$[\text{kg}/\text{m}\cdot\text{s}]$	Turbulence viscosity
$\nu$	$[\text{N}\cdot\text{s}/\text{m}^2]$	Dynamic viscosity
$\lambda$	$[\text{nm}]$	The wavelength of X-ray
$\gamma$	$[-]$	Mixing parameter
$\Gamma$	$[\text{m}^2/\text{s}]$	Turbulent diffusion coefficient
$\Omega$	$[\text{s}^{-1}]$	Cross section average vorticity

### ***Operators***

In the three-dimensional coordinates (x, y, z) with the unit vectors (i, j, k), the operators can be defined as follows,

$$\nabla = \mathbf{i} \frac{\partial}{\partial x} + \mathbf{j} \frac{\partial}{\partial y} + \mathbf{k} \frac{\partial}{\partial z}$$

$$\Delta = \nabla^2 = \frac{\partial^2}{\partial x^2} + \frac{\partial^2}{\partial y^2} + \frac{\partial^2}{\partial z^2}$$

### **CHPATER 3**

$A_{353}$	$[\text{mol}]$	Absorbance at 353 nm
$A$	$[\text{m}^2]$	Area of the ultrasonic transducer
$c$	$[\text{m}/\text{s}]$	Sound speed in water
$c_i$	$[\text{mol}/\text{m}^3]$	Ion concentration
$C'(t)$	$[\text{mol}/\text{m}^3]$	Standard deviation of concentration
$C'_{max}$	$[\text{mol}/\text{m}^3]$	Maximum deviation

$C_H$	[mol/m <sup>3</sup> ]	Initial acid concentration
$C_\mu$	[-]	Constant coefficient
$C_{1\varepsilon}$	[-]	Constant coefficient
$G_{2\varepsilon}$	[-]	Constant coefficient
$d_i$	[m]	Inlet diameter
$Da$	[-]	Damköhler number
$g$	[kg/s <sup>2</sup> ]	Gravitational acceleration
$G_k$	[kg/(s <sup>3</sup> ·m)]	Generation of turbulent kinetic energy
$I$	[M]	Ionic strength
$I_{us}$	[W/m <sup>2</sup> ]	Sound intensity
$J_i$	[kg/(m <sup>3</sup> ·s)]	Diffusive mass flux of species i
$k$	[m <sup>2</sup> /s <sup>2</sup> ]	Turbulence kinetic energy
$\langle k \rangle$	[m <sup>2</sup> /s <sup>2</sup> ]	Volumetric-averaged turbulent kinetic energy
$K_{eq}$	[-]	Equilibrium constant
$L$	[m]	Thickness of the quartz cell
$P_a$	[pa]	Amplitude of the ultrasound pressure
$P_{ultra}$	[pa]	Ultrasound pressure
$P_{us}$	[W]	Ultrasound power
$P_s$	[W]	Maximum ultrasound power
$Q_1$	[m/s]	Flowrate of mixed solution A
$Q_2$	[m/s]	Flowrate of acid solution B
$R$	[-]	Flowrate ratio of inlet streams
$R_i$	[kg/(m <sup>3</sup> ·s)]	Net rate of production of species i
$Re$	[-]	Reynolds number
$Re_T$	[-]	Turbulent Reynolds number
$t$	[s]	Time
$t_m$	[s]	Micromixing time
$t_r$	[s]	Characteristic reaction time

$T$	[K]	Temperature
$\mathbf{u}$	[m/s]	Instantaneous velocity vector
$V_{H_0}$	[m <sup>3</sup> ]	Initial volume
$X_s$	[-]	Segregation index
$Y_i$	[-]	Mass fraction of species i
$z_i$	[-]	Charge of the ion

***Greek letters***

$\alpha$	[-]	Fluctuation degree
$\beta$	[-]	Temperature exponent
$\varepsilon$	[m <sup>2</sup> /s <sup>3</sup> ]	Energy dissipation rate
$\langle \varepsilon \rangle$	[m <sup>2</sup> /s <sup>3</sup> ]	Averaged energy dissipation rate
$\epsilon_{353}$	[m <sup>-1</sup> ]	Molar extinction coefficient
$\langle \eta \rangle$	[m]	Kolmogorov scale
$\langle \varepsilon \rangle$	[m <sup>2</sup> /s <sup>3</sup> ]	Volumetric-averaged turbulent energy dissipation
$\eta$	[m]	Kolmogorov length
$\theta$	[-]	Mixing degree $\theta$
$\Omega$	[s <sup>-1</sup> ]	Vorticity
$\langle \Omega \rangle$	[s <sup>-1</sup> ]	Volume average vorticity
$\mu_l$	[pa·s]	Molecular viscosity
$\mu_t$	[pa·s]	Turbulent viscosity
$\nu$	[pa·s]	Molecular viscosity of liquid phase
$\rho$	[kg/m <sup>3</sup> ]	Density of fluid
$\sigma_k$	[-]	Constant
$\sigma_\varepsilon$	[-]	Constant
$\omega$	[s <sup>-1</sup> ]	Angular velocity

## CHPATER 4

$a_p$	[m <sup>2</sup> ]	Interfacial area of particles
$C$	[m/s]	The sound speed in the water
$C'$	[mol]	Molar concentration
$C_v$	[-]	Volume fraction of dispersed phase
$C_{l,si}$	[mol/m <sup>3</sup> ]	Concentration of Si(OH) <sub>4</sub>
$C_{l,si}^*$	[mol/m <sup>3</sup> ]	Saturated concentration of Si(OH) <sub>4</sub>
$d_p$	[m]	Particle diameters
$d_o$	[m]	Diameter of the reactor chamber
$D$	[m <sup>2</sup> /s]	Diffusion coefficient
$f$	[Hz]	Frequency of the ultrasound wave
$k$	[s <sup>-1</sup> ]	Rate constant
$k_{sl}$	[m <sup>2</sup> /s]	Solid-liquid mass transfer coefficient
$\langle k \rangle$	[m <sup>2</sup> /s <sup>2</sup> ]	Averaged turbulent kinetic energy
$L$	[m]	Diameter of the inlet tube of SVFR
$I$	[-]	Turbulence intensity
$I_{us}$	[W/m <sup>2</sup> ]	Ultrasound intensity
$\rho$	[kg/m <sup>3</sup> ]	Density
$p$	[pa]	Sound pressure
$p_a$	[pa]	Amplitude of the sound pressure
$P$	[W]	Ultrasound power
$P_A$	[%]	Ultrasound amplitude
$P_s$	[W]	Specified ultrasound power
$Q$	[m <sup>3</sup> /s]	Volumetric flow rates
$r'$	[mol/s]	Reaction rate
$R_v$	[m]	Radius of vortex
$S_{l \rightarrow s}$	[-]	Mass transfer source term of SiO <sub>2</sub>

$t$	[s]	Time
$u_l$	[m/s]	Velocity of liquid phase
$u_p$	[m/s]	Velocity of particles
$u_\theta$	[m/s]	Tangential velocity of Rankine vortex.
$v$	[m/s]	Velocity
$V$	[m <sup>3</sup> ]	Volume of reactor chamber

### ***Greek letters***

$\alpha_l$	[-]	Volume fraction of liquid phase
$\varepsilon$	[m <sup>2</sup> /s <sup>3</sup> ]	Energy dissipation rate
$\langle \varepsilon \rangle$	[m <sup>2</sup> /s <sup>3</sup> ]	Averaged energy dissipation rate
$\langle \eta \rangle$	[m]	Kolmogorov scale
$\mu_L$	[pa·s]	Dynamic viscosity
$\mu_{eff}$	[pa·s]	Effective dynamic viscosity
$\nu$	[m <sup>2</sup> /s]	Molecular viscosity
$\nu_{eddy}$	[m <sup>2</sup> /s]	Eddy viscosity
$\omega$	[s <sup>-1</sup> ]	Angular velocity of vortex
$\varphi$	[-]	Characteristic length ratio
$\tau_c$	[s]	Chemical time scales
$\tau_l$	[-]	Stress strain of liquid phase
$\tau_t$	[s]	Turbulent time scale
$\Gamma_{l,si}$	[pa·s]	Dynamic viscosity of Si(OH) <sub>4</sub>

## **CHPATER 5**

$C_p$	[J/kg·K]	Thermal capacity
$C_D$	[-]	Drag coefficient
$D_T$	[m <sup>2</sup> /s]	Thermal diffusivity

$d_p$	[m]	Particle diameter
$F_b$	[N]	Body force
$F_D$	[N]	Drag force per unit particle mass
$F'$	[N]	External force
$F_t$	[N]	Thermophoretic force
$F_b$	[N]	Buoyancy force
$F_s$	[N]	Drag force
$Gr$	[-]	Grashof number
$g$	[m/s <sup>2</sup> ]	Gravity acceleration
$\langle G \rangle$	[pa]	Volume average Shear rate
$\langle G \rangle_j$	[pa]	Area-weighted average shear rate
$G$	[1/s]	Shear rate
$k$	[W/m·K]	Thermal conductivity
$L$	[m]	Characteristic length of reactor
$m_p$	[g]	Mass of particles
$Pr$	[-]	Prandtl number
$p$	[pa]	Sound pressure
$Re$	[-]	Reynolds number
$Ra$	[-]	Rayleigh number
$t$	[s]	Time
$T$	[K]	Temperature
$T_0$	[K]	Reference temperature
$\Delta T$	[K]	Temperature difference
$u$	[m/s]	Velocity of liquid
$u_p$	[m/s]	Velocity of particles
$V$	[m <sup>3</sup> ]	Volume of reactor chamber

***Greek letters***

$\alpha$	[m <sup>2</sup> /s]	Thermal diffusivity
$\beta$	[1/K]	Coefficient of thermal expansion
$\varepsilon$	[m <sup>2</sup> /s <sup>3</sup> ]	Energy dissipation rate
$\rho_{i,0}$	[kg/m <sup>3</sup> ]	Density
$\mu$	[pa·s]	Viscosity
$\nu$	[m <sup>2</sup> /s]	Molecular viscosity

## **CHAPTER 1**

# **CURRENT STATUS OF MODELLING OF HYDRODYNAMICS AND MASS TRANSFER IN NANO/MICRO PARTICLE SHEAR CONTROLLABLE SYNTHESIS PROCESSES**

### **SUMMARY**

Multiphase flow dynamics in different multiphase reactors for shear controllable synthesis process is a multidisciplinary study intersecting reactor engineering, chemical reaction, molecular dynamics and micro-technology. The functional fine particle produced by shear controllable synthesis has broad applications in pharmaceutical engineering, energy field, electronic technology, environmental engineering and other fields, providing a foundation for modern high-tech industries. The particle is synthesised with desired size, morphology, porosity, and tap density. In particular, fine particles ( $\sim 1 \mu\text{m}$ ) have been found to have a wide range of applications to catalysts, pigments, pharmaceuticals, food, and cosmetics due to their superior properties. However, considering the drawbacks of traditional multiphase reactors including high-energy consumption, low conversion rate, poor mixing performance, thermo-runaway, long reaction time, and novel multiphase reactors are employed to prepare fine particles. In the particle synthesis process, process intensification is effective resulting in higher efficiency, better mixing performance, eco-environment friendly, low capital cost, and low energy requirement. It has been widely realised that controllable synthesis is a complex process with considerations of mass, momentum and energy transport as well as a sophisticated chemical reaction and the deep understanding of such a process is still challengeable. Consequently, there is a necessity to find appropriate models and correlations on multiphase flow dynamics and particle synthesis to achieve the aim of shear controllable synthesis of micro/nanoparticles.

## **1.1 Fundamentals and turbulent-relevant-characteristics of multiphase reactors**

### **1.2.1 Types and characteristics of multiphase reactors**

Multiphase flow has been widely encountered in sewage purification in the environmental industry, flood flow, biological applications, the pharmaceutical industry, and engineering applications such as mineral processing plants. Multiphase reactors are chosen concerning micro and macro-mixing performance and retention time (Pangarkar, 2015). Common multiphase reactors include stirring tank reactors, bubble columns, fluidised beds, trickle beds and fast-mixing reactors. T-junction reactors and jet mixers are classical fast mixer that frequently applied in precipitation reaction for industrial applications. Among these common multiphase reactors, the ones with typical characteristics are reviewed as follows.

#### **Stirring tank reactors (STR)**

The most common and conventional stirring tank reactors (STR), mostly used in chemical and other relevant industries, are vertical cylindrical tanks involving impellers and baffles as shown in Figure 1.1 (Pangarkar, 2015). In industrial applications, there are standards for STR design: the height of liquid dispersion to the tank diameter ratio is one and the impeller is set at a distance equal to the impeller diameter from the bottom of the vessel (Ratcliff, 1986).

The presence of the impellers satisfies the demand of chemical engineering processes such as crystallisation, precipitation, catalytic-involved reactions and slurries-treatment dealing with a stack of dense suspensions involving large solid particles, which are all strongly influenced by the hydrodynamics produced by the impellers (Kazemzadeh *et*

*al.*, 2019). To achieve a highly turbulent hydrodynamic environment, measurements are taken for multiple impellers and impeller modifications are made until a high rotational speed is reached for the impellers. A single impeller is not as efficient as multiple impellers with an intensified effect on the dispersion of the gas phase as well as suspension of solids. In a multiple-impeller STR system, the bottom impeller is predominant for gas dispersion and the suspension of particles. To promote the homogeneity of the solid-liquid distributions, the impellers are designed with parameters such as the number, types and width of blades, in addition to the diameter, location and inclination angle of the impellers with the proper flow pattern for achieving an optimal rotating rate (Kumaresan and Joshi, 2006, Nere *et al.*, 2003). The crucial parameters for choosing impellers can be summarised using the following 5 criteria: peak rate of dissipation of turbulent kinetic energy, peak power requirement, critical speed for surface aeration, power number and momentum number. Paul *et al.* (2004) have emphasised the significance of impellers for a suspending-slurry system considering the balance between the energy delivered by impellers and energy used to lift solid particles susceptible to turbulent flow. Kazemzadeh *et al.* (2019) have compared the homogeneity degree in the particle suspension process under the condition with three types of impellers (A310, PF3 and PBT) as shown in Figure 1.2 via coupling CFD modelling with the Eulerian-Eulerian multiphase model. The results displayed show that the impeller type PBT is can achieve the highest suspension homogeneity (Figure 1.3) and the highest particles' velocity of 9.88 m/s compared with the same ones of 2.79 m/s for A310, PF3 acting under the same impeller rotating speed of 950 rpm. Furthermore, two circulation loops are generated as PBT and A310-type impellers are equipped with minimised turbulent energy loss. However, the impellers of PF3 have split the main streams and produced circulation loops upwards and downwards resulting in inefficient suspension mixing (Kazemzadeh *et al.*, 2019). The suspension homogeneity is quantified by Equation (1-1),

$$H_o = 1 - \sqrt{\frac{\sum_1^n (X_v - X_{av})^2}{n}} \quad (1-1)$$

where  $n$  is the number of planes,  $X_v$  is the volume fraction of solid at each plane, and  $X_{av}$  is the average volume fraction of solid at all planes.

Satjaritanun *et al.* (2018) have reported that the design of contra-rotating impellers can eliminate vortex and dead zones. Gelves *et al.* (2014) have applied a Rushton-type impeller to the reactor due to its design of inhomogeneous mixing zones and high local dissipation rates of turbulent kinetic energy. With the increased rotating speed of impellers, the vortices generated by the liquid transferring in the tangential direction without the radial or axial component of velocity lead to a poor mixing performance (Pangarkar, 2015).

In order to overcome such a drawback, baffles that are vertical plates are used to adhere to the wall of the vessel as obstacles to minimise the vortex formation and break the tangential components into the radial and axial directions (Hao *et al.*, 2013). Pukkella *et al.* (2019) have confirmed mixing performance in a solid-liquid system is improved by enhancing the mixing performance of solid suspensions in a stirred tank attached by interface baffles between gas and liquid that break apart the vortices and redistribute the flow field. The CFD results have demonstrated that the baffle helps break apart vortices and leads to energy dissipation throughout particle distribution in the stirring tank. Ahmadi *et al.* (2021) has investigated the passive micromixer with baffles and found that baffles take advantage of the geometry to enhance the micromixing performance and the configuration and the number have impact on inertial mixing in a curved serpentine micromixer.

### **Taylor-Couette reactor (TCR)**

The Taylor–Couette reactor (TCR) is a typical shear-induced reactor consisting of a rotating inner cylinder and a coaxial immobile outer cylinder with viscous fluid inside as shown in Figure 1.4. Taylor (1922) found special patterns generated in these types of reactors and invented the concept of Taylor-Couette flow with an array of vortices as seen in Figure 1.4 (Kim *et al.*, 2013). TCRs provide a stable shear-stress environment as an alternative to crystalliser and phase-transformation device and encourages more homogenous mixing in the process of particle synthesis with high uniformity (Kim *et al.*, 2013, Jung *et al.*, 2010). Jung *et al.* (2010) have prepared calcium carbonate at different initial concentrations, resulting in rhombic and spindle-like nanoparticles in STR and homogenous morphology in TCR as shown in Figure 1.5.

There are several prototypes of TCRs employed in the industry such as cyclonic separators and heat exchangers (Naseem *et al.*, 2019). It has reported that the crystals synthesised showed a narrow size distribution with the benefits of energy-saving and reduced cost in post-treatment. Haut *et al.* (2003) used TCR as a bioreactor with suspended cells at low Reynold number regimes. Santiago *et al.* (2011) utilised TCR to culture cells in micro-carriers with its characteristic of highly effective oxygen transfer and mass transfer. Liu *et al.* (2020b) have synthesised barium sulfate particles in TCR with a modified inner cylinder of narrower shear rate distribution resulting in smaller-sized particles.

As an alternative to crystallisation, the size distribution of synthesised particles is reliant on flow patterns susceptible to parameters like inner cylinder geometry, annulus width, flow velocity, the rotational velocity of the inner cylinder, density ratio of particle-to-fluid (Kim *et al.*, 2013). It has been found by Ohmura *et al.* (2005) that the large particles were always traced in the vicinity of the exterior edge of the vortices and swiftly relocated caused by bypass flow. Taylor number ( $Ta$ ) and Reynolds number ( $Re$ ) are the dimensionless parameters used to characterise TCRs, which are defined as follows by Equations (1-2) and (1-3),

Taylor number ( $Ta$ )

$$Ta = \frac{d^3 R \omega^2}{\nu^2} \quad (1-2)$$

Reynolds number ( $Re$ )

$$Re = \frac{d \bar{u}}{\nu} \quad (1-3)$$

where  $\omega$  represents the angular velocity of the inner cylinder;  $\bar{u}$  represents the axial velocity of fluid;  $d$  is the annulus width;  $R$  represents the mean radius of the inner cylinder and outer cylinder;  $\nu$  is the kinematic viscosity of the fluid.

Taylor (1922) determined that the existence of the transition state from stable flow to Taylor-Couette flow can be quantitatively described by the critical Taylor number. Couette-flow is defined where the velocity profile appears to be purely tangential at low Taylor number and the  $Ta$  number gradually increases to a transition state with a periodic structure. Further increments may result in increasing the inner cylinder rotational speed superior to the threshold and toroidal-liked vortices are superposed to the tangential flow. With a continuous increase in the  $Ta$  number, the vortices begin to oscillate leading to a random velocity-fluctuation field that is a wavy vortex flow (Haut *et al.*, 2003).

Vaezi *et al.* (1997) have carried out experimental work to prove the linear relationship between the average cylinder surface speed and turbulence intensities. Work done by Lewis and Swinney (1999) determined that turbulent Taylor vortices remained at a  $Re$  number equal to  $5 \times 10^5$  and Smith (1982) verified the commencement of homogenous turbulence in TC reactors when the  $Re$  number exceeds  $5 \times 10^5$ . However, Anabaraonye *et al.* (2021) has gave an in-depth analysis on decoupling transport effects of its intrinsic chemical reactions by computational fluid dynamics (CFD) approach and claimed that the assumption of turbulent isotropy in TC reactor is fundamentally

incorrect and leads to erroneous results. The simulation results of TC reactor has successfully defined a new local turbulent Peclet numbers ( $Pe$ ) to quantify the relative enhancement in diffusivity compared with turbulent advection and an increment of 29% has been observed in the turbulence intensity as Reynolds number ( $Re$ ) is doubled (Anabaraonye et al., 2021). Kim *et al.* (2013) have investigated the impact of vortex movement on particles dynamics using CFD by comparing particle classification at both vortices' stationary region (5 mL/min) and moving region (60 mL/min). Both regions operate under the inner rotating speed of 200rpm and the behaviour of the particles inside the TCR is shown in Figure 1.6, which demonstrate that the larger particles quickly fall due to the gravitational effect and the smaller particles are trapped inside a Taylor vortex and move with vortices in the upper region. Meanwhile, the stationary region particle vortices are trapped without movement (Kim *et al.*, 2013). The results indicate that the impact of vortices on particles is susceptible to the vortices' movement itself and the particle size distribution.

Furthermore, researchers have demonstrated the rotational speed of the inner cylinder in TCRs exert significant diversity on particle morphology and particle distributions in the particle synthesis process. Tang *et al.* (2019) have reported that particles exhibit hexagonal-shaped nanoplates when the rotational speed increased from 5 rpm- 85 rpm and become nanofibers as the rotational speed experienced an upsurge from 90 rpm to 1000 rpm (SEM images are shown in Figure 1.7). Guérin *et al.* (2017) have investigated the sequence flocculation of latex particles at a low shear rate and high shear rate in TCR. Latex aggregates exhibit a smaller equivalent diameter of spherical-shaped particles and are back to being loose-structured and irregularly shaped at a low shear rate as shown in Figure 1.8.

### **Impinging jet reactor (IJR)**

IJR comprises a limited chamber with two injecting streams impinging intensively to achieve a high mixing rate at the micro-scale, which has been broadly employed in industrial processes such as gasification, extraction, combustion and nanoparticle synthesis (Wang *et al.*, 2012, Luo *et al.*, 2013). Figure 1.9 displays the schematic diagram of a typical IJR, which has the advantage of outstanding mixing performance that is much faster than conventional reactors and also has an outstanding capability to deliver fast reaction processes. When IJR is used for fast-precipitation processes at high levels of supersaturation, high mixing intensities are required for the thermodynamic driving force of phase transition (Schwarzer and Peukert, 2004). The micromixing efficiency of IJR is attributed to parameters such as the Reynolds number of inlet jet ( $Re_j$ ), ratio of two volumetric flow ( $R'$ ), outlet length ( $L$ ) and inlet diameter ( $d_i$ ), Root Mean Square (RMS) velocity, turbulent kinetic energy and stagnation point offset (Liu *et al.*, 2019). Luo *et al.* (2019) have scaled up the Jet-In-Cross-Flow (JICF) reactor and the Forward-Impinging-Back (FIB) Reactor with an increased diameter from 30 mm to 390 mm. The yield of  $C_2$  in the FIB reactor is approximately 64% and exhibits superior scale-up performance compared to the JICF reactor with a decreasing yield from 64.4% to 43.8% as the diameter of the reactor increases as shown in Figure 1.10.

Liu *et al.* (2014) have investigated the hydrodynamics in a micro-impinging stream reactor with a diameter of 1mm. The impingement region became thinner with an increasing Reynolds number  $Re_j$ , signifying higher local turbulent kinetic energy for higher  $Re_j$  as observed in Figures 1.11 and 1.12. A high  $Re_j$  value contributes to a high turbulent energy dissipation rate in the central impingement region. Liu *et al.* (2014) and Schwertfirm *et al.* (2007) have simulated hydrodynamics in IJR and the results displayed a region of high intensity of turbulent kinetic energy and dissipation at the centre of the impingement zone, whereas the intensity drops dramatically in the vicinity of the outlet.

The numerical results produced by Liu *et al.* (2014) agree well with experimental results and show that the mixing performance is susceptible to the Reynolds number ( $Re_j$ ) of both inlets and the diameter of the inlets. For a low  $Re_j$  value, two injecting streams behave as segregated flow distributed by layers and the mixing is the result of the diffusion across the vertical interface of two streams (Bothe *et al.*, 2006). As  $Re_j$  increases, the flow becomes asymmetric and gradually develops into steady engulfment flow due to two inlet streams concurrently meet and collide generating two co-rotating vortices along the chamber (Kumaresan and Joshi, 2006). Landreth and Adrian (1990) have considered the flow and vortex structure by measuring the velocity magnitude in 2D-dimension of a turbulent circular jet impinging using Particle Image Velocimetry (PIV). Liu *et al.* (2014) have compared the instantaneous flow field captured by PIV and simulated results via LES by displaying the small-scale eddies changing over time with regards to location and intensity as shown in Figures 1.11 and 1.12. Generation of turbulent vortices lead to higher energy dissipation rate locally and contributes to enhancement of mixing performance. Tu *et al.* (2015) have detected the half deflecting oscillation behaviour in IJR by increasing the value of  $Re_j$ . Somashekar *et al.* (2012) have analysed the flow field through micro-PIV and displayed the pointwise and spatial statistics of turbulence with Reynolds stresses and spatial correlations of velocity fluctuations. Krupa *et al.* (2014) have proved that the mixing efficiency can be enhanced by a larger ratio between the mixing chamber width and inlet jet diameter. Tsaoulidis and Angeli (2017) have reported that the drop path (Figure 1.19) and the shape of the liquid jet (Figure 1.20) change due to the flow field being affected by the chamber size, especially for the jet under a low Reynolds number. The drops circulate in the impingement zone at the areas with a smaller diameter of impingement zone and high Reynolds number, increasing the likelihood for drop collision and coalescence.

### 1.1.2 Fundamentals and relevance to turbulence

In order to maintain a high level of efficiency among the diverse phases in multiphase reactors, a high level of energy in terms of turbulence is required (Pangarkar, 2015). Energy input is a feasible approach to strengthen the turbulence intensity leading to high mass/heat transport rate as the consequence of high diffusion rate. Osborne and Reynolds (1883) have put forward the concept of turbulence in pipe flow. Parameters used to quantify the turbulence include turbulent length scales, turbulent intensity and the turbulent kinetic energy budgets. The fluid velocity vector is derived as the sum of time average velocity and the instantaneous fluctuating component as follows in Equation (1-4) for one direction.

$$u_x = \overline{u_x} + u_x' \quad (1-4)$$

Pangarkar (2015) has shown that the instantaneous fluctuating velocity  $u_x'$  is essential to determine crucial factors like turbulence intensity and the mass transfer coefficient at the gas-liquid and solid-liquid interphase. The turbulent intensity can be expressed as follows by Equation (1-5).

$$I = \frac{\sqrt{u_x'^2}}{\overline{u_x}} \quad (1-5)$$

For a three-dimensional system, the instantaneous fluctuating components in 3 directions are  $u_x'$ ,  $u_y'$ ,  $u_z'$  with alike interpretations of the turbulence intensity. There Homogenous turbulence and isotropic turbulence are two important concepts. Homogeneous turbulence is defined independent of direction and isotropic turbulence is referred to three identical fluctuating components as shown by Equation (1-6). Isotropic turbulence is always homogeneous.

$$\sqrt{\overline{u_x'^2}} = \sqrt{\overline{u_y'^2}} = \sqrt{\overline{u_z'^2}} \quad (1-6)$$

Completely random fluctuations in space are without any correlation between the different directional fluctuations, which can be written as Equation (1-7).

$$\overline{u_x' u_y'} = 0 \quad (1-7)$$

### **Theoretical models**

The mean turbulent flow can be classified as steady or unsteady as well as zero, one, two or three-dimensional, with simple, smooth structures, dominated by one or two length and time scales. Once a flow does become turbulent, it is always unsteady, three-dimensional, and characterised by a spectrum of scales where viscous dissipation will convert mechanical energy to thermal energy (Durbin and Shih, 2005). The use of Computational Fluid Dynamics (CFD) has been widely applied in academic research as well as industrial applications analysing the characteristics of multi-phase fluid flows. Based on Navier–Stokes (N–S), the mathematical expression of turbulence flows can be expressed into four categories as shown in Table 1.1.

Among all these models, RANS is less computationally intensive compared with DNS and LES by simplifying the flow and making it smoother. It is dominated by only a few length and time scales, although the turbulent flow is always 3-D and unsteady. RANS equation quantities are given by Equation (1-8).

$$\frac{\partial u_i}{\partial t} + u_j \frac{\partial u_i}{\partial x_j} = -\frac{1}{\rho} \frac{\partial p}{\partial x_i} + \frac{\partial}{\partial x_j} \left( \frac{\mu}{\rho} \frac{\partial u_i}{\partial x_j} \right) \quad (1-8)$$

The continuity equation is denoted as follows by Equation (1-9).

$$\frac{\partial u_i}{\partial x_i} = 0 \quad (1-9)$$

The Reynolds-averaged quantities are defined by Equations (1-10) and (1-11).

$$U_i(x_k, t) = U_i(x_k) + u'(x_k, t) \quad (1-10)$$

$$U_i(x_k) = \lim_{T \rightarrow \infty} \frac{1}{T} \int_0^T u_i(x_k, t) dt \quad (1-11)$$

The equations above can be substituted and averaged to produce Equation (1-12):

$$\frac{\partial u_i}{\partial t} + u_j \frac{\partial u_i}{\partial x_j} = -\frac{1}{\rho} \frac{\partial p}{\partial x_i} + \frac{\partial}{\partial x_j} \left( \frac{\mu}{\rho} \frac{\partial u_i}{\partial x_j} \right) + \frac{\partial (-\overline{u_i' u_j'})}{\partial x_j} \quad (1-12)$$

The first term in Equation (1-12) can be eliminated due to averaging principles and the last term triggers the closure problem. In the past few decades, more than 200 models have been developed in accordance with the number of solved transport equations other than RANS equations, such as the standard  $k-\varepsilon$  model, Realizable  $k-\varepsilon$  model, Shear Stress Transport (SST)  $k-\omega$  model and Reynolds stress model (RSM). The turbulence intensity, kinetic turbulent energy and energy dissipation are investigated and compared to quantify the variances between the computational turbulence models. These turbulence models are often chosen with a comprehensively accurate description of turbulence flows (Akin and Kahveci, 2019). The Reynolds stress model (RSM) has been widely investigated in open literature. The Algebraic RSM was derived by Lahey *et al.* (1993) for predicting the accuracy of bubbly flows in triangular ducts. Moureh and Flick (2005) have established a small-scale CFD model to assess the performance of turbulence closure models consisting of the  $k-\varepsilon$  model and the RSM under the circumstances of high and low Reynolds number. Mimouni *et al.* (2008) and Mimouni *et al.* (2011) have applied RSM to the thermal hydraulics of a nuclear reactor. Colombo

and Fairweather (2019) employed a near-wall RSM to capture the anisotropy of the turbulence structure and its impact on the radial distribution of the bubbles.

Zhou *et al.* (2017a) have compared the Nusselt number to test the applicability of RSM and LES with the experimental data of the tube flow displayed in Figure 1.14, indicating that the models are most practical at different ranges of the Reynolds number. In this case, the heat transfer performance is accurately predicted, referring to the result that LES agrees well with experimental data at a  $Re$  number range of  $10^4$  to  $10^5$ , whereas RSM is more applicable at a  $Re$  number larger than  $10^5$  (Zhou *et al.*, 2017a). In addition, a LES/RANS hybrid turbulence model has been reported in the open literature especially in the application of hydro-turbines and draft tubes (Javadi and Nilsson, Foroutan and Yavuzkurt, 2015). Defraeye *et al.* (2013) have stated that the evaluation of the turbulence model performance can be achieved by comparing the flow parameters with experimental data such as the Nusselt number, separation index, drag coefficient, Nusselt number and recirculation length. Sadiki *et al.* (2017) have analysed the turbulent modelling impact of the oxy-coal combustion on devolatilisation and coal burnout by comparing both the RANS (realisable  $k-\varepsilon$  model) and LES (WALE and Smagorinsky SGS models) coupled with the Eulerian-Lagrangian approach in gas-solid system. Figure 1.13 displays the particle trajectories without turbulent dispersion as tracers in the flow field simulated by RANS and LES. The simulation results of RANS appear to be more homogeneously distributed with a dilute two-phase regime compared with LES and the particles are dispersed in the radial direction. Javadi and Nilsson (2015) have simulated swirling flow with rotor-stator interaction to estimate the applicability of high-Reynolds RANS (standard  $k-\varepsilon$  and RNG  $k-\varepsilon$ ), low-Reynolds RANS (Launder-Sharma  $k-\varepsilon$ ) and RANS-LES hybrid method (DES Spalart-Allmaras) with great unsteadiness and high kinetic turbulence energy. The iso-surface pressure under different eddy-viscosity models is displayed in Figure 1.15, indicating similar results for high-RANS models no matter whether the standard  $k-\varepsilon$  model or RNG  $k-\varepsilon$  model is applied. However, a compacted rope-like vortex rope under low-Reynolds

RANS and detailed structure with hybrid method is shown (Javadi and Nilsson, 2015). Vorticity contours under the RANS-LES hybrid method at a horizontal plane downstream shown in Figure 1.16 also displayed a more detailed picture compared with others (Javadi and Nilsson, 2015). Kang and Chester (2003) have verified that the LES model is the most accurate at predicting the turbulence in the resolved scales.

### **Turbulent energy spectrum**

The prediction of turbulent solid-liquid multiphase flow is tough due to the wide spectrum of length scales and time scales being susceptible to the microscopic physics of particles and both fine and large structures of turbulences (Octau *et al.*, 2020). Anisotropic turbulence in a multiphase system is triggered by primary energy input. However, energy is dissipated due to bulk viscosity ultimately causing isotropic turbulence resulting from the small eddies according to Kolmogorov's theory (Pangarkar, 2015). Kolmogorov-energy-spectrum is used to quantify the energy transfer through different scales of vortices. Kolmogorov's length scale is defined as follows by Equation (1-13),

$$\eta = (\nu^3/\epsilon)^{1/4} \quad (1-13)$$

where  $\nu$  represents the fluid viscosity and the  $\epsilon$  is the energy dissipation rate.

According to Lynch (2007), vortices in turbulent flow have interactions in an energy cascade that are defined for the energy transformation of vortices in diverse scales. Bak and Kalmár-Nagy (2018) have analogically displayed the transformation of vortices at different scale using a mechanistic model of a binary tree of masses and springs as shown in Figure 1.17. The “mass” stands for the vortices of different scales and the “spring” is the transforming connection of vortices at different vortices. The largest-scale vortices are incurred by eternal energy input that is unstable and it can affect

several vortices of a smaller size. Those smaller sized vortices may cause a larger effect on viscosity and the turbulent kinetic energy may dissipate due to the viscosity effect.

Pope (2000) has qualitatively analysed the well-known Kolmogorov-spectrum of 3D-homogeneous turbulence in terms of Fourier-transform of the total kinetic energy  $E$  (see Figure 1.18) given by Equation (1-14),

$$E = \hat{E}(\kappa)d\kappa \quad (1-14)$$

where  $\kappa$  is the wavenumber reciprocal to the characteristic eddy size  $L$  as  $\kappa \sim L$ .

The peak of the spectrum is located in the energy spectrum containing the range that covers the smallest wavenumbers. The external energy input is located at this range as well. The intermediate values of wave numbers are called the inertial range where the energy spectrum follows the scaling law, namely,  $\hat{E}(\kappa) \sim \kappa^{-5/3}$ . For a wavenumber larger than  $1/\eta$ , the energy drops off due to significant dissipation. Another crucial hypothesis by Kolmogorov is that the energy spectrum in the inertial spectrum is dependent on the energy dissipation rate as shown by Equation (1-15),

$$\hat{E}(\kappa) = C\epsilon^{2/3}\kappa^{-5/3} \quad (1-15)$$

where  $C$  represents a Kolmogorov constant.

The qualitative graph of the 3D Kolmogorov-spectrum for homogeneous turbulence is shown in Figure 1.18. Researchers have shown that their results agree with Kolmogorov's hypotheses. For instance, Stalp *et al.* (1999), Kurian and Fransson (2009) have all verified the Kolmogorov hypotheses in the past few decades. Kang and Chester (2003) have compared the results from grid turbulence measurement and Large Eddy Simulation (LES) has shown that LES models are able to accurately predict low-

order statistics of resolved scales in isotropic turbulence during the decay process. The turbulent dissipation rate can be assessed through experimental techniques such as hot wires, LDV, PIV and PTV via the velocity processing methods (Wang et al., 2021). Hoque *et al.* (2014) have applied Particle Image Velocimetry (PIV) to measure the velocity vector field as well as the integral length scale and spatial energy spectrum and used it to obtain the energy spectrum from grid generated homogeneous turbulence velocity data.

## **1.2 Process of mixing, chemical reaction and particle formation in the multiphase flow system**

### **1.2.1 Mixing process in multiphase reactors**

#### **Qualification of mixing performance**

Baldyga and Pohorecki (1995) have distinguished the complicated mixing processes into three mixing categories, that is, macromixing, mesomixing and micromixing. They also defined the mixing of various scales:

- Macro-mixing is defined as the motion of large-scale vortices motion in a turbulent flow field with a scalar integral scale.
- Mesomixing is defined as the length-scale of vortices between the Kolmogorov scale (Equation (1-16)) and the Batchelor scale (Equation (1-17)).
- Micro-mixing is referred to the length scale at the level of molecular diffusion (Baldyga and Bourne, 1999).

Among the rest, micromixing has an intensive influence on many industrial processes such as polymerisation, crystallisation and precipitation (Ying *et al.*, 2008).

The Kolmogorov scale is given by Equation (1-16).

$$\eta_k = \left(\frac{\nu^3}{\varepsilon}\right)^{\frac{1}{4}} \quad (1-16)$$

The Batchelor scale is given by Equation (1-17),

$$\eta_k = \eta_B Sc^{-1/2} \quad (1-17)$$

where  $\nu$  is the kinematic viscosity of the fluid,  $\varepsilon$  is the local dissipation rate of turbulent kinetic energy and  $Sc$  is the Schmidt number, defined as the ratio of fluid viscosity and the mass diffusivity denoted by Equation (1-18).

$$Sc = \nu/D \quad (1-18)$$

One common criterion used to determine the mixing efficiency is the mixing time or homogenisation time  $t_m$ , which is defined by Grein *et al.* (2016) who claim that there are requirements for macro-mixing that the system achieves with a certain level of homogeneity for all the components regardless of meso-mixing and micro-mixing. However, Schwertfirm *et al.* (2007) defined the total mixing time  $t_m$  as the total time required to reduce the initial spatial segregation of the reactants over the cascade of macro-mixing, meso-mixing, and micro-mixing down to a molecular segregation scale where the reactants can react. This is important for the setup and hydrodynamic regime adjustment to predict the mixing efficiency of the process scaled-up. Baldyga and Bourne (1999) have proposed the concept of turbulent mixing defined by turbulent mixing time and it is predominant for the processes of particle nucleation, growth,

agglomeration, and aggregation in a precipitation process when it is slower than or similar to the chemical reaction time  $t_r$ . Schwertfirm *et al.* (2007) suggested that the mixing time in the impinging jet reactor is a function of the Reynolds number ( $Re$ ), inflow condition and mixer geometry. Vicum and Mazzotti (2007) have provided the expression of the macro-mixing as follows where the macro-mixing time  $\tau_c$  is given by Equation (1-19),

$$\tau_c = \frac{V}{Q_c} \quad (1-19)$$

and the circulation capacity  $Q_c$  is denoted by Equation (1-20),

$$Q_c = C_1 N d_{imp}^3 \quad (1-20)$$

where  $V$  is the liquid volume in the reactor,  $N$  represents the stirring rate,  $d_{imp}$  is the impeller diameter and  $C_1$  is a constant related to the pumping capacity of the impeller. The expression of the characteristic time for meso-mixing is proposed by (Baldyga and Pohorecki, 1995) by Equation (1-21),

$$\tau_s = \frac{k}{2\varepsilon} \quad (1-21)$$

where  $k$  is the turbulent kinetic energy and  $\varepsilon$  is the energy dissipation rate.

Baldyga and Bourne (1989) have also illustrated that micro-mixing is driven by the viscous convective deformation of fluid elements and the molecular diffusion, also known as the engulfment time constant given by Equation (1-22).

$$\tau_E = \frac{1}{E} = 17.24 \left( \frac{\nu}{\varepsilon} \right)^{1/2} \quad (1-22)$$

The characteristic time for molecular diffusion is related to the micro-mixing time denoted by Equation (1-23).

$$\tau_G = \tau_E \left( 0.030 + \frac{17050}{s_c} \right)^{-1} \quad (1-23)$$

Another approach to quantify (Vicum and Mazzotti, 2007) the mixing performance is to obtain the targeted species concentration profile. Numerical simulation by computational fluid dynamics (CFD) has been applied to explore the mixing performance owing to the change of reaction species concentration. Van den Akker (2010) has put forward two approaches to acquiring the flow characteristics as a means of interpreting mixing performance: one method solves the momentum equation only and the other method solves both the momentum equation and mass transfer equation. Engler *et al.* (2004) have quantified the mixing through diffusion efficiency of the artificial diffusive species by solving Navier–Stokes equation coupled with mass transfer equation. It was also found by Engler *et al.* (2004) that increasing the vorticity in the mixer, even at low Reynolds numbers ( $Re \leq 200$ ), is able to improve the mixing quality defined by Equation (1-24),

$$\alpha = 1 - \sqrt{\frac{\sigma_M^2}{\sigma_{max}^2}} \quad (1-24)$$

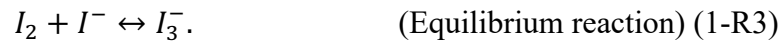
where the  $\sigma_{max}^2$  represents the maximum variance of the mixture and  $\sigma_M^2$  is defined as follows by Equation (1-25),

$$\sigma_M^2 = \frac{1}{n} \sum_{i=1}^n (c_i - \bar{c}_M)^2 \quad (1-25)$$

where  $n$  is the number of grid points inside the cross-section,  $c_i$  is the concentration at the grid point  $i$  and  $\bar{c}_M$  is the optimal mixing concentration ( $\bar{c}_M = 0.5$  represents symmetrical boundary conditions).

Although there are various approaches to evaluating micromixing performance, the Villiermaux /Dushman reaction is widely used as a parallel competing reaction due to its simplicity and low cost, firstly proposed by Villiermaux *et al.* (1994) and Fournier *et al.*, (1996), which evaluates the impact of operating parameters on the segregation index serving as an indicator for micromixing performance.

The Villiermaux /Dushman reaction comprises of three parts as follows:



The segregation index ( $X_S$ ) is defined as the relative amount of  $H^+$  consumed by Reaction (1-R2) and is denoted by Equation (1-26),

$$X_S = \frac{Y}{Y_{ST}} = \frac{n_{I_2} + n_{I_3^-}}{n_{H^+}} \left( 2 + \frac{n_{H_2BO_3^-,0}}{3n_{IO_3^-,0}} \right) \quad (1-26)$$

where  $X_S = 0$  represents perfect micromixing and  $X_S = 1$  means total segregation.

However, the debate on the options of acid and the reactant impact on reaction rate constant in Villiermaux-Dushman reaction has been revived in recent year. Arian and Pauer (2021) proposed a newly obtained reaction rate constant considering the integrated effect of reaction rate constant and equilibrium of sulphuric acid based on

incorporation model. This makes the calculation of mixing time via Villermaux-Dushman experiments independent of the acid choice. Rahimi *et al.* (2014) have investigated the acid concentrations and the ultrasound irradiation on micromixing performance by employing the T-type microreactor with a low frequency (42 kHz) piezoelectric transducer. The results shown in Figure 1.21 reveal that  $X_s$  trends show lower activity with low  $H^+$  concentration and ultrasound waves, leading to a significant reduction in mixing times and segregation index values.

### **Impact of mechanical factors on the mixing performance**

Mixing can be categorised into positive mixing and passive mixing. The mixing triggered spontaneously is defined as passive mixing and active mixing is intensified by the external energy input through mechanical, pneumatic, or ultrasonic forces leading to the enhancement of local turbulence and mixing quality (Engler *et al.*, 2004). The external driving field such as magnetic actuation, microwave and ultrasound irradiation will be introduced in section 1.4.2: Process intensification (PI) for multiphase flows. Metzger and Kind (2016) claimed that the particle size distribution is strongly reliant on the mixing characteristics of the reaction apart from the intrinsic kinetics. Zhendong *et al.* (2012) have validated that the mixing efficiency goes up as the flow rate increases at the convergence region in a T-mixer. This was proved by Kockmann *et al.* (2003) who showed that the laminar flow can exist in three different regimes as the mass flow rate increases as shown in Figure 1.22 (Engler *et al.*, 2004).

At low flow rates, the stratified flow regime occurring at streamlines are scarcely bent and follow the channel walls. At medium flow velocity, the vortex flow regime contributes to a slight improvement of mixing quality by dragging fluid from the middle to the top and bottom side of the mixing channel. At high flow rates, the engulfment flow regime and streamlines intertwine and reach the opposite sides of the wall leading to a dramatic improvement in mixing performance (Engler *et al.*, 2004). However,

Saadat *et al.* (2020) have illustrated that the mixing efficiency is not monotonous anymore with an optimum point although an increase in inlet velocity may result in the deterioration of the mixing performance in a rough trend. Brito *et al.* (2020) have conducted work on the visualisation of mixing in the confined impinging jet reactor at different Reynolds numbers derived from inlet flowrate  $v_{in}$ . The different flow types and their characterisation is shown in Figure 1.23. They tend to behave as a segregated flow regime at  $Re = 103$  characterised by the clear division of two flows, which changes to a chaotic flow regime with the generation of vortices up and down the jets that engulf fluid from both jets as the Reynolds number increases from 111 to 505. In addition, Cheng *et al.* (2019) have carried out similar work on the estimation of micromixing time under different Reynolds number in a single countercurrent-flow microchannel reactor as shown in Figures 1.24 (a) and 1.24 (b) and demonstrated that  $t_m$  decreases with increasing a  $Re$  value to achieve a rather high-level micromixing efficiency (Cheng *et al.*, 2019). Furthermore, Rahimi *et al.* (2014) have investigated the effect of flow rate on micromixing in a T-junction via CFD modelling by applying five different total flow rates and the velocity magnitude vector is shown in Figure 1.25. An iodide–iodate reaction is employed and the low amount of produced  $I_3^-$  indicates high micromixing. It can be seen from Figure 1.26 that a higher flow rate contributes to better micromixing performance due to its high turbulent kinetic energy and generation of vortices (Rahimi *et al.*, 2014).

The geometry and structure of the impinging jet affect the pressure drop in the channel as well as the mixing performance. Faryadi *et al.* (2014) have measured the pressure drop in microchannels of three different geometry as shown in Figure 1.27 and the results show that the pressure drop is higher in the Lambda type microchannel and lower in the T-type microchannel (Figure 1.28 (a)). They have also defined the performance ratio through the segregation index and friction factor based conditions with and without ultrasound as equation and revealed that the T-type microchannel performs the best with a maximum increment of 34.1% in the calculated performance

ratio once the piezoelectric transducer is activated (Figure 1.28 (b)), denoted by Equation (1-27).

$$\text{Performance ratio} = \frac{X_s/X_{s0}}{(f/f_0)^{1/3}} \quad (1-27)$$

Zhendong *et al.* (2012) have validated that broadening the width of the dispersed fluid channel also weakens the intensity of mixing in an asymmetrical T-shaped micromixer. Another experiment done by Zhou *et al.* (2019) has illustrated that the impact of the thickness of the injection ring and the installation of the rectifying ring has a significant effect on the mixing performance in the radial multiple jets-in-crossflow mixing system as shown in Figure 1.29. Moreover, Wu *et al.* (2014) have also shown that the effect of the length and convergence angle of the mixing chamber affect the mixing performance of the steam ejector. The optimum range to acquire the best mixing performance of the mixing chamber length and angle can be obtained with its largest entrainment ratio.

Vicum and Mazzotti (2007) have pointed out that although the concentration of the reactant cannot affect small-scale mixing and particle formation, it strongly acts on macro-mixing by producing an inhomogeneous environment on a large scale resulting in low saturation, which eliminates the precondition of particle nucleation.

## 1.2.2 Intrinsic kinetics of multiphase reactions

### Gas-liquid two-phase reaction

Gas-liquid two-phase contactor is the most common and representative apparatus for the investigation of bubbles hydrodynamics such as bubble size distribution, bubble-liquid interfacial as a function of superficial gas velocity, superficial liquid velocity, temperature, pressure and phase types (inert/reactive) (Feng *et al.*, 2019). Davies (1985) displayed the typical concentration profiles for a reaction involving gas-liquid phases,

depicting the gaseous solute dissolving in the liquid phase and overcoming the resistance to transfer into the liquid phase using a film model as a basis. Except for the chlorination and sulfonation reactions with gaseous  $\text{SO}_3$ , the common reactions encountered in industrial processes are hydrogenation and oxidation with sparingly soluble gases. the gas film resistance is negligible in reactions with low solubility (Pangarkar, 2015). As the diffusional processes and the subsequent reaction occur in series and the slowest step acts as the rate-governing rule that controls the overall rate, considering a general type of reaction:



where  $\psi$  is the stoichiometric factor.

Pangarkar (2015) has classified the two-phase mass transfer rate  $R_v$  expression into different regimes with the corresponding equations under different situations discussed below. The film model is applied here and the mechanism of the four models is shown in Figure 1.30. The characterised parameter to determine the reaction rate and define the regime is the Hatta number ( $Ha$ ), as given by Equation (1-28). The  $Ha$  number is defined as the ratio of chemical reaction rate to the mass transfer rate in the gas-liquid film.

$$Ha = \frac{\sqrt{D_A k_2 [B_B]}}{k_L} \quad (1-28)$$

The mass transfer rate and the chemical reaction rate are characterised by the characteristic diffusion time  $\tau_D$  and the reaction time  $\tau_R$  (Decoursey, 1987). The characteristic time is defined as the reciprocals of the respective rate coefficients,  $R_D$  and  $R_R$ , with the characteristic diffusion time and reaction time given by Equations (1-29) and Equation (1-30), respectively.

$$\tau_D \propto \left(\frac{1}{k_L a}\right) \quad (1-29)$$

$$\tau_R \propto \left(\frac{1}{R_R}\right) \quad (1-30)$$

**a) Regime A: Extremely Slow Reaction That Occurs Only in the Bulk Liquid Phase**

As the reaction rate is slow without any reaction occurring in the liquid film, the concentration of bulk gas equals to that at liquid film as shown in Figure 1.30 (a), that is,  $[A^*] \approx [A_B]$ . Thus, the reaction takes place exclusively in the bulk liquid phase and the Hatta number satisfies  $Ha \ll 1$  for this regime. Therefore, the volumetric rate of the reaction in the bulk liquid is given by Equation (1-31),

$$R_R = \varepsilon_L k_{p-q} [A^*]^p [B_B]^q \quad (1-31)$$

where  $k_{p-q}$  is the intrinsic reaction rate constant.  $p$  and  $q$  represent the orders of the reactions concerning the gaseous and liquid-phase reactant, respectively.

**b) Regime B: Diffusion-Controlled Slow Reaction**

Regime B defines the sufficiently slow reaction without occurrence at the diffusion film whereas physical diffusion occurs in the liquid film and the Hatta number satisfies  $Ha \ll 1$  for this regime. However, the homogeneous reaction is considerably faster than the diffusion process in the film compared to regime A, running out of A in the bulk liquid phase as shown in Figure 1.30 (b). The volumetric rate of mass transfer in this case is given by Equation (1.32),

$$R_R = k_L a [A^*] \quad (1-32)$$

where  $a$  is the interfacial area.

The specific rate per unit effective interfacial area or flux of A is given by Equation (1-33).

$$R_{Ri} = k_L[A^*] \text{ (mol/m}^2\text{s)} \quad (1-33)$$

**c) Regime C: Fast Reaction Occurring in the Diffusion Film**

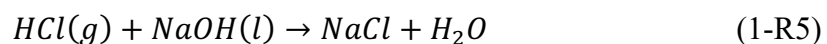
Regime C refers to the fast occurrence of both reaction and diffusion in the diffusion film. Under this regime, the Hatta number satisfies  $Ha > 3$  when  $Ha \ll B_B/(\psi A^*)$ . For this scenario, the specific rates of mass transfer accompanied by a general  $(p-q)^{\text{th}}$  order reaction are given by Equation (1-34),

$$R_{Ri} = A_m \sqrt{\frac{2}{p+1} D_A k_{p-q} [B_B]^q [A^*]^{p-1}} \quad (1-34)$$

where  $A_m$  is the molecular diffusivity of dissolvable gaseous species A.

**d) Regime D: Instantaneous Reaction**

The instantaneous reaction occurs when  $\tau_R$  is extremely low and the concentration profiles for this regime are shown in Figure 1.30 (d). Under this regime, the Hatta number satisfies  $Ha \gg 3$  when  $Ha \gg B_B/(\psi A^*)$ . One typical example is the neutralisation reaction as follows.



Under these conditions, the specific rate of mass transfer is given by Equation (1-35).

$$R_{Ri} \sim k_L \left( \frac{D_B^{B_B}}{\psi_{D_A}} \right) \quad (1-35)$$

### **Gas-liquid-solid three-phase reaction**

The traditional technologies for hosting gas-liquid-solid three-phase reactions are fixed-bed, slurry bubble column and fluidised-bed reactors (Durán Martínez *et al.*, 2016). The three-phase reaction always comprises of a solid phase as the catalyst and the prediction of the mass transfer coefficients is restricted to the gas-liquid ( $k_L a$ ) and solid-liquid mass transfer ( $K_{SL}$ ) steps in terms of the general nature of concentration profiles for the gaseous solute (Pangarkar, 2015). The typical concentration profiles for the solid-catalysed gas-liquid reaction is shown in Figure 1.30.

Lefebvre *et al.* (2018) have explored the three-phase CO<sub>2</sub> methanation reaction kinetics in a CSTR, implying that the gas concentration in the liquid phase is the kinetic driving force and the gas concentration available on the catalyst surface is decided by the liquid phase. Lefebvre *et al.* (2019) also investigated two-phase CO<sub>2</sub> methanation reaction kinetics in a plug flow laboratory reactor and have successfully applied a two-phase kinetic rate equation to a three-phase reaction (catalyst involved) with good agreement. Durán Martínez *et al.* (2016) have developed Monolith reactors as a novel gas-liquid-solid reactor involving hydrogenation reactions with advantages of minimised internal diffusional resistances, enlarged mass transfer interfacial area and a low-pressure drop without reactor fouling and clogging. Conclusively, the main focus should be on achieving the intrinsic rate afforded by a given catalyst from an industrial point of view and the solid-liquid mass transfer ( $k_{sL}$ ) is based on catalyst surface area per unit volume of the reaction mixture (Pangarkar, 2015).

As depicted in Figure 1.31 at steady state, the volumetric mass transfer rate of a first-order reaction is given by Equation (1-36),

$$R_R = k_L a ([A^*] - [A_B]) = \left( K_{SL} \left( \frac{A_p}{V} \right) \right) ([A_B] - [A_S]) = k_R [A_S] \quad (1-36)$$

where  $A_p/V$  is the surface area per unit volume of the reaction mixture. The overall mass transfer rate is decided by the relative values of  $k_L$ ,  $K_{SL}$  and  $k_R$  in the gas-liquid and solid-liquid mass transfer steps.

### 1.2.3 Effect of hydrodynamics on particle formation in multiphase reactors

#### **Particle nucleation, growth and its influence factors in multiphase reactors**

Once the chemical time scales  $\tau_R$  are in a similar range or faster than the turbulent time scales, the turbulent mixing determines the reaction rate and thus has a dominating influence on all consecutive steps, such as nucleation, growth, agglomeration and aggregation in a precipitation process. Fan *et al.* (2013) have divided the heterogeneous condensation process into two stages, nucleation and growth process, in their investigation of insoluble spherical particles.

Variables that can have an impact on the nucleation process include supersaturation, particle size distribution, surface properties, solubility, particle composition and the electric charge of a particle (Xu *et al.*, 2017, Tammaro *et al.*, 2012, Chen and Tao, 2000, Wu *et al.*, 2016). Lv *et al.* (2020) have shown the visualisation process of vapour condensation on a single SiO<sub>2</sub> particle through the time-resolved images recorded by an Environmental Scanning Electron Microscopy (ESEM) system (Wu *et al.*, 2016). Hogrefe and Keesee (2002) have determined the critical supersaturation point using the characteristics of the oscillation period and amplitude of micron-sized glass particle by using a Charge Coupled Device (CCD) camera. Furthermore, work done by Harrison

*et al.* (2011) also illustrates the struvite growth kinetics as a function of solution supersaturation relevant to the mean particle size. Mousavi *et al.* (2019) have utilised the Computational Fluid Dynamics (CFD) coupled with Population Balance Modelling (PBM) to model the growth of crystals in the reactor as a function of the supersaturation index (SI).

The nucleation and growth model was firstly developed by Reiss (1951) and indicated that the growth of particle is via uniform diffusion. Over the past few decades, the developed nucleation and growth processes have been prevalent and quantitatively illustrated by the LaMer burst nucleation and Ostwald ripening theory based on particle size changes (LaMer, 1952, LaMer and Dinegar, 1950). Thanh *et al.* (2014) have derived the nucleation rate  $J$  as a function of the crystal free energy  $\Delta G_v$ , assuming the nuclei formation is homogeneous and the total free energy is the sum of the surface free energy and the bulk free energy.

The bulk free energy is given by Equation (1-37).

$$\Delta G_v = \frac{-k_B T \ln(S)}{v} \quad (1-37)$$

The total free energy is given by Equation (1-38).

$$\Delta G = 4\pi r^2 \gamma + \frac{4}{3}\pi r^3 \Delta G_v \quad (1-38)$$

where  $k_B$  is the Boltzmann's constant,  $S$  is the supersaturation of the solution,  $v$  is molar volume and  $r$  is the radius of the particles. The critical radius can be estimated at the minimum size when a particle can survive in the solution without being re-dissolved, whereas the differentiation of  $\Delta G$  equals 0 when the status of the stable nucleus is

$d\Delta G/dr = 0$ . Therefore, the rate of nucleation  $J$  of  $N$  particles during time  $t$  is given by  
rate of surface reaction

$$J = \frac{dN}{dt} = A \exp\left(-\frac{16\pi\gamma^3 v^2}{3k_B^3 T^3 (\ln S)^2}\right) \quad (1-39)$$

where  $A$  is the pre-exponential factor.

The derivation of the growth model is reliant on the mechanisms of the surface reaction and the monomer's diffusion to the surface in terms of Fick's first law (Sugimoto and Tadao, 2001). The growth rate of nanoparticles by differentiating the change of particles radius with time is decided by limiting factors (Thanh *et al.*, 2014). When diffusion acts as the limiting factor, the particle growth rate is given by Equation (1-40).

$$\frac{dr}{dt} = \frac{Dv}{r} (C_b - C_r) \quad (1-40)$$

Likewise, if the limiting factor is surface reaction, the nucleation rate is given by Equation (1-41),

$$\frac{dr}{dt} = kv(C_b - C_r) \quad (1-41)$$

where  $D$  is diffusion coefficient,  $k$  is the rate of surface reaction,  $v$  is the molar volume of the bulk crystal,  $C_b$  is the concentration of the bulk solution and  $C_r$  is the solubility of the particle.

The morphology of particles is determined by its primary phase and sequential growth, dependent on its reagents, reaction condition, hydrodynamics and calcination

conditions. Most of all, the target is to obtain the desired morphology with a narrow particle distribution, high crystallinity, good dispersibility and high uniformity. Figure 1.33 shows the LaMer curve depicting the process of atoms generation, self-nucleation, formation of seed and growth versus concentration (You and Fang, 2016). For different reaction modes, the LaMer curve can provide a quantitative evaluation of status relevant to particle nucleation or growth from the viewpoint of reaction engineering to control its final morphology and size more easily. You and Fang (2016) have modified the morphology of Ag mesoparticles by controlling particle-mediated growth via  $\text{Ag}^+$  ion concentration and found various well-controlled nanostructures with 1D, 2D, and 3D morphologies as shown in Figure 1.34. Janulevicius *et al.* (2020) have also proved that the best way to control the particle morphology and of  $\text{GdPO}_4$  particles is to change the  $\text{PO}_4^{3-}/\text{Gd}^{3+}$  ratio in the reaction mixture as the primary seeds tend to grow in different ways as the  $\text{PO}_4^{3-}/\text{Gd}^{3+}$  ratio changes from 10 to 100, leading to nanosheets, nanorods or nanospheres (see Figure 1.35). Furthermore, the approach to synthesise particles also affects its morphology and particles size. For instance, the synthesis of  $\text{LnPO}_4$  particles has been studied extensively through different routes (combustion, solid-state, sol-gel, ultrasound, co-precipitation, solvothermal synthesis, hydrothermal microwave treatment) producing diverse morphologies such as nanorods, nanowires, nanofibers, nanocubes, hexagonal nanoprisms, microspheres and submicrostars (Hernández *et al.*, 2014, Kumar *et al.*, 2016, Janulevicius *et al.*, 2020, Dai *et al.*, 2015). Except for the reaction route and reactant concentration, the reaction time can also have an impact on the particle crystal structures and morphologies. Lai *et al.* (2014) have fabricated  $\text{YPO}_4$  through hydrothermal treatment at 180 °C with different additives for different reaction times and have found that  $\text{YPO}_4$  is formed in a variety of patterns (Figure 1.32) with the assistance of additives under different reaction times.

Delgado-Licona *et al.* (2020) have conducted a systematic investigation to fully control the particle size and morphology on the effect of mixing intensities and reaction conditions on the mechanism of particle nucleation and growth via synthesis of  $\text{ZnO}$  in

different Coiled Flow Inverters (CFIs) as shown in Figure 1.36. The experiments reveal that the ratio of  $\text{OH}^-/\text{Zn}^{2+}$  has an obvious effect on the particle shape (spindle-shaped and flower-shaped) with various particle sizes at different CFIs (Figure 1.37 (C)) where its proposed mechanism of ZnO particle formation due to a change in hydrodynamics and reaction conditions in CFIs is shown in Figures 1.37 (A) and 1.37 (B) (Delgado-Licona *et al.*, 2020). Another novel work done by Delgado-Licona *et al.* (2020) is the identification of the limiting factor of nucleation or growth on particles size by determining the Dean number and  $[\text{OH}^-/\text{Zn}^{2+}]$  ratios as shown in Figure 1.38. It has been concluded that small particles may experience higher “local” residence times than those experienced by bigger particles leading to a homogenisation of the particle growth, which is in good agreement with observations from Wiedmeyer *et al.* (2017a) and Wiedmeyer *et al.* (2017b).

### **Particle aggregation, agglomeration, breakage and its influence factors in multiphase reactors**

Except for particle nucleation and growth, the solid particles are also affected by dynamic agglomeration and breakage. The agglomerates are referred to particles rigidly joining together due to the partial fusion (sintering) owing to forces between primary particles as a result of high surface-to-volume ratio and short distance. The assembly of agglomerates significantly changes the properties of bulk powders such as flowability and chemical reactivity (Yao *et al.*, 2002). Aggregates are the assemblage of particles that are loosely coherent (Nichols *et al.*, 2002). Usually, the aggregation is followed by an agglomeration process. Boverhof *et al.* (2015) have demonstrated the particle formation procedure through a bottom-up synthesis approach for synthetic amorphous silica through a pyrogenic process (see Figure 1.39).

Zhou *et al.* (2018) have quantified the impact of agglomerates on the hydrodynamics of fluid flows, demonstrating that the growth and breakage rate increases as the

agglomerates increases. The mode class of particle size of agglomerates is decided by the balance of growth and breakage of agglomerates. In their simulation work, the complex agglomerates are assumed to be “particles” with equivalent size and density in the simulation work (Zhou *et al.*, 2018). Liu *et al.* (2016a) have employed an adhesive CFD-DEM model to hydrodynamics in a fluidised bed with agglomerate breakage and reunion in the process of uniform fluidisation to defluidisation. In another publication, Liu *et al.* (2016b) have visualised agglomerate breakage at different conditions and evaluated the particle dynamics as a function of a dispersion coefficient, indicating that the increment in cohesion is the exact reason for the dispersion coefficient decrement (Ferron *et al.*, 2013).

Chen *et al.* (2016) have claimed that the agglomeration and growth of fine particles is susceptible to the structure and arrangement characteristics of the vortex and a dimensionless agglomeration number  $A_g$  was proposed to evaluate the agglomeration ability of the vortex generator (Liu *et al.*, 2020a). The agglomeration process is accelerated to turbulence due to the disturbance of the flow field leading to the particles colliding and forming larger agglomerates. However, the agglomeration force caused by turbulence is weak and the aggregates are easily fragmented (Chen *et al.*, 2016). In order to increase  $PM_{2.5}$  removal efficiency in electrostatic precipitators (ESP), a pretreatment process was proposed coupling effect of chemical and turbulent agglomeration together (Bin *et al.*, 2018). In addition to chemical reagents, the agglomeration agent molecular chain adsorbs submicron particles to form stable aggregates after the droplets evaporated. Turbulent agglomeration using the disturbance of flow field promotes the particles collide and forms larger agglomerates.

Unlike agglomeration, aggregates are defined as the physical adhesion of crystals by inter bonding. The occurrence of the particle aggregates can be summarised into two major mechanisms: Brownian diffusion (perikinetic aggregation) and fluid motion (*orthokinetic* aggregation) (Gregory, 2009). The process of formation of aggregates is

shown in Figure 1.40 (a) indicating that the aggregates are initiated from the destabilisation of colloidal stable suspension by certain additives (coagulants or flocculants) or hydrodynamic conditions. Gregory (2009) has plotted the ratio of aggregated particle number and an initial primary particle number  $n_T/n_0$  as a function of time is shown in Figure 1.40 (b). The results indicate that the rate of decrease in the total number of particles in the early stages for both mechanisms are similar and the orthokinetic rate becomes relatively much faster at longer times and orthokinetic mechanism is responsible for large aggregates when time is sufficient. Oles (1992) has claimed that an increasing shear rate accelerated the growth and decreased the stable size of the aggregates. Gmachowski (2005) has shown that a small difference in the structure of aggregates results in slightly different hydrodynamic behaviour in both regimes and Gmachowski (2007) has determined that the kinetics of solid–liquid separation can be improved by the aggregation of particles.

Similar to the particle aggregation in continuous phase flow, the breakage of aggregates is significantly influenced by continuous phase hydrodynamics and interfacial interactions. Normally, the concept of “breakage” is referred to the reduction of the size of aggregates that is susceptible to the fluid flow overcoming the attractive inter-particle force holding the individual solid particle together within the aggregates. Research has found that the fragility of an aggregate is generally proportional to its size, that is, as the aggregate increases in size, it becomes more vulnerable to breakage increases as the aggregate particle is enlarged (Pandya and Spielman, 1983, Vassileva *et al.*, 2007). Fluid shear can change the trajectories of the colliding particles and apply a force on the aggregates leading to the breakup of the aggregates resulting in a balance between growth and breakup (Oles, 1992). Xiao *et al.* (2015) have simulated shear-induced particle breakage using the improved breakage kernel, together with the sectional modelling technique, showing internal bonding forces is decisive to the strength of the aggregates and the hydrophobic bonding forces are much stronger than van der Waals’ forces for holding the aggregates against shear breakage. Another conclusion is that

high shear leads to an increase in the aggregation rate and to a decrease of the stable size and vice versa (Oles, 1992).

Although the behaviour of particles are difficult to predict, there are approaches to predict aggregates. Skillas *et al.* (2005) have used a monodisperse particle model tracking the total number concentration of the aggregates, total surface area concentration, total aggregate volume concentration coupled with fluid dynamics of the process and mass transfer of particle generation. However, this model still lacks the feature to track the aggregate shape. Boje *et al.* (2019) have developed a hybrid particle model by employing a particle-number description for small particles to illustrate the complicated particle morphology of particle aggregates by primaries. As shown in Figure 1.41, the mass transfer between the gas-phase and the particle systems from small primary particles with size less than  $N_{\text{thresh}}$  and assembly of aggregate particles, where  $N_{\text{thresh}}$  is the size of the largest particle, is tracked by the particle-number model before the transfer to the space of aggregate particles (Boje *et al.*, 2019). Naseri and Thomson (2019) have done modelling work of carbon black formation to predict aggregates structure in flow reactors considering hydrocarbon (PAH) addition, hydrogen abstraction carbon addition (HACA), particle volume fraction ( $F_V$ ) and particle size distribution (PSD). In their work, the number of primary particles is required to identify with constant-diameter circles as shown in Figure 1.42.

### **1.3 Fluid dynamics effects in particle precipitation processes in multiphase flow system**

#### **1.3.1 Applicable numerical techniques to analyse multiphase system**

In this section, the particle-fluid interactions mainly in liquid-solid system are critically reviewed. When considering the interactions between particles and liquid, the size of the particles must be comparable to the domain dimension (Hashemi *et al.*, 2016). The

bidirectional hydrodynamic interactions between the host fluid and suspended particles should be accurately considered involving the flow pattern and the dynamic properties in the multiphase system. In the aforementioned research, computational fluid dynamics (CFD) is considered as a typically applicable technique rather than an analytical solution for numerical simulations of such problems, which can be classified into direct numerical simulations (DNS), Eulerian-Eulerian methods and the Eulerian-Lagrangian methods (Hashemi *et al.*, 2016). To solve the problem, the Navier-Stokes (NS) equations are used to handle the fluid phase and the equations related to the motion of the particles including particles nucleation, growth, agglomeration and breakup should be carefully considered in such systems.

### **Direct numerical simulation (DNS) approach**

The Direct Numerical Simulation (DNS) approach is one of the most important tools for the investigation of turbulence physics due to the increasing capability of high-performance-computing techniques. The DNS method can resolve all the essential turbulent scales, especially for complicated physical phenomena (turbulent flames (Chen, 2011), bubbles and drops (Esmaeeli and Tryggvason, 1998), acoustics of supersonic and hypersonic flows (Bodony and Lele, 2008)) by numerically solving the Navier-Stokes equations with physically consistent accuracy in space and time. The errors produced from dispersion and dissipation can be minimised once the mesh is sufficiently fine and the time step is short (Alfonsi, 2011). Although DNS resolves all the scales in hydrodynamics and delivers satisfactory results, such intensive work can usually only be performed by high-performance computing (HPC).

Based on the preparation steps in the mesh generation process, the proposed DNS method can be classified into two groups: boundary-fitted methods and non-boundary-fitted methods (Hashemi *et al.*, 2016). The boundary-fitted method is referred to the unstructured grid with an arbitrary shape that completely conforms to the boundaries.

Furthermore, it always quantified with low quality and low accuracy in the interpolation process as shown in Figure 1.43 (a). In addition, the inefficiency of boundary-fitted DNS methods proposed by Feng and Michaelides (2009) revealed that it is not applicable for the system consisting of a large number of particles in the system. On the other hand, the non-boundary-fitted methods defined for a computational mesh do not require being conformed to the real physical boundary and can be generated more easily to circumvent the difficulties and inefficiency of boundary-fitted methods in simulating a large number of particles with the use of a stationary structured or unstructured computational mesh. This removes the requirement for the remeshing procedure as shown in Figure 1(b) (Feng and Michaelides, 2009). Furthermore, the non-boundary-fitted methods can be further categorised into the fictitious domain methods (Glowinski *et al.*, 1999), immersed boundary methods (Peskin) and Lattice Boltzmann method (Ladd, 1993, Ladd and Verberg, 2001), which are different types of non-boundary-fitted DNS methods that have been used to capture the interaction of fluid and particles. Among all these methods, the main idea is that a fixed grid is constructed over the whole fluid domain, containing both the exterior and interior regions of the particle and the appropriate boundary condition is enforced on the particle-fluid interface.

In a number of works, Grötzbach (1983) has provided suggestions on the accuracy of DNS calculations with some reliable but less stringent criteria for those of the Kolmogorov scales as follows:

- Sufficient large domain to record all structures of large-scale;
- Distribute more grid points near the wall to record steep gradients of velocity;
- Select the computational grid smaller than turbulent elements;
- Make the time step smaller than the Kolmogorov time scale.

Del Alamo *et al.* (2004) have reported that the execution of DNS of turbulent channel flow up to  $Re_\tau = 1900$  and they have investigated the spectra and correlations of the velocity fluctuations especially above the buffer layer validating corrections to the similarity assumptions in the logarithmic and outer layer of wall-bounded turbulence. On that basis, Jiménez *et al.* (2004) extended these investigations to the sublayer and buffer regions of the turbulent channel flow. However, the numerical simulation in the logarithmic layer has not been fully feasible (Alfonsi, 2011). DNS is considered as the only numerical way to investigate turbulence physics, especially in a 3D time-dependent turbulent flow.

DNS gives the most exact, error-free solution but there are typically some numerical and other forms of errors. As all length scales from the largest to the smallest are explicitly resolved, DNS requires a grid size smaller than the Kolmogorov scale as described in Equation (1-42)

$$\eta = (\nu/\varepsilon)^{1/4} \quad (1-42)$$

where  $\nu$  is the kinematic viscosity and  $\varepsilon$  is the turbulent kinetic energy dissipation.

### **Eulerian-Eulerian (EE) approach**

The multi-scale attribute is complicated to estimate since the micro-scale and the macro-scale and micro-scale may have mutual effects and the range of the scales is hard to be captured without an advanced experimental or CFD approach (Sardina *et al.*, 2019). The macro-scale is defined as a grid size that is of an order of magnitude larger than the bubble/particle diameter based on Reynolds averaging or volume filtering of the system conservation laws (Fox and O.). The unclosed terms should contain the dynamics of the unresolved scales smaller than the grid size, while their current parametrisation is mostly based on global empirical correlations with suitable

coefficients that can depend on a particular configuration. This micro-scale is referred to grid size much smaller than the bubble/particle diameter that requires a large amount of computational time. A mesoscale CFD simulation resolves these intermediate scales where the liquid phase is usually resolved in a fixed Eulerian grid and discretising the Navier-Stokes equations that include a momentum exchange term with the dispersed phase (Sardina *et al.*, 2019). As to the discretised phase, Eulerian or Lagrangian techniques are applied. Thus, two strategies are practical for mesoscale, that is, Eulerian- Eulerian (EE) and Eulerian-Lagrangian (EL) frameworks.

Both gas and solid phases are treated as interpenetrating continua in the Eulerian-Eulerian (EE) modelling method for multiphase system solving the diluted particle dispersion and it is considered as a computationally less-expensive alternative (Lan *et al.*, 2009). For the Eulerian-Eulerian (EE) model, the main assumption is that the phases interpenetrate at which point both phases have the same dynamic properties in the time-space domain (Meier *et al.*, 2011).

Compared with the Lagrangian approach, less information is available on the overall distribution, residence time and mixing behaviour (Shi *et al.*, 2019). The EE model is also called the two-fluid model by treating two phases that are considered as interpenetrating continua and is computational fast without tracking individual bubbles/particles. The conservation equations of mass and momentum are solved by assuming slow spatial variations of the phasic properties like the volume fractions which is considered as the major drawback for two-fluid model (Lahey and Drew). Another problem appears in the bubble/fluid phase since the two-fluid model governing equation system is non-hyperbolic with the initial-value problem but this cannot affect the particle-gas/liquid system due to the density of particles being always larger than the liquid/gas phase with the drag force larger than the other contributions in the momentum transfer expression (Prosperetti and Tryggvason, 2009). To circumvent this weakness, Sardina *et al.* (2019) raised a solution by adding a dispersion term in the

momentum transfer express to guarantee the hyperbolicity of the incompressible two-fluid model for gas-liquid flows. Additionally, Lucas and Tomiyama (2011) raised a solution by assuming the momentum transfer term between the two phases is expressed as total contributions of drag, virtual mass and lift, addressing the effects induced by the existence of the lift force. Both these approaches stabilise the two-phase model, however, this interpretation is not physically meaningful and remains an open question of the aforementioned investigation (Lhuillier *et al.*, 2013).

The continuity equation of the two-phase model can be derived by volume averaging as follows by Equation (1-43),

$$\frac{\partial \alpha_{vi} \rho_i}{\partial t} + \nabla \cdot (\alpha_{vi} \rho_i \mathbf{u}_i) = 0 \quad (1-43)$$

where the index  $i$  denotes the phase,  $\alpha_v$  denotes the phase volume fraction,  $\rho$  is the density and  $\mathbf{u}$  denotes the velocity vector.

The momentum conservation equation is given by Equation (1-44),

$$\frac{\partial \alpha_i \rho_i \mathbf{u}_i}{\partial t} + \nabla \cdot (\alpha_i \rho_i \mathbf{u}_i \otimes \mathbf{u}_i) = \alpha_i \nabla p + \nabla \cdot (\alpha_i \boldsymbol{\tau}_i) + \alpha_i \rho_i \mathbf{g} + \mathbf{M}_i \quad (1-44)$$

where the pressure  $p$  is shared by both phases,  $\boldsymbol{\tau}_i$  is the viscous stress tensor,  $\mathbf{g}$  is the gravity acceleration and  $\mathbf{M}$  is the interfacial momentum transfer. The flow is postulated to be Newtonian so that the stress tensor can be expressed by Equation (1-45),

$$\boldsymbol{\tau}_i = \mu_i (\nabla \mathbf{u}_i + \nabla \mathbf{u}_i^T) - \frac{2}{3} \mathbf{I} \nabla \cdot \mathbf{u}_i \quad (1-45)$$

where  $\mu_i$  is the dynamic viscosity of one phase.

### **Lagrangian-Eulerian (LE) approach**

The Lagrangian-Eulerian (LE) approach, like the Discrete Element Method (DEM), presents a statistical scheme of the dispersed phase in terms of a stochastic point process based on the forces acting on each particle and their dynamic trajectory according to Newton's laws of motion, which is hard to validate by experimental measurement (Zhu *et al.*, 2008, Subramaniam, 2013). However, the presented DEM models are normally inadequate to simulate full-scale reactor containing millions or more of particles due to computational restrictions (Shi *et al.*, 2015). The mass transfer, momentum and energy for interphase can be signified by the coupling terms in the Eulerian conservation equations for fluid phase with a corresponding closure in the Eulerian-Eulerian two-fluid theory (Subramaniam, 2013).

The continuity and momentum equations are derived by neglecting the contributions of liquid volume fraction with small bubble loadings and the impacts of the collisions-coalescence phenomena (Druzhinin and Elghobashi). In this way, the liquid velocity field satisfies the incompressible Navier-Stokes equations as follows by Equation (1-46).

$$\nabla \cdot (\mathbf{u}_l) = 0 \quad (1-46)$$

The momentum equation including the bubble-induced back-reaction is described by Equation (1-47),

$$\frac{\partial \mathbf{u}_l}{\partial t} + \mathbf{u}_l \cdot \nabla \mathbf{u}_l = -\frac{\nabla p}{\rho_l} + \nu_l \nabla^2 \mathbf{u}_l + (\alpha_i \rho_i \mathbf{u}_i \otimes \mathbf{u}_i) = \alpha_i \nabla p + \mathbf{g} + \mathbf{f}_b \quad (1-47)$$

where  $\mathbf{u}_l$  is the liquid velocity field,  $\rho_l$  and  $\nu_l$  represent the density and kinematic viscosity and  $\mathbf{f}_b$  is the back-reaction term.

## **Comparison between Eulerian-Eulerian (EE) and Lagrangian-Eulerian (EL) approaches**

Patel *et al.* (2017) have compared EE and EL approaches in cluster-induced turbulence of a gas-solid system, revealing that the EE approach exhibits convergence issues under grid refinement, whereas the EL approach can produce reasonable simulation results as a benchmark for EE while it undergoes extracting convergence. Although the direct comparisons between the EE and EL approaches are rarely provided in the aforementioned literature, Sokolichin *et al.* (1997) has offered quantitatively matching results from both strategies in two-dimensional computation.

Hirche *et al.* (2019) have provided a brief overview of gas-solid multiphase methods in Figure 1.44 (a), indicating that both the Eulerian-Eulerian approach and the Eulerian-Lagrangian approach model the gas-phase as a continuum on the basis of the Eulerian theory. However, Eulerian-Eulerian approach models the granular phase as a continuum by applying the Kinetic Theory of Granular Flow (KTGF) (Ding and Gidaspow, 1990), while Eulerian-Lagrangian approach models the granular phase by Lagrangian Particle Tracking (LPT), including:

- Discrete Phase Model (DPM) tracking individual particle according to Newton's Second Law of Motion without considering particle-particle collisions.
- Discrete element method (DEM) resolving each particle individually and the particles undergo a 4-way coupling (Tsuji *et al.*, 1993).
- Multiphase Particle-In-Cell (MP-PIC) considering forces and stresses owing to particle interactions like drag force or interparticle stresses.

Among these methods, DEM is the most accurate and computationally demanding of the three models presented for the Lagrangian treatment of particles.

With the combination of the Eulerian and Lagrangian treatment of the granular phase, the Eulerian solid phase will be transformed into pseudo Lagrangian particles (pseudo L-Particles). The transformed Eulerian solid phase or rather the pseudo L-particles are marked as inactive but inherit the velocities of the Eulerian solid phase as shown in Figure 1.45 (b). The inactive nature of the pseudo L-Particles excludes those particles from the calculation in the LPT. Therefore, the collision detection mechanism by the LPT only detects collisions between Lagrangian particles and Lagrangian particles, Lagrangian particles and pseudo L-Particles, as well as Lagrangian particles and the wall (Hirche *et al.*, 2019).

Furthermore, Chiesa *et al.* (2005) have investigated the flow behaviour of a lab-scale fluidised bed via Eulerian-Eulerian (EE) and Lagrangian-Eulerian (EL) approaches and compared them as shown in Figure 1.46. The results of the particle and bubbles' movement and hydrodynamics are roughly corresponding and the bubble upwards and bubble breakage can be identified in the results of both EE and EL approach, of which the bubble travelling time obtained from the EL agrees much better with the experimental results (Figure 1.47) (Chiesa *et al.*, 2005). Ali and Pushpavanam (2011) compared the EE method and the EL method at low gas flowrates with a modified low Reynolds  $k-\varepsilon$  turbulence mode with analogous results, but there were mismatched results at the high gas flowrates with a standard  $k-\varepsilon$  model. Recent work done by Sardina *et al.* (2019) has proposed the same results in mesoscale dynamics in the gas-liquid system but the EE approach has been found with instabilities compared with the better performance of the EL approach with closure models for mesoscale dynamics. Pouraria *et al.* (2020) has employed Eulerian-Eulerian-Lagrangian approach to model both dilute and dense particulate flows where the continuous phase is modelled on a fixed Eulerian grid and particles are tracked by using Lagrangian model.

Xu *et al.* (2020b) have compared the Lagrangian and Eulerian approaches under the same operating conditions with an emphasis on their performance in predicting particle deposition in turbulent flows (Figure 1.48) and the non-dimensional deposition velocity for the two approaches at the same depth are presented in Figure 1.49. Four regions represent the non-dimensional deposition velocity on the four-floor plates along the flow direction and the non-dimensional deposition velocity on the first plate is significantly larger than that of the other three plates behind it. Xu *et al.* (2020b) also demonstrated the difference between Lagrangian (Figure 1.50 (a)) and Eulerian approaches (Figure 1.50 (b)) on the total deposition mass and removal mass of particulate fouling and total fouling mass on the floor with time under the same conditions. Compared with the Eulerian approach, the Lagrangian approach predicts a higher fouling mass on the floor than the Eulerian approach because the Lagrangian approach predicts a higher concentration gradient near the floor, which will directly lead to increased particle deposition (Xu *et al.*, 2020b). Octau *et al.* (2020) have compared the accuracy and computational cost of EE and EL approaches and concluded DEM-CFD coupled with Euler-Lagrange is the most computationally intensive method to resolve hydrodynamics with specific particles-particles interactions. Figure 1.51 shows instantaneous velocity vectors and volume fraction of particles and both simulation through Eulerian-Eulerian (EE) and Lagrangian-Eulerian (EL) approaches showed discrete particles and Eulerian solid particle phase move from high velocity (HV) chamber to low velocity (LV) chamber through the baffle and back via a slot (Zhang *et al.*, 2018).

### **1.3.2 Hydrodynamic interactions between particles and fluid/gas shear flows**

#### **Interfacial momentum transfer**

The momentum transfer between phases is principally a function of relative velocity highly relevant to flow regime. The vertical flow consists of basic flow regimes of bubbly flow, slug flow, chum flow, annular flow and inverted annular flow (Govier and Aziz, 1972). The interfacial friction in general is highest in those flow regimes, which result in high interfacial areas. In relating the interphase friction to the difference in average phase velocities, the effect of non-uniform velocity (velocity profile) needs to be considered, as does the effect of averaging flow structures (for example, the use of a single droplet diameter) (Aksan, 2017).

The interfacial momentum transfer can be analysed by separating the terms containing the drag and lift force, virtual mass force, wall forces, turbulent dispersion force and history forces (Rzehak *et al.*, 2017). The wall effect can be neglected without solid boundaries (Rzehak *et al.*, 2017) and the turbulent dispersion force is ignorable turbulent fluctuations of liquid velocity is linearly proportional to the liquid turbulent viscosity (Burns *et al.*, 2004). As for the dispersion term, Panicker *et al.* (2018) suggested that it should be taken into account for both laminar and turbulent flow as well as the drag force due to the disturbances in the flow caused by the presence of other bubbles. However, in the multiphase flow with low bubble-loadings, the drag force can be neglected (Sardina *et al.*, 2019). The ratio between the history and drag forces is monotonous to the particle size but independent of the particle density (Daitche, 2015). They also stated that the previous effects are negligible for small bubbles. Therefore, drag, virtual mass and lift are the main forces to be considered in both EE and EL approaches as shown in Table 1.2.

For expressions for both frameworks,  $d_b$  is the bubble diameter and  $C_D$  is the drag coefficient which is calculated based on the bubble Reynolds number  $Re_b$  according to the Schiller-Naumann correlation Schiller-Naumann correlation. The major challenge in the multiphase system is to model interphase forces, especially the drag force and

the lift force. Based on the phases grouping, specific models can be applied as shown in Table 1.3.

### **Interfacial mass transfer**

According to the investigation done by Higbie (1935), mass transfer correlation can be based on the penetration theory and the boundary layer equations. The expression of interphase mass transfer coefficient is based on these two models. Besides, other mass transfer models have been suggested such as the surface renewal model (Danckwerts, 1951), the film penetration model (Toor and Marchello, 1958) and the eddy cell model (Lamont and Scott, 1970). Zhou *et al.* (2020) have summarised the gas-liquid mass transfer models in their work. For the gas-liquid system, the mass transfer rate is related to the solubility of the gas. The mass transfer rate is predominately controlled by the gas film for soluble gas but is controlled by liquid film for insoluble gas (Muroyama and Fan, 1985). Most of the aforementioned research have laid their emphasis on the correlation of the gas-liquid volumetric mass transfer parameter  $k_l a$  where both parameters  $k_l$  (mass transfer coefficient) and the  $a$  (interfacial area) are highly correlated with hydrodynamic characteristics. Nevertheless,  $k_l a$  serves as a global parameter and is of vital importance to analyse  $k_l$  and  $a$  separately. The mass transfer coefficient  $k_l$  is decided by the turbulence energy dissipation rate, the bubble slip velocity and the average bubble diameter on the basis of various models (Wang and Wang, 2007).

Lewis and Whitman (1924) have proposed Two-film model by assuming the interface of two phases as two stationary films on the basis of molecular diffusion in the interphase retention layer. The mass transfer coefficient can be expressed by Equation (1-48),

$$k_l = \frac{D_L}{\delta} \quad (1-48)$$

where  $D_L$  is the diffusion coefficient and  $\delta$  is the thickness of the gas film and the liquid film.

Higbie (1935) has proposed the Penetration model based on the penetration of dissolved gas into the liquid phase through the molecular diffusion in equal residence time and the expression of mass transfer coefficient is given by Equation (1-49),

$$k_l = \frac{2}{\sqrt{\pi}} \sqrt{D_L} \left( \frac{\varepsilon}{\nu_l} \right)^{1/4} \quad (1-49)$$

where  $\nu_l$  is the kinematic viscosity of liquid.

Danckwerts (1951) developed the Surface renewal model by counting the residence time following the random age distribution with a variable interphase retention layer. The expression for surface renewal model is given by Equation (1-50)

$$k_l = \frac{2}{\sqrt{\pi}} \sqrt{\frac{D_L v_b}{d_b}} \quad (1-50)$$

where  $v_b$  is the bubble slip velocity and  $d_b$  bubble diameter.

Lamont and Scott (1970) have developed the Eddy cell model with isotropic turbulence through the effect of turbulence at the interface, which can be expressed by Equation (1-51),

$$k_l = K \sqrt{D_L} \left( \frac{\varepsilon}{\nu_l} \right)^{1/4} \quad (1-51)$$

where  $\varepsilon$  is the local rate of turbulence energy dissipation or volume fraction.

The gas-liquid interfacial area  $a$  is dependent on the gas holdup and the average bubble diameter ( $d_b$ ) based on the population balance model (PBM) is denoted by Equation (1-52).

$$a = \frac{6\varepsilon_g}{d_b} \quad (1-52)$$

In a gas-liquid system the mass transfer source term of gas can be expressed as Equation (1-53).

$$S_{g \rightarrow l} = k_l a (C_l^* - C_l) \quad (1-53)$$

The term  $(C_l^* - C_l)$  represents the concentration difference between the saturated state and the actual state in the specialised liquid.

In a three-phase system, the existence of solid particles may have two-sided effects on the gas-liquid mass transfer behaviour concerning the effect of the superficial gas, liquid velocities and particle circulating rate (Zhou *et al.*, 2017b).  $k_l a$  is monotonically increased with rising gas velocity irrespective of the diameter of the particles (Zhou *et al.*, 2020). Additionally, the liquid velocity is relevant to the particle size: the mass transfer coefficient of large particles larger than 1 mm is independent of liquid velocity, but the mass transfer coefficient is significantly enhanced when liquid velocity increases (Nguyen-Tien *et al.*, 1985). Moreover, Yang *et al.* (2001) also experimentally verified that  $k_l a$  increases at low solid hold-up due to enhanced turbulence caused by the existence and movement of particles, whereas it decreases at low solid hold-up with enhanced apparent viscosity and bubble breakage. Zhang *et al.* (2015) have carried out studies of liquid-liquid mass transfer in a slug flow through circular capillaries based on computational fluid dynamics (CFD) and the flow field within individual slugs with interphase mass transfer with reactions between two consecutive slugs of the organic

phase and aqueous phase was investigated (see Figure 1.52). The concentration field over the computational domain is governed by the general convective-diffusive equations given by Equations (1-54) and (1-55),

$$\frac{\partial C_{11}}{\partial t} + \mathbf{u}_1 \cdot \nabla C_{11} = D_{11} C_{11} \quad (1-54)$$

$$\frac{\partial C_{12}}{\partial t} + \mathbf{u}_2 \cdot \nabla C_{12} = D_{12} C_{12} \quad (1-55)$$

where  $u$  is the velocity field, and  $C_{11}$  and  $C_{12}$  are the concentrations of species 1 in phase 1 (organic phase) and phase 2 (aqueous phase), respectively.

Thus, the volumetric mass transfer coefficient  $k_L a$  is then given by Equation (1-56) involving the logarithmic-mean driving force,

$$k_L a = \frac{1}{t} \ln \left( \frac{C_{2,sat} - C_{2,t=0}}{C_{2,sat} - C_{2,t=t}} \right) \quad (1-56)$$

where  $C_{2,sat}$  is the saturated concentration of species A in phase 2 and  $C_{2,t=0}$  is the transient concentration at time  $t$ .

The aqueous phase diffusivity can greatly affect the mass transfer process as shown in Figure 1.53 (a), which indicates that greater diffusivity makes species transfer easier in the aqueous phase (Zhang *et al.*, 2015). Besides, the mass transfer performance varies greatly among different types of reactions. It can be seen from Figure 1.53 (b) that there are remains at very low concentrations in the aqueous phase during the reaction period at large reaction rate constants  $k_2 = 650 \text{ m}^3/(\text{kmol}\cdot\text{s})$  and  $k_2 = 65 \text{ m}^3/(\text{kmol}\cdot\text{s})$  and it is regarded as a relatively fast reaction and mass transfer-dominated. For those slow reactions at  $k_2 = 6.5 \text{ m}^3/(\text{kmol}\cdot\text{s})$ ,  $k_2 = 0.65 \text{ m}^3/(\text{kmol}\cdot\text{s})$  and  $k_2 = 0.325 \text{ m}^3/(\text{kmol}\cdot\text{s})$ , the concentration of the aqueous phase increases fast and it is the dominant chemical

reaction (Zhang *et al.*, 2015). Lu *et al.* (2018) have simulated the mass transfer problems of a nine-sphere cuboid cluster and a random generated spherical cluster composed of active catalysts and inert particles via direct numerical simulation (DNS) and the mutual influence of particles on their mass transfer performance were investigated. The active ratio (AR) is defined as the ratio of the number of active particles to the total particle number as denoted by Equation (1-57).

$$AR = \frac{N_{active}}{N_{total}} \quad (1-57)$$

The results are shown in Figure 1.54 where clustering is found to have a negative influence on the mass transfer performance, which can be improved by dilution with inert particles and higher Reynolds numbers with the distribution of active/inert particles potentially leading to large variations in the cluster mass transfer performance and the individual particle deep inside the cluster may possess a high Sherwood number (Lu *et al.*, 2018).

Additionally, an attempt was made by Haugen *et al.* (2018) to correlate the effects of the turbulence on the droplet's mass transfer rate by using the Sherwood number. The expressions for the mass and heat transfer rate are similar and denoted by Equations (1-58) and (1-59), respectively.

$$\kappa = \frac{ShD}{d_p} \quad (1-58)$$

$$\kappa_{th} = \frac{NuD_{th}}{d_p} \quad (1-59)$$

where  $d_p$  is the particle radius,  $Sh$  is the Sherwood number;  $Nu$  is the Nusselt number;  $D$  and  $D_{th}$  are the mass and thermal diffusivities. The  $Sh$  and  $Nu$  numbers, expressed

by Equations (1-60) and (1-61), are related to the dimensionless Schmidt number ( $Sc$ ) and Prandtl number ( $Pr$ ) at low and medium Reynolds numbers.

$$Sh = 2 + 0.69Re_p^{1/2}Sc^{1/3} \quad (1-60)$$

$$Nu = 2 + 0.69Re_p^{1/2}Pr^{1/3} \quad (1-61)$$

where the Schmidt number is the ratio of fluid viscosity and the mass diffusivity,  $Sc = \nu/D$ , and the Prandtl is the ratio of fluid viscosity and the heat diffusivity,  $Pr = \nu/\alpha$ .

Haugen *et al.* (2017) have used the Sherwood to define the reactant consumption rate as denoted by Equation (1-62),

$$\alpha_{hom} = n_p A_p \bar{\kappa} = n_p A_p \frac{\overline{Sh}D}{d_p} \quad (1-62)$$

where  $n_p$  is the particle number density,  $A_p$  is the external surface area of the particles number density, and  $\bar{\kappa}$  and  $\overline{Sh}$  are the mass transfer coefficient and Sherwood number averaged over all particles, respectively.

When particles are sufficiently small and the relative velocity can be neglected ( $Re_p=0$ ), the modelled reactant consumption can be expressed by Equation (1-63).

$$\alpha_{Sh, Da} = \lim_{h \rightarrow 2, Da \rightarrow 0} \alpha = n_p A_p \frac{2D}{d_p} \quad (1-63)$$

$Da$ , the Damköhler number, is defined as the ratio of the typical turbulent and chemical time scales and is expressed by Equation (1-64).

$$Da = \frac{\tau_L}{\tau_c} \quad (1-64)$$

Furthermore, the normalised reactant consumption rate can be expressed by Equation (1-65).

$$\tilde{\alpha} = \frac{\alpha}{\alpha_{Sh, Da}} = \frac{\alpha_c \tau_L}{\alpha_c \tau_L + Da \overline{Sh}/2} \frac{\overline{Sh}}{2} \quad (1-65)$$

For diffusion-controlled reactions, the modified reactant decay rate is considered to be a measure of the relative modification to the mass transfer rate due to the effect of turbulence. This means that a modified Sherwood number that accounts for the effect of turbulence can now be defined as shown by Equation (1-66).

$$Sh_{mod} = 2\tilde{\alpha} = \overline{Sh} \frac{\alpha_c \tau_L}{\alpha_c \tau_L + Da \overline{Sh}/2} \quad (1-66)$$

For the limit of small Damköhler numbers, this expression reduces to  $Sh_{mod} = Sh$ , as expected (Haugen *et al.*, 2017).

Al-Sood and Birouk (2007) have also attempted to correlate the effect of the freestream turbulence on the droplet's mass transfer rate by using the Sherwood number over a wide range of freestream temperatures. The general form of the correlation between the Sherwood number and Schmitt number is expressed by Equation (1-60) but a turbulent coefficient  $C_T$  has been added into the original equation that considers the effect of turbulence, defined by Equation (1-67),

$$Sh = A' + B' Re^{1/2} Sc^{1/3} (C_T) \quad (1-67)$$

where  $A'$  and  $B'$  are constants.

Previous research has considered different constants and turbulent coefficient based on different correlations. Yearling (1996) denoted the correlations as shown in Equation (1-68).

$$Sh = 2.0 + Re^{\frac{1}{2}}Sc^{\frac{1}{3}}(0.562 + 0.1807d^{\frac{1}{2}} + 0.0672I_{\infty}(I_{\infty} + 0.05)Re_{\infty}^{1/2}) \quad (1-68)$$

Hiromitsu and Kawaguchi (1995) have developed the correlations by considering the influence of flow turbulence on the evaporation rate of the suspended droplet in a hot air flow as shown in Equation (1-69).

$$Sh = 0.549Re^{1/2}Sc^{1/3}(ReI)^{0.066} \quad (1-69)$$

Birouk *et al.* (1996) have developed the correlations by considering the turbulence effects on the vaporisation of mono-component single droplets, as shown in Equation (1-70).

$$Sh = 2.0 + 0.52Re^{\frac{1}{2}}Sc^{\frac{1}{3}}(1 + 3.397I^{0.843}) \quad (1-70)$$

Based on these previous studies, Al-Sood and Birouk (2007) have developed their correlations as shown in Equation (1-71).

$$Sh = 2.0 + 0.914Re^{\frac{1}{2}}Sc^{\frac{1}{3}}(1 + 1.235I^{0.372}) \quad (1-71)$$

From the results above, the effect of turbulence weakens as the freestream temperature increases although the freestream turbulence has an effect on the droplet mass transfer even at temperatures higher than the liquid boiling temperature. This can be attributed to the fact that as the temperature increases the molecular vapour diffusion increases as well, which reduces the residence time of the vapour around the droplet and thus

decreases the time for turbulence to act (Al-Sood and Birouk, 2007). Park and Farrell (1987) developed a two-dimensional numerical model to predict the effect of freestream turbulence on the evaporation of *n*-hexane droplet. Although Park's numerical model lacked experimental validation, Park and Farrell (1987) concluded that the freestream turbulence enhances the evaporation rate particularly at elevated Reynolds numbers. This affects the turbulence on the mass transfer rate and surface reaction rates on both sides. The formation of particle clustering decreases the mass transfer rate owing to the quick consumption of gas reactant inside the cluster and few particles left outside the cluster. On the other hand, the increased difference of mean velocity between the particle and gas phase may potentially increase the overall mass transfer rate (Haugen *et al.*, 2018).

#### **1.4 Fundamental methodologies of controllable synthesis of nano- and micro-sized particles and process intensification (PI) for multiphase flows**

##### **1.4.1 Approaches to synthesise ultrafine particle synthesis**

The production of micro/nanoparticles of various morphologies like nanorods, nanowires, nanofibers, nanocubes, hexagonal nanoprisms, microspheres, submicrostars have been reported in nano-technological applications recently. The particles size, as well as other physical properties involving density, porosity, specific surface area, solubility, reactivity of synthesised particles are desired to be precisely controlled in the preparation process (Barnard, 2006). Various techniques have been employed in order to synthesise ultrafine particles such as combustion, sol-gel, solid state, vapor deposition method, template method, co-precipitation, solvothermal synthesis, hydrothermal synthesis, pulse laser ablation, microwave, ultrasound irradiation treatment and biological synthesis.

#### **Combustion and calcination**

Combustion is the most direct way to prepare a stable powder product such as metallic oxide and ceramic with an intensive consumption of energy. An example is nanometer ceramics-structural alumina  $\text{Al}_2\text{O}_3$  powder with a high melting point ( $\sim 2050^\circ\text{C}$ ) and thermodynamic stable phase at high temperature. Zhang *et al.* (2012) have prepared  $\text{Al}_2\text{O}_3$  of well-distributed in a narrow range (20~30nm) by combustion chemical deposition with a low concentration of reactants, proper detention time and fast cooling technology condition. However, the morphology of products are non-uniform with the majority being either spherically shaped or of an orthohexagonal columnar shape. Few of these products are of a rhombohedral shape (Zhang *et al.*, 2012). Storozhev and Yermakov (2015) have carried out the combustion of gaseous nano-sized  $\text{Al}_2\text{O}_3$  and its fast condensation. Lewis (2009) has invented technology for the application of metal oxide coatings onto substrates via combustion deposition, which is able to provide mixed or graded microstructure metal oxide coatings in addition to the situ nanoparticle matrix loading of metal oxide coatings.

Calcination is solid-state combustion acting as post-process of which temperature also affects the morphology and texture of crystalized particles. Juibari and Tarighi (2020) have investigated the thermal effect on the framework of  $\text{CuO}@NiO$  nanocomposites at two different calcinated temperatures (400 and 500 °C) following the precipitation of copper nitrate by NaOH (Cu:Ni molar ratio of 1:2). The SEM images of  $\text{CuO}@NiO$  at 400 °C ( $\text{CuO}@NiO$ -400) and 500 °C ( $\text{CuO}@NiO$ -500) are presented in Figure 1.55 and show that the calcination temperature dominates the morphology and texture of nanocomposites with more agglomeration occurring at higher calcination temperature (Juibari and Tarighi, 2020). By observing the results of nitrogen adsorption-desorption isotherms of  $\text{CuO}@NiO$  nanocomposites, it can be suggested that the calcination process at 500 °C destroys the porous structure of the nanoparticle where the surface area of  $\text{CuO}@NiO$ -500 and  $\text{CuO}@NiO$ -400 is  $2.183 \text{ m}^2 \text{ g}^{-1}$  and  $94.02 \text{ m}^2 \text{ g}^{-1}$ , respectively as shown in Figure 1.56 (Juibari and Tarighi, 2020). Purnama *et al.* (2019)

have also discussed the calcination temperature dependence of the structural and magnetic properties of co-precipitated cobalt ferrite and found that the nanoparticle organisation changes from single particles separating from one another (calcination temperatures at 600 °C and 800 °C) to compact nanoparticle granules. This result demonstrates that the heat energy from the temperature calcination is used by the nanoparticles to conglomerate and then diffuse in order to form larger granular particles and for a greater distribution (Purnama *et al.*, 2019). The calcination temperature also has a significant effect on the hysteresis of cobalt ferrite nanoparticles. Figure 1.57 presents a hysteresis curve for cobalt ferrite nanoparticle samples at three different calcination temperatures (600°C, 800 °C and 1000°C). The typical SEM images and particles size distribution analysis (inset) for cobalt ferrite after calcination for six hours under three different temperatures are shown in Figure 1.58 (Purnama *et al.*, 2019).

The magnetisation, denoted by  $M_s$ , is enhanced as the calcination temperature increases, which is attributed to the cation's redistribution where the  $Fe^{3+}$  ions migrate to octahedral sites with an increase in the calcination temperature (Purnama *et al.*, 2019). Similar work concerning the effects of calcination temperature on the phase formation and particle size of  $Zn_2Nb_3O_{11}$  powder was carried out by Xiang *et al.* (2019). They indicated that a continuous increment in crystallinity with broader diffraction lines as the calcination temperature increases (see Figure 1.59 (b)) and its morphology tends to regular and angular as shown in Figure 1.59 (a).

### **Hydrothermal treatment**

Another thermal technique is hydrothermal and is considered to be an easy, clean and fast way of preparing the particles in an aqueous solution at moderate temperatures without producing hazardous waste. The hydrothermal method is a chemical reaction in water sealed in a pressure vessel with both high temperature and pressure. Janulevicius *et al.* (2020) have applied the hydrothermal route to produce stable

precursors material  $\text{GdPO}_4 \cdot n\text{H}_2\text{O}$  using tartaric acid as a chelating agent without surface modification. Zhang *et al.* (2019) have reported the preparation of silver nanoparticles-nanocellulose with improved high bactericidal efficiency via the hydrothermal method. Li *et al.* (2016) have displayed a novel, facile and eco-friendly approach to synthesise nano-ZnO nanoflakes through a novel co-gelation and low-temperature hydrothermal synthesis with lamellar thickness of about 100 nm. Xiang *et al.* (2019) clearly illustrated that the particle growth process of Alumina ( $\text{Al}_2\text{O}_3$ ) in hydrothermal reaction in autoclave signifies the great impact of raw material ratio, reaction temperature and filling factor on the properties of on thermal behaviour, functional groups, phase composition, microstructure and the specific surface of precursors (Figure 1.60). Figure 1.61 displays the SEM images of products prepared at different hydrothermal reaction temperatures of a) 120 °C; b) 140 °C; c) 160 °C; d) 180 °C. Spherical particles are obtained at 120 °C with a particle size of about 2µm and turn into coral-like alumina particles, which become aggregated together when the temperature rises to 140 °C (Xiang *et al.*, 2019). Products are alumina with acicular morphology as the temperature continually increases.

It is found that the hydrothermal treatment can affect the physical-chemical structures of lignite and help lignite liquefaction through hydrothermal treatment at low temperatures (130°C~190°C). Habib *et al.* (2008) have investigated the effect of temperature and time on the particle characterisation of Barium titanate ( $\text{BaTiO}_3$ ) nanopowder using  $\text{TiO}_2$  powder precursors. XRD results show that the crystallite size of obtained  $\text{BaTiO}_3$  for the type-A precursor is in the range of 40–95 nm and the type-B precursor is in the range 35–52 nm under different hydrothermal temperatures as shown in Figure 1.62. However, one of the drawbacks is that the process of crystal growth is invisible since the autoclaves are stainless steel. Furthermore, the amorphous and crystalline regions for  $\text{BaTiO}_3$  sample under temperatures of 60°C, 90°C and 150 °C for 48 hours using type-B Ti precursor can be observed by HRTEM images (Figure 1.63) and the amorphous structure tends to be regularly crystallised as the

hydrothermal temperature increases from 60°C to 150°C (Habib *et al.*, 2008). From the SEM images shown in Figure 1.64, the change can be seen from irregular to spherical and a final compact faceted shape for BaTiO<sub>3</sub> is obtained using the type-B precursor (Habib *et al.*, 2008).

### **Sol-gel method**

The sol-gel method is another well-established synthetic approach to prepare novel metal oxide nanoparticles as well as mixed oxide composites and its schematic process is shown in Figure 1.65. It is considered to be a wet-chemical process involving the formation of colloidal suspension (Lefebvre and Sol) and gelation (gel) of the colloidal in the continuous liquid phase, followed by hydrolysis, condensation and the drying process. This method has achieved potential control over the texture by providing a highly entangled network of nanofibers and surface properties of the materials. Over the previous decade, sol-gel processing is finding applications ranging from new catalysts and separations media to the composites of inorganic and biological systems and complex hierarchical structures that mimic life itself (Loy, 2003).

One of the most important applications of sol-gel treatment is coating with the most commonly reported coating material to be TiO<sub>2</sub> and SiO<sub>2</sub> (Uhlmann *et al.*, 1997). It has been reported that SiO<sub>2</sub>, ZrO<sub>2</sub>, Al<sub>2</sub>O<sub>3</sub>, TiO<sub>2</sub> and CeO<sub>2</sub> are the most familiar coating materials due to their good protection and stability and can be used for metallic materials such as stainless steel, aluminium, copper and magnesium via sol-gel treatment (Wang and Bierwagen, Tian *et al.*, 2017). Sol-gel treatment is also used for compounds with reinforced structure and matrix, such as SiC and alumina reinforced nanocomposites (Mo *et al.*, 2005). The preparation of nanometre to millimetre-sized TiO<sub>2</sub> nanostructure has been recorded by researchers recently using cellulose hydrogel nanofibers template via sol-gel, which demonstrate outstanding features of high surface area and improved photocatalytic activity (Habibi and Jamshidi, 2020, Gunji *et al.*,

2016). However, compared with coating techniques, this method suffers from a slow process and inherently demonstrates cracks in the body of the solidified gel. Besides, most of the sol-gel materials like TEOS and TMOS have proven to be somewhat toxic and expensive to implement.

The condensation of colloidal suspension is greatly affected by reaction circumstances such as reagent concentration, pH and temperature. Considering the hydrolysis and condensation reactions involving the net formation of a siloxane bond from a silanol and an alkoxysilane, the condensation rate is decisive by pH in the aqueous solution and the first condensation reaction of an alkyltriol only occurs at a minimum pH of 4.5. Varying pH changes are shown in Figure 1.66 (Loy, 2003). Baqiah *et al.* (2020) have prepared  $\beta$ - $\text{Bi}_2\text{O}_3$  films via sol-gel method process from solutions with varying precursor concentration and found that the contact angle (CA) of  $\beta$ - $\text{Bi}_2\text{O}_3$  films increases as the molarity increases from 0.05 to 0.20 and the corresponding contact angles are  $\sim 60^\circ$  to  $\sim 101^\circ$  as shown in Figure 1.67. Muthee and Dejene (2020) have examined structural and optical properties of titanium dioxide ( $\text{TiO}_2$ ) nanoparticles (NPs) via sol-gel method with variation of concentration of tetra isopropyl orthotitanate (TIP). The information about crystallite size, structure and lattice strain is given in Figure 1.68 as the ethanol volume ratios of 1:63 is suggested as the best volume ratio to obtain the smallest crystal size mostly preferred for the lower electron-hole recombination rate (Muthee and Dejene, 2020).

### **Co-precipitation**

Co-precipitation is a technique used to synthesise composites from aqueous solutions by means of reduction from nonaqueous solutions, electrochemical reduction, and decomposition of metalorganic precursors with simultaneous particle nucleation, growth, coarsening, and/or agglomeration occurring in the process (Rane *et al.*, 2018). Co-precipitation methods are mostly used to synthesize precursors fluoride-, oxide-, or

oxyfluoride-based nanophosphors and most precursors are in the form of chloride, nitrate, or acetate with a solvent such as distilled water, ethanol, cyclohexane or *N,N*-dimethyl formaldehyde (Nair *et al.*, 2018). Both metals and metal oxides are formed from aqueous solution and the metal chalcogenides are formed by reactions of molecular precursors. Li *et al.* (2020) have reported that the feasible and effective co-precipitation of  $\text{Fe}^{2+}$ ,  $\text{Cu}^{2+}$ ,  $\text{Zn}^{2+}$ ,  $\text{Cd}^{2+}$  and  $\text{Ni}^{2+}$  mechanochemical activation with  $\text{CaCO}_3$  to stabilize metals in water with a neutral pH. Buinachev *et al.* (2021) has found that the size, shape and porosity of hydrous zirconia particles are determined by the pH of precipitation and the effect of pH precipitation on the phase composition and crystallite size of calcined samples are also discussed. Mirzaee *et al.* (2020) have prepared Manganese doped Nickel ferrites nanoparticles by means of precipitation of  $\text{Fe}^{3+}$  and  $\text{Ni}^{2+}$  ions in an aqua solution of NaOH and modified the process by adding dopant ions after nucleation leading to enhanced strain in the structure and intensified orientation peak preferred. Cao *et al.* (2021) has demonstrated that potassium hydroxide is predominant to sphericity and dense structures to synthesise spherical carbon particles through a spray drying method.

Furthermore, a reverse co-precipitation method has been reported to synthesise cobalt ferrite nanoparticles with perfect cubic spinel ferrite type structure by adding precursor ions into the precipitant solution in advance and ensuring precipitant in a supersaturated state and generation of nanoparticles of a smaller size (Huixia *et al.*, 2014). Conclusively, the coprecipitation process is readily controlled and provides possibilities to modify the particle surface state and the overall homogeneity at low temperatures without any organic solvent being involved. However, the coprecipitation process is time-consuming and does not work well with reactants of various precipitation rates (Rane *et al.*, 2018). Massart (1981) has fabricated the iron oxides and metal ferrite nanoparticles by co-precipitation. Aqueous solutions of Fe(III) and M(II) salts are usually mixed in an alkaline solution leading to the formation of the

magnetic precipitate as shown in Figure 1.69. Massart (1981) also claimed that the control of the particle characteristics can be achieved through adjusting molar ratio between M(II) and Fe(III) cations, reaction temperature, pH value, and type/concentration of alkaline agent, resulting in different nanoparticle characterization such as size, shape, and chemical composition. Xu *et al.* (2020a) have synthesised  $\text{Na}_3\text{GaF}_6:\text{Mn}^{4+}$  red phosphors through a mild co-precipitation method and the result of the XRD patterns of  $\text{Na}_3\text{GaF}_6:\text{Mn}^{4+}$  synthesised with different  $\text{Mn}^{4+}$  doping concentrations is shown in Figure 1.70. They indicated that doping small amounts of  $\text{Mn}^{4+}$  does not alter the crystal structure of  $\text{Na}_3\text{GaF}_6$  at the diffraction peaks but it can change the crystallinity. Figure 1.71 displays the SEM images of  $\text{Na}_3\text{GaF}_6:\text{Mn}^{4+}$  samples prepared with different hydrofluoric acid concentrations and irregular polyhedron morphology of  $\text{Na}_3\text{GaF}_6:\text{Mn}^{4+}$  samples are affected when HF concentration increases from 10 wt% to 30 wt% (Xu *et al.*, 2020a). Although sol-gel is considered to be a simple and effective approach to synthesis particles, previous research has attempted to modify the process and realise controllable synthesis through the alteration of reaction temperature, pH value and type/concentration in the sol-gel process.

#### **1.4.2 Process intensification (PI) for ultrafine particle synthesis in the multiphase system**

Process intensification has been put forward with the concept of “any chemical engineering development that leads to a substantially smaller, cleaner and more energy-efficient technology” (Stankiewicz and Moulijn, 2000). The aforementioned research on process intensification has ranged widely in microstructure reactors, multifunctional reactors, microwave/ultrasound-assisted processes, alternative energy sources involving laser and luminous energy (Pangarkar, 2017). The targets of process intensification can be specified as (1) high atom efficiency of sustainable processes, (2) eco-environment friendly, (3) low capital cost, (4) low energy requirement, (5)

elimination of reagents or catalysts, (6) low pressure/temperature and (7) safe operation (Pangarkar, 2017).

### **Ultrasound irradiation**

Among these methods, ultrasound synthesis has been frequently applied and considered as facile and a fast approach for producing nanoparticles with controlled morphology. With the assistance of ultrasound irradiation, ultrasonic cavitation generates and produces cavitation micro-bubbles that undergo bubble growth, violent oscillations and finally collapse releasing energy with high local temperature and pressure and giving rise to acoustic streaming, liquid jets and shock waves (Dong *et al.*, 2020).

The general effect of ultrasound can be summarised into two aspects: acoustic streaming due to the impulse from shock wave produced by the ultrasound transducer and ultrasonic cavitation owing to the bubble collapse and burst as the result of the ultrasound irradiation. To investigate the cavitation effect induced by ultrasound, Lebon *et al.* (2017) have simulated the bubble behaviour below the sonotrode in water by a high-order acoustic model with validation of the measurement of pressure in liquid aluminium. It can be seen from Figure 1.72 that bubbles tend to be a cloud-like structure after an initial transient period ( $<100 \mu\text{s}$ ), which develops into a stable cone-like structure below the sonotrode afterwards. Further investigation was carried on the position away from the sonotrode and its effect produced by the ultrasound transducer. In Lebon's research, 5 points were selected to predict pressure in aluminium domain as shown in Figure 1.73 (a) and its acoustic pressure predicted is displayed in Figure 1.73 (b). It shows that the pressure is dependent on the distance and the acoustic pressures predicted decrease dramatically with distance away from the sonotrode and away from the axis, with the point 2 cm below the sonotrode axis registering the highest pressure of 9.5 MPa (Lebon *et al.*, 2017). Sajjadi *et al.* (2015) have analysed the fluid flow pattern and acoustic streaming under ultrasound irradiation with the power range of

100W-400W using Particle Image Velocimetry (PIV) and the experimental setup is shown in Figures 1.74 and 1.75.

The employment of an ultrasound transducer can significantly enhance the mixing performance. Parvizian *et al.* (2011) have proved the improvement of both macro-mixing and micro-mixing due to convection by its cavitation effect via employing a Dushman reaction coupled with a neutralisation reaction with the adoption of activation of piezoelectric transducers (PTZs) in the tank. The comparison between ultrasound-activated system and the non-activated system is shown in Figure 1.76. Parvizian *et al.* (2012) also employed the Dushman reaction and the piezoelectric wave transducers at the same frequency in a novel continuous flow tubular sonoreactor (Figures 1.77 (a) and 1.77 (b)). In addition, the macromixing was examined through the residence time related to the location of piezoelectric transducers (PTZs) as shown in Figure 1.77 (c) and the effect of micromixing in terms of segregation index ( $X_S$ ) and micromixing time ( $t_m$ ).

According to the PIV results, the velocity increases with power amplitude until the maximum jet-flow velocity of about 1.23 m/s in the system is reached and the velocity at the highest power (400 W) was almost 5 times greater than that of the lowest power setting which occurred at about 24 cm/s, indicating that the recirculation flow also increased slightly with power (Sajjadi *et al.*, 2015). Consequently, the measured velocity behaved similarly as estimated one by CFD simulation, in which velocity also increased with ultrasound power.

The combination of micro-channel and the ultrasound can provide a confined environment with merit of enhanced heat/mass transfer and intrinsic safety with high specific surface area and solving the clogging problem (Yue *et al.*, 2007). Furthermore, it has been reported that the size-controlled gold nanoparticles can be optimised by the number of induced-ultrafine bubbles and the pulsed-off time of pulsed ultrasound

(Yasuda *et al.*, 2020). It was shown that the presence of the ultrasound bubbles intensified the cavitation effect with ultrafine gold particle being adsorbed onto the surface of bubbles and the particle size decreasing with increasing ultrafine bubbles (Yasuda *et al.*, 2020).

With the assistance of ultrasound, the synthesis process is intensified, and the reaction rate achieved is high. However, this method is only feasible with heat-insensitive reactions and the process is difficult to scale up since the turbulent micro-streaming is complex and difficult to enlarge.

### **Microwave**

The preparation of nanoparticle with the assistance of microwave has become a new method in recent years. The presence of microwave is used in an intensified and combined way with those fundamental processes for producing fine particles such as microwave-assisted hydrothermal synthesis, microwave-assisted hydrolysis, microwave-assisted and -precipitation as shown in Figure 1.78 (Komarneni and Katsuki, A.Gerbec *et al.*, 2005). Goyal and Vlachos (2020) elucidated that the microwave takes effect through heating by resolving the electromagnetic field from the single particle to the entire cavity. Microwave-assisted routes have been applied for the one-pot synthesis of a large number of bimetallic nanoparticles and nanostructures such as Au, Ag, Pd, Pt, Cu, In, and combinations thereof in the solution (Polshettiwar *et al.*, 2009). The microwave-hydrothermal method provides access to a large variety of binary and ternary oxides such as ZnO, CuO, SnO<sub>2</sub>, BaTiO<sub>3</sub>, etc (Huang *et al.*, 2008, Zhao *et al.*, 2004, Nyutu *et al.*, 2008). Nyutu *et al.* (2008) have proved that the particle size, phase purity and morphology of tetragonal BaTiO<sub>3</sub> is susceptible to microwave frequency. A.Gerbec *et al.* (2005) hves proved that microwave heating not only enhances the rate of formation but also enhances the material quality and size distribution without suffering thermal gradient effects. Kheradmandfard et al. (2021) has argued the excellence of microwave-assisted

synthesis of high-entropy oxide nanoparticles for Li-ion battery applications, including ultrafast speed, low temperature, nanoscale and high-purity products, and low cost.

Caminata *et al.* (2020) have argued that the employment of microwave is able to greatly reduce the synthesis duration to generate the polymeric precursor for nanometric powders of  $\text{BaZr}_{0.08}\text{Ti}_{0.92}\text{O}_3$  from 15 hours to 2 hours without increasing the reaction temperature. Another advantage pointed out by Caminata *et al.* (2020) is that microwave heating requires lower energies for the heat treatment of the crystallisation of BZT powders, making it possible to support the hypothesis that the high distribution of the binding sites between the polymer chains and the cations is promoted at a greater distance between the citrate groups, therefore generating more crystallisation nuclei. Except for the aforementioned merits, the application of the microwave is expected to enhance crosslinking reactions that produce more resistant structures within shorter synthesis timeframes and at a moderate temperature. In the process of microwave-assisted acid-basic catalysed synthesis of silica gels, as shown in Figure 1.79, a gelled polymeric network is formed in a shorter time with a higher degree of cross-linking. A stronger structure during the gelation stage since microwave interactions with the polar functional groups produce vibrations that promote certain reactions to a greater extent than conventional methods. It increases the condensation rate between partial and total hydrolysed-molecules (Flores-López *et al.*, 2020). The microwave-assisted synthesis of silica gels offers not only the clear advantage of reducing the synthesis time, but also the possibility of using moderate operating conditions of temperature and pressure with a preferred structure and texture.

Bilecka and Niederberger (2010) have summarised the pros and cons of microwave technology. It plays a significant role in a future environmentally friendlier in the process intensification of chemical reactions especially in synthetic nanotechnology due to its simple operation, high heating rates, indirect contact between the heating source and the reactants, control of the reaction parameters, higher yields, better selectivity due to reduced side

reactions, improved reproducibility and automation, and high throughput synthesis. However, it suffers the defects of high cost and scale-up problems.

### **1.4.3 Controllable synthesis of micro/nanoparticles via hydrodynamic interaction**

The whole process of particle synthesis can be summarised into the steps of reactant mixing, chemical reaction, particle formation (nucleation, growth, agglomeration and breakage), particle shaping. However, the well-known particles synthesis control approaches considering the crystallisation mechanism of nanostructures with classical models are overly simplistic, assuming constant surface and bulk energies while disregarding particle interactions, mass transfer effects, competing kinetics, and external forces. However, the hydrodynamic mechanisms should be considered into the particle synthesis control including flow pattern and liquid/particle interaction. It is the final but vital stage for growing properly sized and good quality crystals by controlling the shear-induced flow pattern that is controlled by hydrodynamics with the concepts of ‘hydrodynamic assembly’ and ‘shear controllable synthesis’.

Experimental work and complementary simulations were completed to build a universal stability criterion, demonstrating that hydrodynamic interactions alone drive this process of pattern formation independent of the particle size, shape, and chemical composition (Varga *et al.*, 2019). Attempts have been made by Jose *et al.* (2018) to mechanistically explain the effects of shear on nucleation, growth, and oriented assembly using insights gleaned from liquid transmission electron microscopy (LTEM), atomic force microscopy (AFM), powder X-ray diffraction (XRD) and shear-induced aggregation kinetic modelling. It has been found that the high shear rates accelerate the crystallisation of 2D nanoplatelets via oriented attachment and speed up mixing performance in a high shear microfluidic annular flow resulting in changes of particle size distribution (see Figure 1.80 (a)). In addition, the mixing region produced by

collision and hydrodynamics focuses on two-liquid annular flows, which stabilises into a wavy annular thin film and the film thickness remains unchanged resulting in a constant shear rate (see Figure 1.80 (b)) (Jose *et al.*, 2018, Han *et al.*, 2015).

Conversely, Wessel and Ball (1992) have claimed that the suspended particles display weak attractive interactions resulting in the formation of clusters disrupted by the stresses induced underflow. Consequently, the overall behaviour of a suspension of weakly attractive particles is susceptible to a subtle competition between shear and attraction, shaping both the cluster size and cluster shape. The addition of ultrasound may produce cavitation bubbles and speed up the mixing, but it can also change the hydrodynamic behaviour.

In a reactor with stator and rotor assembly, the characteristics of shear rate and pressure area are quite different based on the magnitude of the rotation velocity of the rotor and the bubble behaviour changes drastically under turbulent conditions where bubbles undergo transient turbulent condition and resembles the behaviour of a cavity under acoustic conditions (Pandit, 1997). Further modelling of hydrodynamic cavitation was conducted by Badve *et al.* (2015) indicating that the number of vortices is higher with strengthened turbulence being responsible for the generation of transient cavitation in the hydrodynamic cavitation reactor. The influence on particle could be attributed to the synergistic hydrodynamic effect of shear-induced flow and micro-streaming behaviour. The consecutive work done by Ferron *et al.* (2013) and Mao *et al.* (2019) has verified that the ultrasound-induced cavitation bubbles may impact the particle aggregation and shape modification processes.

### **1.5 Scale-up of multiphase reactor on basis of similarity principle**

A bench-scale laboratory cannot satisfy the requirements of industrial processes, but upscaling to the full industrial scale is a complex and troublesome endeavour (Durán

Martínez *et al.*, 2016). In particular, the scale-up of multiphase reactors is not only relevant to geometry size but closely associated with hydrodynamics and chemical conversion inside the multiphase reactor subject to many eventualities and pitfalls causing a drastic deterioration in the reactor's performance and economy. Furthermore, important design parameters especially in the multiphase flow are manifold, like particle properties, mass and heat transfer, bubble growth (Rüdisüli *et al.*, 2012). Glicksman (1988) has put forward the full set of characteristic parameters by scaling of fluidised bed using two-fluid model via nondimensionalising the governing mass and momentum conservation equations. Those microreactors with excellent transport properties are expected to be embraced by researchers, however, scaling the benefits associated with the microenvironment has proven to be a daunting challenge (Dong *et al.*, 2021).

### **1.5.1 Scale-up process**

The procedure of the scale up a reactor to commercial size is based on proper simplifications and approximations and educated guesses. In this way, except for applying feasible and reasonable scaling-up laws, the successful scale-up relies on the combination of computer simulations and experimental models. Kelkar and Ng (2002) have given an example of scaling up the fluidised bed and summarised a referable process as shown in Figure 1.81. The screening procedure is the first step that the fluid regime should be implemented by considering the hydrodynamics of bubbling, turbulence and circulation. This is followed by the construction of the lab-scale reaction and the pilot-scale process before full-scale plant construction for the test. The final and most important step is to construct the full-scale plant referring to the scaling-up laws and modification.

### 1.5.2 Scaling laws

The conventional scale-up is mostly based on the criteria of geometric similarity, thermal similarity and chemical similarity while more considerations of hydrodynamic effects have been put forward and applied. Rüdüsüli *et al.* (2012) claimed that the most popular approach nowadays is to achieve hydrodynamic and reactive similarity in multiphase flow like two fluidised beds is to use sets of dimensionless numbers, which have to be kept constant at both scales. Nevertheless, there is an additional similarity should be taken into account such as bioreactors with consideration of physiological similarity (Pangarkar, 2015).

#### **Geometric similarity**

Generally, geometric similarity is the most direct way of maintaining similarity between two reactors (denoted as reactor 1 and reactor 2) that have corresponding points (Rane *et al.*, 2018). The given coordinates satisfy the relationship expressed by Equation (1-72).

$$\frac{x_1}{x_2} = \frac{y_1}{y_2} = \frac{z_1}{z_2} = \text{const} \quad (1-72)$$

Except for the entire geometric ratios, multiple elements such as impeller and baffles and their dimensional relationship to the vessel diameter should ideally be the same as in the laboratory. For instance, the ratio of the impeller diameter to the vessel diameter and the ratio of the clearance of the impeller from the bottom to the vessel diameter are two important parameters that have an impact on the overall performance of the stirred vessel (Alfaro-Ayala *et al.*, 2015).

#### **Mechanical similarity-dynamic, hydrodynamics and turbulence similarity**

Mechanical similarity consists of three subseries: static similarity, kinematic similarity and dynamic similarity (Worstell, 2014). Static similarity is referred to deformations on two bodies and is relevant under a constant applied stress that is usually applicable in Civil Engineering. Dynamic similarity demands that the ratios of various forces affecting the motion are equal as shown in Equation (1-73).

$$\frac{F_1}{F_2} = \frac{F_1}{F_2} = const \quad (1-73)$$

Another approach to realise the dynamic similarity is to require the ratios of different forces in the same system constant as shown in Equation (1-74).

$$\frac{F'_1}{F_1} = \frac{F'_2}{F_2} = const \quad (1-74)$$

An example is Reynolds number that is a ratio of parameters representing inertial and viscous forces. The similarity is shown in Equation (1-75).

$$Re_1 = Re_2 = const \quad (1-75)$$

Although the gross assumptions were made to be empirically correlated to experimental data, they may deviate as the *Re* number varies due to the features of the structure. The force varies significantly in space in a given multi-phase reactor as is evident from Kolmogorov's theory on the decay of turbulence from a large scale to the final stage where viscous dissipation is predominant (Pangarkar, 2015). For instance, the inertial energy is highest in the stream discharged from the impeller in the stirred reactor and decays as the fluid moves away from the impellers to the least and farthest point away from the impellers where the viscous forces dominate. In this case, the Reynolds number decreases from the highest to the lowest far from the impellers. With rigorous treatment, the representative Reynolds number should be a value obtained by the triple

integration of the local Reynolds number over the entire reactor space using the velocity that prevails at the various locations. Analogous common-used dimensionless groups pertinent to multiphase reactors are listed in Table 1.4.

The final subcategory is the hydrodynamic similarity which is most complex and reliable on equipment geometry and operation conditions. It relates to scaling approaches where the sets of dimensionless groups are kept similar in reactors of different sizes. This ensures that the physical phenomena at the two scales are similar.

Sanderson *et al.* (2007) have applied the full set and simplified scaling criteria to simulate 2D and 3D bubbling fluidised beds using a coupling of Computation Fluid Dynamics (CFD) and the Discrete Element Method and concluded that the simplified scaling criteria performed well at low velocities and performed poorly for 2D simulations. Link *et al.* (2009) have applied hydrodynamics similarity to the fluidised beds by keeping the similarity of Reynolds number and minimum fluidisation velocity in the base and scaled cases with the same geometry of a fluidised bed but with a lower computational time due to the smaller number of particles and larger time step. Unfortunately, the scaling factor has to be limited by the grid and the mesh size is required to be larger than the particle size in the case (Link *et al.*, 2009). Qi *et al.* (2008) have modified the scaling parameter  $G_s/(\rho_p U_g)$  by adding the effect of Froude number as  $Fr_D^{-0.3} G_s/(\rho_p U_g)$  and fully developing the zone of the risers of the gas–solid flow, which achieves similarity under different operating conditions.

Nevertheless, Shaikh and Al-Dahhan (2010) have argued that hydrodynamic similarity is a necessary but not sufficient condition in the case of gas holdup in bubble columns and have shown that mere hydrodynamic similarity on the global level does not yield similar mixing or turbulence structure. Besides, hydrodynamic similarity is inadequate to yield similar transport properties in the multiphase systems since some hydrodynamic regime similarity is based on global parameters that are indirectly related

to the local parameters as shown by several investigators (Nikhade and Pangarkar, 2007, Shaikh and Al-Dahhan, 2010).

Therefore, a new concept of ‘turbulence similarity’ is induced to specify the level of turbulence experienced by the particles by tracing out similar paths. Besides, it is of vital importance to determine the heat and mass transfer (Pangarkar, 2015). It is defined by Nikhade and Pangarkar (2007), referring to particles in their path experiencing the same turbulence intensity related to the microscopic mixing. Chasnov (1996) has achieved turbulence similarity by developing three distinct high Reynolds number similarity states by means of invariance of the low wavenumber coefficients of the three-dimensional kinetic or potential energy spectrum considering the decay of statistically homogeneous velocity and density fluctuations in a stably stratified fluid. Cafiero and Vassilicos (2018) have developed the turbulence similarity by hypotheses of the dissipation scaling with the constant dissipation coefficient  $C_\varepsilon$  defined as the ratio of the turbulence dissipation rate to the rate of non-linear energy losses by the largest turbulent eddies. This was supported by the experimental data of self-similarity from 18 to at least 54 nozzle sizes. The rate of energy losses is proportional to the  $3/2$  power of the turbulent kinetic energy  $k$  divided by a length-scale which characterises the size of the largest turbulent eddies (Cafiero and Vassilicos, 2018). Once the same inverse power-law relation of energy spectrum is applied, it does not matter that the Reynolds number changes.

The combination of turbulence similarity with hydrodynamics similarity ensures that particles travel similar paths while experiencing similar local hydrodynamics. It should be noted that the principles of turbulence similarity are still vague and requires further discussion.

### **Other similarities**

Thermal similarity and chemical similarity are commonly used and work well with the aforementioned scaling laws in the industrial scaling up process. Thermal similarity demands that the ratio of the temperature difference at corresponding locations of a geometrically similar mechanism or process are equal and is usually assisted with geometric similarity and kinematic similarity (Pangarkar, 2015).

Chemical similarity occurs when the ratio of concentration differences at all corresponding locations. This procedure is inefficient to predict the similar status of mass and heat transfer rates, hydrodynamic regime and turbulence similarity in a multiphase flow. Thus, the prerequisite is that geometrically and thermally similar systems, which also exhibit hydrodynamic regime and turbulence similarity, are chemically similar when the corresponding concentration differences bear a constant ratio to one another (Pangarkar, 2015). The concept has explicitly exhibited equality of the ratios of rate of product formation to the rate of bulk flow and rate of product formation to the rate of convective mass/heat transfer.

However, the scale-up approaches applied nowadays from lab-scale to industrial scale is integrated with the consideration of mixing, chemical reaction, hydrodynamics, heat and mass transfer, and economic factors. Rehage *et al.* (2020) have successfully proposed a novel scale-up method based on complete similarity named “complete similarity approach” (CSA) through keeping the dominant mixing time scale equal by realising similarity of the Damköhler number ( $Da$ ), Reynolds number ( $Re$ ) and reactant concentration (see Figure 1.82).

### **1.5.3 Validation of scaling**

After applying the scaling laws in multiphase flow reactor discussed above, the consecutive step is to validate the hydrodynamic or chemical behaviour by measuring and quantitatively comparing dependent hydrodynamic phenomena such as the flow

regime, turbulence intensity, vortex structure, bubble and particle characteristics, which are supposed to be identical at both scales (Pangarkar, 2015). However, the prerequisite to achieve hydrodynamic similarity is that the two reactors have equivalent geometrical properties and that all relevant physical quantities governing the particular physical problem are identical (Grace and Taghipour, 2004). Both direct and indirect experimental validation can be applied. The direct methods include the measurement of bubble properties like diameter, growth rate, size distribution, frequency and rise velocity through the technique of high-speed camera, particle image velocimetry, video analysis (Stein *et al.*, 2002). Indirect experimental validation comprises the measurement of the fluctuations and calculation of validation quantity by means of time series analysis (Stein *et al.*, 2002).

The specific validation tools are introduced in this part. An example is to measure the pressure fluctuation inside non-reactive bed fluidized bed retrieve information on the hydrodynamic state of fluidised beds (van der Schaaf *et al.*, 2002). Ommen *et al.* (2006) have reported an indirect approach to validate the enlarged bubbling fluidised beds via power spectral density (PSD) of which periodic wave signal yields the power carried by each frequency of the wave. Sanderson *et al.* have reported a similar approach applied to scale-up validation regarding circulating beds (Sanderson *et al.*, 2004). Based on scaling-up principles, the pressure and frequency should be nondimensionalised as shown in Equations (1-76) and (1-77), respectively,

$$p^* = \frac{p}{\rho_0 g H_s} \quad (1-76)$$

$$f^* = \frac{f D}{u_{mf}} \quad (1-77)$$

where  $p$  is the measured pressure (Pa),  $\rho_0$  is the packed bed bulk density (kg/m<sup>3</sup>),  $g$  is the acceleration due to gravity (m/s<sup>2</sup>),  $H_s$  is the settled bed height (m),  $f$  is the measured

frequency (Hz),  $D$  is the bed diameter (m) and  $u_{mf}$  is the minimum fluidisation velocity (m/s).

Another indicator to validate the scaling-up performance is the Probability Density Function (PDF) that is closely relevant to the superficial gas velocity. The particle size also depends on the fluidisation regime and the reactor geometry (Sanderson and Rhodes, 2005). Moreover, in the case of the bubble column or bubble-induced fluidised bed, the bubble characteristics can be used as validation tools such as the mean bubble volume fraction, the nondimensional mean bubble frequency, the mean pierced bubble length, the mean bubble rise velocity and the local mean visible bubble flow rate per unit area (Brown and Brue, 2001). L fstrand *et al.* (1995) have derived the dimensionless drag coefficient (Equation (1-78)). Wiman and Almstedt verified that it serves as a good validation parameter as long as the particles do not respond to gas velocity fluctuations (Wiman and Almstedt, 1998). Nevertheless, the drag coefficient is an inadequate scaling parameter for comprehensively describing fluidisation.

$$F^* = \frac{F_D}{m_p g} = \frac{1}{(1-\epsilon_{mf})g\rho_p} \left[ \frac{\Delta p}{H} \right]_{\epsilon=\epsilon_{mf}} = \frac{Re_p}{\epsilon_{mf}\phi^2 Ar_p} \left( 150 \frac{1-\epsilon_{mf}}{\epsilon_{mf}} + 1.75\phi Re_p \right) \quad (1-78)$$

Here,

$$Re_p = \frac{d_p U_{f1} \rho_g}{\epsilon_{mf} \mu_g} \quad (1-79)$$

and

$$Ar_p = \frac{d_p^3 \rho_p \rho_g g}{\mu_g^2} \quad (1-80)$$

where  $F_D$  is drag force acting on the individual particles ( $N$ ),  $m_p$  is mass of single particle (kg);  $U_{f1}$  is the superficial fluidisation velocity (m/s),  $\rho_g$  is gas density (kg/m<sup>3</sup>),  $\rho_p$  is particle density (kg/m<sup>3</sup>),  $\epsilon$  is the bed voidage,  $\epsilon_{mf}$  is the bed voidage at minimum

fluidisation,  $\phi$  is the sphericity of particles,  $Ar_p$  is the Archimedes number and  $\mu_g$  is dynamic viscosity of gas (kg/ms).

## 1.6 Concluding remarks and recapitulation

It is challenging to accurately predict the behaviour of turbulent solid-liquid multiphase flow since (1) the wide spectrum of length scales and time scales are affected by the microscopic physics of particles and both the fine and large structures of turbulences; (2) the high resolution of the turbulence scale is due to the small-scale of particles; (3) the low universality of the turbulence model and highly reliable on experience (Octau *et al.*, 2020). Consequently, it is of vital importance to understand the fundamentals behind the hydrodynamics of multiphase systems and the particle synthesis process. To achieve this, five criteria have been discussed and reviewed (1) multiphase reactors; (2) the mixing, chemical reaction and particle synthesis process; (3) the fluid dynamics effects; (4) controllable synthesis and process intensification; (5) reactor scale-up.

Multiphase reactors are selected based on characteristics such as mixing performance, retention time, chemical reaction and hydrodynamic properties. Among the wide variety of multiphase reactors, the stirring tank reactor, the Taylor-Couette reactor and the impinging jet reactor have been introduced and their distinctive features analysed. Stirring tank reactors are the most conventional and widely used reactors with the merits of ease of use and maintenance under moderate conditions. In order to break part of the vortices and avoid dead zones in order to increase mixing efficiency, impellers are installed with the proper number, type, location and degree of baffling.

In the multiphase reactor, the turbulent environment is of vital importance for particle synthesis. Therefore, the turbulence fundamentals and turbulence models are presented including Direct numerical simulation (DNS), Large-eddy simulation (LES), Reynolds averaged Navier-Stokes (Kurian and Fransson) and the hybrid method. To further

investigate the behaviour of turbulence in multiphase reactors, the turbulent energy spectrum is introduced, which refers to energy transfer on the basis of vortices size.

After introducing multiphase reactors and their interiors, the process of mixing, chemical reactions and the particle synthesis process have been presented. For this research, the focus is on meso- and micro- mixing behaviour, quantitatively described by the mixing time and mixing quality factor. The chemical reactions were discussed based on gas-liquid two-phase reactions and gas-liquid-solid three-phase reactions. The gas-liquid two-phase reactions can be sub-categorised into 4 regimes based on the reactor rate with a different expression for the mass transfer rate. For gas-liquid-solid three-phase reactions where the intrinsic rate is afforded by a given catalyst, the mass transfer rate is determined by both gas-liquid and solid-liquid mass transfer steps. The particle synthesis process comprises particle nucleation, growth, aggregation, agglomeration and breakage.

In part 1.3, the fluid dynamics effects and particle-fluid interactions mainly in the liquid-solid system were critically reviewed. Simulation work of computational fluid dynamics (CFD) has been reviewed and describe direct numerical simulations (DNS), Eulerian-Eulerian methods and the Eulerian-Lagrangian methods. The particle-fluid interactions were introduced via interfacial momentum transfer and interfacial mass transfer.

The fundamental and intensified methodology of the particle synthesis process was next discussed. Techniques that comprise of combustion, hydrothermal, sol-gel method and co-precipitation have been employed. The process intensification has been put forward with the purpose of higher efficiency, better mixing performance, eco-environment friendly, low capital cost, and low energy requirement. Ultrasound irradiation is used for process intensification with intensified local turbulence caused by cavitation micro-streaming. The microwave is usually coupled with other processes like microwave-

assisted hydrothermal synthesis, microwave-assisted hydrolysis, microwave-assisted co-precipitation with high heating rates. Both of these techniques play a significant role in shaping an environmentally friendlier future in the process intensification of chemical reactions, especially in synthetic nanotechnology due to its simplistic operation. Regardless of the methodologies employed, the objective is to realise controllable synthesis and the mechanism of the hydrodynamics effect on particles should be further discussed.

After achieving the bench-scale particles synthesis process, there is a need to upscale it to the full industrial scale. The subsequent process is the screening procedure, lab-scale, pilot-scale and full-scale. The entire scaling-up process is reliant on scaling laws especially geometric similarity. Hydrodynamic similarity and turbulence similarity are achieved by proportionality to the dimensionless number pertinent to multiphase reactors. Thermal similarity and chemical similarity are not used individually but assist with geometric similarity and hydrodynamic similarity. Considering the energy consumption, construction of concentration spectrum is done by Large-eddy-simulation (LES) simulation. After scaling up the reactor, the full-scaled plant is validated experimentally either through direct or indirect means by comparing the result with hydrodynamic effects. The scale-up of particle synthesis process is carefully designed in aspect of both efficiency and economy.

## References

- A.GERBEC, J., MAGANA, D., WASHINGTON, A. & F.STROUSE, G. 2005. Microwave-Enhanced Reaction Rates for Nanoparticle Synthesis. *Journal of the American Chemical Society*, 127, p.15791-15800.
- AKIN, A. & KAHVECI, H. S. 2019. Effect of turbulence modeling for the prediction of flow and heat transfer in rotorcraft avionics bay. *Aerospace Science and Technology*, 95, 105453.
- AKSAN, N. 2017. Target phenomena in nuclear thermal-hydraulics. *Thermal-Hydraulics of Water Cooled Nuclear Reactors*. Elsevier.
- AL-SOOD, M. A. & BIROUK, M. 2007. A numerical study of the effect of turbulence on mass transfer from a single fuel droplet evaporating in a hot convective flow. *International journal of thermal sciences*, 46, 779-789.
- ALCAMO, R., MICALÉ, G., GRISAFI, F., BRUCATO, A. & CIOFALO, M. 2005. Large-eddy simulation of turbulent flow in an unbaffled stirred tank driven by a Rushton turbine. *Chemical Engineering Science*, 60, 2303-2316.
- ALFARO-AYALA, J. A., AYALA-RAMÍREZ, V., GALLEGOS-MUÑOZ, A. & URIBE-RAMÍREZ, A. R. 2015. Optimal location of axial impellers in a stirred tank applying evolutionary programming and CFD. *Chemical Engineering Research and Design*, 100, 203-211.
- ALFONSI, G. 2011. On direct numerical simulation of turbulent flows. *Applied Mechanics Reviews*, 64.
- ALI, B. A. & PUSHPAVANAM, S. 2011. Analysis of unsteady gas–liquid flows in a rectangular tank: Comparison of Euler–Eulerian and Euler–Lagrangian simulations. 37, 268-277.

BADVE, M. P., ALPAR, T., PANDIT, A. B., GOGATE, P. R. & CSOKA, L. 2015. Modeling the shear rate and pressure drop in a hydrodynamic cavitation reactor with experimental validation based on KI decomposition studies. *Ultrasonics Sonochemistry*, 22, 272-277.

BAK, B. D. & KALMÁR-NAGY, T. 2018. A linear model of turbulence: reproducing the Kolmogorov-spectrum. *IFAC-PapersOnLine*, 51, 595-600.

BALDYGA, J. & BOURNE, J. 1999. Turbulent mixing and chemical reactions. . Chichester: Wiley.

BALDYGA, J. & BOURNE, J. R. 1989. Simplification of micromixing calculations. I. Derivation and application of new model. 42, 83-92.

BALDYGA, J. & POHORECKI, R. 1995. Turbulent micromixing in chemical reactors — a review. *Chemical Engineering Journal & the Biochemical Engineering Journal*, 58, 183-195.

BAQIAH, H., TALIB, Z. A., LIEW, J. Y. C., SHAARI, A. H., ZAINAL, Z. & F, L. M. 2020. Effects of precursor concentration on the microstructural, optical and photoelectrochemical properties of Bi<sub>2</sub>O<sub>3</sub> films synthesized by sol-gel method. *Optik*, 206, 164303.

BARNARD, A. S. 2006. Using theory and modelling to investigate shape at the nanoscale. *Journal of Materials Chemistry*, 16, 813.

BILECKA, I. & NIEDERBERGER, M. 2010. Microwave chemistry for inorganic nanomaterials synthesis. *Nanoscale*, 2, 1358-0.

BIN, H., YANG, Y., CAI, L., ZHULIN, Y., ROSZAK, S. & LINJUN, Y. 2018. Experimental study on particles agglomeration by chemical and turbulent agglomeration before electrostatic precipitators. *Powder Technology*, 335, 186-194.

- BIROUK, M., CHAUVEAU, C., SARH, B., QUILGARS, A. & GÖKALP, I. 1996. Turbulence effects on the vaporization of monocomponent single droplets. *Combustion science and technology*, 113, 413-428.
- BODONY, D. J. & LELE, S. K. 2008. Current status of jet noise predictions using large-eddy simulation. *AIAA journal*, 46, 364-380.
- BOJE, A., AKROYD, J. & KRAFT, M. 2019. A hybrid particle-number and particle model for efficient solution of population balance equations. *Journal of Computational Physics*, 389, 189-218.
- BOTHE, D., STEMICH, C. & WARNECKE, H.-J. 2006. Fluid mixing in a T-shaped micro-mixer. *Chemical Engineering Science*, 61, 2950-2958.
- BOVERHOF, D. R., BRAMANTE, C. M., BUTALA, J. H., CLANCY, S. F., LAFRANCONI, M., WEST, J. & GORDON, S. C. 2015. Comparative assessment of nanomaterial definitions and safety evaluation considerations. *Regulatory Toxicology and Pharmacology*, 73, 137-150.
- BRITO, M. S. C. A., DIAS, M. M., SANTOS, R. J., LOPES, J. C. B. & FONTE, C. P. 2020. Fully resolved modelling and simulation of micromixing in confined impinging jets. *Chemical Engineering Science*, 211, 115299.
- BROWN, R. & BRUE, E. 2001. Resolving Dynamical Features of Fluidized Beds from Pressure Fluctuations. *Powder Technology*, 119, 68-80.
- BURNS, A. D., FRANK, T., HAMILL, I. & SHI, J. M. The Favre Averaged Drag Model for Turbulent Dispersion in Eulerian Multi-Phase Flows. 5th International Conference on Multiphase Flow, ICMF'04, 2004.
- CAFIERO, G. & VASSILICOS, J. 2018. Non-equilibrium turbulence scalings and self-similarity in turbulent planar jets. *Proceedings of the Royal Society A: Mathematical, Physical and Engineering Sciences*, 475.

CAMINATA, L. P., PERDOMO, C. P. F. & KIMINAMI, R. H. G. A. 2020. Effect of microwave heating during evaporation solvent and polymeric precursor formation in synthesis of BaZr<sub>0.08</sub>Ti<sub>0.92</sub>O<sub>3</sub> nanopowders. *Journal of Solid State Chemistry*, 121586.

CHASNOV, J. R. 1996. Some similarity states of stably stratified homogeneous turbulence. *Dynamics of Atmospheres and Oceans*, 23, 183-192.

CHEN, C. C. & TAO, C. J. 2000. Condensation of supersaturated water vapor on submicrometer particles of SiO<sub>2</sub> and TiO<sub>2</sub>. *Journal of Chemical Physics*, 112, 9967-9977.

CHEN, D., WU, K. & MI, J. 2016. Experimental investigation of aerodynamic agglomeration of fine ash particles from a 330 MW PC-fired boiler. *Fuel*, 165, 86-93.

CHEN, J. H. 2011. Petascale direct numerical simulation of turbulent combustion—fundamental insights towards predictive models. *Proceedings of the Combustion Institute*, 33, 99-123.

CHENG, K., LIU, C., GUO, T. & WEN, L. 2019. CFD and experimental investigations on the micromixing performance of single countercurrent-flow microchannel reactor. *Chinese Journal of Chemical Engineering*, 27, 1079-1088.

CHIESA, M., MATHIESEN, V., MELHEIM, J. A. & HALVORSEN, B. 2005. Numerical simulation of particulate flow by the Eulerian–Lagrangian and the Eulerian–Eulerian approach with application to a fluidized bed. *Computers & Chemical Engineering*, 29, 291-304.

COLOMBO, M. & FAIRWEATHER, M. 2019. Influence of multiphase turbulence modelling on interfacial momentum transfer in two-fluid Eulerian-Eulerian CFD models of bubbly flows. *Chemical Engineering Science*, 195, 968-984.

DAI, J., LI, G. C., LV, M., ZHOU, R. S. & LI, X. Hydrothermal synthesis and

luminescent properties of spherical LaPO<sub>4</sub>: Ln<sup>3+</sup> (Ln<sup>3+</sup>= Eu<sup>3+</sup>, Dy<sup>3+</sup>, Ce<sup>3+</sup>, Tb<sup>3+</sup>). *Advanced Materials Research*, 2015. Trans Tech Publ, 396-400.

DAITCHE, A. 2015. On the role of the history force for inertial particles in turbulence. *Journal of Fluid Mechanics*, 782, 567-593.

DANCKWERTS, P. 1951. Significance of liquid-film coefficients in gas absorption. *Industrial & Engineering Chemistry*, 43, 1460-1467.

DAVIES, J. T. 1985. *Heterogeneous Reactions*. : by L.K. Doraiswamy and M.M. Sharma. John Wiley and Sons, New York, 1984, 2 Vols. 40, 1808-1809.

DECOURSEY, W. J. 1987. MASS TRANSFER WITH CHEMICAL REACTION. 21, 164-167.

DEFRAEYE, T., VERBOVEN, P. & NICOLAI, B. 2013. CFD modelling of flow and scalar exchange of spherical food products: Turbulence and boundary-layer modelling. *Journal of Food Engineering*, 114, 495---504.

DEL ALAMO, J. C., JIMÉNEZ, J., ZANDONADE, P. & D MOSER, R. 2004. Scaling of the energy spectra of turbulent channels. *Journal of Fluid Mechanics*, 500, 135.

DELGADO-LICONA, F., LÓPEZ-GUAJARDO, E. A., GONZÁLEZ-GARCÍA, J., NIGAM, K. D. P. & MONTESINOS-CASTELLANOS, A. 2020. Intensified tailoring of ZnO particles in a continuous flow reactor via hydrothermal synthesis. *Chemical Engineering Journal*, 396, 125281.

DING, J. & GIDASPOW, D. 1990. A bubbling fluidization model using kinetic theory of granular flow. *Aiche Journal*, 36, 523-538.

DONG, Z., UDEPURKAR, A. P. & KUHN, S. 2020. Synergistic effects of the alternating application of low and high frequency ultrasound for particle synthesis in microreactors. *Ultrasonics Sonochemistry*, 60, 104800.

DRUZHININ, O. A. & ELGHOBASHI, S. Direct numerical simulations of bubble-laden turbulent flows using the two-fluid formulation. *Physics of Fluids*, 10, 685.

DURÁN MARTÍNEZ, F. L., JULCOUR, C., BILLET, A.-M. & LARACHI, F. 2016. Modelling and simulations of a monolith reactor for three-phase hydrogenation reactions — Rules and recommendations for mass transfer analysis. *Catalysis Today*, 273, 121-130.

DURBIN, P. & SHIH, T. 2005. An overview of turbulence modeling. *Modelling and Simulation of Turbulent Heat Transfer*, 16, 3-31.

DUROUDIER, J.-P. 2016. 1 - Stirring in a Vat: Homogenization of Pasty Products. In: DUROUDIER, J.-P. (ed.) *Solid-Solid, Fluid-Solid, Fluid-Fluid Mixers*. Elsevier.

ENGLER, M., KOCKMANN, N., KIEFER, T. & WOIAS, P. 2004. Numerical and experimental investigations on liquid mixing in static micromixers. *Chemical Engineering Journal*, 101, 315-322.

ESMAEELI, A. & TRYGGVASON, G. 1998. Direct numerical simulations of bubbly flows. Part 1. Low Reynolds number arrays. *Journal of Fluid Mechanics*, 377, 313-345.

FAN, Y., QIN, F., LUO, X., LIN, L., GUI, H. & LIU, J. 2013. Heterogeneous condensation on insoluble spherical particles: Modeling and parametric study. *Chemical Engineering Science*, 102, 387-396.

FARYADI, M., RAHIMI, M., SAFARI, S. & MORADI, N. 2014. Effect of high frequency ultrasound on micromixing efficiency in microchannels. *Chemical Engineering and Processing: Process Intensification*, 77, 13-21.

FENG, D., FERRASSE, J.-H., SORIC, A. & BOUTIN, O. 2019. Bubble characterization and gas-liquid interfacial area in two phase gas-liquid system in bubble column at low Reynolds number and high temperature and pressure. *Chemical Engineering Research and Design*, 144, 95-106.

FENG, Z.-G. & MICHAELIDES, E. E. 2009. Heat transfer in particulate flows with Direct Numerical Simulation (DNS). *International Journal of Heat and Mass Transfer*, 52, 777-786.

FERRON, R. D., SHAH, S., FUENTE, E. & NEGRO, C. 2013. Aggregation and breakage kinetics of fresh cement paste. *Cement and Concrete Research*, 50, 1-10.

FLORES-LÓPEZ, S. L., VILLANUEVA, S. F., MONTES-MORÁN, M. A., CRUZ, G., GARRIDO, J. J. & ARENILLAS, A. 2020. Advantages of microwave-assisted synthesis of silica gels. *Colloids and Surfaces A: Physicochemical and Engineering Aspects*, 604, 125248.

FOROUTAN, H. & YAVUZKURT, S. 2015. Unsteady Numerical Simulation of Flow in Draft Tube of a Hydroturbine Operating Under Various Conditions Using a Partially Averaged Navier–Stokes Model. *Journal of Fluids Engineering*, 137.

FOURNIER, M.-C., FALK, L. & VILLERMAUX, J. 1996. A new parallel competing reaction system for assessing micromixing efficiency—determination of micromixing time by a simple mixing model. *Chemical Engineering Science*, 51, 5187-5192.

FOX & O., R. On multiphase turbulence models for collisional fluid–particle flows. *Journal of Fluid Mechanics*, 742, 368-424.

FREGNI, A., ANGELI, D., CIMARELLI, A. & STALIO, E. 2019. Direct Numerical Simulation of a buoyant triple jet at low-Prandtl number. *International Journal of Heat and Mass Transfer*, 143, 118466.

GELVES, R., DIETRICH, A. & TAKORS, R. 2014. Modeling of gas–liquid mass transfer in a stirred tank bioreactor agitated by a Rushton turbine or a new pitched blade impeller. *Bioprocess and Biosystems Engineering*, 37, 365-375.

GLICKSMAN, L. R. 1988. Scaling relationships for fluidized beds. *Chemical Engineering Science*, 43, 1419-1421.

GLOWINSKI, R., PAN, T. W., HESLA, T. I. & JOSEPH, D. D. 1999. A distributed Lagrange multiplier/fictitious domain method for particulate flows. *International Journal of Multiphase Flow*, 25, 755-794.

GMACHOWSKI, L. 2005. Aggregate structure and hydrodynamics of aggregated systems. *Colloids and Surfaces A: Physicochemical and Engineering Aspects*, 255, 105-110.

GMACHOWSKI, L. 2007. Hydrodynamics of aggregates with mixed statistics. *Colloids and Surfaces A: Physicochemical and Engineering Aspects*, 295, 34-37.

GOVIER, G. W. & AZIZ, K. 1972. *The flow of complex mixtures in pipes*, Van Nostrand Reinhold Company New York.

GRACE, J. R. & TAGHIPOUR, F. 2004. Verification and validation of CFD models and dynamic similarity for fluidized beds. *Powder Technology*, 139, 99-110.

GREGORY, J. 2009. Monitoring particle aggregation processes. *Advances in Colloid and Interface Science*, 147-148, 109-123.

GREIN, T. A., LEBER, J., BLUMENSTOCK, M., PETRY, F., WEIDNER, T., SALZIG, D. & CZERMAK, P. 2016. Multiphase mixing characteristics in a microcarrier-based stirred tank bioreactor suitable for human mesenchymal stem cell expansion. *Process Biochemistry*, 51, 1109-1119.

GRÖTZBACH, G. 1983. Spatial resolution requirements for direct numerical simulation of the Rayleigh-Bénard convection. *Journal of computational physics*, 49, 241-264.

GUÉRIN, L., COUFORT-SAUDEJAUD, C., LINÉ, A. & FRANCES, C. 2017. Dynamics of aggregate size and shape properties under sequenced flocculation in a turbulent Taylor-Couette reactor. *Journal of Colloid and Interface Science*, 491, 167-178.

GUNJI, S., SHIMOTSUMA, Y. & MIURA, K. 2016. Synthesis and photocatalytic properties of SiO<sub>2</sub>/TiO<sub>2</sub>nanofibers using templates of TEMPO-oxidized cellulose nanofibers. *Journal of Sol-Gel Science and Technology*, 79, 151-159.

HABIB, A., HAUBNER, R. & STELZER, N. 2008. Effect of temperature, time and particle size of Ti precursor on hydrothermal synthesis of barium titanate. *Materials Science and Engineering: B*, 152, 60-65.

HABIBI, S. & JAMSHIDI, M. 2020. Synthesis of TiO<sub>2</sub> nanoparticles coated on cellulose nanofibers with different morphologies: Effect of the template and sol-gel parameters. *Materials Science in Semiconductor Processing*, 109, 104927.

HAN, Y., KANNO, H., AHN, Y.-J. & SHIKAZONO, N. 2015. Measurement of liquid film thickness in micro tube annular flow. *International Journal of Multiphase Flow*, 73, 264-274.

HAO, Z. R., XU, J., BIE, H. Y. & ZHOU, Z. H. 2013. Study of Flow Characteristics of Oil and Water in the Process of Stirring. *Applied Mechanics & Materials*, 353-356, 3190-3193.

HARRISON, M., JOHNS, R., WHITE, E. & MEHTA, C. 2011. *Growth Rate Kinetics for Struvite Crystallisation*.

HASHEMI, Z., ABOUALI, O. & AHMADI, G. 2016. Direct Numerical Simulation of Particle–Fluid Interactions: A review. *Iranian Journal of Science and Technology, Transactions of Mechanical Engineering*, 41.

HAUGEN, N. E. L., KRÜGER, J., MITRA, D. & LØVÅS, T. 2018. The effect of turbulence on mass transfer rates of small inertial particles with surface reactions. *Journal of Fluid Mechanics*, 836, 932-951.

HAUGEN, N. E. L., KRÜGER, J., MITRA, D. & LØVÅS, T. 2017. The effect of turbulence on mass transfer rates of small inertial particles with surface reactions.

HAUT, B., AMOR, H. B., COULON, L., JACQUET, A. & HALLOIN, V. 2003. Hydrodynamics and mass transfer in a Couette–Taylor bioreactor for the culture of animal cells. *Chemical Engineering Science*, 58, 777-784.

HERNÁNDEZ, A. G., BOYER, D., POTDEVIN, A., CHADEYRON, G., MURILLO, A. G., DE J. CARRILLO ROMO, F. & MAHIOU, R. 2014. Hydrothermal synthesis of lanthanide-doped GdPO<sub>4</sub> nanowires and nanoparticles for optical applications. *physica status solidi (a)*, 211, 498-503.

HIGBIE, R. 1935. The rate of absorption of a pure gas into a still liquid during short periods of exposure. *Trans. AIChE*, 31, 365-389.

HIRCHE, D., BIRKHOLZ, F. & HINRICHSEN, O. 2019. A hybrid Eulerian-Eulerian-Lagrangian model for gas-solid simulations. *Chemical Engineering Journal*, 377, 119743.

HIROMITSU, N. & KAWAGUCHI, O. 1995. Influence of flow turbulence on the evaporation rate of a suspended droplet in a hot air flow. *Heat transfer. Japanese research*, 24, 689-700.

HOGREFE, O. V. & KEESEE, R. G. 2002. Heterogeneous Vapor-to-Liquid Nucleation of Water on Individual Glass Particles. *Aerosol Science and Technology*, 36, 239-247.

HOQUE, M. M., SATHE, M. J., JOSHI, J. B. & EVANS, G. M. 2014. Analysis of Turbulence Energy Spectrum by Using Particle Image Velocimetry. *Procedia Engineering*, 90, 320-326.

HUANG, J., XIA, C., CAO, L. & ZENG, X. 2008. Facile microwave hydrothermal synthesis of zinc oxide one-dimensional nanostructure with three-dimensional morphology. *Materials Science and Engineering: B*, 150, 187-193.

HUIXIA, F., BAIYI, C., DEYI, Z., JIANQIANG, Z. & LIN, T. 2014. Preparation and characterization of the cobalt ferrite nano-particles by reverse coprecipitation. *Journal*

*of Magnetism and Magnetic Materials*, 356, 68-72.

JANULEVICIUS, M., KLIMKEVICIUS, V., VANETSEV, A., PLAUSINAITIENE, V., SAKIRZANOVAS, S. & KATELNIKOVAS, A. 2020. Controlled hydrothermal synthesis, morphological design and colloidal stability of GdPO<sub>4</sub>·nH<sub>2</sub>O particles. *Materials Today Communications*, 23, 100934.

JAVADI, A. & NILSSON, H. K. Time-accurate Numerical Simulations of Swirling Flow with Rotor-stator Interaction. *Flow Turbulence & Combustion*, 95, 755-774.

JAVADI, A. & NILSSON, H. K. 2015. Time-accurate Numerical Simulations of Swirling Flow with Rotor-stator Interaction. *Flow Turbulence & Combustion*, 95, 755-774.

JIMÉNEZ, J., DEL ALAMO, J. C. & FLORES, O. 2004. The large-scale dynamics of near-wall turbulence. *Journal of Fluid Mechanics*, 505, 179.

JOSE, N. A., ZENG, H. C. & LAPKIN, A. A. 2018. Hydrodynamic assembly of two-dimensional layered double hydroxide nanostructures. *Nature Communications*, 9, 4913.

JUIBARI, N. M. & TARIGHI, S. 2020. Metal–organic framework-derived nanocomposite metal-oxides with enhanced catalytic performance in thermal decomposition of ammonium perchlorate. *Journal of Alloys and Compounds*, 832, 154837.

JUNG, W.-M., HOON KANG, S., KIM, K.-S., KIM, W.-S. & KYUN CHOI, C. 2010. Precipitation of calcium carbonate particles by gas–liquid reaction: Morphology and size distribution of particles in Couette-Taylor and stirred tank reactors. *Journal of Crystal Growth*, 312, 3331-3339.

KANG, H. & CHESTER, S. 2003. Decaying turbulence in an active-grid-generated flow and comparisons with large-eddy simulation. *Journal of Fluid Mechanics*, 480,

129-160.

KAZEMZADEH, A., EIN-MOZAFFARI, F. & LOHI, A. 2019. Effect of impeller type on mixing of highly concentrated slurries of large particles. *Particuology*.

KELKAR, V. V. & NG, K. M. 2002. Development of fluidized catalytic reactors: Screening and scale-up. *Aiche Journal*, 48.

KEWALRAMANI, G. V., HEDAU, G., SAHA, S. K. & AGRAWAL, A. 2019. Study of laminar single phase frictional factor and Nusselt number in In-line micro pin-fin heat sink for electronic cooling applications. *International Journal of Heat and Mass Transfer*, 138, 796-808.

KIM, J. S., KIM, D. H., GU, B., KIM, D. Y. & YANG, D. R. 2013. Simulation of Taylor–Couette reactor for particle classification using CFD. *Journal of Crystal Growth*, 373, 106-110.

KOCKMANN, N., ENGLER, M., FÖLL, C. & WOIAS, P. Liquid Mixing in Static Micro Mixers With Various Cross Sections. ASME 2003 1st International Conference on Microchannels and Minichannels, 2003.

KOMARNENI, S. & KATSUKI, H. Nanophase materials by a novel microwave-hydrothermal process. *Pure & Applied Chemistry*, 74, 1537---1543.

KRUPA, K., NUNES, M. I., SANTOS, R. J. & BOURNE, J. R. 2014. Characterization of micromixing in T-jet mixers. *Chemical Engineering Science*, 111, 48-55.

KUMAR, G., BALLI, N. R., KAILASNATH, M., MIMUN, L. C., DANNANGODA, C., MARTIROSYAN, K. S., SANTHOSH, C. & SARDAR, D. K. 2016. Spectroscopic and magnetic properties of neodymium doped in GdPO<sub>4</sub> sub-micron-stars prepared by solvothermal method. *Journal of Alloys and Compounds*, 672, 668-673.

KUMARESAN, T. & JOSHI, J. B. 2006. Effect of impeller design on the flow pattern

and mixing in stirred tanks. *Chemical engineering journal*, 115, 173-193.

KURIAN, T. & FRANSSON, J. H. M. 2009. INVITED PAPER: Grid-generated turbulence revisited. 41.

LARUBIA GARCÍA, M. D., PACHECO, R., SÁNCHEZ, A., LÓPEZ, A., SÁNCHEZ, S. & CAMACHO, F. 2012. Kinetic Study of the Absorption of Carbon Dioxide by Aqueous Triethanolamine Solutions. *International Journal of Chemical Reactor Engineering*.

LADD, A. J. C. 1993. Numerical Simulations of Particulate Suspensions via a Discretized Boltzmann Equation Part I. Theoretical Foundation. *Physics of Fluids*, 271, 285-310.

LADD, A. J. C. & VERBERG, R. 2001. Lattice-Boltzmann Simulations of Particle-Fluid Suspensions. *Journal of Statistical Physics*, 104, 1191-1251.

LAHEY, R. T., BERTODANO, M. L. D. & JR., O. C. J. 1993. Phase distribution in complex geometry conduits. *Nuclear Engineering & Design*, 141, 177-201.

LAHEY, R. T. & DREW, D. A. The Three-Dimensional Time and Volume Averaged Conservation Equations of Two-Phase Flow.

LAI, H., DU, Y., ZHAO, M., SUN, K. & YANG, L. 2014. Effects of different organic additives on the formation of YPO<sub>4</sub>:Eu<sup>3+</sup> nano-/microstructures under hydrothermal conditions with enhanced photoluminescence. *Ceramics International*, 40, 1885-1891.

LAMER, V. 1952. Kinetics in phase transitions. *Ind. Eng. Chem*, 44, 1270-1277.

LAMER, V. K. & DINEGAR, R. H. 1950. Theory, production and mechanism of formation of monodispersed hydrosols. *Journal of the American Chemical Society*, 72, 4847-4854.

LAMONT, J. C. & SCOTT, D. 1970. An eddy cell model of mass transfer into the

surface of a turbulent liquid. *AIChE Journal*, 16, 513-519.

LAN, X., XU, C., WANG, G., WU, L. & GAO, J. 2009. CFD modeling of gas–solid flow and cracking reaction in two-stage riser FCC reactors. *Chemical Engineering Science*, 64, 3847-3858.

LANDRETH, C. C. & ADRIAN, R. J. 1990. Impingement of a low Reynolds number turbulent circular jet onto a flat plate at normal incidence. *Experiments in Fluids*, 9, 74-84.

LEBON, G. B., TZANAKIS, I., DJAMBAZOV, G., PERICLEOUS, K. & ESKIN, D. 2017. Numerical modelling of ultrasonic waves in a bubbly Newtonian liquid using a high-order acoustic cavitation model. *Ultrasonics sonochemistry*, 37, 660-668.

LEFEBVRE, J., BAJOHR, S. & KOLB, T. 2019. A comparison of two-phase and three-phase CO<sub>2</sub> methanation reaction kinetics. *Fuel*, 239, 896-904.

LEFEBVRE, J., TRUDEL, N., BAJOHR, S. & KOLB, T. 2018. A study on three-phase CO<sub>2</sub> methanation reaction kinetics in a continuous stirred-tank slurry reactor. *Fuel*, 217, 151-159.

LEFEBVRE, L. & SOL, D. 2008. Brains, lifestyles and cognition: Are there general trends? *Brain, Behavior and Evolution*, 72, 135-144.

LEWIS, G. S. & SWINNEY, H. L. 1999. Velocity structure functions, scaling, and transitions in high-Reynolds-number Couette-Taylor flow. *Physical Review E Statistical Physics Plasmas Fluids & Related Interdisciplinary Topics*, 59, 5457-5467.

LEWIS, M. M., DAVID, 2009. IN SITU NANO-PARTICLE MATRIX LOADING OF METAL OXIDE COATINGS VIA COMBUSTION DEPOSITION.

LEWIS, W. & WHITMAN, W. 1924. Principles of gas absorption. *Industrial & Engineering Chemistry*, 16, 1215-1220.

- LHUILIER, D., CHANG, C.-H. & THEOFANOUS, T. G. 2013. On the quest for a hyperbolic effective-field model of disperse flows. *Journal of Fluid Mechanics*, 731, 184-194.
- LI, X., ZHANG, Q. & YANG, B. 2020. Co-precipitation with CaCO<sub>3</sub> to remove heavy metals and significantly reduce the moisture content of filter residue. *Chemosphere*, 239, 124660.
- LI, X., ZHANG, X., LI, L., HUANG, L., ZHANG, W., YE, J. & HONG, J. 2016. Preparation of nano-ZnO/regenerated cellulose composite particles via co-gelation and low-temperature hydrothermal synthesis. *Materials Letters*, 175, 122-125.
- LI, Y. Z. & INGASON, H. 2018. Discussions on critical velocity and critical Froude number for smoke control in tunnels with longitudinal ventilation. *Fire Safety Journal*, 99, 22-26.
- LINK, J., GODLIEB, W., TRIPP, P., DEEN, N., HEINRICH, S., KUIPERS, J., SCHÖNHERR, M. & PEGLOW, M. 2009. Comparison of fibre optical measurements and discrete element simulations for the study of granulation in a spout fluidized bed. *Powder technology*, 189, 202-217.
- LIU, D., VAN WACHEM, B. G., MUDDE, R. F., CHEN, X. & VAN OMMEN, J. R. 2016a. An adhesive CFD-DEM model for simulating nanoparticle agglomerate fluidization. *AIChE Journal*, 62, 2259-2270.
- LIU, D., VAN WACHEM, B. G. M., MUDDE, R. F., CHEN, X. & VAN OMMEN, J. R. 2016b. Characterization of fluidized nanoparticle agglomerates by using adhesive CFD-DEM simulation. *Powder Technology*, 304, 198-207.
- LIU, H., YANG, F., TAN, H., LI, Z., FENG, P. & DU, Y. 2020a. Experimental and numerical investigation on the structure characteristics of vortex generators affecting particle agglomeration. *Powder Technology*, 362, 805-816.

LIU, L., YANG, X., LI, G., HUANG, X. & XUE, C. 2020b. Shear controllable synthesis of barium sulfate particles using lobed inner cylinder Taylor-Couette flow reactor. *Advanced Powder Technology*.

LIU, M., GAO, Z., YU, Y., LI, Z., HAN, J., CAI, Z. & HUANG, X. 2019. PIV experiment and large eddy simulation of turbulence characteristics in a confined impinging jet reactor. *Chinese Journal of Chemical Engineering*, 27, 10-20.

LIU, Y., ZHANG, H., WANG, S. & WANG, J. 2008. Prediction of Pressure Gradient and Holdup in Small Eötvös Number Liquid-Liquid Segregated Flow\* \*Supported by the National High Technology Research and Development Program of China (2006AA09Z333). *Chinese Journal of Chemical Engineering*, 16, 184-191.

LIU, Z., GUO, L., HUANG, T., WEN, L. & CHEN, J. 2014. Experimental and CFD studies on the intensified micromixing performance of micro-impinging stream reactors built from commercial T-junctions. *Chemical Engineering Science*, 119, 124-133.

LÖFSTRAND, H., ALMSTEDT, A. E. & ANDERSSON, S. 1995. Dimensionless expansion model for bubbling fluidized beds with and without internal heat exchanger tubes. *Chemical Engineering Science*, 50, 245-253.

LOY, D. A. 2003. Sol–Gel Processing. In: MEYERS, R. A. (ed.) *Encyclopedia of Physical Science and Technology (Third Edition)*. New York: Academic Press.

LU, J., PETERS, E. A. & KUIPERS, J. A. 2018. Direct numerical simulation of fluid flow and mass transfer in particle clusters. *Industrial & engineering chemistry research*, 57, 4664-4679.

LUCAS, D. & TOMIYAMA, A. 2011. On the role of the lateral lift force in poly-dispersed bubbly flows. *International Journal of Multiphase Flow*, 37, 1178-1190.

LUO, J., WANG, J. & WANG, T. 2019. A new forward-impinging-back reactor for the scale-up of partially decoupled oxidation of ethane to produce ethylene and acetylene.

*Chemical Engineering and Processing - Process Intensification*, 145, 107646.

LUO, P., JIA, H., XIN, C., XIANG, G., JIAO, Z. & WU, H. 2013. An experimental study of liquid mixing in a multi-orifice-impinging transverse jet mixer using PLIF. *Chemical Engineering Journal*, 228, 554-564.

LV, L., ZHANG, J. & XU, J. 2020. Microscopic visualization of heterogeneous nucleation process on smooth spherical particle: Method and results. *Chemical Engineering Science*, 213, 115411.

LYNCH, F. B. P. 2007. *Weather Prediction by Numerical Process*.

MAO, Y., CHEN, Y., BU, X. & XIE, G. 2019. Effects of 20 kHz ultrasound on coal flotation: The roles of cavitation and acoustic radiation force. *Fuel*, 256, 115938.

MASSART, R. 1981. Preparation of aqueous magnetic liquids in alkaline and acidic media. *IEEE transactions on magnetics*, 17, 1247-1248.

MEIER, H., VEGINI, A. & MORI, M. 2011. Four-Phase Eulerian-Eulerian Model for Prediction of Multiphase Flow in Cyclones. *The Journal of Computational Multiphase Flows*, 3, 93-105.

METZGER, L. & KIND, M. 2016. Influence of mixing on particle formation of fast precipitation reactions—A new coarse graining method using CFD calculations as a “measuring” instrument. *Chemical Engineering Research and Design*, 108, 176-185.

MIMOUNI, S., F, A., BOUCKER, M., LAVIÉVILLE, J. & MOREL, C. 2008. A Second-Order Turbulence Model Based on a Reynolds Stress Approach for Two-Phase Flow—Part I: Adiabatic Cases. *Science and Technology of Nuclear Installations*, 2009.

MIMOUNI, S., LAVIÉVILLE, J., SEILER, N. & RUYER, P. 2011. Combined evaluation of second order turbulence model and polydispersion model for two-phase

boiling flow and application to fuel assembly analysis. 241, 4523-4536.

MIRZAEI, S., AZIZIAN-KALANDARAGH, Y. & RAHIMZADEH, P. 2020. Modified co-precipitation process effects on the structural and magnetic properties of Mn- doped nickel ferrite nanoparticles. *Solid State Sciences*, 99, 106052.

MO, C. B., CHA, S. I., KIM, K. T., LEE, K. H. & HONG, S. H. 2005. Fabrication of carbon nanotube reinforced alumina matrix nanocomposite by sol-gel process. *Materials Science and Engineering: A*, 395, 124-128.

MOUREH, J. & FLICK, D. 2005. Airflow characteristics within a slot-ventilated enclosure. *International Journal of Heat & Fluid Flow*, 26, 12-24.

MOUSAVI, S. E., CHOUDHURY, M. R. & RAHAMAN, M. S. 2019. 3-D CFD-PBM coupled modeling and experimental investigation of struvite precipitation in a batch stirred reactor. *Chemical Engineering Journal*, 361, 690-702.

MUROYAMA, K. & FAN, L. S. 1985. Fundamentals of gas-liquid-solid fluidization. *AIChE Journal*, 31, 1-34.

MUTHEE, D. K. & DEJENE, B. F. 2020. The effect of tetra isopropyl orthotitanate (TIP) concentration on structural, and luminescence properties of titanium dioxide nanoparticles prepared by sol-gel method. *Materials Science in Semiconductor Processing*, 106, 104783.

NAIR, G. B., PAWADE, V. B. & DHOBLE, S. J. 2018. Chapter 13 - White Light-Emitting Novel Nanophosphors for LED Applications. *In: BHANVASE, B. A., PAWADE, V. B., DHOBLE, S. J., SONAWANE, S. H. & ASHOKKUMAR, M. (eds.) Nanomaterials for Green Energy*. Elsevier.

NASEEM, U., AWAN, M. B., SAEED, B., ABBAS, N., NAWAZ, S. & HUSSAIN, M. 2019. Experimental investigation of flow instabilities in a wide gap turbulent rotating Taylor-Couette flow. *Case Studies in Thermal Engineering*, 14, 100449.

NASERI, A. & THOMSON, M. J. 2019. Development of a numerical model to simulate carbon black synthesis and predict the aggregate structure in flow reactors. *Combustion and Flame*, 207, 314-326.

NERE, N. K., PATWARDHAN, A. W. & JOSHI, J. B. 2003. Liquid-phase mixing in stirred vessels: turbulent flow regime. *Industrial & engineering chemistry research*, 42, 2661-2698.

NGUYEN-TIEN, K., PATWARI, A. N., SCHUMPE, A. & DECKWER, W.-D. 1985. Gas-liquid mass transfer in fluidized particle beds. *AIChE Journal*, 31, 194-201.

NICHOLS, G., BYARD, S., BLOXHAM, M. J., BOTTERILL, J., DAWSON, N. J., DENNIS, A., DIART, V., NORTH, N. C. & SHERWOOD, J. D. 2002. A review of the terms agglomerate and aggregate with a recommendation for nomenclature used in powder and particle characterization. *Journal of pharmaceutical sciences*, 91, 2103-2109.

NIKHADE, B. P. & PANGARKAR, V. G. 2007. Theorem of Corresponding Hydrodynamic States for Estimation of Transport Properties: Case Study of Mass Transfer Coefficient in Stirred Tank Fitted with Helical Coil. *Industrial & Engineering Chemistry Research*, 46, 3095-3100.

NYUTU, E. K., CHEN, C.-H., DUTTA, P. K. & SUIB, S. L. 2008. Effect of Microwave Frequency on Hydrothermal Synthesis of Nanocrystalline Tetragonal Barium Titanate. *The Journal of Physical Chemistry C*, 112, 9659-9667.

OCTAU, C., DBOUK, T., WATREMEZ, M., MERESSE, D., LIPPERT, M., SCHIFFLER, J., KEIRSBULCK, L. & DUBAR, L. 2020. Liquid–solid two-phase jet in a turbulent crossflow: Experiments and simulations. *Chemical Engineering Research and Design*, 155, 156-171.

OHMURA, N., SUEMASU, T. & ASAMURA, Y. 2005. Particle classification in Taylor

vortex flow with an axial flow. *Journal of Physics: Conference Series*, 14, 64-71.

OLES, V. 1992. Shear-induced aggregation and breakup of polystyrene latex particles. *Journal of Colloid and Interface Science*, 154, 351-358.

OMMEN, J. R. V., TEULING, M., NIJENHUIS, J. & WACHEM, B. G. M. V. 2006. Computational validation of the scaling rules for fluidized beds. *Powder Technology*, 163, 32-40.

OSBORNE & REYNOLDS 1883. An Experimental Investigation of the Circumstances Which Determine Whether the Motion of Water Shall Be Direct or Sinuous, and of the Law of Resistance in Parallel Channels.

PANDIT, A. 1997. Bubble Behavior in Hydrodynamic Cavitation: Effect of Turbulence. *AIChE Journal*, 43, 1641-1648.

PANDYA, J. D. & SPIELMAN, L. A. 1983. Floc breakage in agitated suspensions: Effect of agitation rate. *Chemical Engineering Science*, 38, 1983-1992.

PANGARKAR, V. 2015. Design of Multiphase Reactors. *Design of Multiphase Reactors*, 1-512.

PANGARKAR, V. G. 2017. Process intensification in multiphase reactors: From concept to reality. *Chemical Engineering and Processing - Process Intensification*, 120, 1-8.

PANICKER, N., PASSALACQUA, A. & FOX, R. O. 2018. On the hyperbolicity of the two-fluid model for gas-liquid bubbly flows. *Applied Mathematical Modelling*, 57.

PARK, J.-K. & FARRELL, P. Droplet vaporization in turbulent flow. 1st National Fluid Dynamics Conference, 1987. 3683.

PARK, S., KIM, C.-H., LEE, W.-J., SUNG, S. & YOON, M.-H. 2017. Sol-gel metal oxide dielectrics for all-solution-processed electronics. *Materials Science and*

*Engineering: R: Reports*, 114, 1-22.

PARVIZIAN, F., RAHIMI, M. & AZIMI, N. 2012. Macro- and micromixing studies on a high frequency continuous tubular sonoreactor. *Chemical Engineering and Processing: Process Intensification*, 57-58, 8-15.

PARVIZIAN, F., RAHIMI, M. & FARYADI, M. 2011. Macro- and micromixing in a novel sonochemical reactor using high frequency ultrasound. *Chemical Engineering and Processing: Process Intensification*, 50, 732-740.

PATEL, R. G., DESJARDINS, O., BO, K., CAPECELATRO, J. & FOX, R. O. 2017. Verification of Eulerian–Eulerian and Eulerian–Lagrangian simulations for turbulent fluid–particle flows. *Aiche Journal*, 63.

PAUL, E. L., ATIEMO-OBENG, V. A. & KRESTA, S. M. 2004. *Handbook of industrial mixing: science and practice*, John Wiley & Sons.

PESKIN, C. S. Flow patterns around heart valves: A numerical method. *Journal of Computational Physics*, 10, 252-271.

POLSHETTIWAR, V., NADAGOUDA, M. N. & VARMA, R. S. 2009. Microwave-Assisted Chemistry: a Rapid and Sustainable Route to Synthesis of Organics and Nanomaterials. *Australian Journal of Chemistry*, 62, 16-26.

POPE, S. B. 2000. *Turbulent Flows*, Cambridge, Cambridge University Press.

PROSPERETTI, A. & TRYGGVASON, G. 2009. *Computational methods for multiphase flow*, Cambridge university press.

PUKKELLA, A. K., VYSYARAJU, R., TAMMISHETTI, V., RAI, B. & SUBRAMANIAN, S. 2019. Improved mixing of solid suspensions in stirred tanks with interface baffles: CFD simulation and experimental validation. *Chemical Engineering Journal*, 358, 621-633.

PURNAMA, B., WIJAYANTA, A. T. & SUHARYANA 2019. Effect of calcination temperature on structural and magnetic properties in cobalt ferrite nano particles. *Journal of King Saud University - Science*, 31, 956-960.

QI, X., ZHU, J. & HUANG, W. 2008. Hydrodynamic similarity in circulating fluidized bed risers. *Chemical Engineering Science*, 63, 5613-5625.

RAHIMI, M., AGHEL, B., HATAMIFAR, B., AKBARI, M. & ALSAIRAFI, A. 2014. CFD modeling of mixing intensification assisted with ultrasound wave in a T-type microreactor. *Chemical Engineering and Processing: Process Intensification*, 86, 36-46.

RANE, A. V., KANNY, K., ABITHA, V. K. & THOMAS, S. 2018. Chapter 5 - Methods for Synthesis of Nanoparticles and Fabrication of Nanocomposites. *In: MOHAN BHAGYARAJ, S., OLUWAFEMI, O. S., KALARIKKAL, N. & THOMAS, S. (eds.) Synthesis of Inorganic Nanomaterials*. Woodhead Publishing.

RATCLIFF, G. A. 1986. Unit operations of chemical engineering. . 6, 287-0.

REHAGE, H., BARTSCH, M. & KIND, M. 2020. A new scale-up method for competitive chemical model reactions based on complete similarity. *Chemical Engineering Journal*, 400, 125763.

REISS, H. 1951. The growth of uniform colloidal dispersions. *The Journal of Chemical Physics*, 19, 482-487.

RÜDISÜLI, M., SCHILDHAUER, T. J., BIOLLAZ, S. M. A. & VAN OMMEN, J. R. 2012. Scale-up of bubbling fluidized bed reactors — A review. *Powder Technology*, 217, 21-38.

RZEHAKE, R., ZIEGENHEIN, T., KRIEBITZSCH, S., KREPPER, E. & LUCAS, D. 2017. Unified modeling of bubbly flows in pipes, bubble columns, and airlift columns. *Chemical Engineering Science*, 157, 147-158.

SAADAT, M., SHAFII, M. B. & GHASSEMI, M. 2020. Numerical investigation on mixing intensification of ferrofluid and deionized water inside a microchannel using magnetic actuation generated by embedded microcoils for lab-on-chip systems. *Chemical Engineering and Processing - Process Intensification*, 147, 107727.

SADIKI, A., AGREBI, S., CHRIGUI, M., DOOST, A. S., KNAPPSTEIN, R., DI MARE, F., JANICKA, J., MASSMEYER, A., ZABRODIEC, D., HEES, J. & KNEER, R. 2017. Analyzing the effects of turbulence and multiphase treatments on oxy-coal combustion process predictions using LES and RANS. *Chemical Engineering Science*, 166, 283-302.

SAJJADI, B., RAMAN, A. A. A. & IBRAHIM, S. 2015. Influence of ultrasound power on acoustic streaming and micro-bubbles formations in a low frequency sono-reactor: Mathematical and 3D computational simulation. *Ultrasonics Sonochemistry*, 24, 193-203.

SANDERSON, J. & RHODES, M. 2005. Bubbling fluidized bed scaling laws: Evaluation at large scales. *AIChE Journal*, 51, 2686-2694.

SANDERSON, J., RHODES, M. J., WANG, X. S. & LIM, K. S. 2007. An investigation of fluidized bed scaling laws by DEM simulation.

SANDERSON, P. J., LIM, K. S., SIDORENKO, I. & RHODES, M. J. 2004. Hydrodynamic Similarity in Bubbling Fluidized Beds: The Importance of the Solid-to-Gas Density Ratio. *Industrial & Engineering Chemistry Research*, 43, 5466-5473.

SANTIAGO, P. A., GIORDANO, R. D. C. & SUAZO, C. A. T. 2011. Performance of a vortex flow bioreactor for cultivation of CHO-K1 cells on microcarriers. *Process Biochemistry*, 46, 35-45.

SARDINA, G., JARETEG, K., STRÖM, H. & SASIC, S. 2019. Assessing the ability of the Eulerian-Eulerian and the Eulerian-Lagrangian frameworks to capture mesoscale

dynamics in bubbly flows. *Chemical Engineering Science*, 201, 58-73.

SATJARITANUN, P., BRINGLEY, E., REGALBUTO, J., REGALBUTO, J., REGISTER, J., WEIDNER, J., KHUNATORN, Y. & SHIMPALEE, S. 2018. Experimental and computational investigation of mixing with contra-rotating, baffle-free impellers. *Chemical Engineering Research and Design*, 130, 63-77.

SCHWARZER, H. C. & PEUKERT, W. 2004. Combined Experimental/Numerical Study on the Precipitation of Nanoparticles. *Aiche Journal*, 50, 3234-3247.

SCHWERTFIRM, F., GRADL, J., SCHWARZER, H. C., PEUKERT, W. & MANHART, M. 2007. The low Reynolds number turbulent flow and mixing in a confined impinging jet reactor. *International Journal of Heat and Fluid Flow*, 28, 1429-1442.

SHAIKH, A. & AL-DAHMAN, M. 2010. A new methodology for hydrodynamic similarity in bubble columns. 88, 503-517.

SHI, X., RONSSE, F., ROEGIERS, J. & PIETERS, J. G. 2019. 3D Eulerian-Eulerian modeling of a screw reactor for biomass thermochemical conversion. Part 1: Solids flow dynamics and back-mixing. *Renewable Energy*, 143, 1465-1476.

SHI, X., WU, Y., LAN, X., LIU, F. & GAO, J. 2015. Effects of the riser exit geometries on the hydrodynamics and solids back-mixing in CFB risers: 3D simulation using CPFD approach. *Powder Technology*, 284, 130-142.

SKILLAS, G., BECKER, C., MÜHLENWEG, H. & BEHNISCH, J. 2005. Simulation of particulates in a carbon black reactor. *Journal of Nanoparticle Research*, 7, 15-27.

SMITH, G. P. 1982. Turbulent Couette Flow Between Concentric Cylinders at Large Taylor Number. *Journal of Fluid Mechanics*, 123, 187-217.

SOKOLICHIN, A., EIGENBERGER, G., LAPIN, A. & LÜBERT, A. 1997. Dynamic

numerical simulation of gas-liquid two-phase flows Euler/Euler versus Euler/Lagrange. *Chemical Engineering Science*, 52, 611-626.

SOMASHEKAR, V., LIU, Y., FOX, R. O. & OLSEN, M. G. 2012. Turbulence measurements in a rectangular mesoscale confined impinging jets reactor. *Experiments in Fluids*, 53, 1929-1941.

STALP, S. R., SKRBEEK, L. & DONNELLY, R. J. 1999. Decay of Grid Turbulence in a Finite Channel. *Phys.rev.lett*, 82, 4831-4834.

STANKIEWICZ, A. & MOULIJN, J. A. 2000. Process Intensification: Transforming Chemical Engineering. *Chemical Engineering Progress*, 96, 22-33.

STEIN, M. J., DING, Y. L. & SEVILLE, J. P. K. 2002. Experimental verification of the scaling relationships for bubbling gas-fluidised beds using the PEPT technique. *Chemical Engineering Science*, 57, 3649-3658.

STOROZHEV, V. B. & YERMAKOV, A. N. 2015. Combustion of nano-sized aluminum particles in steam: Numerical modeling. *Combustion and Flame*, 162, 4129-4137.

SUBRAMANIAM, S. 2013. Lagrangian–Eulerian methods for multiphase flows. *Progress in Energy and Combustion Science*, 39, 215-245.

SUGIMOTO & TADAO 2001. Monodispersed Particles || Growth. 86-117.

TAMMARO, M., NATALE, F. D., SALLUZZO, A. & LANCIA, A. 2012. Heterogeneous condensation of submicron particles in a growth tube. *Chemical Engineering Science*, 74, 124-134.

TANG, Z., KIM, W.-S. & YU, T. 2019. Studies on morphology changes of copper sulfide nanoparticles in a continuous Couette-Taylor reactor. *Chemical Engineering Journal*, 359, 1436-1441.

- TAYLOR, G. I. 1922. The motion of a sphere in a rotating liquid. 102, 180-189.
- THANH, N. T. K., MACLEAN, N. & MAHIDDINE, S. 2014. Mechanisms of Nucleation and Growth of Nanoparticles in Solution. *Chemical Reviews*, 114, 7610-7630.
- TIAN, T., ZENG, Z., VULPE, D., CASCO, M. E., DIVITINI, G., MIDGLEY, P. A., SILVESTRE-ALBERO, J., TAN, J.-C., MOGHADAM, P. Z. & FAIREN-JIMENEZ, D. 2017. A sol-gel monolithic metal-organic framework with enhanced methane uptake. *Nature Materials*.
- TOOR, H. & MARCHELLO, J. 1958. Film-penetration model for mass and heat transfer. *AIChE Journal*, 4, 97-101.
- TSAOULIDIS, D. & ANGELI, P. 2017. Liquid-liquid dispersions in intensified impinging-jets cells. *Chemical Engineering Science*, 171, 149-159.
- TSUJI, Y., KAWAGUCHI, T. & TANAKA, T. 1993. Discrete particle simulation of two-dimensional fluidized bed. *Powder Technology*, 77, 79-87.
- TU, G.-Y., LI, W.-F., QIAN, W.-W., SHI, Z.-H., LIU, H.-F. & WANG, F.-C. 2015. Experimental study on oscillation behaviors in T-jets reactor with excitation. *Chemical Engineering Science*, 134.
- UHLMANN, D. R., SURATWALA, T., DAVIDSON, K., BOULTON, J. M. & TEOWEE, G. 1997. Sol-gel derived coatings on glass. 218, 113-122.
- VAEZI, V., OH, E. S. & ALDREDGE, R. C. 1997. High-intensity turbulence measurements in a Taylor-Couette flow reactor. *Experimental Thermal and Fluid Science*, 15, 424-431.
- VAN DEN AKKER, H. 2010. Toward A Truly Multiscale Computational Strategy For Simulating Turbulent Two-Phase Flow Processes. *Industrial & Engineering Chemistry*

*Research*, 49, 10780-10797.

VAN DER SCHAAF, J., SCHOUTEN, J. C., JOHNSON, F. & VAN DEN BLEEK, C. M. 2002. Non-intrusive determination of bubble and slug length scales in fluidized beds by decomposition of the power spectral density of pressure time series. *International Journal of Multiphase Flow*, 28, 865-880.

VARGA, Z., GREARD, V., PECORARIO, S., TABERLET, N., DOLIQUE, V., MANNEVILLE, S., DIVOUX, T., MCKINLEY, G. & SWAN, J. 2019. Hydrodynamics control shear-induced pattern formation in attractive suspensions. *Proceedings of the National Academy of Sciences*, 116, 201901370.

VASSILEVA, N. D., VAN DEN ENDE, D., MUGELE, F. & MELLEMA, J. 2007. Fragmentation and Erosion of Two-Dimensional Aggregates in Shear Flow. *Langmuir the Acs Journal of Surfaces & Colloids*, 23, 2352-2361.

VICUM, L. & MAZZOTTI, M. 2007. Multi-scale modeling of a mixing-precipitation process in a semibatch stirred tank. *Chemical Engineering Science*, 62, 3513-3527.

VILLERMAUX, J., FALK, L. & FOURNIER, M. Potential use of a new parallel reaction system to characterise micromixing in stirred reactors. AIChE Symposium Series, 1994. New York, NY: American Institute of Chemical Engineers, 1971-c2002., 50-54.

WANG, D. & BIERWAGEN, G. P. Sol-gel coatings on metals for corrosion protection. 64, 327-338.

WANG, T. & WANG, J. 2007. Numerical simulations of gas-liquid mass transfer in bubble columns with a CFD-PBM coupled model. *Chemical engineering science*, 62, 7107-7118.

WANG, W., ZHAO, S., SHAO, T., JIN, Y. & CHENG, Y. 2012. Visualization of micro-scale mixing in miscible liquids using  $\mu$ -LIF technique and drug nano-particle

preparation in T-shaped micro-channels. 192, 252-261.

WEEKS, D. E. 2001. Newton Morton's influence on genetics: The Morton number. *Advances in Genetics*. Academic Press.

WESSEL, R. & BALL, R. C. 1992. Fractal aggregates and gels in shear flow. *Physical Review A*, 46, R3008-R3011.

WIEDMEYER, V., ANKER, F., BARTSCH, C., VOIGT, A., JOHN, V. & SUNDMACHER, K. 2017a. Continuous crystallization in a helically coiled flow tube: Analysis of flow field, residence time behavior, and crystal growth. *Industrial & Engineering Chemistry Research*, 56, 3699-3712.

WIEDMEYER, V., VOIGT, A. & SUNDMACHER, K. 2017b. Crystal population growth in a continuous helically coiled flow tube crystalliser. *Chemical Engineering & Technology*, 40, 1584-1590.

WIMAN, J. & ALMSTEDT, A. E. 1998. Influence of pressure, fluidization velocity and particle size on the hydrodynamics of a freely bubbling fluidized bed. *Chemical Engineering Science*, 53, 2167-2176.

WORSTELL, J. 2014. Chapter 5 - Scaling Fixed-Bed Reactors. In: WORSTELL, J. (ed.) *Adiabatic Fixed-Bed Reactors*. Boston: Butterworth-Heinemann.

WU, H., LIU, Z., HAN, B. & LI, Y. 2014. Numerical investigation of the influences of mixing chamber geometries on steam ejector performance. *Desalination*, 353, 15-20.

WU, H., PAN, D., HUANG, R., HONG, G., YANG, B., PENG, Z. & YANG, L. 2016. Abatement of fine particle emission by heterogeneous vapor condensation during wet limestone-gypsum flue gas desulfurization. *Energy & Fuels*, acs.energyfuels.6b00673.

XIANG, H., WANG, Z., YIN, Q., WANG, L., ZHANG, L., WANG, H., XU, H., ZHANG, R. & LU, H. 2019. Effect of process factors on properties of high dispersion

spherical  $\alpha$ -Al<sub>2</sub>O<sub>3</sub> particles prepared by hydrothermal method. *Ceramics International*, 45, 22007-22014.

XIAO, F., XU, H., LI, X.-Y. & WANG, D. 2015. Modeling particle-size distribution dynamics in a shear-induced breakage process with an improved breakage kernel: Importance of the internal bonds. *Colloids and Surfaces A: Physicochemical and Engineering Aspects*, 468, 87-94.

XU, H., HONG, F., PANG, G., LIU, G., DONG, X., WANG, J. & YU, W. 2020a. Co-precipitation synthesis, luminescent properties and application in warm WLEDs of Na<sub>3</sub>GaF<sub>6</sub>:Mn<sup>4+</sup> red phosphor. *Journal of Luminescence*, 219, 116960.

XU, J., YU, Y., YIN, Y., ZHANG, J. & ZHONG, H. 2017. Heterogeneous condensation coupled with partial gas circulation for fine particles abatement. *Chemical Engineering Journal*, 330, 979-986.

XU, Z., HAN, Z. & QU, H. 2020b. Comparison between Lagrangian and Eulerian approaches for prediction of particle deposition in turbulent flows. *Powder Technology*, 360, 141-150.

YANG, W., WANG, J., WANG, T. & JIN, Y. Experimental study on gas-liquid interfacial area and mass transfer coefficient in three-phase circulating fluidized beds. *Chemical Engineering Journal*, 84, 485-490.

YAO, W., GUANGSHENG, G., FEI, W. & JUN, W. 2002. Fluidization and agglomerate structure of SiO<sub>2</sub> nanoparticles. *Powder Technology*, 124, 152-159.

YASUDA, K., SATO, T. & ASAKURA, Y. 2020. Size-controlled synthesis of gold nanoparticles by ultrafine bubbles and pulsed ultrasound. *Chemical Engineering Science*, 217, 115527.

YEARLING, P. R. A. 1996. Experimental determination of convective heat and mass transfer rates from single evaporating liquid droplets in a turbulent air flow.

YING, Y., CHEN, G., ZHAO, Y., LI, S. & YUAN, Q. 2008. A high throughput methodology for continuous preparation of monodispersed nanocrystals in microfluidic reactors. *Chemical Engineering Journal*, 135, 209-215.

YOU, H. & FANG, J. 2016. Particle-mediated nucleation and growth of solution-synthesized metal nanocrystals: A new story beyond the LaMer curve. *Nano Today*, 11, 145-167.

YUE, J., CHEN, G., YUAN, Q., LUO, L. & GONTHIER, Y. 2007. Hydrodynamics and mass transfer characteristics in gas-liquid flow through a rectangular microchannel. *Chemical Engineering Science*, 62, 2096-2108.

ZHANG, Q., WANG, S., LU, H., WANG, Q., TAO, M. & LIU, G. 2018. Impact velocity-dependent restitution coefficient using a coupled Eulerian fluid phase-Eulerian solid phase-Lagrangian discrete particles phase model in gas-monodisperse particles internally circulating fluidized bed. *International Journal of Multiphase Flow*, 105, 142-158.

ZHANG, X., SUN, H., TAN, S., GAO, J., FU, Y. & LIU, Z. 2019. Hydrothermal synthesis of Ag nanoparticles on the nanocellulose and their antibacterial study. *Inorganic Chemistry Communications*, 100, 44-50.

ZHANG, Y., ZHANG, X., XU, B., CAI, W. & WANG, F. 2015. CFD simulation of mass transfer intensified by chemical reactions in slug flow microchannels. *The Canadian Journal of Chemical Engineering*, 93, 2307-2314.

ZHANG, Z., ZHOU, S. & CHEN, Z. 2012. Preparation and morphology of single crystal ( $\alpha$ - $\text{Al}_2\text{O}_3$  nano- particles by combustion chemical deposition. *Procedia Engineering*, 27, 1284-1291.

ZHAO, Y., ZHU, J.-J., HONG, J.-M., BIAN, N. & CHEN, H.-Y. 2004. Microwave-Induced Polyol-Process Synthesis of Copper and Copper Oxide Nanocrystals with

Controllable Morphology. *European Journal of Inorganic Chemistry*, 2004, 4072-4080.

ZHENDONG, L., YANGCHENG, L., JIAWEI, W. & GUANGSHENG, L. 2012. Mixing characterization and scaling-up analysis of asymmetrical T-shaped micromixer: Experiment and CFD simulation. *Chemical Engineering Journal*, 181-182, 597-606.

ZHOU, B., YANG, M., LI, Z., WANG, Z. & ZHANG, Y. 2017a. Numerical simulations of forced convection across a single tube to evaluate applicability of the DNS, LES and RSM methods. *Applied Thermal Engineering*, 123, 123-130.

ZHOU, L., WANG, J., GE, W., LIU, S., CHEN, J., XU, J., WANG, L., CHEN, F., YANG, N., ZHOU, R., ZHANG, L., CHANG, Q., RICOUX, P. & FERNANDEZ, A. 2018. Quantifying growth and breakage of agglomerates in fluid-particle flow using discrete particle method. *Chinese Journal of Chemical Engineering*, 26, 914-921.

ZHOU, M., JIANG, H., HU, Y., LU, Z., JIANG, H. & LI, C. 2019. Analyzing of mixing performance determination factors for the structure of radial multiple jets-in-crossflow. *Chinese Journal of Chemical Engineering*, 27, 2626-2634.

ZHOU, R., YANG, N. & LI, J. 2017b. CFD simulation of gas-liquid-solid flow in slurry bubble columns with EMMS drag model. *Powder Technology*, 314, 466-479.

ZHOU, X., MA, Y., LIU, M. & ZHANG, Y. 2020. CFD-PBM simulations on hydrodynamics and gas-liquid mass transfer in a gas-liquid-solid circulating fluidized bed. *Powder Technology*, 362, 57-74.

ZHU, H. P., ZHOU, Z. Y., YANG, R. Y. & YU, A. B. 2008. Discrete particle simulation of particulate systems: A review of major applications and findings. *Chemical Engineering Science*, 63, 5728-5770.

## Figures and Graphs

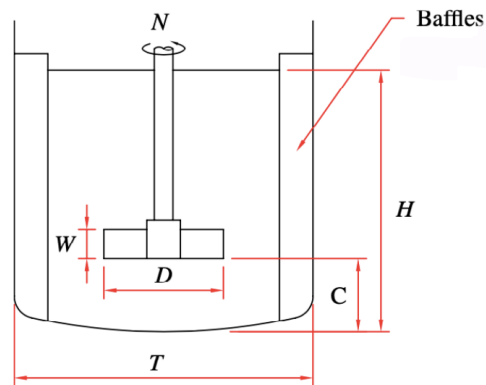


**Figure 1.1** configuration of typical stirred tank reactor (Pangarkar, 2015).

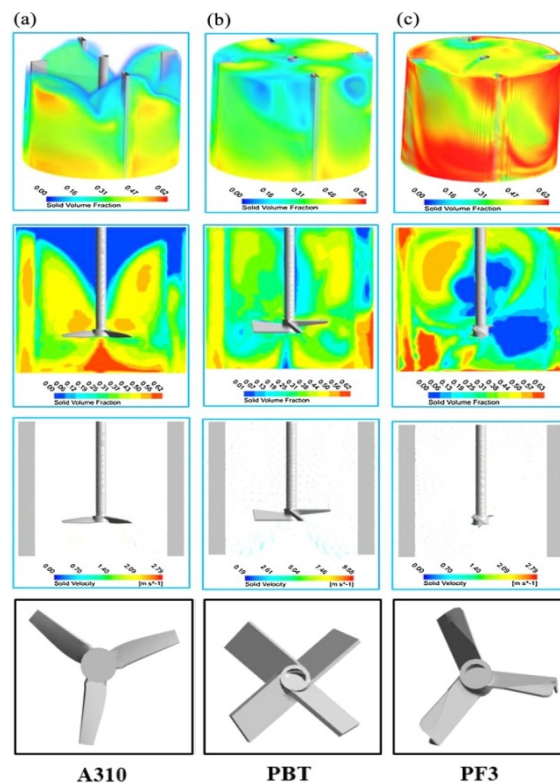


**Figure 1.2** 3D- and 2D-dimensional contour of solid volume fraction and the solid velocity-vector at impeller speed of 950rpm for (a) A310, (b) PBT, and (c) PF3 (Kazemzadeh *et al.*, 2019).

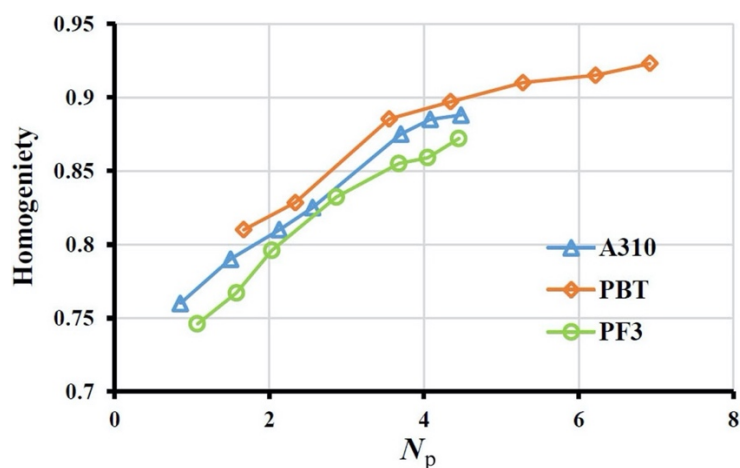


**Figure 1.3** Homogeneity versus power consumption for different types of impellers (Kazemzadeh *et al.*, 2019).

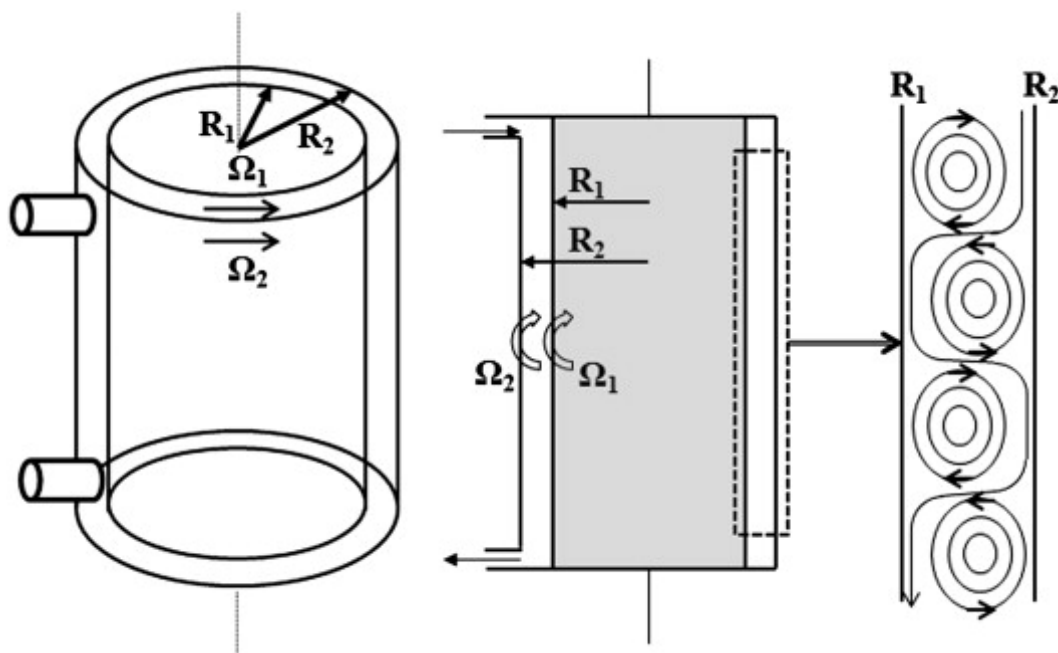


**Figure 1.4** Schematic diagram of Taylor-Couette reactor from side view and bottom view (Kim *et al.*, 2013).

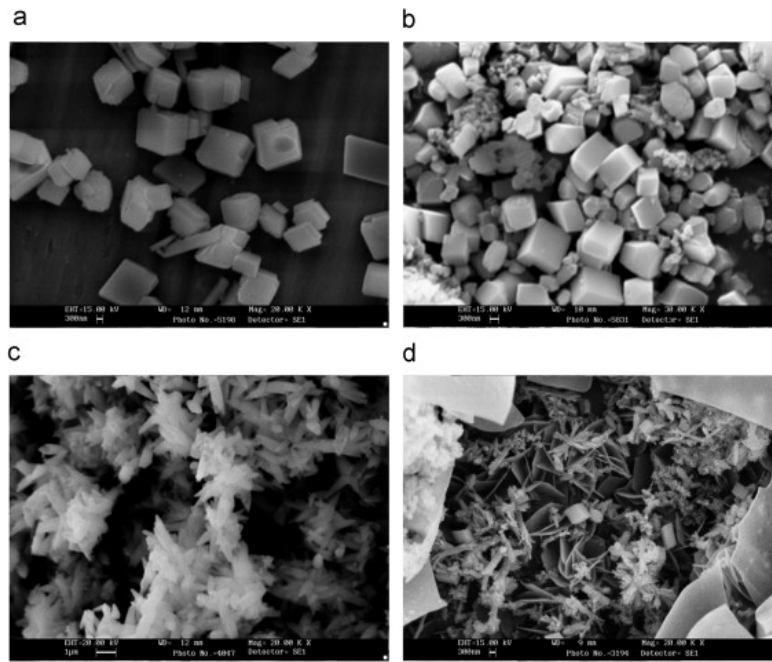


**Figure 1.5** SEM images of calcium carbonate synthesised in (a) CTR at  $C_{BO} = 5 \text{ mol/m}^3$ ; (b) STR at  $C_{BO} = 5 \text{ mol/m}^3$ ; (c) CTR at  $C_{BO} = 48 \text{ mol/m}^3$ ; (d) STR at  $C_{BO} = 48 \text{ mol/m}^3$  (Jung *et al.*, 2010).

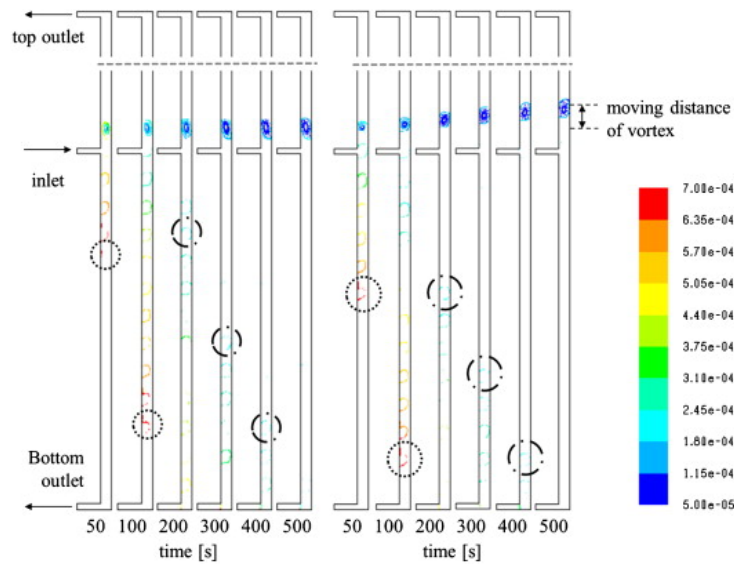


**Figure 1.6** Particle distribution at stationary region (left: 200 rpm, 5 mL/min) and moving region (right: 200 rpm, 60 mL/min) (Kim *et al.*, 2013).

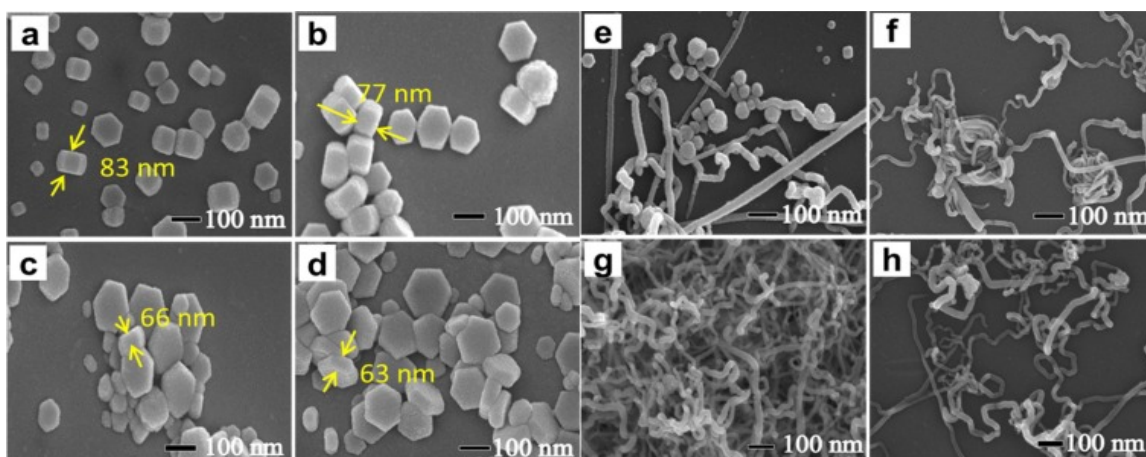


**Figure 1.7** SEM images of copper sulfide nanoparticles with different morphology synthesized in CTR under different rotational speed. (a) 90 rpm; (b) 200 rpm; (c) 500 rpm; (d) 1000 rpm; (e) 85 rpm; (f) 80 rpm; (e) 50 rpm, and (h) 5 rpm respectively (Tang *et al.*, 2019).

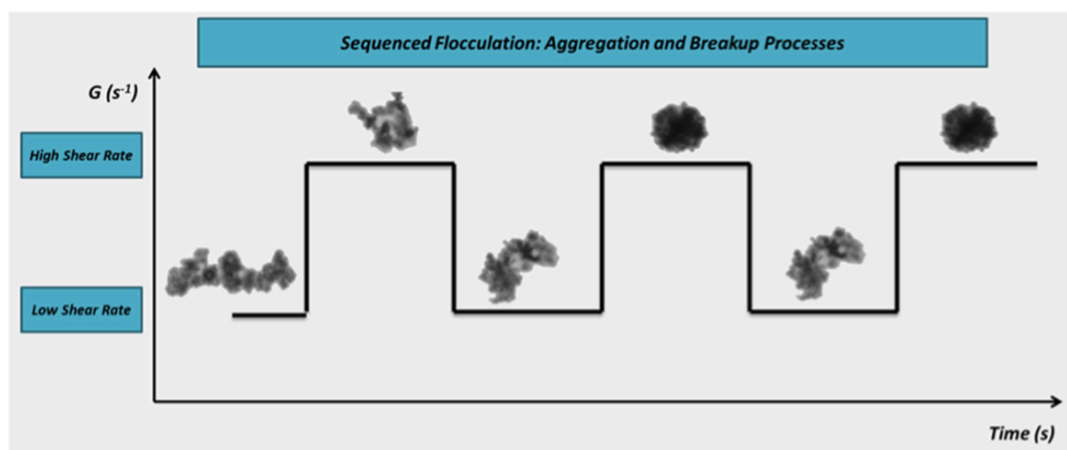


**Figure 1.8** Morphology of latex aggregates experiencing alternative steps of high-shear rate and the low-shear rate (Guérin *et al.*, 2017).

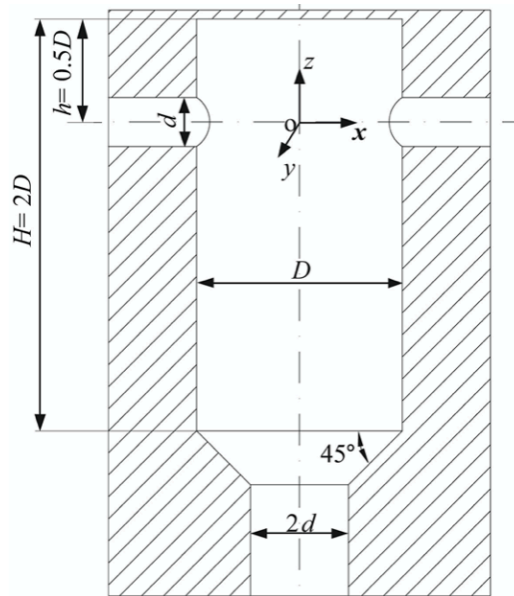


**Figure 1.9** Cross-sectional of confined impinging jets reactor (Schwarzer and Peukert, 2004).

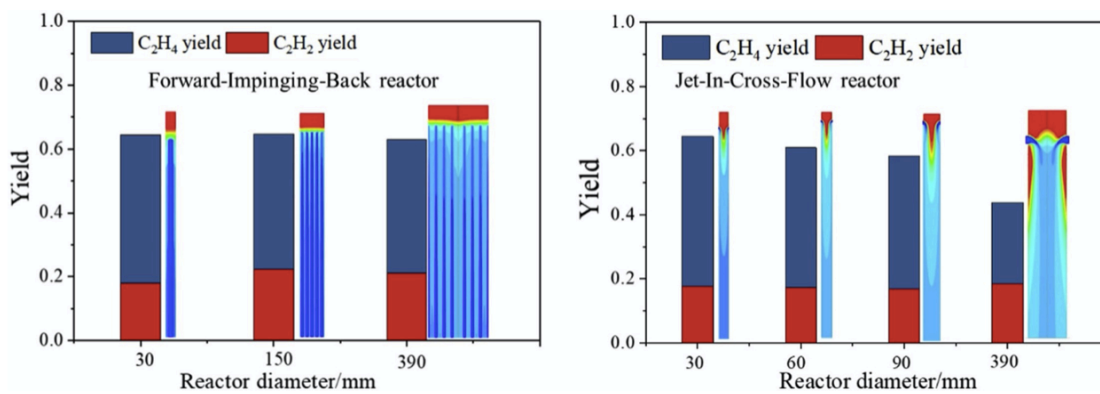


**Figure 1.10** The yield of  $C_2$  ( $C_2H_2 + C_2H_4$ ) of different diameter in Jet-In-Cross-Flow (JICF) reactor and Forward-Impinging-Back (FIB) Reactor (Luo *et al.*, 2019).

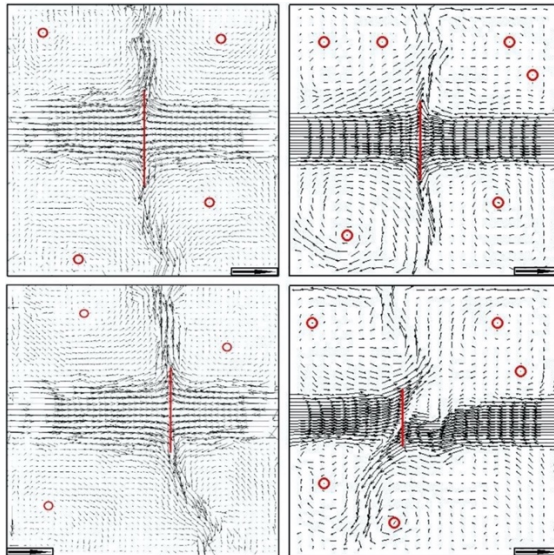


**Figure 1.11** Instantaneous flow field of confined impinging jet reactors on XZ planes with denote of vortex (the scale of arrow is 10 m/s) (Liu *et al.*, 2014).

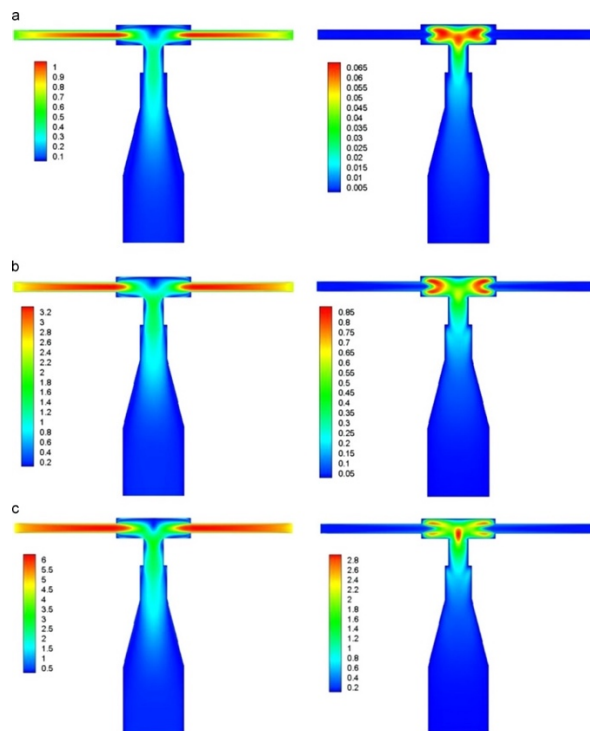


**Figure 1.12** Contour of velocity magnitude and turbulent kinetic energy of micro-impinging stream reactor (MISR) at (a)  $Re_j = 395$ ; (b)  $Re_j = 1500$ ; (c)  $Re_j = 3161$  (Liu *et al.*, 2014).

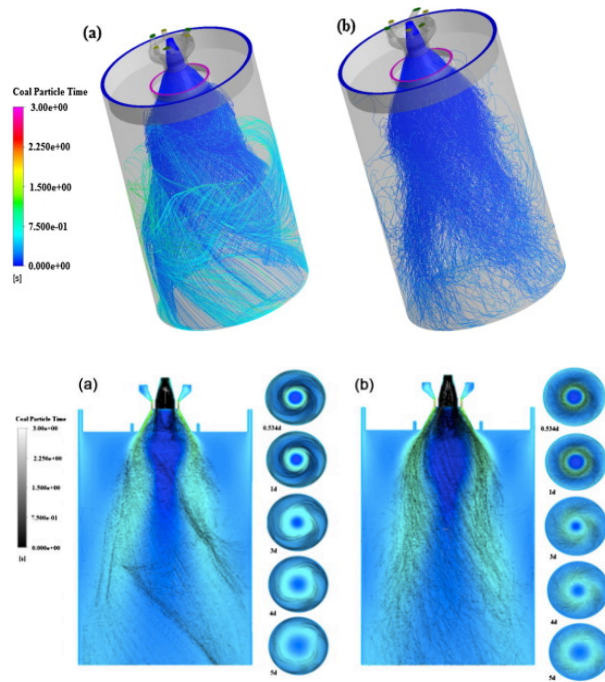


**Figure 1.13** 3D and 2D-dimensional particles trajectories without turbulent dispersion simulated by (a) RANS and (b) LES (Sadiki *et al.*, 2017).

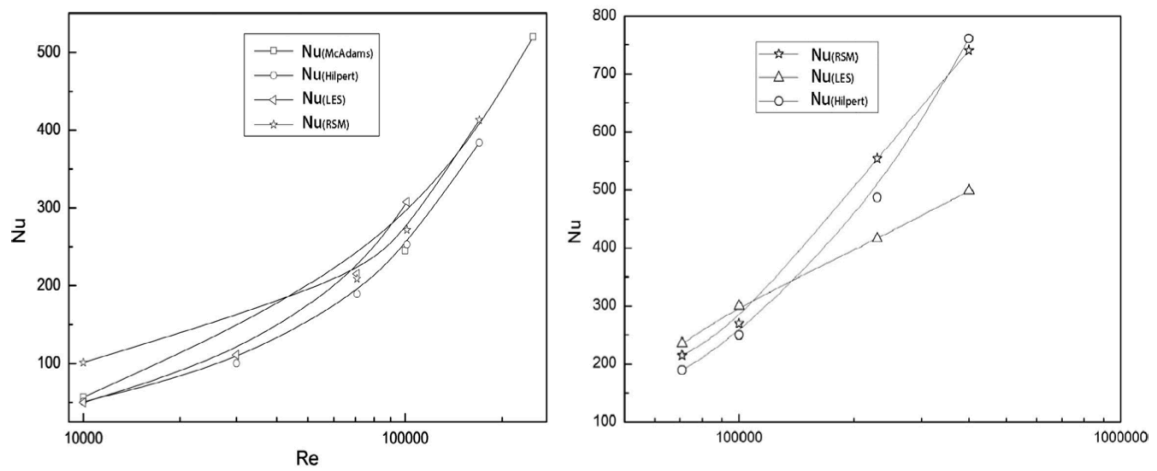


**Figure 1.14** Nusselt number  $Nu$  simulated from LES and RSM with experimental data (Zhou *et al.*, 2017a).

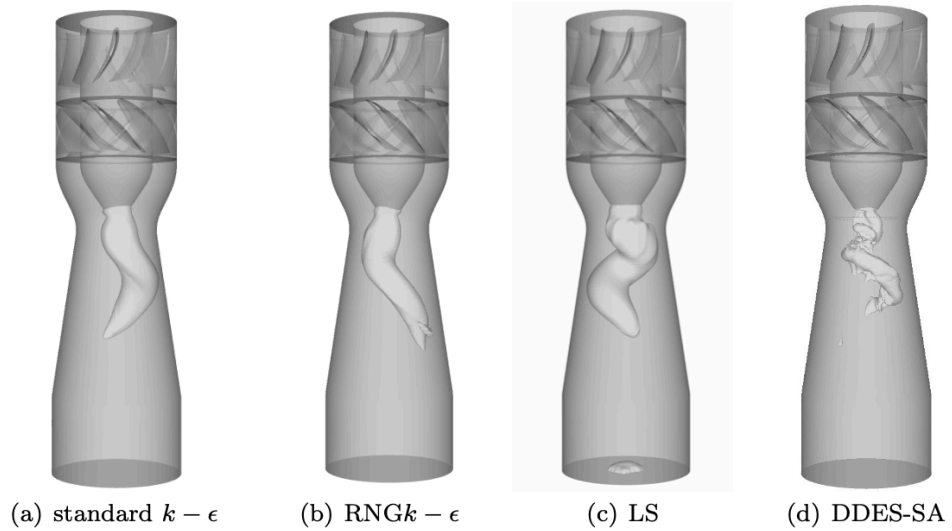


**Figure 1.15** Iso-surface of pressure, visualizing the vortex rope simulated from models of (a) standard  $k-\epsilon$ ; (b) RNG  $k-\epsilon$ ; (c) DDES-SA; (d) LS (Javadi and Nilsson, 2015).

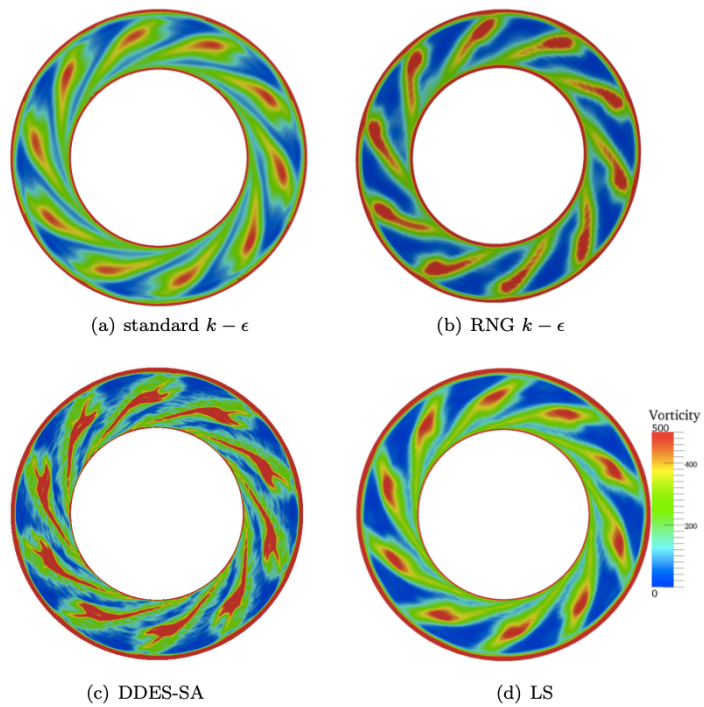


**Figure 1.16** Contours of vorticity magnitude at a horizontal plane simulated by (a) standard  $k-\epsilon$ ; (b) RNG  $k-\epsilon$ ; (c) DDES-SA; (d) LS (Javadi and Nilsson, 2015).

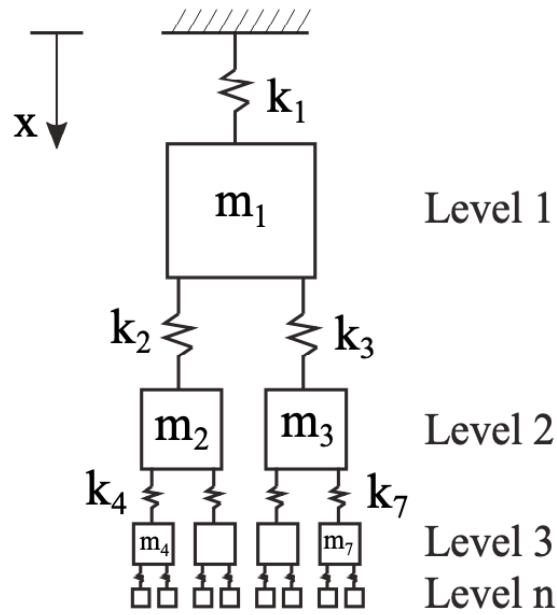


**Figure 1.17** Mechanistic model of a binary tree of masses and springs (Bak and Kalmár-Nagy, 2018).

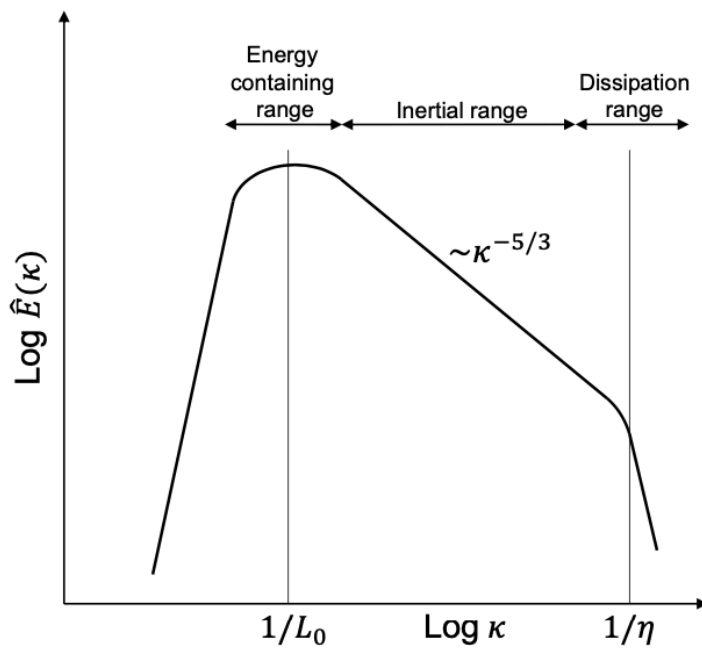


**Figure 1.18** Qualitative graph of the Kolmogorov-spectrum for 3D homogeneous turbulence (Pope, 2000).

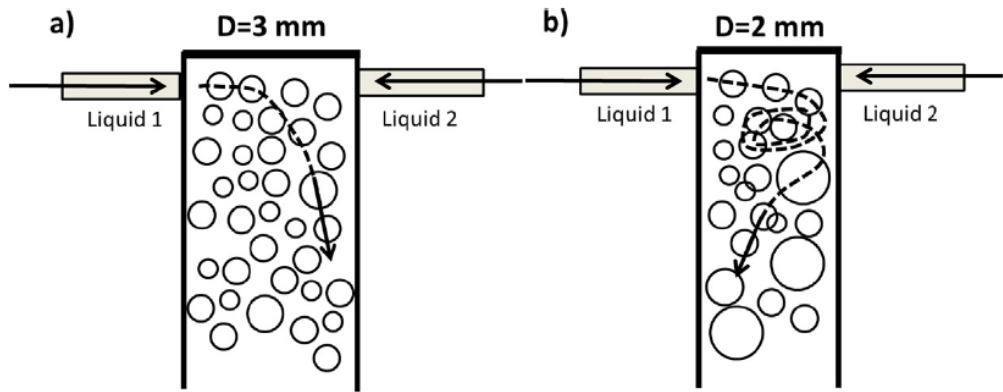


**Figure 1.19** Schematic representation of the path the drops following in the channel with a)  $D=3\text{mm}$ ; b)  $D=2\text{mm}$  at low jet velocities (Tsaoulidis and Angeli, 2017).

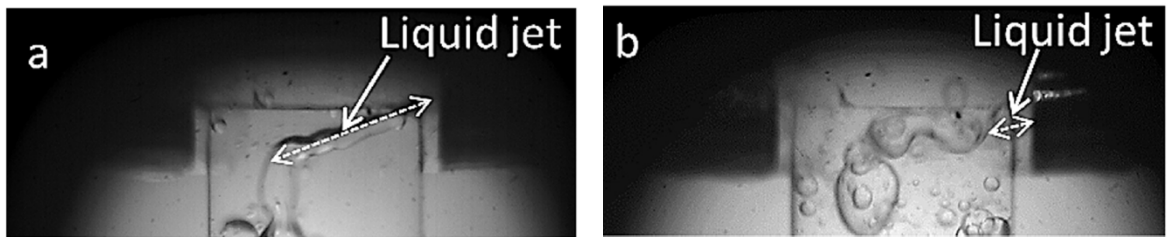


**Figure 1.20** Photos of the liquid jet at (a) low and (b) high jet velocities (Tsaoulidis and Angeli, 2017).

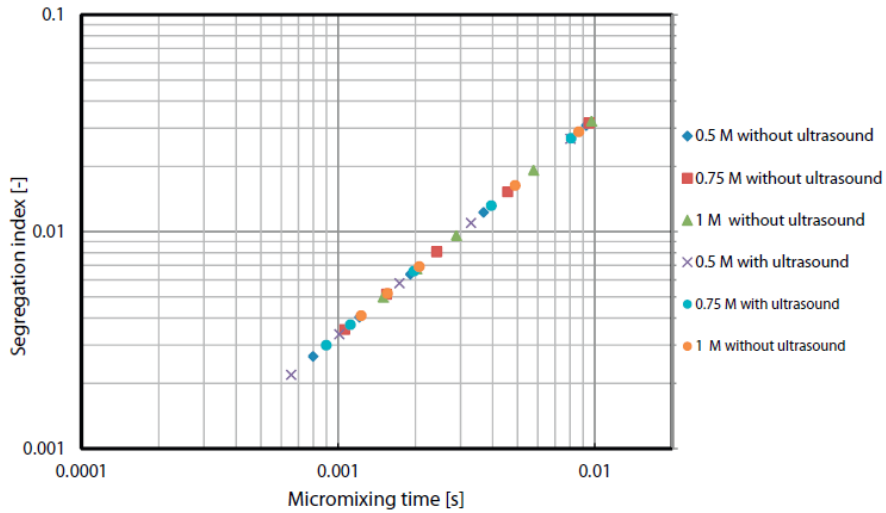


**Figure 1.21** Relationship between segregation index and micromixing time at various conditions (Rahimi *et al.*, 2014).

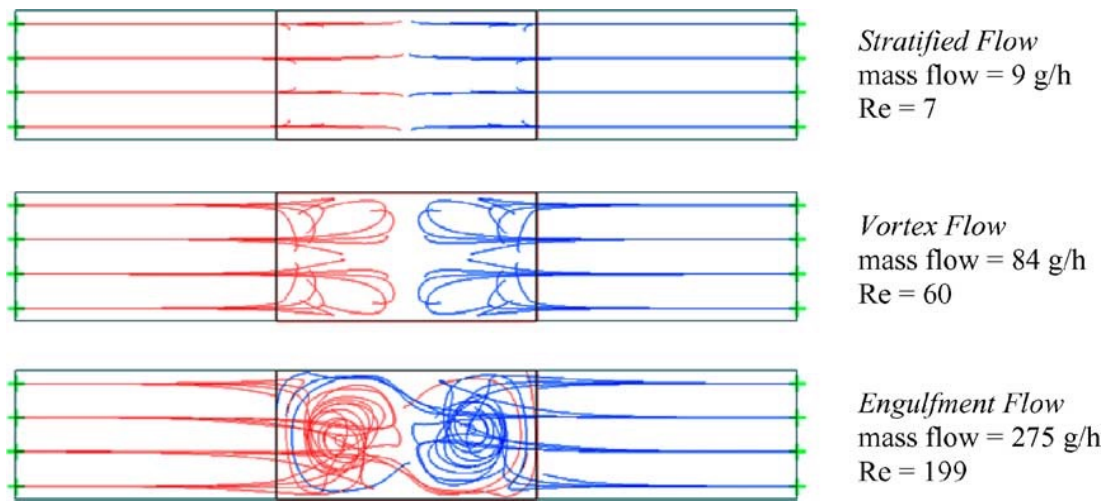


**Figure 1.22** Configuration of streamlines inside a T-mixer at different mass flows (Engler *et al.*, 2004).

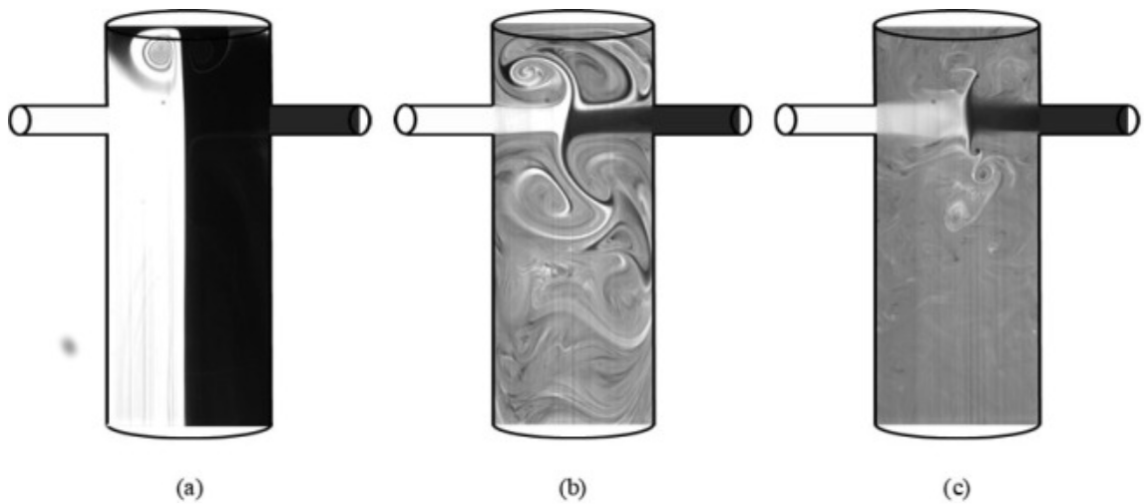


**Figure 1.23** Concentration field of a jet dyed with rhodamine in the confined impinging jet reactor under different Reynolds number (a)  $Re=103$ , (b)  $Re=111$  and (c)  $Re=505$  (Brito *et al.*, 2020).

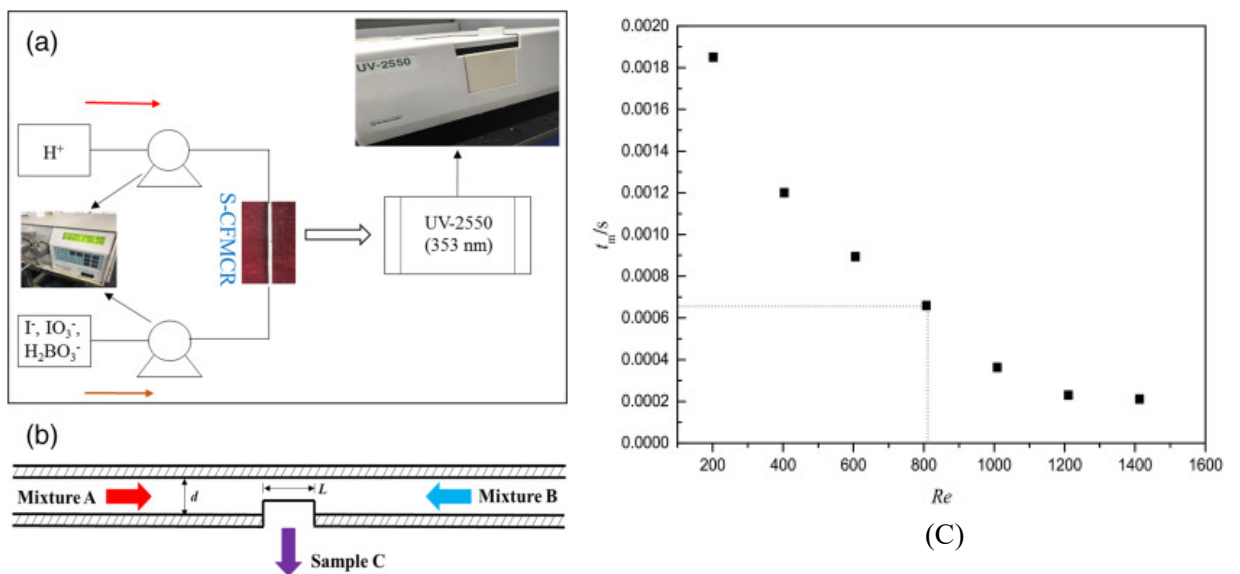


**Figure 1.24** (a) Experimental flowchart for the iodide-iodate tests; (b) Schematic illustration of a single countercurrent-flow micro-channel reactor; (c) micromixing time  $t_m$  versus Reynolds number  $Re$  (Cheng *et al.*, 2019).

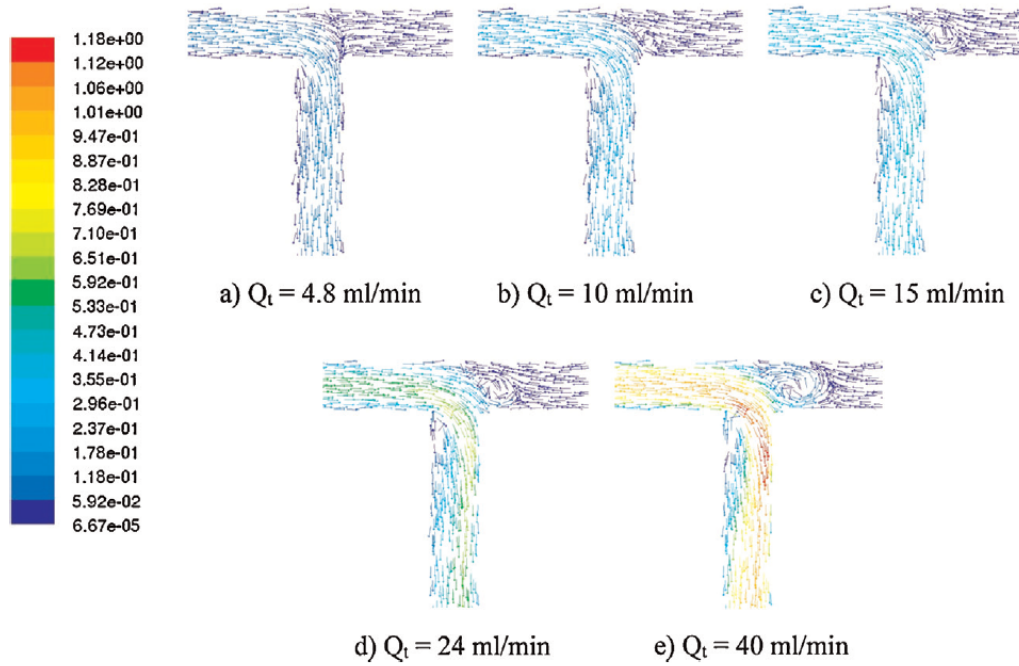


**Figure 1.25** Velocity magnitude vectors at horizontal intersecting face and various total flow rates (Rahimi *et al.*, 2014).

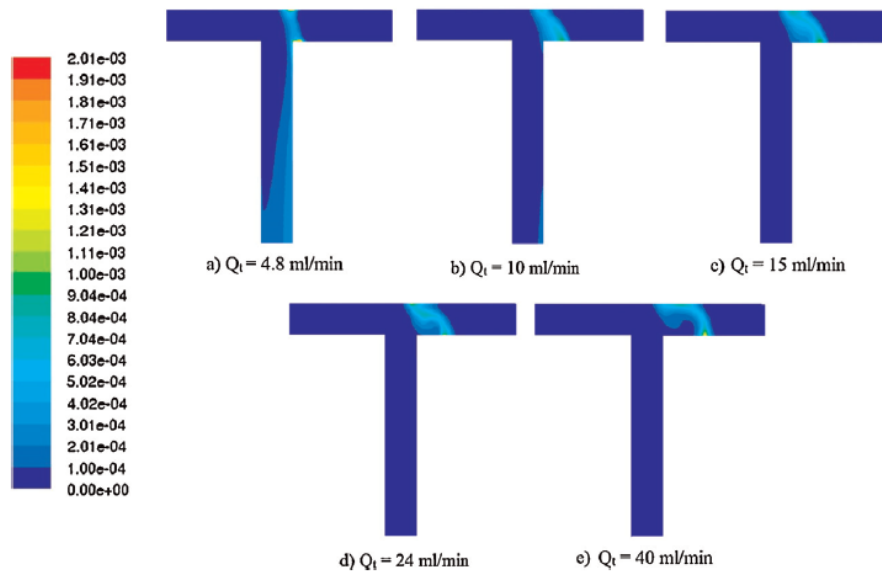


**Figure 1.26** Contour plots of  $I_3^-$  mass fraction fields at horizontal intersecting face and various total flow rates (Rahimi *et al.*, 2014).

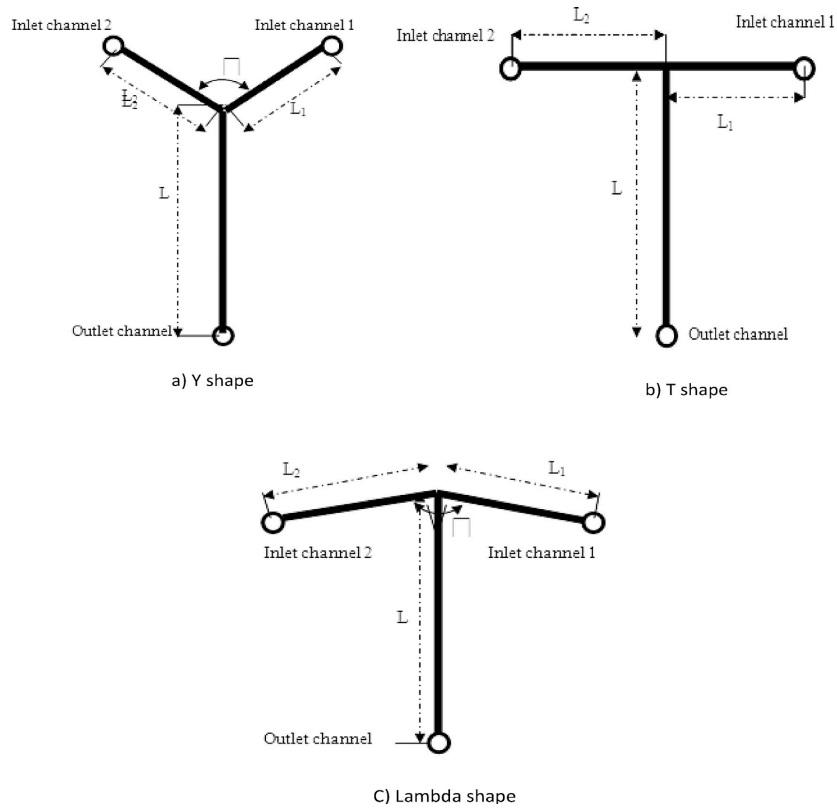


**Figure 1.27** Schematic of the different-types of microchannel reactors (a) Y-shape; (b) T-shape; (c) Lambda shape (Faryadi *et al.*, 2014).

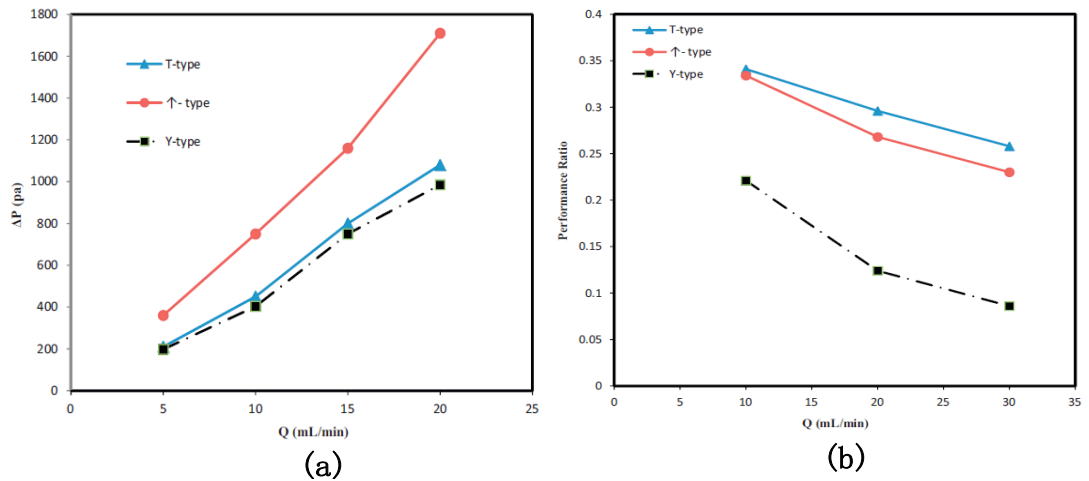


**Figure 1.28** (a) Pressure drop in microchannels of different geometry; (b) the performance ratio microchannels of different geometry (Faryadi *et al.*, 2014).

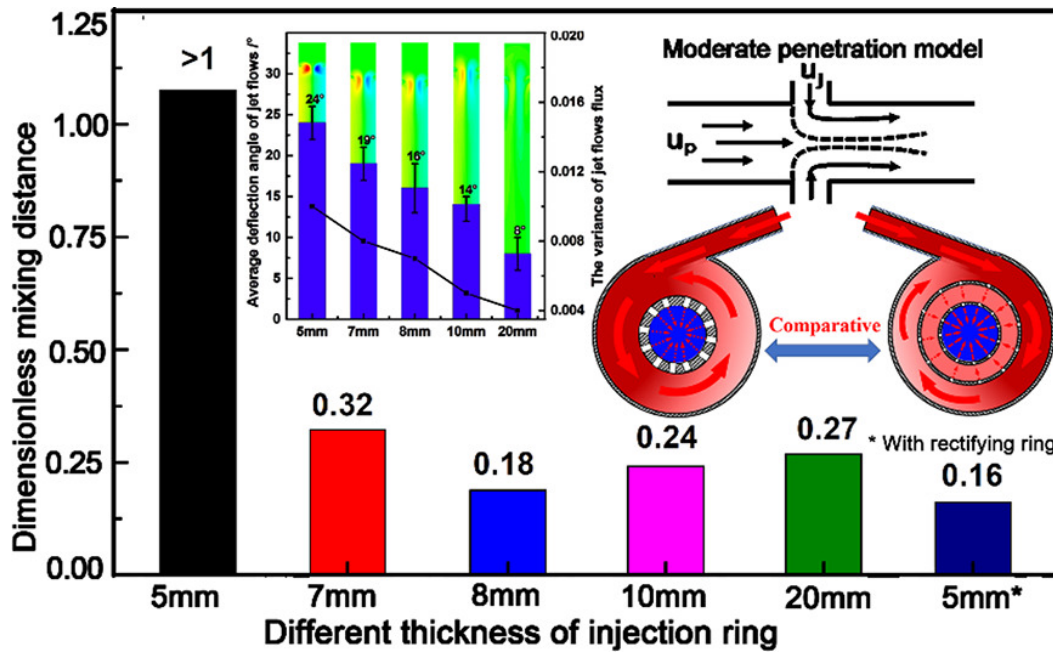


Figure 1.29 The dimensionless mixing distance versus different thickness of injection ring and schematic diagram of moderated penetration model (Zhou *et al.*, 2019).

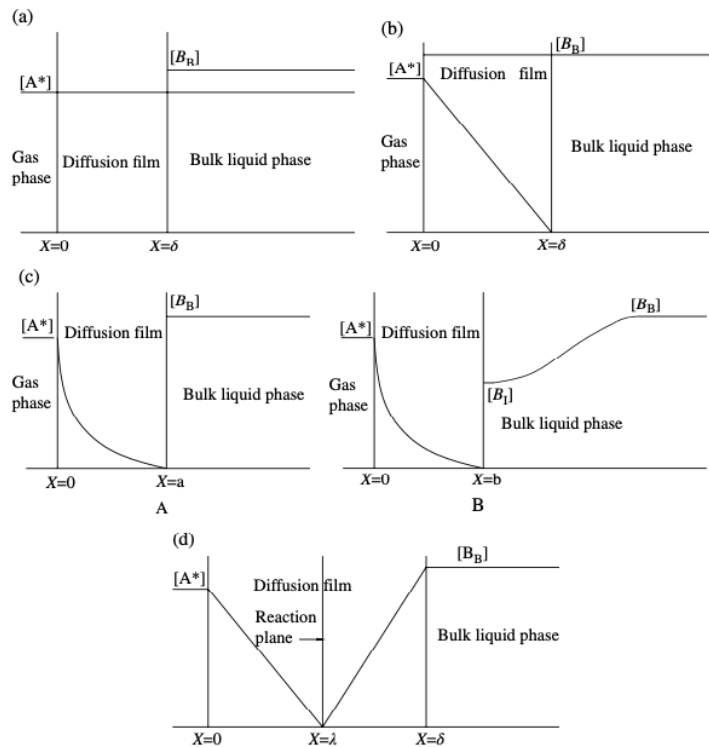
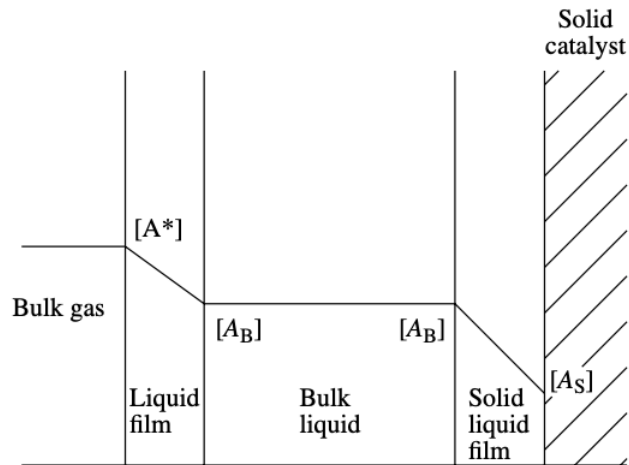
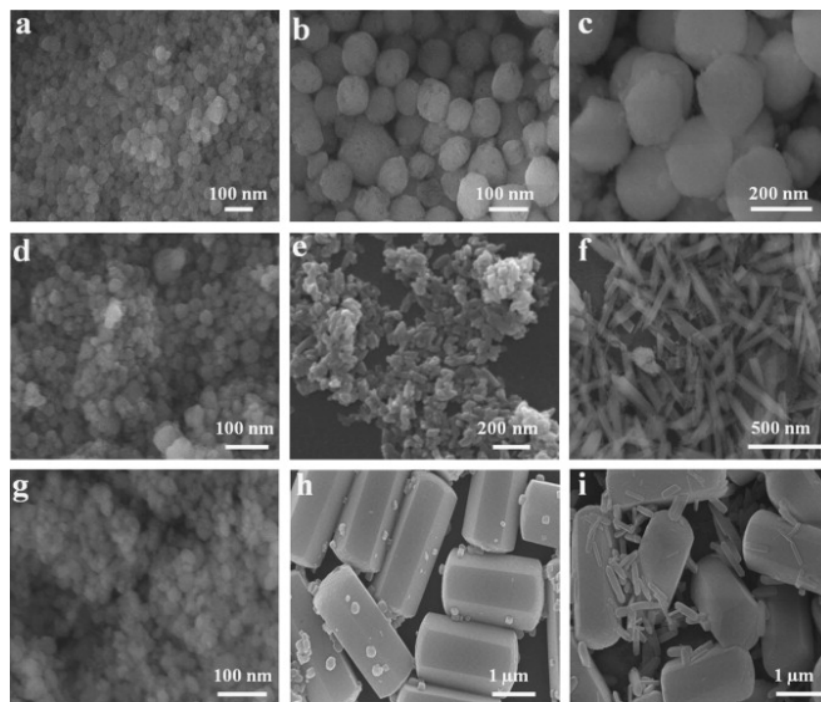


Figure 1.30 Typical concentration profiles for a gas–liquid reaction (Pangarkar, 2015).



**Figure 1.31** Typical concentration profiles for solid-catalyzed gas–liquid reaction (Pangarkar, 2015).



**Figure 1.32** SEM images of  $\text{YPO}_4$  synthesized under hydrothermal treatment at  $180\text{ }^\circ\text{C}$  with different additives for different reaction time: (a, b, c) citric acid for 2 h, 6 h, and 12 h, respectively; (d, e, f) oxalate for 2 h, 6 h, and 12 h, respectively; and (h, i, j) EDTA for 2 h, 6 h, 12 h, respectively (Lai *et al.*, 2014).

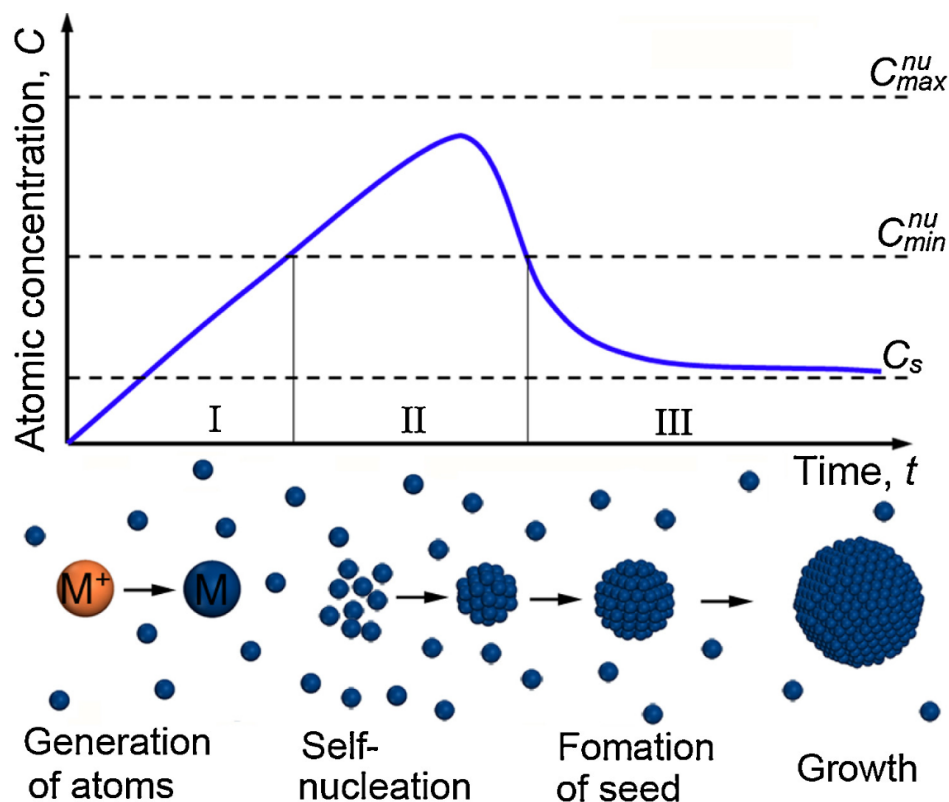


**Figure 1.33** LaMer curve describing the three stages of metal nanocrystal formation in solution system. Stage I: Atom-producing, stage II: nucleation, and stage III: seed formation and growth (You and Fang, 2016).

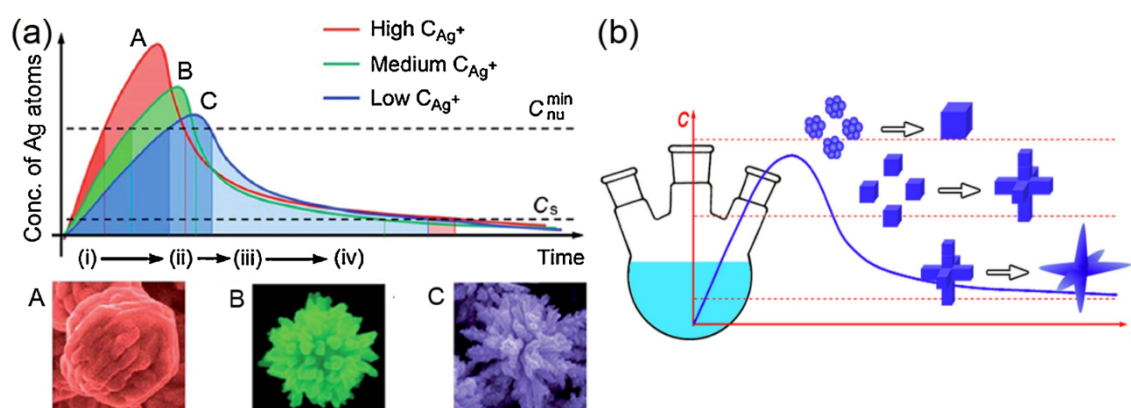


**Figure 1.34** (a) Schematic illustration of the effect of  $\text{Ag}^+$  ion concentration on the morphology of Ag mesoparticles. (b) Schematic diagram of 1D, 2D, and 3D morphologies have been prepared via particle-mediated growth (You and Fang, 2016).

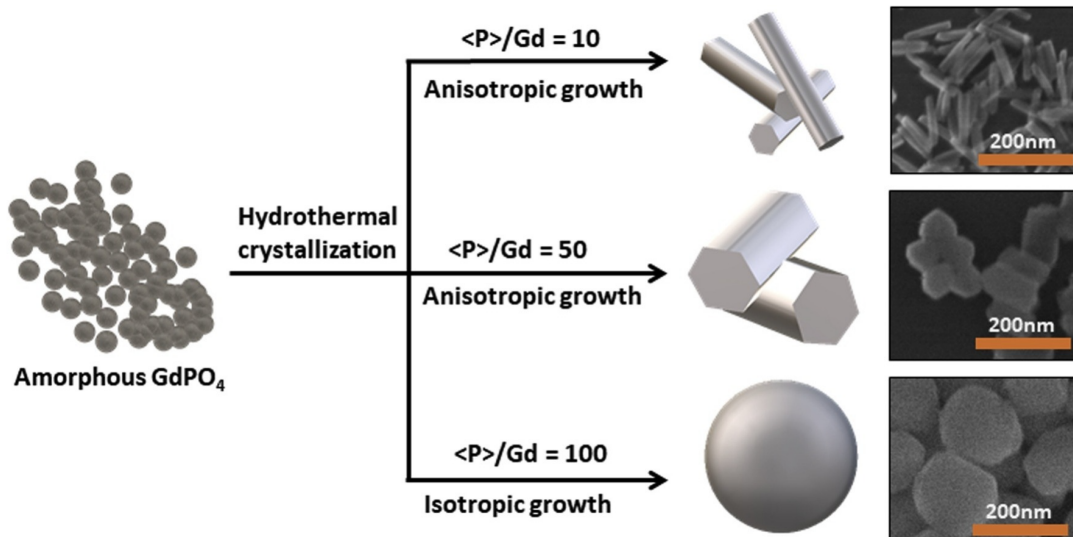


**Figure 1.35** Crystallisation of the  $\text{GdPO}_4$  into different morphology and size under different  $\text{PO}_4^{3-} / \text{Gd}^{3+}$  ratio in the reaction mixture.

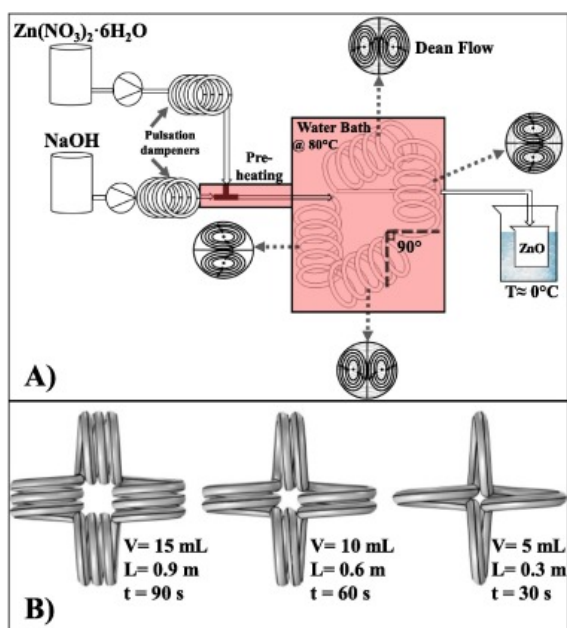


**Figure 1.36** A) Experimental set-up for synthesis of  $\text{ZnO}$  particles in a CFI. Dashed arrows represent the change of direction of the secondary flow (Dean flow) due to  $90^\circ$  bends; B) Different CFIs used for carrying out the  $\text{ZnO}$  synthesis at different residence times (Delgado-Licona *et al.*, 2020).

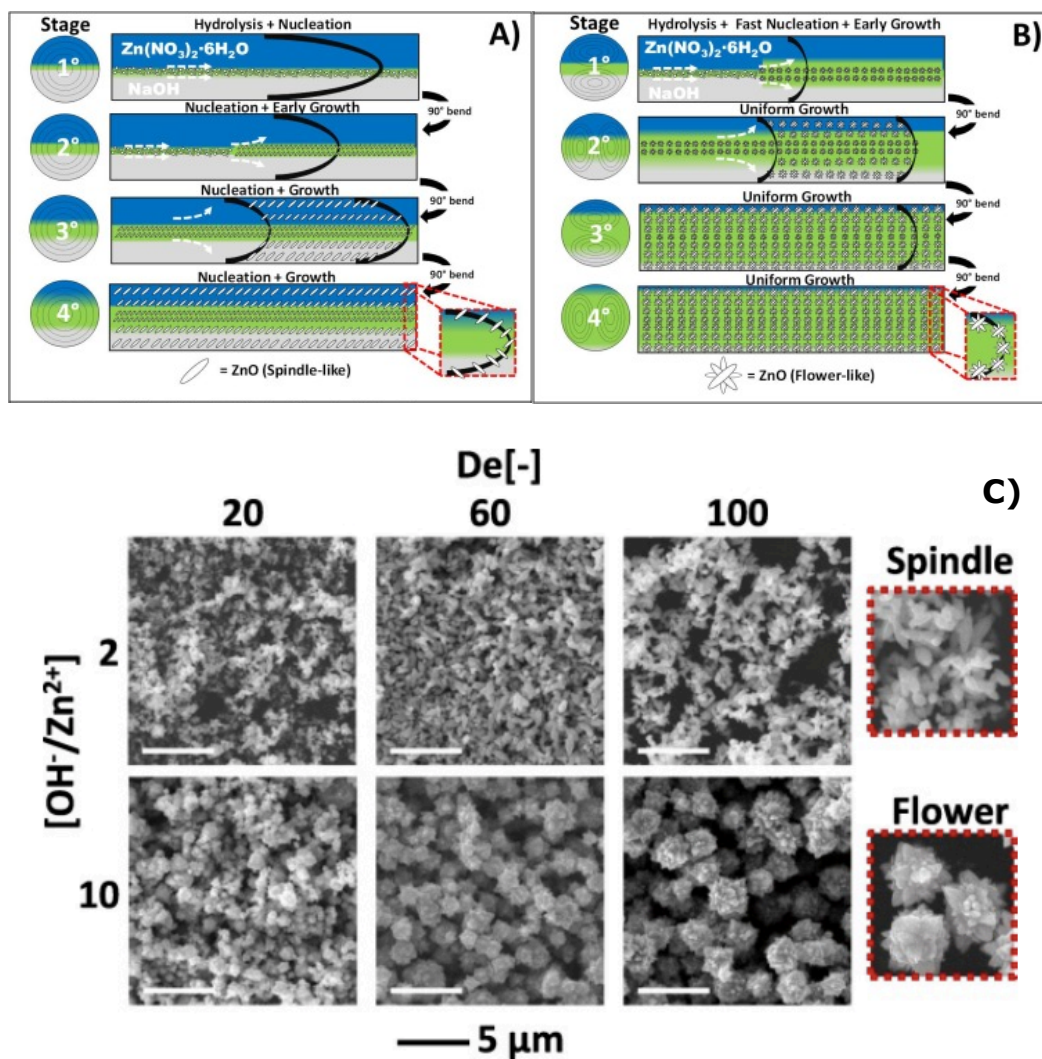


**Figure 1.37** Schematic representation of the ZnO formation mechanism by a change in hydrodynamics and reaction conditions: A)  $De \leq 20$  and  $[OH^-/Zn^{2+}] = 2$  where mass transfer controls the nucleation rate and B)  $De \geq 60$  and  $[OH^-/Zn^{2+}] = 10$ , where the growth of the particle is favored due to a formation of Dean flow. Colour contours represents the concentration of each reactants, whereas the green interface represents the concentration of the formed ZnO. Bold black lines represent the velocity profile in axial direction; C) SEM images of Spindle-like ZnO particles obtained at  $[OH^-/Zn^{2+}] = 2$ ; Flower-like ZnO particles obtained at  $[OH^-/Zn^{2+}] = 10$  (Delgado-Licona *et al.*, 2020).

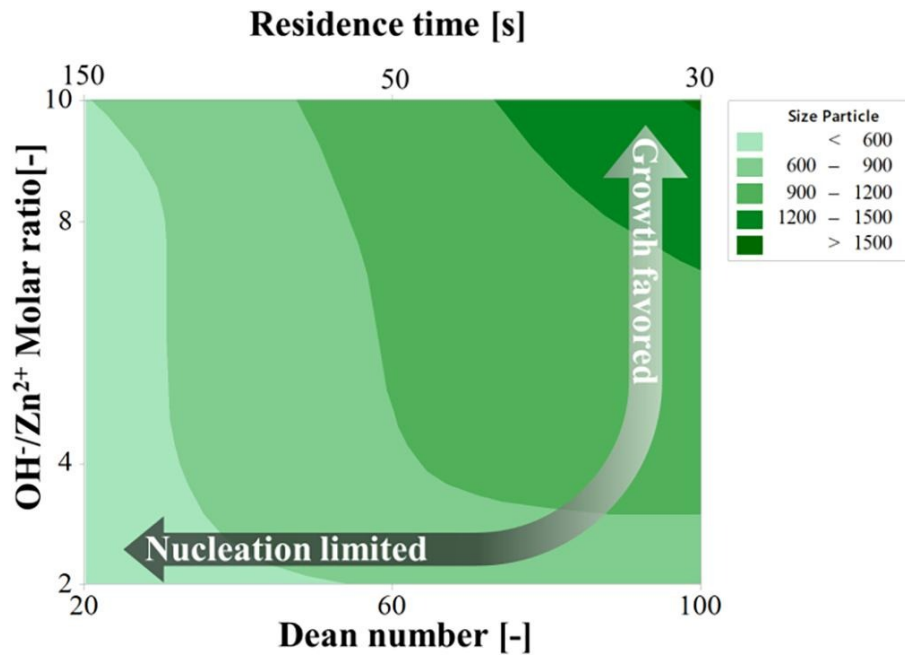


**Figure 1.38** Predicted contour graph of the relationship between  $[\text{OH}^-/\text{Zn}^{2+}]$  molar ratios, Dean numbers and residence time on the particle size (Delgado-Licona *et al.*, 2020).

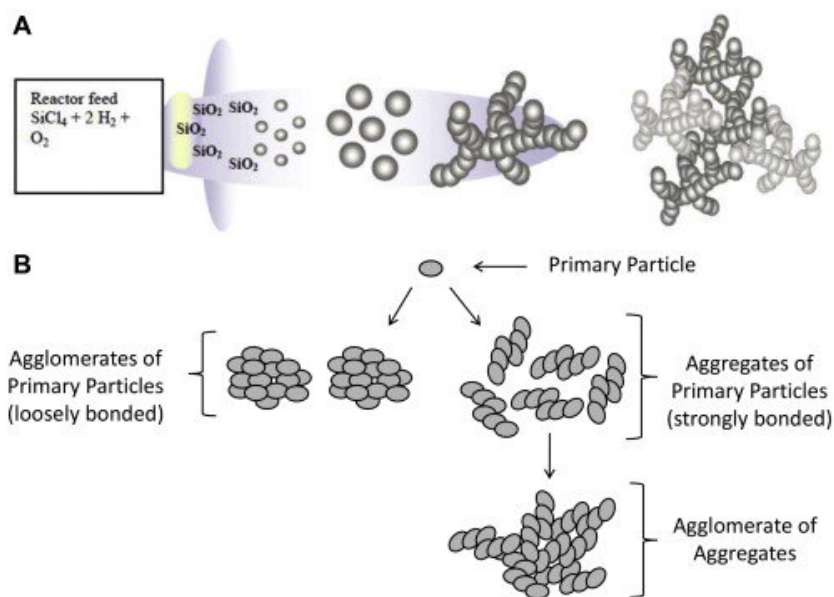


**Figure 1.39** Considerations for primary particles, aggregates and agglomerates. (A) synthesis approach of synthetic amorphous silica through a pyrogenic process; (B) aggregates and agglomerates of primary particles (Boverhof *et al.*, 2015).

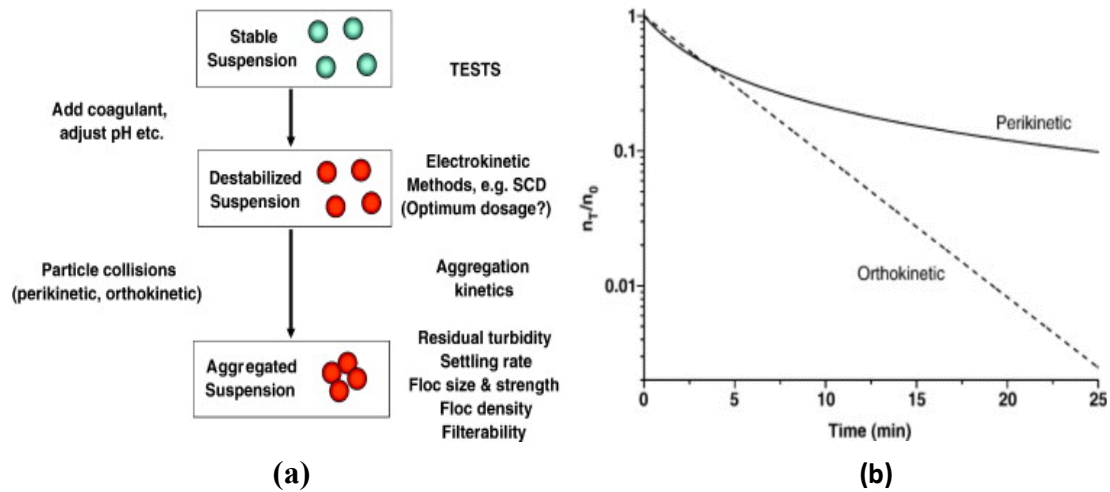


**Figure 1.40** (a) Schematic aggregation process with possible test methods; (b) Relative decrease in total particle concentration for perikinetic and orthokinetic aggregation (Gregory, 2009).

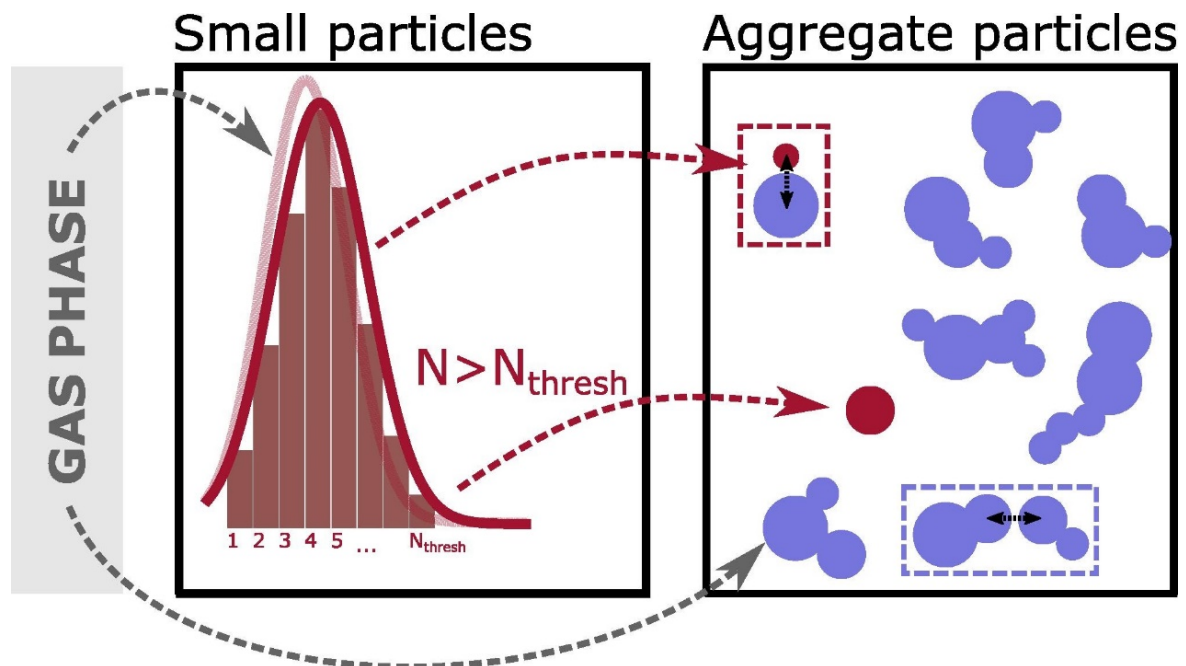
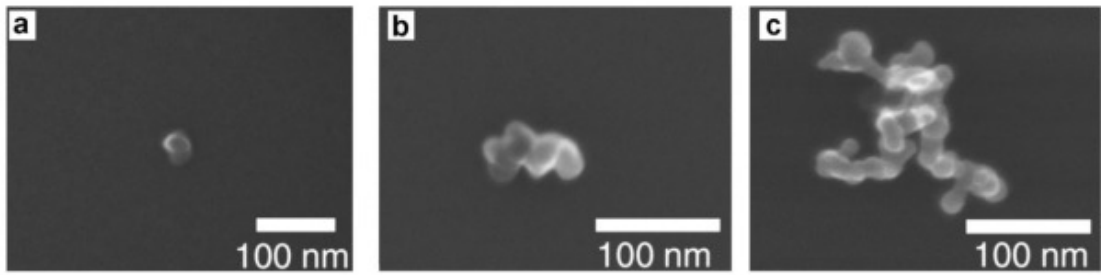
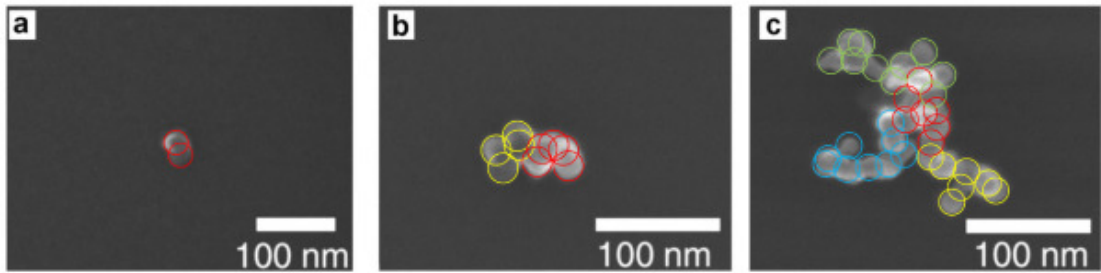


**Figure 1.41** Schematic diagram of hybrid particle state and mass transfer between the gas-phase and the particle systems (Boje *et al.*, 2019).

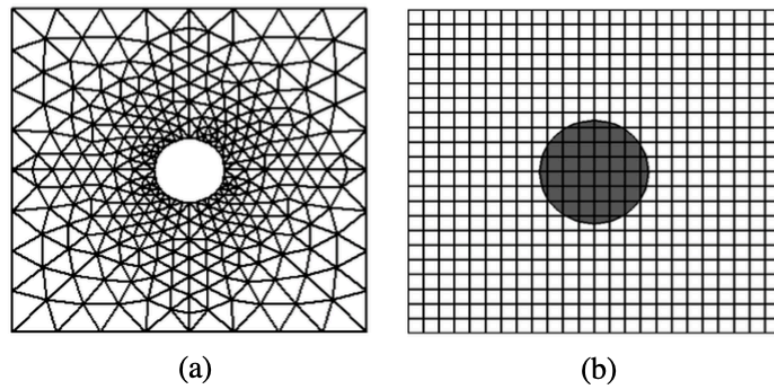


(A)

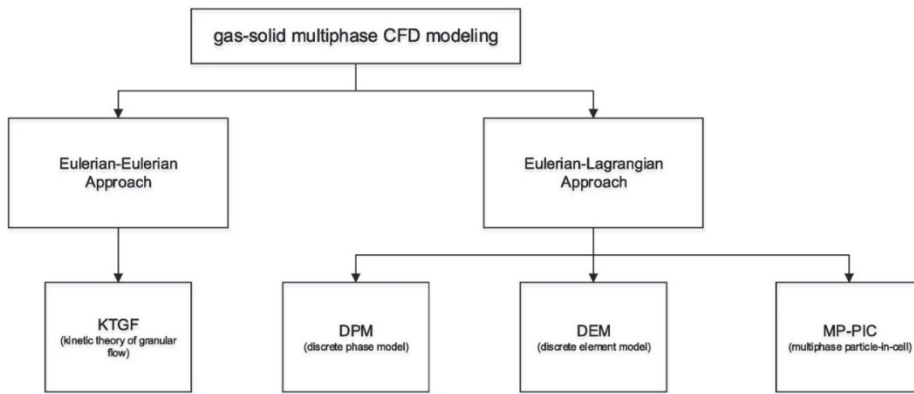


(B)

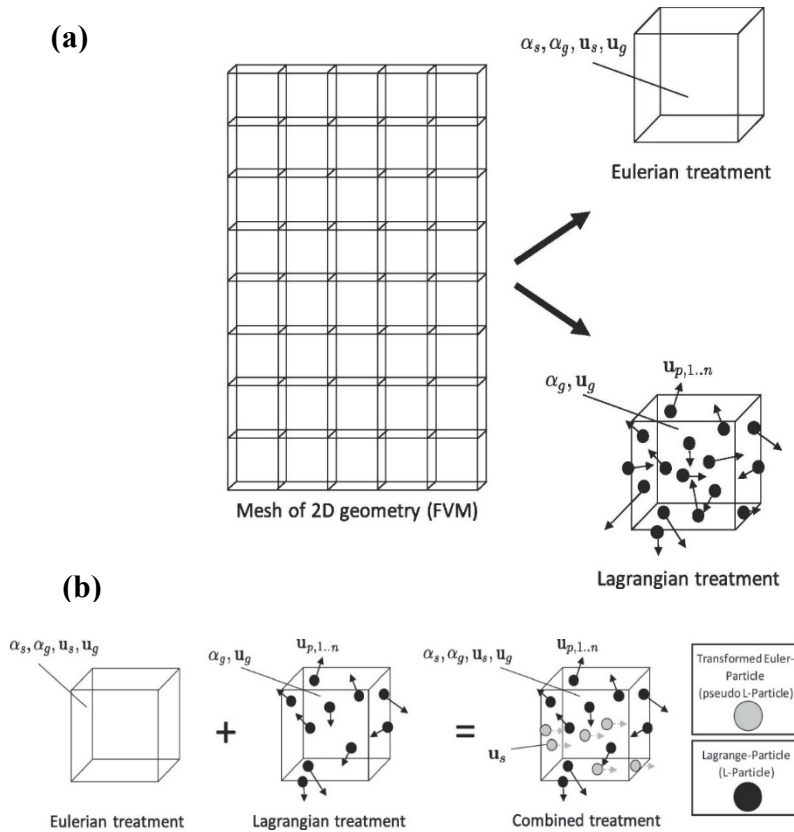
**Figure 1.42** SEM images of aggregates with mobility diameters of (a) 30 nm, (b) 50 nm, and (c) 100 nm for (A) Original SEM images and (B) SEM images with sketched representative primary particle circles (Naseri and Thomson, 2019).



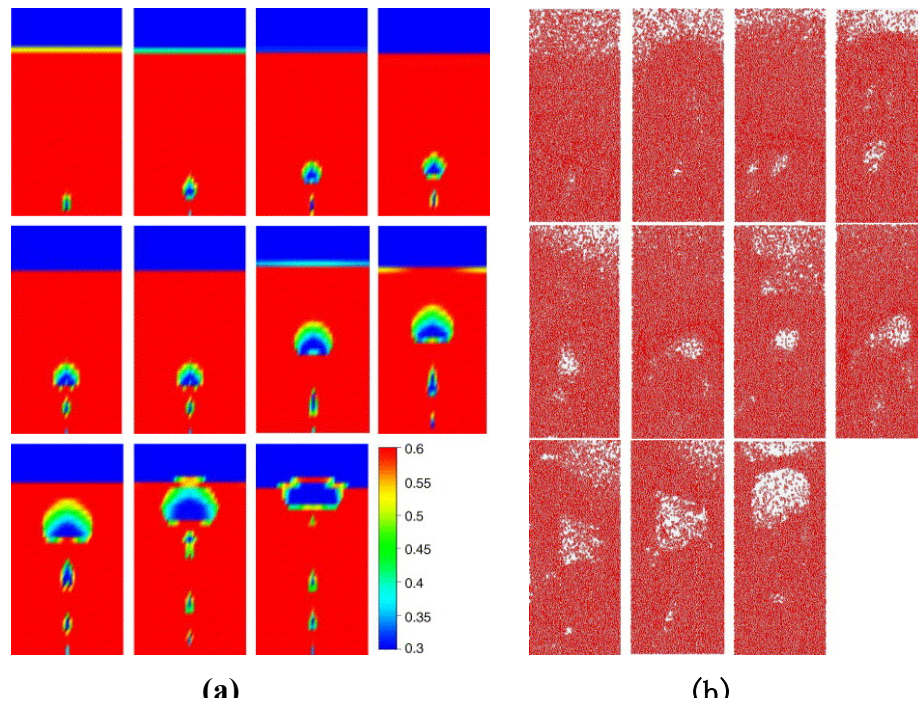
**Figure 1.43** (a) Structured boundary-fitted mesh (b) Unstructured boundary-fitted mesh around a circular particle (Feng and Michaelides, 2009).



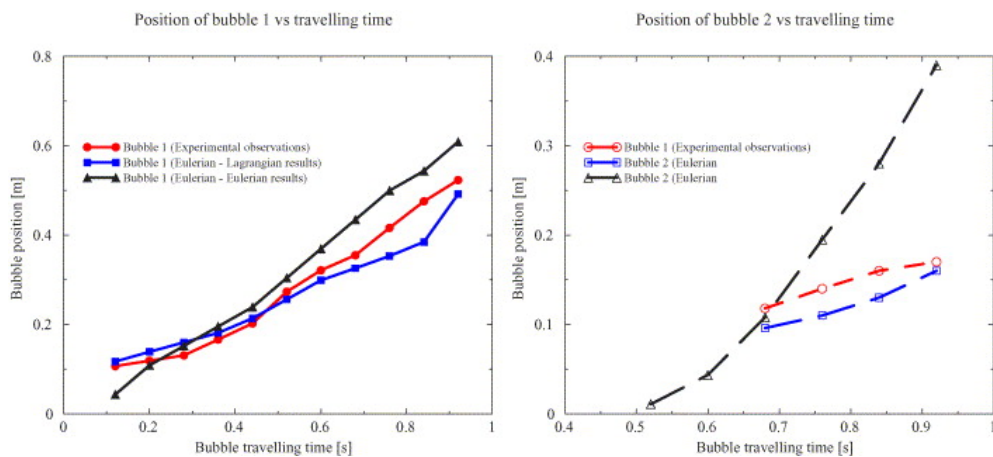
**Figure 1.44** Overview of gas-solid multiphase CFD models with an Eulerian-Eulerian and an Eulerian-Lagrangian approach (Hirche *et al.*, 2019).



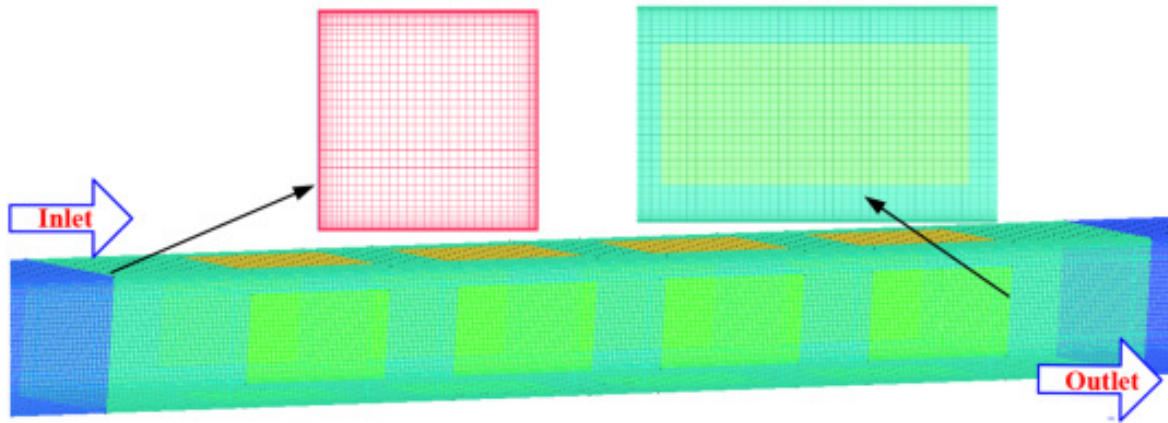
**Figure 1.45** (a) Eulerian-Eulerian and Eulerian-Lagrangian treatment for a 2D geometry with finite volume method (FVM) method; (b) Coupling overview of Eulerian and Lagrangian treatment and introduction of transformed Eulerian particles as pseudo Lagrangian particles (Hirche *et al.*, 2019).



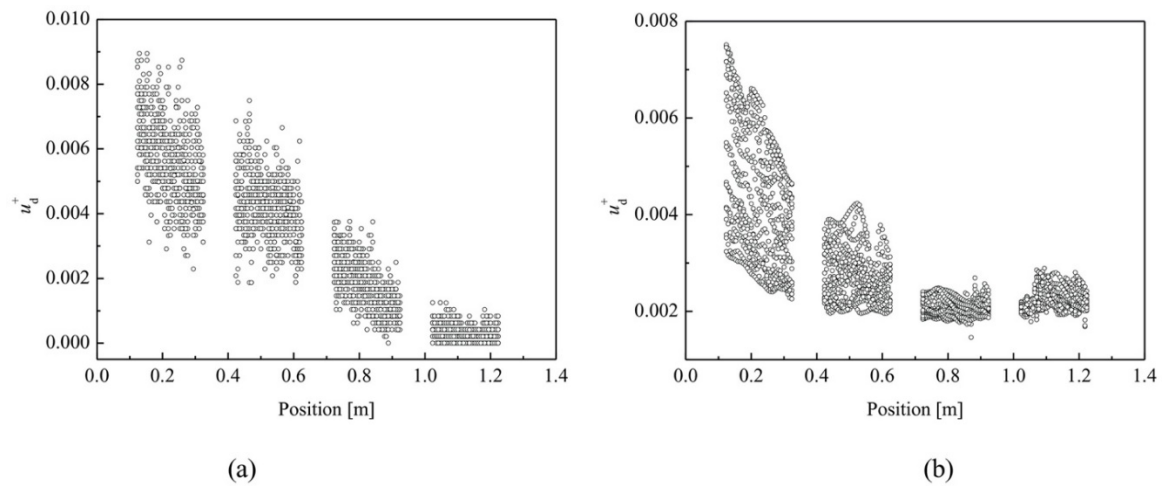
**Figure 1.46** (a) Numerical observations of a two-dimensional fluidised bed formulated with a Eulerian–Eulerian approach (time interval  $\Delta t = 80$  ms); (b) Numerical observations of a two-dimensional fluidised bed formulated with an Eulerian-Lagrangian (EL) approach (Chiesa *et al.*, 2005).



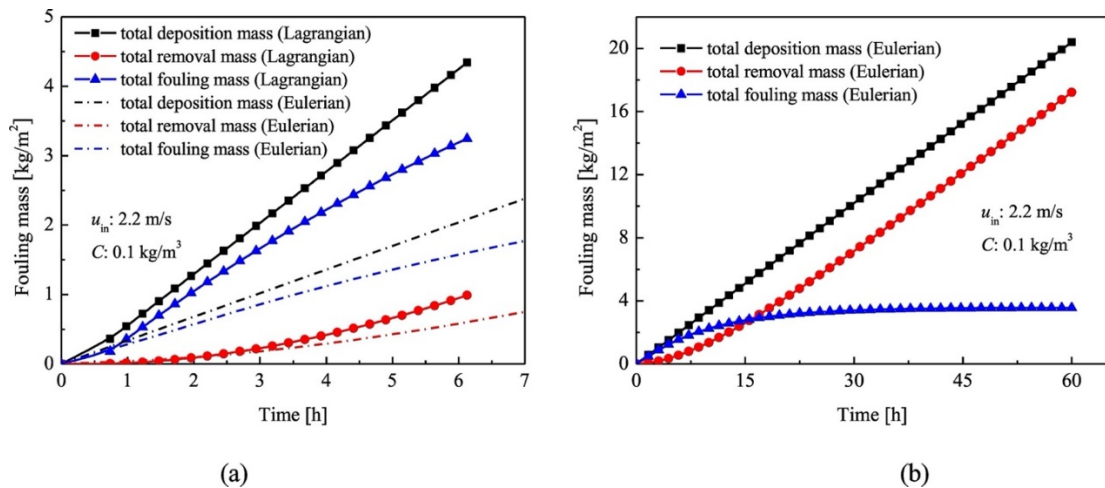
**Figure 1.47** Position of bubbles in fluidised bed as a function of time for both Eulerian-Eulerian and Eulerian-Lagrangian approaches compared with experimental data (Chiesa *et al.*, 2005).



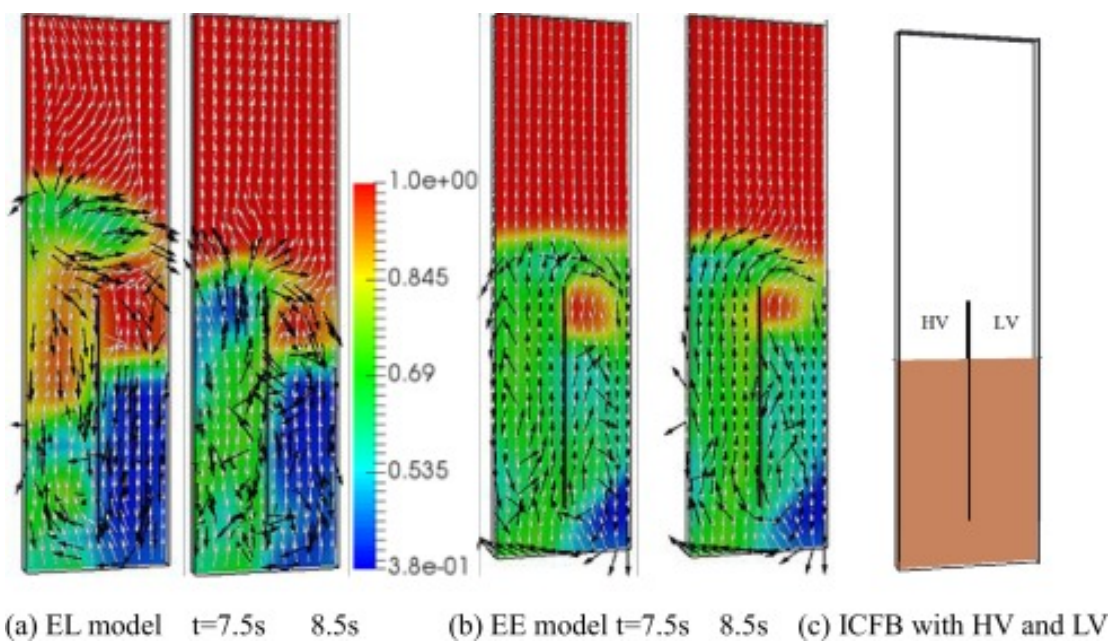
**Figure 1.48** Structural grids for ventilation ducts (Xu *et al.*, 2020b).



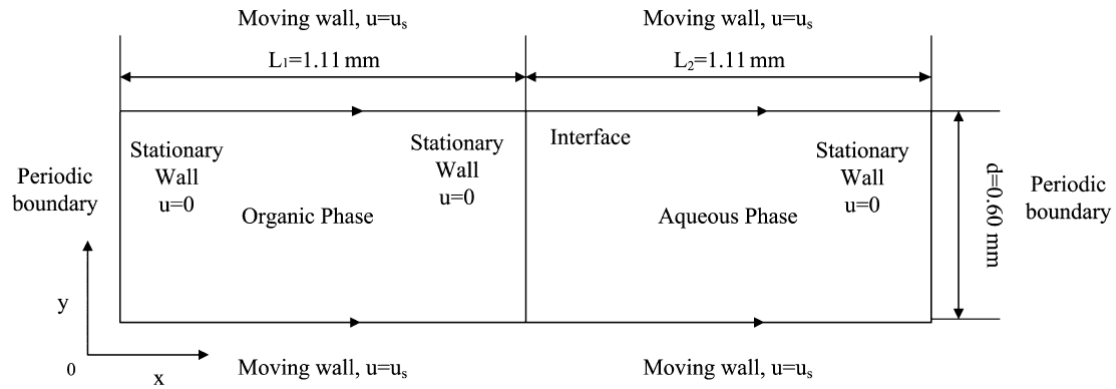
**Figure 1.49** Non-dimensional deposition velocity at different positions: (a) Lagrangian approach; (b) Eulerian approach (Xu *et al.*, 2020b).



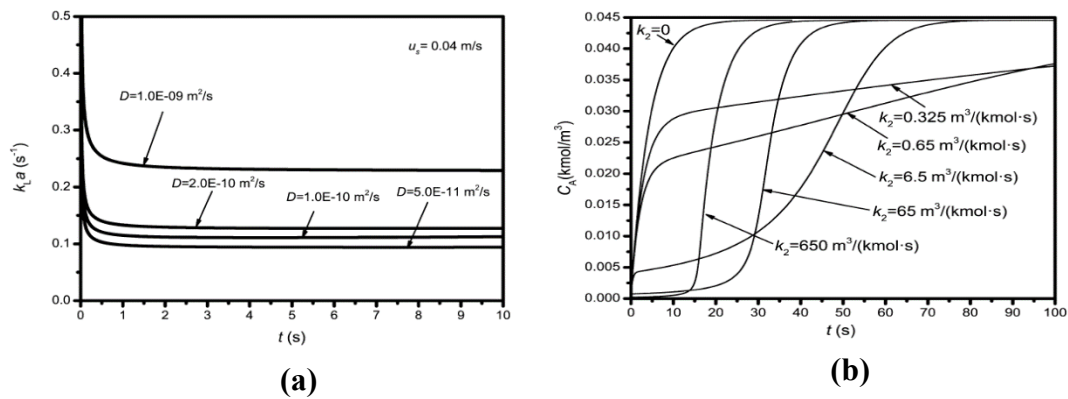
**Figure 1.50** Variation of fouling mass on floor with time for  $d_p = 5 \mu\text{m}$ : (a) Comparison of two approaches; (b) Eulerian approach (Xu *et al.*, 2020b).



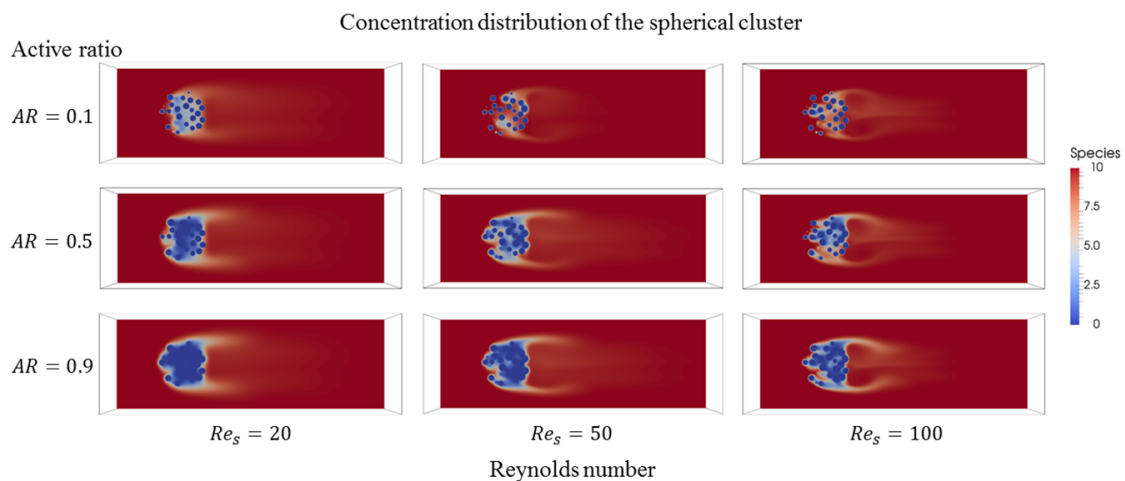
**Figure 1.51** Instantaneous gas volume fraction and velocity vectors (color snapshots for gas volume fraction, white vector for gas phase, and black vector for discrete particles of (a) EL model; (b) solid phase of EE model; (c) Schematic of the internally circulating fluidized bed) (Zhang *et al.*, 2018).



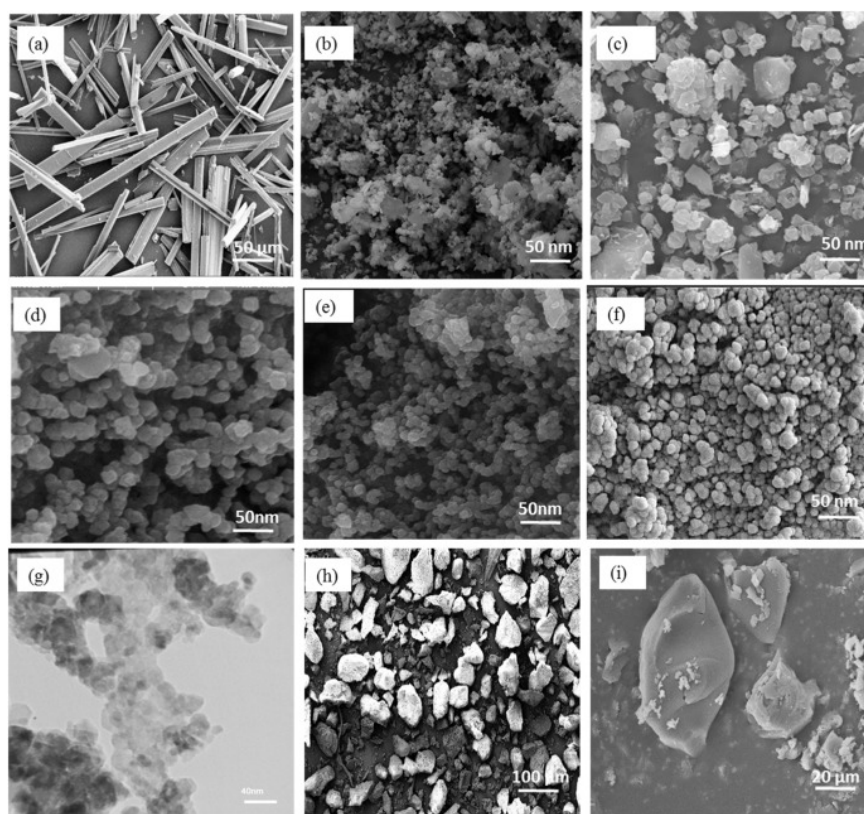
**Figure 1.52** Schematic diagrams of the computational domain and boundary conditions for mass transfer simulation (Zhang *et al.*, 2015).



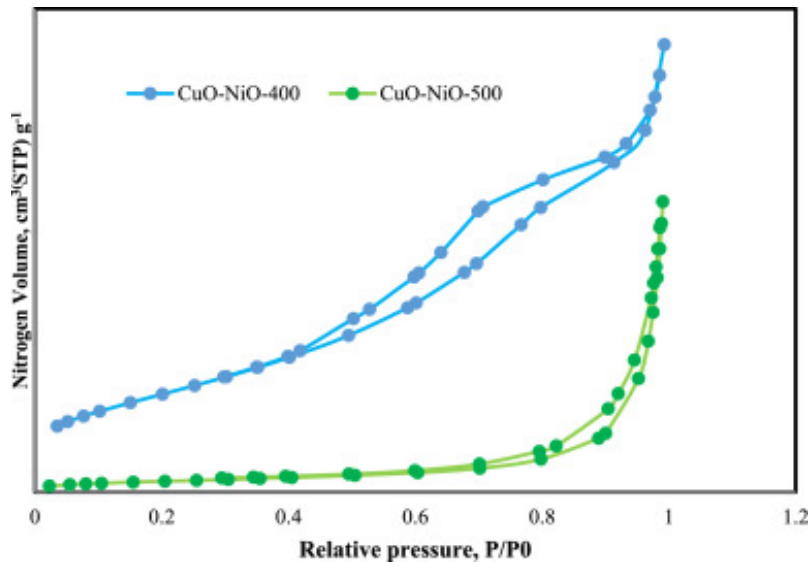
**Figure 1.53** (a) Effect of diffusivity on mass transfer coefficient at different residence times; (b) Dependence of concentrations of mass transfer species in aqueous phase on residence time for different types of reactions (Zhang *et al.*, 2015).



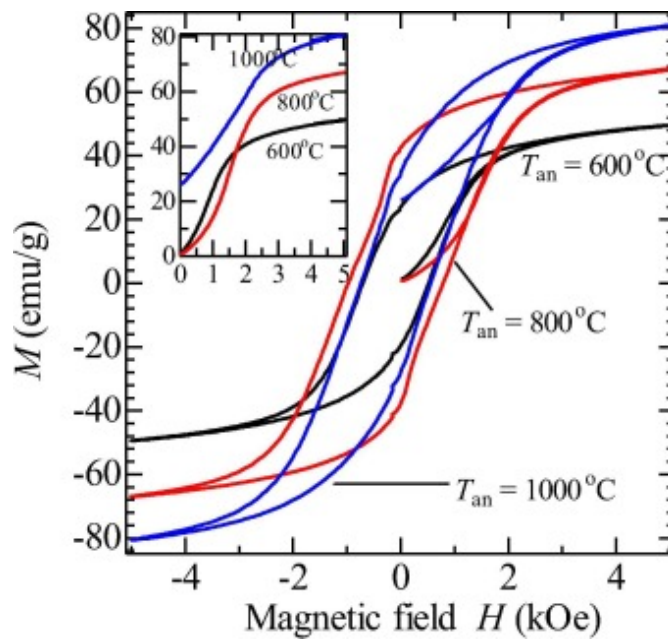
**Figure 1.54** Concentration distribution of the spherical cluster at different Reynolds number (Lu *et al.*, 2018).



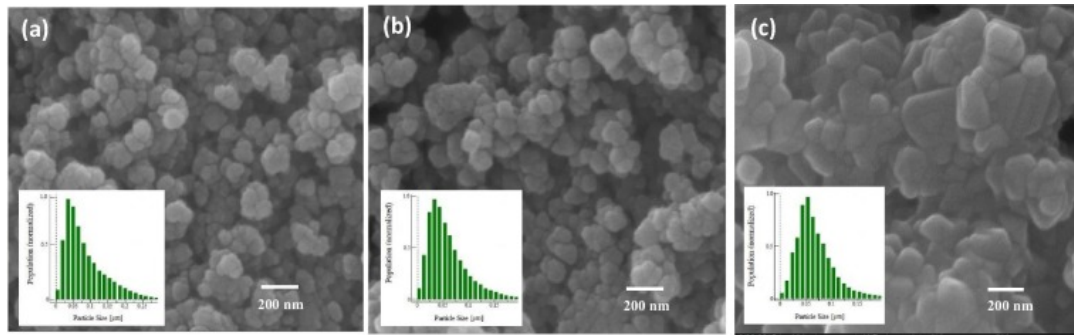
**Figure 1.55** SEM images of (a) Ni-MOF; (b) CuO@NiO-400(1:2); (c) CuO@NiO-500(1:2); (d) CuO@NiO-400(1:1); (e) CuO@NiO-500(2:1); (f) NiO nanoparticles; (g) TEM image of CuO@NiO-400(1:2); (i) AP Pure(AP0) (h) and AP1 samples (Juibari and Tarighi, 2020).



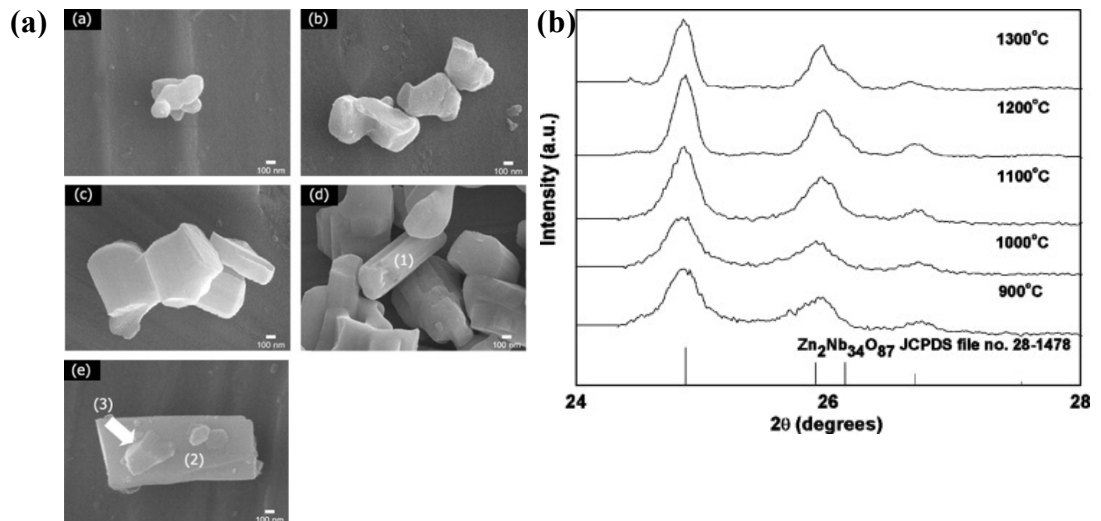
**Figure 1.56** Adsorption–desorption isotherms of  $N_2$  on  $CuO@NiO-400(1:2)$  and  $CuO@NiO-500 (1:2)$  nanocomposites determined at 77.35 K (Juibari and Tarighi, 2020).



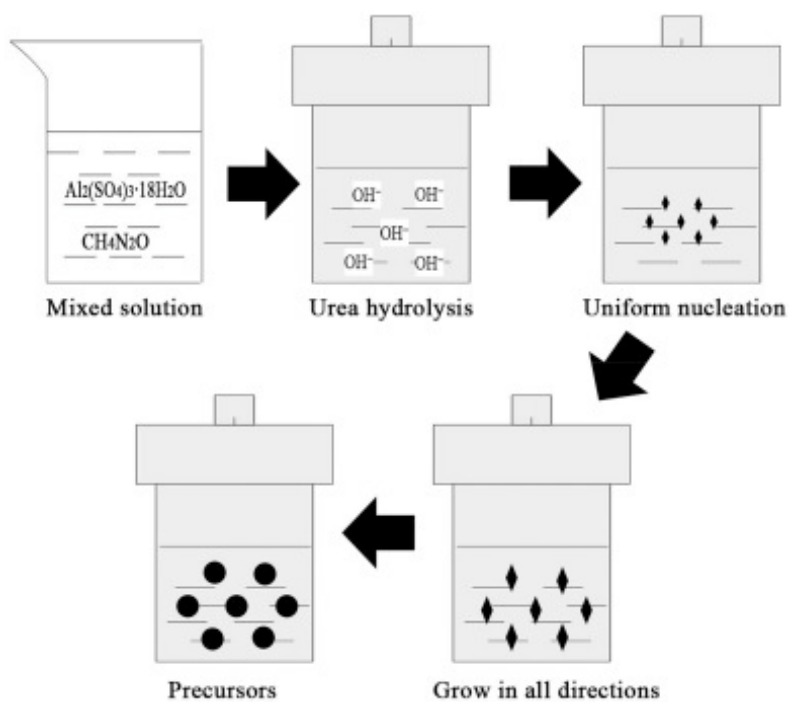
**Figure 1.57** A typical hysteresis curve for co-precipitated cobalt ferrite nanoparticles at the three different calcination temperatures (600 °C, 800 °C and 1000 °C). The magnetisation step from the initial magnetised state (cobalt ferrite nano-magnetic particles) to saturated magnetisation, when a magnetic field of 5000 Oe is applied (Inset) (Purnama *et al.*, 2019).



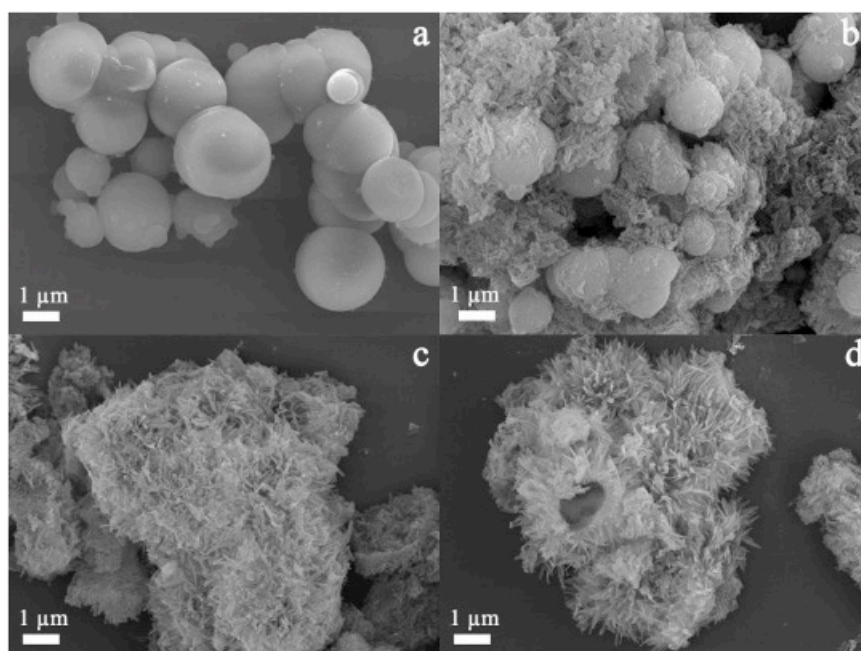
**Figure 1.58** Typical SEM images and particles size distribution analysis (inset) for cobalt ferrite after calcination for six hours under three different temperatures: (a) 600 °C, (b) 800 °C and (c) 1000 °C (Purnama *et al.*, 2019).



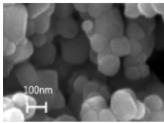
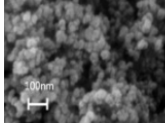
**Figure 1.59** (a) SEM micrographs of the  $Zn_2Nb_{34}O_{87}$  powders calcined for 4 h with heating/cooling rates of  $5\text{ }^\circ\text{C min}^{-1}$  at (a) 900 °C, (b) 1000 °C, (c) 1100 °C (d) 1200 °C and (e) 1300 °C; (b) Enlarged zone of XRD patterns showing peak broadening as a function of calcination temperature (Xiang *et al.*, 2019).



**Figure 1.60** The schematic diagram of precursor growth process (Xiang *et al.*, 2019).



**Figure 1.61** SEM images of products after calcining of precursors prepared at different hydrothermal reaction temperatures a) 120 °C; b) 140 °C; c) 160 °C; d) 180 °C (Xiang *et al.*, 2019).

Type	Brand name	Particle size	Phase	SEM	Type	Brand name	Particle size	Phase	SEM
A	TiO <sub>2</sub> Tronox	110- 125 nm	Anatase		B	P25 Degussa	25 nm	Rutile 30%, Anatase 70%	

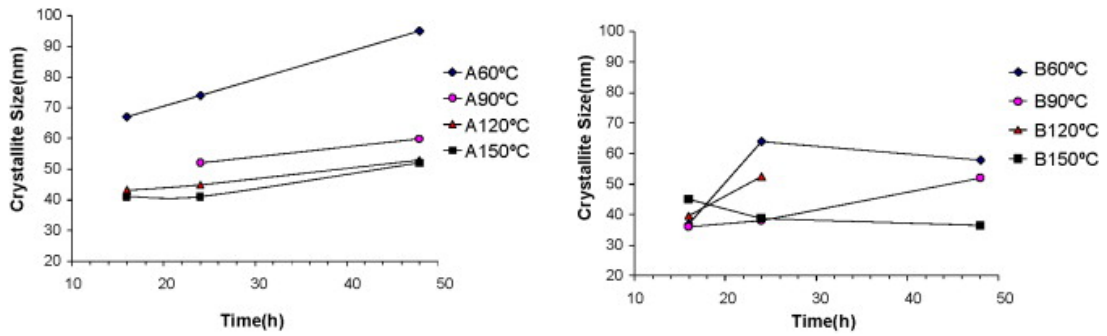


**Figure 1.62** Description of Type A and Type B crystallite size of two TiO<sub>2</sub> precursors and variation of BaTiO<sub>3</sub> obtained using type-A and type-B Ti precursors with temperature and time (Habib *et al.*, 2008).

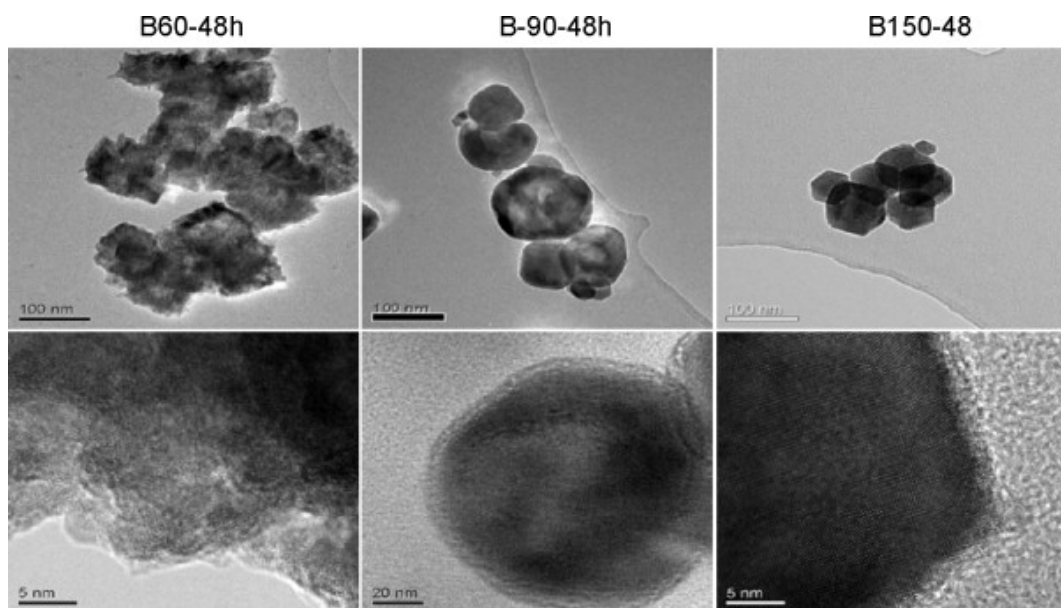


**Figure 1.63** TEM micrograph for BaTiO<sub>3</sub> sample obtained at 60, 90 and 150 °C for 48 h using type-B Ti precursor (Habib *et al.*, 2008).

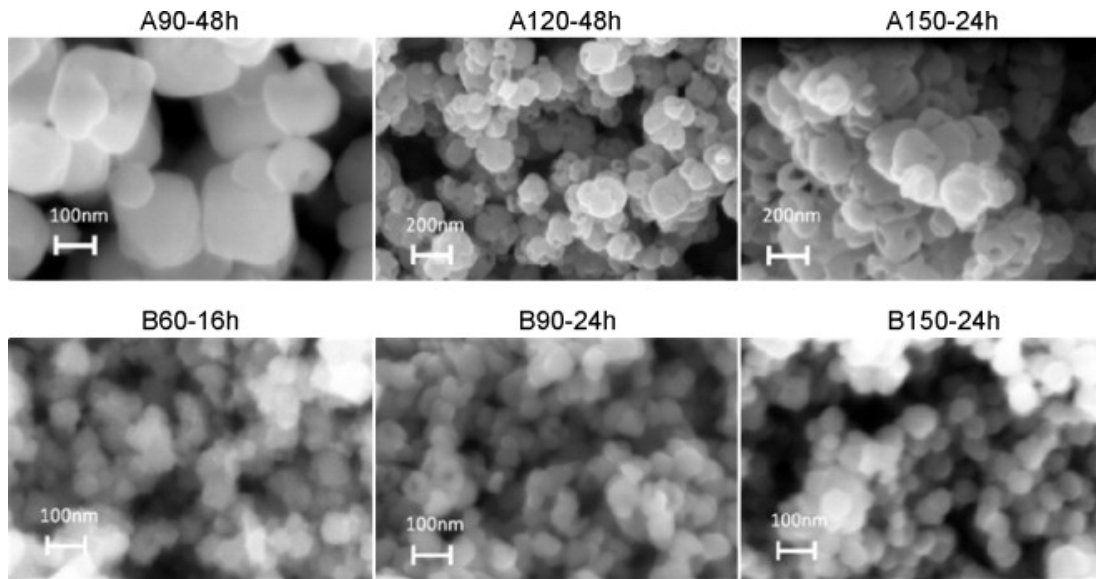


**Figure 1.64** SEM images of BT samples obtained at 90 °C for 48 h, 120 °C for 48 h and 150 °C for 24 h using type-A Ti precursor and BT samples obtained at 60 °C for 16 h, 90 °C for 24 h and 150 °C for 24 h using type-B Ti precursor (Habib *et al.*, 2008).

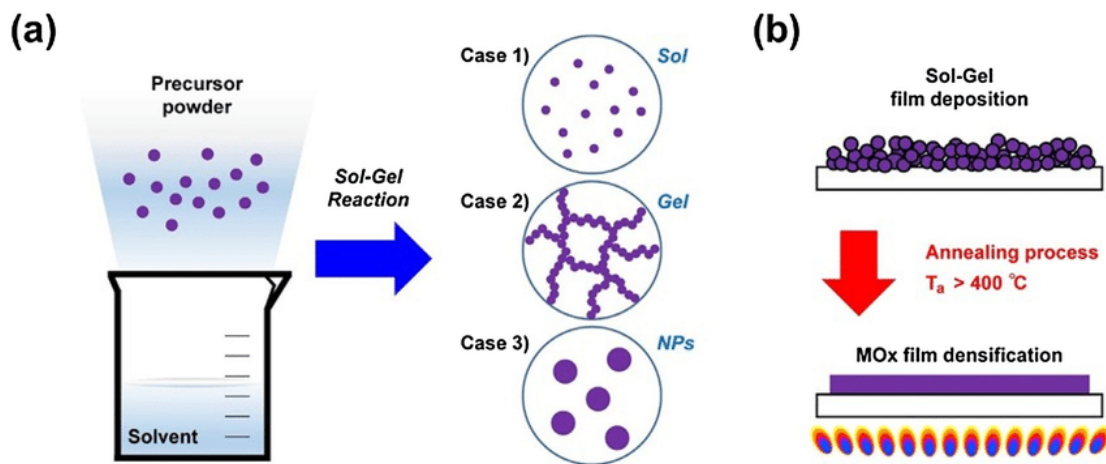


**Figure 1.65** Fabrication of sol-gel metal oxide films. (a) Typical sol-gel metal oxide reaction products (i.e., sol, gel, and nanoparticles) (Park *et al.*, 2017).

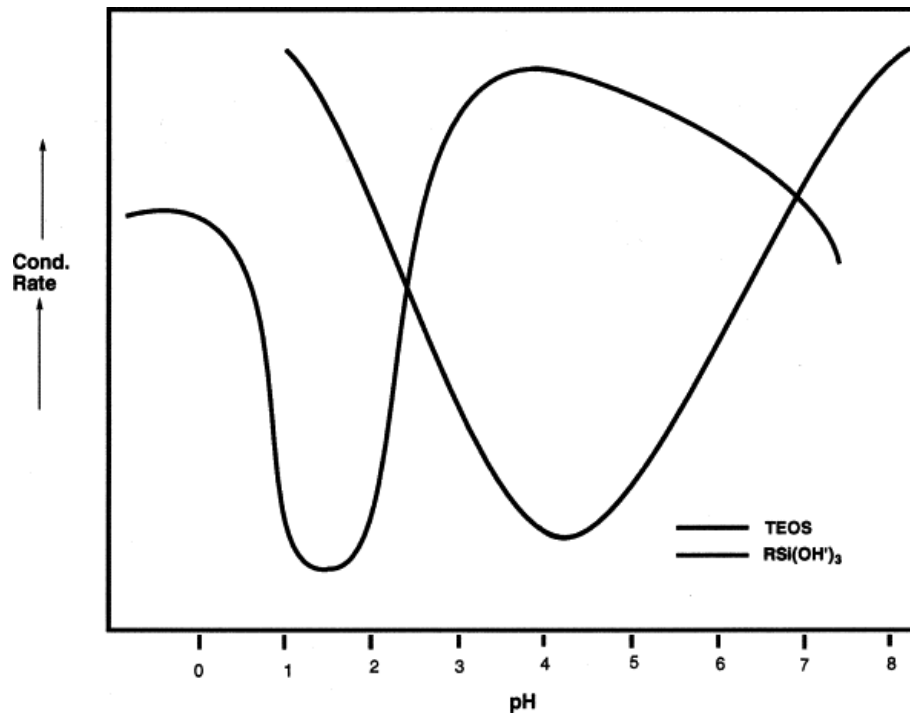


**Figure 1.66** Condensate rate-pH profile for an alkylsilanetriol and the average condensation rate for tetraethoxysilane (1/tgel) (Loy, 2003).

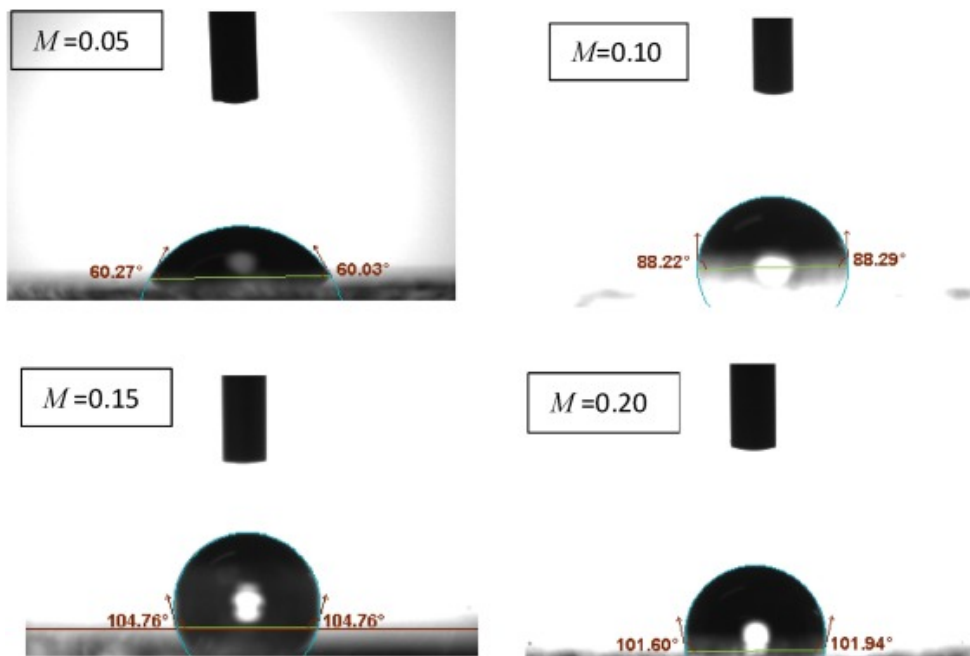


**Figure 1.67** Contact angle of  $\beta$ - $\text{Bi}_2\text{O}_3$  films with different concentration of the precursors (Baqiah *et al.*, 2020).

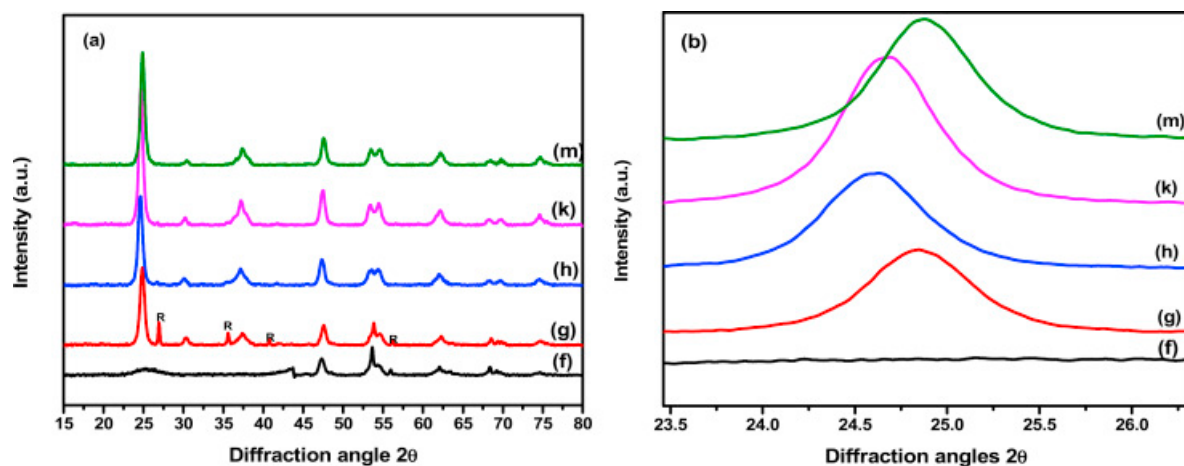


**Figure 1.68** (a) XRD pattern for TiO<sub>2</sub> NPs prepared with different TIP: ethanol volume ratios of (f = 1:63, g = 1:21, h = 1:13, k = 1:9, m = 1:7). (b) XRD peak shift of the most intense peak (101) (Muthee and Dejene, 2020).

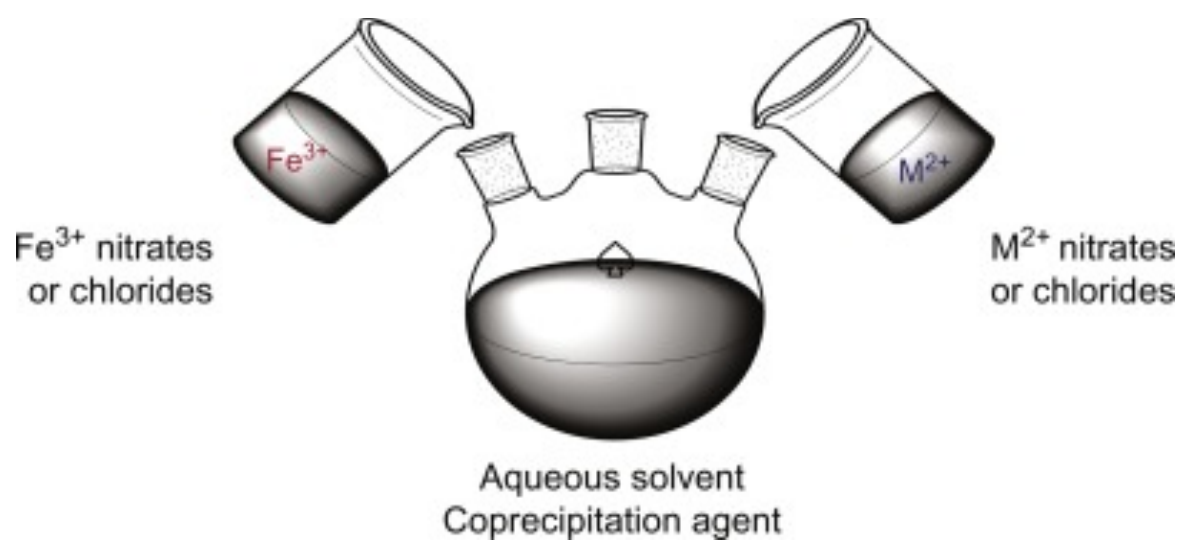


**Figure 1.69** Schematic representation of the synthesis of MFe<sub>2</sub>O<sub>4</sub> MNPs by coprecipitation (Massart, 1981).

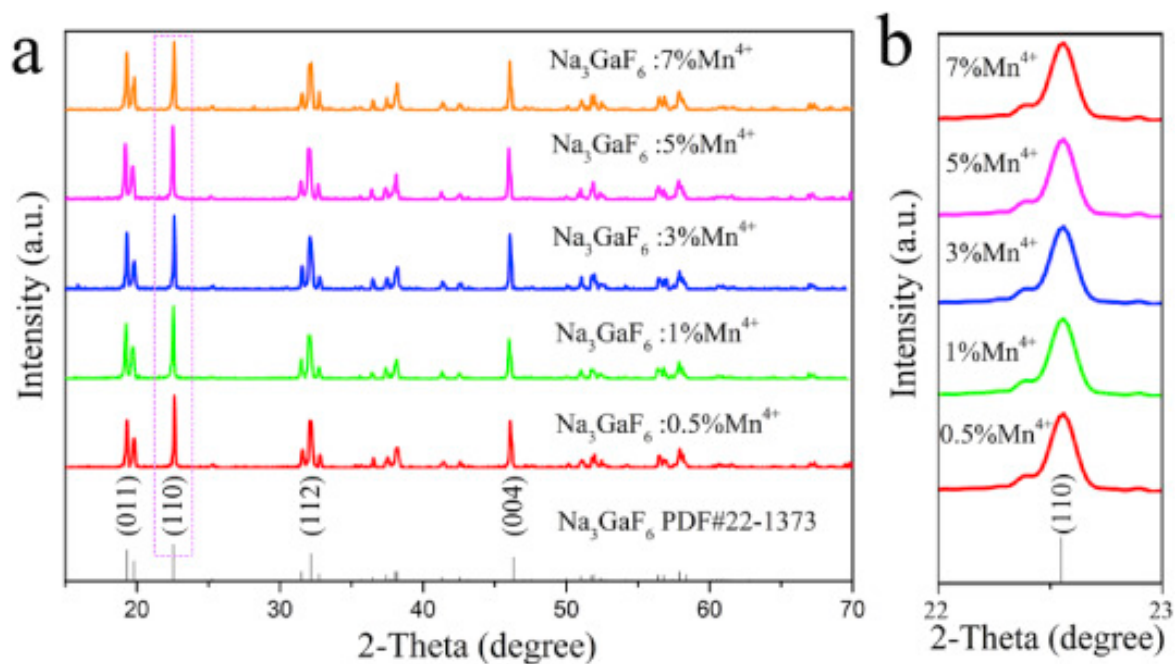


**Figure 1.70** (a) XRD patterns of  $\text{Na}_3\text{GaF}_6:\text{Mn}^{4+}$  synthesised with various  $\text{Mn}^{4+}$  doping concentrations; (b) XRD patterns of amplified (110) diffraction peaks (Xu *et al.*, 2020a).

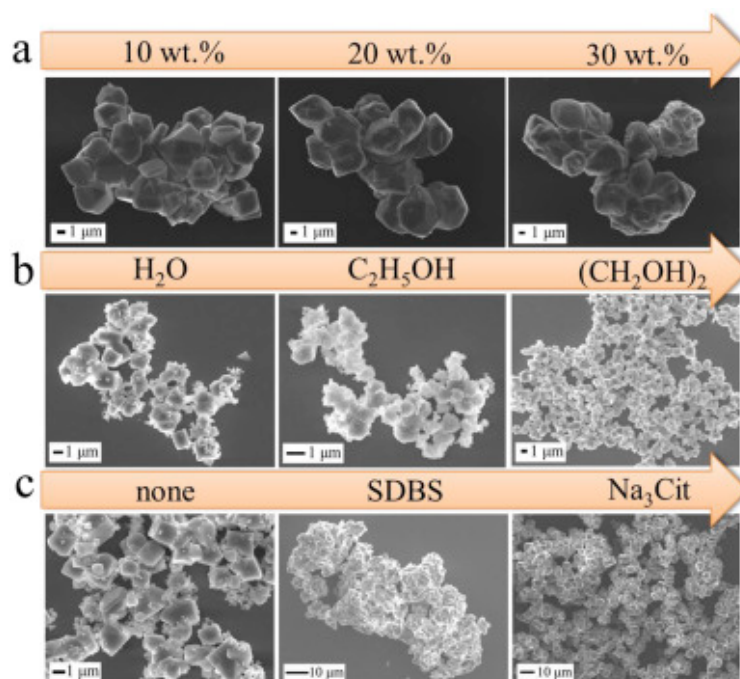


**Figure 1.71** SEM images of  $\text{Na}_3\text{GaF}_6:\text{Mn}^{4+}$  prepared with different (a) hydrofluoric acid concentrations; (b) solvents and (c) surfactants (Xu *et al.*, 2020a).

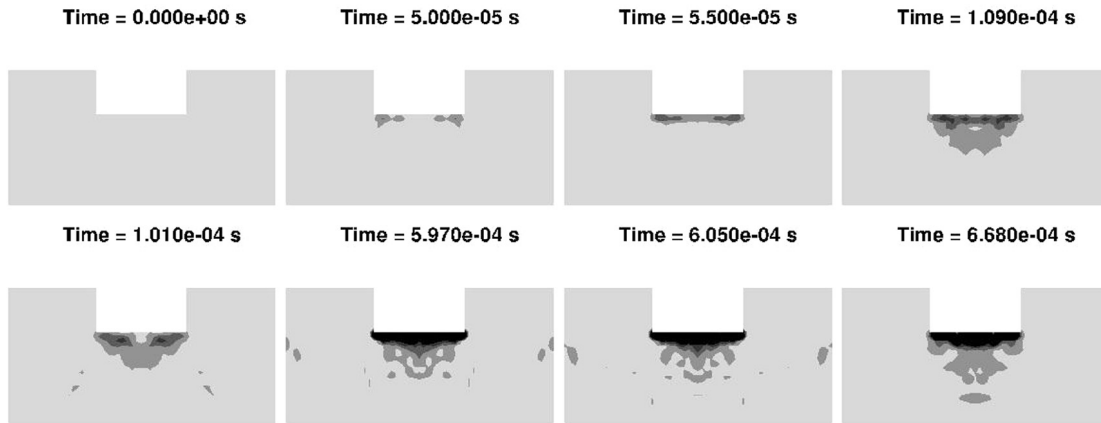


**Figure 1.72** Development of the bubble cloud below the sonotrode in aluminium. Light grey contours represent volume fractions of 0.1% and darker contours represent volume fractions of 0.5% (Lebon *et al.*, 2017).

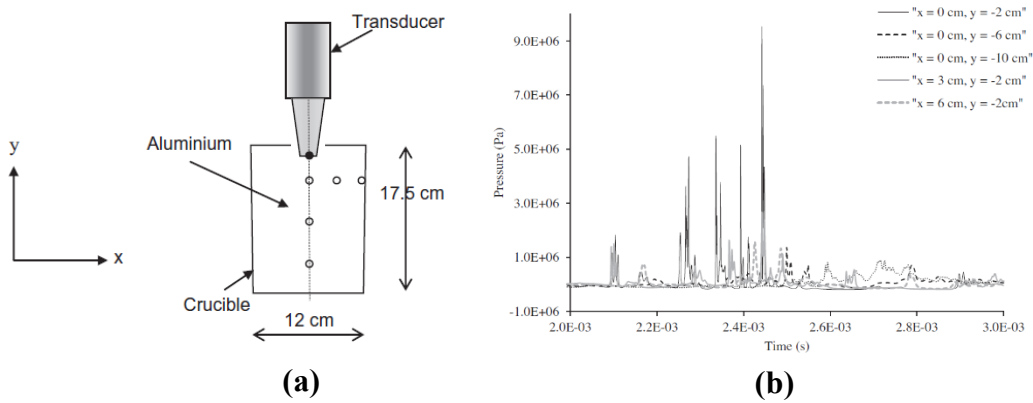


**Figure 1.73** (a) Schematic of aluminium treatment setup; (b) Acoustic pressure predictions at selected points in aluminium domain (Lebon *et al.*, 2017).

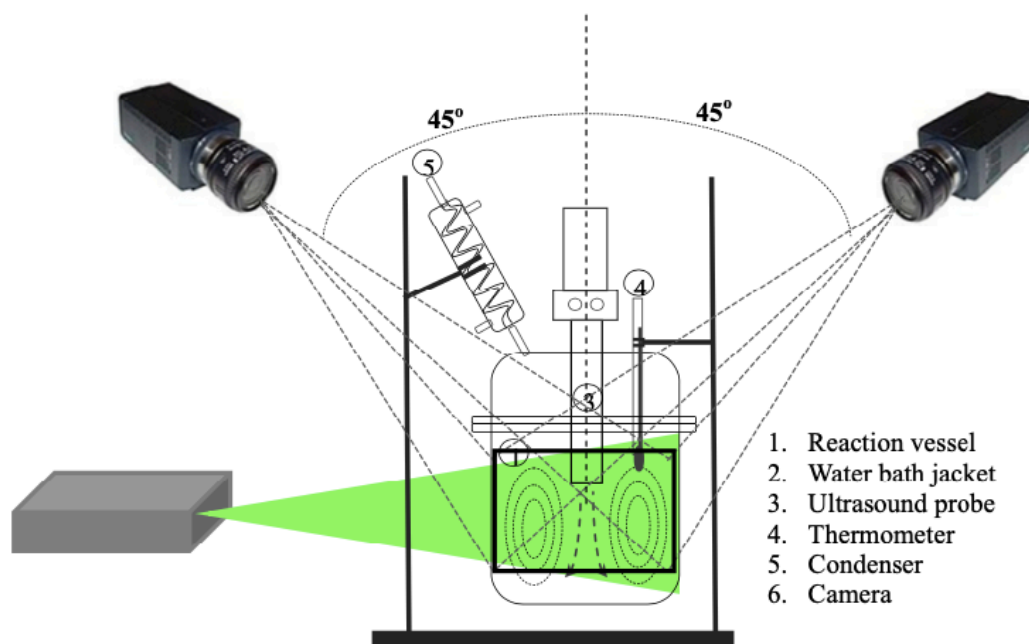


**Figure 1.74** Experimental setup used for ultrasound assisted transesterification (Sajjadi *et al.*, 2015).

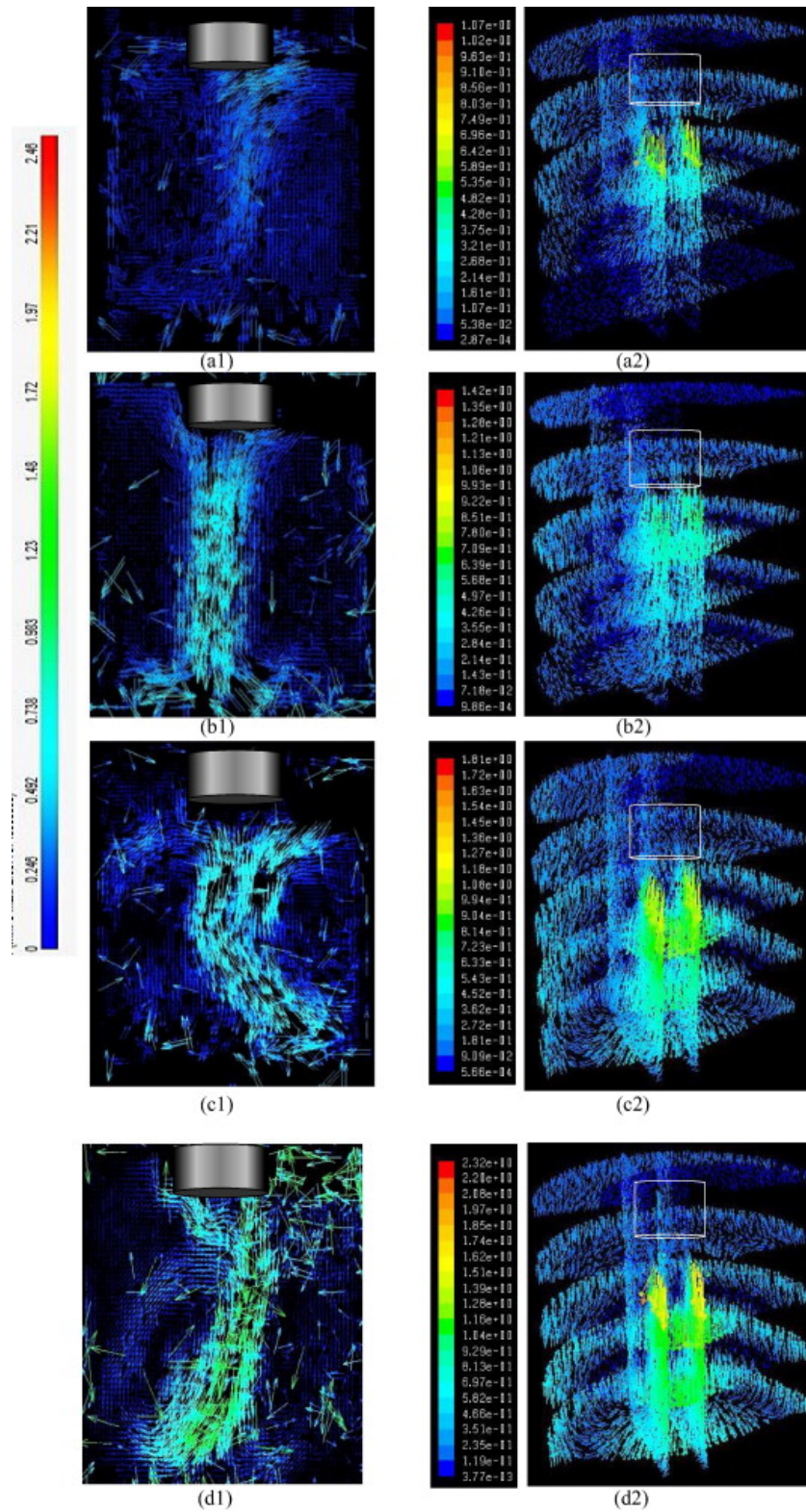


**Figure 1.75** Liquid flow pattern induced by ultrasound irradiation presented by (1) PIV and (2) CFD, under power amplitude of (a) 100 W, (b) 200 W, (c) 300 W and (d) 400 W (Sajjadi *et al.*, 2015).

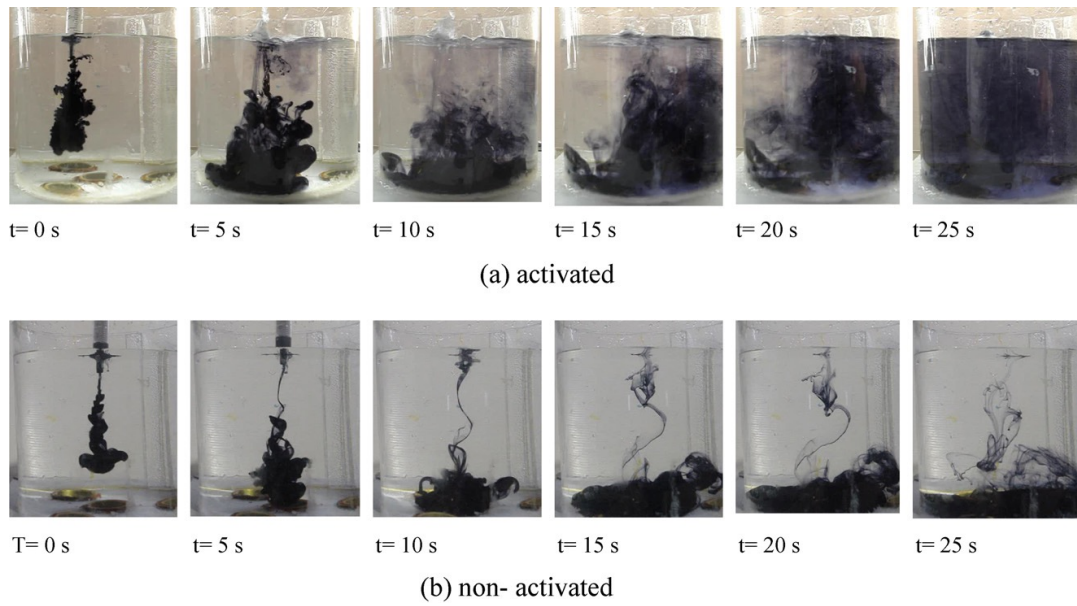


**Figure 1.76** Ink dispersion in the tank at circumstance of (a) activated ultrasound with  $f=1.7\text{MHz}$  and  $P_{\text{elec}} = 60\text{ W}$  and (b) non-activated ultrasound ( $T = 298\text{ K}$ ,  $P = 1\text{ atm}$ ) (Parvizian *et al.*, 2011).

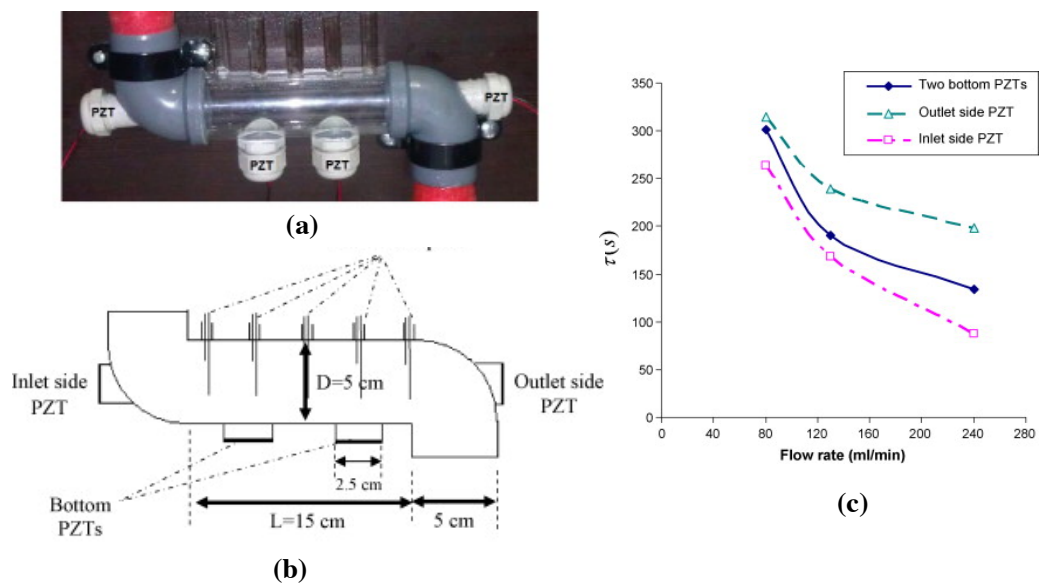


**Figure 1.77** (a) Photograph of continuous tubular sonoreactor; (b) Details of tubular sonoreactor design parameters; (c) The effect of feed flow rate on mean residence time ( $T = 298\text{ K}$ ,  $P = 1\text{ atm}$ ,  $f = 1.7\text{ MHz}$ ) (Parvizian *et al.*, 2012).

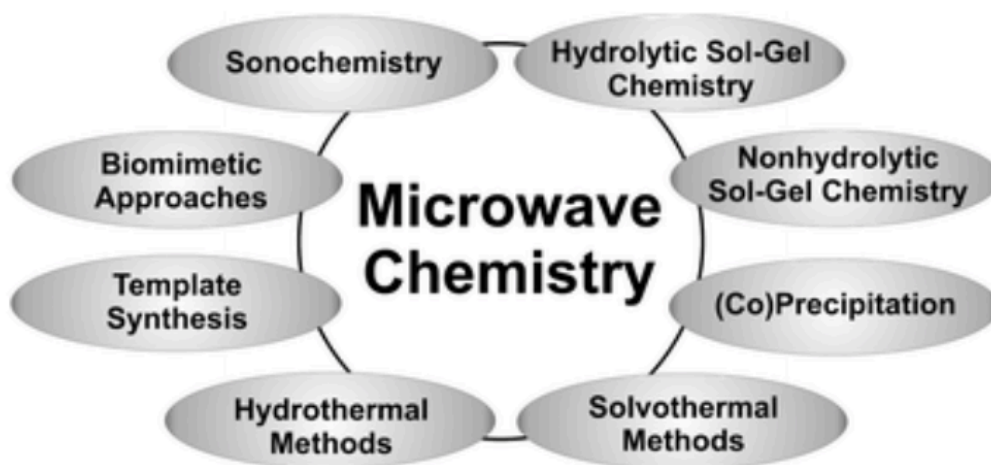


**Figure 1.78** Possible combinations of microwave chemistry with well-established liquid-phase synthesis routes (Komarneni and Katsuki).

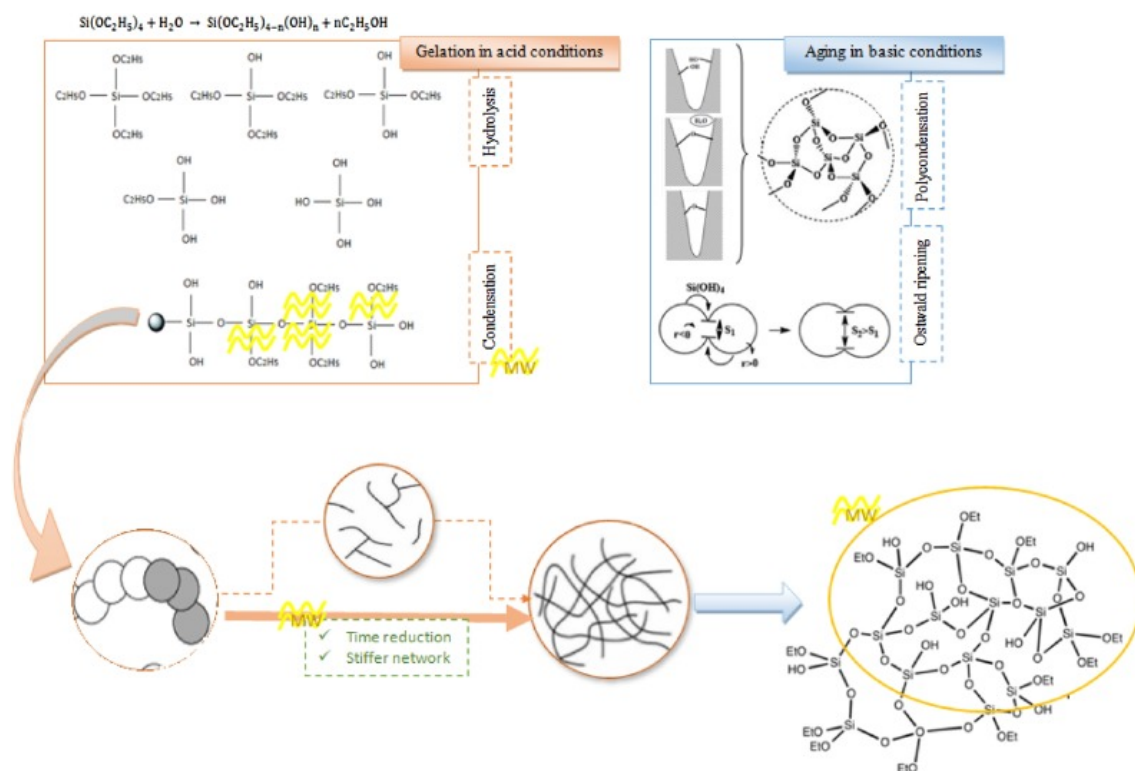


**Figure 1.79** Hypothetical synthesis pathways of silica gels with (→) and without (---) microwave-assistance (Flores-López *et al.*, 2020).

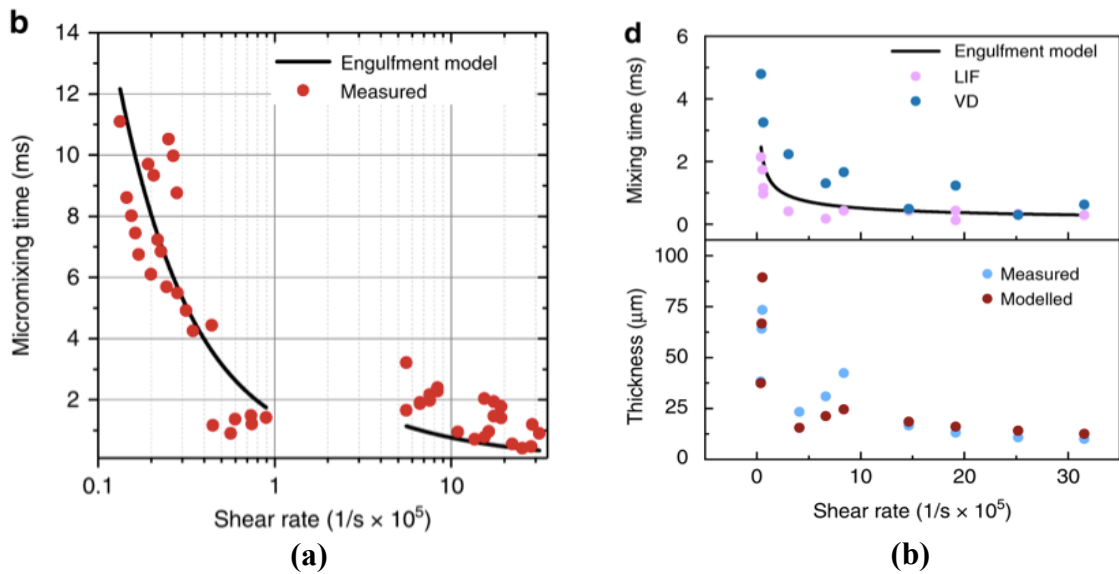


**Figure 1.80** (a) Predicted and measured characteristic micromixing times using Villiermaux–Dushman test reaction; (b) Measurements and model predictions of macromixing time and film thickness (bottom) of film thickness in annular flow as a function of shear rate (Jose *et al.*, 2018).

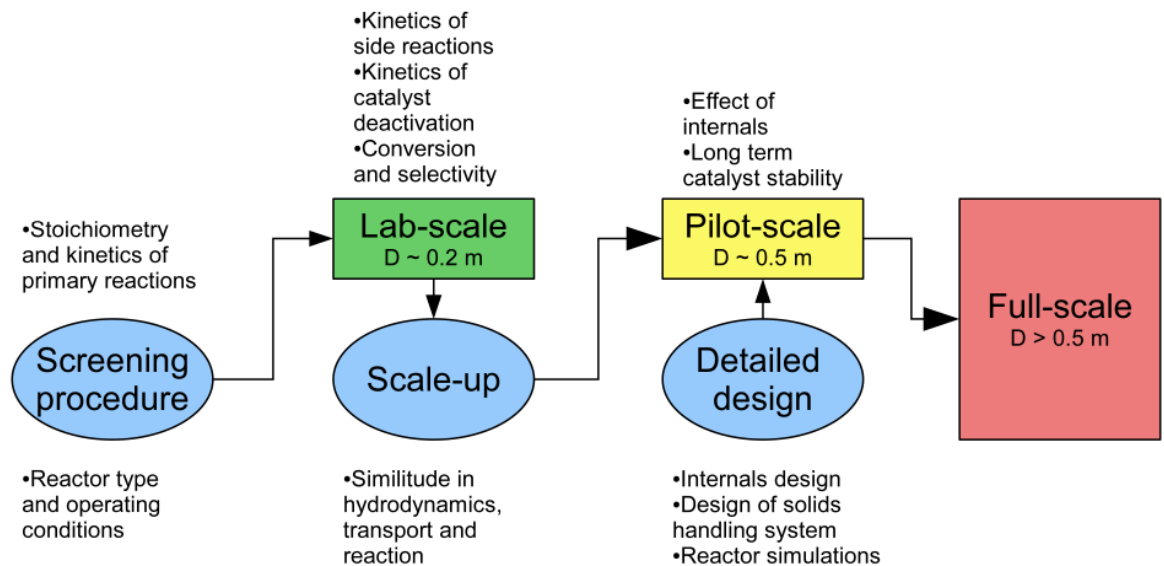


**Figure 1.81** Scale-up procedure to establish an industrial full-scale reactor (Kelkar and Ng, 2002).

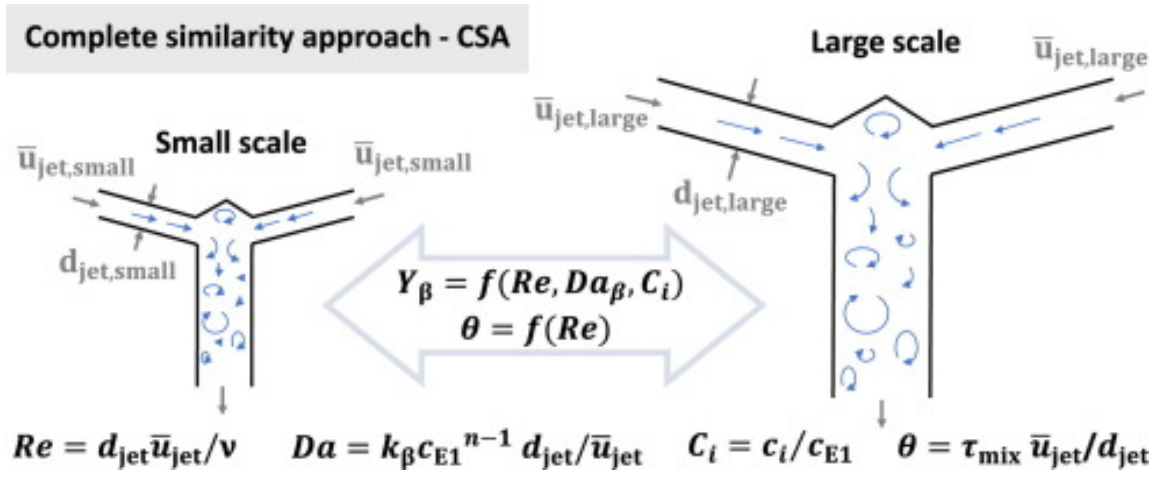


**Figure 1.82** Schematic illustration of scale-up methods for predicting the product distribution of competitive chemical reactions (CCRs) (Rehage et al., 2020).

## Tables

**Table 1.1** Theoretical model based on the N–S equations.

<b>Approaches</b>	<b>Applicable cases</b>	<b>Derivative models</b>
<b>Direct</b>		
<b>numerical simulation (DNS)</b>	Those that analyse the unaveraged/ Unfiltered 3-D, unsteady N–S equations	
<b>Large-eddy simulation (LES)</b>	Those that analyse spatially filtered, 3-D, unsteady N–S equations	Subgrid scales (SGS) model
<b>Reynolds averaged Navier–Stokes (Kurian and Fransson)</b>	Those that analyse ensemble or density-weighted ensemble, averaged N–S equations	Differential Reynolds stress models (DSMs) Algebraic Reynolds stress models (ASMs) Nonlinear constitutive relations (NCRs) Eddy viscosity models (EVMs)
<b>Hybrid methods</b>	Those that analyse the turbulence field with different approaches	Detached eddy simulation (DES)

**Table 1.2** The comparison of Eulerian-Eulerian (EE) Lagrangian–Eulerian (EL) frameworks (Sardina *et al.*, 2019)

	<b>Eulerian-Eulerian (EE) framework</b>	<b>Lagrangian–Eulerian (EL) framework</b>
<b>DRAG TERM</b>	$M_{g,drag} = \frac{3C_D\rho_l\alpha_g\alpha_l \mathbf{u}_l - \mathbf{u}_g }{4d_b}(\mathbf{u}_l - \mathbf{u}_g)$	$F_{drag} = C_D \frac{1}{2} \rho_l \pi \frac{d_b^2}{4}  \mathbf{u}_l - \mathbf{u}_g (\mathbf{u}_l - \mathbf{u}_g)$
<b>VIRTUAL MASS TERM</b>	$M_{g,drag} = C_{vm}\rho_l\alpha_g\alpha_l\left(\frac{D\mathbf{u}_l}{Dt} - \frac{D\mathbf{u}_g}{Dt}\right)$	$F_{VM} = C_{vm}m_l\left(\frac{D\mathbf{u}_l}{Dt} - \frac{D\mathbf{u}_g}{Dt}\right)$
<b>LIFT FORCE</b>	$M_{g,lift} = C_L\rho_l\alpha_g\alpha_l(\mathbf{u}_l - \mathbf{u}_g) \times (\nabla \times \mathbf{u}_l)$	$F_{lift} = C_L m_l(\mathbf{u}_g - \mathbf{u}_l) \times (\nabla \times \mathbf{u}_l)$

**Table 1.3** The drag models and lift models of multiphase system (Zhou *et al.*, 2020).

	<b>MULTIPHASE SYSTEM</b>	<b>GAS- LIQUID</b>	<b>LIQUID- SOLID</b>	<b>GAS-SOLID</b>
<b>DRAG MODELS</b>	Model applied	Tomiyama (PBM- customized) model	Schiller- Naumann (PBM- customized) model	Schiller- Naumann (PBM- customized) model
<b>LIFT MODELS</b>	Model applied	Tomiyama model	Moraga model	/

**Table 1.4** Dimensionless groups relevant to multiphase systems

Dimensionless number	Symbol	Formula	Meaning
<b>Eötvös number</b>	Eo	$\left(\frac{\Delta\rho g l^2}{\sigma_L}\right)$	Ratio of buoyancy force and surface tension force (Liu <i>et al.</i> , 2008)
<b>Froude number</b>	Fr	$\left(\frac{N^2 D}{g}\right)$	Ratio of inertial force and gravitational force (Li and Ingason, 2018)
<b>Hatta number</b>	Ha	$\left(\frac{\sqrt{2/(p+1)} D_A k_{p-q} [B_B]^q [A^*]^{p-1}}{k_L}\right)$	Ratio of rate of mass transfer in the presence of a chemical reaction and that in the absence of a chemical reaction (La Rubia García <i>et al.</i> , 2012)
<b>Morton number</b>	Mo	$\left(\frac{g \mu_c^4 \Delta\rho}{\rho_c^2 \sigma^3}\right)$	Ratio of viscous force and interfacial force (Weeks, 2001)
<b>Nusselt number</b>	Nu	$\left(\frac{hl}{k_c}\right)$	Ratio of heat transfer by convection and that by conduction (Kewalramani <i>et al.</i> , 2019)

<b>Power number</b>	Np	$\left(\frac{P}{\rho N^3 D^5}\right)$	Ratio of drag force on impeller and inertial force (Duroudier, 2016)
<b>Prandtl number</b>	Pr	$\left(\frac{C_P \mu}{k_c}\right)$	Ratio of momentum and thermal diffusivity (Fregni <i>et al.</i> , 2019)
<b>Reynolds number</b>	Re	$\left(\frac{l u_c \rho}{\mu}\right)$	Ratio of inertial and viscous force
<b>Schmidt number</b>	Sc	$\left(\frac{\mu}{\rho D_M}\right)$	Ratio of kinematic viscosity and molecular diffusivity
<b>Sherwood number</b>	Sh	$\left(\frac{k_M l}{D_M}\right)$	Ratio of mass transfer by convection and that by molecular diffusion (Haugen <i>et al.</i> , 2018)
<b>Weber number</b>	We	$\left(\frac{N^2 D^3 \rho_L}{\sigma}\right)$	Ratio of inertial and surface tension force

## **CHAPTER 2**

# **EFFECT OF ULTRASONIC INTENSIFICATION ON SYNTHESIS OF NANO-SIZED PARTICLES WITH AN IMPINGING JET REACTOR**

### **SUMMARY**

This chapter presents a fast approach to the synthesis of nano-sized  $\text{FePO}_4$  in the impinging jet reactor (IJR). The nano-sized  $\text{FePO}_4$  is then used as a precursor to produce appealing cathode material  $\text{LiFePO}_4$  battery. Overall improved features of  $\text{LiFePO}_4$  with high bulk density, discharge rate, and capacity, can be realised by controlling the crystal size, structure, morphology of  $\text{FePO}_4$ . The preparation of  $\text{FePO}_4$  nanoparticles can be conducted in a more efficient way by intensifying the effect of micromixing due to the enhanced turbulence in an impinging jet Reactor (IJR) where two linear liquid jets are introduced into the IJR and collide at high velocity to diminish the segregation. However, micromixing is significantly affected by the existence of a stagnant region that may partially block/clog the reaction chamber. By imposing ultrasound to the IJR, micro-scale turbulent eddies generated as the result of the collapse of ultrasonically generated micro cavitation bubbles may generate a strong local shear. Such micro-scale turbulent vortices exert shear on the interface between the particles and surrounding fluid, resulting in uniform particle morphology and high surface area for chemical reaction. This chapter aims to optimise the ultrasonic intensification effect on the synthesis of nano-sized particles with the desired homogeneity, expound on the governing mechanisms and present a kinetic model to describe the multiphase flow

dynamics in the IJR. Both experimental and numerical analysis are conducted to demonstrate the impact of fluid dynamics on particle synthesis.

## 2.1 Introduction

With the gradual upgrading of standards and requirement in the aspect of environmental protection and safety control as well as the emergence of novel reactor technologies, many industrial fields are facing a crisis of washout and the urgently forced to renovate also as consequences of drawbacks including high energy consumption, low conversion rate, thermo-runaway, etc. Under this circumstance, techniques like imping jet reactor and its process intensification have been developed rapidly. The modularity, flexible and customized production capacity, high efficiency and high safety performance of microreactor technology attract people's attention. The mixing performance of different reacting components can be promoted by using hybrid reactor systems. Among these reactors, impinging jet reactor (IJR) provides a facile and direct way of process intensification for microscale chemical precipitation reactions and nanoparticles synthesis (Abiev *et al.*, 2017). In the IJR, two linear liquid jets collide with each other at relatively high velocity in the impingement zone, thus achieving better micromixing performance by means of diminishing the segregation and improving mass transfer rate (Nie *et al.*, 2018, Ying *et al.*, 2008). It has been reported that the use of IJR provides a homogeneous local environment for the formation of nanoparticles with high supersaturation in milliseconds or less time (Liu *et al.*, 2013, Mahajan and Kirwan, 1996). Due to the violent collision of two streams in the IJR, high dissipation of kinetic energy of the jets in a confined volume leads to local strong shear due to the generation of localized turbulent eddies. However, the mixing performance can be significantly affected by the existence of a stable separated regime and a stagnant region. Fonte *et al.* (2015) have shown that the imbalance of branch jet always has negative effects on mixing quality and the mixing efficiency in an IJR mainly depends on the scale of small eddy engulfment but not the amount of energy dissipation of the system.

Due to the particular geometry of IJR, the reaction chamber might be partially choked because of the precipitation process (Guo *et al.*, 2017). In order to overcome this drawback and promote the mixing efficiency, ultrasound intensification was imposed to improve the mixing performance due to strong acoustic impact following the collapse of microbubbles characterized by occurrence of micro-streaming, shock waves and micro-scale turbulent eddies. The maximum volume fraction of cavitation bubbles takes up to 0.016% of the total sonoreactor and micro-bubble collapse may lead to intensive local heat ( $\sim 5000$  K), high pressure ( $\sim 1000$  atm), high-speed jet streams ( $\sim 400$  km/h) and strong local shear (Mahajan and Kirwan, 1996, Hielscher, 2007, Sajjadi *et al.*, 2017). Such energy transfer from acoustic streaming within the fluid at a localized scale exerts a shear force on the interface between the particles and surrounding fluid, resulting in narrower particle size distribution and high surface area for particle synthesis (Jamei *et al.*, 2013). It has been recognized that acoustic cavitation affects nuclei growth in a liquid media under low-pressure cycles and contributes to micro-bubble collapse under a high-pressure cycle, which may be responsible for mass transfer rates enhancement (Sajjadi *et al.*, 2017).

Most of the previous studies focus on the effect of ultrasonic energy dissipation while having overlooked the influence of flow dynamics caused by acoustic streaming and mixing zone (Zhao *et al.*, 2007). In CFD modelling, this was compensated by either superposing the pressure field change or introducing a boundary vibration that is resonant to the ultrasonic field imposed. Based on the existing numerical studies on ultrasound, the acoustic streaming contributes to both the mass transfer and heat transfer improvement of reaction at low viscosity (Laugier *et al.*, 2008, Monnier *et al.*, 2000, Abolhasani *et al.*, 2012). Moreover, the segregation index has reduced up to 20% with low ultrasound intensity (Rahimi *et al.*, 2014). The numerical simulation initially conducted by Nyborg (1953) has demonstrated that the second-order nonlinear ultrasound wave propagation is responsible for acoustic streaming and the inertia term

can be neglected in the simulation. However, Lighthill (1954) argued that the elimination of the inertia term is acceptable only when the flow is in the regime of low Reynolds number ( $Re < 1$ ), known as “creeping motion”. Considering the inertial effect, Van Wijngaarden (1968) proposed a more complex model to reproduce the transient shock waves in a bubbly mixture. Based on Wijngaarden’s model, both Jamshidi *et al.* (2012) and Lebon *et al.* (2017) introduced acoustic cavitation into the fluid as a source term for the momentum transfer because micro-bubbles have an impact on wave propagation and bulk properties. Whereas, Sajjadi *et al.* (2017) investigated ultrasound effect in liquid bulk by introducing it as a boundary condition in terms of pressure profile change. In addition, to investigate the ultrasound effect on mass transfer coefficient, Jiao *et al.* (2014) came up with a computational model to predict the ultrasonic enhancement on mass transfer coefficient and considered the effect of extrinsic factors such as temperature, transducer geometry and the distance between the transducer and ultrasound source. Xu *et al.* (2013) also quantitatively determined the flow field in a sonochemical reactor and found that average stream velocity increased with acoustic power increment. In addition, Niazi *et al.* (2014) have investigated the pressure and temperature distribution of liquid bulk in a sonoreactor and the collapse pressure and temperature of acoustic bubbles were predicted around 3040 bar and 3200 K.

The ultrasound-assist impinging jet reactor has the characteristics of flexibility, customization, high efficiency and safety performance, widely used in the field of pharmaceutical manufacturing and gradually replacing the traditional stirring reactors owing to its small scale and high mixing performance. This chapter aims at investigating the intensified effects of low-frequency ultrasonic irradiation (20 kHz) on nano-sized  $\text{FePO}_4$  (FP) powder synthesis using an IJR system with the downstream sudden expansion chamber. Both experimental and computational analysis were conducted to explore the effect of ultrasound on synthesized nano-sized FP particles that can be used as precursor contributing to  $\text{LiFePO}_4$  (LFP) cathode materials with

excellent electrochemical performance for rechargeable lithium-ion batteries (De Castro and Priego-Capote, 2007).

## **2.2 Experimental Methods**

### **2.2.1 Experimental setup and product characterization**

The experimental setup is shown in Figure 2.1 Solution A ( $1 \text{ mol L}^{-1} \text{ Fe(NO}_3)_3$ , Sinopharm Chemical Reagent Co., Ltd, 99%) and solution B ( $1 \text{ mol L}^{-1} \text{ (NH}_4)_2\text{HPO}_4$ , Sinopharm Chemical Reagent Co., Ltd, 99%) were introduced into two separated inlets of the IJR by peristaltic pumps with a flow rate of  $85.74 \text{ ml min}^{-1}$ . In order to stabilise the pH value at 1.7, aqueous ammonia ( $1.5 \text{ mol L}^{-1}$ ) was simultaneously pumped from the third inlet with automatic pH controller. In the mixing process, the IJR system was irradiated by ultrasound with a power of 360 W, 480 W, 600 W, 720 W and 960 W, respectively. Mixing was also carried out in the same system without imposing ultrasound for purpose of comparison. The samples prepared under different ultrasound intensities were analysed (herein referred to as FP-ultrasound power). FP precipitation was washed by deionized water (DI), filtrated and dried in air at  $100 \text{ }^\circ\text{C}$  for 12 h. Then the sample was calcined in air at  $600^\circ\text{C}$  for 10 h to obtain anhydrous crystalline  $\text{FePO}_4$ .

The structures of synthesised FP powder were identified by X-ray diffraction (XRD, D8 ADVANCE DAVINCI, BRUKE) with  $\text{Cu K}\alpha$  radiation source ( $\lambda=1.5406\text{\AA}$ ) and scanning angle ranging from  $10^\circ$  to  $90^\circ$ . The morphology and microstructure were obtained using scanning electron microscope (SEM, sigma VP, ZEISS, Germany). The Brunauer-Emmett–Teller (BET) surface area was determined using ASAP 2020 (Micrometrics, U.S.A). Thermal gravimetric was conducted by a thermal analyser (TG, NETZSCH STA 449 F3 Jupiter, Germany).

### 2.2.2 LFP/C preparation

The electrochemical properties of the LFP/C synthesised from prepared FP at different ultrasound power were investigated by galvanostatic method using LFP/C half-cells. Anhydrous FP samples were mixed with  $\text{Li}_2\text{CO}_3$  (Sinopharm Chemical Reagent Co., Ltd, 99%) and glucose (Sinopharm Chemical Reagent Co., Ltd, 99%) by ball-milled method of 500rpm for 5h. Then the mixture was calcined in nitrogen atmosphere at  $650^\circ\text{C}$  for 10h.

Electrochemical measurements were performed using CR2032 coin-type cell assembled in an argon-filled glove box. Cathode electrodes were fabricated from the synthesised LFP/C, polyvinylidene fluoride (PVDF) binder and the acetylene black at a weight ratio of 80:10:10 and pasted on pure aluminum foil. Pure lithium foil was used as the counter electrode. The electrolyte is consisted of a solution of 1 M  $\text{LiPF}_6$  in ethylene carbonate and diethyl carbonate (EC+DMC, 1:1 volume ratio). The charge/discharge tests were carried out using a LAND Cell test CT2001A (Wuhan LAND Electronic Co.Ltd., China) between the voltage of 2.5V and 4.2V.

### 2.2.3 Description on synthesis reaction

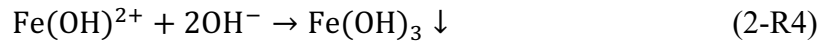
On exposing to ultrasound irradiation, sonolysis of water is realised through sonochemical reductants such as  $\text{H}\cdot$  radicals. Furthermore, these produced radicals are added to produce secondary radical species that may promote the reduction rate (Bang and Suslick, 2010). In the present work, the sonolysis of water is characterised by Kohno *et al.* (2011) as:



$\text{Fe}(\text{NO}_3)_3$  and  $(\text{NH}_4)_2\text{HPO}_4$  were used to synthesise  $\text{FePO}_4$  precursor through the hydrolysis reaction of  $\text{Fe}^{3+}$  and  $\text{HPO}_4^{2-}$  and the main reactions can be described by



In addition, side reaction can be identified as:



Both  $\text{FePO}_4 \cdot x\text{H}_2\text{O}$  and  $\text{Fe}(\text{OH})_3$  are produced in precipitation and they are considered as parallel-competing reactions. In order to promote the occurrence of the main reactions, mixing is intensified via the impinging jets to increase the likelihood of ion collision between  $\text{Fe}^{3+}$  and  $\text{PO}_4^{3-}$ . Adoption of acoustic streaming produced by ultrasound wave propagation helps to accelerate the particle migration, resulting in a higher ratio of  $n(\text{Fe}^{3+})/n(\text{PO}_4^{3-})$  in the solution (Dong *et al.*, 2017). Although the solubility product constant of  $\text{FePO}_4$  is greater than that of  $\text{Fe}(\text{OH})_3$  ( $K_{sp}(\text{FePO}_4) = 1.3 \times 10^{-22}$ ,  $K_{sp}(\text{Fe}(\text{OH})_3) = 2.8 \times 10^{-38}$ ), the side reaction may be ignored as the reaction condition is acidic. It should be noted here that with more  $\text{Fe}^{3+}$  ions being engaged into the complex reaction, the solution tends to be acidic due to  $\text{Fe}^{3+}$  hydrolysis and the precipitation dissolves. To keep the pH value around 1.7 with less induced-impurities, ammonia aqueous solution was added in the mixing process of  $\text{Fe}^{3+}$  and  $\text{PO}_4^{3-}$ .

## 2.3 Numerical simulation

### 2.3.1 Mathematical modelling

The impinge jet flow together with the flow in the expansion chamber with and without ultrasound irradiation was analysed at ultrasound frequency of 20 kHz and power ranging from 0 to 960W. Numerical study helps to analyse the intensified effect of

ultrasound on this solid-liquid system. The gas phase in this case is neglected as the volume fraction of cavitation bubbles induced by ultrasound is less than 1%. The governing equation for continuity, momentum and energy can be solved with a simplified model. The  $Re_j$  for the confined impinge jet reactor is defined as

$$Re_j = \frac{\rho u d}{\mu} \quad (2-1)$$

where  $u$  is the mean velocity in the inlet of the T-shape junction and  $d$  is the hydraulic diameter of the circular tube inlet. The mean velocity is 0.2022 m/s based on the feed flow rate, corresponding to  $Re_j$  of 606. However, it should be pointed out that it may be inappropriate to consider the flow to be laminar as the intensive mixing in the chamber of the confined impinge jet will generate small turbulent eddies and the flow will become highly turbulent although the Reynolds number is less than 2000. The ultrasound waves may lead to a sharp localised pressure reduction and the formation of local cavitation due to acoustic streaming (Rahimi *et al.*, 2014). This will give rise to local turbulence with huge amounts of micro-cavitated bubble collapse in an extremely short time and in a very small volume. To describe the flow in the impinge jet system with a sudden expansion chamber, the following governing equations were employed. The general mass conservation equation for incompressible fluid takes the following form,

$$\nabla \cdot \vec{u} = 0 \quad (2-2)$$

where  $\vec{u}$  is the mass-average velocity and the momentum conservation equation in 3-D dimension is given by,

x-Momentum equation,

$$\frac{\partial}{\partial t}(\rho u) + \nabla \cdot (\rho u \vec{u}) = -\frac{\partial p}{\partial x} + \mu \nabla^2 u - \left[ \frac{\partial(\overline{\rho u'^2})}{\partial x} + \frac{\partial(\overline{\rho u'v'})}{\partial y} + \frac{\partial(\overline{\rho u'w'})}{\partial z} \right] \quad (2-3)$$

y-Momentum equation,

$$\frac{\partial}{\partial t}(\rho v) + \nabla \cdot (\rho v \vec{u}) = -\frac{\partial p}{\partial y} + \mu \nabla^2 u - \left[ \frac{\partial(\overline{\rho v' u'})}{\partial x} + \frac{\partial(\overline{\rho v'^2})}{\partial y} + \frac{\partial(\overline{\rho v' w'})}{\partial z} \right] \quad (2-4)$$

z-Momentum equation,

$$\frac{\partial}{\partial t}(\rho w) + \nabla \cdot (\rho w \vec{u}) = -\frac{\partial p}{\partial z} + \mu \nabla^2 u - \left[ \frac{\partial(\overline{\rho u' w'})}{\partial x} + \frac{\partial(\overline{\rho v' w'})}{\partial y} + \frac{\partial(\overline{\rho w'^2})}{\partial z} \right] \quad (2-5)$$

where  $\rho$  is the fluid density,  $\vec{u}$  is the velocity vector,  $\mu$  is the dynamic viscosity and  $p$  is the pressure. The standard  $k$ - $\varepsilon$  model is employed for liquid phase and it is proven to be appropriate to simulate the flow in the impinge jet based on Gavi's work as follows (Gavi *et al.*, 2007),

$$\frac{\partial(\rho k)}{\partial t} + \nabla \cdot (\rho k \vec{u}) = \nabla \cdot \left[ \left( \mu + \frac{\mu_t}{\sigma_k} \right) \Delta k \right] + G_k - \rho \varepsilon \quad (2-6)$$

$$\frac{\partial(\rho \varepsilon)}{\partial t} + \nabla \cdot (\rho \varepsilon \vec{u}) = \nabla \cdot \left[ \left( \mu + \frac{\mu_t}{\sigma_\varepsilon} \right) \Delta \varepsilon \right] + C_1 \frac{\varepsilon}{k} G_k - C_2 \rho \frac{\varepsilon^2}{k} \quad (2-7)$$

where  $G_k$  is the generation of turbulence kinetic energy due to the mean velocity gradients as shown in Equation (2-8),  $\mu_t$  is the turbulent dynamic viscosity and the coefficients used in this standard  $k$ - $\varepsilon$  model take the following values  $C_\mu=0.09$ ,  $C_1=1.42$ ,  $C_2=1.92$ ,  $\sigma_k=1.0$  and  $\sigma_\varepsilon=1.3$ .

$$G_k = \mu_t \left\{ 2 * \left[ \left( \frac{\partial u}{\partial x} \right)^2 + \left( \frac{\partial v}{\partial y} \right)^2 + \left( \frac{\partial w}{\partial z} \right)^2 \right] + \left( \frac{\partial u}{\partial y} + \frac{\partial v}{\partial x} \right)^2 + \left( \frac{\partial u}{\partial z} + \frac{\partial w}{\partial x} \right)^2 + \left( \frac{\partial v}{\partial z} + \frac{\partial w}{\partial y} \right)^2 \right\} \quad (2-8)$$

Considering the chemical reaction in the IJR, species transport equation is shown in Equation (2-9) without considering the energy equation due to the constant value of kinetic constant  $k$  in the temperature range of 293 to 308 K (Guichardon *et al.*, 2000).

$$\frac{\partial(\rho c_i)}{\partial t} + \nabla \cdot (\rho \vec{u} c_i) = \nabla \cdot [(\Gamma_i + \Gamma_t) \Delta c_i] - \left[ \frac{\partial(\rho \overline{u' c_i'})}{\partial x} + \frac{\partial(\rho \overline{v' c_i'})}{\partial y} + \frac{\partial(\rho \overline{w' c_i'})}{\partial z} \right] + S_i \quad (2-9)$$

In Equation (2-9),  $c_i$  represents the concentration of the  $i^{\text{th}}$  specie,  $\Gamma_i$  is the diffusion coefficient of the  $i^{\text{th}}$  specie and  $\Gamma_t$  is the turbulent diffusion coefficient and  $S_i$  is the formation rate of the  $i^{\text{th}}$  specie. However, the species transport equation can be solved only if the Probability Density Function (PDF) is known.

### 2.3.2 Numerical simulation

The geometry and computational domain are schematically shown in Figure 2.2 and 3D CFD simulation was conducted using the commercial code FLUENT 15.0. The computation domain contains a T-shaped impinging jet reactor with an ultrasonic transducer installed in the downstream sudden expansion chamber. The inner diameter of the inlet and the outlet are 3 and 8mm, respectively. Ultrasonic wave is generated and propagates from the tip of the ultrasonic transducer which has a length of 60 mm and diameter of 13mm. The location of boundary condition was at the tip of the ultrasonic transducer marked in blue in Figure 2.10, which is 18mm from the bottom of the expanded chamber. The mesh shown in Figure 2.3 was generated by using ANSYS ICEM with the feature of grid being orthogonal. Trial simulations were conducted and it was found that when the number of the meshes is greater than 160000, there is no noticeable change observed in the time-averaged concentration distributions in the IJR system. As such, all the simulations were conducted using this mesh setup throughout the present work.

In CFD modelling of the hydrodynamics in the confined impinge jet reactor, the pressure-velocity coupling was realised by SIMPLE algorithm with the second-order upwind discretisation scheme (Rahimi *et al.*, 2014). Standard  $k$ - $\varepsilon$  model was employed as the mixing in the core of the confined impinge jet reactor could be highly turbulent although the calculated Reynolds number at the reactor inlet is smaller than 2000. Velocity inlet boundary condition has been imposed for both IJR inlets while the pressure outlet boundary condition was specified for the outlet of the IJR where the synthesised product was collected. The tip of the ultrasonic transducer was set as a pressure inlet. No-slip boundary condition was applied to all the walls. Numerical simulations were performed with and without ultrasonic exposure.

Ultrasound of different amplitudes was imposed with a fixed ultrasound frequency of 20 kHz. The solutions were treated as being converged when the residuals of all the variables are smaller than  $1 \times 10^{-7}$  since the time step used for CFD modelling to capture the ultrasound wave fluctuation should be at least smaller than a period of the ultrasound wave. The numbers of max iterations per time step are set to be 100 to ensure convergence. When considering the effect of ultrasound on the bulk flow, the cyclic sound pressure equation of ultrasound wave was induced to describe the distribution of sound field according to the following equation (Cai *et al.*, 2009).

$$p_u = p_a \cos(2\pi ft) + \frac{1}{2} \rho v^2 \quad (2-10)$$

Where  $p_a$  is the amplitude of the sound pressure (pa),  $f$  is the frequency (Hz),  $t$  is the time (s),  $\rho$  is the average density of liquid bulk ( $\text{kg}/\text{m}^3$ ) and  $v$  is the velocity (m/s).

$$p_a = \sqrt{2I\rho C} \quad (2-11)$$

$$I = \frac{p_{us}}{A} \quad (2-12)$$

where  $I$  is the sound intensity ( $\text{W}/\text{m}^2$ ),  $p_{\text{us}}$  is the ultrasonic power ( $\text{W}$ ),  $A$  is the tip area of the ultrasonic transducer ( $\text{m}^2$ ) and  $C$  is the sound speed in the water ( $\text{m}/\text{s}$ ). In the present work, synthesis was proceeded under different conditions by changing the input power of the ultrasound as listed in Table 2.1.

## **2.4 Results and discussion**

### **2.4.1 Effect of ultrasound power intensity on crystallinity and morphology of FP precursors**

Thermal gravimetric analysis (TG) and Differential Thermal Analysis (DTA) were used to confirm the thermal properties of FP precursors and Figure 2.4 shows TG-DTA curves of sample FP-600 at a heating rate of  $10\text{ }^\circ\text{C min}^{-1}$  in the air. The TG curves indicated mass loss of samples. The absorbed water begins to lose at  $100\text{ }^\circ\text{C}$  and there is a strong endothermic peak near  $120\text{ }^\circ\text{C}$  indicating the loss of crystallized where  $\text{FePO}_4 \cdot x\text{H}_2\text{O}$  transformed to anhydrous hexagonal  $\text{FePO}_4$  crystal residues. Therefore,  $x$  for  $\text{FePO}_4 \cdot x\text{H}_2\text{O}$  is calculated in the range of 0.73 to 2.50. In addition, the gradual weight loss from  $200\text{ }^\circ\text{C}$  to  $600\text{ }^\circ\text{C}$  is ascribed to the decay of hydroxide and thus  $600\text{ }^\circ\text{C}$  is considered to be the minimum temperature needed for the calcination process to obtain the product with high purity.

The crystallinity and phase of FP specimens prepared under different ultrasound intensities were analysed by XRD as shown in Figure 2.5. The morphology and size of FP nano-particles were detected by SEM imaging as shown in Figure 2.6. It can be seen from the figures that the relative intensity of sample peaks is well consistent with that of hexagonal  $\text{FePO}_4$  crystal (JCPDS No.70-1793), which indicates high purity and crystallinity. The intensity of diffraction peaks has a noticeable change once ultrasound wave is imposed. A similar trend can be observed in Figure 2.5 (b), implying ultrasound

waves strengthen the crystal structure of LiFePO<sub>4</sub> crystal (JCPDS No.81-1173). Noticeably at ultrasound power as high as 960W, the intensity of peaks for both FP and LFP specimens becomes smaller. From XRD patterns, the average crystallite size  $L$  can be calculated through the Scherrer equation (Liu and Fox, 2006).

$$L = \frac{K\lambda}{\beta \cos\theta} \quad (2-13)$$

where  $K$  is the crystallite shape factor or denoted as Scherrer's constant equals to 0.9,  $\lambda$  is the wavelength of X-ray taken as 0.145056 nm,  $\beta$  is the peak width of the diffraction peak profile at half maximum height and  $\theta$  is the degree. The average crystallite size in nanometres of different samples is listed in Table 2.2. Sample prepared without applying ultrasound exposure has the largest average crystallite size of 191nm while that prepared under ultrasound power of 600 W has the smallest diameter of 107 nm. A similar appearance was also observed in a series of SEM images of FP samples as shown in Figure 2.6, indicating that higher intensity of ultrasound irradiation may cause a noticeable change in particles size and uniform microstructure. There may exist a threshold of the applied ultrasound intensity that is most optimum for particle synthesis with the most uniform microstructure and smallest particle size.

#### **2.4.2 Effect of ultrasound power on particle size and porosity of FP precursors**

Apart from crystallinity and morphology, ultrasound has an impact on particle size and porosity as well. The particle size distribution of FP precursors under different conditions are shown in Figure 2.6 It shows that the main peaks of the particle size distribution of FP samples have fallen into the range of 90 -130 nm. FP samples prepared without applying ultrasound present a broader size distribution and less than 47 % of particles are in the range of 90 -130 nm. In contrast, samples for cases of FP-600 and FP-720 exhibit a narrower particle size distribution, corresponding to a

percentage up to 77 % and 68 % of the particles falling into this size range. The broader size distribution is contributed by non-uniform products that is consistent with the average crystallite size of samples shown in Table 2.2. In addition, samples FP-600 and FP-720 give narrow particle size distribution but that of FP-960 is broader. The impact of ultrasound intensity on particle size and porosity can be also reflected by results of BET test as shown in Figure 2.7, verifying that product with smaller particle size in the presence of ultrasound irradiation can be obtained. As can be observed from Figure 2.7, the adsorption of N<sub>2</sub> at very low pressure indicates that the micropores fill with nitrogen gas. At the knee monolayer formation is beginning and multilayer formation occurs at medium pressure. At the higher pressures, capillary condensation occurs. The plots of sample FP-0 and FP-360 are approximately fitted by type II (Bulliard-Sauret et al., 2019). However, the gaps between the N<sub>2</sub> adsorption and release curve of samples such as FP-600 and FP-960 demonstrate the existence of pores and the plots are well described by type IV. Brunauer *et al* (1940) claimed that BET surface area characterized by mesoporous materials with pore diameters between 2 - 50 nm gives such type of isotherm. Consequently, the porosity of the FP particles is increased with the adoption of the ultrasound irradiation compared with the samples synthesised without ultrasound. In specific, the sample of FP-600 is the most mesoporous among all the samples. This may be ascribed to micro-bubble collapse in an extremely short time to generate the bombarding on the particle surfaces to form the porous structures, leading to increment in porosity.

The ultrasound irradiation in the IJR intensifies the reactant mixing and encourages rapid reaction to form the nuclei of FePO<sub>4</sub> with smaller size, which have been shown from experimental results. The turbulent eddies induced by acoustic streaming may exert strong shear force on the nanoparticles to diminish and smooth its ragged surface. This can be interpreted as the fact that the synthesised micro-particles that are entrained by the turbulent eddies experience a higher local shear so that the particle size may be reduced due to surface rip-off. This can be also supported by turbulent kinetic energy

(k) distribution in the IJR system as shown in Figure 2.8. Figure 2.8 (a) shows the iso-surface distribution of turbulent kinetic energy ( $k$ ) under the ultrasound power of 960W in the IJR while Figure 2.8 (b) shows the turbulent kinetic energy ( $k$ ) distribution under diverse ultrasound power. It can be seen from Figure 2.9 that enhancement of the turbulent kinetic energy  $k$  in the vicinity of the tip of ultrasound transducer and the reactor outlet is observed as the acoustic streaming is introduced at 0.0023 s of 46 periods of ultrasound wave. As an effect of ultrasound intensification, the pressure change gives rise to the change in the velocity field. Such velocity fluctuation would have an impact on the turbulent kinetic energy  $k$  due to the periodical fluctuation of acoustic wave. Consequently, it can be reasonably assumed that the application of ultrasound can strengthen the local turbulent shear as more small length scale turbulent eddies could be generated, which will enhance turbulent kinetic energy  $k$  (see Figure 2.9).

When the ultrasound power used is higher than its threshold, the aggregate of particles becomes prevalent and leads to larger particle size as can be seen from Figure 2.8 (b). An explanation is that small particles tend to agglomerate to diminish the high surface energy induced by ultrasound and regress to a steady state (Vollath *et al.*, 2018). Another cause for aggregation is attributed to temperature impact. Larger ultrasound energy causes higher temperature change and this enlarges the enthalpy change with a negative value when it cools down. At room temperature however, enthalpy enhancement owing to the release of water drives aggregation process (Yu *et al.*, 2007). Thus, temperature increment is the result of turbulence energy dissipation which  $\varepsilon$  can be estimated by the following equation (Burton *et al.*, 2009),

$$\varepsilon = \frac{\Delta PQ}{\rho V} \quad (2-14)$$

Flow in ultrasound-assisted IJR is pressure-driven since the solution is pumped into the IJR while the effect of ultrasound wave can be expressed in terms of pressure. From the numerical works, the total pressure distribution varies under different power of ultrasound as shown in Figure 2.10 (a). The pressure from the inlet is predominant and pressure drops as with flow upwards. From Equation (2-13), the large pressure drop is responsible for high-energy dissipation rate leading to intense temperature increase. Under the impact of ultrasound waves, the dynamic pressure profile was predicted theoretically to be the sectorial shape and was acoustically generated from a fictitious “orifice” as shown in Figure 2.10 (b).

### 2.4.3 Effect of adoption of different ultrasound power intensities on the mixing

There are generally two scales used to describe mixing performance, namely macromixing for blending and micro-mixing for turbulent mixing. In this case, acoustic streaming helps to intensify micro-mixing as a result of ultrasound wave propagation and mixing parameter  $\gamma$  is used to define the micromixing time as,

$$t_m = \frac{1}{2\gamma} \quad (2-15)$$

$$\gamma = \frac{C_\phi \varepsilon}{2k} \quad (2-16)$$

Where  $C_\phi$  is a function of local turbulent Reynolds number  $Re_t$  in Equation (2-17),  $k$  and  $\varepsilon$  are the turbulent kinetic energy and the turbulent dissipation rate that can be derived from numerical works.

$$Re_t = \frac{k}{(\varepsilon\nu)^{1/2}} \quad (2-17)$$

In this case,  $C_\phi \approx 2$  is used for turbulent flow and it is overestimated for this case (Liu and Fox, 2006). The mixing time shown in Figure 2.11 reveals that the adoption of

ultrasound can noticeably reduce the mixing time up to 98.6%. In the presence of ultrasound, the mixing performance is intensified and an empirical relationship between Kolmogorov time scale  $\left(\frac{k}{\varepsilon}\right)$  and micromixing time  $t_m$  based on power law relation as follows,

$$t_m = 0.0005 \left(\frac{k}{\varepsilon}\right)^{-0.0285} \quad (2-18)$$

From the velocity magnitude in Figure 2.11, the ultrasound waves lead to an “active” zone near the tip of ultrasound transducer where eddies are induced owing to ultrasound wave propagation. These turbulence-like micro-streams entrain the particles to convey with these eddies. The intensity of the vortices changes along with the amplitude of the ultrasound waves. In order to illustrate the effect of ultrasound on the mixing behaviour in the IJR, especially for the zone just downstream of the impinging jet, a special correlation between cross-section area average turbulent dissipation rate and cross-section area average vorticity is proposed. The results of such correlation are shown in Figure 2.12. The  $R_{\varepsilon,\Omega}$  represents the correlation factor and it can be calculated by Equation (2-19) as given,

$$R_{\varepsilon,\Omega} = \frac{\varepsilon(h,t)|\Omega(h+\Delta h,t)|}{\sqrt{\varepsilon(h,t)^2} \sqrt{\Omega(h,t)^2}} \quad (2-19)$$

$$\varepsilon(h,t) = \frac{1}{A} \int_0^A \varepsilon \, dA \quad (2-20)$$

$$\Omega(h,t) = \frac{1}{A} \int_0^A |\Omega| \, dA \quad (2-21)$$

where  $\varepsilon$  is the cross-section area-weighted average turbulent dissipation rate and  $\Omega$  is the cross-section average area-weighted vorticity. Spatial correlation  $R_{\varepsilon,\Omega}$  starts from 1 since all the spatial correlation is corresponding to the first point at the tip of the

ultrasound transducer. Without adopting ultrasound, correlation factor gradually decreases where energy dissipation rate contributes less to the formation of vortices. On the other hand,  $R_{\epsilon,\Omega}$  approaches to 1.2 where vortices are strengthened in the core of impingement zone of T-junction with the assistance of sonication. It can be observed from Figure 2.12 that there exists a toroidal vortex just above the sudden expansion of the exit of the confined impinge jet reactor chamber when ultrasound is used. Thus, the correlation between turbulent energy dissipation and vorticity will be significantly affected by the existence of such a vortex. Generally speaking, high turbulent energy dissipation will take place at the core of such vortex. With ultrasound intensification, the dissipation will increase with increasing the ultrasound power. As the ultrasound power increases, the spatial correlation factor has a slower decline, indicating ultrasound has a significant impact on flow patterns. High correlation factor indicates the great contribution to intensified turbulence thus leading to enhanced mixing performance via inducing ultrasound waves. Simultaneously, intensified eddies may exert a strong shear force to shape the particles or carry the particles in circulation. Such correlation not only provides interpretation on the intensification of mixing performance as a result of the increment of ultrasound power, the correlation may also help to optimise flow conditions for particle preparation. Figure 2.13 shows that fluid near the ultrasound transducer has diverse pathway due to the impact of the ultrasound period ( $T = 5 \times 10^{-5}$  s). It shows the streamline flow of the fluid in the period from  $44T$  to  $45T$  (0.0022 s to 0.0023 s) and this verifies the vortices changes near the ultrasound transducer.

#### **2.4.4 Effect of ultrasound power on electrochemical performance**

The electrochemical performance of LFP/C prepared with FP-precursors under different ultrasound power is as shown in the Figure 2.14. The initial charge/discharge of LFP/C composites was performed at 0.1 C and the applied voltage is in the range of

2.5-4.2V. As can be seen from Figure 2.14 (a), the initial discharge specific capacities of samples synthesised with FP without ultrasound power is 141.02 mAh/g and the initial discharge specific capacities for battery samples synthesised under ultrasound power of 600W is 158.05 mAh/g. The electrochemical performance is enhanced up to 10.78 % by when using ultrasonic prepared LFP as the battery precursor under ultrasound power of 600W. 6 groups of electrical tests have been carried out employing assembled batteries from LFP precursors synthesised under ultrasound power. The cell is being discharged with discharge rate from 0.1 C to 5 C. There exists an apparent trend that intensified ultrasound power in the synthesis process has a positive impact on the electrochemical performance of the LFP products. It is noticed that the LFP prepared under ultrasound power of 600 W and 960 W present higher discharge capacity than others at charging/discharging rate from 0.1 C to 5 C.

The enhanced electrochemical performance by employing LFP precursors synthesised under the intensified ultrasound power may attribute to increased potential difference between the charge and discharge plateaus. Good performance of LFP under 600 W and 960 W can be explained by narrow potential polarization and other aspects such as degree of crystallization, particle size, porosity and purity. To be specific, ultrasound power has impact on LFP/C half-cell electrochemical performance by influencing the transport of lithium-ion (Doyle and Newman, 1995). The governing equation of transport of lithium-ion inside the electrolyte is related to concentration of lithium-ion and its flux as shown below,

$$\alpha \frac{\partial c_e}{\partial t} = \frac{\partial}{\partial x} \left( D_{eff} \frac{\partial c_e}{\partial x} \right) + a_p (1 - t_+^0) \quad (2-22)$$

where  $\alpha$  is the electrode porosity;  $c_e$  is the concentration of lithium-ion inside electrolyte;  $D_{eff}$  is effective diffusivity;  $a_p$  is the specific surface area which is interfacial surface area per unit volume of electrode;  $t_+^0$  is the transference number of

the lithium-ion in the solution that is assumed to be constant (Newman and Tiedemann, 1975).

According to Newman and Tiedemann (1975), the enhanced electrochemical performance is reliant on a large interfacial area per unit volume porous electrode can compensate for this by providing a large interfacial area per unit that is decisive by the porosity  $\epsilon$  and electrode particle size  $d_p$ , as follows,

$$a = \frac{3(1-\epsilon)}{d_p} \quad (2-23)$$

This theory has clearly explained the consistency of the tendency of particle size and electrochemical performance. It can be concluded that smaller particle size with narrow particles size distribution can enhance cycling stability with a high capacity leading to better electrochemical performance (Wu *et al.*, 2018).

## 2.5 Conclusions

In this work, impinging jet reactor with a downstream sudden expansion chamber that is equipped with ultrasound transducer was employed to assess the effect of intensification of ultrasound on the synthesis of FePO<sub>4</sub> particles. It was found that FePO<sub>4</sub> particles could be obtained with higher crystallinity and uniformity, higher porosity and smaller size with ultrasound intensification. However, adoption of excess high ultrasound intensity may induce free radicals and generate other compounds due to local high temperature and pressures, leading to unpredictable changes in physical and chemical properties and excessive energy waste (Jambrak *et al.*, 2014). However, the application of ultrasound can be still considered as an effective means for the synthesis of FP nanoparticles if the threshold of the applied ultrasound intensity is suitable. It has been clearly indicated that the ultrasound-assisted impinging jet reactor

system can effectively intensify micro-mixing as the result of enhancement on the local turbulent dissipation rate. The increase of the local turbulent dissipation rate gives rise to an increase of the local shear which can assist in the controllable synthesis of nanoparticles with desired characteristics. It has been demonstrated from experimental results that particles with expected characteristics such as smaller size and higher porosity can be obtained as the consequence of increase in the ultrasound power applied, which has reaffirmed that with ultrasonic intensification, the synthesized particles tend to aggregate due to the locally enhanced shear strain from the occurrence of high turbulent kinetic energy dissipation.

## References

ABIEV, R., ALMYASHEVA, O., IZOTOVA, S. & GUSAROV, V. 2017. Synthesis of cobalt ferrite nanoparticles by means of confined impinging-jets reactors. *J Chem Tech App. 2017; 1 (1): 7-13. 8 J Chem Tech App 2017 Volume 1 Issue, 1.*

ABOLHASANI, M., RAHIMI, M., DEHBANI, M. & SHABANIAN, S. R. CFD modeling of low, medium and high frequency ultrasound waves propagation inside a liquid medium. 4rd National Conference on CFD Applications in Chemical & Petroleum Industries, Ahwaz, Iran, 2012.

BANG, J. H. & SUSLICK, K. S. 2010. Applications of ultrasound to the synthesis of nanostructured materials. *Advanced materials*, 22, 1039-1059.

BULLIARD-SAURET, O., BERINDEI, J., FERROUILLAT, S., VIGNAL, L., MEMPONTEIL, A., PONCET, C., LEVEQUE, J. M. & GONDREXON, N. 2019. Heat transfer intensification by low or high frequency ultrasound: Thermal and hydrodynamic phenomenological analysis. *Experimental Thermal and Fluid ence (EXP THERM FLUID )*, 104, 258-271.

BURTON, A. W., ONG, K., REA, T. & CHAN, I. Y. 2009. On the estimation of average crystallite size of zeolites from the Scherrer equation: a critical evaluation of its application to zeolites with one-dimensional pore systems. *Microporous and Mesoporous Materials*, 117, 75-90.

BRUNAUER, S., DEMING, L. S., DEMING, W. E. & TELLER, E. 1940. On a Theory of the van der Waals Adsorption of Gases. *J.am.chem.soc*, 62, 1723-1732.

CAI, J., HUAI, X., YAN, R. & CHENG, Y. 2009. Numerical simulation on enhancement of natural convection heat transfer by acoustic cavitation in a square enclosure. *Applied Thermal Engineering*, 29, 1973-1982.

- DE CASTRO, M. L. & PRIEGO-CAPOTE, F. 2007. Ultrasound-assisted crystallization (sonocrystallization). *Ultrasonics sonochemistry*, 14, 717-724.
- DONG, B., HUANG, X., YANG, X., LI, G., XIA, L. & CHEN, G. 2017. Rapid preparation of high electrochemical performance LiFePO<sub>4</sub>/C composite cathode material with an ultrasonic-intensified micro-impinging jetting reactor. *Ultrasonics sonochemistry*, 39, 816-826.
- DOYLE, M. & NEWMAN, J. 1995. The use of mathematical modeling in the design of lithium/polymer battery systems. *Electrochimica Acta*, 40, 2191-2196.
- FONTE, C. P., SULTAN, M. A., SANTOS, R. J., DIAS, M. M. & LOPES, J. C. B. 2015. Flow imbalance and Reynolds number impact on mixing in Confined Impinging Jets. *Chemical Engineering Journal*, 260, 316-330.
- GAVI, E., MARCHISIO, D. L. & BARRESI, A. A. 2007. CFD modelling and scale-up of confined impinging jet reactors. *Chemical engineering science*, 62, 2228-2241.
- GUICHARDON, P., FALK, L. & VILLERMAUX, J. 2000. Characterisation of micromixing efficiency by the iodide-iodate reaction system. Part II: kinetic study. *Chemical Engineering Science*, 55, 4245-4253.
- GUO, T., RUAN, B., LIU, Z., JAMAL, M. A., WEN, L. & CHEN, J. 2017. Numerical and experimental investigations of liquid mixing in two-stage micro-impinging stream reactors. *Chinese Journal of Chemical Engineering*, 25, 391-400.
- HIELSCHER, T. 2007. Ultrasonic production of nano-size dispersions and emulsions. *arXiv preprint arXiv:0708.1831*.
- JAMBRAK, A. R., MASON, T. J., LELAS, V., PANIWNYK, L. & HERCEG, Z. 2014. Effect of ultrasound treatment on particle size and molecular weight of whey proteins. *Journal of Food engineering*, 121, 15-23.

JAMEI, M. R., KHOSRAVI, M. R. & ANVARIPOUR, B. 2013. Investigation of ultrasonic effect on synthesis of nano zero valent iron particles and comparison with conventional method. *Asia-Pacific Journal of Chemical Engineering*, 8, 767-774.

JAMSHIDI, R., POHL, B., PEUKER, U. A. & BRENNER, G. 2012. Numerical investigation of sonochemical reactors considering the effect of inhomogeneous bubble clouds on ultrasonic wave propagation. *Chemical engineering journal*, 189, 364-375.

JIAO, Q., TAN, X. & ZHU, J. 2014. Numerical simulation of ultrasonic enhancement on mass transfer in liquid–solid reaction by a new computational model. *Ultrasonics sonochemistry*, 21, 535-541.

KOHNO, M., MOKUDAI, T., OZAWA, T. & NIWANO, Y. 2011. Free radical formation from sonolysis of water in the presence of different gases. *Journal of clinical biochemistry and nutrition*, 49, 96-101.

LAUGIER, F., ANDRIANTSIFERANA, C., WILHELM, A.-M. & DELMAS, H. 2008. Ultrasound in gas–liquid systems: Effects on solubility and mass transfer. *Ultrasonics sonochemistry*, 15, 965-972.

LEBON, G. B., TZANAKIS, I., DJAMBAZOV, G., PERICLEOUS, K. & ESKIN, D. 2017. Numerical modelling of ultrasonic waves in a bubbly Newtonian liquid using a high-order acoustic cavitation model. *Ultrasonics Sonochemistry*, 37, 660-668.

LIGHTHILL, M. J. 1954. On sound generated aerodynamically II. Turbulence as a source of sound. *Proceedings of the Royal Society of London. Series A. Mathematical and Physical Sciences*, 222, 1-32.

LIU, X.-M., YAN, P., XIE, Y.-Y., YANG, H., SHEN, X.-D. & MA, Z.-F. 2013. Synthesis of superior fast charging–discharging nano-LiFePO<sub>4</sub>/C from nano-FePO<sub>4</sub> generated using a confined area impinging jet reactor approach. *Chemical Communications*, 49, 5396-5398.

- LIU, Y. & FOX, R. O. 2006. CFD predictions for chemical processing in a confined impinging-jets reactor. *AIChE Journal*, 52, 731-744.
- MAHAJAN, A. J. & KIRWAN, D. J. 1996. Micromixing effects in a two-impinging-jets precipitator. *AIChE Journal*, 42, 1801-1814.
- NEWMAN, J. & TIEDEMANN, W. 1975. Porous-electrode theory with battery applications. *AIChE Journal*, 21, 25-41.
- MONNIER, H., WILHELM, A. & DELMAS, H. 2000. Effects of ultrasound on micromixing in flow cell. *Chemical Engineering Science*, 55, 4009-4020.
- NIAZI, S., HASHEMABADI, S. H. & RAZI, M. M. 2014. CFD simulation of acoustic cavitation in a crude oil upgrading sonoreactor and prediction of collapse temperature and pressure of a cavitation bubble. *Chemical Engineering Research and Design*, 92, 166-173.
- NIE, A., GAO, Z., XUE, L., CAI, Z., EVANS, G. M. & EAGLESHAM, A. 2018. Micromixing performance and the modeling of a confined impinging jet reactor/high speed disperser. *Chemical Engineering Science*, 184, 14-24.
- NYBORG, W. L. 1953. Acoustic streaming due to attenuated plane waves. *The journal of the acoustical society of America*, 25, 68-75.
- RAHIMI, M., AGHEL, B., HATAMIFAR, B., AKBARI, M. & ALSAIRAFI, A. 2014. CFD modeling of mixing intensification assisted with ultrasound wave in a T-type microreactor. *Chemical Engineering and Processing: Process Intensification*, 86, 36-46.
- SAJJADI, B., ASGHARZADEHAHMADI, S., ASAITHAMBI, P., RAMAN, A. A. A. & PARTHASARATHY, R. 2017. Investigation of mass transfer intensification under power ultrasound irradiation using 3D computational simulation: A comparative analysis. *Ultrasonics sonochemistry*, 34, 504-518.

VAN WIJNGAARDEN, L. 1968. On the equations of motion for mixtures of liquid and gas bubbles. *J. Fluid Mech*, 33, 465-474.

VOLLATH, D., FISCHER, F. D. & HOLEC, D. 2018. Surface energy of nanoparticles— influence of particle size and structure. *Beilstein journal of nanotechnology*, 9, 2265-2276.

WU, S., YU, B., WU, Z., FANG, S., SHI, B. & YANG, J. 2018. Effect of particle size distribution on the electrochemical performance of micro-sized silicon-based negative materials. *RSC Advances*, 8, 8544-8551.

XU, Z., YASUDA, K. & KODA, S. 2013. Numerical simulation of liquid velocity distribution in a sonochemical reactor. *Ultrasonics sonochemistry*, 20, 452-459.

YING, Y., CHEN, G., ZHAO, Y., LI, S. & YUAN, Q. 2008. A high throughput methodology for continuous preparation of monodispersed nanocrystals in microfluidic reactors. *Chemical Engineering Journal*, 135, 209-215.

YU, J. A., OH, S. H., PARK, Y. R. & KIM, J. S. Enthalpy-Entropy Compensation in Aggregation of Poly (styrene-co-sodium methacrylate) Ionomers in Aqueous Solution. *Macromolecular Symposia*, 2007. Wiley Online Library, 445-449.

ZHAO, Y., CHEN, G. & YUAN, Q. 2007. Liquid–liquid two-phase mass transfer in the T-junction microchannels. *AIChE journal*, 53, 3042-3053.

## Figures and graphs

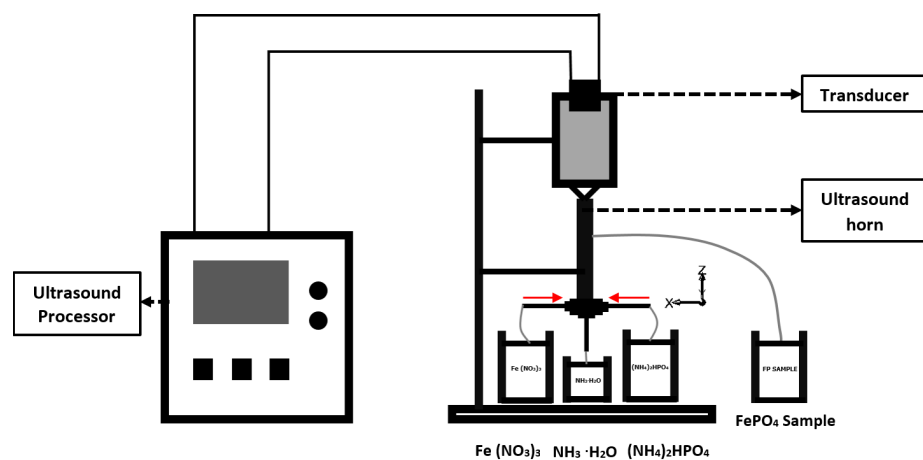


**Figure 2.1** Schematic diagram of the experimental setup of FePO<sub>4</sub> synthesis in the IJR.

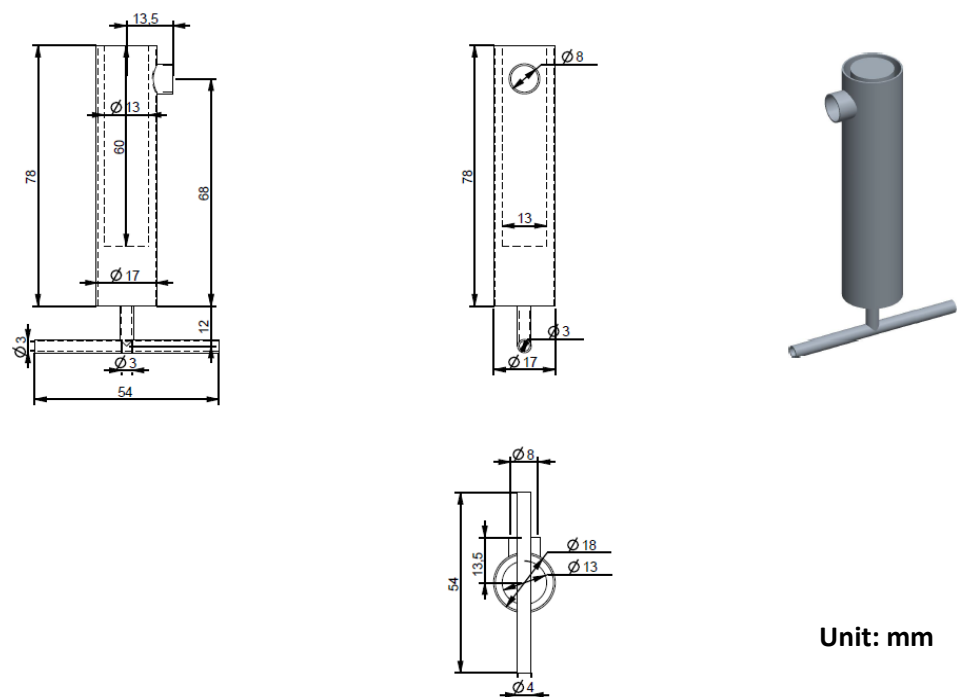


**Figure 2.2** Configuration of IJR with ultrasound transducer with scaled dimensions in millimetres.

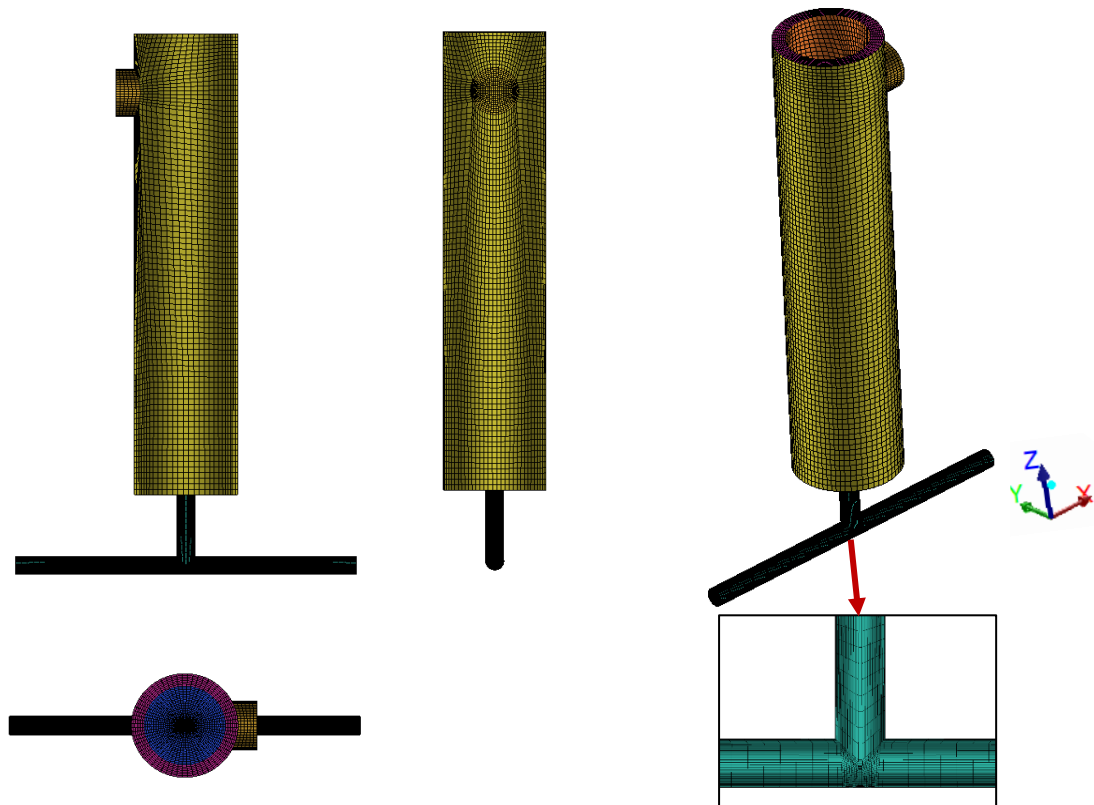


**Figure 2.3** 3D view of the computational domain and mesh structure of IJR.

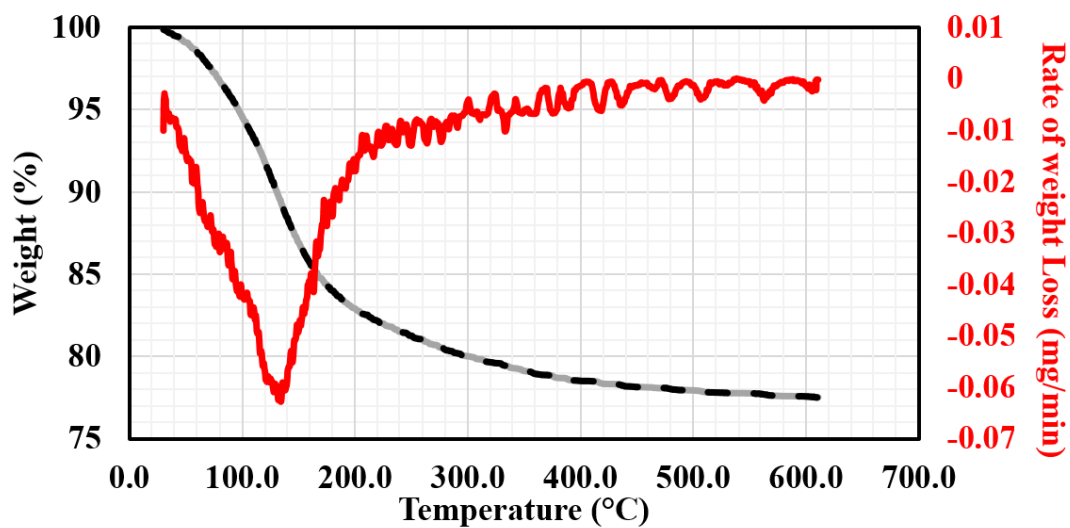


**Figure 2.4** TG-DTA curves of sample FP-600 before calcination at heating rate of 10 °C min<sup>-1</sup> in air.

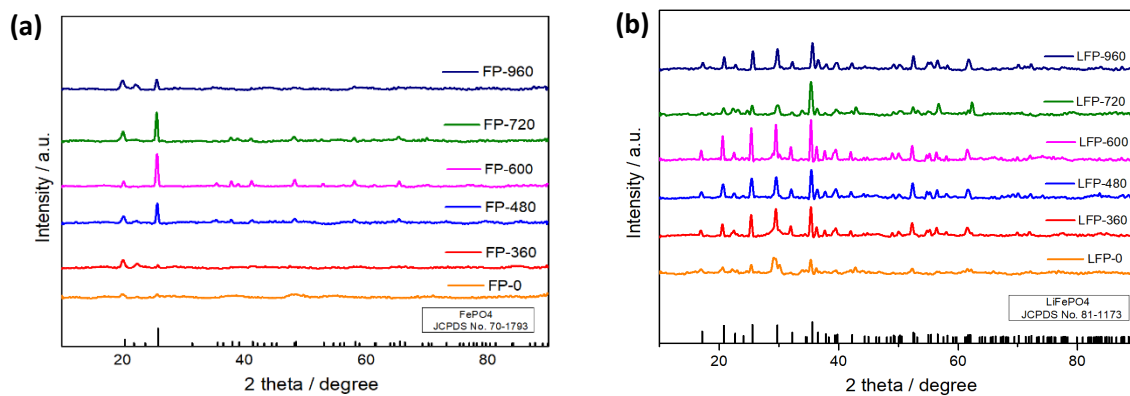


**Figure 2.5** XRD patterns of (a)  $\text{FePO}_4$  and prepared (b)  $\text{LiFePO}_4$  from  $\text{FePO}_4$  in degree of from  $10^\circ$  to  $90^\circ$ .

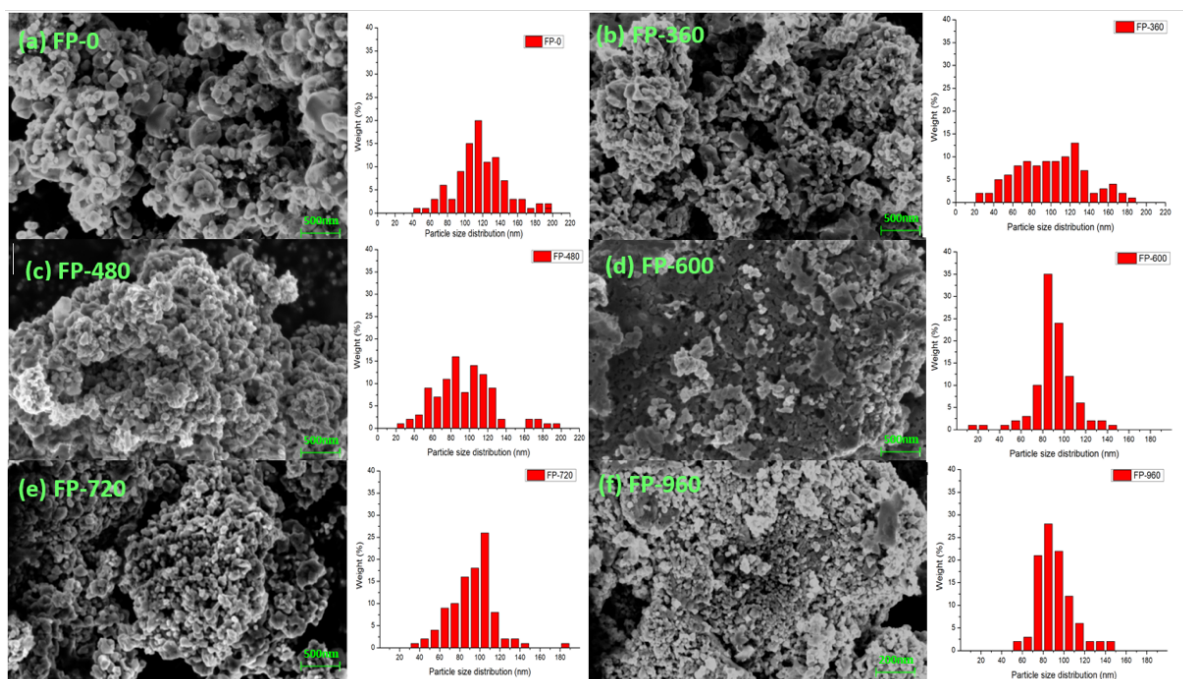
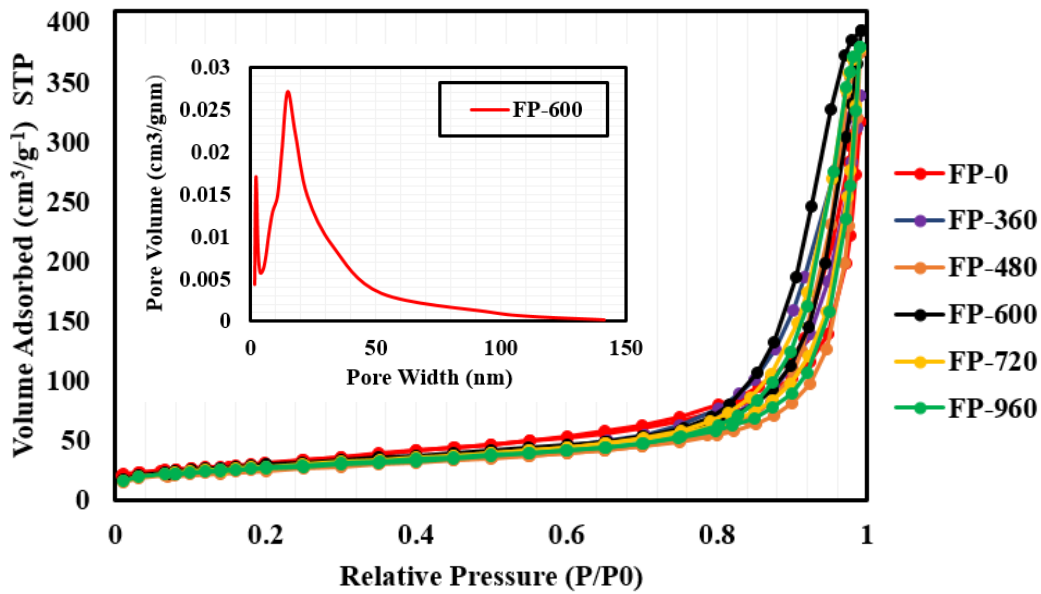
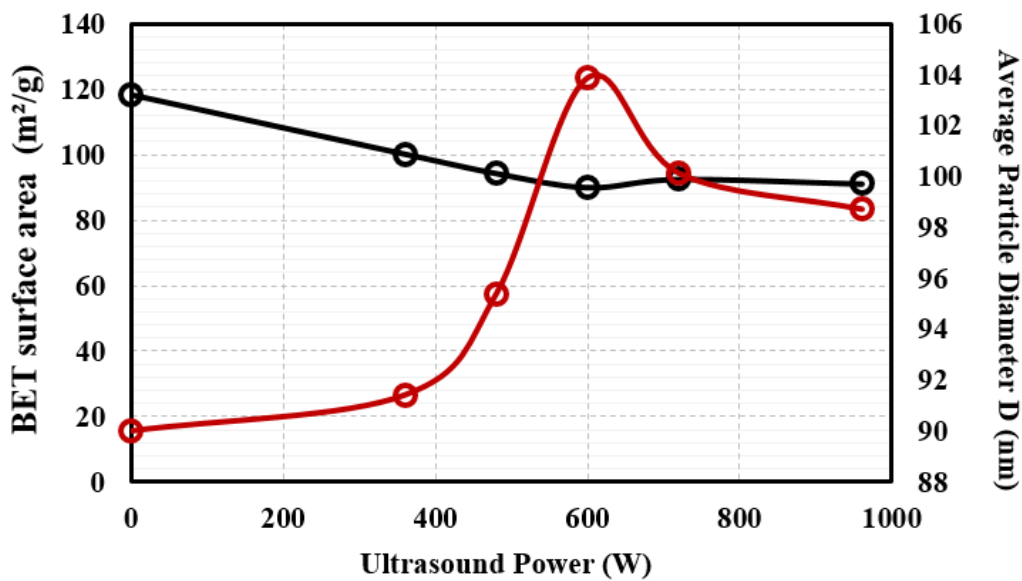


**Figure 2.6** The SEM images of  $\text{FePO}_4$  synthesized under the conditions of applying different ultrasound powers and corresponding size distribution of  $\text{FePO}_4$  samples synthesized under the conditions of applying different ultrasound powers.

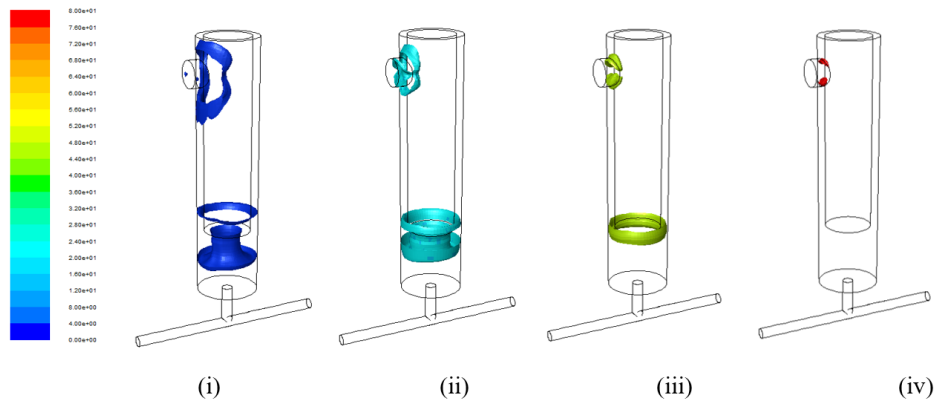


(a)

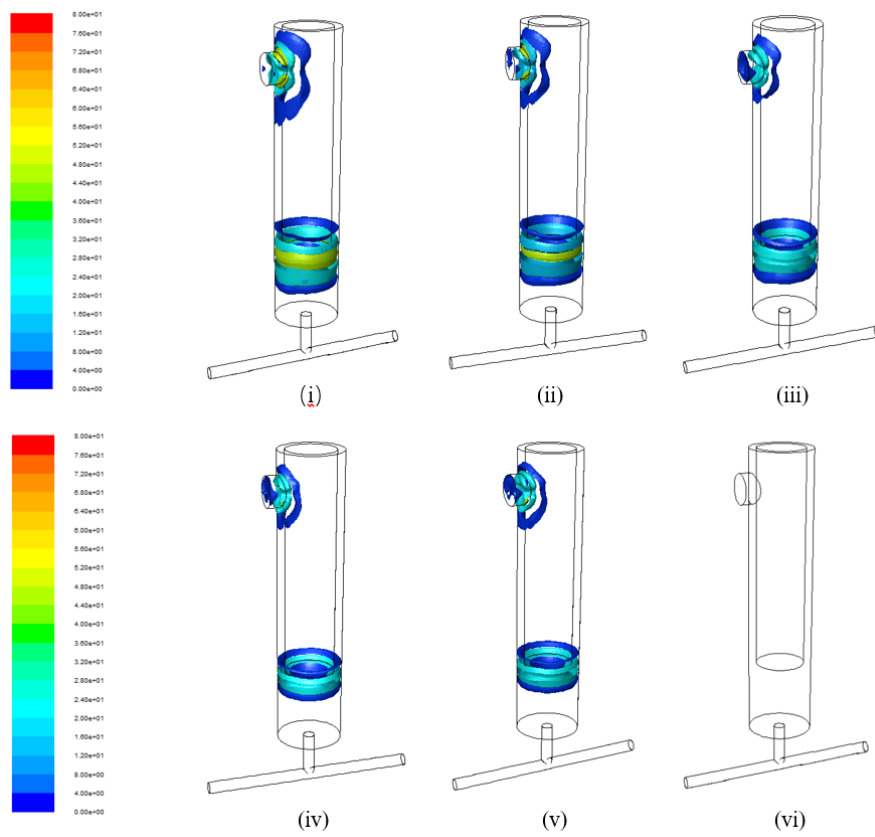


(b)

**Figure 2.7** (a)  $N_2$  adsorption–desorption isotherm at 77 K and pore size distribution (the inset) calculated by the BJH method from the desorption branch of  $\text{FePO}_4$ ; (b) Average particles size and BET surface area of the sample prepared under different ultrasound power.

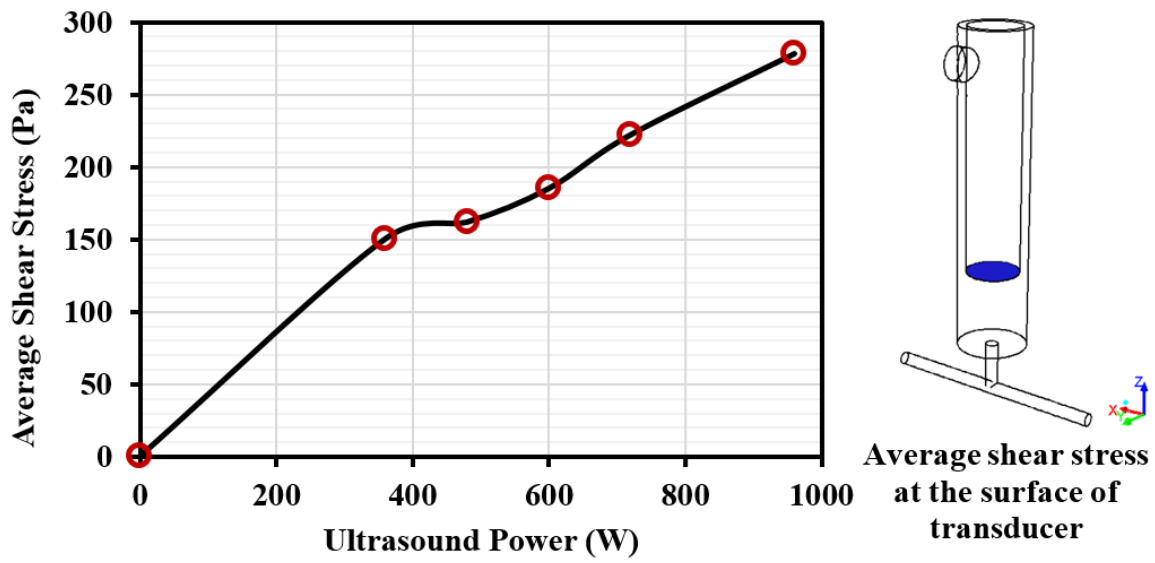


(a)

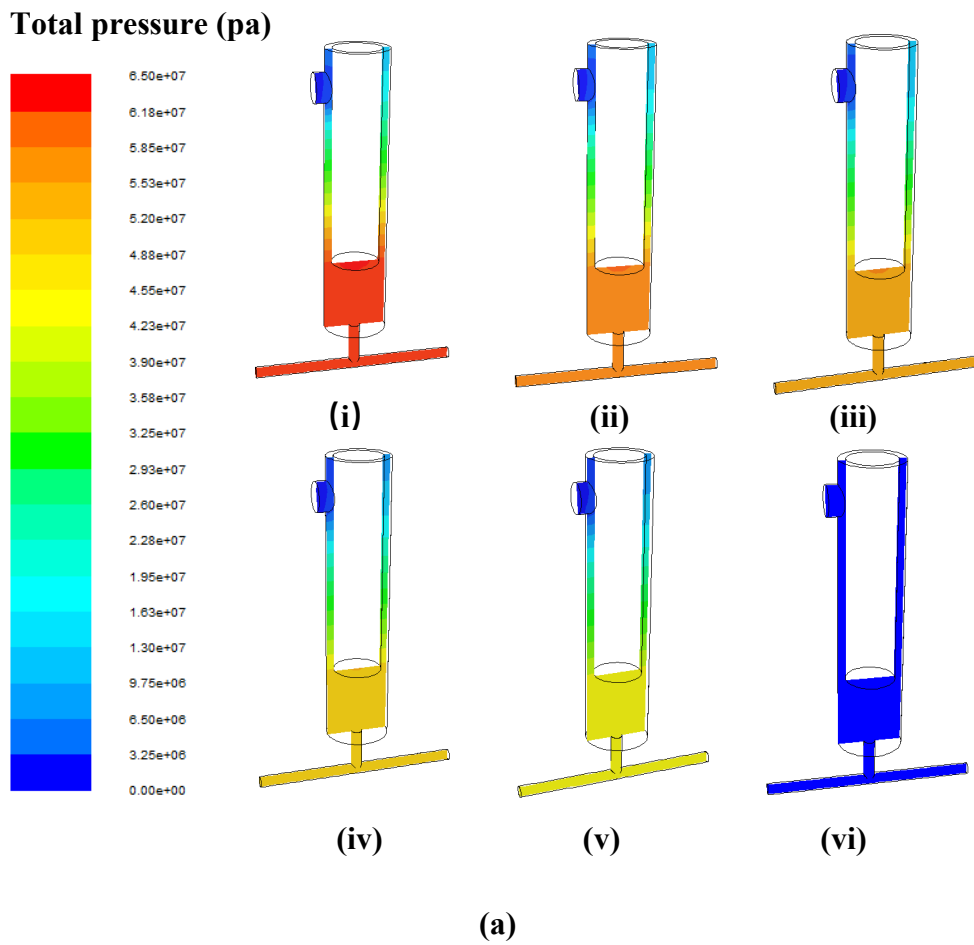


(b)

**Figure 2.8** (a) Iso-surface distribution of turbulent kinetic energy ( $k$ ) in IJR under the ultrasound power of 960W at 0.0023s. (i)  $5 \text{ m}^2/\text{s}^2$ , (ii)  $20 \text{ m}^2/\text{s}^2$ , (iii)  $50 \text{ m}^2/\text{s}^2$  and (iv)  $80 \text{ m}^2/\text{s}^2$ ; (b) Turbulence Kinetic Energy ( $k$ ) distribution of IJR under different power of ultrasound at 0.0023s. (i) 960W, (ii) 720W, (iii) 600w, (iv) 480W, (v) 360W and (vi) 0W.



**Figure 2.9** Cross-section averaged shear stress at the transducer surface under the conditions of applying different ultrasound powers.



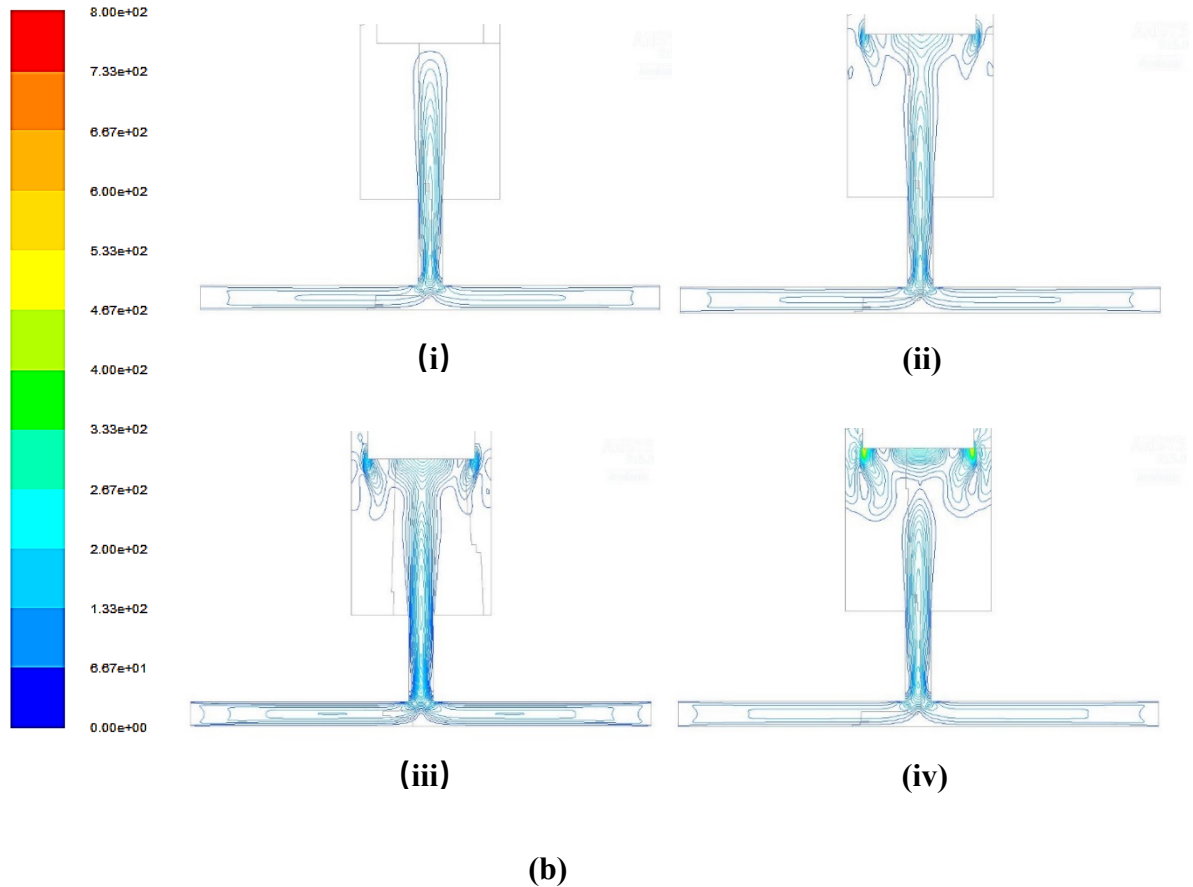


**Figure 2.10** (a) Total pressure distribution (Pa) of x-z plane of IJR under different power of ultrasound at 0.0023s. (i) 960W, (ii) 720W, (iii) 600w, (iv) 480W, (v) 360W and (vi) 0W. (b) Dynamic pressure distribution (P) of x-z plane of IJR under different power of ultrasound at 0.0023s. (i) 960W, (ii) 600W, (iii) 360w, (iv) 0W.

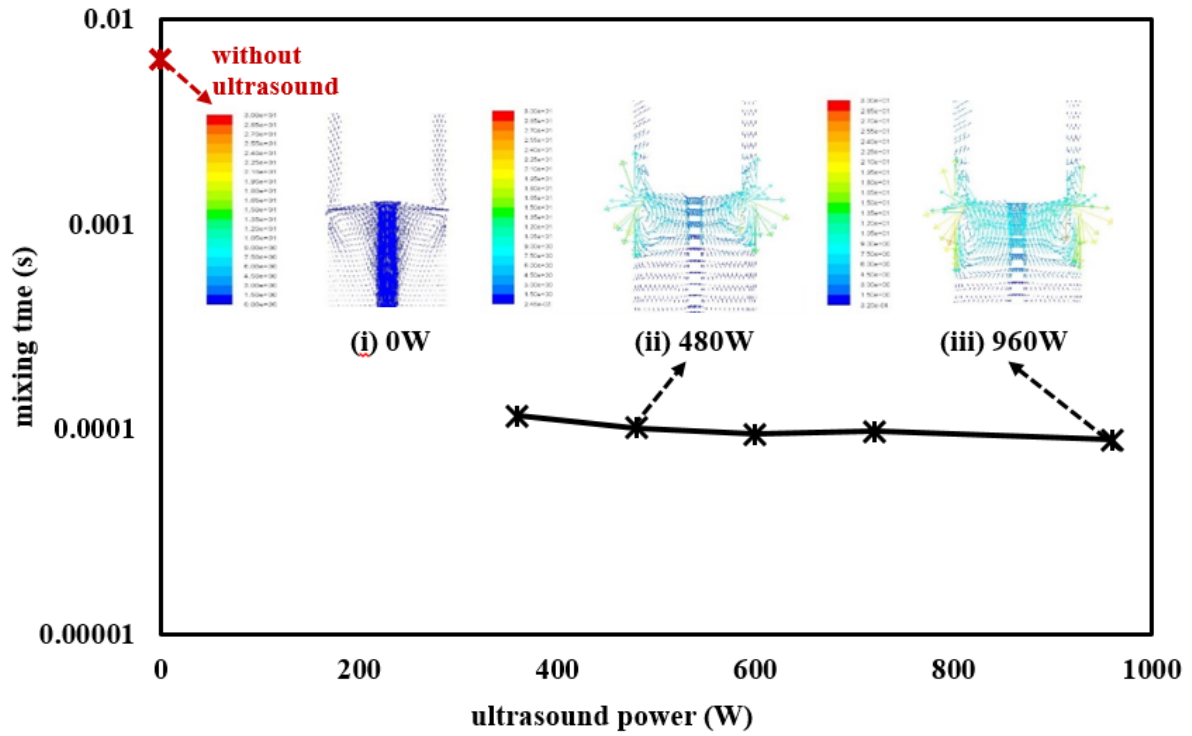


**Figure 2.11** Micromixing time  $t_m$  as a function of ultrasound power  $P$  and velocity Magnitude (m/s) of x-z plane of IJR under different power of ultrasound at 0.0023s.

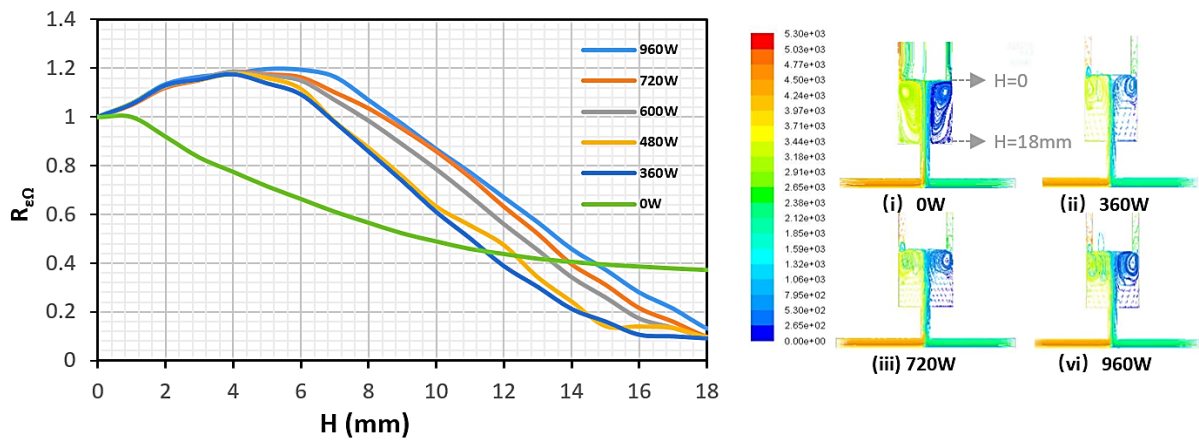


**Figure 2.12** Spatial correlation  $R_{\epsilon, \Omega}$  along the reaction chamber from the tip of the ultrasound transducer ( $H=0$ ) to the bottom of expansion ( $H=18\text{mm}$ ) under different power of ultrasound at 0.0023s.

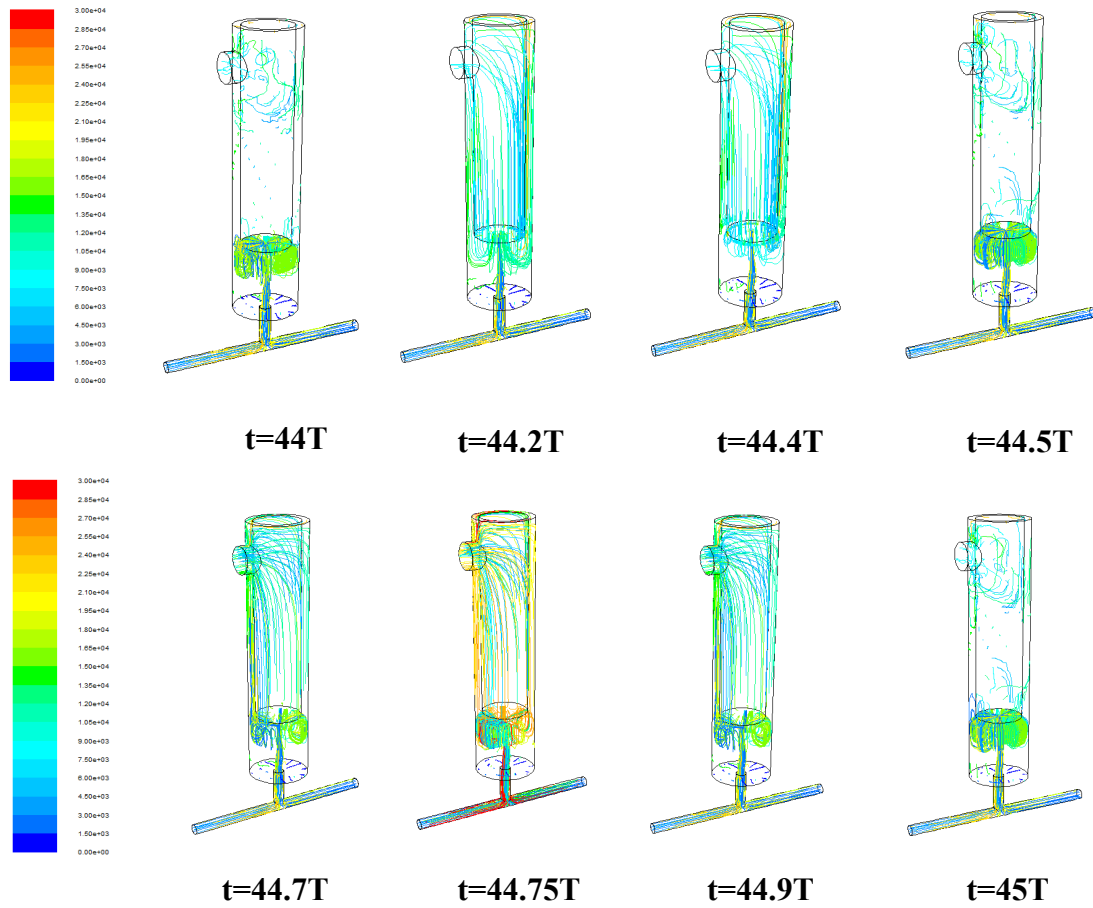


**Figure 2.13** The streamline flow of the fluid in the period from 44T to 45T (0.0022 s to 0.0023 s) in the IJR.

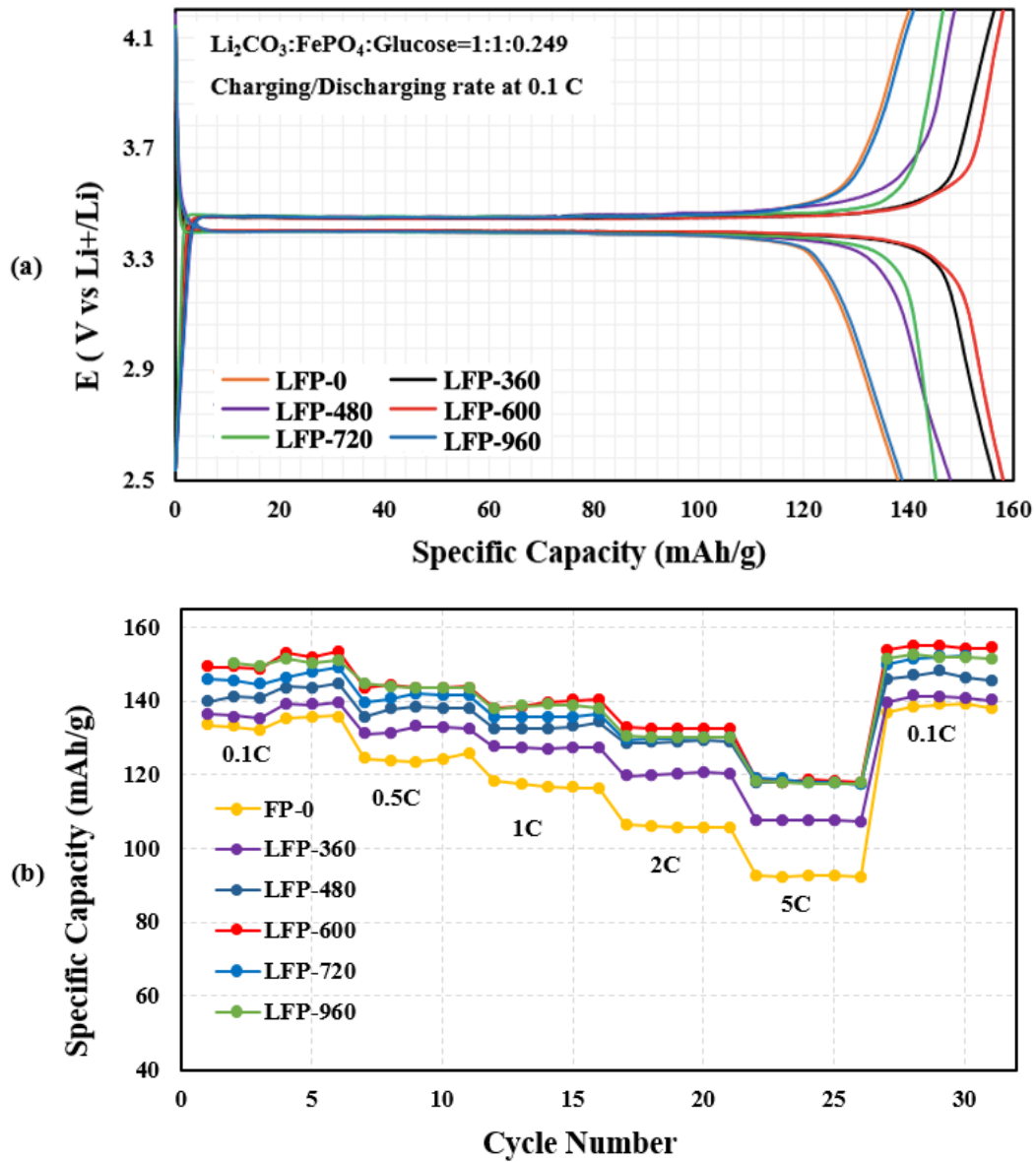


**Figure 2.14** (a) Initial charge/discharge curves of the LFP/C composites at different ultrasound power at 0.1 C synthesized with anhydrous FePO<sub>4</sub>; (b) Cycle number of the LFP samples synthesized by different FP precursors.

## Tables

**Table 2.1** Samples with different ultrasound power and intensity.

<b>Samples</b>	<b>Ultrasound Power Input (W)</b>	<b>Ultrasound Intensity×10<sup>6</sup> (W/m<sup>2</sup>)</b>
<b>FP-0</b>	0	0
<b>FP-360</b>	360	2.713
<b>FP-480</b>	480	3.617
<b>FP-600</b>	600	4.521
<b>FP-720</b>	720	5.426
<b>FP-960</b>	960	7.234

**Table 2.2** The average crystallite size of samples under different conditions.

<b>Sample</b>	<b>FP-0</b>	<b>FP-360</b>	<b>FP-480</b>	<b>FP-600</b>	<b>FP-720</b>	<b>FP-960</b>
<b>Average crystallite size L (nm)</b>	191	184	149	107	121	134



## **CHAPTER 3**

# **TURBULENT MICROMIXING INTENSIFICATION IN THE IMPINGING JET REACTOR ASSISTED BY ULTRASOUND IRRADIATION AND CHARACTERISATION BY VILLERMAUX-DUSHMAN REACTION**

### **SUMMARY**

In the previous chapter, hydrodynamics has been verified to have a significant impact on FePO<sub>4</sub> fine particle synthesis. The particle synthesis in the impinging jet reactor has been verified to be intensified in the previous Chapter and the mixing has been correlated with the turbulence indicator. Study of hydrodynamic mechanism would be further performed down to the molecular level with consideration of chemical reaction taking place in the impinging jet reactor (IJR). This Chapter focuses on characterisation of the micromixing occurring in the IJR with and without applying the ultrasound irradiation. The ultrasound irradiation assisted turbulent micromixing intensification in the impinging jet flow in a T-junction mixer has been realised by imposing a frequency of 20 kHz ultrasound generator with different input power amplitudes. The effect on micromixing enhancement by applying ultrasound irradiation is quantitatively characterised and analysed based on the segregation index using the Villermaux-Dushman reaction. Such turbulent micromixing intensification has been also studied using CFD modelling on various operating conditions such as the acid concentration in the Villermaux-Dushman reaction, turbulent Reynolds number and ultrasound irradiation power, and compared with the experimental measurements. It was found from both experiments and CFD simulation that the use of higher acid concentration of

Villermaux-Dushman reaction in the impinging jet flow can promote the conversion of side reactions and show a higher segregation index and poor mixing performance. The experimental results with the characterisation through Villermaux-Dushman reaction have clearly verified that the turbulent micromixing in the impinging jet flow T-junction reactor can be significantly improved by applying the ultrasound irradiation. In particular, when the ultrasound irradiation with an input power amplitude up to 70 % (840 W) was applied, it was found that the segregation index has been significantly reduced to 54.9%. CFD simulation also confirmed such turbulent micromixing intensification in the impinging jet flow reactor by applying ultrasound irradiation.

### 3.1 Introduction

Turbulent mixing is important in process engineering by affecting chemical reaction and thus dominating product properties (Schwertfirm *et al.*, 2007, Baldyga and Bourne., 1999). According to the mixing concept proposed by Baldyga and Bourne (1999), mixing can be classified into (i) macro mixing, (ii) meso-mixing and (iii) micromixing mixing. Among them, micromixing is also known as “molecular-level mixing” as the result of laminar stretching to striation, turbulent erosion and shrinking and molecular diffusion (Baldyga and Bourne, 1999, Villermaux and David, 1983). The segregation index  $X_s$  is used as an indicator to quantify the micromixing performance, ranging from 0 to 1, and the mixing time  $t_m$  is defined as the total time required to reduce the initial spatial segregation of the reactants until reaching a molecular contact. Segregation index  $X_s$  has been widely employed to estimate micromixing performance by adopting models such as the incorporation model (Fournier *et al.*, 1996a), interexchange with the mean model (Villermaux and Devillon, 1972), the engulfment deformation diffusion model and the engulfment model (Baldyga and Bourne, 1990) and droplet erosion and diffusion model (Ou and Ranz, 1983).

IJR is used as a fast-mixing unit operation in chemical process and its turbulent mixing performance has been investigated with higher demand in heat and mass transfer rates, effective process control and on-demand or on-site synthesis in fields of chemical, biological and pharmaceutical industries (Kumar *et al.*, 2011, Mills *et al.*, 2007, Rahimi *et al.*, 2014a). IJR consists of two opposing feeding streams leading to an impingement in a confined space, where the mixing is controlled by its geometry, inflow speed and flow field. The characteristic time scale of IJR is small and is capable to achieve rapid mixing (Kashid *et al.*, 2011). It allows chemical reaction taking place at the high specific surface area with enhanced heat and mass transfer rates due to the improved diffusion and convection inside the impingement chamber.

The mixing performance in the IJR is affected by factors such as flowrate (Nie *et al.*, 2018), reactor geometry (Kashid *et al.*, 2011) and external field (Akbari *et al.*, 2017). It can be further intensified by generating small-scale eddies via the adoption of an external field (Faryadi *et al.*, 2014). The ultrasound irradiation is a promising intensified technique, contributing to heat and mass transfer enhancement through turbulence intensification (Zhang *et al.*, 2021, Bulliard-Sauret *et al.*, 2019, Chen *et al.*, 2020). The ultrasound frequency has a significant influence on hydrodynamic phenomena. High-frequency ultrasound irradiation (100 kHz–1 MHz) is mainly responsible for convective acoustic streaming while low-frequency ultrasound irradiation (20 to 100 kHz) often induces major cavitation effect attributed to micro-jets, which are produced by strong shock waves due to cavitation bubble collapse (Bulliard-Sauret *et al.*, 2019). Furthermore, high-frequency ultrasound irradiation can also be applied to the field of image detection, medical scanning, velocity measurement and low-frequency ultrasound irradiation due to its considerable mechanical and chemical effects (Smirnov *et al.*, 2017, Karimi *et al.*, 2014). It has been widely reported that turbulence can be triggered and enhanced by the adoption of ultrasound irradiation (Nomura *et al.*, 2002, Bulliard-Sauret *et al.*, 2015). Bulliard-Sauret *et al.* (2015) and Nomura *et al.* (2002) have argued that the turbulence can be intensified by acoustic effect. Therefore, improved mixing, mass and heat transfer performance can be expected with the assist of ultrasound. Zhang *et al.* (2021) have proved that the overall volumetric mass transfer coefficient for the gas-liquid mass transfer process in microreactors can be enhanced

by 22 times at an ultrasound frequency of 20 kHz with power intensity of 0.14 W/mL. It has been highlighted by Bulliard-Sauret *et al.* (2017) that the heat transfer coefficient can be enhanced by induced acoustic streaming and other researchers have experimentally verified the heat transfer enhancement up to 27% (Kurbanov and Melkumov, 2003, Duan *et al.*, 2004, Yao *et al.*, 2010). Mass transfer coefficient  $K_{La}$  enhancement has been improved about 50–110% in a base solution of oxygen transfer into pure water assisted by an ultrasound horn. Furthermore, it was reported by Dange *et al.* (2015) that the maximum time for equilibrium conversion (91.64%) in process of esterification of butyric acid with methanol in an isothermal batch reactor can be decreased from 180 min to 120 min with the presence of ultrasound.

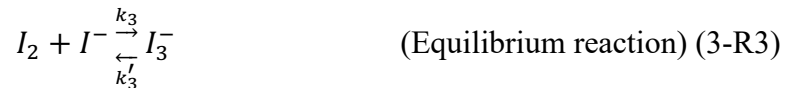
Although the micromixing for different types of reactors have been investigated and ultrasound is used as a technique to intensify the mixing process, rare works on modulation of ultrasound and validation by experimental performance have been reported. To demonstrate the hydrodynamics induced by ultrasound waves, the physical model of ultrasound wave propagation through numerical simulation have been proposed. The ultrasound effect was introduced in terms of sound pressure as a boundary condition based on Cai's model (Cai *et al.*, 2009) and it has been widely accepted and applied to CFD modelling on ultrasound (Sajjadi *et al.*, 2017, Rahimi *et al.*, 2014b, Abolhasani *et al.*, 2012). In the present study, the efficient mixing performance was characterized via Villermaux-Dushman reaction in IJR in the range of Reynolds number from 2070 to 4461 under the conditions with and without the assist of ultrasound. Ultrasound effects are expressed as pressure waves produced by the ultrasound transducer in the flow domain in the following discussion. Both experimental and numerical approaches are employed to investigate the ultrasound effects on the mixing behaviour of two inlet streams. The mixing time is correlated with segregation index  $X_s$  based on models including incorporation model, drop erosion and diffusion model (Ou and Ranz, 1983), and engulfment model (Palmer *et al.*, 1984). Among these approaches, the incorporation model is most widely used to estimate micromixing time  $t_m$ . Moreover, the effect of turbulence on micromixing performance has been captured below the Kolmogorov scale via simulation work (Zhang *et al.*, 2020a). The objective of the study in this chapter is to investigate the ultrasound effects on the mixing behaviour in the impinging jet reactor in both experimental and numerical

approaches. Further, the model of ultrasound wave propagation is validated and manipulated by the experimental results.

## 3.2 Experimental

### 3.2.1 Reaction descriptions

For better characterisation of the effect on turbulent micromixing intensification with or without applying ultrasound irradiation to the impinging jet flow for the synthesis of nano/microparticles, parallel competing reaction system, Villermaux Dushman reaction which has been widely used to evaluate the impact of operating parameters on micromixing performance (Faryadi *et al.*, 2014, Parvizian *et al.*, 2012), was adopted in the present study due to its simplicity and low cost. The Villermaux /Dushman reaction includes three-step reactions as follows,



The reaction rate in the above reaction (3-R1) is dependent on reactants concentration. Guichardon *et al.* (2000) have proposed the reaction rate equation for Dushman reactions at the room temperature of 298 K to be given by

$$r_1 = k_1[H^+][H_2BO_3^-] \quad (3-1)$$

with  $k_1 = 10^{11} \text{ l mol}^{-1}\text{s}^{-1}$ . The rate constant  $k_2$  in step (3-R2) depends on the ionic strength  $I$  that changes during the micromixing process (Rahimi *et al.*, 2014a, Guichardon and Falk, 2000), which can be described by

$$r_2 = k_2[H^+]^2[I^-]^2[IO_3^-] \quad (3-2)$$

If  $I \leq 0.166 \text{ M}$ ,

$$\log_{10}k_2 = 9.28 - 3.66\sqrt{I} \quad (3-3)$$

If  $I > 0.166 \text{ M}$ ,

$$\log_{10}k_2 = 8.38 - 1.51\sqrt{I} + 0.23I \quad (3-4)$$

The ionic strength  $I$  is calculated by following equations,

$$I = \sum_{i=1}^n c_i z_i^2 \quad (3-5)$$

where  $c_i$  is the ion concentration in the solution and  $z_i$  is the charge of the ion,  $z$ , to the power of 2. For reaction rate of reaction (3-R3), one has

$$r_3 = r_3^+ - r_3^- = k_3^+[I^-][I_2] - k_3^-[I_3^-] \quad (3-6)$$

with  $k_3^+ = 5.9 \times 10^9 \text{ l mol}^{-1}\text{s}^{-1}$  and  $k_3^- = 7.5 \times 10^6 \text{ s}^{-1}$ .

In order to explicitly quantify the micromixing quality, segregation index  $X_S$  was employed as an indicator, whose value lies between 0 and 1. Perfect mixing occurs only

when  $X_S = 0$  and total segregation takes place when  $X_S = 1$ .  $X_S$  is defined as follows (Guichardon and Falk, 2000, Fournier *et al.*, 1996a, Guichardon *et al.*, 2000),

$$X_S = \frac{Y}{Y_S} \quad (3-7)$$

where  $Y$  is defined as the mole ratio of proton consumed by reaction (3-R2) to the total moles of acid fed in the case of complete segregation,  $Y_S$  denotes the value of mole ratio of the  $Y$  in the poor mixing condition. Both  $Y$  and  $Y_S$  can be calculated by the following relations,

$$Y = \frac{2(n_{I_2} + n_{I_3^-})}{n_{H^+}} = \frac{2(Q_1 + Q_2)([I_2] + [I_3^-])}{Q_2[H^+]_0} = 2(1 + R) \frac{([I_2] + [I_3^-])}{[H^+]_0} \quad (3-8)$$

and

$$Y_S = \frac{6n_{IO_3^-}}{6n_{IO_3^-} + n_{H_2BO_3^-}} = \frac{6[IO_3^-]_0}{6[IO_3^-]_0 + [H_2BO_3^-]_0} \quad (3-9)$$

where  $[H^+]_0$ ,  $[IO_3^-]_0$  and  $[H_2BO_3^-]$  represents the initial concentration at inlets.  $R$  is the flowrate ratio of  $Q_1$  and  $Q_2$ . Accordingly,  $X_S$  can be written as follows,

$$X_S = \frac{Y}{Y_S} = \frac{(1+R)([I_2] + [I_3^-])}{[H^+]_0} \left( 2 + \frac{1}{3} \frac{[H_2BO_3^-]_0}{[IO_3^-]_0} \right) \quad (3-10)$$

where  $R$  is the specific flowrate ratio of inlet streams for IJR. The concentration of  $[I_3^-]$  can be estimated from the absorbance test and the iodine concentration is determined via material balance equation as follows,

$$[I^-] = [I^-]_0 - \frac{5}{3}([I_3^-] + [I_2]) - [I_3^-] \quad (3-11)$$

In addition, the equilibrium constant for reaction (3-R3) is calculated by the following equation:

$$K_{eq} = \frac{[I_3^-]}{[I_2][I^-]} \quad (3-12)$$

The equilibrium constant,  $K_{eq}$ , depends on temperature  $T$ , which can be estimated using the following relationship:

$$\log_{10}K_{eq} = \frac{555}{T} + 7.355 - 2.575\log_{10}T \quad (3-13)$$

Combing Equation (3-12) and (3-13), it reads,

$$-\frac{5}{3}[I_2]^2 + \left([I^-]_0 - \frac{8}{3}[I_3^-]\right)[I_2] - \frac{[I_3^-]}{K_{eq}} = 0 \quad (3-14)$$

### 3.2.2 Calibration curve of UV spectrophotometer

The concentration of  $I_3^-$  served as an indicator of micromixing performance was measured by a UV spectrophotometer at a wavelength of 353 nm. To ensure the calibration to have high accuracy, the calibration curve was predetermined on basis of the Beer-Lambert equation for  $[I_3^-] < 10^{-3}$  and the selected acid concentration was required to ensure the produced concentration of  $[I_3^-]$  in a range of linear correlation with absorbance. The correlation between the concentration of  $I_3^-$  and absorbance gives (Guichardon *et al.*, 2000),

$$[I_3^-] = \frac{A_{353}}{\epsilon_{353}L} \quad (3-15)$$

where  $[I_3^-]$  is the concentration of  $I_3^-$ ,  $\epsilon_{353}$  is the molar extinction coefficient,  $A$  is the absorbance of the solution; and  $L$  is the thickness of the quartz cell (0.01 m). The

calibration curve is obtained by evaluating the light absorption at various concentration of  $I_3^-$  as shown in Figure 3.1.

### 3.2.3 Experimental setup and product characterisation

Solution A which is composed of  $H_3BO_3$  solution was mixed with KI and  $KIO_3$  solutions together. NaOH was added to KI and  $KIO_3$  solution in advance as a buffer solution (Guichardon and Falk, 2000, Guichardon *et al.*, 2000). The concentration of the reactants is as described in Table 3.1. Solution B was prepared by diluting the sulfuric acid with the concentration of 0.01, 0.02, 0.05 M. All reactants were purchased from Sinopharm Chemical Reagent Co., Ltd.

The experimental setup in this work is shown in Figure 3.2. The IJR was mounted with an ultrasound transducer (20kHz, UH1200-T, Shanghai Ouhor Co., Ltd. China) with the sensor tip being pointing downwards to allow the ultrasound wave to propagate against the upflow in the part of the expansion chamber of the outlet of the impinging jet flow reactor. The ultrasonic horn with a diameter of 13 mm was inserted inside the chamber. The Villiermaux-Dushman reaction was taking place in the IJR by pumping solution A (composed of  $H_3BO_3$ , NaOH, KI and  $KIO_3$ ) and B (dilute sulfuric acid) from the two inlets of the impinging jet flow reactor at the selected flow rate ratios as shown in Table 3.2. The concentration of the indicator ion  $I_3^-$  was measured via UV spectrophotometer (UNICO SQ4802 UV/VIS Spectrophotometer, U.S.A) at the wavelength of 353 nm to ensure its stability. Both the experiments and the sample measurement were conducted at the room temperature of 25 °C by varying the acid concentration, and inlet velocities with the given flow rate ratios ( $R = 1\sim 10$ ) as listed in Table 3.2. For each absorption intensity test, 3 mL sample solution was collected for UV test from the outlet of the reactor. It should be mentioned that the given flow rate ratio  $R$ , defined as the ratio of the flowrate  $Q_1$  of the main solution A (KI,  $KIO_3$ , NaOH and  $H_3BO_3$ ) to the flowrate  $Q_2$  of solution B (diluted acid), covers a range of the

Reynolds number  $Re$  based on the inlet guide tube of the reactor  $Re = \rho u d_i / \mu$  from 2070 to 4461 while different nominal ultrasound input powers (0 W~ 840 W) was applied.

### 3.3 Numerical Modelling

#### 3.3.1 Governing equations

In this study, a set of conservation equations of continuity, momentum and species transport were employed to model the solution flow motion and the mixing of the impinging jet flow. Also, the energy equation was considered as the temperature change has an impact on chemical kinetics of reaction (3-R2) as described by Equations (3-21) and (3-22). The turbulence in the reactor was modelled by the standard k- $\epsilon$  viscous model due to its successful applications in similar cases (Liu *et al.*, 2014, Liu and Fox, 2006, Woo *et al.*, 2009). Notice that the turbulent dissipation rate in the T-junction impinging jet flow has a significant impact on the local shear and micromixing (Chen *et al.*, 2020). The pressure boundary conditions are applied to the ultrasound probe modulating the ultrasound wave propagation as elucidated in section 3.4.2.

#### Continuity, Momentum and Species transport equations

*Continuity equation:*

$$\frac{\partial}{\partial t}(\rho) + \nabla \cdot (\rho \mathbf{u}) = 0 \quad (3-16)$$

*Momentum equation:*

$$\frac{\partial}{\partial t}(\rho \mathbf{u}) + \nabla \cdot (\rho \mathbf{u} \mathbf{u}) = -\nabla p + \nabla \cdot \mu_{eff} \left( (\nabla \mathbf{u} + (\nabla \mathbf{u})^T) - \frac{2}{3} (\nabla \cdot \mathbf{u}) \mathbf{I} \right) + \rho \mathbf{g} + S_{ultram} \quad (3-17)$$

*Species transport equation:*

$$\frac{\partial}{\partial t}(\rho Y_i) + \nabla \cdot (\rho \mathbf{u} Y_i) = -\nabla \cdot (\mathbf{J}_i) + R_i \quad (3-18)$$

where  $\rho$ ,  $\mathbf{u}$ ,  $\mathbf{g}$  and  $p$  denote the density, instantaneous velocity vector gravitational acceleration and pressure respectively.  $Y_i$ ,  $J_i$  and  $R_i$  are the mass fraction of species  $i$ , the diffusive mass flux and net rate of production of species  $i$  due to chemical reaction, respectively. Effective viscosity  $\mu_{eff}$  can be expressed as the sum of molecular viscosity and turbulent eddy viscosity, i.e.  $\mu_{eff} = \mu + \mu_T$ . Concentration of individual species was determined using the species transport equation. A simplification on reaction  $R_i$  for the Villiermaux-Dushman reaction has been made to predict the micromixing by using the concentration of  $I_2$  instead of  $I_3^-$ , which may be better to represent the actual segregation conditions. Considering the temperature can influence the kinetic rate constant  $k_2$ , Equations (3-3) and (3-4) were modified following the suggestions (Guichardon and Falk, 2000) (Fournier *et al.*, 1996b), which read

$$\log_{10} k_2 = 9.28 - 3.66\sqrt{I}T^\beta \quad \text{for } I \leq 0.166 \text{ M} \quad (3-19)$$

$$\log_{10} k_2 = 8.38 - 1.51\sqrt{I} + 0.23IT^\beta \quad \text{for } I > 0.166 \text{ M} \quad (3-20)$$

where  $I$  is the ionic strength and  $\beta$  is the temperature exponent.

### 3.3.2 Turbulence modelling

The standard  $k$ - $\varepsilon$  turbulence model was used in CFD simulations as given by Equations (3-21) and (3-22) while turbulent eddy viscosity  $\mu_t$  was estimated using the local turbulence kinetic energy  $k$  and the corresponding turbulent energy dissipation rate  $\varepsilon$  defined by Equation (3-27).

$$\frac{\partial}{\partial t}(\rho k) + \nabla \cdot (\rho u k) = \nabla \cdot \left( \frac{\mu_t}{\sigma_k} \nabla k \right) + G_k - \rho g \varepsilon + S_{ultrak} \quad (3-21)$$

$$\frac{\partial}{\partial t}(\rho \varepsilon) + \nabla \cdot (\rho u \varepsilon) = \nabla \cdot \left( \frac{\mu_t}{\sigma_\varepsilon} \nabla \varepsilon \right) + \frac{\varepsilon}{k} (C_1 G_k - C_2 \rho \varepsilon) + S_{ultrad} \quad (3-22)$$

$$G_k = \mu_t (\nabla u + (\nabla u)^T) \nabla u \quad (3-23)$$

$$\mu_t = \frac{C_\mu \rho k^2}{\varepsilon} \quad (3-24)$$

where  $G_k$  represents the generation of turbulent kinetic energy due to the turbulent shear. With the caution, the coefficients in Equations (3-21) to (3-24) were still to adopt the widely used values, i.e.  $C_\mu = 0.09$ ,  $C_{1\varepsilon} = 1.44$ ,  $G_{2\varepsilon} = 1.92$ ,  $\sigma_k = 1.0$  and  $\sigma_\varepsilon = 1.0$ .

### 3.3.3 Modelling of ultrasound effect on boundary condition

Following the previous studies (Cai *et al.*, 2009, Sajjadi *et al.*, 2017, Rahimi *et al.*, 2014b, Abolhasani *et al.*, 2012), the perturbation to the turbulent shear flow in the impinging jet flow as the result of applying the ultrasound irradiation which causes the pressure changes in the field can be expressed as:

$$P_{ultra} = P_a \cos(\omega(t + y/c)) \quad (3-25)$$

where  $\omega$ ,  $t$ ,  $y$  and  $c$  denote the angular frequency, elapsed time, distance between the location and tip of the ultrasound transducer but measured in vertical direction and local sound speed in the solution, respectively. The amplitude of the ultrasound pressure  $P_a$  can be estimated by

$$P_a = \sqrt{2I_{us}\rho c} \quad (3-26)$$

where  $I_{us}$  represents the ultrasound intensity which can be estimated by  $P_{us}/A$ , where  $P_{us}$  is the ultrasound power while  $A$  is the area of tip of the ultrasonic transducer.

### 3.3.4 Numerical Simulation

In the present work, 3D CFD numerical simulations were conducted using the commercial code-FLUENT 18.0. The geometry and computational domain are schematically shown in Figure 3.3. The computation domain contains a T-junction impinging jet flow reaction chamber and a sudden expansion chamber where the ultrasonic transducer can be inserted and just mounted downstream of the sudden expansion. The domain also includes two circular tube inlets of diameter 3 mm and the outlet of diameter 8 mm. The ultrasound transducer with diameter of 13 mm generates ultrasound wave, propagating from the tip of ultrasound. The mesh shown in Figure 3.3 was generated by using ANSYS ICEM to achieve the feature that the grids are orthogonally formed. Trial simulations were conducted and the mesh with 109800 cells can provide the mesh independent results. Further refinement of the mesh does not bring out any noticeable changes in the time-averaged concentration distributions in the IJR. Consequently, all the simulations were conducted using such mesh setup. In the simulations, the pressure-velocity coupling was realised by SIMPLE algorithm with the second-order upwind discretisation scheme. The mixing occurring in the core of the confined chamber of the T-junction impinge jet flow reactor is highly turbulent, judged by the calculated Reynolds number at the reactor inlet. Velocity inlet boundary condition was imposed for both impinging jet inlets while the pressure outlet boundary condition was specified for the outlet of the IJR where the synthesised product was collected. The tip of the ultrasonic transducer was set as a pressure inlet. No-slip boundary condition was applied to all the walls. Numerical simulations were performed with and without applying ultrasound irradiation. For cases of applying ultrasound

irradiation, different amplitudes of input powers were imposed with a fixed ultrasound frequency of 20 kHz. The CFD simulations were treated as being converged when the normalized residuals of all the variables are smaller than  $1 \times 10^{-5}$  and the time step adopted in the simulation is  $1.0 \times 10^{-6}$  s so as to capture the ultrasound wave fluctuation and satisfy the requirement that the time step should be smaller than a period of the ultrasound wave.

### 3.4 Results and discussion

#### 3.4.1 Effect of $H^+$ concentration on micromixing performance in the IJR

Micromixing performance in the T-junction impinging jet flow reactor is characterised by Villermaux-Dushman reaction and the appropriate range of acid should be selected so as to ensure the proper amount of  $I_3^-$  generated for test. The experiments were conducted under the different acid concentrations of 0.02 M, 0.04 M, 0.1 M with the same flowrate of 6.43 mL/s for both inlet streams with an estimated inlet Reynolds number of 2714. The total acid concentration should be lower than the stoichiometric amount in reactions (3-R1) and (3-R2) to guarantee the acid being totally consumed. To investigate the effect of acid concentration, acid solution of different concentration (0.02 M, 0.04 M, 1 M) was used to react with the iodide-iodate solution as displayed in Table 3.2 (Sample 21-23). The experimental results have shown that the segregation index  $X_s$  increases as the acid concentration increases (see Figure 3.4 (a)) and the corresponding segregation index  $X_s$  under acid concentration of 0.02 M, 0.04 M, 0.1 M are  $X_s = 0.04$ ,  $X_s = 0.09$ , and  $X_s = 0.12$ , respectively. The acid concentration was also changed by changing the volume flowrate ratio  $R$  ( $R = Q_1/Q_2$ ), varying within the range from 0.13 m/s to 1.25 m/s.  $Q_1$  is the flowrate of mixed solution A composed of KI,  $KIO_3$ , NaOH and  $H_3BO_3$  and  $Q_2$  is the flowrate of acid solution B. As the volume ratio increases by increasing the mixed solution A, the acid solution will be definitely diluted and this can be seen from the estimation of the concentration of acid, defined by

$$C_2 = \frac{n_2}{V_2} = \frac{C_H \times Q_2}{Q_1 + Q_2} = \frac{C_H}{1+R} \quad (3-27)$$

where  $C_H$  is the initial acid concentration and  $R$  is the volume flowrate ratio.

Figure 3.4 (b) has clearly shown a remarkable reduction of segregation index caused by dilution of acid solution owing to increasing the flowrate ratio. As the flowrate ratio increases from 1 to 10, the segregation index gradually drops from 0.105 to 0.017. The experiments have clearly indicated that at lower concentration of acid  $C_H$ , micromixing in the core of the impinging jet flow reactor becomes intensified with increase of the flowrate ratio but this will bring out more  $H^+$  engulfed by turbulent eddies to create the locally enhanced acidic environment. Consequently, this may favour the occurrence of reaction (3-R2), thus delivering undesirable products. As the reaction rate of reaction (3-R2) is twice as high as that of reaction (3-R1) in terms of acid concentration as shown in Equations (3-1) and (3-2), the production of  $I_2$  and therefore  $I_3^-$  is more sensitive to acid concentration. With increasing in the concentration of acid introduced by  $Q_2$ , more  $I_3^-$  may be trapped by smaller turbulent eddies. In contrast, a reduction in the acid concentration reduces the overall reaction due to Reaction (3-R2), thus having a lower segregation index as the micromixing occurring in the eddies can achieve a better engulfment so that the mass transfer between the solution slabs engulfed is much improved. Based on this consideration and the measurement capability and accuracy of the UV spectrophotometry approach, the acid concentration of 0.04 M was found to be suitable for characterisation of the micromixing in all the other experiments.

### 3.4.2 Effect of local turbulence on mixing performance in the IJR

As defined in Equation (3-16), the calculated Reynolds number  $Re$  based on the inlet diameter  $d_i$  covers the range from 2070 to 4461, which is safe to be considered as a

turbulent flow. The distribution of turbulent kinetic energy in the intersecting surfaces downstream of the impingement region is displayed in Figure 3.5. As marked in Figure 3.5, the impinging stagnant point is centrally located since the flowrates of two impinging jets are equal and constant. It is obvious that the turbulent kinetic energy is intensified as Reynold number  $Re$  increases. The intensified turbulence is caused by the violent collision and engulfment effect at the impingement zone caused by strengthened impulse due to the increased inlet flowrate. Figure 3.6 shows the volumetric-averaged turbulent kinetic energy  $\langle k \rangle$  versus different Reynolds numbers  $Re$ . At low Reynolds number  $Re=2070$ , the volumetric-averaged turbulent kinetic energy  $\langle k \rangle$  is  $0.018 \text{ m}^2/\text{s}^2$  while this has been increased more than four times as Reynolds number  $Re$  increases to 4461. The Kolmogorov length  $\eta$  as defined in Equation (3-28) is calculated in the range of  $1.49 \times 10^{-5} \text{ m}$  to  $2.67 \times 10^{-5} \text{ m}$  (Pope, 2000) for the impinging jet flows in the present study:

$$\eta = \left( \frac{\nu^3}{\langle \varepsilon \rangle} \right)^{1/4} \quad (3-28)$$

where  $\nu$  is the specific molecular viscosity of the liquid phase and  $\langle \varepsilon \rangle$  is the volumetric-averaged turbulent energy dissipation, obtained from CFD simulation. To further discuss the impact of local turbulence level on mixing performance in the IJR, turbulent Reynolds number  $Re_T$  estimated from CFD simulation, defined by equation (3-29), was introduced.

$$Re_T = \frac{\langle k \rangle}{(\langle \varepsilon \rangle \nu)^{1/2}} \quad (3-29)$$

where  $\langle k \rangle$  and  $\langle \varepsilon \rangle$  are the volumetric-averaged turbulent kinetic energy and turbulent energy dissipation rate, respectively.

The calculated turbulent Reynolds number  $Re_T$  versus the inlet Reynolds number  $Re$  is also shown in Figure 3.6, revealing that  $Re_T$  increases from 12.6 to 17.4 as  $Re$  increases from 2070 to 4461. Their correlation can be fitted by the relationship of  $Re_T = 0.53 Re^{0.42}$ .

It can be seen from the relationship that a monotonous rise in the curve demonstrates that the turbulence is intensified when Reynolds number increases. The intensified turbulence has a positive effect on micromixing. Figure 3.7 displays both the experimental and simulated results of segregation index  $X_s$  versus turbulent Reynolds number  $Re_T$  under the conditions of inactive ultrasound irradiation (0 W) and active ultrasound power of 600W for a given constant flowrate ratio. As expected, there is a descending trend of segregation index  $X_s$  as the turbulent Reynolds number  $Re_T$  increases. It can be found from experimental results that the segregation index  $X_s$  gradually drops from 0.105 to 0.076 while the  $Re_T$  increases from 12.6 to 15.3. With continuous increases of  $Re_T$  from 15.3 to 17.4, the corresponding  $X_s$  slowly reduces to 0.07. The modelling results have shown a good agreement with the experimental results, however, the segregation indices obtained from the simulation results are nearly 10% lower than the experimental ones. The difference between the segregation index obtained from the experiments and the simulations may be attributed to the simplifications introduced in the model to describe the micromixing in CFD modelling. To be specific, finite-rate model was employed in this case, which means the turbulence-chemistry interaction is merely affected by the hydrodynamics and ion strength inside the impinging jet reaction as described in Equations (3-19) and (3-20). It is worth noting that the ignorance of Reaction (3-R3) in the simulations may result in a significant deviation of the segregation index. Although the segregation index is calculated from the concentration of  $I_2$  rather than  $I_3^-$  for simplification, Reaction (3-R3) is an equilibrium reaction with fixed conversion once equilibrium state is achieved. Consequently, the simplification of reaction steps in CFD modelling would not make a great difference on simulation results.

### 3.4.3 Effect of ultrasound amplitude on mixing performance in the IJR

In order to investigate the effect of ultrasound irradiation on mixing performance, an indicator defining maximum capability of ultrasound irradiation, ultrasound amplitude  $P_a$  is expressed as follows:

$$P_a = \frac{P}{P_s} \times 100 \% \quad (3-30)$$

where  $P_s$  is the maximum ultrasound power applied (1200W). Both experiment and simulation works have quantitatively measured the micromixing efficiency. Imposing ultrasound wave propagation in CFD modelling was realised in terms of pressure profile as expressed in Equations (3-25) and (3-26). The experiments were carried out by comparing the segregation index  $X_s$  under different turbulent Reynolds numbers at ultrasound amplitude ( $P_a = 50\%$ ) with constant acid concentration and flowrate ratio in the IJR. As shown in Figure 3.7, the segregation index  $X_s$  calculated from the experiment with activated ultrasound amplitude of  $P_a = 50\%$  is smaller than  $X_s$  without assist of ultrasound. The simulation results of  $X_s$  are in good agreement with the experiment results, especially at  $Re_T = 13.3$  and  $Re_T = 17.6$ . Further work is to explore the ultrasound effect at constant turbulent Reynolds number by adopting different ultrasound amplitudes from 30% to 70%. The relationship of segregation index  $X_s$  against ultrasound amplitude  $P_a$  is shown in Figure 3.8. Generally, the segregation index calculated from experiments decreases with intensified ultrasound, where the simulation results display a similar trend. From the experimental data shown in Figure 3.8, the segregation index  $X_s$  is found to be around 0.096 and it then decreases to 0.081 when exposed ultrasound amplitude increases from 30% to 40%. Its further enhancement to 70% leads to the segregation index  $X_s$  decreasing to

0.041. While the simulation results show some deviation from experimental results. That may be caused by the local turbulent effect generated by small eddies being challengeable to be captured by the current applied model.

Such enhanced micromixing performance due to ultrasound irradiation might be attributed to local turbulence intensification caused by acoustic streaming from ultrasound wave propagation. It is recognised that the acoustic streaming is an intrinsic feature, which is strongly dependent on the ultrasound frequency (Bulliard-Sauret *et al.*, 2019). In this study, ultrasound transducer with frequency of 20 kHz was employed. The acoustic streaming is generated and intensified in the process of collision of two opposite inlet streams in IJR's assisted by ultrasound. Also, engulfment of fluid elements takes place and then triggers perturbation. Figure 3.9 displays the contour of velocity magnitude and streamlines under the ultrasound amplitude of 0%, 30%, 60% downstream of the impinging region where the acoustic streaming has notably affected the flow pattern. As shown in Figure 3.9 (a), the adoption of ultrasound significantly changes the flow pattern as well as velocity distribution. In the case without applying the ultrasound irradiation, the symmetric vortex rings are generated in the vicinity of the ultrasound horn because the jet flows exit the impingement region and are pulsed to the tip of ultrasound in the normal direction. When the ultrasound irradiation applied with an amplitude of 60 %, such annular vortex rings start to lose the original symmetry, deforming and twisting. Such acoustic streaming significantly affects the flow in the expanded chamber. As a result of the ultrasound irradiation, once the ultrasound amplitude is amplified to up to 60%, regular patterns of large vortices evolve into totally turbulent but are still affected by the periodical fluctuation of acoustic wave. In this way, the local turbulent kinetic energy is greatly enhanced. The small-scale eddies are generated due to the periodical fluctuation of acoustic wave. In order to explore such ultrasound-induced fluctuation on micromixing, the volumetric-averaged fluctuation degree  $\alpha(t)$  as a function of time at downstream of impingement region is introduced, defined as follows (Zhang *et al.*, 2019),

$$\alpha(t) = \frac{\overline{C'(t)}}{\overline{C'}} \quad (3-31)$$

where  $C'(t)$  is the volumetric average standard deviation of concentration and  $\overline{C'}$  is time average of  $C'(t)$ . It is thus possible to calculate the mixing degree by time averaging as follows,

$$\theta = \frac{1}{T} \int_0^T \sqrt{(1 - \alpha(t))^2} dt \quad (3-32)$$

As can be seen from Figure 3.10, the volume-averaged concentration of I<sub>2</sub> dramatically increases and then tends to be almost unchanged when the reaction proceeds for 2 seconds, signifying that the reaction has reached an equilibrium state. It takes shorter time once ultrasound irradiation is applied (<1.5 s). Thus, it is reasonable to take samples after 2 seconds to ensure the accuracy and effectiveness of calculation of segregation index. The micromixing degree could be calculated from Equation (3-32). It was found that the ultrasound irradiation can cause the fluctuation on the concentration of produced iodine. Notice that the mixing degree is 0.016 when there is no ultrasound pulse. With the ultrasound amplitude of 30 %, 50 % and 70 %, the corresponding mixing degree  $\theta$  calculated are 0.090, 0.096 and 0.131, respectively. This again affirms the finding that the ultrasound wave propagation with a higher amplitude can trigger micromixing to take place in turbulent eddies at an environment with small concentration fluctuations.

To quantify the existence of turbulent vortex rings and the likely effect on micromixing, the time-averaged vorticity  $\Omega = \nabla \times \mathbf{u}$  was also employed to describe the turbulence induced shear coupled with micromixing (Liu and Li, 2018). A correlation of between vorticity  $\Omega$  and mixing degree  $\theta$  was proposed to quantitatively describe the turbulence effect on micromixing performance, defined by

$$R_{\theta,\Omega} = \frac{\overline{\theta_j \langle \Omega \rangle_j}}{\theta_{\text{ref}} \langle \Omega \rangle_{\text{ref}}} \quad (3-33)$$

where  $\langle \Omega \rangle_j$  is the volume average vorticity, subscript  $j$  denotes different conditions.

Figure 3.11 displays the correlation factor  $R_{\theta,\Omega}$  versus the ultrasound amplitude  $P_a$  and iso-surface of vorticity magnitude distribution ( $50 \text{ s}^{-1}$ ,  $500 \text{ s}^{-1}$ ,  $1000 \text{ s}^{-1}$  and  $2000 \text{ s}^{-1}$ ) in the impinging jet reactor at flow time  $t = 2.0 \text{ s}$  from simulation. The correlation factor  $R_{\theta,\Omega} = 1$  for case without ultrasound as the reference point. As can be seen from the figure, the vorticity  $\Omega$  and mixing degree  $\theta$  of concentration is highly correlated. The correlation factor  $R_{\theta,\Omega}$  dramatically increases to thousands-fold compared with the reference value, once the ultrasound irradiation is applied. To be specific, when ultrasound amplitude increases to 70 % (840 W), the correlation factor  $R_{\theta,\Omega}$  increases to 7167. This indicates that high level of vorticity which greatly contributes to shear turbulence intensification, thus enhancing micromixing in the T-junction IJR as more small turbulence eddies will be generated. In addition, the distribution of vorticity is also shown in Figure 3.11. High vorticity level ( $\Omega = 2000 \text{ s}^{-1}$ ) is achieved especially in vicinity of the tip of ultrasound horn as acoustic streaming is periodically fluctuated. The effect of ultrasound irradiation intensification on the pressure change results can also bring out the changes in the vorticity, consequently reinforcing the micromixing.

#### 3.4.4 The mixing time scale in the T-junction IJR

The turbulent mixing performance estimated by the segregation index and the corresponding timescales are discussed in this section. The micromixing time can be estimated based on the incorporation model developed by Villiermaux and his co-authors (Villiermaux *et al.*, 1992, Villiermaux, 1990), assuming that the inlet stream ( $H^+$ ) is composed of several aggregates with initial volume  $V_{H_0}$  which is immediately

invaded by the surrounding substance containing iodide and iodate from the other stream. An aggregate involves the complete occurrence of micromixing with chemical reaction taking place. Therefore, the characteristic incorporation time equates the micromixing time (Rahimi *et al.*, 2014a). As the initial volume  $V_{H_0}$  grows with the growth rate  $g(t)$ , the new volume is calculated as follows (Kashid *et al.*, 2011),

$$V_H = V_{H_0}g(t) \quad (3-34)$$

The growth rate is as a function of micromixing time  $t_m$ ,

$$g(t) = 1 + \frac{t}{t_m} \quad (3-35)$$

and

$$g(t) = \exp\left(\frac{t}{t_m}\right) \quad (3-36)$$

Ultimately, the concentration change rate is presented as follows (Kashid *et al.*, 2011),

$$\frac{dC_j}{dt} = (C_{j,s} - C_j)\frac{1}{g}\frac{dg}{dt} + r_j \quad (3-37)$$

where  $C_{j,s}$  is the surrounding fluid concentration of the acid solution and  $r_j$  is the total generation rate of the product  $j$  in the reaction. Linear growth rate function is assumed for this reaction and the Runge-Kutta method is used to solve conservation equations of component concentration by adopting the nomenclature for conciseness as outlined in appendix (Rahimi *et al.*, 2014a).

Figure 3.12 (a) shows the estimation results between the relevant micromixing mixing time  $\frac{t_m}{t_{Ref}}$  and  $X_s$  derived from the incorporation model based on the experimental conditions. The reference mixing time  $t_{Ref}$  refers to the micromixing time of cases

without ultrasound. The applicable range of micromixing time  $t_m$  is in the range of 0.05 to 0.1 ms, where the results are fitted using a power, given by

$$\frac{t_m}{t_{Ref}} = 10.45X_s^{1.0506} \quad (3-38)$$

Based on the above relationship, the results are plotted in Figure 3.12 (b) for different Reynolds number and ultrasound power. As indicated, the micromixing performance is poorest when the ultrasound transducer is not activated at turbulent Reynolds number  $Re_T = 12.7$  with micromixing time of  $1.80 \times 10^{-4}$  s. Compared with the condition without ultrasound irradiation, the micromixing time is reduced by 9.4 % once adopting an ultrasound amplitude of 50 % (600 W). The micromixing time dramatically reduces to  $6.74 \times 10^{-5}$  s once the intensification of ultrasound power is further increased to 70% (840 W). Consequently, a conclusion is drawn that the adoption of ultrasound considerably improves micromixing performance up to 62.5% and the micromixing can be enhanced by shear turbulence intensification.

In order to achieve high selectivity in the fast reaction system, micromixing is expected to enhance the performance and subsequently the micromixing time  $t_m$  is required to be smaller than the reaction time ( $t_r$ ) (Zhang *et al.*, 2020b). The characteristic reaction time  $t_r$  is dependent on the intrinsic kinetics and consequently the rate of reaction. Since the reaction rate for reaction (3-R1) is constant, the rate of reaction is determined by  $k_2$  which depends on the ionic strength involved in chemical reaction as described in Equations (3-3) and (3-4). The characteristic reaction time  $t_r$  is then defined according to follows (Zhang *et al.*, 2020b),

$$t_r = \frac{\text{Min} \left( \frac{3}{5}[I^-]_0, 3[IO_3^-]_0, \frac{1}{2}[H^+]_0 \right)}{(r_2)_{t=0}} \quad (3-39)$$

where  $(r_2)_{t=0}$  is the reaction rate for reaction (3-R2) when  $t=0$ . For convenience, a dimensionless Damköhler number  $Da$  is introduced to characterise the significance of micromixing on the chemical reaction, defined as the ratio of the micromixing time scale (typical turbulent eddy time scale) to the chemical reaction time scale, expressed as

$$Da = \frac{t_m}{t_r} \quad (3-40)$$

The reaction rate  $(r_2)_{t=0}$  is a constant at  $t=0$  and it is equal to  $0.017 \text{ mol}\cdot\text{L}^{-1}\text{s}^{-1}$ . Based on Equation (3-40), the estimated Damköhler number  $Da$  for all conditions is in range of  $5.74 \times 10^{-5}$  s to  $1.53 \times 10^{-4}$  s, was found to be smaller than 1. This may indicate that Reaction (3-R2) is affected by micromixing occurring in the turbulent eddies as the micromixing time  $t_m$  is much smaller than  $t_r$ . It is thus concluded that the value of the Damköhler number  $Da$  can indicate the appropriateness of the use of Villiermaux-Dushman reaction to characterise micromixing performance in the T-junction impinging jet flow reactor.

### 3.5 Conclusions

In the present work, the micromixing performance in the impinging jet flow T-junction reactor with or without application of the ultrasound irradiation is characterised by means of a parallel competing reaction as described by the Villiermaux-Dushman reaction system. Both experimental validation and CFD simulations have been carried out to further reveal the effect of shear turbulence intensification on the micromixing occurring in the impinging jet T-junction reactor by applying ultrasound irradiation. The micromixing performance can be well quantitatively indicated by the segregation index  $X_s$  and the local time-dependent fluctuation degree  $\alpha$ . The experiments with the Villiermaux-Dushman reaction were performed based on the conditions that different

acid concentrations ( $H^+$ ) and various turbulent Reynolds numbers together with the adoption of different ultrasound irradiation input power amplitudes were applied. The results drawn from this study can be summarised as follows:

- (1) Turbulent micromixing intensification can be realised by increasing the impinging jet flow reactor inlet flow rate, corresponding to an increase in the turbulent Reynolds number ( $Re_T$ ). Such micromixing intensification as the result of local shear turbulence intensification can be attributed to the stronger eddy engulfment effect due to the mixing occurring in the turbulent eddies that have the sizes down to the Kolmogorov scale. As an example, it was found that as the turbulent Reynolds number  $Re_T$  increases from 12.7 to 17.4, the corresponding segregation index  $X_s$  obtained from the Villermaux-Dushman reaction experiments has reduced from 0.105 to 0.07, clearly indicating an improved micromixing being achieved. CFD simulation results were also in a good agreement with the experiment results, with a difference smaller than 10%.
  
- (2) The adoption of ultrasound irradiation has a significant favourable influence on micromixing performance. The implement of the ultrasound irradiation effect into CFD modelling has been realised by applying the pressure inlet boundary condition. CFD simulation results indicate that the turbulent eddy engulfment is enhanced with the application of ultrasound irradiation. When increasing the ultrasound amplitude, shear vortex rings in the chamber where the ultrasound transducer is inserted are deformed, twisted and small turbulent eddies are generated as the result of acoustic streaming. The segregation index decreases as ultrasound amplitude increases. In addition, the corresponding mixing degree  $\theta$  in terms of  $I_2$  concentration in the IJR is found to be enhanced from 0.016 to 0.131 as ultrasound amplitude increases from 0 % to 70 %. Correlation between the vorticity  $\Omega$  and mixing degree  $\theta$  has been proposed, which shows that the correlation coefficient dramatically increases with enhanced ultrasound

amplitude. A high level of vorticity greatly contributes to shear turbulence intensification, thus giving rise to a better micromixing due to the improved engulfment.

- (3) CFD simulation by implementing the incorporation model into the modelling has shown that the predicted micromixing time of the flow in the impinging jet flow reactor used in this study falls into the range of  $1.7 \times 10^{-4}$  to  $2.3 \times 10^{-5}$  s. It should be noted that the CFD model for ultrasound sonication process only accounts for the ultrasound irradiation effect by acoustic streaming in the CFD simulation, which is not able to reflect the impact of microbubble collapse induced turbulent small-eddies due to the cavitation on the local shear turbulence intensification. This becomes necessary to consider such effect in the model which should thoroughly consider the effect of ultrasound irradiation on turbulence generation and to improve the engulfment model proposed by Baldyga *et al.* (1999).

## References

- ABOLHASANI, M., RAHIMI, M., DEHBANI, M. & ALSAIRAFI, A. A. 2012. CFD modeling of heat transfer by 1.7 MHz ultrasound waves. *Numerical Heat Transfer, Part A: Applications*, 62, 822-841.
- AKBARI, M., RAHIMI, M. & FARYADI, M. 2017. Gas-liquid flow mass transfer in a T-shape microreactor stimulated with 1.7MHz ultrasound waves. *Chinese Journal of Chemical Engineering*, 25, 1143-1152.
- BALDYGA, J. & BOURNE, J. Turbulent mixing and chemical reactions, 1999. Chichester: Wiley.
- BALDYGA, J. & BOURNE, J. 1984. A fluid mechanical approach to turbulent mixing and chemical reaction part III computational and experimental results for the new micromixing model. *Chemical Engineering Communications*, 28, 259-281.
- BALDYGA, J. & BOURNE, J. 1990. Comparison of the engulfment and the interaction-by-exchange-with-the-mean micromixing models. *The Chemical Engineering Journal*, 45, 25-31.
- BULLIARD-SAURET, O., BERINDEI, J., FERROUILLAT, S., VIGNAL, L., MEMPONTEIL, A., PONCET, C., LEVEQUE, J. M. & GONDREXON, N. 2019. Heat transfer intensification by low or high frequency ultrasound: Thermal and hydrodynamic phenomenological analysis. *Experimental Thermal and Fluid Science*, 104, 258-271.
- BULLIARD-SAURET, O., FERROUILLAT, S., VIGNAL, L., MEMPONTEIL, A. & GONDREXON, N. 2017. Heat transfer enhancement using 2 MHz ultrasound. *Ultrasonics sonochemistry*, 39, 262-271.
- BULLIARD-SAURET, O., FERROUILLAT, S., VIGNAL, L., PASHMI, E., MEMPONTEIL, A. & GONDREXON, N. 2015. Experimental study of heat transfer

enhancement using ultrasound on a flat plate in forced convection. *Turbulence, Heat and Mass Transfer*, 8.

CAI, J., HUAI, X., YAN, R. & CHENG, Y. 2009. Numerical simulation on enhancement of natural convection heat transfer by acoustic cavitation in a square enclosure. *Applied Thermal Engineering*, 29, 1973-1982.

CHEN, L., DONG, B., GUO, Y., YANG, X. & LI, G. 2020. CFD modelling of the effects of local turbulence intensification on synthesis of LiFePO<sub>4</sub> particles in an impinging jet reactor. *Chemical Engineering and Processing - Process Intensification*, 155, 108065.

DANGE, P., KULKARNI, A. & RATHOD, V. 2015. Ultrasound assisted synthesis of methyl butyrate using heterogeneous catalyst. *Ultrasonics Sonochemistry*, 26, 257-264.

DUAN, X. L., WANG, X. Y., WANG, G., CHEN, Y. Z. & QIU, X. Q. 2004. Experimental study on the influence of ultrasonic vibration on heat transfer and pressure drop in heat exchanger tubes. *Petrochemical Equipment*, 33, 1-4.

FARYADI, M., RAHIMI, M., SAFARI, S. & MORADI, N. 2014. Effect of high frequency ultrasound on micromixing efficiency in microchannels. *Chemical Engineering and Processing: Process Intensification*, 77, 13-21.

FOURNIER, M.-C., FALK, L. & VILLERMAUX, J. 1996a. A new parallel competing reaction system for assessing micromixing efficiency—determination of micromixing time by a simple mixing model. *Chemical Engineering Science*, 51, 5187-5192.

FOURNIER, M. C., FALK, L. & VILLERMAUX, J. 1996b. A new parallel competing reaction system for assessing micromixing efficiency—Experimental approach. *Chemical Engineering Science*, 51, 5053-5064.

GUICHARDON, P. & FALK, L. 2000. Characterisation of micromixing efficiency by the iodide–iodate reaction system. Part I: experimental procedure. *Chemical Engineering Science*, 55, 4233-4243.

- GUICHARDON, P., FALK, L. & VILLERMAUX, J. 2000. Characterisation of micromixing efficiency by the iodide–iodate reaction system. Part II: kinetic study. *Chemical Engineering Science*, 55, 4245-4253.
- KARIMI, M., JENKINS, B. & STROEVE, P. 2014. Ultrasound irradiation in the production of ethanol from biomass. *Renewable and Sustainable Energy Reviews*, 40, 400-421.
- KASHID, M., RENKEN, A. & KIWI-MINSKER, L. 2011. Mixing efficiency and energy consumption for five generic microchannel designs. *Chemical Engineering Journal*, 167, 436-443.
- KUMAR, V., PARASCHIVOIU, M. & NIGAM, K. D. P. 2011. Single-phase fluid flow and mixing in microchannels. *Chemical Engineering Science*, 66, 1329-1373.
- KURBANOV, U. & MELKUMOV, K. Use of ultrasound for intensification of heat transfer process in heat exchangers. Proceedings of the international congress of refrigeration, 2003. 1-5.
- LIU, Y. & FOX, R. O. 2006. CFD predictions for chemical processing in a confined impinging-jets reactor. *AIChE Journal*, 52, 731-744.
- LIU, Z., GUO, L., HUANG, T., WEN, L. & CHEN, J. 2014. Experimental and CFD studies on the intensified micromixing performance of micro-impinging stream reactors built from commercial T-junctions. *Chemical Engineering Science*, 119, 124-133.
- LIU, Z. & LI, B. 2018. Scale-adaptive analysis of Euler-Euler large eddy simulation for laboratory scale dispersed bubbly flows. *Chemical Engineering Journal*, 338, 465-477.
- MILLS, P. L., QUIRAM, D. J. & RYLEY, J. F. 2007. Microreactor technology and process miniaturization for catalytic reactions—A perspective on recent developments and emerging technologies. *Chemical Engineering Science*, 62, 6992-7010.

- NIE, A., GAO, Z., XUE, L., CAI, Z., EVANS, G. M. & EAGLESHAM, A. 2018. Micromixing performance and the modeling of a confined impinging jet reactor/high speed disperser. *Chemical Engineering Science*, 184, 14-24.
- NOMURA, S., MURAKAMI, K. & KAWADA, M. 2002. Effects of turbulence by ultrasonic vibration on fluid flow in a rectangular channel. *Japanese journal of applied physics*, 41, 6601.
- OU, J.-J. & RANZ, W. E. 1983. Mixing and chemical reactions: Chemical selectivities. *Chemical Engineering Science*, 38, 1015-1019.
- PALMER, D. A., RAMETTE, R. & MESMER, R. 1984. Triiodide ion formation equilibrium and activity coefficients in aqueous solution. *Journal of solution chemistry*, 13, 673-683.
- PARVIZIAN, F., RAHIMI, M. & AZIMI, N. 2012. Macro-and micromixing studies on a high frequency continuous tubular sonoreactor. *Chemical Engineering and Processing: Process Intensification*, 57, 8-15.
- POPE, S. B. 2000. *Turbulent Flows*, Cambridge, Cambridge University Press.
- RAHIMI, M., AGHEL, B., HATAMIFAR, B., AKBARI, M. & ALSAIRAFI, A. 2014a. CFD modeling of mixing intensification assisted with ultrasound wave in a T-type microreactor. *Chemical Engineering and Processing: Process Intensification*, 86, 36-46.
- RAHIMI, M., AZIMI, N., PARVIZIAN, F. & ALSAIRAFI, A. A. 2014b. Computational Fluid Dynamics modeling of micromixing performance in presence of microparticles in a tubular sonoreactor. *Computers & chemical engineering*, 60, 403-412.
- SAJJADI, B., ASGHARZADEHAHMADI, S., ASAITHAMBI, P., RAMAN, A. A. A. & PARTHASARATHY, R. 2017. Investigation of mass transfer intensification under

power ultrasound irradiation using 3D computational simulation: A comparative analysis. *Ultrasonics sonochemistry*, 34, 504-518.

SCHWERTFIRM, F., GRADL, J., SCHWARZER, H. C., PEUKERT, W. & MANHART, M. 2007. The low Reynolds number turbulent flow and mixing in a confined impinging jet reactor. *International Journal of Heat and Fluid Flow*, 28, 1429-1442.

SMIRNOV, L. P., KULAGINA, T. P. & ANDRIANOVA, Z. S. 2017. Influence of low-frequency vibrations on the chemical reaction rate in the liquid phase for reagent association. *Russian Chemical Bulletin*, 66, 30-33.

VILLERMAUX, J. Micromixing and chemical reaction semi-quantitative criteria based on comparison of characteristic time constants. AI Ch. E. Meeting, Chicago, 1990.

VILLERMAUX, J. & DAVID, R. 1983. Recent advances in the understanding of micromixing phenomena in stirred reactors. *Chemical Engineering Communications*, 21, 105-122.

VILLERMAUX, J. & DEVILLON, J. Représentation de la coalescence et de la redispersion des domaines de ségrégation dans un fluide par un modèle d'interaction phénoménologique. Proceedings of the 2nd International symposium on chemical reaction engineering, 1972. Elsevier New York, 1-13.

VILLERMAUX, J., FALK, L., FOURNIER, M.-C. & DETREZ, C. Use of parallel competing reactions to characterize micromixing efficiency. AIChE Symposium Series, 1992. American Institute of Chemical Engineers, 6-6.

WOO, X. Y., TAN, R. & BRAATZ, R. D. 2009. Modelling and Computational Fluid Dynamics-Population Balance Equation-Micromixing Simulation of Impinging Jet Crystallizers. *Crystal growth and design*, 9, 156-164.

YANG, H.-J., CHU, G.-W., ZHANG, J.-W., SHEN, Z.-G. & CHEN, J.-F. 2005. Micromixing Efficiency in a Rotating Packed Bed: Experiments and Simulation. *Industrial & Engineering Chemistry Research*, 44, 7730-7737.

YAO, Y., ZHANG, X. & GUO, Y. 2010. Experimental study on heat transfer enhancement of water-water shell-and-tube heat exchanger assisted by power ultrasonic.

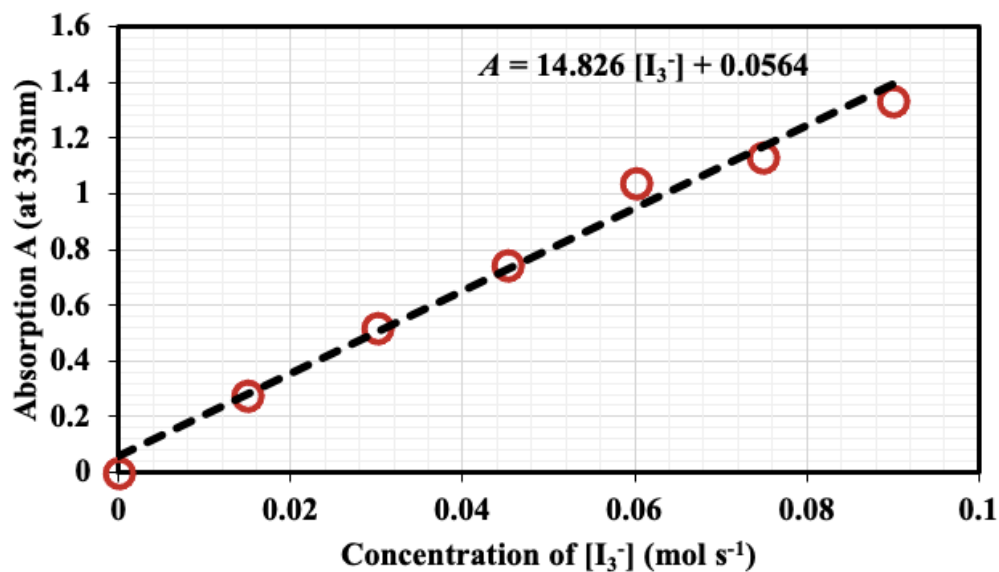
ZHANG, F., MARRE, S. & ERRIGUIBLE, A. 2020a. Mixing intensification under turbulent conditions in a high pressure microreactor. *Chemical Engineering Journal*, 382, 122859.

ZHANG, J.-W., LIU, S.-F., CHENG, C., LI, W.-F., XU, X.-L., LIU, H.-F. & WANG, F.-C. 2019. Investigation of three-dimensional flow regime and mixing characteristic in T-jet reactor. *Chemical Engineering Journal*, 358, 1561-1573.

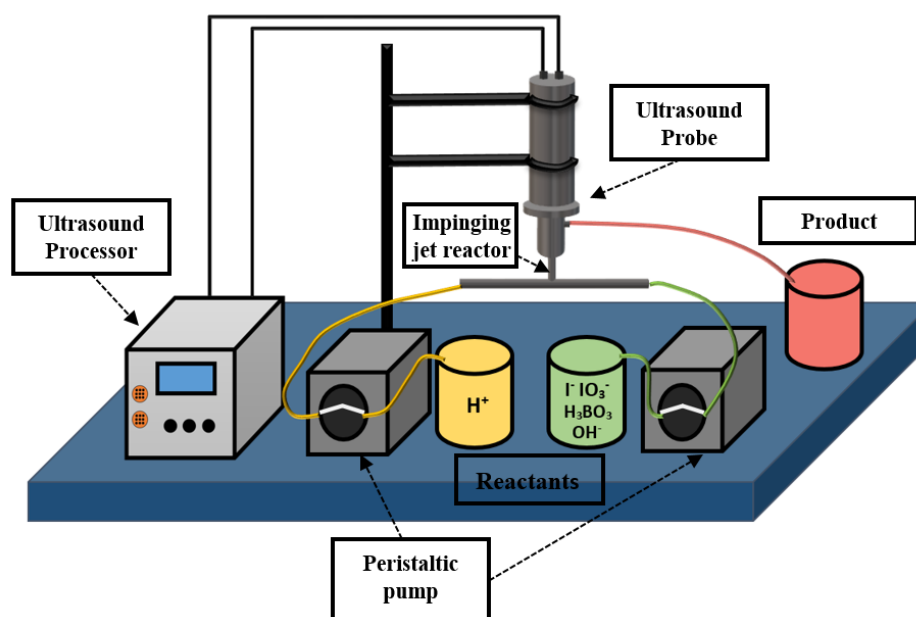
ZHANG, L., SRINIVASAKANNAN, C., LI, S., HE, Y., CHEN, K. & YIN, S. 2020b. Mixing performance in T-shape microchannel at high flow rate for Villermaux-Dushman reaction. *Microchemical Journal*, 155, 104662.

ZHANG, Q., DONG, Z., ZHAO, S., LIU, Z. & CHEN, G. 2021. Ultrasound-assisted gas-liquid mass transfer process in microreactors: The influence of surfactant, channel size and ultrasound frequency. *Chemical Engineering Journal*, 405, 126720.

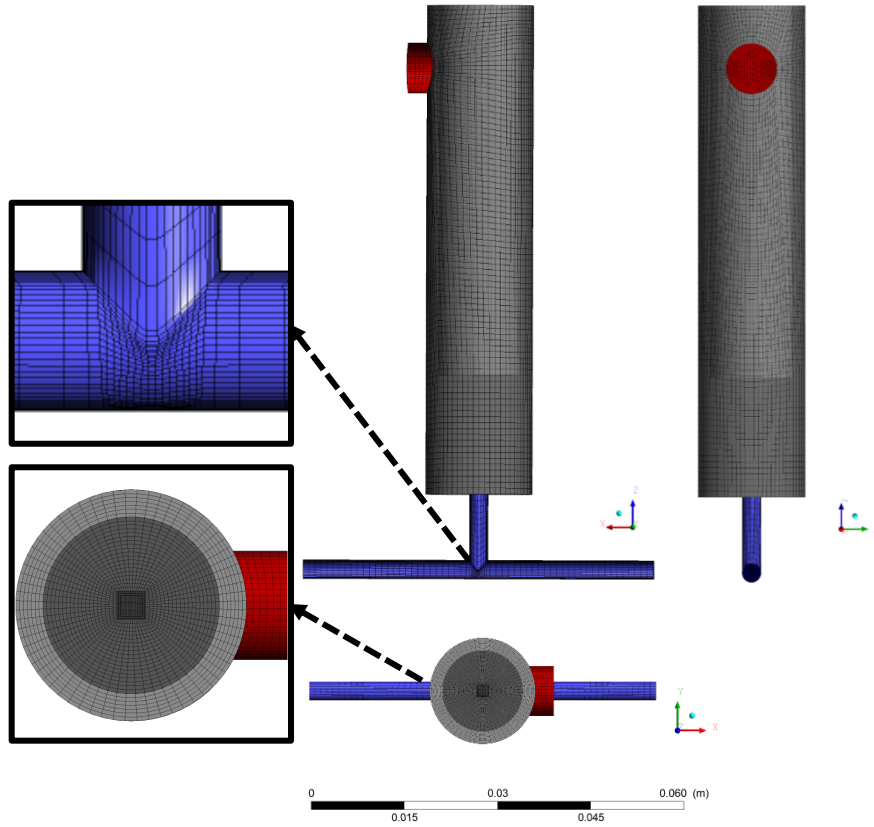
## Figures and Graphs



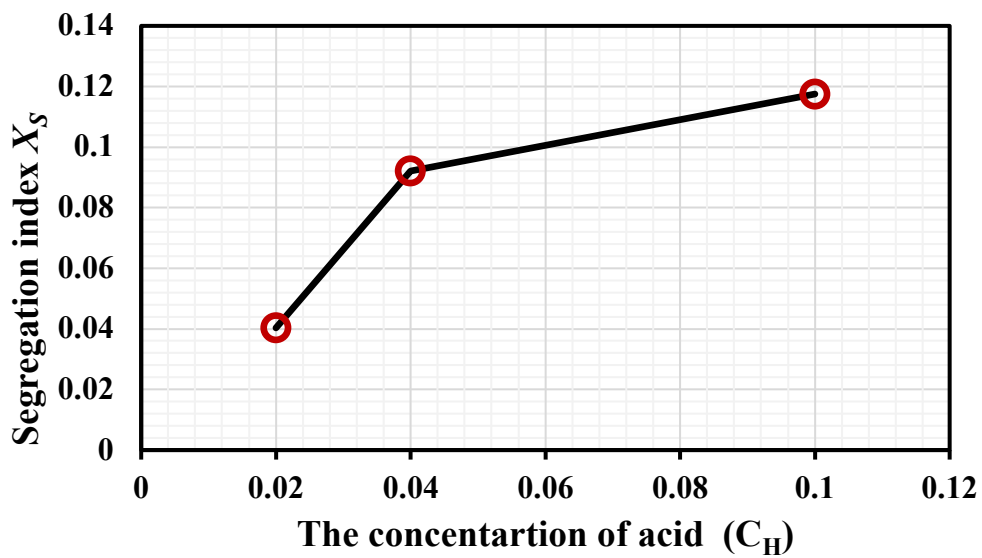
**Figure 3.1** Calibration curve of  $[I_3^-]$  concentration by a UV spectrophotometer at wavelength of 353 nm.



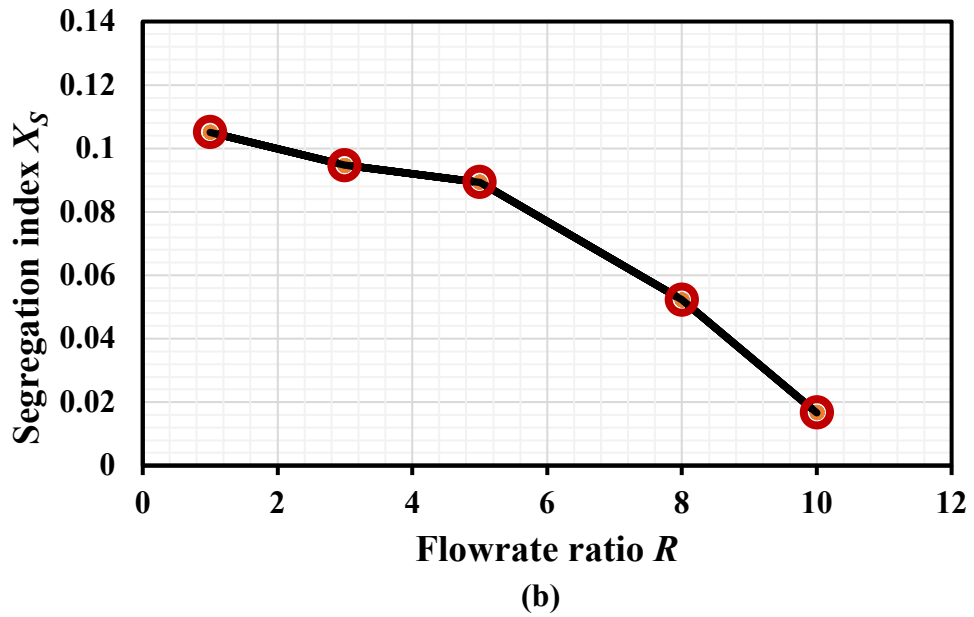
**Figure 3.2** Schematic diagram of experimental setup of micromixing in the impinging jet reactor with assist of ultrasound irradiation via Villermaux-Dushman reaction.



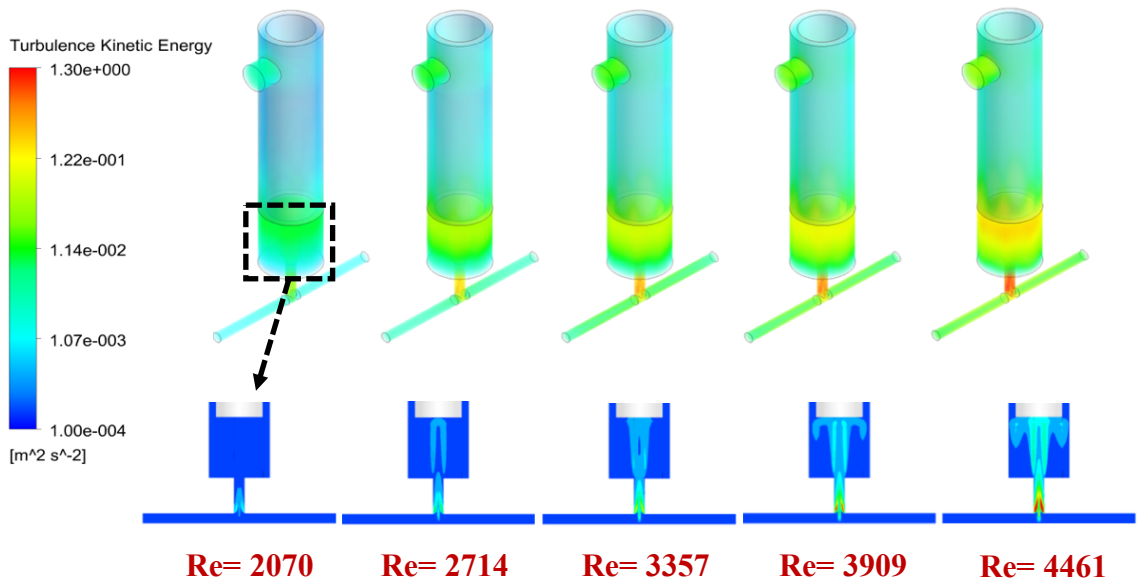
**Figure 3.3** 3D view and mesh of the computational domain and mesh structure of impinging jet obtained from ANSYS ICEM.



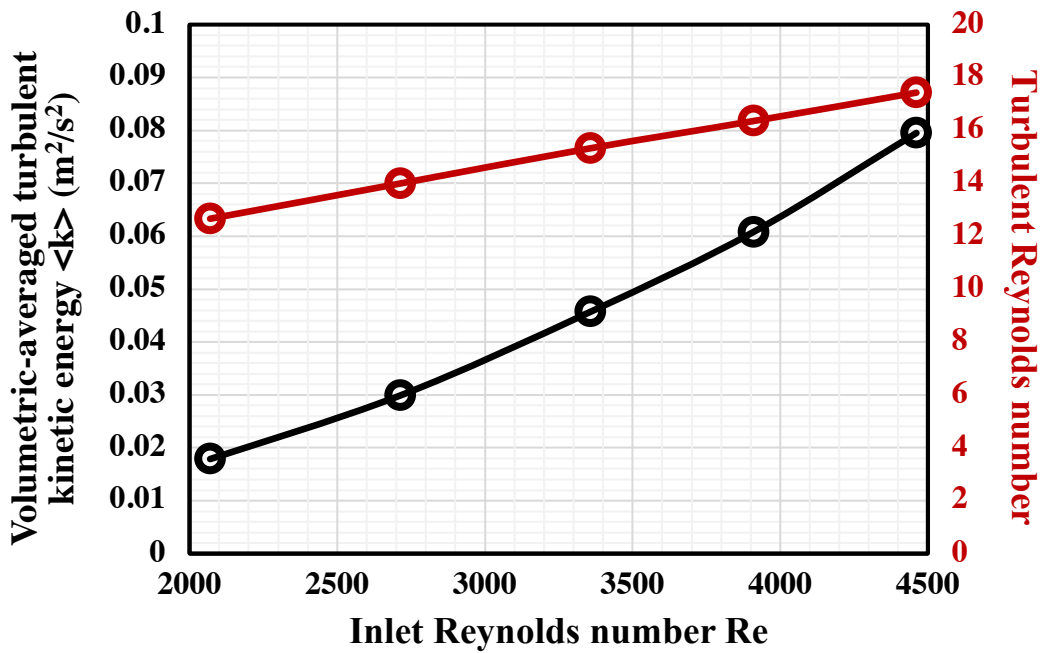
(a)



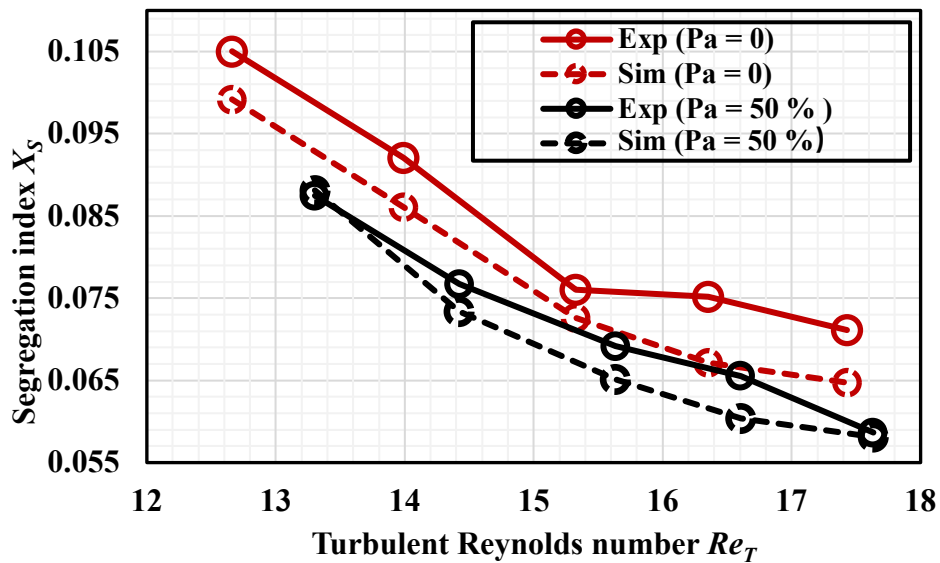
**Figure 3.4** Experimental results of segregation index  $X_s$  under (a) different concentration  $C_H$  of acid under the Reynolds number  $Re = 2714$  and flowrate ratio  $R=1$ ; (b) different flowrate ratio  $R$  ( $R=1 \sim R=10$ ) with constant initial acid concentration  $C_H$ .



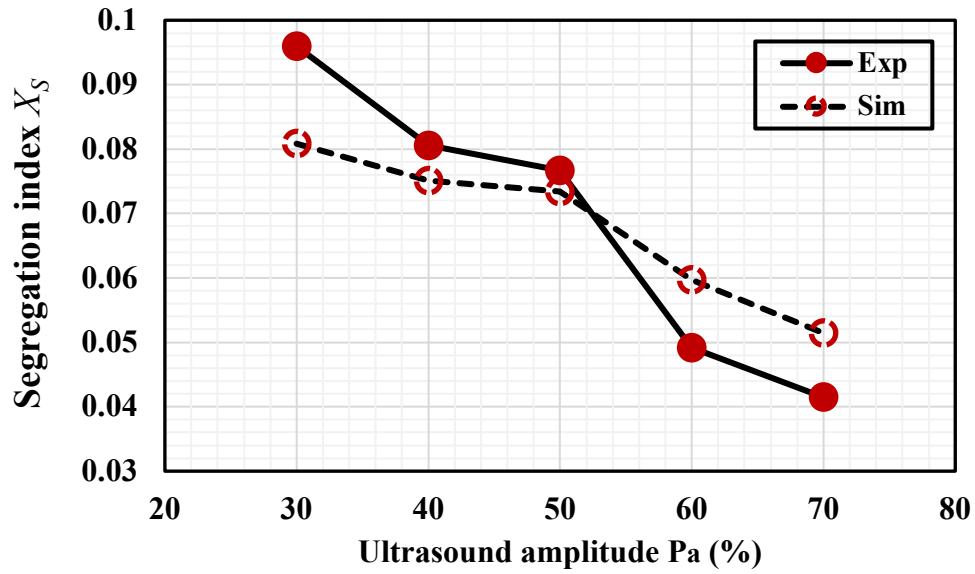
**Figure 3.5** The 3D contour plot of turbulent kinetic energy (TKE) in the impinging jet reactor and the 2D plot of chamber downstream the impingement region the with different inlet flowrate without ultrasound irradiation.



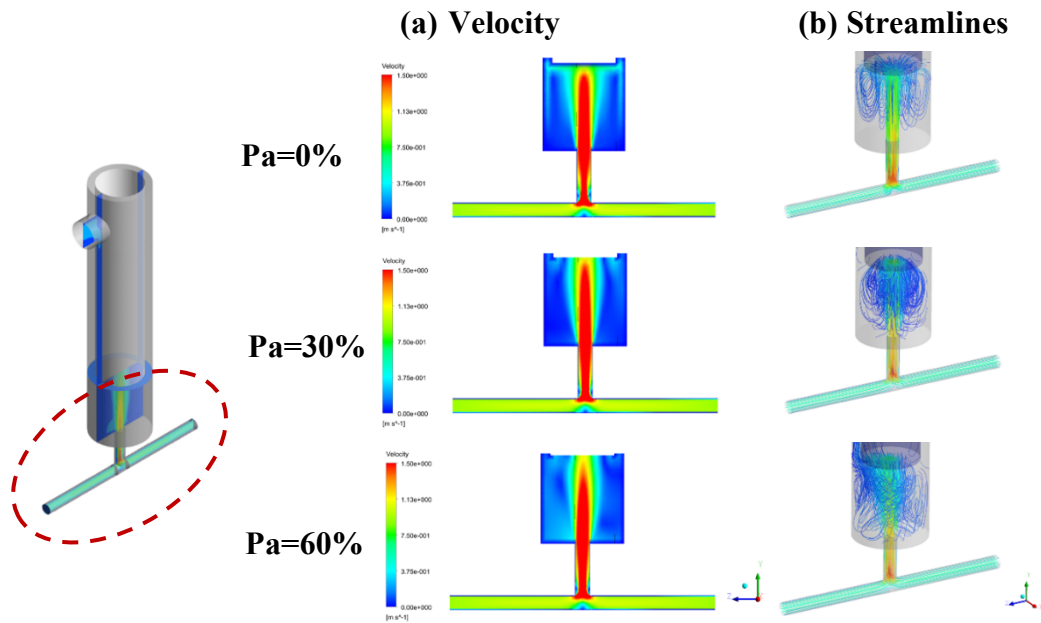
**Figure 3.6 (a)** The volumetric-averaged turbulent kinetic energy  $k$  (m<sup>2</sup>/s<sup>2</sup>) and the turbulent Reynolds number  $Re_T$  versus inlet Reynolds number  $Re$ .



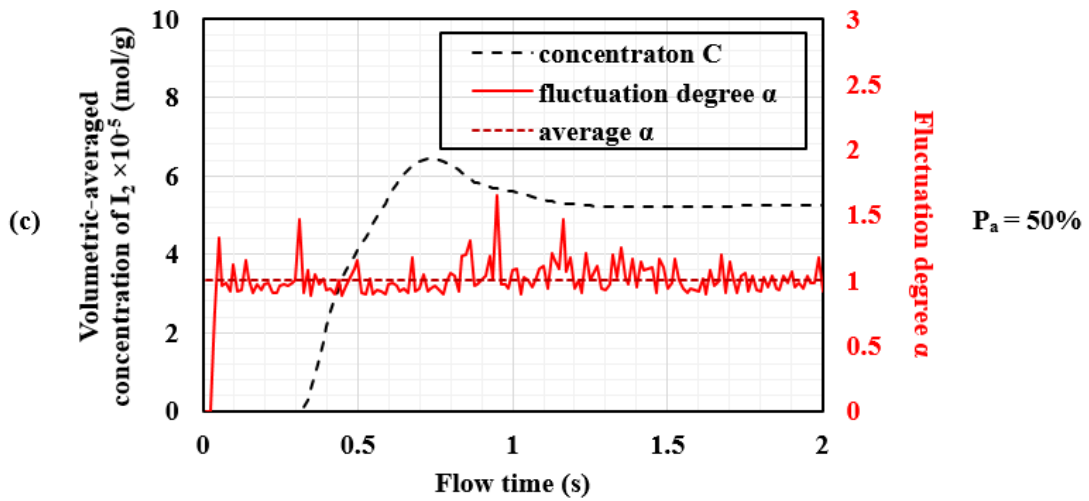
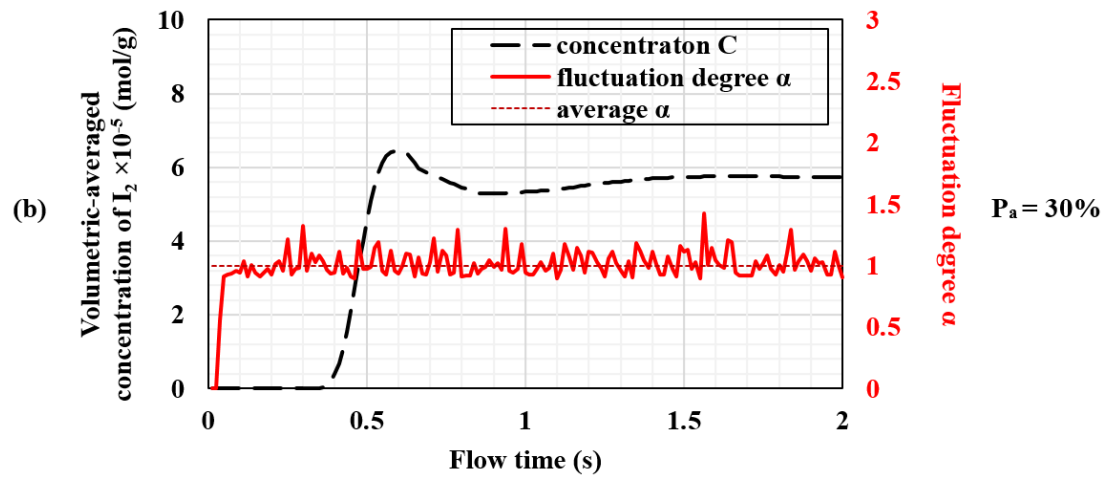
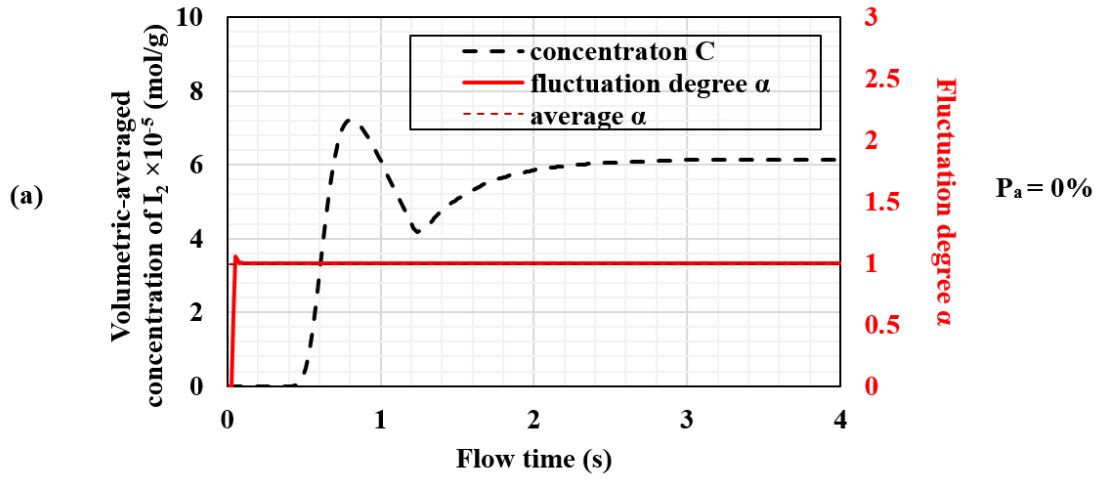
**Figure 3.7** Experimental and simulation results of segregation index  $X_s$  versus turbulent Reynolds number without ultrasound (Exp ( $P_a = 0$ ) and Sim ( $P_a = 0$ )) and ultrasound amplitude of 50 % (Exp ( $P_a = 50\%$ ) and Sim ( $P_a = 50\%$ )) at constant acid concentration.



**Figure 3.8** Experimental and simulated results of segregation index  $X_s$  versus ultrasound amplitude under different ultrasound amplitude at turbulent Reynolds number  $Re_T = 14.0$  and constant acid concentration.



**Figure 3.9** (a) Contour of velocity magnitude and (b) streamlines under the ultrasound amplitude of 0%, 30%, 60% at downstream of impingement region at flow time  $t = 2.0$  s from simulation.



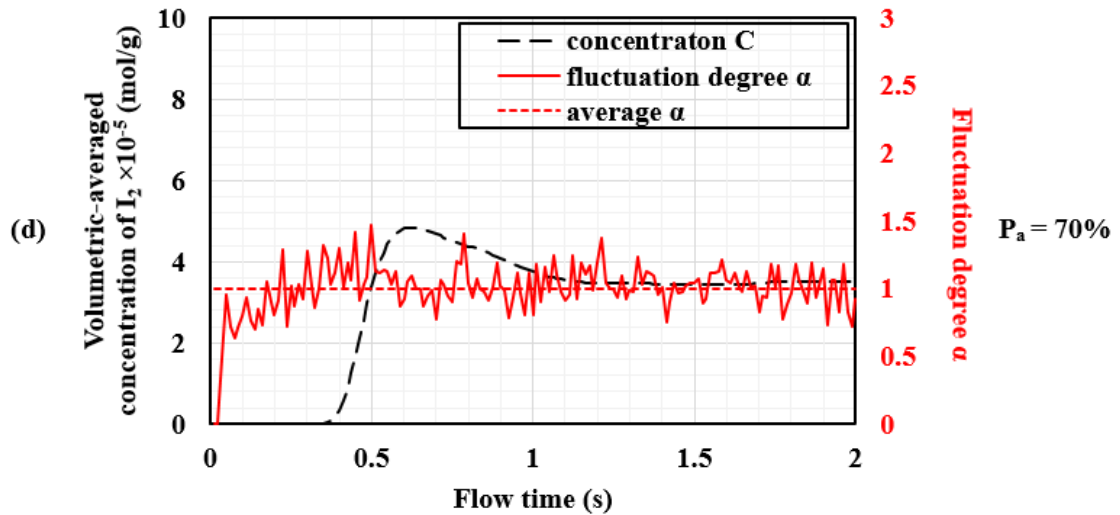


**Figure 3.10** The volumetric-averaged concentration of  $I_2$  and fluctuation degree  $\alpha$  in impinging jet reactor versus flow time  $t$  under the conditions of ultrasound amplitude of (a)  $P_a = 0\%$ ; (b)  $P_a = 30\%$ ; (c)  $P_a = 50\%$  and (d)  $P_a = 70\%$  at constant acid concentration at flow time  $t = 2.0$  s from simulation.

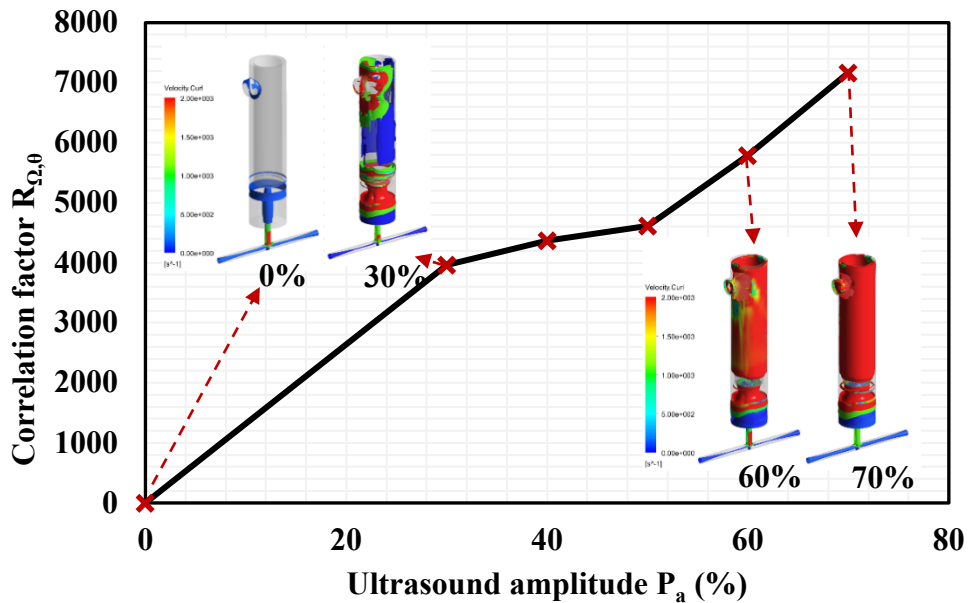
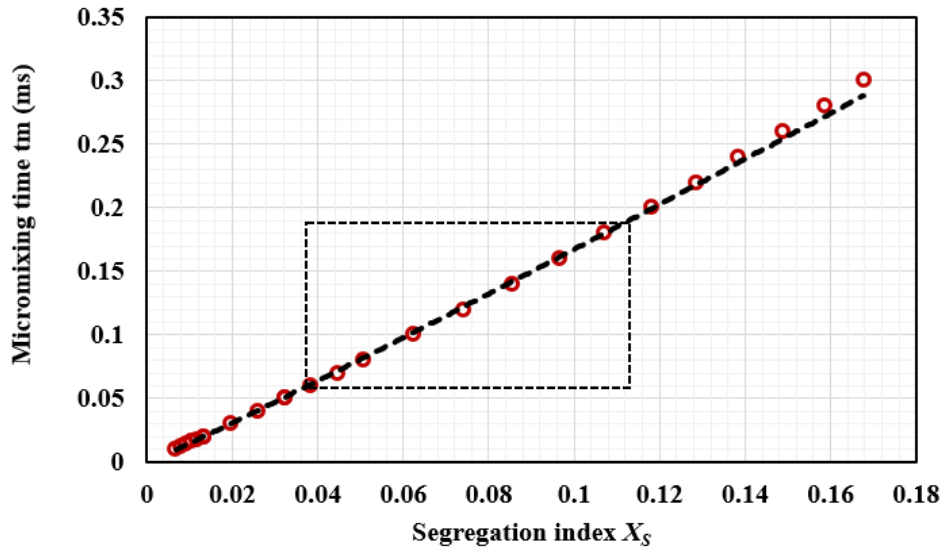
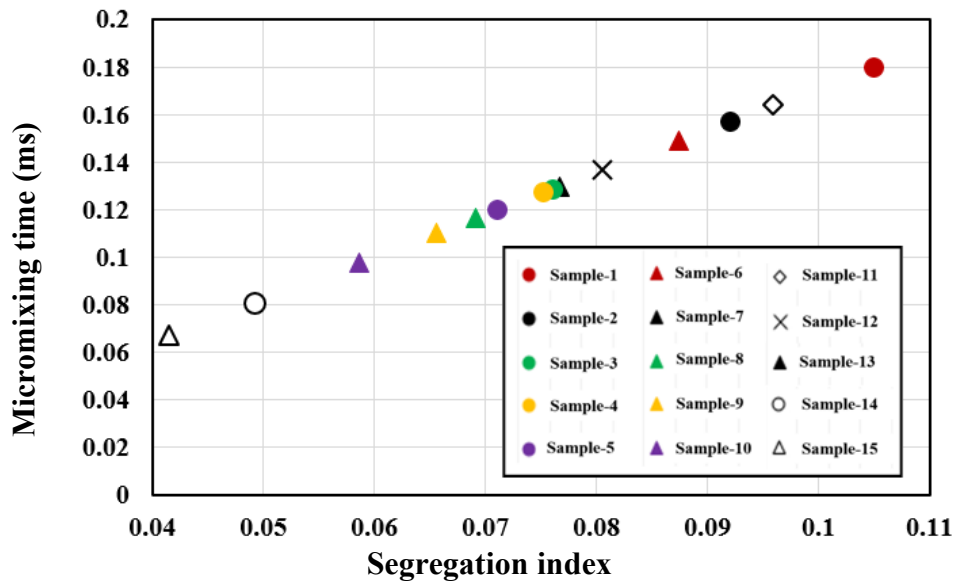


**Figure 3.11** The correlation factor  $R_{\Omega,0}$  versus ultrasound amplitude  $P_a$  and iso-surface distribution of various vorticity magnitude of  $50\text{ s}^{-1}$ ,  $500\text{ s}^{-1}$ ,  $1000\text{ s}^{-1}$  and  $2000\text{ s}^{-1}$  in the impinging jet reactor with constant inlet flowrate at flow time  $t = 2.0$  s from simulation.



(a)



(b)

**Figure 3.12** (a) Relationship between micromixing time  $t_m$  and segregation index  $X_s$  based on Incorporation model; (b) Relationship between micromixing time  $t_m$  and segregation index  $X_s$  at various experimental conditions.

## Tables

**Table 3.1** The concentration of reactants

Reactant	Range
H <sub>3</sub> BO <sub>3</sub> (mol/L)	0.1818
NaOH (mol/L)	0.0909
KI (mol/L)	0.0116
KIO <sub>3</sub> (mol/L)	0.00233
H <sub>2</sub> SO <sub>4</sub> (mol/L)	0.01-0.02-0.05

**Table 3.2** Samples prepared under different conditions

No.	Conc. of [H <sup>+</sup> ] (mol/l)	Q <sub>1</sub> (ml/s)	Q <sub>2</sub> (ml/s)	v <sub>1</sub> (m/s)	v <sub>2</sub> (m/s)	Flowrate ratio R	Re	Ultrasound amplitude (%)
<b>under different flowrate without ultrasound power</b>								
1	0.04	4.91	4.91	0.69	0.69	1	2070	0
2	0.04	6.43	6.43	0.91	0.91	1	2714	0
3	0.04	7.96	7.96	1.13	1.13	1	3357	0
4	0.04	9.27	9.27	1.31	1.31	1	3909	0
5	0.04	10.57	10.57	1.50	1.50	1	4461	0
<b>under different flowrate with constant ultrasound power</b>								
6	0.04	4.91	4.91	0.69	0.69	1	2070	50
7	0.04	6.43	6.43	0.91	0.91	1	2714	50
8	0.04	7.96	7.96	1.13	1.13	1	3357	50
9	0.04	9.27	9.27	1.31	1.31	1	3909	50
10	0.04	10.57	10.57	1.50	1.50	1	4461	50
<b>under different ultrasound power at constant flowrate</b>								
11	0.04	6.43	6.43	0.91	0.91	1	2714	30

<b>12</b>	0.04	6.43	6.43	0.91	0.91	1	2714	40
<b>13</b>	0.04	6.43	6.43	0.91	0.91	1	2714	50
<b>14</b>	0.04	6.43	6.43	0.91	0.91	1	2714	60
<b>15</b>	0.04	6.43	6.43	0.91	0.91	1	2714	70
<b>under different flowrate ratio without ultrasound power</b>								
<b>16</b>	0.04	4.91	4.91	0.69	0.69	1	-	0
<b>17</b>	0.04	7.36	2.45	1.04	0.35	3	-	0
<b>18</b>	0.04	8.18	1.64	1.15	0.23	5	-	0
<b>19</b>	0.04	8.72	1.09	1.23	0.15	8	-	0
<b>20</b>	0.04	8.92	0.89	1.25	0.13	10	-	0
<b>with different acid concentration at constant flowrate without ultrasound power</b>								
<b>21</b>	0.02	6.43	6.43	0.91	0.91	1	2714	0
<b>22</b>	0.04	6.43	6.43	0.91	0.91	1	2714	0
<b>23</b>	0.1	6.43	6.43	0.91	0.91	1	2714	0

## Appendix

Runge-Kutta method is used to solve conservation equations of component concentration by adopting the following nomenclature for conciseness as following steps,

$$A = \text{H}_2\text{BO}_3^-, B = \text{H}^+, C = \text{I}^-, D = \text{IO}_3^-, E = \text{I}_2, F = \text{I}_3^-.$$

On basis on concentration change rate presented as Equation (3-41), the mass conservation of each components can be calculated as follows (Yang *et al.*, 2005),

$$\frac{dC_A}{dt} = -\frac{C_A}{t_m} + R_1 \quad (3-a1)$$

$$\frac{dC_B}{dt} = -\frac{C_B}{t_m} - R_1 - 6R_2 \quad (3-a2)$$

$$\frac{dC_C}{dt} = \frac{C_{C,s} - C_C}{t_m} - 5R_2 - R_3 + R_4 \quad (3-a3)$$

$$\frac{dC_D}{dt} = \frac{C_{D,s} - C_D}{t_m} - R_2 \quad (3-a4)$$

$$\frac{dC_E}{dt} = -\frac{C_E}{t_m} + 3R_2 - R_3 + R_4 \quad (3-a5)$$

$$\frac{dC_F}{dt} = -\frac{C_F}{t_m} + R_3 - R_4 \quad (3-a6)$$

In order to simplify the Equations (3-a1) to (3-a6), method of transformation is used by rearrangement (Baladyga and Bourne, 1984).

Let  $W = C_B - C_A$ ,  $Z = C_B - C_E$  and  $U = C_C - C_F$ . Then the rate of concentration for components can be rewritten as,

$$\frac{dW}{dt} = -\frac{W}{t_m} - 6R_2 \quad (3-a7)$$

$$\frac{dZ}{dt} = \frac{C_{C,s} - Z}{t_m} - 8R_2 \quad (3-a8)$$

$$\frac{dU}{dt} = \frac{C_{C,s}-U}{t_m} - 5R_2 \quad (3-a9)$$

$$\frac{dC_D}{dt} = \frac{C_{D,s}-C_D}{t_m} - R_2 \quad (3-a10)$$

The segregate index can be rewritten as,

$$X_s = \frac{Y}{Y_s} = \frac{(1+R)(U-Z)}{[H^+]_0} \left( 2 + \frac{1}{3} \frac{[H_2BO_3^-]_0}{[IO_3^-]_0} \right) \quad (3-a11)$$

By using Runge-Kutta method to solve the problem, the initial conditions are given as follows,

$$W = C_{H,0}, Z = 0, U = 0 \text{ and } C_D = 0.$$

The iteration ends up once the concentration of acid approaches to 0. For equilibrium constant  $K_{eq}$  as described in Equation (3-13), substituted by the following equation:

$$K_{eq} = \frac{C_F}{C_C C_E} \quad (3-a12)$$

where  $C_F$  and  $C_E$  can be substituted with  $U - C_c$  and  $C_c - Z$ . A 2<sup>th</sup>-order equation can be obtained as follows,

$$C_c^2 + (1/K_B - Z)C_c - U/K_B = 0 \quad (3-a13)$$

By solving the equation, the  $C_c$  can be solved as,

$$C_c = \frac{Z-1/K_B + \sqrt{(Z-1/K_B)^2 + 4U/K_B}}{2} \quad (3-a14)$$

Thus,

$$R_2 = k_2 [H^+]_0^2 \left( \frac{Z-1/K_B + \sqrt{(Z-1/K_B)^2 + 4U/K_B}}{2} \right)^2 C_D \quad (3-a15)$$

## **CHAPTER 4**

# **SHEAR TURBULENCE CONTROLLABLE SYNTHESIS OF AGGREGATED NANO-PARTICLES USING A SWIRLING VORTEX FLOW REACTOR ASSISTED BY ULTRASOUND IRRADIATION**

### **SUMMARY**

In Chapter 2 and 3, the hydrodynamic characteristics and mixing performance in the impinging jet reactor has been discussed. Considering the narrowly confined impingement region for mixing in the impinging jet reactor and the limitation of the enhancement of the electrochemical performance of FePO<sub>4</sub> precursor by turbulence intensification, this chapter concerns another type of fine particle synthesis process using a proposed novel type of structured mixer, so-called 'swirling vortex flow reactor (SVFR)'. The shear controllable synthesis process especially mass transfer in SVFR is investigated. This type of reactor is able to generate a strong 'Rankine vortex-like' flow with a great shear gradient in the radial direction, trapping the synthesised SiO<sub>2</sub> aggregated nanoparticles into the vortex core to form enhanced engulfment for particle aggregation. The aggregated particles are further agglomerated to form larger particles with high uniformity under the action of turbulent shear and subsequent mass transfer due to engulfment occurring in the turbulent eddies. The mass transfer is enhanced by engulfment between the slabs of the liquid streams tangentially entering into the reactor while the local shear in the turbulent eddies with the length scales down to the Kolmogorov scale shape the particles, yielding well spherical morphology and narrower size distribution. In addition, the mass transfer performance can be further

improved by intensifying the local turbulent shear by applying the ultrasound to the synthesis process. The instantaneous collapse of cavitation bubbles in the vortex due to the introduction of ultrasound results in intensified micro-turbulent streaming. The particle characteristics, chemical reaction and mass transfer performance are found to be correlated with the local turbulence characteristics in the vortex. The mass transfer can be characterised using the film surface renewal model via the Sherwood number by considering the agglomerated particles response to the turbulent eddies. Both numerical simulation and experimental results clearly indicate the existence of the correlation in synthesis of aggregated nano-particles in swirling vortex reactor between the mass transfer and turbulence shear by using ultrasound irradiation.

#### 4.1 Introduction

A so-called SVFR has been proposed as a high-shear mixer used for synthesis of nanoparticles, due to its unique hydrodynamic characteristics of mixing and mass transfer (Usune *et al.*, 2019, Shoukry and Shemilt, 1985). This swirling vortex reactor consists of two fast tangential inlet streams strongly recirculating and evolving in a swirling chamber with engulfment of two inlet streams presenting a rotating vortex structure in the core. Pressure in the central part of the swirling turbulence vortex reduces owing to centrifugal forces pushing the liquid and particles to the outside when particles' density is higher than the solution. Kockmann *et al.* (2003) proposed engulfment flow in a T-shaped mixer and attributed the enhanced mass transfer to the emergence of vortices as the result of energy dissipation. The vortex structure in engulfment flow was numerically simulated by Mariotti *et al.* (2019) and quantified by vortex indicator  $\lambda^2$ , which is susceptible to the tilt angle of inlets. Shoukry and Shemilt (1985) have illustrated the enhancement of the mass transfer coefficient of up to 320% in swirling annular pipe flow compared with developed axial flow. The decay of the swirl leads to a reduction in the mass transfer augmentation along the flow path. Legentilhomme *et al.* (1993) have further increased the mass transfer coefficient up to

550% by the modification of geometric factors in annular swirling flow. Contigiani *et al.* (2018) illustrated that the mass-transfer enhancement factor of recirculating flow increases due to intensive forced convection and the sudden expansion at the inlet of tangential streamflow. The SVFR presents a deviation of mass transfer in a wide range of Re numbers of two streams in both symmetrical and asymmetrical scenarios.

It has been recognised that acoustic cavitation affects nuclei growth in a liquid medium under low-pressure cycles and contributes towards micro-bubble collapse under high-pressure cycles, which may be responsible for the enhancement in mass transfer rates. The adoption of ultrasound acts as an active enhancing approach by inputting external energy with oscillation and swirling of vortices resulting in the folding and stretching of the interface, which improves the mixing and mass transfer performance (Zhang *et al.*, 2019). Conversely, ultrasound irradiation in terms of shock waves induces a cavitation effect, which triggers oscillation and the collapse of microbubbles producing micro-streaming and turbulent eddies (Sajjadi *et al.*, 2015a, Hielscher, 2007). Sajjadi *et al.* (2017) have numerically simulated ultrasound pressure via an inhomogeneous Helmholtz equation as a boundary condition by claiming that the ultrasound helps to produce extra turbulence that overcomes the mass transfer restriction. They also proved that the propagation of acoustic streaming doubles the turbulent intensity of the mechanical stirring. In addition to the intense turbulence driving the mass transfer process, particles are modified while they are pushed and engulfed at the core of vortices with strong local shear that is responsible for particles of high uniformity. Pioneering studies have also claimed that ultrasound intensity has a significant influence on particle morphology, particles size distribution (PSD) and tap density with a threshold existing for the effect on PSD instead of being monotonous (Zhang *et al.*, 2009, Jeevanandam *et al.*, 2001, Jordens *et al.*, 2015). Jordens *et al.* (2015) have experimentally verified that lower frequencies and higher intensities of ultrasound may contribute towards particles with higher sphericity. Rahimi *et al.* (2014) have simulated the Villermaux-Dushman reactions in a T-type microreactor assisted by ultrasound

waves and indicated that the segregation index can be increased up to 10-20% by the employment of a piezoelectric transducer at 42 kHz.

Mesoporous silica dioxide (SiO<sub>2</sub>) nano-particles were explored as stable supporters and synthesised in the swirling reactor with its outstanding properties including high mechanical strength and non-interference effectivity (Dai *et al.*, 2020). The functionalised agents are immobilised on mesoporous SiO<sub>2</sub> as composite materials enable a high rate of mass transfer and are potentially beneficial to the adsorption process with their high-cost effectiveness and are widely applied in catalysts (Wang *et al.*, 2019), carriers (Hafizi *et al.*, 2019), surfactants (Tian *et al.*, 2020), stabilizers (Morita *et al.*, 2017, Keyvanloo *et al.*, 2014, Gobinath *et al.*, 2020) and biosensor (Harpaz *et al.*, 2020). The polymerisation of hydrous silicon dioxide is able to result in the complex branching of polymers due to the tetra-functional hydrolysed monomer Si(OH)<sub>4</sub> (Brinker and Scherer, 2013). The synthesis of porous SiO<sub>2</sub> microspheres in the presence of organic templates and/or additives has also been intensively investigated in recent years. Yu *et al.* (2006) have prepared monodispersed microporous SiO<sub>2</sub> microspheres of high porosity up to 61.4% in the range of 0.52 to 1.25 μm by adjusting the amount of dodecylamine (DDA). These hydrolysis catalysts through the hydrolysis of TEOS in water-ethanol mixture suggest that the concentration of silicon source and DDA play significant roles in the size and porosity control of SiO<sub>2</sub> synthesis. Yano and Fukushima (2003) controlled the size and porosity of monodispersed particles by synthesising the temperature and the ratio of methanol and water in solvent to the silica source, with the particle size ranging from 0.52 to 1.25 μm.

It should be noted that the morphology of amorphous SiO<sub>2</sub> particles can be modified owing to its amorphous nature, the various coordination states of Si-O pairs (Gurav *et al.*, 2009) and the controllable kinetics of the silica sol-gel process (Kim *et al.*, 2002). Thus, based on the above reviews and discussion on synthesis of nano-sized particles using the turbulence engulfment or ultrasound irradiation assisted processes, it can be

postulated that the mesoporous silica material synthesised and controlled by a sol-gel process can be affected by local turbulence embedded in the swirling vortex flow, which may change the characteristics of the mesoporous silica particle in both structure and morphology.

In this Chapter, SVFR is used for the intensified reaction manufacturing process to synthesis value-added and productive products of various scales. To overcome the drawbacks of discontinuous production, nonuniformity, low conversion rate, thermo-runaway and so on. The present study aims to investigate the hydrodynamics and mass transfer in the process of SiO<sub>2</sub> synthesis using a SVFR, focusing on the liquid-solid mass transfer coefficient and particle characteristics such as particle morphology and particle size distribution in a wide range of Reynolds number of inlet streams. The mass transfer enhancement is also explored with the employment of ultrasound ranging from 120 W to 600 W at a constant frequency of 20 kHz.

## **4.2 Experimental**

### **4.2.1 Solution preparation**

SiO<sub>2</sub> floccule was synthesised by adding 1 g of Cetyltrimethyl Ammonium Bromide (CTAB) and 3.5 ml of NaOH solution (2 M), purchased from Sinopharm Chemical Reagent Co., Ltd., into 480 ml of deionised water. After the CTAB was fully dissolved at the constant temperature of 80 °C, 5 ml of tetraethyl orthosilicate (TEOS > 28.5 %), purchased from Sinopharm Chemical Reagent Co., Ltd., was added into the mixture solution as mentioned in order to prepare mixture A.

### **4.2.2 Experimental setup and product characterization**

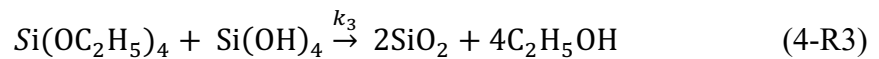
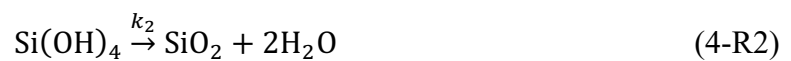
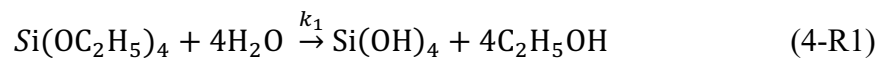
The experimental setup is shown in Figure 4.1. The simulated SVFR consists of a short circular cylindrical chamber ( $D = 20$  mm,  $H = 10$  mm) embedded in a stainless-steel block with two guided introduction thin pipes that allow the solution to tangentially enter the chamber to form the so-called Rankine vortex flow. An ultrasound probe ( $D = 20$  mm) (UH1200, 20 kHz, Ouhor Shanghai Co., Ltd) was imposed as the ultrasonic source immersed into the solution from the top of reactor chamber. Sample S-0 was obtained without assist of ultrasound irradiation at a constant flow rate of 5.75 ml/s for each inlet, circulating in the SVFR for 30 min at 80 °C. Samples S-1 to S-5 were obtained at a constant flow rate of 5.75 ml/s from introducing mixture A into the two inlet streams of swirling vortex reactor via peristaltic pumps and were circulated for 30 min under ultrasonic powers of 0 W, 120 W, 240 W, 360 W, 480 W and 600 W, respectively. Samples S-6 to S-10 were obtained with the inlet flow rate of 1.92 ml/s, 3.83 ml/s, 5.75 ml/s, 7.66 ml/s and 9.58 ml/s Reynolds number ranging from 2620 to 13196 under the ultrasound power level of 240 W. Samples S-11 to S-15 were obtained by altering the ratio of volumetric flow rate of two inlet streams from 1 to 5 under the ultrasound power level of 240 W. All the samples synthesised under different conditions are listed in Table 4.1 After the sample flocs were collected from the outlet of the reactor to cool down to the room temperature, the flocs were then filtered by a vacuum circulating pump and washed 3 times with the deionised water. The obtained gel was dried for 5 hours at 100 °C in the oven and then transferred to a muffle oven for calcination of 6 hour at 550 °C. After free cooling, the white powdery solid product, i.e. SiO<sub>2</sub> particles, were obtained.

The stability of synthesised SiO<sub>2</sub> particles was investigated using thermogravimetric analysis (TGA) from 20°C to 600°C, NETZSCH STA 449 F3 Jupiter, Germany, 10 °C/min, in synthetic air (20 vol% O<sub>2</sub> and 80 vol% N<sub>2</sub>). The morphology and microstructure were investigated by a scanning electron microscope (SEM), Sigma VP, ZEISS, Germany and the Brunauer-Emmett–Teller analysis (BET), ASAP 2020

Micrometrics, United States. The aggregated particle size was measured from SEM images using software ImageJ 6.5.

### 4.2.3 Description of synthesis reaction

The silicate was prepared through a sol-gel approach and the hydrolysis process proceeds in the presence of a NaOH solution acting as a homogenising agent (Brinker and Scherer, 2013). When TEOS was added into the solution containing NaOH and CTAB, it could be rapidly hydrolysed to produce  $\text{Si(OH)}_4$  under alkaline environments on the basis of multi-step chemical reactions that can be described by the following equations (De *et al.*, 2000, Zhao Rui-Yu, 1995) :



where reaction (4-R1) involves a homogenous hydrolysis reaction, reaction (4-R2) is a heterogeneous condensation reaction by converting aqueous silicate into silica and reaction (4-R3) is the condensation of alcohol. The parameters  $k_1$ ,  $k_2$  and  $k_3$  represent the reaction rate constant of hydrolysis, main step of condensation and condensation of alcohol, respectively. Practically, the process of hydrolysis and condensation occurs concurrently. There are two limiting cases: hydrolysis reaction is predominant and complete when the hydrolysis reaction rate constant is much greater than that of condensation ( $k_2 \gg k_3$ ); condensation occurs once after hydrolysis and the condensation rate is proportional to the hydrolysis reaction rate when the hydrolysis reaction rate constant is smaller than that of condensation ( $k_2 < k_3$ ) (Brinker and

Scherer, 2013). Water is excessive and sufficient to complete the hydrolysis reaction, thereby the hydrolysis can be assumed to be dominant in this particular case. The overall hydrolysis–condensation reaction rate followed the first-order reaction with the rate constant ( $k$ ),

$$r' = -\frac{d[\text{Si}(\text{OC}_2\text{H}_5)_4]}{dt} = k[\text{Si}(\text{OC}_2\text{H}_5)_4] \quad (4-1)$$

Here, the rate constant  $k$  of hydrolysis-condensation reaction is presumed to be  $3.6 \times 10^{-3} \text{ s}^{-1}$  (Zhao Rui-Yu, 1995).

### 4.3 Numerical simulation

#### 4.3.1 Governing equations

The approach employed during this investigation is based on Euler-Euler fully coupled two-fluid model. The liquid is set as a continuous primary phase and solid phase is considered as the dispersed phase. The continuity equation for liquid phase ( $l$ ) and solid phase ( $s$ ) are expressed as

Liquid phase:

$$\frac{\partial}{\partial t} (\alpha_l \rho_l) + \nabla \cdot (\alpha_l \rho_l \mathbf{u}_l) = -\dot{m}_{l \rightarrow s} \quad (4-2)$$

Solid phase:

$$\frac{\partial}{\partial t} (\alpha_s \rho_s) + \nabla \cdot (\alpha_s \rho_s \mathbf{u}_s) = \dot{m}_{l \rightarrow s} \quad (4-3)$$

where  $\mathbf{u}_l$  is the velocity of the liquid phase and  $\dot{m}_{l \rightarrow s}$  is the mass transfer source term from liquid to the solid phase. The conservation equations for momentum for both phases take the following form:

Liquid phase:

$$\frac{\partial}{\partial t} (\alpha_l \rho_l \mathbf{u}_l) + \nabla \cdot (\alpha_l \rho_l \mathbf{u}_l \mathbf{u}_l) = -\alpha_l \nabla p + \nabla \cdot \boldsymbol{\tau}_l + \alpha_l \rho_l \mathbf{g} + \mathbf{R}_{sl} \quad (4-4)$$

Solid phase:

$$\frac{\partial}{\partial t} (\alpha_s \rho_s \mathbf{u}_s) + \nabla \cdot (\alpha_s \rho_s \mathbf{u}_s \mathbf{u}_s) = -\alpha_s \nabla p + \nabla \cdot \boldsymbol{\tau}_s + \alpha_s \rho_s \mathbf{g} + \mathbf{R}_{sl} \quad (4-5)$$

where  $\mu_l$  and  $\lambda_l$  are the shear and bulk viscosity of liquid phase  $l$ ,  $\mathbf{R}_{sl}$  is the interaction force between phases. The interaction term is expressed in the following form:

$$\mathbf{R}_{sl} = K_{sl} (\mathbf{u}_s - \mathbf{u}_l) \quad (4-6)$$

where  $K_{sl}$  is the interphase momentum exchange coefficient. In the present study, drag force derived from the model of Wen and Yu has been adopted which is appropriate for the description of the dilute system (Wen, 1966). The fluid-solid exchange coefficient takes the following form:

$$K_{sl} = \frac{3}{4} C_D \frac{\alpha_s \alpha_l \rho_l |\mathbf{u}_s - \mathbf{u}_l|}{d_s} \alpha_l^{-0.265} \quad (4-7)$$

and

$$C_D = \frac{24}{\alpha_l Re_s} [1 + 0.15 (\alpha_l Re_s)^{0.687}] \quad (4-8)$$

where  $Re_s$  relative Reynolds number.

$$Re_s = \frac{\rho_l d_p |\mathbf{u}_s - \mathbf{u}_l|}{\mu_l} \quad (4-9)$$

Eulerian dispersed turbulence model has been chosen for this case. It is suitable when there is clearly one primary continuous phase and the other is dispersed dilute secondary phase. For the current case, the mass fraction of particles is smaller than 1% and it is assumed to be granular in the simulation. The turbulent prediction for continuous phase  $l$  has been modified with the term considering interphase turbulent momentum transfer as follows,

$$\frac{\partial}{\partial t}(\alpha_l \rho_l k_l) + \nabla \cdot (\alpha_l \rho_l \mathbf{u}_l k_l) = \nabla \cdot \left( \alpha_l \frac{\mu_{t,l}}{\sigma_k} \nabla k_l \right) + \alpha_l G_{k,l} - \alpha_l \rho_l \varepsilon_l + \alpha_l \rho_l \Pi_{k_l} \quad (4-10)$$

and

$$\frac{\partial}{\partial t}(\alpha_l \rho_l \varepsilon_l) + \nabla \cdot (\alpha_l \rho_l \mathbf{u}_l \varepsilon_l) = \nabla \cdot \left( \alpha_l \frac{\mu_{t,l}}{\sigma_k} \nabla \varepsilon_l \right) + \alpha_l \frac{\varepsilon_l}{k_l} (C_{1\varepsilon} G_{k,l} - C_{2\varepsilon} \rho_l \varepsilon_l) + \alpha_l \rho_l \Pi_{\varepsilon_l} \quad (4-11)$$

where  $\Pi_{k_l}$  and  $\Pi_{\varepsilon_l}$  are the source terms representing the influence of the dispersed phase  $s$  on the continuous phase  $l$ , and  $G_{k,l}$  is the production of turbulent kinetic energy. The terms  $\Pi_{k_l}$  and  $\Pi_{\varepsilon_l}$  take the following form,

$$\Pi_{k_l} = C_s \sum_{p=1}^M \frac{K_{sl}}{\alpha_l \rho_l} X_{sl} (\langle \mathbf{u}''_l \cdot \mathbf{u}''_s \rangle + (\mathbf{u}_s - \mathbf{u}_l) \cdot \mathbf{u}_{dr}) \quad (4-12)$$

which can be simplified as

$$\Pi_{k_l} = C_s \sum_{p=1}^M \frac{K_{sl}}{\alpha_l \rho_l} X_{sl} (k'_{sl} - 2k_l + \mathbf{u}_{sl} \cdot \mathbf{u}_{dr}) \quad (4-13)$$

where  $C_s$  is the model constant ( $C_s=1$  as default);

$k'_{sl}$  is the covariance of the velocities of the continuous phase  $q$  and dispersed phase  $p$ ;

$\mathbf{u}_{sl}$  is the relative velocity;

$\mathbf{u}_{dr}$  is the drift velocity;

$X_{sl} = \frac{\rho_l}{\rho_l + C_{VM}\rho_l}$  for granular flows,  $X_{sl} \sim 1$ .

$\Pi_{\varepsilon_l}$  can be modelled based on the work by Elghobashi and Abou-Arab (1983):

$$\Pi_{\varepsilon_l} = C_{3\varepsilon} \frac{\varepsilon_l}{k_l} \Pi_{k_l} \quad (4-14)$$

where  $C_{3\varepsilon} = 1.2$ . The turbulent viscosity  $\mu_{t,q}$  is written in terms of the turbulent kinetic energy of liquid phase  $l$ :

$$\mu_{t,l} = \rho_l C_\mu \frac{k_l^2}{\varepsilon_l} \quad (4-15)$$

### 4.3.2 Mass transfer models

The mass transfer from aqueous silicate to solid silicon dioxide floccule driven by the diffusion process is from saturated solution to the surface of particles. The general mass fraction transport equation in multiphase flow is expressed by Equation (4-16) (Zhou *et al.*, 2020):

$$\frac{\partial}{\partial t} (\alpha_l \rho_l C_{l,si}) + \nabla \cdot (\alpha_l \rho_l v_l C_{l,si} - \alpha_l \Gamma_{l,si} C_{l,si}) = -S_{l \rightarrow s} \quad (4-16)$$

where  $C_{l,si}$  and  $C_{l,si}^*$  represent concentration and of saturated concentration of silicon source ( $\text{Si(OH)}_4$ ),  $\Gamma_{l,si}$  is the dynamic viscosity of  $\text{Si(OH)}_4$  and  $S_{l \rightarrow s}$  is the mass transfer source term of  $\text{SiO}_2$ . The diffusional mass transfer source term can be written as Equation (4-17) (Bong *et al.*, 2015),

$$-S_{l \rightarrow s} = k_{sl} \alpha_p (C_{l,si}^* - C_{l,si}) \quad (4-17)$$

where  $k_{sl}$  is the solid-liquid mass transfer coefficient and  $a_p$  is the interfacial area per unit volume. The saturation concentration of silicate,  $C_{l,si}^*$ , is calculated on the basis of Henry's law and  $C_{l,si}$  represents the silicate concentration in liquid phase. The volumetric mass transfer coefficient,  $k_{sl}a_p$ , can be obtained from the change of concentration of silicate via the Equation (4-18) (Kato *et al.*, 1998, SCREEN *et al.*, 1972),

$$\ln \left( \frac{[C_{l,si}]}{[C_{l,si}]_0} \right) = -k_{sl}a_p t \quad (4-18)$$

where  $[C_{l,si}]$  and  $[C_{l,si}]_0$  are the silicate concentrations at time  $t = 0$  and  $t = t_1$ , respectively. The value of  $k_{sl}a_p$  can be obtained by the slope of  $\ln \left( [C_{l,si}]/[C_{l,si}]_0 \right)$  against time  $t$ . The solid-liquid mass transfer coefficient,  $k_{sl}$ , can be obtained by dividing the interfacial area of solid particles,  $a_p$ , which is estimated using Equation (4-19) (Sajjadi *et al.*, 2017, Bong *et al.*, 2015),

$$a_p = \frac{6C_v}{d_p} \quad (4-19)$$

where  $C_v$  is the volume fraction of dispersed phase and  $d_p$  is the Sauter mean diameter of particles.

### 4.3.3 Numerical Simulation

To model the swirling vortex flow in the reactor, the Eulerian-Eulerian two-fluid fully coupled model was adopted to simulate the hydrodynamics and the mass transfer characteristics in the confined geometry as shown in Figure 4.2. The grid was generated using the software ANSYS ICEM 15.0. Grid sensitivity trial simulation was carried out and it was found that the adoption of a total amount of about 304,000 cells was

appropriate. Further refining of the mesh has little impact on the simulation results, especially on the turbulence kinetic energy and turbulent dissipation rate.

The governing equations were solved by using commercial software FLUENT 18.0. The modelling approach to simulate hydrodynamics and mass transfer for particle-liquid multiphase system is based on Eulerian-Eulerian two-fluid fully coupled model by treating liquid and particles as two independent pseudo-continuum phases. In the simulation, liquid is set as a continuous primary phase while particles (solid phase) is considered as dispersed phase. The properties of dispersed phase are shown in Table 4.2. Two phases are interpenetrated and interacted with each other. The dominant interphase force is drag force (Wen-yu model). As the swirling flow in the reactor is highly turbulent, RNG k- $\epsilon$  model has been adopted. Phase coupled SIMPLE algorithm has been used for velocity-pressure coupling. The first-order upwind scheme was used for momentum and species transport equation spatial discretization while QUICK scheme was used in continuity discretisation to ensure better estimation of phase volume fraction. For transient simulation, a maximum number of iterations was set to 100 each time step. The solutions were considered to be converged when the residuals of all the variables were less than  $10^{-5}$ . The boundary conditions for inlet 1 and inlet 2 were set to velocity inlet and the outlet of the SVFR was set as the pressure outlet with the static pressure there being specified to be the atmospheric one. This is consistent with the actual experimental condition as the samples are collected from the outlet. Modelling of chemical reaction and ultrasound irradiation was implemented into the simulation once the simulated turbulent flow field in the reactor had been well established. Ultrasound irradiation with a fixed frequency of 20 kHz was imposed as the boundary condition of cyclic sound pressure at the probe tip surface in terms of pressure amplitude  $p_a$  and was evaluated based on Equations (4-20) and (4-21) (Sajjadi *et al.*, 2017, Roohi *et al.*, 2019, Sajjadi *et al.*, 2015b),

Pressure amplitude:

$$p_a = \sqrt{2I_{us}\rho C} \quad (4-20)$$

Pressure:

$$p = p_a \cos(2\pi ft) + \frac{1}{2}\rho v^2 \quad (4-21)$$

where  $C$  is the sound velocity (m/s),  $f$  is the frequency (Hz),  $t$  is the time (s),  $\rho$  is the average density of liquid bulk (kg/m<sup>3</sup>) and  $v$  is the velocity of liquid phase due to propagation of ultrasound waves (m/s).

## 4.4 Results and discussions

### 4.4.1 Synthesised particle characterisation

As the result of shear turbulence controllable synthesis of nano-sized particles in the SVFR and intensification by applying ultrasound irradiation, the morphology of nano-sized mono particles and aggregated particle size distribution of SiO<sub>2</sub> were detected by SEM as shown in Figure 4.3. In fact, all the mono particles are visualised morphologically spherical-like shaped and it can observe that the average aggregated particle size and its distribution is somewhat affected by hydrodynamic conditions. Particle size distribution of all samples are similarly shaped and exhibit their secondary peak in the range of 5 μm to 10 μm. Mono particle aggregates and the main peak of size are located in the range of 30 μm to 50 μm with a sharp decline indicating particles stop growing due to exerting shear force. Moreover, the Sauter mean diameter ( $d_{32}$ ) of aggregated particles counted from sufficient sample in SEM images is as large as 18.42 μm and the Sauter mean diameter is almost monotonically changeable as the ultrasound power increases as well as local turbulent Reynolds number with identical and non-identical inlet velocity of SVFR. As the Reynolds number  $Re_V$  increases from 2620 to 13196, the Sauter mean diameter,  $d_p$ , decreases from 18.42 μm to 10.94 μm and the size distribution becomes narrower with a reduced coefficient of variation (CV). Here,

coefficient of variation (CV), also recognised as relative standard deviation (RSD), is defined as the ratio of the standard deviation  $\sigma$  to the mean of parameters particle diameters  $\mu$  ( $CV = \sigma/\mu$ ), used to standardise measure of dispersion of a probability distribution. It is very interesting to note that as there is two times ratio of the inlet, the Sauter mean diameter,  $d_p$ , falls from 13.26  $\mu\text{m}$  to 12.04  $\mu\text{m}$  with a narrower distribution. Continuous increases in  $R$  leads to larger particle sizes and broader distribution. This may be attributed to the local mixing behaviour where two swirling streams with different inlet velocities meet and the engulfment is weakened due to the retarding action from the slower stream to the faster stream.

The product before filtration is a colloidal suspension of solid particles in the mixture solution and is small enough to be dominated by the short-range force without consideration of the gravitational forces (Brinker and Scherer, 2013) and these nano-sized particles tend to aggregate in aqueous circumstance as shown in Figure 4.4 (a). It can be seen from the TEM images shown in Figures 4.4 (b), 4.4 (c) and 4.4 (d) that the edge of particles coalesces and overlaps due to aggregation. The sphericity and crystalline microstructure have been magnified under enlargement. Figures 4.5 (a) and 4.5 (b) reveal correlations between the average aggregated particle size and coefficient of variation (CV) as a function of turbulent Reynolds number and ultrasound amplitude. The particles are the smallest with the narrowest size distribution ( $d_p/\langle\eta\rangle < 0.36$ ,  $CV < 0.68$ ) produced when ultrasound amplitude applied reaches 50% (600W) and the Reynolds number,  $Re_V$ , based on the vortex core radius is 7859. In contrast, the largest size particles are synthesised and obtained with a wide size distribution when ultrasound is abandoned at  $Re_V = 7859$  and  $Re_V$  is defined as

$$Re_V = \frac{2\omega R_v^2}{\nu} \quad (4-22)$$

where  $\omega$  is the angular velocity calculated on basis of flowrate of inlet 1 and vortex characteristic length  $R_v$  is approximately equal to  $(D-2d)/2$ . To examine the relationship between the particle size distribution and the turbulent shear rate and the intensification of ultrasound irradiation, the ratio of particle diameter to the mean Kolmogorov scale,  $d_p/\langle\eta\rangle$  is introduced. In general, the characteristic particle length ratio  $d_p/\langle\eta\rangle$  changes from 0.24 to 0.41 when the ultrasound amplitude increases from 0 to 50% and it varies as Reynolds number  $Re_V$  based on the vortex characteristic length  $R_v$ . Here,  $D$  is the diameter of the reactor and  $d$  is the diameter of the inlet tube. The local turbulence level can be estimated from the CFD simulation by a turbulent Reynolds number defined as

$$Re_T = \frac{\langle k \rangle}{(\langle \varepsilon \rangle \nu)^{1/2}} \quad (4-23)$$

where  $\langle k \rangle$  and  $\langle \varepsilon \rangle$  are the volumetric averaged turbulent kinetic energy and turbulent energy dissipation rate, respectively. The correlations of characteristic particle length ratio  $d_p/\langle\eta\rangle$  and CV with  $Re_T$  and the strength of applied ultrasound are found to be well represented by using Equations (4-24) and (4-25) while the correlations are plotted in Figures 4.5 (a) and 4.5 (b),

$$\frac{d_p}{\langle \eta \rangle} = 0.58 Re_T^{-0.13} P_A^{0.11} \quad (4-24)$$

$$CV = 0.87 Re_T^{-0.01} P_A^{-0.08} \quad (4-25)$$

where  $d_p$  is actually obtained from the proportion of particle size  $d_{32}$  of arbitrary samples under the condition of ultrasound amplitude from  $P_A = 0$  to  $P_A = 50\%$  and  $Re_V=7859$ .  $P_A$  is defined by

$$P_A = \frac{P}{P_s} \quad (4-26)$$

where  $P_s$  is the maximum ultrasound power that can be applied (1200W for ultrasound processor in this case). As the synthesised particle size is highly influenced by the local turbulent eddy shear  $\sqrt{\frac{\langle \varepsilon \rangle}{\nu}}$ , the Reynolds number,  $Re_T$ , which is characterised by  $\langle \varepsilon \rangle$  can be associated with the Reynolds number  $Re_V$ . It can be seen from Figure 4.6 that the flow in the SVFR can be well approximated by the turbulent Rankine vortex model with

$$\begin{aligned} u_\theta &= r\omega & r &\leq R_v \\ \frac{\partial u_\theta}{\partial r} &= 0 & r &= R_v \end{aligned} \quad (4-27)$$

The mean turbulent energy dissipation rate  $\langle \varepsilon \rangle$  for the turbulent Rankine vortex is as a function of core radius, i.e.  $\varepsilon = \varepsilon(r)$ . It can be assumed that when the swirling flow in the reactor is turbulent and in dynamic equilibrium, the formed turbulent Rankine vortex is spatially filled with the turbulent eddies with all the scales. Thus,  $\langle \varepsilon \rangle_{exp}$  in the experiment can be estimated by the following relation:

$$\langle \varepsilon \rangle_{exp} = 2\nu_{eff}\omega^2 = 2\nu_{eff} \left( \frac{Q_1+Q_2}{\frac{\pi}{2}d_0^2 R_V} \right)^2 = 2\nu_{eff} \left[ \frac{Q_2(1+R)}{\frac{\pi}{2}d_0^2 R_V} \right]^2 \quad (4-28)$$

where  $Q_1$  and  $Q_2$  are the volumetric flow rates of the faster inlet stream and the slower inlet stream, respectively. The epsilon generated from ultrasound irradiation is estimated from actual ultrasound power  $P_{us}'$ .

The nitrogen adsorption/desorption isotherms for SiO<sub>2</sub> samples has been used to characterise the porosity of material by using the Barrett–Joyner–Halenda (BJH) equation. The adsorption average pore width of samples is shown in Figure 4.7. It can be seen from the figure that the application of ultrasound has an impact on particle porosity. When an increase in the ultrasound power was applied, it was observed that

the porosity of SiO<sub>2</sub> particles monotonically changes together with the average pore diameter varying from 65.9 m<sup>2</sup>/g to 193.0 m<sup>2</sup>/g and the corresponding average pore diameter changing from 8.9 nm to 11.7 nm. When the Reynolds number,  $Re_V$ , is increased from 2620 to 13196, it was found from the tests that the BET surface area gradually increases from 78.9 m<sup>2</sup>/g to 92.9 m<sup>2</sup>/g, then suddenly increases to 116.5 m<sup>2</sup>/g once  $Re_V$  reaches 13196 with the pore width being significantly reduced from 15.4 nm to 9.0 nm. For the cases of imbalanced inlet velocity, i.e.  $R > 1$ , the BET surface area of particles experiences a significant increase, varying from 84.2 m<sup>2</sup>/g to 112.6 m<sup>2</sup>/g, while the pore width decreases from 10.7 nm to 6.1 nm, indicating more pore cavities have formed in the particle. However, when  $R$  increases to 5, this trend is reversed with the corresponding BET surface area of 87.4 m<sup>2</sup>/g and pore width of 12.3 nm. This is likely due to the weak aggregation caused by the reduced local turbulent eddy induced shear.

The synthesised particle characterisation has revealed an important fact that the upturn of Reynolds number  $Re_V$  indicates a reduction in the particle size but with higher porosity. This is strongly associated with local turbulence. This varies when the volumetric flowrate ratio increases and the small particles with higher porosity are synthesised when  $R$  is around 2~3. However, the effect of ultrasound irradiation on particle size and porosity is conspicuous and consistent. Higher intensity of ultrasound leads to reduced particles sizes with a narrower distribution and higher porosity with larger pore diameters.

#### **4.4.2 Effect of turbulent intensity and vorticity strength on the synthesis**

As can be seen from the previous sub-sections, the synthesis is strongly influenced by the local turbulence level while the turbulence level can be associated with the turbulent intensity in the SVFR. To better quantify the turbulent intensity and structure of the “Rankine vortex” inside the SVFR, the following definition for the turbulent intensity is introduced, given by

$$I = \frac{\sqrt{k}}{\omega_{R_V}}. \quad (4-29)$$

The tangential velocity is calculated based on the simulation and is shown in Figure 4.6. The overall distribution of tangential velocity can be well fitted and divided into three segments along the radial direction (Wu *et al.*, 2014). The quasi-forced Rankine vortex core is formed at the centre of the chamber with  $|r/R| \leq 0.6$ , while the quasi-free vortex zone is located at the outer layer of the core ( $0.6 < |r/R| \leq 0.9$ ). A very thin boundary layer zone is found in the vicinity of the wall with  $|r/R| > 0.9$ . The simulated tangential velocity distribution,  $u_\theta$ , of the reactant solution along the radial direction in the SVFR under different ultrasound power levels and Reynolds number are nearly symmetrical due to identical inflow rates. As the ultrasound power level is increased, the gradient of the tangential velocity,  $du_\theta/dr$ , increases with the maximum tangential velocity that takes place at around  $r/R = 0.6$ . When the Reynolds number  $Re_V$  increases, a very similar trend is observed. However, the velocity distribution becomes asymmetrical as the volumetric flowrate ratio  $R$  changes. The inlet stream with fast flow engulfs the weaker one to form a swirling vortex but with the deformed vortex core.

The volumetric average turbulence intensity has been obtained based on the simulation and the results are displayed in Figure 4.8. It can be seen that the turbulence intensity has been dramatically intensified by the adoption of ultrasound irradiation of higher power, changing from 120W to 600W via adjusting ultrasound amplitude ( $P_A$ ) from 10% to 50%. However, the turbulence intensity with different Reynolds number  $Re_V$  gradually increases from 15.41% to 15.67% for the given ultrasound irradiation condition and turbulence intensity varies in the range of 15.57% to 15.64% for different volumetric flowrate ratio  $R$ . This may suggest that the increase of the applied ultrasound power level is more effective than the increase of the inlet stream flow rate

(characterised by the increase in the Reynolds number  $Re_V$ ). This may be attributed to the fact that when increasing the inlet stream speed, the turbulent kinetic energy increases but the turbulent dissipation rate also increases. However, as can be seen from Equation (4-28), the increase in  $\langle \varepsilon \rangle$  will be confined by the swirling vortex core.

To further investigate the effect of ultrasound power on turbulence, turbulent kinetic energy distribution in the reactor chamber under different ultrasound power is shown in Figure 4.9. As the ultrasound power increases, the turbulent kinetic energy at the upper layer tends to reduce and turbulent kinetic energy tends to increase at lower part in the chamber. This may attribute to acoustic streaming imposing in form of pressure impulsing ‘Rankine vortex’ towards away from the tip of ultrasound transducer. In addition, as the intensified effect of ultrasound, the strengthened ‘Rankine vortex’ may centrifuge liquid in upper layer.

Figure 4.10 displays the iso-surface contours of vorticity at  $100 \text{ s}^{-1}$  in the reactor chamber when imposing different ultrasound power levels. It can be seen from the figure that with increasing the ultrasound irradiation level, the larger scale vortex structures have been broken into smaller scale vortex structures in the SVFR for the given  $Re_V$ . This is very likely to indicate that the ultrasound waves generate the acoustic streaming in the flow in terms of the local static pressure change while such local static pressure fluctuation may cause the local vortex stretching and deformed so as to break down the original structure with high irregularity, forcing the core of vorticity to a lower position and increasing the overall turbulent dissipation rate in the synthesis process.

#### **4.4.3 Effects of the interaction between turbulence-induced shear and reaction characteristics on the synthesised particles**

In addition to the effect of the local turbulence-induced shear on the synthesised particles, the interaction between the local turbulence and the particle nuclei growth

dominated by reaction process can be characterised by using the Damköhler number,  $Da$ , as discussed below. The particle synthesis process can be considered to consist of two-step reactions (i) homogenous hydrolysis reaction transforming TEOS to  $\text{Si(OH)}_4$ , and (ii) heterogeneous condensation reaction transforming  $\text{Si(OH)}_4$  to  $\text{SiO}_2$ . The hydrolysis reaction is predominant in the present study case. Following (Bałdyga *et al.*, 1995), the Damköhler number is introduced to characterise the interaction of the local turbulence shear and the chemical reaction, defined as the ratio of the typical turbulent eddy time scale to the chemical reaction time scale, which is expressed as

$$Da = \frac{\tau_t}{\tau_c} = \frac{12 \sqrt{\frac{\nu}{\langle \varepsilon \rangle}}}{c'} r' \quad (4-30)$$

where the Damköhler number,  $Da$ , is volumetric averaged. The estimated  $Da$  as well as mean turbulent energy dissipation rate varying with different Reynolds number  $Re_V$  are displayed in Figure 4.11 (a). The chemical reaction time scale  $\tau_c$  is proportional to the reciprocal of reaction constant  $k$  as described in Equation (4-1) and mixing time ( $\tau_t = 12 \sqrt{\frac{\nu}{\langle \varepsilon \rangle}}$ ) is proportional to the Kolmogorov time scale is calculated by  $\tau = (\nu/\varepsilon)^{1/2}$  (Pope, 2001). In consequence,  $Da$  number is found in the order of  $10^{-7}$  to  $10^{-5}$  since the rate of hydrolysis-dominant reaction is comparably slower than the normal precipitation process, slightly decreasing from  $7.77 \times 10^{-7}$  to  $7.73 \times 10^{-7}$  in the range of Reynolds number from 2620 to 13196 when the ultrasound power level of 240W was applied as shown in Figure 4.11 (b), with respect to turbulent time scale from  $1.80 \times 10^{-5}$  to  $1.79 \times 10^{-5}$ . It is noted that the  $Da$  number has decreased as the  $Re_V$  number increases from 2620 to 10479, indicating the chemical reaction effect becomes less contributed compared with the effect of the turbulence-induced shear. As continuous increment of  $Re_V$  number from 10479 to 13196, the  $Da$  number has slightly increased from  $7.727 \times 10^{-7}$  to  $7.732 \times 10^{-7}$ , indicating that the effect of chemical reaction may be still dominated. An increased  $\varepsilon$  value with a greater  $Re_T$  value indicates that the greater local turbulence level is caused by the stronger swirling turbulent vortex flow with the two

higher inlet velocity streams. Consequently, this leads to an enhanced turbulent mixing, producing higher local turbulent shear stresses and enhancing the local mass transfer. It can be seen from Figure 4.11 (c) that the changes in the volumetric flowrate ratio of two inlet streams  $R$  has an unpredictable impact on the interaction between the turbulence and the synthesis reaction as the  $Da$  number fluctuates in range of  $7.75 \times 10^{-7}$  to  $7.78 \times 10^{-7}$ , with the turbulent eddy time scale from  $1.79 \times 10^{-5}$  to  $1.81 \times 10^{-5}$ . Nevertheless, the adoption of ultrasound has a remarkable influence as the  $Da$  number has reduced significantly from  $7.22 \times 10^{-5}$  to  $5.40 \times 10^{-7}$ . The corresponding turbulent eddy time scale is  $7.52 \times 10^{-4}$  without ultrasound power and it decreases to  $5.63 \times 10^{-6}$  when ultrasound power of 600 W is applied. It is indicated that the mass transfer rate is approximately 200 times larger than the reaction rate when the ultrasound power level reaches 600 W compared with cases without adoption of ultrasound irradiation. As the ultrasound power level increases, the local turbulence is intensified due to the turbulence induced by imposing the ultrasound waves and the acoustic streaming results in the generation of the turbulent eddies that will be superimposed on the existing turbulence shear field, thus leading to the intensified reaction rate.

#### **4.4.4 Effect of turbulence-induced shear on mass transfer rates of the synthesised aggregate particles**

As discussed in the previous subsections, the synthesis of aggregated nano-particles is significantly affected by the local turbulence, implying that the local turbulence has an impact on the mass transfer between the reactant solutions and embedded growing nano-particle aggregates due to the reactions. The Sherwood number ( $Sh$ ) is employed to describe the ratio of the mass transfer to mass diffusion, as defined by Equation (4-31):

$$Sh = \frac{k_{sl}d_p}{D_A} \quad (4-31)$$

The aggregated nano-particle has been assumed to be a sphere with the equivalent diameter of  $d_p$ . In the synthesis, the Sherwood number is a function of the Reynolds number based on the diameter of the aggregate particle,  $Re_p$ , and the Schmidt number,  $Sc$ , based on the correlation described by Armenante and Kirwan (1989) and Miller (1971), which can be written as

$$Sh = 2.0 + ARe_p^{0.5}Sc^{0.33} \quad (4-32)$$

where  $Re_p$  and  $Sc$  is given by

$$Re_p = \frac{|u_l - u_p|d_p}{\nu} \quad (4-33)$$

$$Sc = \frac{\nu}{D_A} \quad (4-34)$$

As the synthesised aggregated nano-particle size is small, typically around  $1.5 \times 10^{-5}$  m from the experimental observation, the corresponding Stokes number,  $St_\eta = \frac{\rho_p d_p^2 \sqrt{\epsilon}}{18\nu^{3/2} \rho_L}$ , based on the volume average turbulent energy dissipation rate and Kolmogorov scale, falls into the range from 0.02 to 2.91 when the ultrasound irradiation power is increased from 0 to 600 W. This clearly indicates that the aggregated particles respond well to the local turbulent eddies with the size down to the Kolmogorov scale and are subject to the shear owing to large swirling turbulent eddies without adoption of the ultrasound irradiation. However, the size of the turbulent eddies that have a strong interaction with the aggregated particles will reduce when the ultrasound irradiation is imposed, but the particles will be subjected to the shear action contributed from a wide-ranging size of turbulent eddies. In this case, the local particle velocity may be estimated by Pope (2001) as follows,

$$u_p = 2.0(\varepsilon d_p)^{1/3} \quad (4-35)$$

Considering the impact of turbulence on mass transfer process, Hiromitsu and Kawaguchi (1995) and Abou Al-Sood and Birouk (2007) made an attempt on correlating the effect of the freestream turbulence on the mass transfer rate by introducing the turbulence coefficient  $C(I)$ . Introducing a similar modification to take the turbulence intensification into account, Equation (4-36) can be modified, expressed as

$$Sh = 2.0 + A'Re_p^{0.5}Sc^{0.33}C(I) \quad (4-36)$$

Equation (4-37) can be further rewritten by relating to the Reynolds number  $Re_V$  as

$$Sh = 2.0 + A'Re_V^{0.5}\varphi^{0.5}Sc^{0.33}C(I) \quad (4-37)$$

where  $\varphi$  represents the aggregated nano-particle size against the Rankine vortex core characteristic length of reactor  $R_v$ , defined by

$$\varphi = \frac{|u_l - u_p|d_p}{2\omega R_v^2} \quad (4-38)$$

The coefficient  $A'$  can be obtained by observing the relationship between  $(Sh - 2)/Re_V^{0.5}\varphi^{0.5}Sc^{0.33}$  against turbulence intensity  $I$  based on the experimental data shown in Figure 4.12 (a). The product of constant  $A'$  and turbulent coefficient  $C(I)$  is found to be well fitted by the following relationship:

$$A'C(I) = a(I - b)^c \quad (4-39)$$

where parameters a, b, c are found from the fitting of the calculated data to be:  $a = 0.07 \pm 0.0053$ ;  $b = 13.40 \pm 0.32$ ;  $c = 0.27 \pm 0.02$ . In this case, the coefficient of determination  $R^2 = 0.99967$  (perfect fit when  $R^2=1$ ). The turbulence coefficient  $C(I)$  as a function of turbulence intensity  $I$  is plotted in Figure 4.12 (b) and the deviation is shown as error bars. We thus obtain the Sherwood number for description of the mass transfer in the synthesis of aggregated nano-particle in the SVFR, given by

$$Sh = 2.0 + 0.07Re_v^{0.5}\varphi^{0.5}Sc^{0.33}(I - 13.4)^{0.27}. \quad (4-40)$$

Figure 4.13 shows the Sherwood number changing as characteristic length ratio  $\varphi$  and turbulence intensity  $I$  at Reynolds number  $Re_v=7859$ . Higher Sherwood number ( $Sh>3.5$ ) occurs when  $\varphi$  is larger than  $1 \times 10^{-3}$  where the intensification of ultrasound irradiation enhances the turbulence so that the mass transfer between the particles and the reactant solution is enhanced. In contrast,  $Sh$  number tends to be smaller as the turbulence intensity decreases contributing less to the mass transfer with  $\varphi$  smaller than  $1 \times 10^{-3}$ . To further investigate the correlation between the mass transfer and local turbulent shear in the swirling turbulent flow, a correlation coefficient  $R_{G,Sh}$  between the predicted local reactant consumption rate and the volume average local turbulent shear rate is proposed, which is defined by

$$R_{G,Sh} = \frac{\overline{\langle G \rangle_j \langle Sh \rangle_j}}{\langle G \rangle_{ref} \langle Sh \rangle_{ref}} \quad (4-41)$$

where  $\langle G \rangle_j$  is the volume average turbulent shear rate, subscript  $j$  denotes different cases. They are estimated by

$$\langle G \rangle_j = \frac{1}{V} \int_0^V G \, dV = \frac{1}{V} \int_0^V \sqrt{\frac{\varepsilon}{\nu}} \, dV \quad (4-42)$$

$$\langle Sh \rangle_j = \frac{1}{V} \int_0^V Sh dV \quad (4-43)$$

Figure 4.14 shows the correlation coefficient  $R_{G,Sh}$  change in the SVFR on the conditions of adoption of different ultrasound power for the given  $\nu$  and variation of  $Re_V$  for the given adopted ultrasound irradiation. The change of the correlation coefficient in the SVFR chamber has the following trend. Considering the case without applying ultrasound irradiation as the reference, the correlation  $R_{G,Sh}$  equals one. It increases monotonically when increasing the applied ultrasound power for the given  $Re_V$ , indicating that the mass transfer process is strongly affected by the local turbulence intensification due to the turbulence generation by acoustic streaming. It is postulated that the effect of ultrasound irradiation may significantly enhance the turbulent eddy fluctuations so that the local turbulent shear stresses are increased. When the ultrasound power increases from 0 W to 600 W, the correlation  $R_{G,Sh}$  for the given  $Re_V$  are almost increased up to 2.5 times greater than that without applying the ultrasound irradiation as can be observed from Figure 4.14 (a). The consequence of the acoustic streaming of ultrasound irradiation is to intensify the local turbulence, resulting in the enhancement of the mass transfer between the particles and the reactant. It can be seen from Figure 4.14 (b) that  $R_{G,Sh}$  also increases up to around 1.4 times with increasing  $Re_V$  for the given ultrasound irradiation of 240 W. It is noted here that as  $\langle \varepsilon \rangle = 2\nu\omega^2$ , an increase in  $Re_V$  means the increase in the rotational angular velocity or vorticity in the Rankine vortex core, thus giving out an increase in the local turbulent shear. As the  $Re_V$  increases, higher dissipation takes place, which results in the improved mass transfer and reactant consumption for the particle growth. However, the Sherwood number and the shear rate are highly correlated when volumetric flowrate ratio  $R=2\sim 3$ , it has an unpredictable correlation as volumetric flowrate ratio increases.

#### 4.5 Conclusions

Shear turbulence controllable synthesis of nano-sized particles using a SVFR assisted by ultrasound irradiation has been investigated using both CFD modelling and experimental validation. The effects of the intensification of turbulence by applying ultrasound irradiation and turbulence level in the Rankine vortex core characterised by using the Reynolds number  $Re_T$  on particle synthesis are studied. Characterisation of the synthesised particle morphology, porosity and size distribution are correlated with the local turbulence generated in the SVFR. The conclusions derived from the present study can be summarised as follows:

(1) It was found that when the Reynolds number  $Re_V$  and the adopted ultrasound power increase, the average synthesised  $\text{SiO}_2$  particle size is reduced, accompanied by a narrower particle size distribution and higher porosity. When increasing the inlet reactant solution volumetric flowrate ratio  $R$ , smaller size  $\text{SiO}_2$  particles with higher porosity are obtained only when  $R$  is around 2 to 3. The effect of change in the volumetric flowrate ratio on the synthesised  $\text{SiO}_2$  particle characteristics is weak due to the enhancement of the turbulence shear stresses acting on the particles being restricted by the variation of the turbulent Rankine vortex formed in the SVFR.

(2) It has been affirmed that increasing the Reynolds number  $Re_V$  and the adopted ultrasound power leads to the reduction of  $Da$  number, indicating that the effect of turbulence-induced shear on the synthesised particles increases compared with the effect of hydrolysis in the synthesis process. The adoption of ultrasound irradiation can significantly enhance the intensity of turbulence embedded in the turbulent Rankine vortex formed in the SVFR and change the local turbulent energy dissipation rate as characterised by the local turbulent shear  $\sqrt{\frac{\varepsilon}{\nu}}$ .

(3) By introducing the modified Sherwood number, the correlation of the mass transfer in the interface of the aggregated nanoparticles and the reactants with the local

turbulent shear stresses has been demonstrated. It has been proved that the intensification of ultrasound will enhance the local turbulence and turbulent shear stresses. As a result, the mass transfer has been enhanced. Such spatial correlation can be used to predict the mass transfer for the particles in the synthesis process.

## References

ABOU AL-SOOD, M. & BIROUK, M. 2007. A numerical study of the effect of turbulence on mass transfer from a single fuel droplet evaporating in a hot convective flow. *International journal of thermal sciences*, 46, 779-789.

ARMENANTE, P. M. & KIRWAN, D. J. 1989. Mass transfer to microparticles in agitated systems. *Chemical Engineering Science*, 44, 2781-2796.

BAKŁDYGA, J., PODGORSKA, W. & POHORECKI, R. 1995. Mixing-precipitation model with application to double feed semibatch precipitation. *Chemical Engineering Science*, 50, 1281-1300.

BONG, E. Y., ESHTIAGHI, N., WU, J. & PARTHASARATHY, R. 2015. Optimum solids concentration for solids suspension and solid–liquid mass transfer in agitated vessels. *Chemical Engineering Research and Design*, 100, 148-156.

BRINKER, C. J. & SCHERER, G. W. 2013. *Sol-gel science: the physics and chemistry of sol-gel processing*, Academic press.

CONTIGIANI, C. C., PÉREZ, O. G. & BISANG, J. M. 2018. Local mass-transfer study in a decaying swirling flow electrochemical reactor under single-phase and two-phase (gas-liquid) flow. *Chemical Engineering Journal*, 350, 233-239.

DAI, Y., LV, R., FAN, J., PENG, H., ZHANG, Z., CAO, X. & LIU, Y. 2020. Highly ordered macroporous silica dioxide framework embedded with supramolecular as robust recognition agent for removal of cesium. *Journal of hazardous materials*, 391, 121467.

DE, G., KARMAKAR, B. & GANGULI, D. 2000. Hydrolysis–condensation reactions of TEOS in the presence of acetic acid leading to the generation of glass-like silica

microspheres in solution at room temperature. *Journal of Materials Chemistry*, 10, 2289-2293.

ELGHOBASHI, S. & ABOU-ARAB, T. 1983. A two-equation turbulence model for two-phase flows. *The Physics of Fluids*, 26, 931-938.

GOBINATH, R., RAJA, G., PRASATH, E., SHYAMALA, G., VILORIA, A. & VARELA, N. 2020. Studies on strength characteristics of black cotton soil by using novel SiO<sub>2</sub> combination as a stabilizing agent. *Materials Today: Proceedings*.

GURAV, J. L., RAO, A. V., RAO, A. P., NADARGI, D. & BHAGAT, S. 2009. Physical properties of sodium silicate based silica aerogels prepared by single step sol-gel process dried at ambient pressure. *Journal of Alloys and Compounds*, 476, 397-402.

HAFIZI, A., RAHIMPOUR, M. & HERAVI, M. 2019. Experimental investigation of improved calcium-based CO<sub>2</sub> sorbent and Co<sub>3</sub>O<sub>4</sub>/SiO<sub>2</sub> oxygen carrier for clean production of hydrogen in sorption-enhanced chemical looping reforming. *International Journal of Hydrogen Energy*, 44, 17863-17877.

HARPAZ, D., KOH, B., SEET, R. C., ABDULHALIM, I. & TOK, A. I. 2020. Functionalized silicon dioxide self-referenced plasmonic chip as point-of-care biosensor for stroke biomarkers NT-proBNP and S100 $\beta$ . *Talanta*, 212, 120792.

HIELSCHER, T. 2007. Ultrasonic production of nano-size dispersions and emulsions. *arXiv preprint arXiv:0708.1831*.

HIROMITSU, N. & KAWAGUCHI, O. 1995. Influence of flow turbulence on the evaporation rate of a suspended droplet in a hot air flow. *Heat transfer. Japanese research*, 24, 689-700.

JEEVANANDAM, P., KOLTYPIN, Y. & GEDANKEN, A. 2001. Synthesis of nanosized  $\alpha$ -nickel hydroxide by a sonochemical method. *Nano Letters*, 1, 263-266.

- JORDENS, J., DE COKER, N., GIELEN, B., VAN GERVEN, T. & BRAEKEN, L. 2015. Ultrasound precipitation of manganese carbonate: The effect of power and frequency on particle properties. *Ultrasonics Sonochemistry*, 26, 64-72.
- KATO, Y., HIRAOKA, S., TADA, Y. & NOMURA, T. 1998. Solid—liquid mass transfer in a shaking vessel for a bioreactor with “current pole”. *The Canadian Journal of Chemical Engineering*, 76, 441-445.
- KEYVANLOO, K., HECKER, W. C., WOODFIELD, B. F. & BARTHOLOMEW, C. H. 2014. Highly active and stable supported iron Fischer–Tropsch catalysts: Effects of support properties and SiO<sub>2</sub> stabilizer on catalyst performance. *Journal of catalysis*, 319, 220-231.
- KIM, KS., KIM, JK. & KIM, WS. 2002. Influence of reaction conditions on sol-precipitation process producing silicon oxide particles. *Ceramics international*, 28, 187-194.
- KOCKMANN, N., FÖLL, C. & WOIAS, P. Flow regimes and mass transfer characteristics in static micromixers. *Microfluidics, BioMEMS, and Medical Microsystems*, 2003. International Society for Optics and Photonics, 319-329.
- LEGENTILHOMME, P., AOUABED, H. & LEGRAND, J. 1993. Developing mass transfer for annular swirling decaying flow induced by means of a tangential inlet. *The Chemical Engineering Journal*, 52, 137-147.
- MARIOTTI, A., GALLETTI, C., SALVETTI, M. V. & BRUNAZZI, E. 2019. Unsteady flow regimes in a T-shaped micromixer: mixing and characteristic frequencies. *Industrial & Engineering Chemistry Research*, 58, 13340-13356.
- MILLER, D. N. 1971. Scale-Up of agitated vessels. Mass transfer from suspended solute particles. *Industrial & Engineering Chemistry Process Design and Development*, 10, 365-375.

MORITA, S., IJIMA, M. & TATAMI, J. 2017. SiO<sub>2</sub> nanoparticles surface modified with polyethyleneimine-oleic acid complex as stabilizers of Ni fine particles in dense nonaqueous suspensions. *Advanced Powder Technology*, 28, 30-36.

POPE, S. B. 2001. Turbulent flows. IOP Publishing.

RAHIMI, M., AGHEL, B., HATAMIFAR, B., AKBARI, M. & ALSAIRAFI, A. 2014. CFD modeling of mixing intensification assisted with ultrasound wave in a T-type microreactor. *Chemical Engineering and Processing: Process Intensification*, 86, 36-46.

ROOHI, R., ABEDI, E., HASHEMI, S. M. B., MARSZALEK, K., LORENZO, J. M. & BARBA, F. J. 2019. Ultrasound-assisted bleaching: Mathematical and 3D computational fluid dynamics simulation of ultrasound parameters on microbubble formation and cavitation structures. *Innovative Food Science & Emerging Technologies*, 55, 66-79.

SAJJADI, B., ASGHARZADEHAHMADI, S., ASAITHAMBI, P., RAMAN, A. A. A. & PARTHASARATHY, R. 2017. Investigation of mass transfer intensification under power ultrasound irradiation using 3D computational simulation: A comparative analysis. *Ultrasonics sonochemistry*, 34, 504-518.

SAJJADI, B., AZIZ, A. A. & IBRAHIM, S. 2015a. Mechanistic analysis of cavitation assisted transesterification on biodiesel characteristics. *Ultrasonics sonochemistry*, 22, 463-473.

SAJJADI, B., RAMAN, A. A. A. & IBRAHIM, S. 2015b. Influence of ultrasound power on acoustic streaming and micro-bubbles formations in a low frequency sono-reactor: mathematical and 3D computational simulation. *Ultrasonics sonochemistry*, 24, 193-203.

- SCREEN, E. O. P. M. I., TO, H. T. F. A. S., SUB-CRITICAL, A. A. S. A. & NUMBER, R. 1972. Particle-liquid hydrodynamics and mass transfer in a stirred vessel Part I- Particle-liquid motion. *Chemical Engineering Research and Design*, 50.
- SHOUKRY, E. & SHEMILT, L. W. 1985. Mass transfer enhancement in swirling annular pipe flow. *Industrial & Engineering Chemistry Process Design and Development*, 24, 53-56.
- TIAN, S., GAO, W., LIU, Y., KANG, W. & YANG, H. 2020. Effects of surface modification Nano-SiO<sub>2</sub> and its combination with surfactant on interfacial tension and emulsion stability. *Colloids and Surfaces A: Physicochemical and Engineering Aspects*, 124682.
- USUNE, S., KUBO, M., TSUKADA, T., KOIKE, O., TATSUMI, R., FUJITA, M., TAKAMI, S. & ADSCHIRI, T. 2019. Numerical simulations of dispersion and aggregation behavior of surface-modified nanoparticles under shear flow. *Powder Technology*, 343, 113-121.
- WANG, H., CHEN, Z., CHEN, D., YU, Q., YANG, W., ZHOU, J. & WU, S. 2019. Facile, template-free synthesis of macroporous SiO<sub>2</sub> as catalyst support towards highly enhanced catalytic performance for soot combustion. *Chemical Engineering Journal*, 375, 121958.
- WEN, C. Y. Mechanics of fluidization. *Chem. Eng. Prog. Symp. Ser.*, 1966. 100-111.
- WU, J.-P., ZHANG, Y.-H. & WANG, H.-L. 2014. Numerical study on tangential velocity indicator of free vortex in the cyclone. *Separation and Purification Technology*, 132, 541-551.
- YANO, K. & FUKUSHIMA, Y. 2003. Particle size control of mono-dispersed super-microporous silica spheres. *Journal of Materials Chemistry*, 13, 2577-2581.

YU, J., ZHAO, L. & CHENG, B. 2006. Preparation of monodispersed microporous SiO<sub>2</sub> microspheres with high specific surface area using dodecylamine as a hydrolysis catalyst. *Journal of Solid State Chemistry*, 179, 226-232.

ZHANG, B., LI, J., CHEN, Q. & CHEN, G. 2009. Precipitation of Al (OH)<sub>3</sub> crystals from supersaturated sodium aluminate solution irradiated with ultrasonic sound. *Minerals Engineering*, 22, 853-858.

ZHANG, J.-W., LIU, S.-F., CHENG, C., LI, W.-F., XU, X.-L., LIU, H.-F. & WANG, F.-C. 2019. Investigation of three-dimensional flow regime and mixing characteristic in T-jet reactor. *Chemical Engineering Journal*, 358, 1561-1573.

ZHAO RUI-YU, D. P., LIANG WEN-JIE 1995. Study of the Hydrolysis Kinetics of Tetraethyl Orthosilicate in the Preparation of Monodisperse Silica System. *Acta Phys.-Chim. Sin.*, 11, 612-616.

ZHOU, X., MA, Y., LIU, M. & ZHANG, Y. 2020. CFD-PBM simulations on hydrodynamics and gas-liquid mass transfer in a gas-liquid-solid circulating fluidized bed. *Powder Technology*, 362, 57-74.

## Figures and Graphs

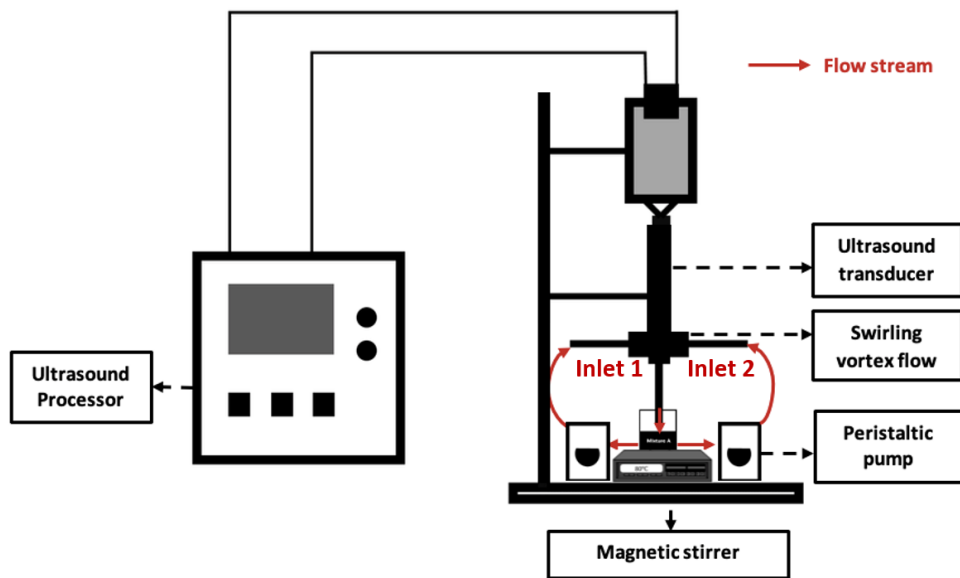


**Figure 4.1** Schematic diagram of the experimental setup of  $\text{SiO}_2$  synthesis using SVFR assist by ultrasound processor.

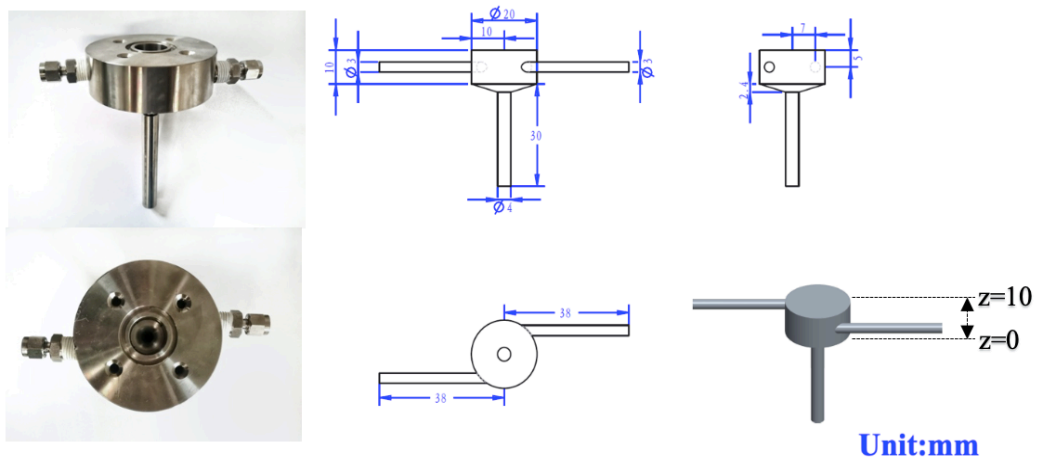
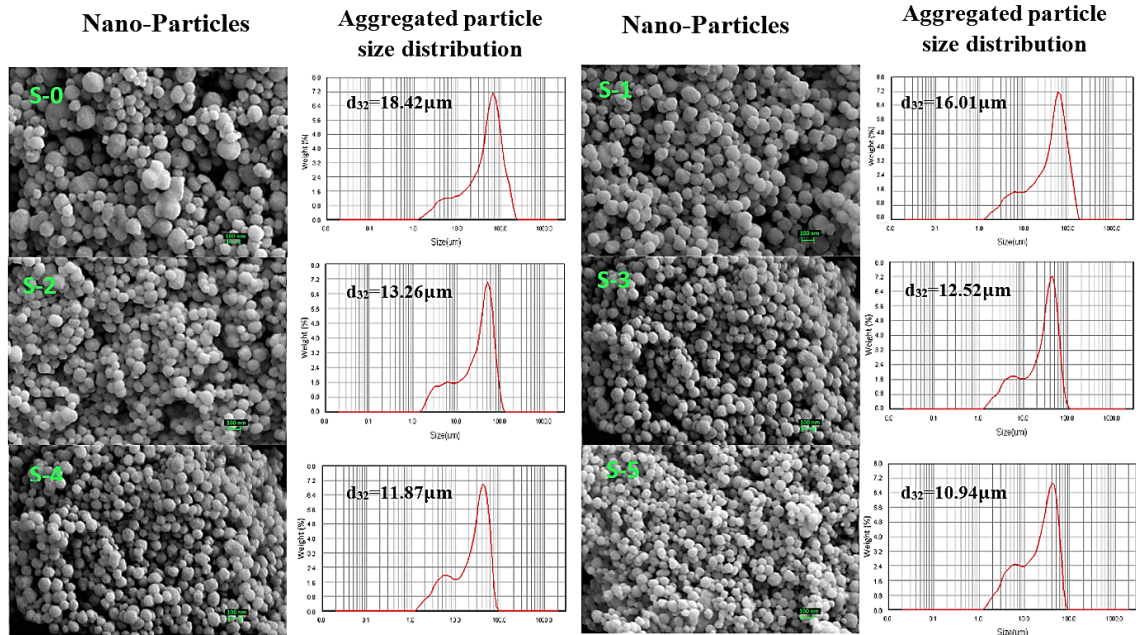
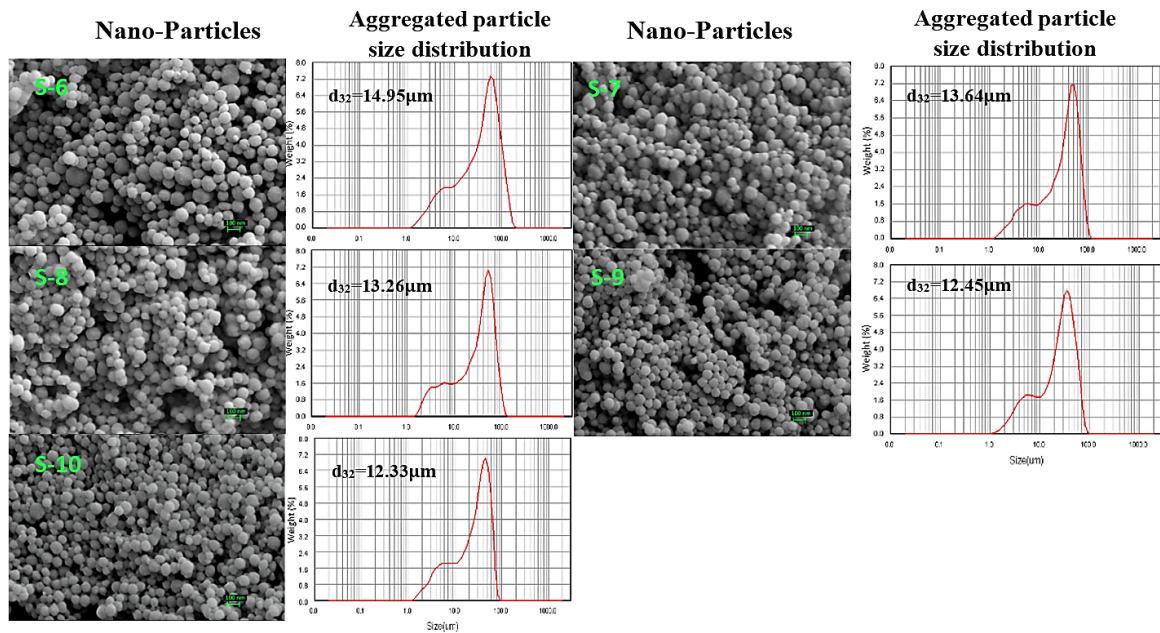


**Figure 4.2** The experimental rig and scaled dimensions of SVFR in millimetres.

(a)



(b)



(c)

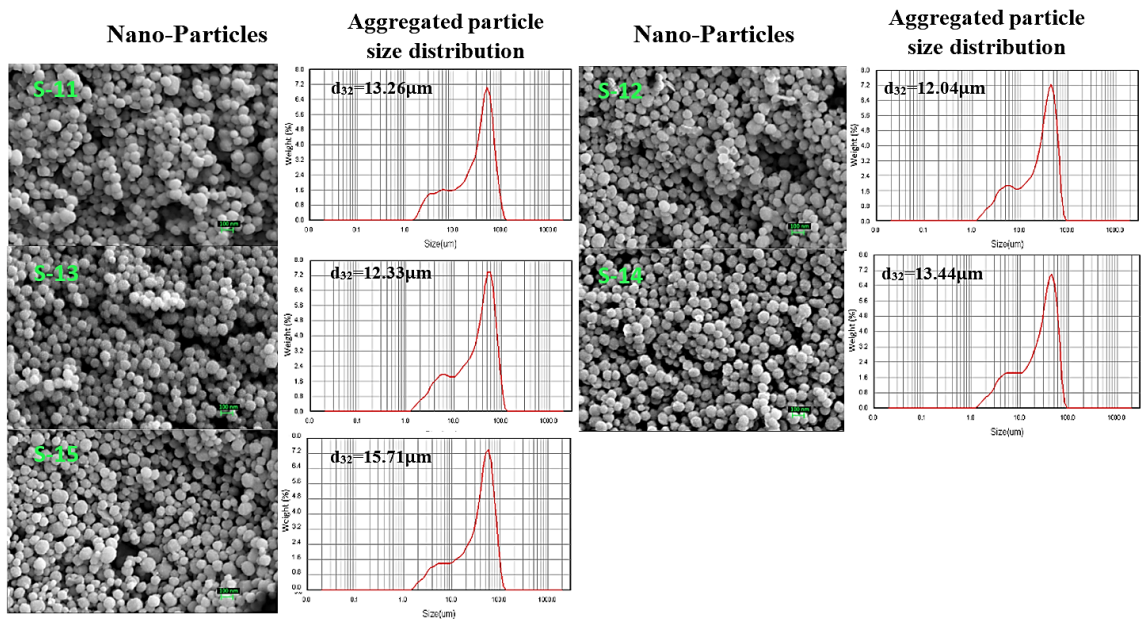


**Figure 4.3** SEM images and the corresponding particle size distribution measured Laser particle size analyzer (LPSA) by of sample SiO<sub>2</sub> synthesised under different condition of (a) Ultrasound power  $P$  at Reynolds number  $Re_V = 7859$ ; (b) Reynolds number  $Re_V$  under the ultrasound power of 240 W; (c) Volumetric flowrate ratio  $R$  under ultrasound power of 240 W.

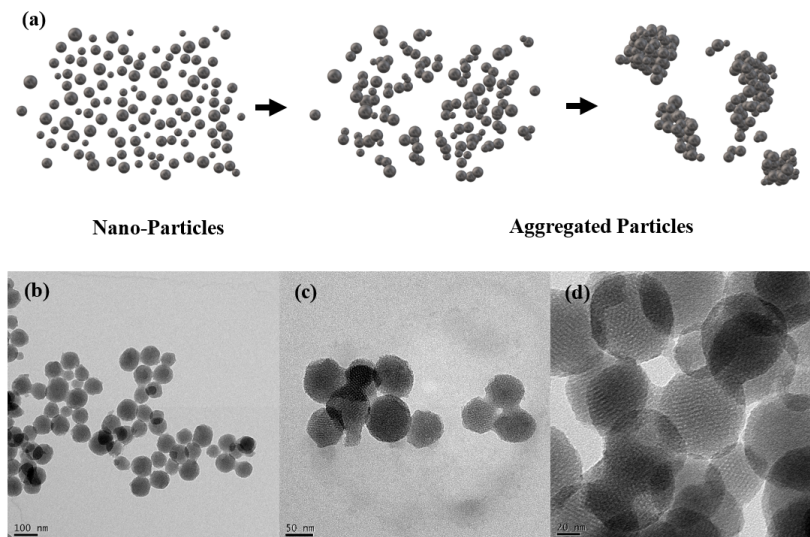


**Figure 4.4** (a) Schematic diagram of SiO<sub>2</sub> nanoparticles aggregation; TEM images of samples synthesised under the ultrasound power of 600 W at Reynolds number  $Re_V = 7859$  under the proportional scale of (b) 100 nm; (c) 50 nm; (d) 20 nm.

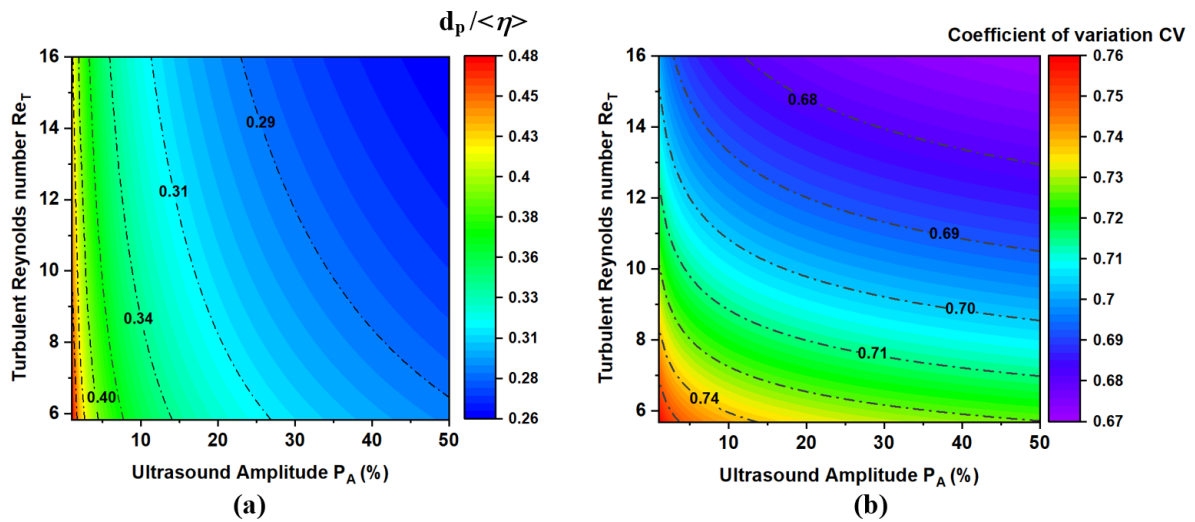


**Figure 4.5** (a) 2D-contour of characteristic particle length ratio  $d_p / \langle \eta \rangle$  versus ultrasound amplitude  $P_A$  (W) and turbulent Reynolds number  $Re_V$  ; (b) 2D-contour of coefficient of variation (CV) versus ultrasound amplitude  $P_A$  (W) and turbulent Reynolds number  $Re_V$ .

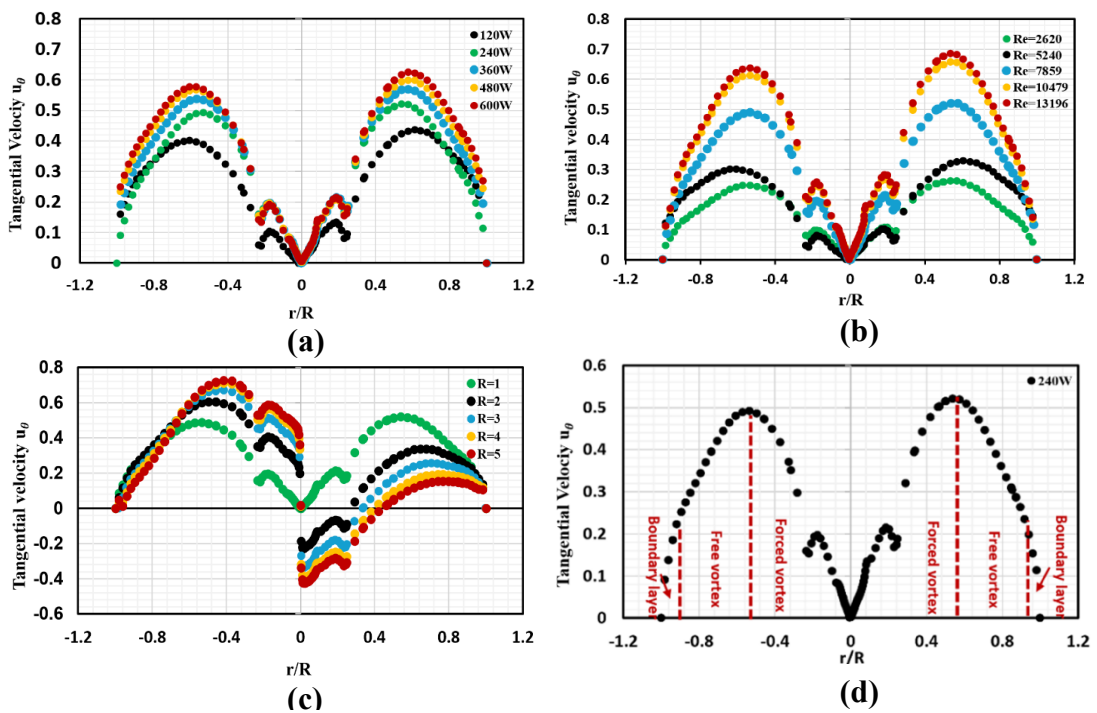


**Figure 4.6** CFD Predicted tangential velocity distribution  $u_\theta$  (m/s) of continuous phase in the SVFR along radial direction at the surface of  $z = 5$  mm for the cases (a) Effect of variation of ultrasound power  $P$  at Reynolds number  $Re_V = 7859$ ; (b) Effect of Reynolds number  $Re_V$  at ultrasound power of 240 W; (c) Effect of variation of volumetric flowrate ratio  $R$  for the given ultrasound power of 240 W; (d) The tangential velocity distribution in radial direction in the Rankine vortex of the SVFR for Reynolds number  $Re_V = 7859$  and the applied ultrasound power of 240 W.

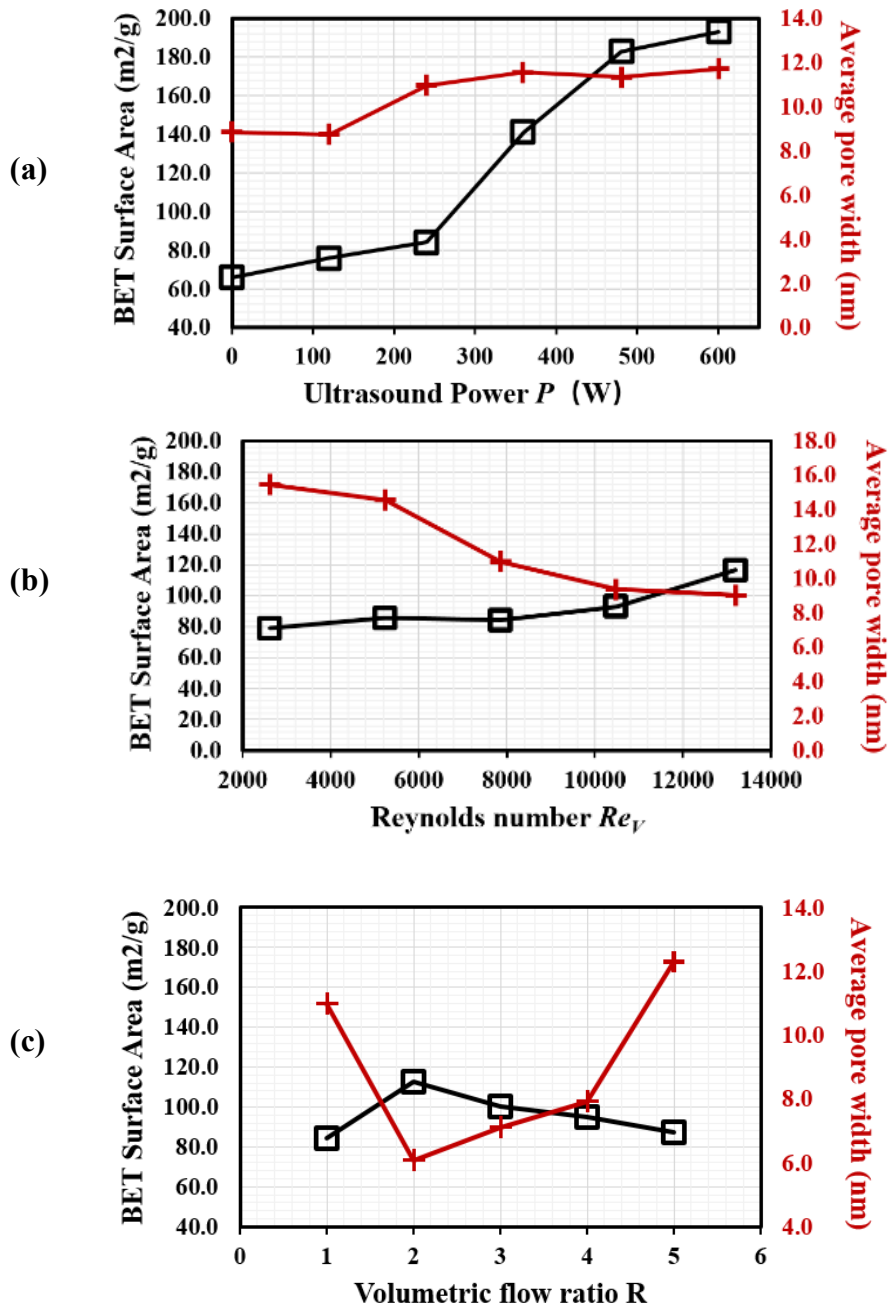


**Figure 4.7** Brunauer-Emmett-Teller (BET) surface area (m<sup>2</sup>/g) and Average pore width (nm) versus (a) Ultrasound power  $P$  at Reynolds number  $Re_V = 7859$ ; (b) Reynolds number  $Re_V$  under ultrasound power of 240 W; (c) Volumetric flowrate ratio  $R$  under ultrasound power of 240 W.

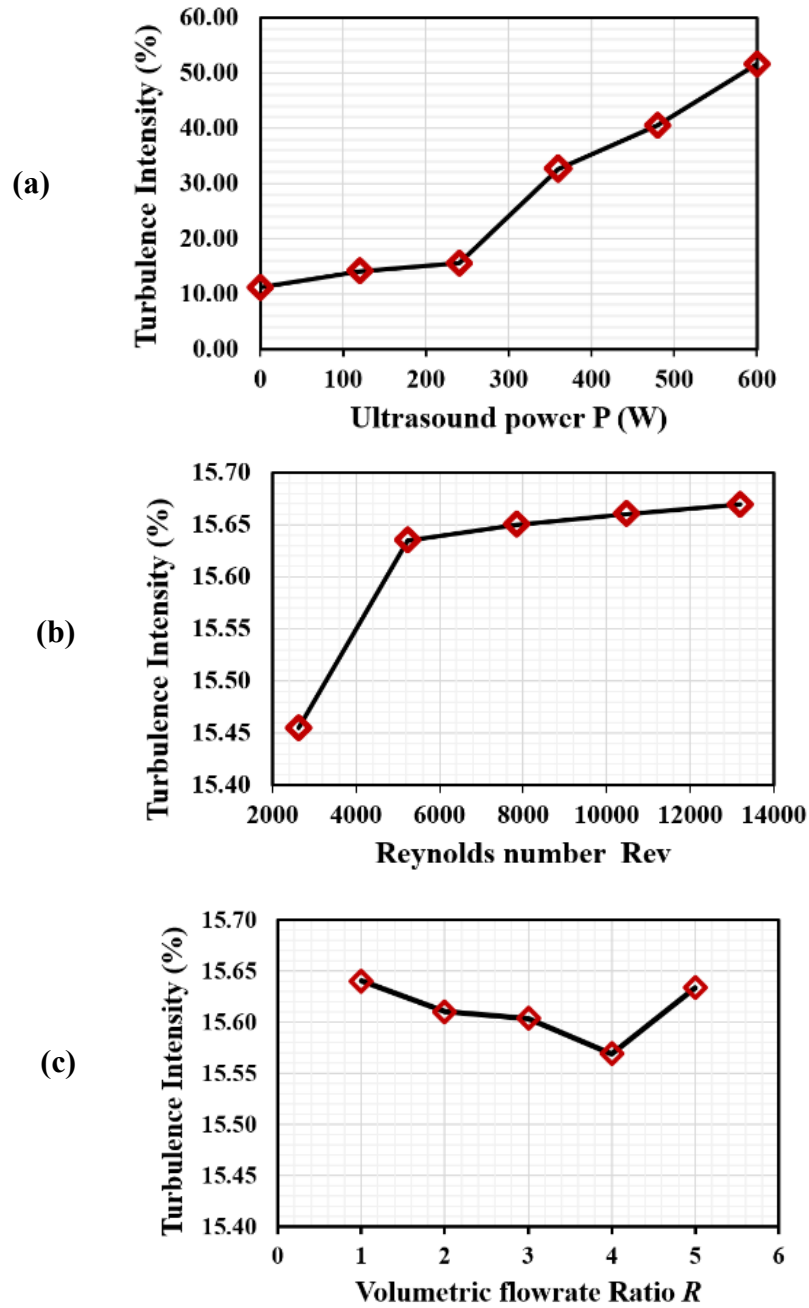


**Figure 4.8** Turbulence intensity versus (a) Ultrasound power  $P$  at Reynolds number  $Re_v = 7859$ ; (b) Reynolds number  $Re_v$  under ultrasound power of 240 W; (c) Volumetric flowrate ratio  $R$  under ultrasound power of 240 W.

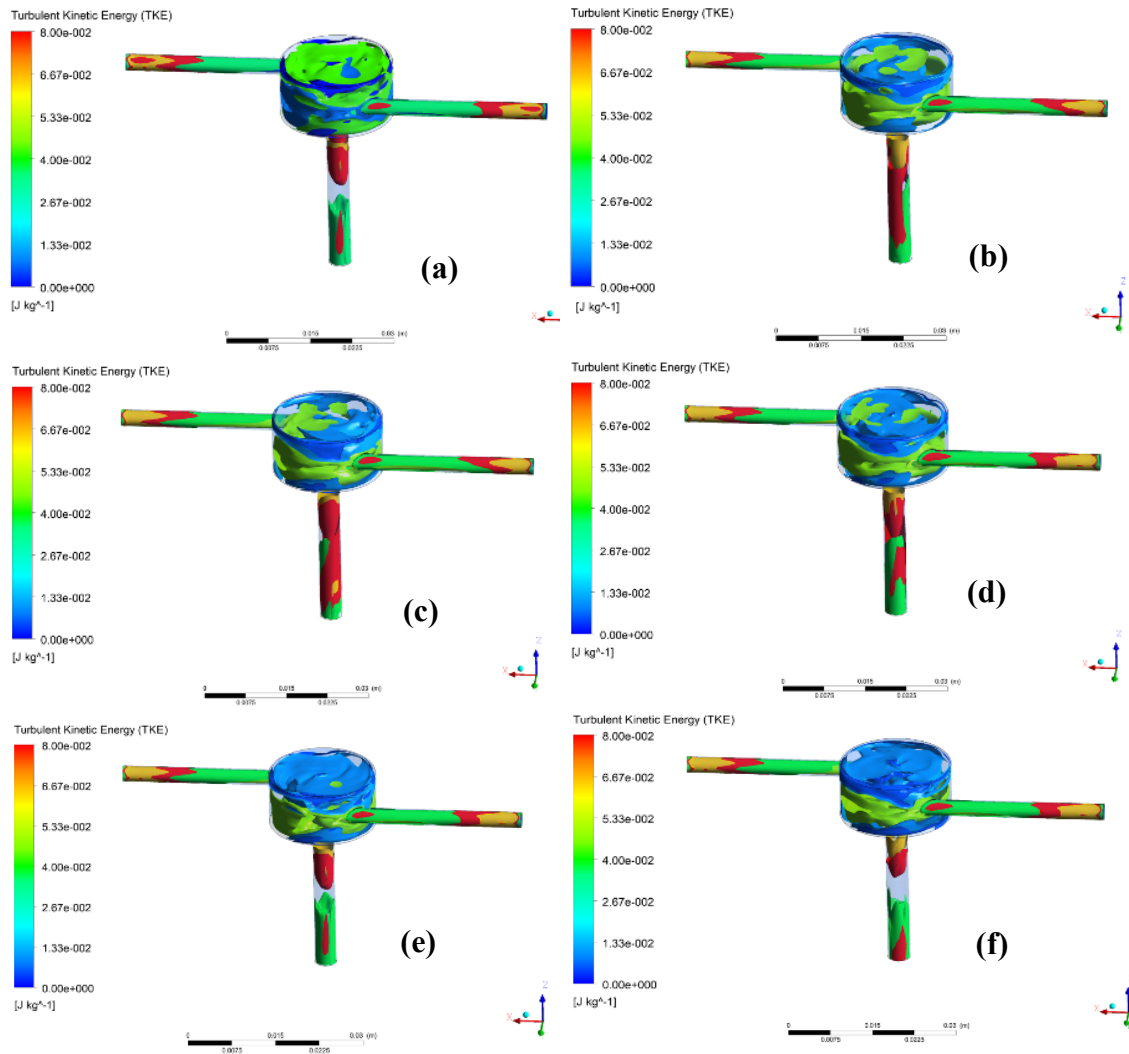


**Figure 4.9** Turbulent kinetic energy distribution in the reactor chamber under ultrasound power of (a) 0 W (b) 120 W (c) 240 W (d) 360W (e) 480 W (f) 600 W at Reynolds number  $Re_V = 7859$  at flow time  $t = 2.0$  s.

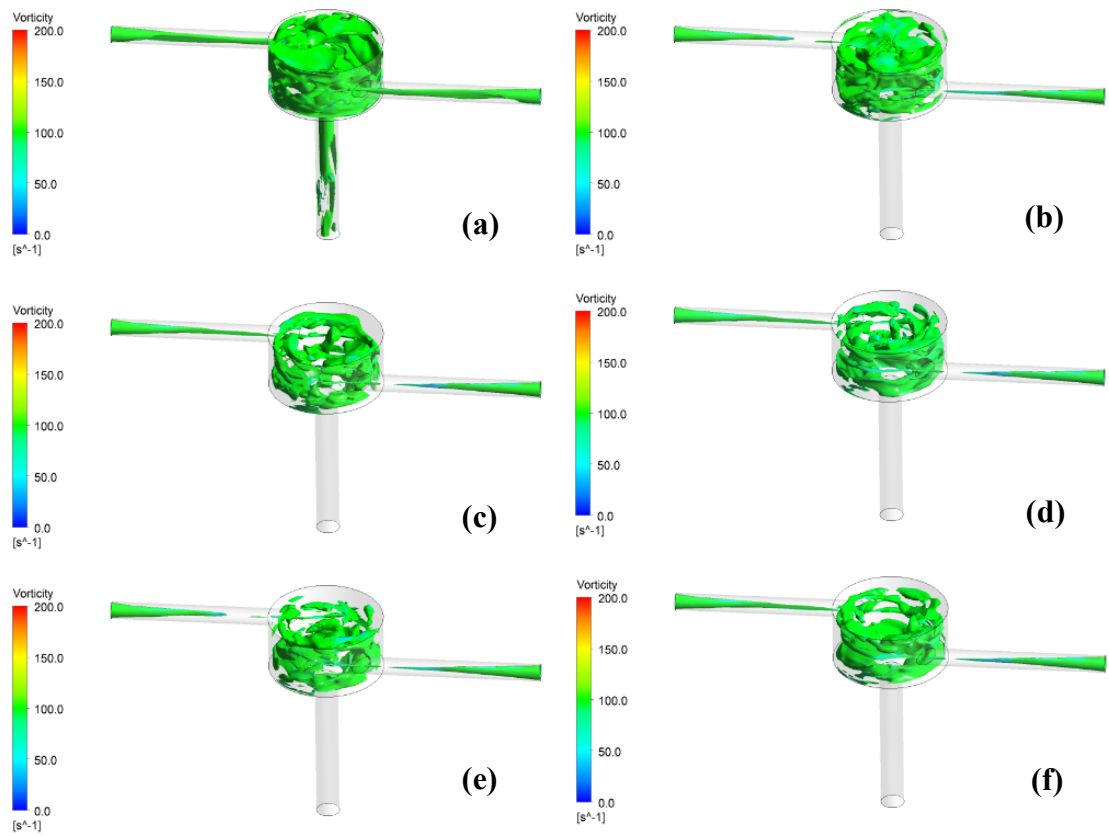


**Figure 4.10** Iso-surface of vorticity at  $100 \text{ s}^{-1}$  in the reactor chamber under ultrasound power of (a) 0 W (b) 120 W (c) 240 W (d) 360 W (e) 480 W (f) 600 W at Reynolds number  $Re_V = 7859$  at flow time  $t = 2.0 \text{ s}$ .

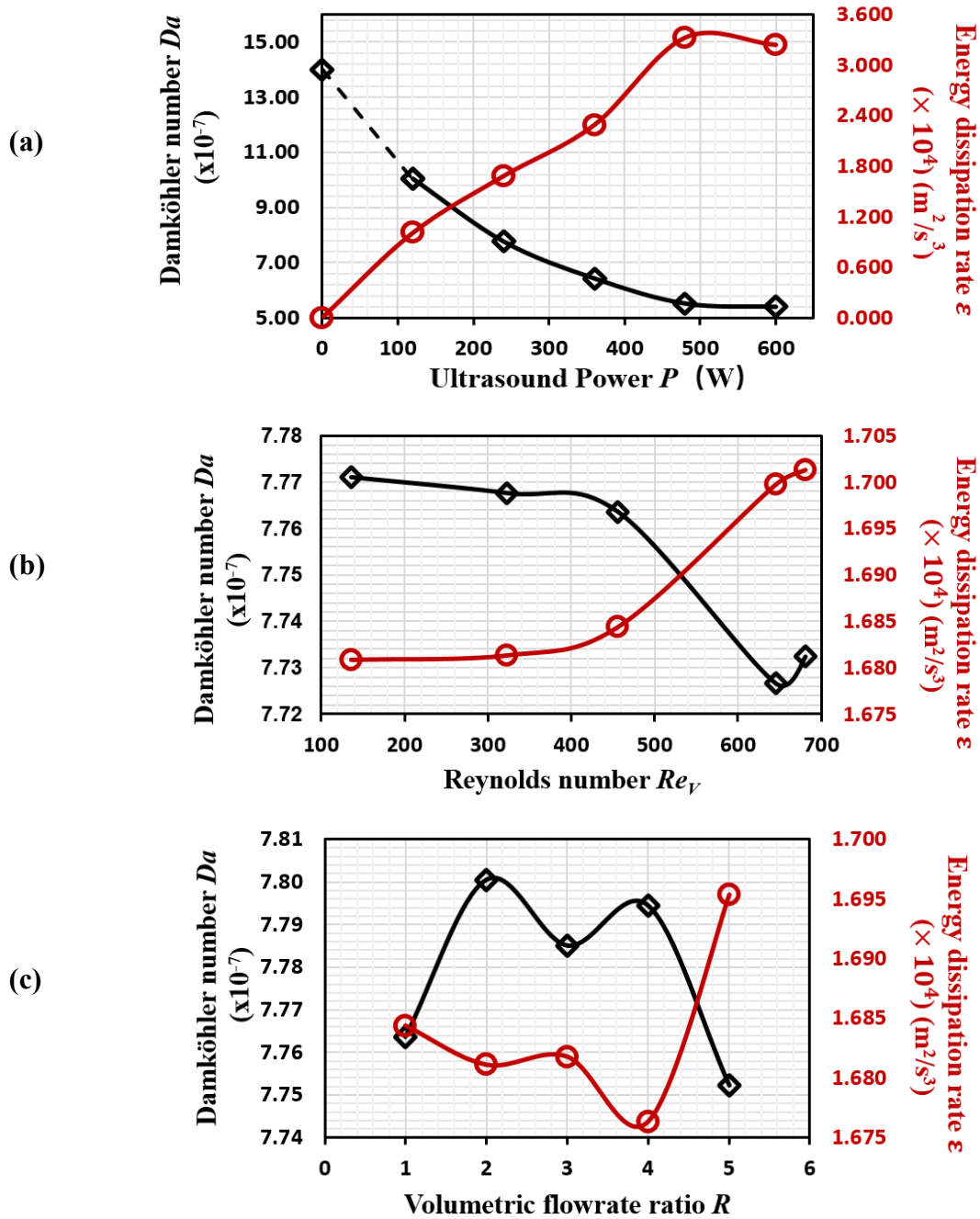


**Figure 4.11** Damköhler number and the mean turbulent energy dissipation rate  $\langle \epsilon \rangle$  versus (a) Ultrasound power  $P$  at Reynolds number  $Re_V = 7859$ ; (b) Reynolds number  $Re_V$  under the ultrasound power of 240 W; (c) Volumetric flowrate ratio  $R$  under the ultrasound power of 240 W.

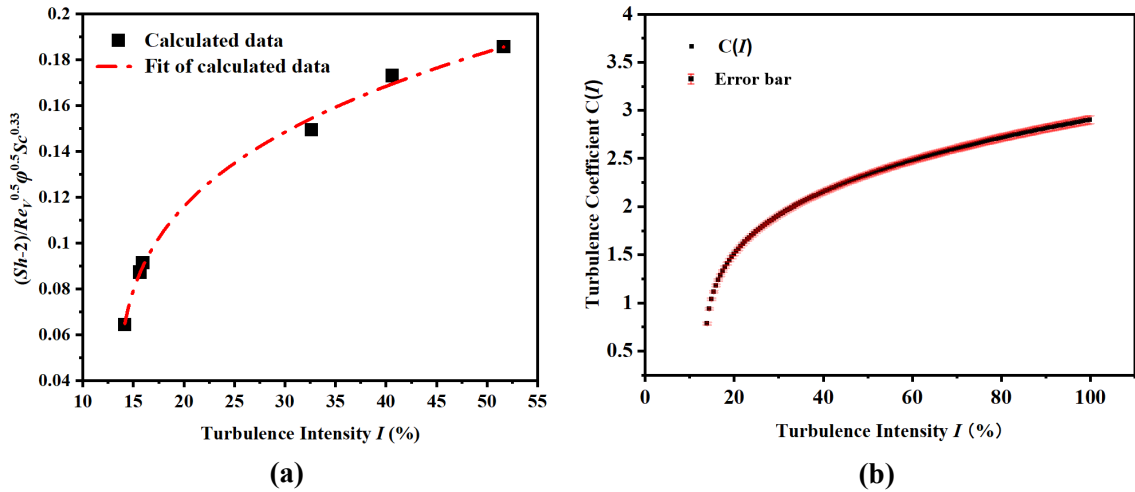


**Figure 4.12** (a)  $(Sh - 2)/Re_V^{0.5} \phi^{0.5} Sc^{0.33}$  versus turbulence intensity  $I$  (%) by adoption of ultrasound power from 0W to 600W and (b) the plot of turbulence coefficient  $C(I)$  as a function of turbulence intensity  $I$  (%) with the error bar of turbulence coefficient.

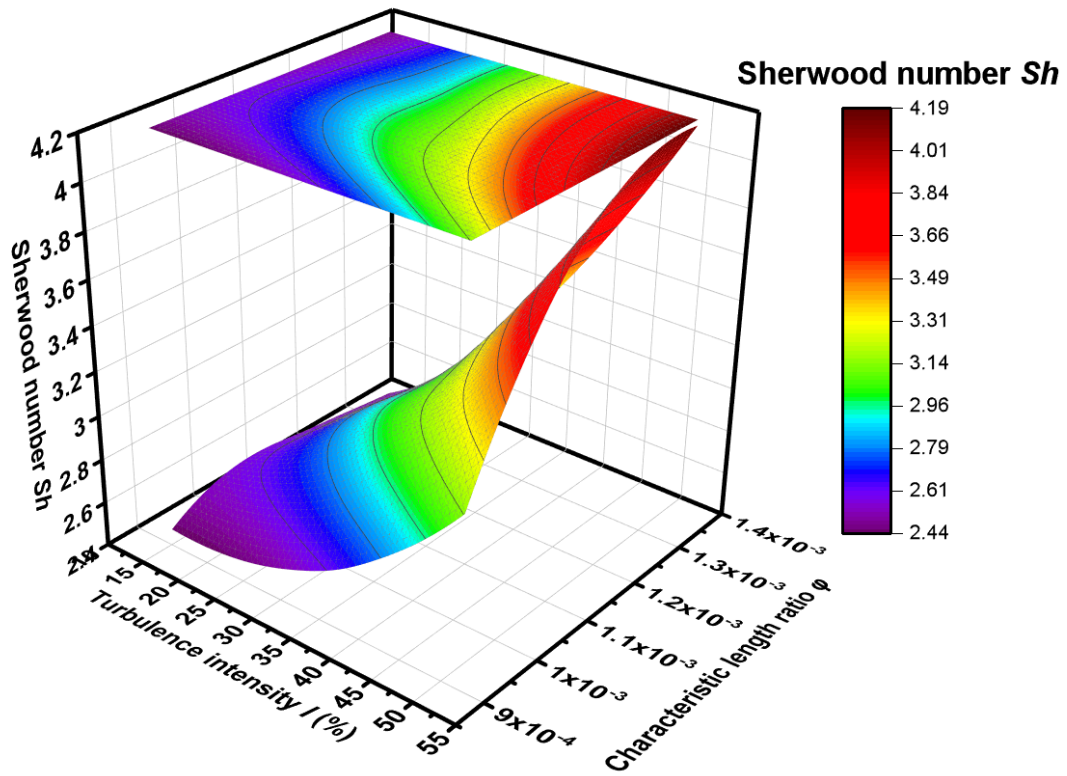


**Figure 4.13** 3D-plot of Sherwood number  $Sh$  versus characteristic length ratio  $\phi$  and turbulence intensity  $I$  (%).

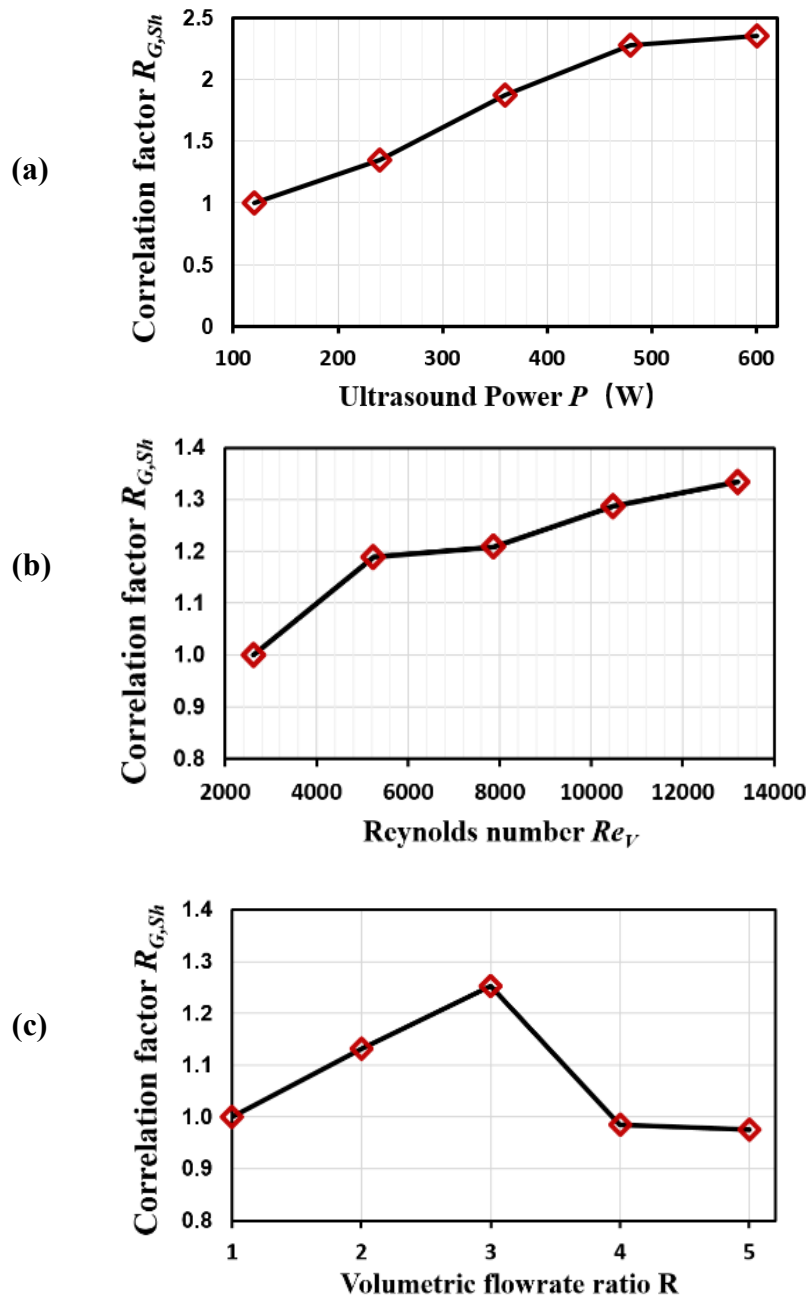


**Figure 4.14** Correlation factor  $R_{G,Sh}$  between the predicted Sherwood number and local shear rate under (a) Ultrasound power  $P$  at Reynolds number  $Re_V = 7859$ ; (b) Reynolds number  $Re_V$ ; (c) Volumetric flowrate ratio  $R$  under ultrasound power of 240 W.

## Tables

**Table 4.1** Samples with different ultrasound power and intensity.

Samples no.	Ultrasound intensity (W)	Ultrasound Amplitude (%)	Reynolds number $Re_V$ for inlet 1	Volumetric flowrate of inlet 1 (ml/s)	Volumetric flowrate of inlet 2 (ml/s)	Volumetric flowrate ratio $R$
<b>Sample Group 1 -Different ultrasound power</b>						
S-0	0	0				
S-1	120	10				
S-2	240	20				
S-3	360	30	7859	5.75	5.75	1
S-4	480	40				
S-5	600	50				
<b>Sample Group 2-Different inlet Reynolds number</b>						
S-6			2620	1.92	1.92	1
S-7			5240	3.83	3.83	1
S-8	240	20	7859	5.75	5.75	1
S-9			10479	7.66	7.66	1
S-10			13196	9.58	9.58	1
<b>Sample Group 3 -Different volumetric flowrate</b>						
S-11				5.75	5.75	1
S-12				7.66	3.83	2
S-13	240	20	-	8.62	2.87	3
S-14				9.2	2.3	4
S-15				9.58	1.92	5

]

**Table 4.2** Properties of dispersed phase.

---

Granular viscosity	Gidaspow
Granular bulk viscosity	Lun <i>et al.</i>
Frictional viscosity	Schaeffer
Granular temperature	Algebraic
Solids pressure	Lun <i>et al.</i>
Radial distribution	Lun <i>et al.</i>

---

## **CHAPTER 5**

# **SHEAR CONTROLLABLE SYNTHESIS OF MESOPOROUS SILICA SPHERICAL PARTICLES USING SWIRLING FLOW REACTORS AND POST-HYDROTHERMAL TREATMENT**

### **SUMMARY**

Chapter 4 has investigated the shear turbulence controllable synthesis of nano-sized particles using a SVFR assisted by ultrasound irradiation using both CFD modelling and experimental validation. The properties of aggregated SiO<sub>2</sub> nanoparticles synthesised in SVFR can be further modified by hydrothermal post-treatment that is discussed in Chapter 5. Unlike IJR and SVFR, the shear force in hydrothermal autoclave driven by natural convection is steady and gentle in laminar flow regimes indicated by Rayleigh number. The precipitated SiO<sub>2</sub> particles were firstly prepared in the swirling flow reactor and then were introduced into the autoclave for a period of up to 1-4 hours subjected to a Rayleigh-Bernard vortex-induced shear. The Rayleigh-Bernard convection in the autoclave using the Rayleigh number characterisation both experimentally and numerically indicates the induced shear flow falls into the regime of laminar shear flow. The post-hydrothermal treatment of the primary particles in the autoclave has clearly indicated that such particles are experiencing the consistent shear owing to the Rayleigh-Bernard induced vortex shear flow driven by the temperature gradient. CFD modelling has reproduced the symmetric vortex flow structure in the hydrothermal autoclave. The particle interactions with such shear flow are modelled using the Euler–Lagrange two-way coupling approach. The particle growth is also investigated based on different hydrothermal conditions for different applied nominal temperatures, treatment duration and the primary particle sizes. The impact of the

exerted shear rate on the particles is particularly studied, focusing on the crystallinity, particle size distribution and porosity. It was found that as the applied nominal temperature surrounding the autoclave increases, the Rayleigh-Bernard convection induced shear is enhanced. A correlation between the Rayleigh convection induced shear rate and aggregated-particle size was proposed to highlight the effect of Rayleigh-Bernard convection induced shear on particle aggregation.

## 5.1 Introduction

Hydrothermal synthesis has been widely adopted to synthesise high-quality single crystal growth and solid-state oxides compounds, as an attractive approach for its simplicity, sustainability and low cost (Hu *et al.*, 2010, Schäfer, 1985, Byrappa and Yoshimura, 2012). Under hydrothermal conditions, the relatively insoluble substances are dissolved and recrystallized from the aqueous solvent under the circumstance of high pressure and temperature gradient (lower than the freezing point at atmospheric pressure) in hydrothermal growth process where a crystal grows under relatively mild shear force and thermal strain producing lower dislocation density compared to the growth under larger temperature gradients (Zunger and Hurle, 1994). The typical hydrothermal system consists of a cylindrical Teflon container and thick wall made from low carbon stainless steel ( $16.3 \text{ W m}^{-1} \text{ K}^{-1}$ , 390 K), vertically placed and designed to maintain good thermal conductivity through the enclosure walls, subjected to pressure and temperature as high as 10 Mpa and 200 °C (Laudise, 1970, Hasany *et al.*, 2012). The aqueous solution inside the hydrothermal vessel reacted in a closed system with air above serving as a thermal insulation layer, leading to buoyancy-driven flow due to the temperature gradient (Ma *et al.*, 2020).

Temperature distribution in the hydrothermal vessel or the temperature gradient applied to the hydrothermal vessel is a decisive factor controlling the particle size and its morphology, which affects the nucleation and grain growth in hydrothermal treatment.

Fu and Ravindra (2012) have studied the thermal effect on the speed of crystal nucleation and growth process, claiming that higher temperature leads to faster nucleation than crystal growth process. Thus, fabrication of smaller sized particles and control of grain growth may be realised by adopting a prolonged reaction duration. Similar conclusions were also drawn from the works done by Habib *et al.* (2008), which indicates crystallite size of BaTiO<sub>3</sub> to decrease at higher temperature and that the treated BaTiO<sub>3</sub> particles are porous irregularly shaped at 90 °C. Consequently, the particles turn to present a compact faceted shape at 150 °C. Another example is BiVO<sub>4</sub> particles preparation via a hydrothermal process by using cetyltrimethyl ammonium bromide (CTAB) as a template-directing reagent. The experimental results have clearly shown the BiVO<sub>4</sub> particles have changed from the shape of the microsphere with mixed tetragonal and monoclinic phases at a relatively low hydrothermal temperature ( $\leq$  160 °C) to the lamellar shape with a pure monoclinic phase at temperature around 200 °C (Ke *et al.*, 2009). Furthermore, owing to the temperature difference in a vessel, ‘Rayleigh-Bénard vortex’ describing annular convection motion in forms of the hexagonal pattern is produced where flows are driven by buoyancy due to the temperature gradient caused by uneven heat conduction (Wesfreid, 2017, Ma *et al.*, 2020). Both thermal impact and hydrodynamics caused by temperature difference were evaluated and analysed in these papers. Other conditions such as solvent type, viscosity, pressure, reaction duration and reactor geometry are also found to affect the particle synthesis, especially for crystal nucleation and growth (Denkbaşı *et al.*, 2016, Wesfreid, 2017, Yu *et al.*, 2007, Kolen'ko *et al.*, 2004). The aforementioned studies have shown the fact that the particle product characteristics such as morphology, size distribution, porosity, microstructures, phase composition, surface chemical properties even photocatalytic activity and magnetism could be modified by manipulating and optimising the operations used in hydrothermal treatment (Yu *et al.*, 2007, McDonnell *et al.*, 2018).

The present study attempts to explore the impact of hydrothermal post-treatment on the

fabrication of silica dioxide particles that have been pre-prepared using a SVFR (Guo *et al.*, 2020). The reactants were mixed and the primary silica dioxide particles were prepared in the SVFR, assisted by applying ultrasound irradiation. The hydrodynamics of post-synthesis using the hydrothermal treatment on modifying the shape of the particles and porosity are investigated by experimental means and CFD modelling approach, focusing on the hydrodynamic conditions in the hydrothermal vessel. It should be noted that hydrothermal methods have been adopted for the synthesis of silica-related micro-/nanomaterials (Yu *et al.*, 2011, Galarneau *et al.*, 2006, Yu *et al.*, 2012). Specifically, the hydrothermal synthesis and post-treatment were found to be effective to improve the hydrothermal stability, mesoscopic regularity and extended pore size (Pan *et al.*, 2009, Sayari, 2000). Martin *et al.* (2002) have developed an approach via alkaline hydrothermal treatment for better controlling the mesoporosity in the pre-formed silica in the dissolution/regrowth kinetics in the range of temperature 373 K to 423 K. Optimization on controlling the particle shape and mesophase self-assembly that is applicable in chromatography applications was also realised as reported in the literature (Galarneau *et al.*, 2006). Bettermann and Liebau (1975) have studied the transformation of amorphous silica in the forms of cristobalite and keatite to crystalline silica on different hydrothermal conditions. Their results have revealed that the routes of the silica transformation process are strongly associated with the pressure, temperature, reaction duration and the starting chemicals in the hydrothermal treatment.

The challenges encountered to conduct the experiment in hydrothermal autoclaves comprise not only extreme operation conditions of high temperature and pressure but also its invisibility. Most importantly, the lack of a clear understanding of the correlations between the hydrodynamics and particle growth mechanism in a hydrothermal vessel is the most obstacle for the application of the hydrothermal approach. Consequently, the CFD simulation approach is usually adopted to investigate the hydrodynamics inside the autoclaves. Li *et al.* (2003) have carried out a series of

numerical simulation to investigate particle crystallisation influenced by Rayleigh natural convections in the hydrothermal autoclaves with different aspect ratios. Their results on the characterisation of bulk flow and particle growth have indicated that an increased aspect ratio would contribute to alternation of Rayleigh instability induced velocity field and likely temperature reduction in the core, giving out a relatively uniform growth of crystals. They have also indicated that buoyancy-driven convection in the hydrothermal autoclave can take place due to the temperature variation in different parts of the autoclaves. Klipov and Shmakov (1991) have claimed that there exists a strong correlation between the fluid flow and the crystal characteristics on its shape, morphology, growth rate, macroscopic defects and inclusion density.

The present work aims to further look into the shear controllable synthesis process in the hydrothermal vessel for silica particle synthesis based on the correlation between the particle characteristics such as particle size distribution, porosity and crystallinity and hydrodynamic conditions used in the hydrothermal treatment. SiO<sub>2</sub> particles were synthesised via a pre-step swirling flow reactor followed by using a post-hydrothermal treatment, where the primary particles or SiO<sub>2</sub> flocs were further subjected to the shear influence through the Rayleigh convection in a hydrothermal autoclave. The hydrodynamics in the autoclave is modelled using the CFD modelling and the correlation between the hydrodynamics and particle properties such as particle diameter, morphology, uniformity and porosity are particularly sought. Section 5.2 presents the experimental details while Section 5.3 presents the theoretical and CFD modelling of the Rayleigh convection in the autoclave for looking into the local shear experienced by SiO<sub>2</sub> particles and the particle dispersion in the autoclave. Section 5.4 presents the results and discussion, especially for the correlation between the local shear and those synthesised SiO<sub>2</sub> particle properties, and finally, Section 5.5 summarises the conclusions derived from the study.

## **5.2 Experimental**

### **5.2.1 Chemicals**

Cetyltrimethyl Ammonium Bromide (CTAB), NaOH solution (2 M) and tetraethyl orthosilicate (TEOS > 28.5 %) were all purchased from Sinopharm Chemical Reagent Co., Ltd. 1g CTAB was required to be fully dissolved in 480 ml of deionised water with 3.5 ml of NaOH solution (2 M) together, which forms the mixture A. After the CTAB was fully dissolved at the constant temperature of 80 °C, 5 ml of tetraethyl orthosilicate (TEOS > 28.5 %) was added into the mixture A dropwise to prepare for SiO<sub>2</sub> floccule.

### **5.2.2 Silica sources preparation**

Primary particles were synthesised in the SVFR which consists of a short circular cylindrical chamber (D = 20 mm, H = 10 mm) embedded in a stainless-steel block with two guided introduction thin pipes that allow the solution to tangentially flow to enter the chamber. Samples of the primary particles were obtained, respectively, by applying the ultrasound irradiation with ultrasound power 120 W, 360 W and 600 W at a constant flow rate of 5.75 ml/s for each inlet, circulating in the SVFR for 30 min at 353 K. The labelling of samples of primary particles synthesised with different experimental conditions are listed in Table 5.1.

### **5.2.3 Hydrothermal post-treatment of the silica sources**

The experimental setup and processes are shown in Figure 5.1. After the sample flocs were collected from the outlet of the pre-step swirling flow reactor, these prepared sample flocs with the flocculent solution were dispersed and the 75 ml formed mixture (containing ~0.21 g primary SiO<sub>2</sub> particles) was then transferred to an autoclave. The autoclave was closely sealed, placed in an oven and hydrothermally heated to the nominally measured temperature in the range of 373 K to 413 K for the different

duration as listed in Table 5.1. After finishing this step, the silica particles were obtained by filtering flocs via a vacuum circulating pump and washed 3 times with the deionised water. The obtained flocs were then dried for 5 hours at 100 °C in the oven. The white powdery SiO<sub>2</sub> particles were obtained after free cooling.

#### **5.2.4 Characterisation**

The prepared white powdery SiO<sub>2</sub> particles were subjected to X-ray diffraction (XRD) characterisation. The X-ray diffraction (XRD) patterns were collected by Bruker AXS D8 ADVANCE using Cu K $\alpha$  radiation ( $\lambda=1.5406 \text{ \AA}$ ) in a range of 10° to 90°. Chemical compositions were verified with Fourier-transform infrared spectroscopy (FT-IR) measurements, Bruker V70, U.S.A. The size distribution and morphology of silica particles were determined by scanning electron microscope (SEM), Sigma VP, ZEISS, Germany and transmission electron microscope (TEM), Hitach H-7500. The Brunauer-Emmett-Teller (BET) surface area was detected by carrying out the nitrogen adsorption experiments using ASAP 2020 (Micrometrics, U.S.A) and thermal gravimetric was conducted by thermogravimetry and differential scanning calorimetry (TG-DSC, NETZSCH STA 449 F3 Jupiter, Germany).

### **5.3 Mathematical Modelling**

#### **5.3.1 Governing equations**

In order to get physical insight into the mechanism of SiO<sub>2</sub> particle growth in the hydrothermal autoclave, a two-dimensional volume of fluid (VOF) coupled with discrete particle motion (DPM) modelling approach has been adopted. It has been assumed that the Rayleigh convection caused by the applied temperature gradient on the autoclave is axisymmetric on the major axis of the hydrothermal autoclave. As there exists an interface between the SiO<sub>2</sub> floc solution and the air inclusive in the autoclave, the VOF is used to model the Rayleigh convection induced vortex flow (van Sint

Annaland *et al.*, 2005) (Brackbill *et al.*) while the DPM model is used to track the SiO<sub>2</sub> particle dispersion in such flow.

### **Rayleigh convection in the hydrothermal autoclave**

The VOF model describing the flow of the SiO<sub>2</sub> floc solution inside the hydrothermal autoclave was adopted, coupling with the energy conservation to consider the effect of the temperature gradient imposed to the hydrothermal autoclave outer-surface. The governing equations to describe such a flow in the hydrothermal autoclave are given by

Continuity equation:

$$\frac{\partial \rho}{\partial t} + \nabla \cdot (\rho \mathbf{u}) = 0 \quad (5-1)$$

Momentum equation:

$$\frac{\partial(\rho \mathbf{u})}{\partial t} + \nabla \cdot (\rho \mathbf{u} \mathbf{u}) = -\nabla p + [\mu(\nabla \mathbf{u} + (\nabla \mathbf{u})^T)] \nabla^2 \mathbf{u} + \rho \mathbf{g} + \mathbf{F}_D + \mathbf{F}_b \quad (5-2)$$

Volume fraction equation:

$$\frac{\partial}{\partial t} (\alpha_L \rho_L) + \nabla \cdot (\alpha_L \rho_L \mathbf{u}) = 0 \quad (5-3)$$

Energy equation:

$$\frac{\partial \rho_L T}{\partial t} + \nabla \cdot (\rho_L \mathbf{u} T) = \frac{k}{c_p} \nabla^2 T \quad (5-4)$$

where  $\mathbf{u}$  is the velocity vector, and  $\alpha_L$  is the solution phase fraction. The volume fraction of the air and solvent liquid phases should sum to be unity, one can calculate the volume fraction of the air phase ( $\alpha_g$ ) based on the following equation:

$$\alpha_L + \alpha_g = 1 \quad (5-5)$$

The volume-fraction-averaged density and viscosity are described by:

$$\rho = \alpha_L \rho_L + (1 - \alpha_L) \rho_g \quad (5-6)$$

$$\mu = \alpha_L \mu_L + (1 - \alpha_L) \mu_g \quad (5-7)$$

Due to the existence of temperature gradient, the induced buoyancy force,  $F_b$ , on basis of Boussinesq approximation considering density variation in the autoclave can be estimated by

$$F_b = \rho_L g \beta (T - T_0) \quad (5-8)$$

As the solvent solution in the hydrothermal autoclave is treated as incompressible fluid, the solution density appeared in the above equations is evaluated using the Boussinesq approximation to consider the buoyancy effect (Li *et al.*, 2006, Scott and Richardson, 1997), given by

$$\rho_L = \rho_{L,0} [1 - \beta (T - T_0)] \quad (5-9)$$

where  $\beta$  is the thermal expansion coefficient;  $T_0$  is the reference temperature based on the average over the temperatures of  $T_1$  and  $T_2$ . With the hydrothermal autoclave reactor adopted in the present study, the Rayleigh number based on the characteristic

length of the reactor,  $Ra_D = g\beta\Delta T L^3/\nu^2 Pr$ , is estimated to be with magnitude of  $10^6$ . The flow with such a Rayleigh number should be in the unsteady laminar regime, since the previous studies have indicated that the flow becomes turbulent when Rayleigh number is in the order of  $1.0 \times 10^8$  (Li *et al.*, 2005, Li *et al.*, 2006). Numerical simulation results presented in the latter section of this paper also affirm that the flow is in the unsteady laminar regime. The boundary condition imposed for the sidewall of the autoclave has been treated as no-slip with constant temperature. For top and bottom walls, it is no-slip and adiabatic conditions.

### **SiO<sub>2</sub> particle dispersion**

In order to reveal the effect of Rayleigh convection induced shear on the particle dispersion, the trajectories of SiO<sub>2</sub> particles in the hydrothermal autoclave were calculated by integrating the equation of motion using the Lagrangian approach, where the forces acting on the particles through the interactions between the particles and the floc solution are mainly the drag and thermophoretic forces (Xu *et al.*, 2013). The equation of motion can be written as

$$\frac{d\mathbf{u}_p}{dt} = f_D(\mathbf{u}_l - \mathbf{u}_p) + \frac{g(\rho_p - \rho_l)}{\rho_p} + \mathbf{F}_T \quad (5-10)$$

where  $f_D(\mathbf{u}_l - \mathbf{u}_p)$  is the drag force per unit mass and the factor  $f_D$  is defined by

$$f_D = \frac{18\mu}{\rho_p d_p^2} \cdot \frac{C_D Re_p}{24} \quad (5-11)$$

where  $Re_p$  is the particle Reynolds number, estimated by  $Re_p = \frac{\rho_L d_p |u_l - u_p|}{\mu_L}$ .

Considering the pre-prepared SiO<sub>2</sub> from the SVFR may possess irregular shapes, the drag coefficient  $C_D$  is defined as:

$$C_D = a_1 + \frac{a_2}{Re} + \frac{a_3}{Re^2} \quad (5-12)$$

where  $a_1$ ,  $a_2$  and  $a_3$  are constants when the particle is assumed to be spherical according to Morsi and Alexander (1972). In addition, as the movement of SiO<sub>2</sub> particles in the floc solution is subjected to a steady temperature gradient, the thermophoresis phenomenon may have a major impact on particle dispersion, such force is also accounted in the modelling, given by

$$\mathbf{F}_T = -D_T \frac{1}{m_p T} \nabla T \quad (5-13)$$

The trajectories of SiO<sub>2</sub> particles were tracked by solving Equation (5-10) coupling with the solution of Equation (5-2) in an Eulerian frame for the velocity distribution in the floc solution in the hydrothermal autoclave.

### 5.3.2 Numerical modelling

To better specify the thermal boundary conditions applied to the outer surfaces of the hydrothermal autoclave, the temperature distribution around the hydrothermal autoclave which was placed in the muffle furnace was measured and validated by CFD modelling. The CFD simulation has adopted a simplified 2D muffle furnace model, which the actual temperature field in the muffle furnace is generated in an enclosure with the double-wall housing and a well-sealed front door as shown in Figure 5.2 (d). The hydrothermal autoclave is placed at the bottom centre of the enclosure wall. The heating is digitally controlled by a temperature sensor, which is located at the top of the autoclave where the feedback regulation can be achieved with the required nominal temperature  $T_s$  (see Figure 5.2). The temperature at the enclosure chamber walls made of polycrystalline alumina fibres,  $T_{ml}$ , was also measured. As can be seen from Figure 5.2, the temperature distribution on the surface of the hydrothermal autoclave since the

free convection taking place in the muffle furnace enclosure will generate a temperature gradient along the surface of the autoclave in the vertical direction. 2D CFD modelling of temperature distribution are displayed in Figures 5.2 (a), 5.2 (b) and 5.2 (c) while the CFD results are also validated by the measurement. Based on the simulation and measurement, the thermal boundary conditions for the hydrothermal autoclave are determined as listed in Table 5.2 and the floc solution properties are given in Table 5.3 (Denys *et al.*, 2003). It should be noted that as the temperature gradient along the hydrothermal autoclave in the vertical direction has been simplified by the temperature difference  $\Delta T = T_2 - T_1$  between the lower part of the autoclave with the temperature  $T_2$ , where the SiO<sub>2</sub> floc solution is filled, and the upper part with the temperature  $T_1$ , where the air is enclosed. This approximation is acceptable as checked from CFD modelling results and the effect is found to be marginal.

CFD modelling for three cases has been conducted under different conditions that the measured temperature  $T_s$  was 373 K, 393 K and 413 K, corresponding to  $T_{ml}$  with 571 K, 592 K and 615 K. It can be seen from the CFD simulation results as shown in Figures 5.2 (a), 5.2 (b) and 5.2 (c) that the temperature profiles in the vicinity of the autoclave along the height exhibit gradual variation with the highest temperature occurs at the bottom of the hydrothermal autoclave wall and lower temperature around the top of the autoclave. Thus, the temperature difference  $\Delta T = T_2 - T_1$  for cases 1 to 3 with 34 K, 43 K and 54 K as the thermal boundary condition applied to the hydrothermal autoclave will be used in the CFD simulation in the present work.

CFD simulation has adopted the commercial CFD software ANSYS Fluent 15.0 with the computational mesh (orthogonal-structured grids) generated by using Gambit 2.4.6 as shown in Figure 5.3. Grid independence check by trial simulation has been conducted by comparison of the wall shear stress  $\langle \tau_w \rangle = \mu \left. \frac{du}{dr} \right|_{r=R}$  among four different mesh setups as listed in Table 5.4. It can be seen from Table 5.4 that the adoption of Grid 3

with a total of 15,200 cells gives shear stress of 0.227 Pa while further refinement on the mesh (Grid 4) has little impact on the predicted wall shear stress. Grid 3 mesh setup was thus employed in all the CFD simulations. The Rayleigh number based on the radius of the hydrothermal autoclave is estimated around  $2 \times 10^6$  and it is safe to assume that the Rayleigh convection established in the hydrothermal autoclave is well falling into the laminar regime. The CFD simulations were run in a transient mode in order to catch up with the Rayleigh convection induced vortex flow. Since the volume fraction of SiO<sub>2</sub> particles is smaller than 5%, the particle trajectories were obtained using the DPM model embedded in the CFD code with a time step of  $10^{-5}$  s.

## **5.4 Results and Discussion**

### **5.4.1 Effects of Rayleigh convection in the hydrothermal autoclave on induced shear flow and temperature distribution**

The temperature difference occurring between the floc solution and the enclosed air will induce the Rayleigh convection. Such convection will generate a vortex shear flow. The particles suspended in the solution will be consequently subjected to such induced shear. The employed hydrothermal autoclave is a 100 ml hydrothermal Teflon reactor with an inner diameter of 48.5 mm and 95 mm height as shown in Figure 5.3. The evolution of the temperature and the velocity distribution in the autoclave for Case-1, predicted by CFD modelling, is shown in Figure 5.4. It can be seen from the figure that at the initial stage of the heating process, there exists a large temperature difference ( $\sim 120$ K) between the wall and the surrounding in the hydrothermal autoclave, which leads to high temperature gradient, inducing an upward flow with a greater velocity near the wall. As revealed from the simulation as shown in Figure 5.4 (a), the Rayleigh convection causes symmetric circulating flow pattern which may be appropriately described as a non-strict Rayleigh–Bénard convection (Yigit *et al.*, 2020). As such convection promotes heat transfer significantly in the hydrothermal autoclave but

gradually weakens the temperature gradient both the air and the floc solution, the induced buoyancy force will gradually reduce while a new equilibrium state will be established, the temperature in the autoclave consequently becomes uniformly distributed as can be seen clearly from Figure 5.5 (a). This process can be evidenced by the CFD simulation results that the velocity near the wall, observed at location p1 and p2, increases initially in the first 10 seconds when heating is applied but temperature steadily decreases afterwards and gradually approaches a constant value when the heating reaches 200 s, e.g. 0.1 m/s for Case-1. However, the velocities recorded in the locations, p4 and p5, at the centreline of the hydrothermal autoclave are almost zero, indicating the induced vortex circulation being weak here. In the air zone, the velocity for Case-1 near the wall is observed to be as high as 0.03 m/s. The predicted velocity and temperature evolution at location p2 are displayed in Figures 5.5 (c) and 5.5 (d) for all the cases. Higher temperature difference induces higher velocities in the vicinity of the autoclave wall. To be specific, the largest temperature difference  $\Delta T = T_2 - T_1$  and induced velocity were found for Case-3 with nominal temperatures of 413 K when the simulation time reaches 200 s with and the corresponding velocity is 0.026 m/s.

To quantitatively characterise the effect of the Rayleigh convection on the induced shear, Grashof number ( $Gr$ ) was adopted, defined by the ratio of the buoyancy to viscous force acting on a fluid particle which is given by

$$Gr = \beta g \Delta T R^3 / \nu^2 \quad (5-14)$$

where  $\beta$  is the coefficient of thermal expansion and  $R$  denotes the radius of the hydrothermal autoclave reactor. For convenience, Rayleigh number ( $Ra$ ) as described in the previous section was also adopted, a product of Grashof number ( $Gr$ ) and Prandtl number  $Pr$ , where  $Pr$  refers to as the ratio of the solution viscosity to thermal diffusivity,

i.e.  $Pr = \frac{\nu}{\alpha} = \frac{c_p \mu}{k}$ .

The strength of the induced shear is described by introducing the volumetric average of the local induced shear rates  $\langle \widetilde{G} \rangle$ , defined by

$$\langle \widetilde{G} \rangle = \frac{1}{\pi R^2 H} \int_0^H \int_0^R \left\{ \sqrt{2 \left[ \left( \frac{\partial U_r}{\partial r} \right)^2 + \left( \frac{U_r}{r} \right)^2 + \left( \frac{\partial U_z}{\partial z} \right)^2 \right]} + \left[ \frac{\partial U_r}{\partial z} + \frac{\partial U_z}{\partial r} \right]^2 \right\} 2\pi r dr dz \quad (5-15)$$

The experiments have been conducted for all the cases loaded with the same primary particles obtained from the pre-preparation using the SVFR with different temperature setup by controlling the temperature difference between the upward and downward parts of the hydrothermal autoclave. The changes of corresponding Rayleigh number for all the cases was estimated based on CFD modelling for 200 s are shown in Figure 5.6. As can be seen from Figure 5.6, the Rayleigh convection induced shear strengths reduces with the time due to the temperature difference gradual reduction. A higher applied temperature difference leads to an increased Rayleigh convection induced shear. It was also noticed that as the Rayleigh number increases, the Rayleigh convection induced vortex shear flow takes place in the region closer to the wall, indicating that the SiO<sub>2</sub> particles may be subjected to stronger shear applied to the particles than the other regions. When heating reaches 180 s, the Rayleigh numbers were found to be  $2 \times 10^6$ ,  $2.52 \times 10^6$  and  $3.17 \times 10^6$  for the setup nominal temperature of 373 K, 393 K and 413 K at the top of the hydrothermal autoclave.

#### **5.4.2 Effect of Rayleigh convection induced shear flow in the hydrothermal autoclave on synthesised characteristics**

In order to affirm the properties of the synthesised particles that have been included in the floc solution especially the chemical compositions, FT-IR spectroscopy measurements have been carried out and the results are shown in Figure 5.7 (a). The

absorption bands at  $1080\text{ cm}^{-1}$  and  $450\text{ cm}^{-1}$  imply the presence of Si-O bonds. The occurrence of the absorption bands at  $2923\text{ cm}^{-1}$  and  $2856\text{ cm}^{-1}$ , however, represent the existence of -CH<sub>2</sub>- bonds because of the formation of the bonding between CTAB and SiO<sub>2</sub>. The extra CTAB can be fully removed after calcination at  $550\text{ }^{\circ}\text{C}$  after 8 h (Zhang *et al.*, 2017). X-Ray diffractometer (XRD) analysis was also performed in the range of  $2\theta$  from  $0^{\circ}$  to  $90^{\circ}$ . The results of XRD pattern analysis of synthesised SiO<sub>2</sub> particles using the hydrothermal post treatment are shown in Figure 5.7 (b). A broad peak appears at the Bragg angles between  $21^{\circ}$  to  $22^{\circ}$ , indicating synthesised SiO<sub>2</sub> particle samples have presented the amorphous phase (Pavlenko *et al.*, 2018). As only one peak was observed, this indicates the product has a high degree of purity while this becomes remarkable as the hydrothermal temperature increases, i.e. Rayleigh number increases. These experimental observations have clearly indicated that the hydrothermal treatment leads to the crystallization of the SiO<sub>2</sub> flocs in the floc solution so that the pre-prepared SiO<sub>2</sub> particles are further aggregated. Although the agglomeration and morphology of the synthesised particles can be controlled due to such one-step crystallization, the step of calcination is still needed to remove the impurities.

The morphology of a primary silica mono-particle exhibits spherical shape, identified by the transmission electron microscope (TEM), which is shown in Figure 5.7 (c). It can be seen from the TEM image that the size of the primary particle is in the range around 100 nm. To further determine the size at its aggregated state, the scanning electron microscope (SEM) was also used to measure the particle size distributions under different setup nominal temperature and primary particles by taking 5 different sample groups as listed in Table 5.1. It can be observed from Figure 5.8 (a) that for sample group, a-373, the pre-prepared silica particles at the first hour of hydrothermal-treatment were loosely distributed with 89.52% of aggregated-particles having the size in the range of 1 to  $100\text{ }\mu\text{m}$  and the surface-weighted average particle size  $d_{32} = 17.77\text{ }\mu\text{m}$ . As the hydrothermal treatment proceeds, aggregated nano-particles start to become smaller and compact in the structure, having a smaller diameter of  $d_{32}$ .

When the particles were hydro-treated in the hydrothermal autoclave at the setup nominal temperature of 373 K (a-373), the aggregated particle size  $d_{32}$  was found to decrease from 17.177 to 14.947  $\mu\text{m}$ . For sample groups a-393 and a-413, the particles sizes were found to decrease from 17.575 to 16.693  $\mu\text{m}$  and 18.419 to 15.711  $\mu\text{m}$ , respectively. A 3D-contour of the particle diameter  $d_p$  for different hydrothermal treatment durations and setup nominal hydrothermal treatment temperatures are displayed in Figures 5.9 (a) and 5.9 (b). For comparison, the primary particle size  $d'$  is also displayed in the figure. It can be observed from Figure 5.9 (a), the product particles size tends to reduce as the hydrothermal treatment time is getting longer and the hydrothermal treatment temperature, i.e. the temperature difference  $\Delta T = T_2 - T_1$  is increased. It should be noted that the primary particles in sample groups a, b and c (see Table 5.1), have the initial sizes of 18.42, 13.26 and 12.52  $\mu\text{m}$ , respectively while the corresponding final synthesised  $\text{SiO}_2$  particles after undergoing the hydrothermal treatment have the sizes of 16.70, 12.33 and 10.94  $\mu\text{m}$ . This is very likely to indicate that the primary particles under the action of Rayleigh convection induced shear will yield the smaller-sized aggregated particles. In other words, this is likely the consequence that the Rayleigh convection induced shear force acting on the particle surfaces may surpass the aggregation bonding force so that the morphology of the  $\text{SiO}_2$  particles can be modified.

To further look into the impact of the Rayleigh convection induced shear on the surface area and porosity of the particles, the nitrogen adsorption-desorption experiments were carried out at 77 K with the synthesised  $\text{SiO}_2$  particle samples that were pre-treated at 473 K for 2 hours to expose to the nitrogen before conducting the measurements. The average surface area and mesoporous-size distribution were calculated from Barrett-Joyner-Halendas (BJH) method and the results are shown in Figure 5.10. It can be seen from the figure that the average pore diameter of the aggregated particles decreases from 25.36 nm to 18.85 nm after 60-minute hydro-treatment and subsequently decreases from 15.02 nm to 13.31 nm after performing a 240-minute treatment as the

setup nominal hydrothermal temperature increases from 373 K to 413 K. In contrast, the BET surface area was also found to reduce from 69.51 m<sup>2</sup>/g to 56.42 m<sup>2</sup>/g after the 240-minute hydrothermal treatment. As a result, the tapped density of the silica powder that consists of the synthesised SiO<sub>2</sub> particles is also affected by such a process. The tapped density of the powder here is defined as the ratio of the mass of the powder to the volume occupied by the powder after being tapped, representing the capability of random dense packing. It can be seen from the histogram as shown in Figure 5.11 (a) that the silica particles synthesised under the condition of Case-1 with the setup nominal temperature 373 K have shown an enhanced tapped density compared with those pre-prepared SiO<sub>2</sub> particles from the SVFR. After tapping, the smaller-sized particles tend to have a compact structure. Consequently, it is speculated that the adoption of higher hydrothermal temperature, i.e. the particles that are exposed to the Rayleigh convection induced shear may be beneficial to the production of the dense silica powder as such shear are very likely to encourage aggregation rather than disaggregation. This is consistent with the observation results of the SEM images as shown in Figure 5.8.

To ensure to have the correct conclusion, the thermal behaviour of SiO<sub>2</sub> powder was also evaluated using the TG-DSC measurement at the temperatures ranging from the room temperature, about 20 °C, to 100 °C and then increasing to 600 °C with slow a heating rate 5 °C /min (Ek *et al.*, 2001), shown in Figure 5.11 (b). The TG curve shown in the figure clearly indicates that the weight loss can be divided into two stages, one characterized by the occurrence of a broad endothermic peak and the other marked by a sharp exothermic one on the DSC curve. It should be noted that the initial weight loss of 40% taking place at 280 °C can be ascribed to the removal of physisorbed water, CTAB, and base from the silica while the mass reduction of less than 10% but with an exothermic DSC peak takes place between 500 °C to 600 °C, which may be caused by the decomposition of dehydration. In fact, decomposition rarely occurs to withstand the working condition at higher temperatures that are approaching 600 °C.

As previously discussed, Rayleigh convection induced shear in the hydrothermal autoclave plays an important role in affecting the synthesised SiO<sub>2</sub> particle properties. The reduction in the synthesised SiO<sub>2</sub> particle size can be attributed to the result that the Rayleigh convection induced shear acting on the particle surface supersedes the aggregation. To evaluate such effect on the synthesised SiO<sub>2</sub> particle size, correlations between the particle size  $d_{32}$  and Rayleigh convection induced shear rate  $\langle G \rangle$ , and the Rayleigh number  $Ra$  have been proposed, defined by

$$R_{G,d} = \frac{\sum_1^n \langle G \rangle_j d_{32,j}}{\langle G \rangle_{ref} d_{32,ref}} \quad (5-16)$$

$$R_{G,Ra} = \frac{\sum_1^n \langle G \rangle_j Ra_j}{\langle G \rangle_{ref} Ra_{ref}} \quad (5-17)$$

where  $\langle G \rangle_j$  is the volumetric average shear rate which can be obtained from Equation (5-15), and subscript  $j$  denotes different cases.

Figure 5.12 shows the correlation coefficients  $R_{G,d}$  and  $R_{G,Ra}$  obtained using different setup nominal hydrothermal temperatures in the hydrothermal autoclave, where Case-1 with the setup nominal temperature of 373 K has been chosen as the reference. It can be seen from the figure that both the correlation coefficients,  $R_{G,d}$  and  $R_{G,Ra}$ , increase as the Rayleigh number increases. Their values change quite significantly from 1.0 to 1.44 for  $R_{G,d}$  and 1.0 to 2.57 for  $R_{G,Ra}$ , respectively. This clearly demonstrates that the particle aggregation during the hydrothermal treatment is strongly affected by the Rayleigh convection induced shear. As the result, the higher induced shear with a greater Rayleigh number may bring out the particle size reduction and promote the compact aggregation, illustrating by reducing the particle diameter  $d_{32}$  (Bubakova *et al.*, 2013). This suggests that the Rayleigh convection induced shear can affect the aggregation process and such induced shear can be modulated by controlling the temperature difference or the setup nominal temperature in the present study (Ehrl *et al.*, 2009).

### 5.4.3 SiO<sub>2</sub> particle dispersion in the hydrothermal autoclave

It can be seen from the previous discussion that the SiO<sub>2</sub> particles pre-prepared from the SVFR will still experience the shear-induced by Rayleigh convection. Such induced shear is generally mild compared with the turbulence-induced shear generated in the SVFR. From materials synthesis point of view, the particle properties such as sphericity and porosity may undergo certain changes in the action of the local shear. Thus, the particle dispersion in the hydrothermal autoclave can be correlated with the synthesised particle property parameters. From the SEM and TEM experimentally obtained images of SiO<sub>2</sub> samples, the sphericity of the synthesised particles in the hydrothermal autoclave can be characterised by introducing the ratio of the surface area of the synthesised particles to that of the spherical particles with the same volume. The SiO<sub>2</sub> particle dispersion in the floc solution can be characterised by the particle trajectories obtained by integrating Equation (5-6) but with the assumption that the particles are not shear-deformed but can be size-changed. In the present study, such size change is not concerned and it will be explored in our further study. The SiO<sub>2</sub> particle dispersion behaviour can be evaluated by considering the radial dispersion in the hydrothermal autoclave. To quantify radial dispersion, an “effective particle diffusion coefficient”, based on the chaotic advection of a large number of SiO<sub>2</sub> particles injected in the flow field, was derived from Lagrangian transient simulations. A radial dispersion coefficient is defined by

$$D_r(t) = \lim_{t \rightarrow \infty} \frac{\left[ \frac{1}{N} \sum_{i=1}^N r_{pi}(t) - \frac{1}{N} \sum_{i=1}^N r_{pi}(0) \right]^2}{2t} \quad (5-18)$$

where  $r_{pi}(t)$  is the radial position of the  $i^{\text{th}}$  particle at time  $t$ ,  $r_{pi}(0)$  is the initial position and  $N$  the total number of SiO<sub>2</sub> particles seeded in the flow. The particles were advected by the Rayleigh convection induced vortex flow. Transport within the induced vortices supplemented by increasing Rayleigh number results in enhanced radial dispersion so

that particles undergo a slightly stronger shear. The mixing property can be also compared with momentum diffusion through the dispersion-based Schmidt number defined as  $Sc = \nu/D_r$ . Figure 5.13 reveals the particle dispersion  $D_r(t)$  in the radial direction as a function of time under different setup nominal temperature. As can be found that the dispersion of particles decreases fast in the first 200 s of hydrothermal treatment and finally keep constant. As the setup nominal temperature increases, particle dispersion tends to larger compared with the others at the same condition and the dispersion ultimately approaches  $2.08 \times 10^7$ ,  $2.30 \times 10^7$  and  $3.65 \times 10^7$   $\text{m}^2/\text{s}$  respectively for cases under setup nominal temperature of 373 K, 393 K and 413 K. Figure 5.14 (a) shows the initial  $\text{SiO}_2$  particle injection positions ( $t=0$ ). The particles are assumed to be uniformly distributed in the solution and to be immediately entrained by Rayleigh convection in the hydrothermal autoclave. It can be seen from Figure 5.14 that at  $t=50$  s, the instantaneous distribution of the particles has presented an almost symmetric pattern with only a few particles escaping from the trapping by Rayleigh convection induced vortex flow. The particles seem to disperse steadily after 100 s to form a distribution to coincide with the Rayleigh–Bénard vortex. In this way, the  $\text{SiO}_2$  particles expose to the Rayleigh convection induced shear, which impacts the particle structure and porosity can be seen from Figure 5.10. Comparing Case-1 (Figure 5.14 (b)) and Case-2 (Figure 5.14 (c)), it can be seen clearly that particles at higher Rayleigh number have undergone an enhanced shear as shown in Figure 5.14 (d). Such enhanced shear acting on the particles may also be attributed to the thermophoresis effect that mobile  $\text{SiO}_2$  particles tend to transport from the hotter region to the cold region as a response to the temperature gradient (Glensvig *et al.*, 2013). However, the impact of the thermophoresis compared with the buoyancy force due to the Rayleigh convection on the particle dispersion can be disregarded.

## 5.5 Conclusions

The effects of hydrothermal post-treatment of SiO<sub>2</sub> in a hydrothermal autoclave with different temperature boundary conditions and initial primary particle sizes on the final synthesised SiO<sub>2</sub> particle properties have been investigated both experimentally and numerically. In the experimental studies, the primary particles obtained from the upstream SVFR assisted by ultrasound were selected according to the particle size and porosity. Consequently, these particles were introduced into a hydrothermal autoclave subjected to the Rayleigh convection induced shear, operating at a nominal scaled temperature range of 373 K to 413 K. The finally synthesised particles were characterised with crystallinity, size distribution, porosity and tapped density. In the modelling aspect, the temperature boundary condition which is applied to the autoclave has been obtained by a 2-D CFD modelling of actual temperature profiles surrounding the autoclave that has been placed inside a muffle furnace. The Rayleigh convection of the solution phase that contains the primary SiO<sub>2</sub> particles was modelled using the Volume of Fluid (VOF) method so as to obtain the velocity and temperature distribution in the autoclave. The dispersion of the synthesised particles was estimated by tracking the particle trajectories based on the Euler-Lagrange approach. The main conclusions reached as the results from the present study are summarised as follows:

(1) CFD modelling results have revealed that the Rayleigh convection in the autoclave generates a symmetric annular flow pattern that can be regarded as Rayleigh–Bénard convection due to the applied temperature profiles around the autoclave. The temperature difference between the up-part region filled with the air and the down-part region filled with the floc solution with pre-prepared primary particles induces the Rayleigh convection induced shear flows inside the autoclave. The Rayleigh number can be used to quantitatively characterise the intensity of the Rayleigh convection.

(2) From the experimental results, the structure and composition of the synthesised SiO<sub>2</sub> particles are affirmed by the FT-IR spectroscopy measurement. Based on the XRD patterns observed for SiO<sub>2</sub> particles, it has been found that although the hydrothermal treatment can lead to better crystallization of the SiO<sub>2</sub> so that one-step particle synthesis control for required particle size without calcination and the impurity removal is necessary via the step of calcination. However, the SEM results show that the synthesised SiO<sub>2</sub> particle sizes become smaller with a prolonged hydrothermal treatment time and an enhanced setup nominal hydrothermal treatment temperature, consequently contributing to a more compacted structure with a higher tapped density.

(3) The calculated particle dispersion coefficient obtained from CFD simulation but based on the experimental thermal conditions imposed to the hydrothermal autoclave has clearly indicated that the SiO<sub>2</sub> particles are dispersed towards the wall with the increment of Rayleigh number. As the consequence, the particles are affected to more extents by Rayleigh convection induced shear in the induced flow in the hydrothermal autoclave. Correlation coefficients,  $R_{G,d}$  and  $R_{G,Ra}$  can be used to indicate the effects on the synthesised SiO<sub>2</sub> particle properties such as particle size and morphology, and aggregation behaviour by the Rayleigh convection induced shear.

## References

BETTERMANN, P. & LIEBAU, F. 1975. The transformation of amorphous silica to crystalline silica under hydrothermal conditions. *Contributions to Mineralogy and Petrology*, 53, 25-36.

BRACKBILL, J. U., KOTHE, D. B. & ZEMACH, C. 1992. A continuum method for modeling surface tension. *Journal of Computational Physics*, 100, 335-354.

BUBAKOVA, P., PIVOKONSKY, M. & FILIP, P. 2013. Effect of shear rate on aggregate size and structure in the process of aggregation and at steady state. *Powder Technology*, 235, 540-549.

BYRAPPA, K. & YOSHIMURA, M. 2012. *Handbook of hydrothermal technology*, William Andrew.

DENKBAŞ, E. B., ÇELİK, E., ERDAL, E., KAVAZ, D., AKBAL, Ö., KARA, G. & BAYRAM, C. 2016. Chapter 9 - Magnetically based nanocarriers in drug delivery. *In: GRUMEZESCU, A. M. (ed.) Nanobiomaterials in Drug Delivery*. William Andrew Publishing.

DENYS, S., PIETERS, J. G. & DEWETTINCK, K. 2003. Combined CFD and Experimental Approach for Determination of the Surface Heat Transfer Coefficient During Thermal Processing of Eggs. *Journal of Food Science*, 68, 943-951.

EHRL, L., SOOS, M., MORBIDELLI, M. & BÄBLER, M. U. 2009. Dependence of initial cluster aggregation kinetics on shear rate for particles of different sizes under turbulence. *AIChE Journal*, 55, 3076-3087.

EK, S., ROOT, A., PEUSSA, M. & NIINISTÖ, L. 2001. Determination of the hydroxyl group content in silica by thermogravimetry and a comparison with <sup>1</sup>H MAS NMR results. *Thermochimica Acta*, 379, 201-212.

FU, C. & RAVINDRA, N. M. 2012. Magnetic iron oxide nanoparticles: synthesis and applications. *Bioinspired, Biomimetic and Nanobiomaterials*, 1, 229-244.

GALARNEAU, A., IAPICHELLA, J., BONHOMME, K., DI RENZO, F., KOOYMAN, P., TERASAKI, O. & FAJULA, F. 2006. Controlling the morphology of mesostructured silicas by pseudomorphic transformation: a route towards applications. *Advanced Functional Materials*, 16, 1657-1667.

GLENSVIG, M., STÖWE, C. & SCHUTTING, E. 2013. Method for active EGR cooler refreshing during cold start. *Vehicle Thermal Management Systems Conference Proceedings (VTMS11)*. Woodhead Publishing.

GUO, Y., YANG, X., LI, G., YANG, J., LIU, L., CHEN, L. & LI, B. 2020. Shear Turbulence Controllable Synthesis of Aggregated Nano-Particles Using a Swirling Vortex Flow Reactor Assisted by Ultrasound Irradiation. *Chemical Engineering Journal*, 126914.

HABIB, A., HAUBNER, R. & STELZER, N. 2008. Effect of temperature, time and particle size of Ti precursor on hydrothermal synthesis of barium titanate. *Materials Science and Engineering: B*, 152, 60-65.

HASANY, S., AHMED, I., RAJAN, J. & REHMAN, A. 2012. Systematic review of the preparation techniques of iron oxide magnetic nanoparticles. *Nanosci. Nanotechnol*, 2, 148-158.

HU, B., WANG, K., WU, L., YU, S. H., ANTONIETTI, M. & TITIRICI, M. M. 2010. Engineering carbon materials from the hydrothermal carbonization process of biomass. *Advanced materials*, 22, 813-828.

KE, D., PENG, T., MA, L., CAI, P. & DAI, K. 2009. Effects of Hydrothermal Temperature on the Microstructures of BiVO<sub>4</sub> and Its Photocatalytic O<sub>2</sub> Evolution Activity under Visible Light. *Inorganic Chemistry*, 48, 4685-4691.

KLIPOV, V. & SHMAKOV, N. Influence of convective flows on the growth of synthetic quartz crystals. Proceedings of the 45th Annual Symposium on Frequency Control 1991, 1991. IEEE, 29-36.

KOLEN'KO, Y. V., MAXIMOV, V. D., GARSHEV, A. V., MESKIN, P. E., OLEYNIKOV, N. N. & CHURAGULOV, B. R. 2004. Hydrothermal synthesis of nanocrystalline and mesoporous titania from aqueous complex titanyl oxalate acid solutions. *Chemical Physics Letters*, 388, 411-415.

LAUDISE, R. A. 1970. *The growth of single crystals*, Prentice Hall.

LI, H., BRAUN, M. J. & PAUDEL, G. 2006. Flow structure and heat transfer in a lower half heated and upper half cooled rectangular enclosure. *International Journal of Heat and Mass Transfer*, 49, 3462-3476.

LI, H., EVANS, E. A. & WANG, G.-X. 2003. Flow of solution in hydrothermal autoclaves with various aspect ratios. *Journal of crystal growth*, 256, 146-155.

LI, H., EVANS, E. A. & WANG, G.-X. 2005. A three-dimensional conjugate model with realistic boundary conditions for flow and heat transfer in an industry scale hydrothermal autoclave. *International journal of heat and mass transfer*, 48, 5166-5178.

MA, Z.-Y., YU, Z.-L., XU, Z.-L., BU, L.-F., HAORAN, L., ZHU, Y., QIN, B., MA, T., ZHAN, H.-J., XU, L., WU, H.-A., DING, H. & YU, S.-H. 2020. Origin of Batch Hydrothermal Fluid Behavior and Its Influence on Nanomaterial Synthesis. *Matter*.

MARTIN, T., GALARNEAU, A., DI RENZO, F., FAJULA, F. & PLEE, D. 2002. Morphological control of MCM-41 by pseudomorphic synthesis. *Angewandte Chemie*, 114, 2702-2704.

MCDONNELL, E., JASZEWSKI, S., YANG, H. Y., ABRAMCHUK, M. & TAFTI, F. 2018. Effect of hydrothermal conditions on superconductivity and magnetism in  $[\text{Li}_{1-x}\text{Fe}_x\text{OH}]\text{FeS}$ . *Materials Chemistry and Physics*, 217, 451-456.

MORSI, S. A. & ALEXANDER, A. J. 1972. An investigation of particle trajectories in two-phase flow systems. *Journal of Fluid Mechanics*, 55, 193-208.

PAN, D., YUAN, P., ZHAO, L., LIU, N., ZHOU, L., WEI, G., ZHANG, J., LING, Y., FAN, Y. & WEI, B. 2009. New understanding and simple approach to synthesize highly hydrothermally stable and ordered mesoporous materials. *Chemistry of Materials*, 21, 5413-5425.

PAVLENKO, V., CHERKASHINA, N. & DEMKINA, L. 2018. Influence of hydrothermal treatment on the crystalline form of SiO<sub>2</sub> synthesized by the sol-gel method.

SAYARI, A. 2000. Unprecedented expansion of the pore size and volume of periodic mesoporous silica. *Angewandte Chemie*, 112, 3042-3044.

SCHÄFER, H. 1985. On the problem of polar intermetallic compounds: the stimulation of E. Zintl's work for the modern chemistry of intermetallics. *Annual Review of Materials Science*, 15, 1-42.

SCOTT, G. & RICHARDSON, P. 1997. The application of computational fluid dynamics in the food industry. *Trends in Food Science & Technology*, 8, 119-124.

VAN SINT ANNALAND, M., DEEN, N. G. & KUIPERS, J. A. M. 2005. Numerical simulation of gas-liquid-solid flows using a combined front tracking and discrete particle method. *Chemical Engineering Science*, 60, 6188-6198.

WESFREID, J. E. 2017. Henri Bénard: Thermal convection and vortex shedding. *Comptes Rendus Mécanique*, 345, 446-466.

XU, Y., LIU, M. & TANG, C. 2013. Three-dimensional CFD-VOF-DPM simulations of effects of low-holdup particles on single-nozzle bubbling behavior in gas-liquid-solid systems. *Chemical Engineering Journal*, 222, 292-306.

YIGIT, S., BRÄUER, F., CHAKRABORTY, N. & KLEIN, M. 2020. Comparison of two and three-dimensional Rayleigh-Bénard convection of power-law fluids in cylindrical and annular enclosures. *International Journal of Heat and Mass Transfer*, 160, 120211.

YU, J., WANG, G., CHENG, B. & ZHOU, M. 2007. Effects of hydrothermal temperature and time on the photocatalytic activity and microstructures of bimodal mesoporous TiO<sub>2</sub> powders. *Applied Catalysis B: Environmental*, 69, 171-180.

YU, Q., HUI, J., WANG, P., XU, B., ZHUANG, J. & WANG, X. 2012. Hydrothermal synthesis of mesoporous silica spheres: effect of the cooling process. *Nanoscale*, 4, 7114-7120.

YU, Q., WANG, P., HU, S., HUI, J., ZHUANG, J. & WANG, X. 2011. Hydrothermal Synthesis of Hollow Silica Spheres under Acidic Conditions. *Langmuir*, 27, 7185-7191.

ZHANG, Y., LIU, C., LUO, L., SHI, Y., CHEN, Y., WANG, S., BIAN, L. & JIANG, F. 2017. One-step hydrothermal synthesis of CTAB-modified SiO<sub>2</sub> for removal of bisphenol A. *Water Science and Technology*, 76, 928-938.

ZUNGER, A. & HURLE, D. 1994. Handbook of crystal growth. Amsterdam: Elsevier) p.

## Figures and Graphs

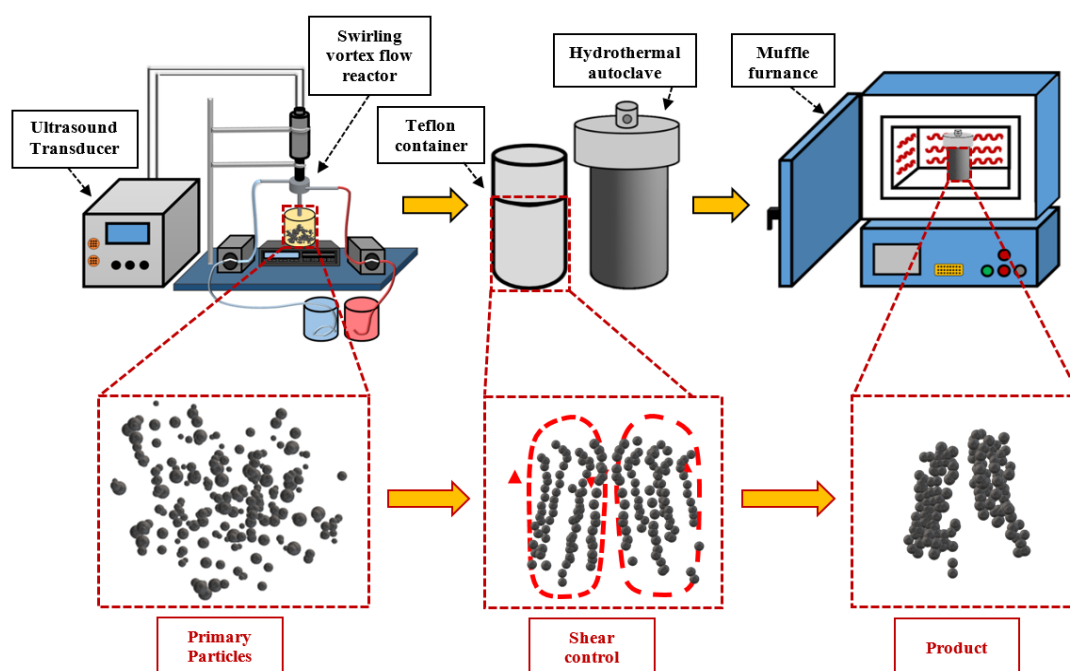


**Figure 5.1** Schematic diagram of experimental setup and post-hydrothermal treatment process of SiO<sub>2</sub> particles following a pre-swirling flow reactor synthesis.

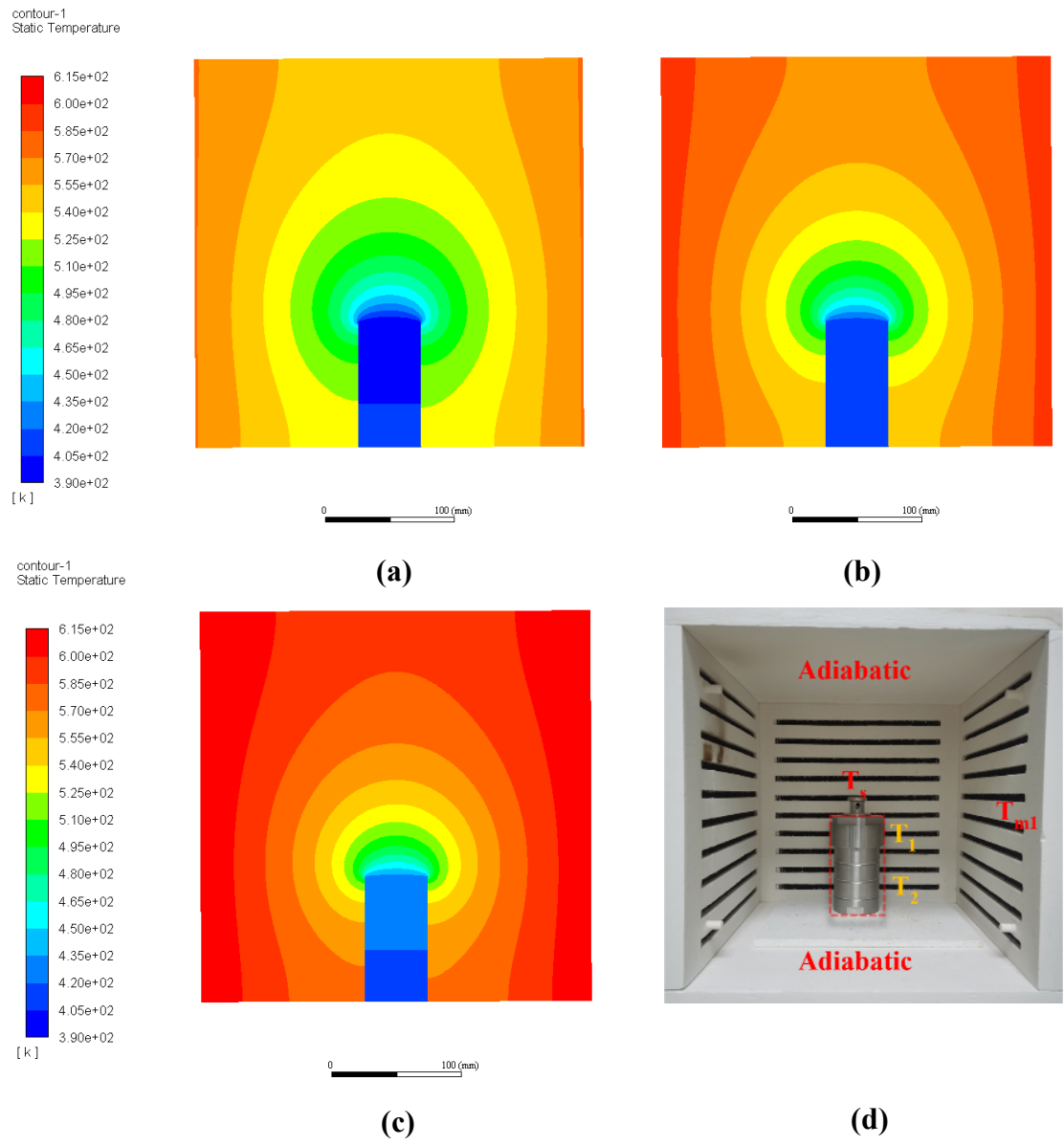
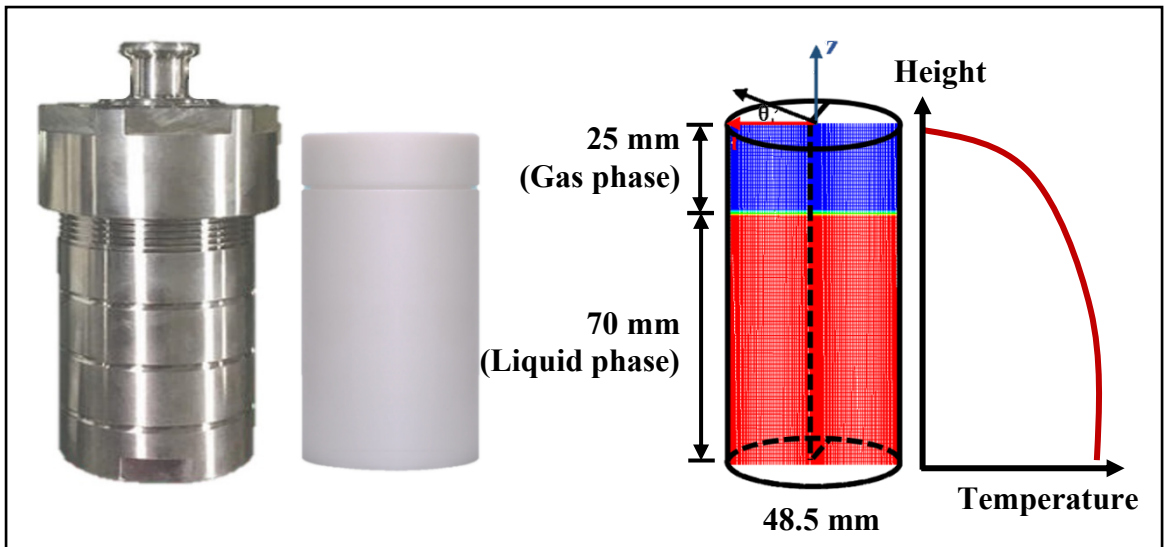


**Figure 5.2** 2-D CFD modelling of the temperature distribution surrounding the hydrothermal autoclave placed inside a muffle furnace under different operation conditions. (a) Case-1; (b) Case-2; (c) Case-3 (as shown Table 5.2); (d) Photos of placement of the hydrothermal autoclave in the muffle furnace.



(a)

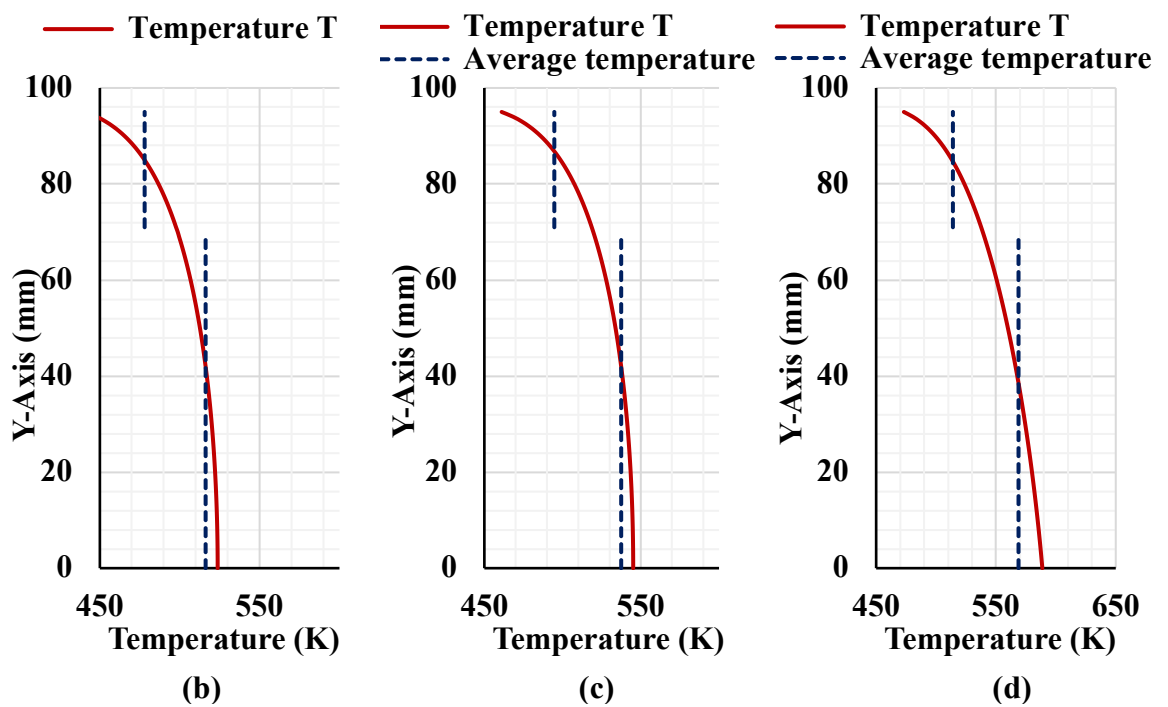


**Figure 5.3** (a) Numerical domain and thermal boundary conditions of 2D autoclave model; Temperature profile and boundary condition ( $T_1$  and  $T_2$ ) for autoclave obtained from simulation of muffle furnace for (a) Case-1; (b) Case-2; (c) Case-3 (as shown Table 5.2).

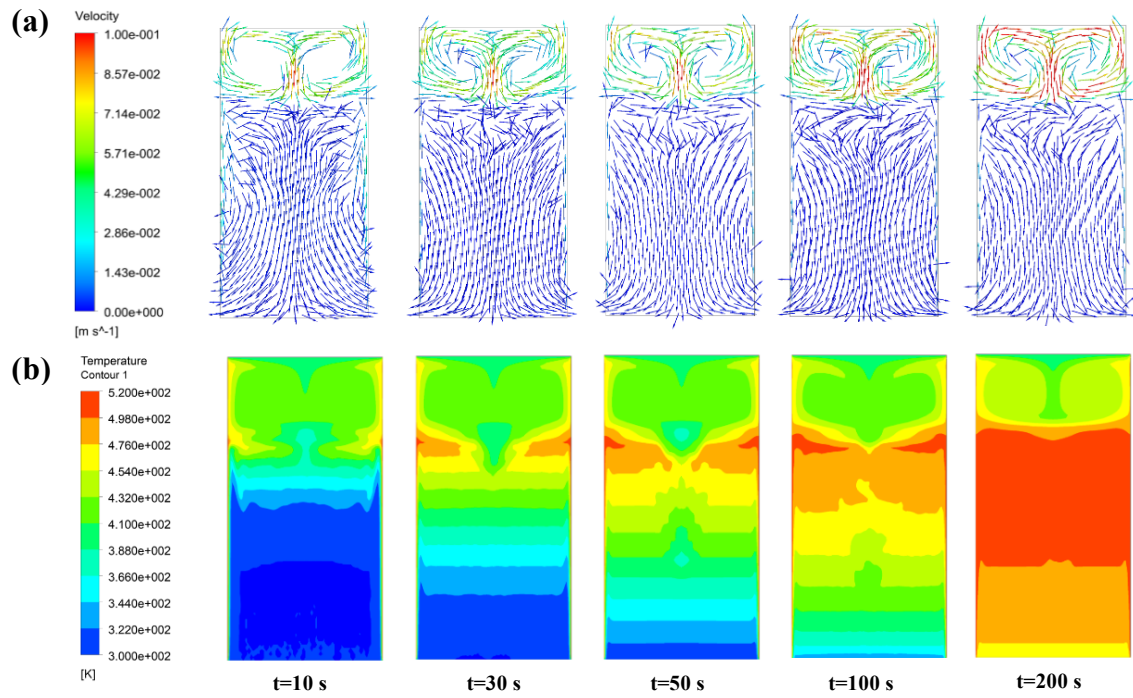


**Figure 5.4** CFD modelling of time-dependant Rayleigh convection induced velocity and temperature distribution in a hydrothermal autoclave, obtained at the time  $t=10\text{ s}$ ,  $30\text{ s}$ ,  $50\text{ s}$ ,  $100\text{ s}$ ,  $200\text{ s}$  for case-1. (a) Velocity distribution and (b) temperature profiles.

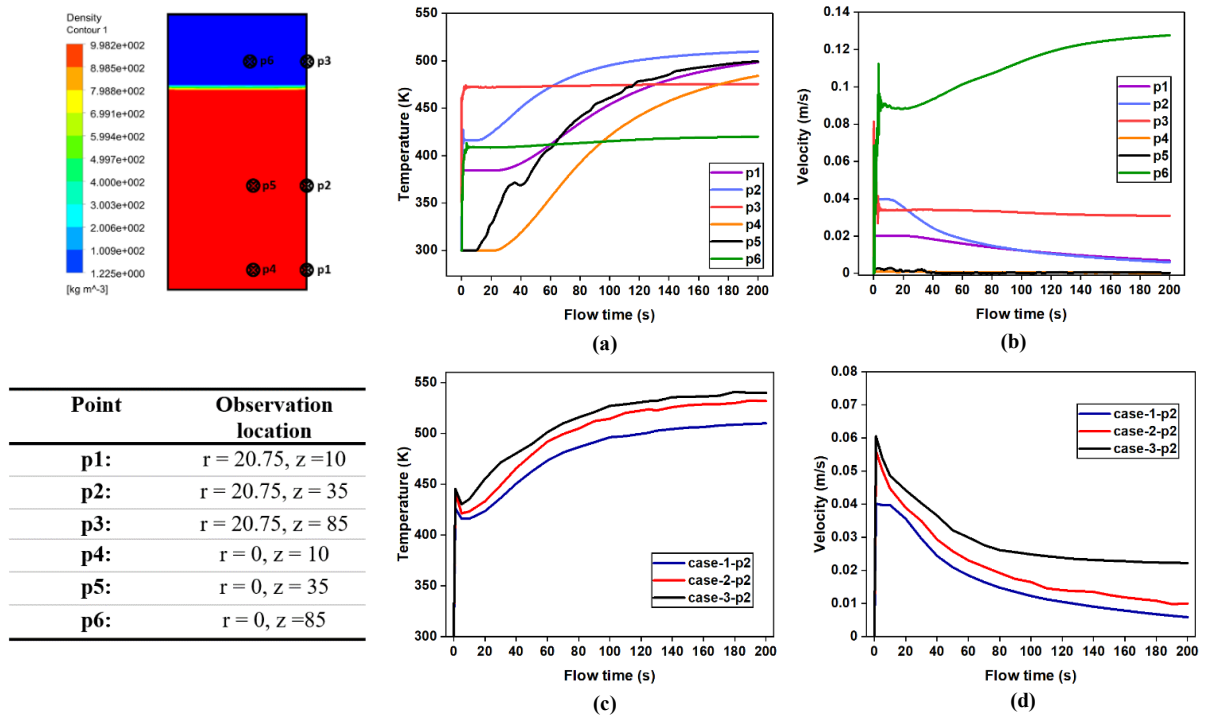


**Figure 5.5** (a) Temperature and (b) velocity of specific points as a function of time under condition of case-1; (c) Temperature and (d) velocity at p2 as function of time under different conditions of case-1, case-2 and case-3.

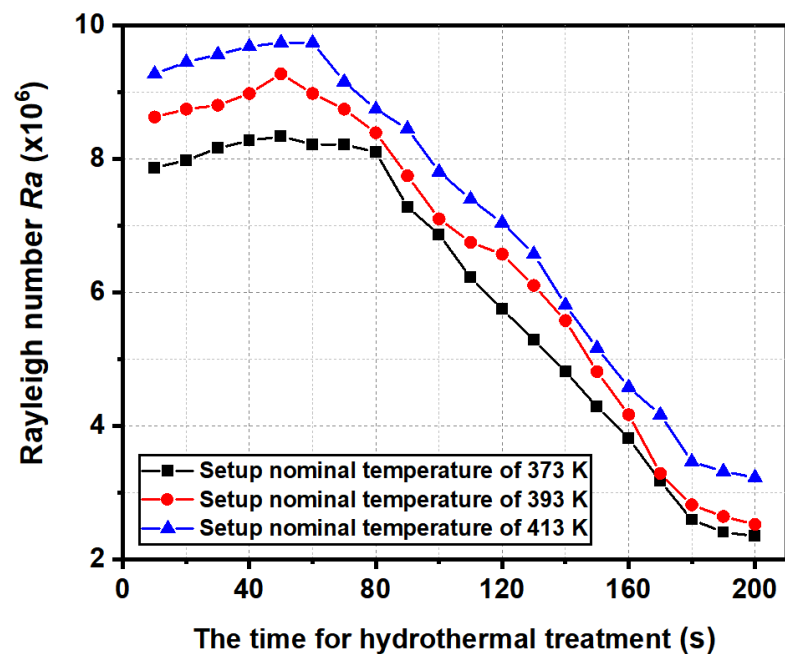


**Figure 5.6** Rayleigh number  $Ra$  versus hydrothermal treatment duration (min) under condition of case-1 at setup temperature of 373 K, 393 K and 413 K.

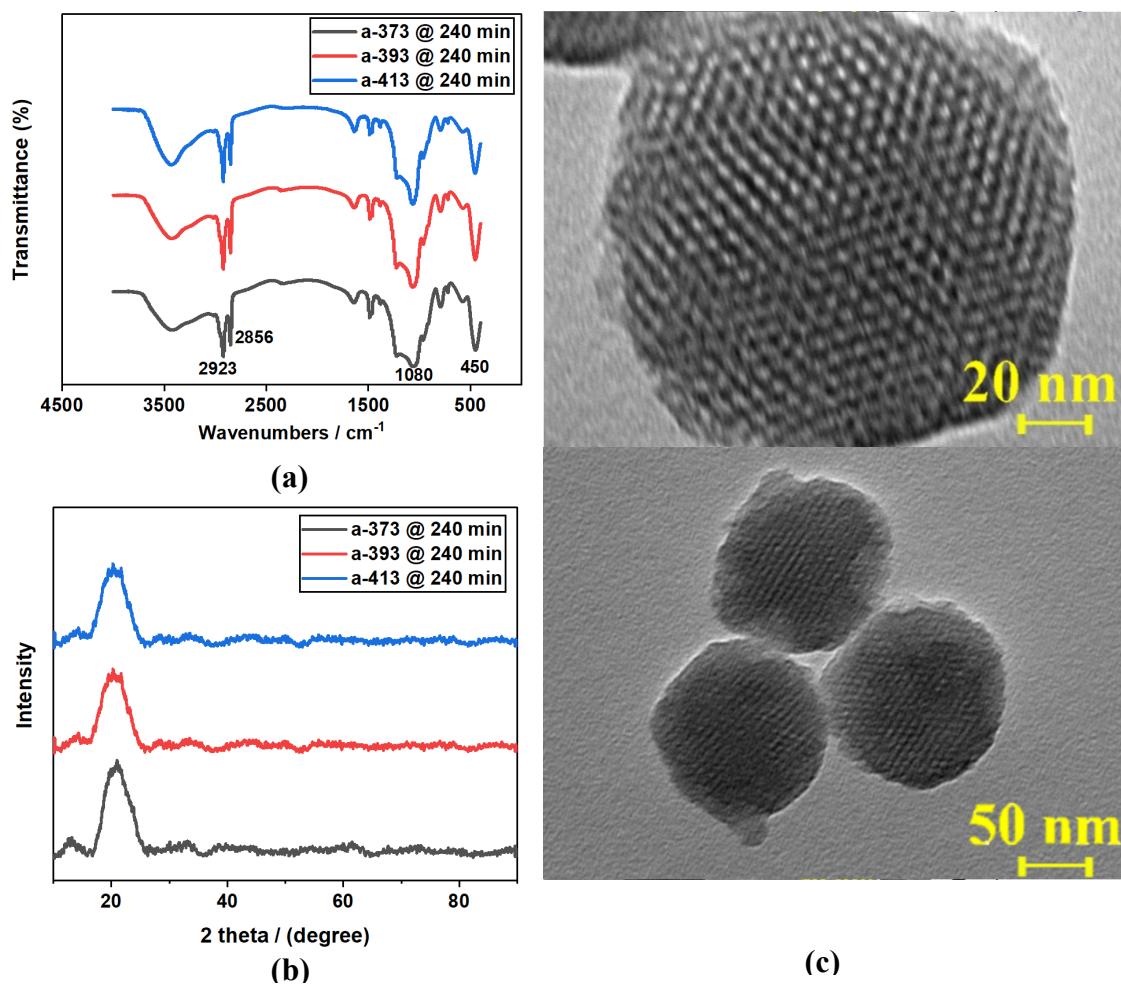


**Figure 5.7** (a) FTIR spectrograms and (b) XRD analysis of SiO<sub>2</sub> synthesized with hydrothermal post-treatment from primary particle a at different temperature a-373 at 240 min, a-393 at 240 min and a-413 at 240 min; (c) TEM images of primary particle of sample a-1 under scale of 20 nm and 50 nm.

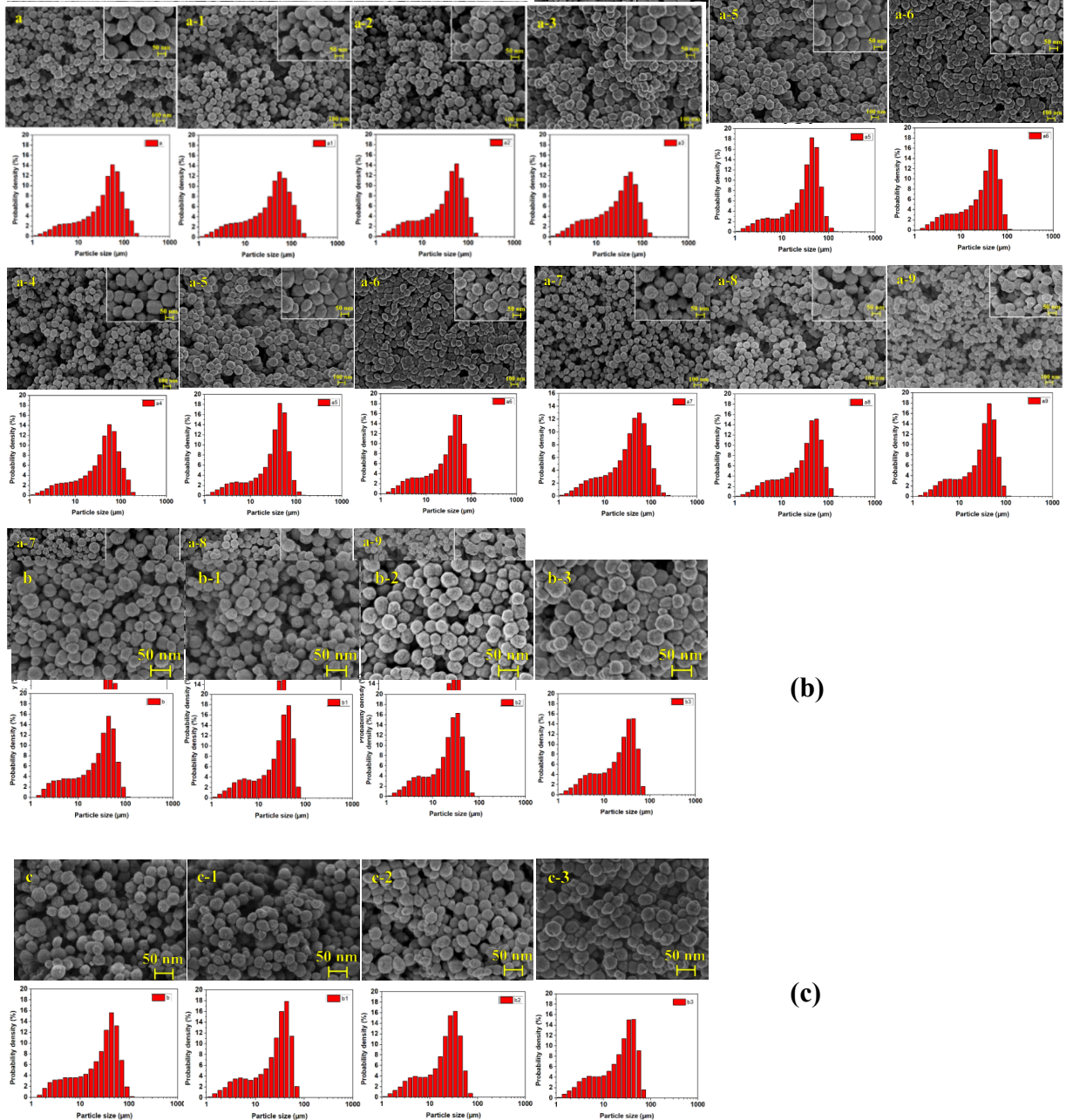


**Figure 5.8** SEM images and particle size distribution of sample SiO<sub>2</sub> samples synthesised after hydrothermal treatment under different condition with different primary particles from sample group (a) a-390, a-410 and a-430; (b) b-390 and (c) c-390.

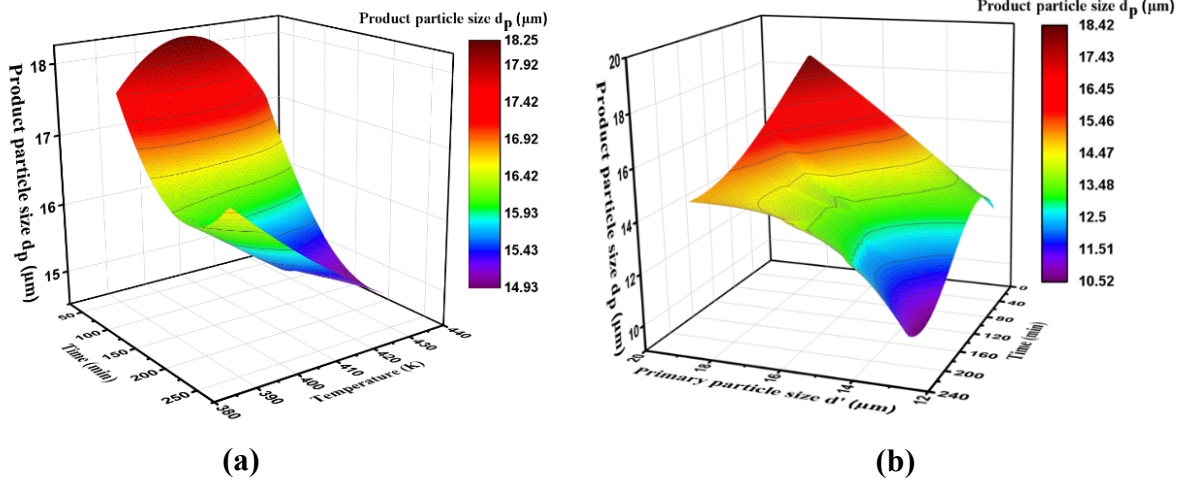


**Figure 5.9** 3D-contour of (a) product particle diameter  $d_p$  versus hydrothermal treatment duration and hydrothermal temperature; (b) product particle diameter  $d_p$  versus primary particle diameter and hydrothermal treatment duration.

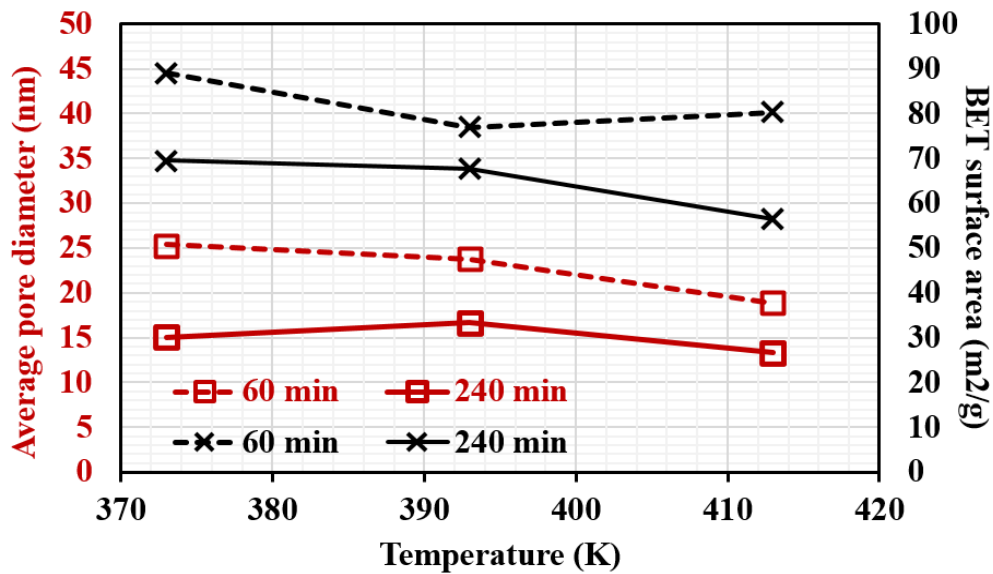


**Figure 5.10** N<sub>2</sub> adsorption–desorption isotherm at 77 K and pore size distribution (the inset) calculated by the BJH method from the desorption branch of presented SiO<sub>2</sub> samples at average particles size and BET surface area of the sample prepared at different hydrothermal temperature.

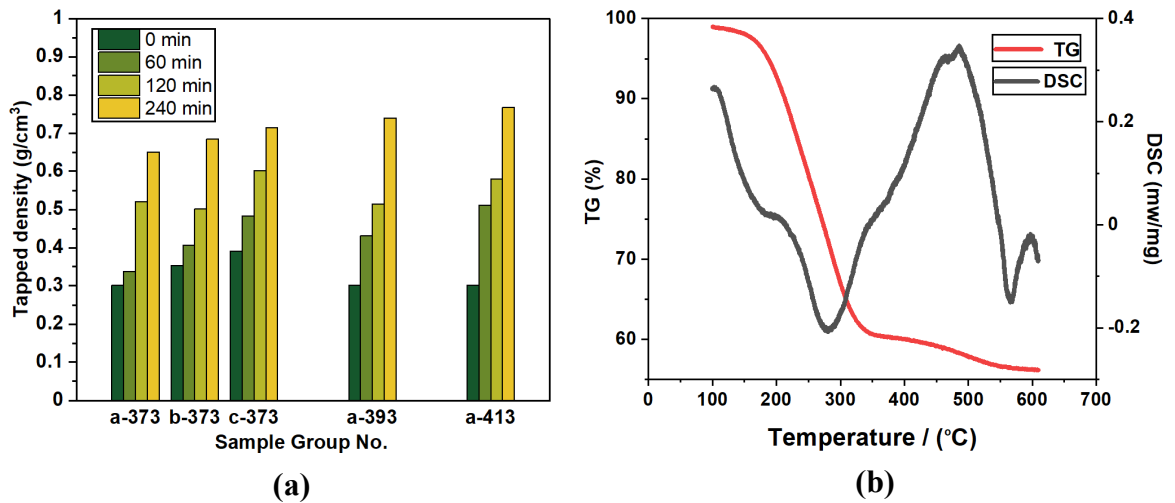


**Figure 5.11** (a) Tapped density of samples under different conditions and (b) TG-DSC for samples of a-373.

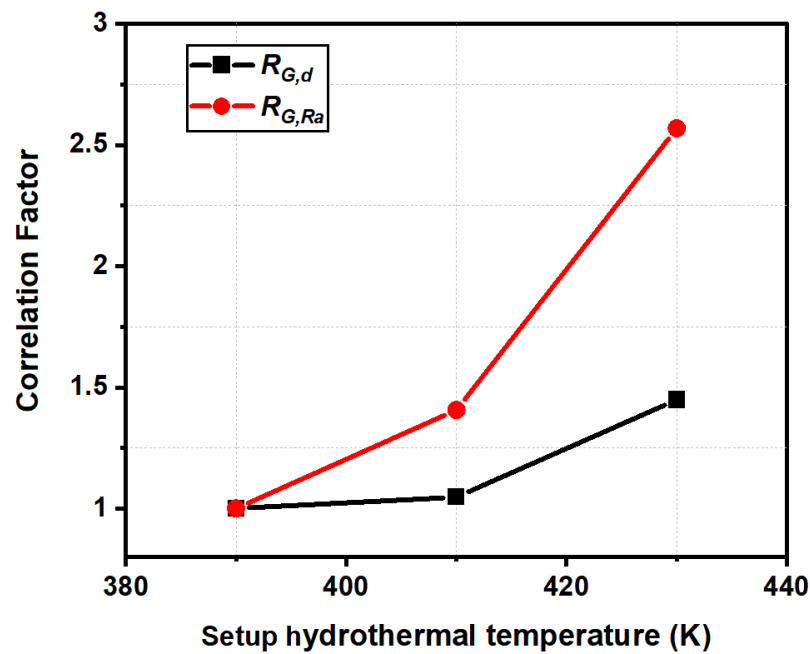


**Figure 5.12** Correlation factor  $R_{G,d}$  and  $R_{G,Ra}$  between the shear rate  $\langle G \rangle$  and Rayleigh number  $Ra$  with the particle size  $d_{32}$  under different setup hydrothermal temperature.

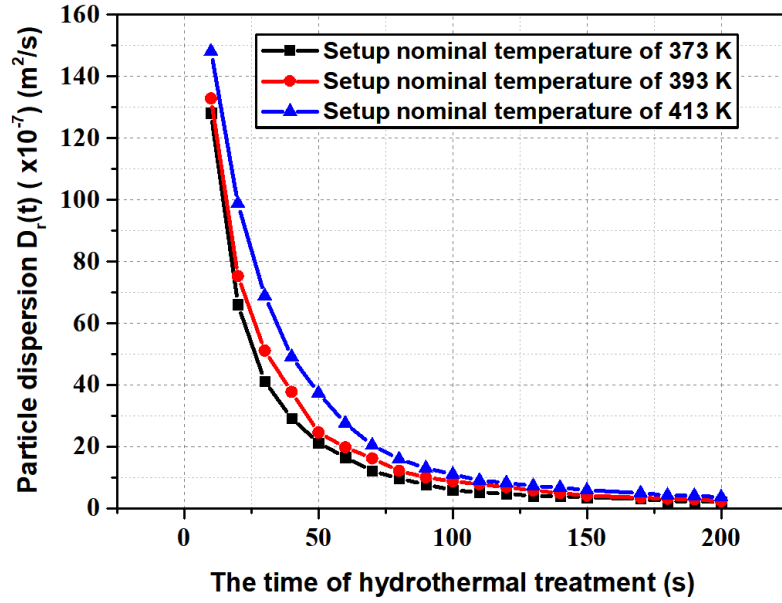


**Figure 5.13** Particle dispersion  $D_r(t)$  versus hydrothermal treatment duration (s) under condition of case-1 at setup temperature of 373 K, 393 K and 413 K.

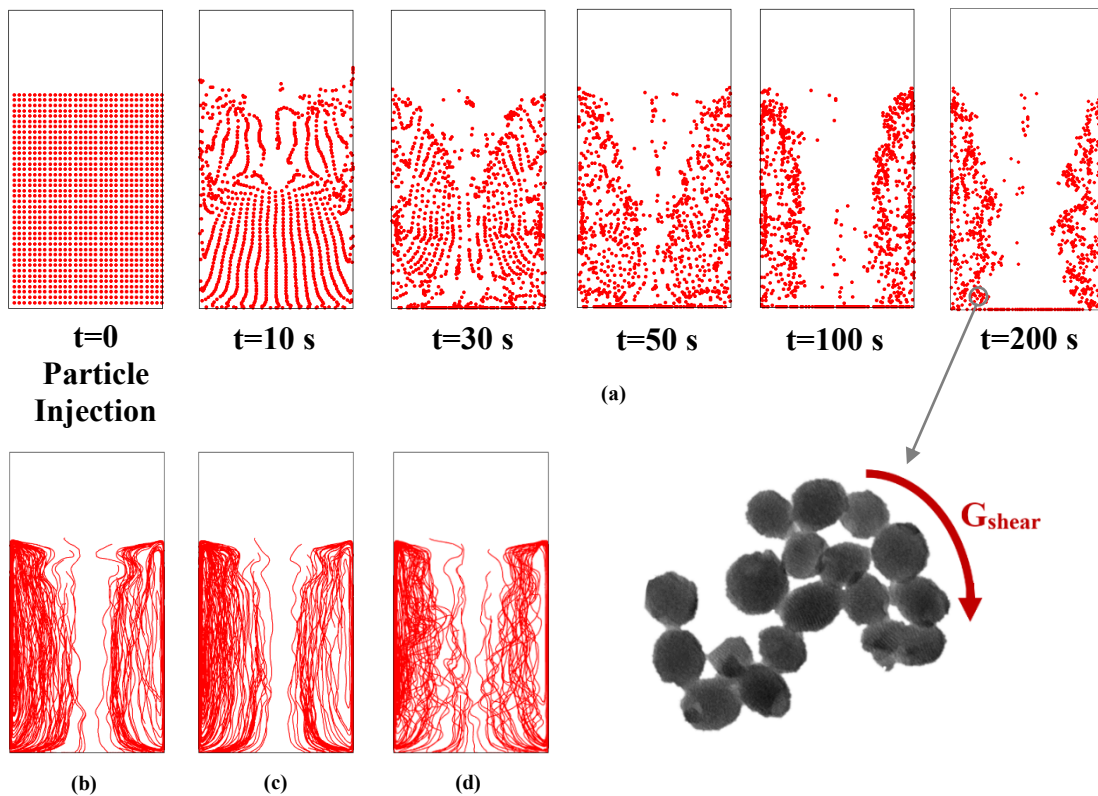


**Figure 5.14** (a) Particle distribution in the hydrothermal autoclave at different time with boundary conditions of case-1; Particle trajectory in the hydrothermal autoclave under different conditions of (b) case-1; (c) case-2; (d) case-3.

## Tables

**Table 5.1** Samples synthesized with different primary particles and post-hydrothermal treatment conditions.

Primary particles		Post-hydrothermal treatment		
Sample Group No.	Ultrasound power (W)	Sample No.	Hydrothermal temperature (K)	Hydrothermal duration (min)
a-373	0	a-1	390	60
		a-2	390	120
		a-3	390	240
a-393	0	a-4	410	60
		a-5	410	120
		a-6	410	240
a-413	0	a-7	430	60
		a-8	430	120
		a-9	430	240
b-373	120	b-1	390	60
		b-2	390	120
		b-3	390	240
c-373	120	c-1	390	60
		c-2	390	120
		c-3	390	240

**Table 5.2** Boundary condition of the muffle furnace and hydrothermal autoclave.

Boundary Condition	Muffle furnace			Hydrothermal autoclave			
	$T_s$ (K)	$T_{m1}$ (K)	top	bottom	$T_1$ (K)	$T_2$ (K)	bottom
Case-1	373	571			482	516	
Case-2	393	592	Adiabatic	Adiabatic	494	537	Adiabatic
Case-3	413	615			514	568	

**Table 5.3** Physical properties of the fluid used in model.

Properties	Water	Air	Stainless steel	Unit
Density ( $\rho$ )	Boussinesq approximation	$4.8078 - 0.0257T + 7 \times 10^{-5}T^2 - 9 \times 10^{-8}T^3 + 4 \times 10^{-11}T^4$	7930	kg/m <sup>3</sup>
Thermal conductivity (k)	$-0.731652 + 0.007321T - 9.492 \times 10^{-6}T^2$	$-1740.2 + 16.619T - 0.0134T^2$	16.2	W/m·K
Specific heat ( $C_p$ )	$3.9912 \times 10^4 - 423.1844T + 1.8799T^2 - 0.0037T^3 + 2.7617 \times 10^{-6}T^4$	$1002.3 + 0.0012T - 0.0189T^2 + 0.0101T^3$	500	J/kg·K
Viscosity ( $\mu$ )	$0.0054 - 0.2 \times 10^{-4}T + 0.2 \times 10^{-7}T^2$	$6 \times 10^{-7} + 8 \times 10^{-7}T - 7 \times 10^{-10}T^2$	-	Pa·s
Thermal expansion coefficient ( $\beta$ )	0.0002	0.0033676	-	1/K

**Table 5.4** Grid independence test for the numerical model.

<b>Grid</b>	<b>Grid size</b>	<b>Shear stress rate (pa) (<math>T_{w,i}</math>)</b>	<b>Difference (%) <math> T_{w,i} - T_{w,i+1}  / T_{w,i+1}</math></b>
Grid (1)	1200	0.015	85.57692308
Grid (2)	7600	0.104	54.18502203
Grid (3)	15200	0.227	0.873362445
Grid (4)	19000	0.229	-

## CHAPTER 6

### RECAPITULATION AND RECOMMENDATIONS

#### 6.1 Shear controllable synthesis of fine particles

This thesis aims to investigate hydrodynamics and complicated transport phenomena involved in the processes of synthesis of fine particles using different multiphase reactors so as to realise the shear controllable synthesis of fine particles. The studies conducted have attempted to provide an insight into the detailed fine particle synthesis processes. CFD modelling of the hydrodynamics in two new types of multiphase reactors (IJR and SVFR) and the actual synthesis of  $\text{FePO}_4$  and  $\text{SiO}_2$  aggregated particles through the experiments using both types of reactors were conducted. Assisted by externally ultrasound irradiation with a frequency of 20 kHz, the mass transfer generated by turbulent eddy engulfment in the IJR and SVFR was found to be intensified, thus having a remarkable impact on chemical reaction and micro-mixing in the reactors. In addition, this thesis has particularly discussed the effects of turbulence induced shear in the IJR and SVFR on aspects of mixing performance, heat transfer and mass transfer and chemical reactions. Such effects on the synthesized particle properties have been carefully investigated and elucidated based on the designed experiments while the obtained experimental results include crystallites, particle morphology, size and size distribution. In order to enhance these concerned properties and improve the production efficiency, fine particles were synthesized by shear controlling approach,

focusing on the eddy turbulence-induced shear impact on the synthesis process while such turbulence-induced shear can be modulated by applying the turbulence intensification measures. To further improve and modify the synthesized particle properties, the pre-prepared particles obtained from the SVFR were also subjected the hydrothermal post-treatment in a hydrothermal autoclave and the hydrodynamics in the hydrothermal autoclave was analysed. CFD modelling has been employed to assist for the acquirement of the hydrodynamic parameters such as shear induced turbulent energy dissipation rate, turbulent kinetic energy distribution and particle-eddy interactions occurring in the IJR and SVFR. Lagrangian tracking of the synthesized particles in the hydrothermal autoclave was conducted to reveal the dynamic process of the particle dispersion in the hydrothermal autoclave.

The investigations conducted in this PhD thesis have made it possible to build the correlations of the hydrodynamics with the synthesised fine particle characteristics and to achieve shear controllable synthesis of fine particles with the required properties. This would benefit the design, upgrade and scale-up of multiphase reactors for particle synthesis process. As the outcomes of the present studies, the main accomplishments of this project can be summarised as:

(1) A fast way of preparation of nano-sized  $\text{FePO}_4$  in the IJR with the assistance of ultrasound irradiation has been proposed. It was found that  $\text{FePO}_4$  particles could be obtained with higher crystallinity and uniformity, higher porosity and smaller size with ultrasound intensification. These characteristics are of vital importance for synthesised  $\text{FePO}_4$  nanoparticles as precursor materials in the fabrication of lithium-ion batteries to

have the features of high capacity and recycling numbers on assembly, where high porosity is particularly important. Both experimental studies and CFD simulations have been carried out for validation of the effectiveness of this approach. The results have clearly indicated that the ultrasound-assisted IJR system can effectively intensify the micro-mixing as the result of enhancement on the local turbulent dissipation rate. However, the application of ultrasound is only effective for the synthesis of FePO<sub>4</sub> nanoparticles when the threshold of the applied ultrasound intensity is reasonable.

(2) The turbulent micromixing in the IJR assisted by ultrasound has been investigated and the micromixing performance was quantitatively analysed by segregation index via the Villermaux-Dushman reaction. The chemical reaction was considered and analysed, validated experimentally and has also been implemented into CFD modelling. A series of experiments have been carried out under different acid concentrations (H<sup>+</sup>) and various turbulent Reynolds numbers. It was found that higher acid concentration leads to higher segregation index and poor mixing performance. The experimental results also clearly indicate that the intensification of local turbulence would give rise to an increase in micromixing efficiency. In addition, the adoption of ultrasound irradiation can have a significant influence on the micromixing as more very small-scale turbulent eddies will be generated, consequently enhancing the turbulence dissipation. The time-scale analysis based on the incorporation model for micromixing has revealed that the estimated micromixing time is in the range of  $1.7 \times 10^{-4}$  to  $2.3 \times 10^{-5}$  s.

(3) A new type of structured mixer, so called ‘swirling vortex flow reactor (SVFR)’, has been proposed and used in the synthesis process for SiO<sub>2</sub> fine particles. The

experimental data have indicated that such reactor is suitable to synthesize the aggregated SiO<sub>2</sub> nano-particles due to its enhanced eddy engulfment feature, which is beneficial to local mass transfer. From both experimental observation and simulation results, the SVFR reactor was found to be able to generate a strong ‘Rankine vortex-like’ flow with a great velocity gradient in the radial direction. Such ‘Rankine vortex’ could trap the synthesised aggregated SiO<sub>2</sub> nanoparticles into the vortex core to form enhanced engulfment for particle aggregation. In this process, the mass transfer characterised by Sherwood number on basis of film refresh model, was found to be enhanced by engulfment and the local shear, which may re-shape the SiO<sub>2</sub> nanoparticles, yielding well spherical morphology and narrower size distribution. Both CFD simulation and experimental results have manifested that the adoption of the ultrasound irradiation assisted SVFR can remarkably enhance the mass transfer due to the intensified micro-turbulent eddy engulfment.

(4) The post-hydrothermal treatment of synthesised aggregated nano-sized SiO<sub>2</sub> particles has been performed in the hydrothermal autoclave. After being synthesised in the SVFR, the SiO<sub>2</sub> primary particles were introduced into the autoclave. These particles are experiencing consistent shear owing to the Rayleigh-Bernard induced vortex shear flow driven by the exerted temperature gradient in the solution held in the hydrothermal autoclave. These synthesized SiO<sub>2</sub> particles were characterised by applying different applied nominal temperature, treatment duration and primary particle sizes. It was found from the study that the Rayleigh-Bernard convection induced shear is enhanced once the applied nominal temperature surrounding the autoclave increases, leading to shear aggregation to supersede the Brownian

aggregation. A correlation of Raleigh number with the shear rate and aggregated-particle size was suggested to highlight the effect of Rayleigh-Bernard convection induced shear on the particle aggregation. In the meantime, CFD modelling has reproduced the symmetric vortex flow pattern occurring in the hydrothermal autoclave and has also indicated that the synthesized SiO<sub>2</sub> particles are dispersed on the action of Rayleigh convection induced vortex shear flow.

## **6.2 Specific realisations**

### **6.2.1 The hydrodynamic effect on synthesis of nanosized FePO<sub>4</sub> in an impinging jet reactor**

The hydrodynamic effect of ultrasound-assisted imping jet reactor on synthesis process of FePO<sub>4</sub> nanoparticles and micromixing efficiency was quantified and analysed in Chapters 2 and 3, respectively. The governing mechanisms of shear turbulence controllable particle synthesis in the impinging jet reactor were proposed, presenting a correlation to assess the properties of FePO<sub>4</sub> particles synthesised in the impinging jet reactor. The particle properties such as crystallinity, particle morphology and particle size distribution have been characterised and analysed in detail as reported in Chapter 2. The XRD results show that the peaks of the relative intensity of synthesized FePO<sub>4</sub> samples are well consistent with typical characteristics of hexagonal FePO<sub>4</sub> crystal, indicating the high purity and crystallinity and the intensity of diffraction peaks becoming noticeably stronger for the synthesis of FePO<sub>4</sub> particles when imposing ultrasound irradiation to the turbulent impinging jet flow. Based on the average

crystallite size  $L$  that is calculated through the Scherrer equation ( $L = \frac{K\lambda}{\beta\cos\theta}$ ) (Liu and Fox, 2006), FePO<sub>4</sub> particle samples prepared in the impinging jet reactor without applying the ultrasound irradiation has an average crystallite size of 191 nm while those prepared with applying the ultrasound irradiation with the input power of 600 W present an average size of 107 nm. The narrower particle size distribution and more uniform microstructure were also observed from a series of SEM images of FePO<sub>4</sub> samples caused by applying higher intensity of the ultrasound. Except for crystallinity and morphology, the applied ultrasound power was also found to have an impact on the porosity of the synthesized FePO<sub>4</sub> particles. The BET test further affirmed that FePO<sub>4</sub> samples have a smaller particle size with higher porosity when applying ultrasound irradiation. The enhanced porosity may be attributed to the ultrasound-induced micro-bubbles collapse which takes place in an extremely short time and the generated tiny eddies bombard the particle surface to form the porous structure. In addition, the uniformity of the particle shapes is improved as the result of local turbulent eddies induced shear while this shear action by acoustic streaming will be likely to have brought an instant strong shear force acting on the nanoparticles to diminish and smooth the ragged surfaces.

To explore such effect, 3D-CFD modelling was conducted to verify the experimental results that the synthesized nanosized particles entrained by the turbulent eddies experience the local shear and the shear stresses. The standard  $k$ - $\epsilon$  model was employed as the mixing in the core of the confined impinge jet reactor is highly turbulent. Considering the effect of ultrasound on the bulk flow, the periodic pressure change of the applied ultrasound irradiation as a boundary condition was introduced

into the CFD modelling to describe the perturbation to the turbulent impinging jet flow field (Cai *et al.*, 2009). The tip of the ultrasonic horn was set as a pressure inlet. The ultrasound intensification results in even strong eddy fluctuations, enhancing the turbulent kinetic energy  $k$ . It was observed from the iso-surface contour distribution of turbulent kinetic energy ( $k$ ) with various applied ultrasound power conditions, the enhancement of the turbulent kinetic energy  $k$  was found to occur in the vicinity of the tip of the ultrasound transducer and the region of the reactor outlet. It was postulated that the ultrasound irradiation intensifies the reactant mixing and encourages rapid reaction to form the nuclei of FePO<sub>4</sub> with smaller size, caused by enhanced interactions between the turbulent eddies and the nuclei of FePO<sub>4</sub>. The micromixing efficiency was also approximately estimated in terms of the micromixing time as a function of turbulent dissipation rate (Liu and Fox, 2010). An empirical relationship was derived from the experiments based on the power-law as  $t_m = 0.0005\varepsilon^{-0.164}$ . The use of this empirical relationship has indicated that the micromixing time is in the order of magnitude of  $10^{-4}$  s and the micromixing time can be reduced up to 98.6% once the ultrasound irradiation with an input power of 960 W is applied compared with the cases without introducing ultrasound irradiation.

An in-depth illustration of the effect of ultrasound irradiation on the micromixing behaviour in the IJR was shown in Chapter 3. In Chapter 3, investigations on the micromixing performance in the impinging jet reactor were performed by employing Villiermaux-Dushman reaction with variables of acid concentration, variations in inlet Reynolds number and amplitude of the ultrasound irradiation. In this chapter, the chemical reaction was considered and analysed through experiments and CFD

simulation. The micromixing performance is quantified by segregation index  $X_s$  and by the local time-dependent fluctuation degree ( $\alpha$ ). To investigate the effect of acid concentration, acid solution of different concentration (0.02 M, 0.04 M, 1 M) was used to react with iodide-iodate solution and the calculated segregation indexed were found to be  $X_s = 0.04$ ,  $X_s = 0.09$ , and  $X_s = 0.12$ , respectively. The experimental results clearly indicate that the excessive acid concentration could trigger the occurrence of Reaction (R-2) leading to more  $I_3^-$  generation and a higher segregation index, resulting in poor micromixing. The micromixing efficiency was also found to be enhanced with an increase in Reynolds number ( $Re_T$ ) when increasing the inlet flow rate. The turbulence intensification at the impingement zone can be attributed to the stronger engulfment effect and turbulent eddies with the sizes down to the Kolmogorov scale. As the turbulent Reynolds number  $Re_T$  increases from 12.7 to 17.4, the corresponding segregation index  $X_s$  obtained from the experimental data changes from 0.105 to 0.07 while the micromixing time is significantly reduced up to 66.7% when the ultrasound power increases 50% ( $P = 840$  W).

CFD simulation results were found to be consistent with the experimental data with a difference of less than 10 %. The micromixing degree defined by  $\theta = 1 - \bar{\alpha}$  was found to enhance from 0.298 to 0.396 as ultrasound amplitude was increased from 30 % ( $P = 360$  W) to 60 % ( $P = 720$  W). The vorticity ( $\Omega$ ) obtained from CFD simulation results, which may be used to describe the local induced shear, is correlated with the mixing degree  $\theta$  to quantitatively explain the effect of turbulence shear on the micromixing performance. The CFD modelling results indicate that the correlation factor  $R_{\theta,\Omega}$  dramatically increases when the ultrasound amplitude applied increases.

A high level of vorticity greatly contributes to turbulence intensification thus enhances the micromixing performance in the impinging jet reactor. The mixing time was also estimated as a function of segregation index  $X_s$  based on the theory of incorporation model implemented in the CFD modelling (Fournier *et al.*, 1996). To be specific, the micromixing time calculated based on CFD modelling was found to be in the range of  $1.7 \times 10^{-4}$  to  $2.3 \times 10^{-5}$  s when the applied ultrasound power amplitude changes from 0 % to 70 % (0 W to 840 W), which is consistent with the micromixing time estimation according to Liu and Fox (2010). In addition, Damköhler number  $Da$  was also found to be far smaller than 1, indicating the appropriateness of adopting the Villermaux-Dushman reaction for evaluation of the micromixing performance in CFD modelling.

### **6.2.2 The hydrodynamic effect on synthesis of aggregated SiO<sub>2</sub> nanoparticles in a swirling vortex flow reactor and post-treatment in a hydrothermal autoclave**

Further studies concentrated on the other new type of structured mixer, so-called ‘swirling vortex flow reactor (SVFR)’. The hydrodynamic effects of SiO<sub>2</sub> synthesis of aggregated nanoparticles in the SVFR and the post-treatment in a hydrothermal autoclave were assessed and analyzed in Chapters 4 and 5. The SVFR consists of two fast tangential inlet streams that strongly mix to form a vortex in the swirling chamber, where the engulfment between the reactants introduced from the two inlet streams can enhance the mass transfer. The strong ‘Rankine vortex-like’ flow generated in the SVFR can have a large shear gradient in the radial direction. The SiO<sub>2</sub> floccule was prepared in such a reactor through a modified sol-gel approach and the hydrolysis process proceeded in the presence of a NaOH solution acting as a homogenising agent.

The overall hydrolysis–condensation reaction rate was assumed to follow the first-order reaction with the rate constant ( $k$ ) as  $r' = -\frac{d[\text{Si}(\text{OC}_2\text{H}_5)_4]}{dt} = k[\text{Si}(\text{OC}_2\text{H}_5)_4]$  in the CFD modelling. The work done as reported in these two chapters has investigated the hydrodynamics and mass transfer in the process of  $\text{SiO}_2$  synthesis using the SVFR for the pre-preparation of  $\text{SiO}_2$  particles, focusing on the liquid-solid mass transfer effect on the synthesized particle characteristics such as particle morphology and particle size distribution in the condition of a wide range of Reynolds numbers. Considering the swirling-vortex structure of reactor, Reynolds number  $Re_V$ , was defined based on the vortex characteristic length  $R_v$ , as  $Re_V = \frac{2\omega R_v^2}{\nu}$ .

The morphology of the synthesized nanosized  $\text{SiO}_2$  mono size particles was detected by the SEM and the size distribution was measured by a laser particle size analyzer. It was observed that all the mono size particles were visualized to present a morphologically spherical shape and the aggregation of such mono size particles were found to be affected by the local turbulence-induced shear. The Sauter mean diameter ( $d_p$ ) of aggregated particles is as large as 18.42  $\mu\text{m}$  and the Sauter mean diameter is almost monotonically changeable when both the ultrasound power imposed to the SVFR and the local turbulent Reynolds number are increased. When the Reynolds number  $Re_V$  and the adopted ultrasound power increase, the average synthesized  $\text{SiO}_2$  particle size is reduced, accompanied by a narrower particle size distribution and higher porosity. Turbulent Reynolds number, defined as  $Re_T = \frac{\langle k \rangle}{((\epsilon)\nu)^{1/2}}$ , was also employed to quantify the local turbulence level, which was obtained from CFD modelling.

In the CFD modelling of the flow in the swirling vortex flow in the reactor, Eulerian-Eulerian two-fluid model approach was adopted to predict the turbulent shear flow and the mass transfer characteristics in the SVFR. In the simulation, the floc solution and SiO<sub>2</sub> particles were treated as two independent pseudo-continuum phases but interacted with each other. RNG k- $\epsilon$  model was adopted as the flow in the reactor is strongly swirling and highly turbulent. Modelling of the chemical reaction and ultrasound irradiation were implemented into the simulation once the turbulent flow field in the reactor has been well established when the simulation without considering these two conditions has been observed to asymptote the steady solution. Ultrasound irradiation with a fixed frequency of 20 kHz was imposed as the boundary condition of cyclic sound pressure at the probe tip surface in terms of pressure amplitude based on Cai's model (Cai *et al.*, 2009) the same as the way mentioned in Chapters 2 and 3. Furthermore, the mass transfer from aqueous silicate to solid silicon dioxide floccule, dominated by diffusion, was described by solving the mass fraction transport equation. A modified Sherwood number Sh (Al-Sood and Birouk; 2007) was introduced to indicate the correlation between the mass transfer in the interface of the aggregated nanoparticles and the local turbulent shear stresses. It has been proved that ultrasound irradiation intensification can enhance the local turbulence and turbulent shear stresses, resulting in the enhanced mass transfer. The spatial correlation between the mass transfer in the interface of the aggregated nanoparticles and the local turbulent shear stresses can be used to predict the mass transfer for the particles in the synthesis process. Moreover, the interaction between the local turbulence and the particle nuclei growth dominated by the reaction process was highlighted by Damköhler number,  $Da$ . It was also affirmed that increasing the Reynolds number  $Re_V$  and the adopted ultrasound

power can lead to a reduction in  $Da$  number, indicating that the effect of turbulence-induced shear on the synthesised particles is reinforced compared with the effect of hydrolysis in the synthesis process.

The prepared  $\text{SiO}_2$  nanoparticles synthesised in the SVFR have the features of narrower particle size distribution and higher porosity and such features can be further modified by the adoption of the hydrothermal post-treatment. Chapter 5 focuses on the effect of Rayleigh-Bernard induced shear on the particle properties in the synthesis of mesoporous spherical  $\text{SiO}_2$  particles by post-hydrothermal treatment using the SVFR for pre-preparation of the  $\text{SiO}_2$  particles. Unlike the IJR and SVFR, the shear generated in a hydrothermal autoclave due to the Rayleigh convection is generally mild, thus being beneficial to the improvement of the properties of the synthesised particles that have been obtained from a pre-synthesis process using the IJR or SVFR reactors. The study proposed the synthesis route for  $\text{SiO}_2$  particles preparation in the SVFR and then particles were introduced into the autoclave for a period of up to 1-3 hours subjected to a shear driven by the Rayleigh-Bernard convection in the autoclave. The particle growth is also investigated based on different hydrothermal conditions for different applied nominal temperature, treatment duration and primary particle sizes. The Rayleigh convection, driven by a temperature gradient, is characterised by Rayleigh number  $Ra$ . Both experimental and CFD simulation results have indicated that the induced shear flow falls into the regime of laminar shear flow. Consequently, it applied a steady and almost constant shear force on the pre-synthesised particles, ensuring to better control the morphology of the synthesised particles. From the XRD patterns of  $\text{SiO}_2$  particles, it can be concluded that the hydrothermal treatment can effectively

improve the crystallization of the SiO<sub>2</sub>, making one-step particle shear controllable synthesis possible without calcination. As can be found from the statistical results of the SEM, the synthesized SiO<sub>2</sub> particle size tends to be smaller with prolonging hydrothermal treatment in the hydrothermal autoclave and an increase in the applied temperature gradient on the hydrothermal autoclave may generate more compacted structures but with higher tapped densities.

CFD modelling results have also reproduced the symmetric vortex flow structure in the hydrothermal autoclave and have shown the particle interactions with such shear flow using the Euler–Lagrange two-way coupling approach. The Rayleigh convection induced shear flow in the floc solution phase was predicted by solving the momentum equation with the Volume of Fluid (VOF) method while the SiO<sub>2</sub> particle dispersion was modelled by tracking the particles using Eulerian-Lagrangian approach, i.e. the use of the DPM model incorporated in the ANSYS Fluent code. The impact of Rayleigh convection induced shear on the size of synthesized particles was illustrated the correlation of Raleigh number with the shear rate and the aggregated particle size. The correlation factor was proposed to highlight the effect of shear-induced by Rayleigh-Bernard convection on particle aggregation. It was found that the shear is greatly enhanced as the applied nominal temperature surrounding the autoclave increases, resulting in shear aggregation to supersede the Brownian aggregation.

### **6.3 Recommendation of future work**

This PhD work has attempted to demonstrate the effects of hydrodynamics in the two multiphase reactors, i.e. IJR and SVFR, on the synthesized particle properties, thus realising the shear controllable synthesis of fine particles for the given particle characteristics using shear modulation technology, including shear turbulence intensification and Rayleigh convection induced shear flow. The adoption of these two fast-mixers with assisted ultrasound irradiation for micro/nano-particle synthesis has been proved to be able to achieve shear turbulence intensification, consequently enhancing the eddy engulfment for better mass transfer between the reactant solution and the synthesized particles so as to circumvent the drawbacks of traditional multiphase reactors such as the mixing tank, that are typically recognized to have the features of high energy consumption, low conversion rate, poor mixing and long reaction time. The revealed correlations between turbulence-induced shear and the properties of the fine particles synthesized in such a reactors may be beneficial to the design of the new types of the reactors and scale-up of the reactors in the industry for better control particle synthesis process. Although ultrasound-assisted IJR and SVFR reactors have been demonstrated to have some important hydrodynamic features in fine-particle synthesis processes, which have significant influences on involved chemical reaction, micromixing and mass transfer taking place in the synthesis, there are remaining several problems needed to be addressed. On basis of the accomplishment of present work, recommendations for future work are summarized as follows:

(1) In the present study, both  $\text{FePO}_4$  and  $\text{SiO}_2$  fine particles synthesised by using the IJR and SVFR, based on the SEM images of the primary mono-particles of the products, were found to be quite spherical and the analysis and CFD modelling have not considered the variances in shapes among individual particles. Nevertheless, such assumption has actually deviated from reality as there still exists a certain amount of irregular shape synthesised particles. It can be envisaged that the shear stresses exerted on the particle surfaces due to the local turbulence-induced shear or the instant pressure changes caused by a sudden collapse of the microbubbles induced by ultrasound irradiation may not be uniformly distributed. This may bring out a noticeable effect on the actual shapes of the particle. As a result, the drag force experienced by the particles may have remarkable changes so that the application of the equation of particle motion in CFD modelling for particle trajectory prediction may yield different results. So far, it is a widely accepted practice in CFD modelling to use the ‘equivalent’ diameter to account for the effect of both shape and size for non-spherical particles on the drag coefficient. The effects of the irregularity and nonuniformity of particles in CFD simulation on the particle dispersion, mass transfer and chemical reaction (especially surface reaction) are still not appropriately addressed. Thus, one of the recommended future studies is to investigate on the effect of turbulence-induced shear on the drag force acting on non-spherical shaped particles such as micro/nano-sheet, micro/nanotube, tetrahedral-shaped and hexahedral-shaped particles. This may require DNS simulation. Also, in the CFD modelling, the effect of roundness and aspect ratios of the individual particle for particle trajectory prediction can be considered through the trial simulations to obtain the drag coefficient. This method can be then applied to the studies for a better

description of the turbulence-induced shear hydrodynamic effects on the synthesised particle properties that are synthesized in various reactors.

(2) To intensify the turbulence-induced shear in the particle synthesis process, external ultrasound irradiation with a frequency of 20 kHz was used in the present study and the adoption of such ultrasound irradiation to induce so-called acoustic streaming in the flow to partially realise the turbulence intensification has been confirmed to be effective. Bulliard-Sauret *et al.* (2019) have argued that the strong disturbance induced by ultrasound irradiation is caused by both convective acoustic streaming and cavitation effects. Acoustic streaming is a generic term defining a liquid or a gas flow driven by acoustic waves while acoustic cavitation contributes to the growing, oscillating and collapsing phenomenon of gas and vapor cavities induced by ultrasound propagation within a liquid. The present study has only considered acoustic streaming to be the predominant mechanism for turbulence shear intensification in CFD modelling, thus implemented the ultrasonic wave propagation in terms of time-dependent pressure profile into the CFD simulation based on Cai's model (Cai *et al.*, 2009). Further work on CFD modelling should consider the ultrasound irradiation effect thoroughly by introducing the cavitation effect in the model. Consequently, a source term to represent the ultrasound irradiation acoustic effect on turbulence-induced shear is proposed to be implemented into the  $k$ - $\varepsilon$  model to account for the ultrasound irradiation modulation on the turbulence intensification in the flow occurring in the synthesis process.

(3) Both CFD simulations and experiments were conducted in the present study to verify the hydrodynamic effect on particle characteristics in the synthesis process,

especially the turbulence-induced shear. Although it has been found that the turbulence-induced shear closely correlates with the synthesised particle properties such as particle size and porosity, the parameters that can be used to characterise the turbulence-induced shear were not directly obtained in the conducted experiments instead obtained by CFD modelling. This will give rise to many limitations as the models implemented in the CFD modelling may not well reflect the hydrodynamic effects. A more direct and simple approach to verify the hydrodynamic effect on particles properties in the multiphase reactor is thus to employ advanced visualization techniques such as holographic PIV, tomographic PIV, 3D PTV or defocusing PIV for measuring and analysis of the turbulence shear in the flows.

(4) Both the IJR and SVFR adopted in the present study can be classified as microreactors with relatively small reactor chamber. They can be used alternatively for semi-batch or continuous synthesis of fine particles coupled with chemical reactions. Owing to their small size, these two reactors have exhibited the advantages of fast mixing, enhanced mass transfer and economical applicability. In spite these advantages, their low throughput will be difficult for industrial scale application. Future studies will seek the scale-up of the two reactors using the CFD modelling and experimental validation. A key step is to identify the law for scaling-up. The turbulence-induced shear, especially based on the local turbulent energy dissipation rate, will be further investigated, focusing on the synthesis processes occurring in the reactors. The turbulent kinetic energy spectra for the turbulent shear flow in these two types of reactors will be studied using the large-eddy simulation (LES), which will be better for

revealing the turbulent eddy induced shear in the reactors so that the interactions between the synthesized particles and such induced shear can be clearly indicated.

## References

AL-SOOD, M. & BIROUK, M. 2007. A numerical study of the effect of turbulence on mass transfer from a single fuel droplet evaporating in a hot convective flow. *International Journal of Thermal Sciences*, 46, 779-789.

BULLIARD-SAURET, O., BERINDEI, J., FERROUILLAT, S., VIGNAL, L., MEMPONTEIL, A., PONCET, C., LEVEQUE, J. M. & GONDREXON, N. 2019. Heat transfer intensification by low or high frequency ultrasound: Thermal and hydrodynamic phenomenological analysis. *Experimental Thermal and Fluid Science*, 104, 258-271.

CAI, J., HUAI, X., YAN, R. & CHENG, Y. 2009. Numerical simulation on enhancement of natural convection heat transfer by acoustic cavitation in a square enclosure. *Applied Thermal Engineering*, 29, 1973-1982.

FOURNIER, M.-C., FALK, L. & VILLERMAUX, J. 1996. A new parallel competing reaction system for assessing micromixing efficiency—determination of micromixing time by a simple mixing model. *Chemical Engineering Science*, 51, 5187-5192.

LIU, Y. & FOX, R. O. 2006. CFD predictions for chemical processing in a confined impinging-jets reactor. *AIChE Journal*, 52, 731-744.



## LIST OF PUBLICATIONS

### Journal articles

[1] Liu, L., Yang, X., Yang, J., Li, G., **Guo, Y.**, Xue C. Modelling of turbulent shear controllable co-precipitation synthesis of lithium ion battery cathode precursor micro-particles in a Taylor-Couette flow reactor with variable configurations of inner cylinder. *Chemical Engineering Journal*. **2021**;411:128571.

[2] Liu, L., Yang, X., Yang, J., Li, G., **Guo, Y.**, Effect of Hydrodynamic Heterogeneity on Micromixing Intensification in a Taylor-Couette Flow Reactor with Variable Configurations of Inner Cylinder. *AIChE Journal*. **2021**(299).

[3] **Guo, Y.**, Yang, X., Li, G., Yang, J., Liu, L., Chen, L., and Li, B., Shear Turbulence Controllable Synthesis of Aggregated Nano-Particles Using a Swirling Vortex Flow Reactor Assisted by Ultrasound Irradiation. *Chemical Engineering Journal*, **2020**:126914.

[4] Chen, L., Dong, B., **Guo, Y.**, Yang, X., and Li, G., CFD modelling of the effects of local turbulence intensification on synthesis of LiFePO<sub>4</sub> particles in an impinging jet reactor. *Chemical Engineering and Processing - Process Intensification*, **2020**; 155:108065.

[5] **Guo, Y.**, Yang, X., Li, G., Dong, B., and Chen, L., Effect of ultrasonic intensification on synthesis of nano-sized particles with an impinging jet reactor. *Powder Technology*, **2019**; 354:218-230.

[6] Kong, Y., Hu, B., **Guo, Y.**, and Wu, Y., Effect of ionic liquids on stability of O/W miniemulsion for application of low emission coating products. *Chinese Journal of Chemical Engineering*, **2016**; 24(1):196-201.

## **Under review**

[1] **Guo, Y.**, Yang, X., Li, G., Dong, B., and Chen, L., 2020. Shear controllable synthesis of mesoporous silica spherical particles using swirling flow reactors and post-hydrothermal treatment. (submitted to Chemical Engineering Journal).

[2] **Guo, Y.**, Chen, L., Yang, X., Li, G., Yang, J., Liu, L., 2020. Turbulent micromixing intensification in the impinging jet reactor assisted by ultrasound irradiation and characterisation by villermaux-dushman reaction. (submitted to Chemical Engineering Journal).



# Shear turbulence controllable synthesis of aggregated nano-particles using a swirling vortex flow reactor assisted by ultrasound irradiation

Yanqing Guo<sup>a</sup>, Xiaogang Yang<sup>a,\*</sup>, Guang Li<sup>a</sup>, Jie Yang<sup>b</sup>, Lu Liu<sup>a</sup>, Luming Chen<sup>c</sup>, Bin Li<sup>a</sup>

<sup>a</sup> Department of Mechanical, Materials and Manufacturing Engineering, University of Nottingham Ningbo China, Ningbo 315100, PR China

<sup>b</sup> School of Mathematical Sciences, University of Nottingham Ningbo China, Ningbo 315100, PR China

<sup>c</sup> Institute of Process Equipment and Control Engineering, Zhejiang University of Technology, Hangzhou 310014, PR China

## HIGHLIGHTS

- Shear turbulence generated in a turbulent swirling Rankine vortex flow reactor.
- Damköhler number  $Da$  describing particle synthesis strongly correlated with the  $ReT$ .
- Mass transfer of synthesis enhanced by shear turbulence and ultrasound irradiation.

## ARTICLE INFO

### Keywords:

Mass transfer  
Vortex flow reactor  
Engulfment  
Nanoparticle preparation  
Ultrasonic intensification

## ABSTRACT

The mass transfer in the shear controllable synthesis process of nano-sized particles using a swirling vortex flow reactor is investigated. This type of a reactor is able to generate a strong 'Rankine vortex-like' flow with a great shear gradient in the radial direction, trapping the synthesised aggregated nano-particles into the vortex core to form aggregation. The aggregated particles are further agglomerated to form larger particles with high uniformity under the action of turbulent shear and subsequent mass transfer due to engulfment occurred in the turbulent eddies. The mass transfer is enhanced by engulfment between the slabs of the liquid streams tangentially entering into the reactor while the local shear in the turbulent eddies with the length scales down to the Kolmogorov scale shape the particles, yielding well spherical morphology and narrower size distribution. In addition, the mass transfer performance can be further improved by intensifying the local turbulent shear by applying the ultrasound to the synthesis process. The instantaneous collapse of cavitation bubbles in the vortex due to the introduction of ultrasound results in intensified micro-turbulent streaming. The particle characteristics, chemical reaction and mass transfer performance are found to be correlated with the local turbulence characteristics in the vortex. The mass transfer can be characterised using the film refresh model via the Sherwood number by considering the agglomerated particles response to the turbulent eddies. Both numerical simulation and experimental results clearly indicate the existence of the correlation in synthesis of aggregated nano-particles in swirling vortex reactor between the mass transfer and turbulence shear by using ultrasound irradiation.

## Nomenclature

$a_p$	[m <sup>2</sup> ]	Interfacial area of particles
$C$	[m/s]	The sound speed in the water
$C_v$	[-]	Volume fraction of dispersed phase
$C_{i,Si}$	[mol/m <sup>3</sup> ]	Concentration of Si(OH) <sub>4</sub>
$C_{i,Si}^*$	[mol/m <sup>3</sup> ]	Saturated concentration of Si(OH) <sub>4</sub>
$d_p$	[m]	Particle diameters
$d_o$	[m]	Diameter of the reactor chamber
$D$	[m <sup>2</sup> /s]	Diffusion coefficient

## Nomenclature (continued)

$\varepsilon$	[m <sup>2</sup> /s <sup>3</sup> ]	Energy dissipation rate
$f$	[Hz]	Frequency of the ultrasound wave
$k$	[s <sup>-1</sup> ]	Rate constant
$k_{sl}$	[m <sup>2</sup> /s]	Solid-liquid mass transfer coefficient
$\langle k \rangle$	[m <sup>2</sup> /s <sup>2</sup> ]	Averaged turbulent kinetic energy
$I$	[-]	Turbulence intensity
$I_{us}$	[W/m <sup>2</sup> ]	Ultrasound intensity
$\rho$	[kg/m <sup>3</sup> ]	Density

(continued on next page)

\* Corresponding author.

E-mail address: [Xiaogang.Yang@nottingham.edu.cn](mailto:Xiaogang.Yang@nottingham.edu.cn) (X. Yang).

<https://doi.org/10.1016/j.cej.2020.126914>

Received 8 July 2020; Received in revised form 25 August 2020; Accepted 2 September 2020

Available online 08 September 2020

1385-8947/ © 2020 Elsevier B.V. All rights reserved.

## Nomenclature (continued)

$p$	[pa]	Sound pressure
$P_a$	[pa]	Amplitude of the sound pressure
$P$	[W]	Ultrasound power
$P_A$	[%]	Ultrasound amplitude
$P_s$	[W]	Specified ultrasound power
$Q$	[m <sup>3</sup> /s]	Volumetric flow rates
$r'$	[mol/s]	Reaction rate
$R_v$	[m]	Radius of vortex
$S_{l \rightarrow s}$	[-]	Mass transfer source term of SiO <sub>2</sub>
$t$	[s]	Time
$u_l$	[m/s]	Velocity of liquid phase
$u_p$	[m/s]	Velocity of particles
$\mu_L$	[pa*s]	Dynamic viscosity
$\mu_{eff}$	[pa*s]	Effective dynamic viscosity
$u_\theta$	[m/s]	Tangential velocity of Rankine vortex.
$v$	[m/s]	Velocity
$V$	[m <sup>3</sup> ]	Volume of reactor chamber
$\alpha_l$	[-]	Volume fraction of liquid phase
$\langle \varepsilon \rangle$	[m <sup>2</sup> /s <sup>3</sup> ]	Averaged energy dissipation rate
$\tau_c$	[s]	Chemical time scales
$\tau_l$	[-]	Stress strain of liquid phase
$\tau_t$	[s]	Turbulent time scale
$\Gamma_{L, Si}$	[pa*s]	Dynamic viscosity of Si(OH) <sub>4</sub>
$\nu$	[m <sup>2</sup> /s]	Molecular viscosity
$\nu_{eddy}$	[m <sup>2</sup> /s]	Eddy viscosity
$\omega$	[s <sup>-1</sup> ]	Angular velocity of vortex
$\langle \eta \rangle$	[m]	Kolmogorov scale
$\varphi$	[-]	Characteristic length ratio

## 1. Introduction

A so-called swirling vortex flow reactor has been proposed as a high-shear mixer used for synthesis of nanoparticles, due to its unique hydrodynamic characteristics of mixing and mass transfer [1,2]. This swirling vortex reactor consists of two fast tangential inlet streams - strongly recirculating and evolving in a swirling chamber with engulfment of two inlet streams presenting a rotating vortex structure in the core. Pressure in the central part of swirling turbulence vortex reduces owing to centrifugal forces pushing the liquid and particles to the outside when particles' density is higher than solution. Kockmann *et al.* [3] proposed engulfment flow in a T-shaped mixer and attributed the enhanced mass transfer to the emergence of vortices as the result of energy dissipation. The vortex structure in engulfment flow was numerically simulated by Mariotti *et al.* [4] and quantified by vortex indicator  $\lambda^2$ , which is susceptible to the tilt angle of inlets. Shoukry and Shemilt [5] have illustrated the enhancement of the mass transfer coefficient of up to 320% in swirling annular pipe flow compared with developed axial flow. The decay of swirl leads to a reduction in the mass transfer augmentation along the flow path. Legentilhomme *et al.* [6] have further increased the mass transfer coefficient up to 550% by the modification of geometric factors in annular swirling flow. Contigiani *et al.* [7] illustrated that the mass-transfer enhancement factor of recirculating flow increases due to intensive forced convection and the sudden expansion at the inlet of tangential stream flow. The swirling vortex flow reactor presents a deviation of mass transfer in a wide range of Re numbers of two streams in both symmetrical and asymmetrical scenarios.

It has been recognised that acoustic cavitation affects nuclei growth in a liquid medium under low-pressure cycles and contributes towards micro-bubble collapse under high-pressure cycles, which may be responsible for the enhancement in mass transfer rates. Adoption of ultrasound acts as an active enhancing approach by inputting external energy with oscillation and swirling of vortices resulting in the folding and stretching of the interface, which improves the mixing and mass transfer performance [8]. Conversely, ultrasound irradiation in terms of shock waves induces a cavitation effect, which triggers oscillation and

the collapse of microbubbles producing micro-streaming and turbulent eddies [9,10]. Sajjadi *et al.* [11] have numerically simulated ultrasound pressure via an inhomogeneous Helmholtz equation as a boundary condition by claiming that the ultrasound helps to produce extra turbulence that overcomes the mass transfer restriction. They also proved that the propagation of acoustic streaming doubles the turbulent intensity of the mechanical stirring. In addition to the intense turbulence driving the mass transfer process, particles are modified while they are pushed and engulfed at the core of vortices with strong local shear that are responsible for particles of high uniformity. Pioneering studies have also claimed that ultrasound intensity has a significant influence on particle morphology, particles size distribution (PSD) and tap density with a threshold existing for the effect on PSD instead of being monotonous [12–14]. Jordens *et al.* [14] have experimentally verified that lower frequencies and higher intensities of ultrasound may contribute towards particles with higher sphericity. Rahimi *et al.* [15] have simulated the Villermaux-Dushman reactions in a T-type microreactor assisted by ultrasound waves and indicated that the segregation index can be increased up to 10–20% by the employment of a piezoelectric transducer at 42 kHz.

Mesoporous silica dioxide (SiO<sub>2</sub>) nano-particles were explored as stable supporters and synthesised in the swirling reactor with its outstanding properties including high mechanical strength and non-interference effectivity [16]. The functionalised agents are immobilised on mesoporous SiO<sub>2</sub> as composite materials enable a high rate of mass transfer and are potentially beneficial to the adsorption process with their high cost effectiveness and are widely applied in catalysts [17], carriers [18], surfactants [19], stabilizers [20–22] and biosensor [23]. The polymerisation of hydrous silicon dioxide is able to result in the complex branching of polymers due to the tetra-functional hydrolysed monomer Si(OH)<sub>4</sub> [24]. The synthesis of porous SiO<sub>2</sub> microspheres in the presence of organic templates and/or additives has also been intensively investigated in recent years. Yu *et al.* [25] have prepared monodispersed microporous SiO<sub>2</sub> microspheres of high porosity up to 61.4% in the range of 0.52 to 1.25  $\mu\text{m}$  by adjusting the amount of dodecylamine (DDA). These hydrolysis catalysts through the hydrolysis of TEOS in water-ethanol mixture suggest that the concentration of silicon source and DDA play significant roles in the size and porosity control of SiO<sub>2</sub> synthesis. Yano and Fukushima [26] controlled the size and porosity of monodispersed particles by synthesising the temperature and the ratio of methanol and water in solvent to the silica source, with the particle size ranging from 0.52 to 1.25  $\mu\text{m}$ .

It should be noted that the morphology of amorphous SiO<sub>2</sub> particles can be modified owing to its amorphous nature, the various coordination states of Si-O pairs [27] and the controllable kinetics of the silica sol-gel process [28]. Thus, based on the above reviews and discussion on synthesis of nano-sized particles using the turbulence engulfment or ultrasound irradiation assisted processes, it can be postulated that the mesoporous silica material synthesised and controlled by a sol-gel process can be affected by local turbulence embedded in the swirling vortex flow, which may change the characteristics of the mesoporous silica particle both in structure and in morphology.

The aim of the present study is to investigate the hydrodynamics and mass transfer in the process of SiO<sub>2</sub> synthesis using a swirling reactor, focusing on the liquid-solid mass transfer coefficient and particle characteristics such as particle morphology and particle size distribution in a wide range of Reynolds number of inlet streams. The mass transfer enhancement is also explored with the employment of ultrasound ranging from 120 W to 600 W at a constant frequency of 20 kHz.

## 2. Experimental

## 2.1. Solution preparation

SiO<sub>2</sub> floccule were synthesised by adding 1 g of Cetyltrimethyl Ammonium Bromide (CTAB) and 3.5 ml of NaOH solution (2 M),

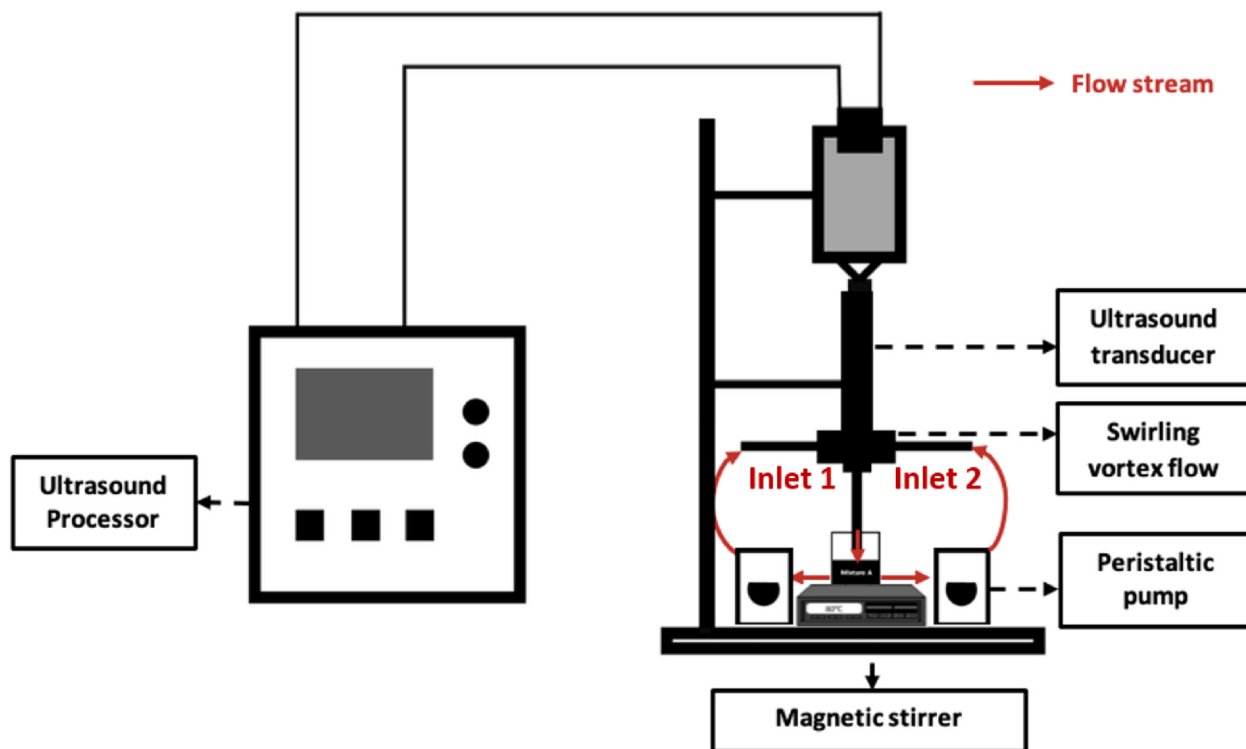


Fig. 1. Schematic diagram of the experimental setup.

purchased from Sinopharm Chemical Reagent Co., Ltd., into 480 ml of deionised water. After the CTAB was fully dissolved at the constant temperature of 80 °C, 5 ml of tetraethyl orthosilicate (TEOS > 28.5%), purchased from Sinopharm Chemical Reagent Co., Ltd., was added into the mixture solution as mentioned in order to prepare mixture A.

## 2.2. Experimental setup and product characterization

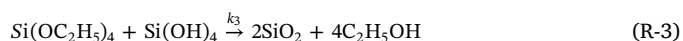
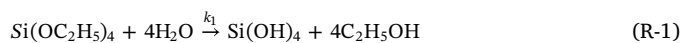
The experimental setup is shown in Fig. 1. The simulated swirling vortex flow reactor (SVFR) consists of a short circular cylindrical chamber (D = 20 mm, H = 10 mm) embedded in a stainless-steel block with two guided introduction thin pipes that allow the solution to tangentially enter the chamber to form the so-called Rankine vortex flow. An ultrasound probe (D = 20 mm) (UH1200, 20 kHz, Ouhor Shanghai Co., Ltd) was imposed as the ultrasonic source immersed into the solution from the top of reactor chamber. Sample S-0 was obtained without assist of ultrasound irradiation at a constant flow rate of 5.75 ml/s for each inlet, circulating in the SVFR for 30 min at 80 °C. Samples S-1 to S-5 were obtained at a constant flow rate of 5.75 ml/s from introducing mixture A into the two inlet streams of swirling vortex reactor via peristaltic pumps and were circulated for 30 min under ultrasonic powers of 0 W, 120 W, 240 W, 360 W, 480 W and 600 W, respectively. Samples S-6 to S-10 were obtained with the inlet flow rate of 1.92 ml/s, 3.83 ml/s, 5.75 ml/s, 7.66 ml/s and 9.58 ml/s Reynolds number ranging from 2620 to 13,196 under the ultrasound power level of 240 W. Samples S-11 to S-15 were obtained by altering the ratio of volumetric flow rate of two inlet streams from 1 to 5 under the ultrasound power level of 240 W. All the samples synthesised under different conditions are listed in Table 1. After the sample flocs were collected from the outlet of the reactor to cool down to the room temperature, the flocs were then filtered by a vacuum circulating pump and washed 3 times with the deionised water. The obtained gel was dried for 5 h at 100 °C in the oven and then transferred to a muffle oven for calcination of 6 h at 550 °C. After free cooling, the white powdery solid product, i.e. SiO<sub>2</sub> particles, was obtained.

The stability of synthesised SiO<sub>2</sub> particles were investigated using

thermogravimetric analysis (TGA) from 20 °C to 600 °C, NETZSCH STA 449 F3 Jupiter, Germany, 10 °C/min, in synthetic air (20vol%O<sub>2</sub> and 80vol% N<sub>2</sub>). The morphology and microstructure were investigated by a scanning electron microscope (SEM), Sigma VP, ZEISS, Germany and the Brunauer-Emmett-Teller analysis (BET), ASAP 2020 Micrometrics, United States. The aggregated particle size was measured by laser particle size analyser, Bettersize 2000, adopted the technology of single-beam dual-lens with size range 0.02–2000 μm.

## 2.3. Description on synthesis reaction

The silicate was prepared through a sol-gel approach and the hydrolysis process proceeds in the presence of a NaOH solution acting as a homogenising agent [24]. When TEOS was added into the solution containing NaOH and CTAB, it could be rapidly hydrolysed to produce Si(OH)<sub>4</sub> under alkaline environments on the basis of multi-step chemical reactions that can be described by [29,30]:



where R-1 involves a homogenous hydrolysis reaction, R-2 is a heterogeneous condensation reaction by converting aqueous silicate into silica and R-3 is the condensation of alcohol. The parameters  $k_1$ ,  $k_2$  and  $k_3$  represent the reaction rate constant of hydrolysis, main step of condensation and condensation of alcohol, respectively. Practically, the process of hydrolysis and condensation occurs concurrently. There are two limiting cases: hydrolysis reaction is predominant and complete when the hydrolysis reaction rate constant is much greater than that of condensation ( $k_2 \gg k_3$ ); condensation occurs once after hydrolysis and the condensation rate is proportional to the hydrolysis reaction rate when the hydrolysis reaction rate constant is smaller than that of condensation ( $k_2 < k_3$ ) [24]. Water is excessive and sufficient to complete the hydrolysis reaction, thereby the hydrolysis can be assumed to

**Table 1**  
Samples with different ultrasound power and intensity.

Samples no.	Ultrasound intensity (W)	Ultrasound Amplitude (%)	Reynolds number Rev for inlet 1	Volumetric flowrate of inlet 1 (ml/s)	Volumetric flowrate of inlet 2 (ml/s)	Volumetric flowrate ratio R
<i>Sample Group 1 – Different ultrasound power</i>						
S-0	0	0	7859	5.75	5.75	1
S-1	120	10				
S-2	240	20				
S-3	360	30				
S-4	480	40				
S-5	600	50				
<i>Sample Group 2 – Different inlet Reynolds number</i>						
S-6	240	20	2620	1.92	1.92	1
S-7			5240	3.83	3.83	1
S-8			7859	5.75	5.75	1
S-9			10,479	7.66	7.66	1
S-10			13,196	9.58	9.58	1
<i>Sample Group 3 – Different volumetric flowrate</i>						
S-11	240	20	–	5.75	5.75	1
S-12				7.66	3.83	2
S-13				8.62	2.87	3
S-14				9.2	2.3	4
S-15				9.58	1.92	5

be dominant in this particular case. The overall hydrolysis–condensation reaction rate followed a first order reaction with the rate constant ( $k$ ),

$$r' = -\frac{d[\text{Si}(\text{OC}_2\text{H}_5)_4]}{dt} = k[\text{Si}(\text{OC}_2\text{H}_5)_4]. \quad (1)$$

here, the rate constant  $k$  of hydrolysis–condensation reaction is presumed to be  $3.6 \times 10^{-3}\text{s}^{-1}$  [30].

### 3. Numerical simulation

#### 3.1. Governing equations

The approach employed during this investigation is based on Euler–Euler fully coupled two–fluid model. Liquid is set as a continuous primary phase and solid phase is considered as dispersed phase. The continuity equation for liquid phase ( $l$ ) and solid phase ( $s$ ) are expressed as

Liquid phase:

$$\frac{\partial}{\partial t}(\alpha_l \rho_l) + \nabla \cdot (\alpha_l \rho_l \mathbf{u}_l) = -\dot{m}_{l \rightarrow s} \quad (2)$$

Solid phase:

$$\frac{\partial}{\partial t}(\alpha_s \rho_s) + \nabla \cdot (\alpha_s \rho_s \mathbf{u}_s) = \dot{m}_{l \rightarrow s} \quad (3)$$

where  $\mathbf{u}_l$  is the velocity of liquid phase and  $\dot{m}_{l \rightarrow s}$  is the mass transfer source term from liquid to solid phase. The conservation equations for momentum for both phases take the following form:

Liquid phase:

$$\frac{\partial}{\partial t}(\alpha_l \rho_l \mathbf{u}_l) + \nabla \cdot (\alpha_l \rho_l \mathbf{u}_l \mathbf{u}_l) = -\alpha_l \nabla p + \nabla \cdot \boldsymbol{\tau}_l + \alpha_l \rho_l \mathbf{g} + \mathbf{R}_{sl} \quad (4)$$

Solid phase:

$$\frac{\partial}{\partial t}(\alpha_s \rho_s \mathbf{u}_s) + \nabla \cdot (\alpha_s \rho_s \mathbf{u}_s \mathbf{u}_s) = -\alpha_s \nabla p + \nabla \cdot \boldsymbol{\tau}_s + \alpha_s \rho_s \mathbf{g} + \mathbf{R}_{sl} \quad (5)$$

where  $\mu_l$  and  $\lambda_l$  are the shear and bulk viscosity of liquid phase  $l$ ,  $\mathbf{R}_{sl}$  is the interaction force between phases. The interaction term is expressed in the following form:

$$\mathbf{R}_{sl} = K_{sl}(\mathbf{u}_s - \mathbf{u}_l) \quad (6)$$

where  $K_{sl}$  (is equal to  $K_{ls}$ ) is the interphase momentum exchange coefficient. In the present study, drag force derived from the model of

Wen and Yu (Wen, 1966) has been adopted which is appropriate for description of the dilute system. The fluid–solid exchange coefficient takes the following form:

$$K_{sl} = \frac{3}{4} C_D \frac{\alpha_s \alpha_l \rho_l |\mathbf{u}_s - \mathbf{u}_l|}{d_s} \alpha_l^{-0.265} \quad (7)$$

and

$$C_D = \frac{24}{\alpha_l Re_S} [1 + 0.15(\alpha_l Re_S)^{0.687}] \quad (8)$$

where  $Re_S$  relative Reynolds number.

$$Re_S = \frac{\rho_l d_p |\mathbf{u}_s - \mathbf{u}_l|}{\mu_l} \quad (9)$$

Eulerian dispersed turbulence model has been chosen for this case. It is suitable when there is clearly one primary continuous phase and the other is dispersed dilute secondary phase. For the current case, the mass fraction of particles is smaller than 1% and it is assumed to be granular in the simulation. The turbulent prediction for continuous phase  $l$  has been modified with the term considering interphase turbulent momentum transfer as follows,

$$\frac{\partial}{\partial t}(\alpha_l \rho_l k_l) + \nabla \cdot (\alpha_l \rho_l \mathbf{u}_l k_l) = \nabla \cdot \left( \alpha_l \frac{\mu_{t,l}}{\sigma_k} \nabla k_l \right) + \alpha_l G_{k,l} - \alpha_l \rho_l \varepsilon_l + \alpha_l \rho_l \Pi_{kl} \quad (10)$$

and

$$\frac{\partial}{\partial t}(\alpha_l \rho_l \varepsilon_l) + \nabla \cdot (\alpha_l \rho_l \mathbf{u}_l \varepsilon_l) = \nabla \cdot \left( \alpha_l \frac{\mu_{t,l}}{\sigma_\varepsilon} \nabla \varepsilon_l \right) + \alpha_l \frac{\varepsilon_l}{k_l} (C_{1\varepsilon} G_{k,l} - C_{2\varepsilon} \rho_l \varepsilon_l) + \alpha_l \rho_l \Pi_{\varepsilon l} \quad (11)$$

where  $\Pi_{kl}$  and  $\Pi_{\varepsilon l}$  are the source terms representing the influence of the dispersed phase  $s$  on the continuous phase  $l$ , and  $G_{k,l}$  is the production of turbulent kinetic energy.

The terms  $\Pi_{kl}$  and  $\Pi_{\varepsilon l}$  take the following form,

$$\Pi_{kl} = C_s \sum_{p=1}^M \frac{K_{sl}}{\alpha_l \rho_l} X_{sl} (\langle \mathbf{u}_l \cdot \mathbf{u}_s \rangle + (\mathbf{u}_s - \mathbf{u}_l) \cdot \mathbf{u}_{dr}) \quad (12)$$

which can be simplified as

$$\Pi_{kq} = C_s \sum_{p=1}^M \frac{K_{sl}}{\alpha_l \rho_l} X_{sl} (k'_{sl} - 2k_l + \mathbf{u}_s \cdot \mathbf{u}_{dr}) \quad (13)$$

where  $C_s$  is the model constant ( $C_s = 1$  as default);

$k'_{sl}$  is the covariance of the velocities of the continuous phase  $q$  and the dispersed phase  $p$ ;

$\mathbf{u}_{sl}$  is the relative velocity;

$\mathbf{u}_{dr}$  is the drift velocity,

$X_{sl} = \frac{\rho_l}{\rho_l + C_{VM}\rho_l}$  for granular flows,  $X_{sl} = 1$ .

$\Pi_{el}$  can be modelled based on the work by Elghobashi and Abou-Arab [31]:

$$\Pi_{el} = C_{3\epsilon} \frac{\epsilon_l}{k_l} \Pi_{kl} \quad (14)$$

where  $C_{3\epsilon} = 1.2$ . The turbulent viscosity  $\mu_{t,q}$  is written in terms of the turbulent kinetic energy of liquid phase  $l$ :

$$\mu_{t,l} = \rho_l C_\mu \frac{k_l^2}{\epsilon_l} \quad (15)$$

### 3.2. Mass transfer models

The mass transfer from aqueous silicate to solid silicon dioxide floccule driven by the diffusion process is from saturated solution to the surface of particles. The general mass fraction transport equation in multiphase flow is expressed by Eq. (16) [32]:

$$\frac{\partial}{\partial t} (\alpha_l \rho_l C_{l,si}) + \nabla \cdot (\alpha_l \rho_l \mathbf{v}_l C_{l,si} - \alpha_l \Gamma_{l,si} C_{l,si}) = -S_{l \rightarrow s} \quad (16)$$

where  $C_{l,si}$  and  $C_{l,si}^*$  represent concentration and of saturated concentration of silicon source ( $\text{Si}(\text{OH})_4$ ),  $\Gamma_{l,si}$  is the dynamic viscosity of  $\text{Si}(\text{OH})_4$  and  $S_{l \rightarrow s}$  is the mass transfer source term of  $\text{SiO}_2$ . The diffusional mass transfer source term can be written as Eq. (17) [33],

$$-S_{l \rightarrow s} = k_{sl} a_p (C_{l,si}^* - C_{l,si}) \quad (17)$$

where  $k_{sl}$  is the solid-liquid mass transfer coefficient and  $a_p$  is the interfacial area per unit volume. The saturation concentration of silicate,  $C_{l,si}^*$ , is calculated on the basis of Henry's law and  $C_{l,si}$  represents the silicate concentration in liquid phase. The volumetric mass transfer coefficient,  $k_{sl} a_p$ , can be obtained from the change of concentration of silicate via the Eq. (18) [34,35],

$$\ln \left( \frac{[C_{l,si}]}{[C_{l,si}]_0} \right) = -k_{sl} a_p t \quad (18)$$

where  $[C_{l,si}]$  and  $[C_{l,si}]_0$  are the silicate concentrations at time  $t = 0$  and  $t = t_i$ , respectively. The value of  $k_{sl} a_p$  can be obtained by the slope of  $\ln([C_{l,si}]/[C_{l,si}]_0)$  against time  $t$ . The solid-liquid mass transfer coefficient,  $k_{sl}$ , can be obtained by dividing the interfacial area of solid particles,  $a_p$ , which is estimated using equation (19) [11,33],

$$a_p = \frac{6C_v}{d_p} \quad (19)$$

where  $C_v$  is the volume fraction of dispersed phase and  $d_p$  is the Sauter mean diameter of particles.

### 3.3. Numerical simulation

To model the swirling vortex flow in the reactor, the Eulerian-Eulerian two-fluid fully coupled model was adopted to simulate the hydrodynamics and the mass transfer characteristics in the confined geometry as shown in Fig. 2. The grid was generated using the software ANSYS ICEM 15.0. Grid sensitivity trial simulation was carried out and it was found that the adoption of a total amount of about 304,000 cells was appropriate. Further refining of the mesh has little impact on the simulation results, especially on the turbulence kinetic energy and turbulent dissipation rate.

The governing equations were solved by using commercial software FLUENT 18.0. The modelling approach to simulate hydrodynamics and mass transfer for particle-liquid multiphase system is based on Eulerian-

Eulerian two-fluid fully coupled model by treating liquid and particles as two independent pseudo-continuum phases. In the simulation, liquid is set as a continuous primary phase while particles (solid phase) is considered as dispersed phase. The properties of dispersed phase is shown in table 2. Two phases are interpenetrated and interacted with each other. The dominant interphase force is drag force (Wen-yu model). As the swirling flow in the reactor is highly turbulent, RNG  $k-\epsilon$  model has been adopted. Phase coupled SIMPLE algorithm has been used for velocity-pressure coupling. The first-order upwind scheme was used for momentum and species transport equation spatial discretization while QUICK scheme was used in continuity discretization to ensure better estimation of phase volume fraction. For transient simulation, a maximum number of iterations was set to 100 each time step. The solutions were considered to be converged when the residuals of all the variables were less than  $10^{-5}$ . The boundary conditions for inlet 1 and inlet 2 were set to velocity inlet and the outlet of the swirling vortex flow reactor was set as the pressure outlet with the static pressure there being specified to be the atmospheric one. This is consistent with the actual experimental condition as the samples are collected from the outlet. Modelling of chemical reaction and ultrasound irradiation was implemented into the simulation once the simulated turbulent flow field in the reactor had been well established. Ultrasound irradiation with a fixed frequency of 20 kHz was imposed as the boundary condition of cyclic sound pressure at the probe tip surface in terms of pressure amplitude  $p_a$  and was evaluated based on Eqs. (20) and (21) [11,36,37],

Pressure amplitude:

$$p_a = \sqrt{2I_{us}\rho C} \quad (20)$$

Pressure:

$$p = p_a \cos(2\pi f t) + \frac{1}{2} \rho v^2 \quad (21)$$

where  $C$  is the sound velocity (m/s),  $f$  is the frequency (Hz),  $t$  is the time (s),  $\rho$  is the average density of liquid bulk ( $\text{kg}/\text{m}^3$ ) and  $v$  is the velocity of liquid phase due to propagation of ultrasound waves (m/s).

## 4. Results and discussion

### 4.1. Synthesised particle characterization

As the result of shear turbulence controllable synthesis of nano-sized particles in the swirling vortex flow reactor and intensification by applying ultrasound irradiation, the morphology of nano-sized mono particles and aggregated particle size distribution of  $\text{SiO}_2$  were detected by SEM as shown in Fig. 3. In fact, all the mono particles are visualised morphologically spherical-like shaped and it can observe that the average aggregated particle size and its distribution is somewhat affected by hydrodynamic conditions. Particle size distribution of all samples are similarly shaped and exhibit their secondary peak in the range of  $5 \mu\text{m}$  to  $10 \mu\text{m}$ . Mono particle aggregates and the main peak of size are located in the range of  $30 \mu\text{m}$  to  $50 \mu\text{m}$  with a sharp decline indicating particles stop growing due to exerting shear force. Moreover, the Sauter mean diameter ( $d_{32}$ ) of aggregated particles is as large as  $18.42 \mu\text{m}$  and the Sauter mean diameter is almost monotonically changeable as the ultrasound power increases as well as local turbulent Reynolds number with identical and non-identical inlet velocity of SVFR. As the Reynolds number  $Re_v$  increases from 2620 to 13196, the Sauter mean diameter,  $d_p$ , decreases from  $18.42 \mu\text{m}$  to  $10.94 \mu\text{m}$  and the size distribution becomes narrower with a reduced coefficient of variation (CV). Here, coefficient of variation (CV), also recognised as relative standard deviation (RSD), is defined as the ratio of the standard deviation  $\sigma$  to the mean of parameters particle diameters  $\mu$  ( $CV = \sigma/\mu$ ), used to standardise measure of dispersion of a probability distribution. It is very interesting to note that as there is two times ratio of the inlet, the Sauter mean diameter,  $d_p$ , falls from  $13.26 \mu\text{m}$  to

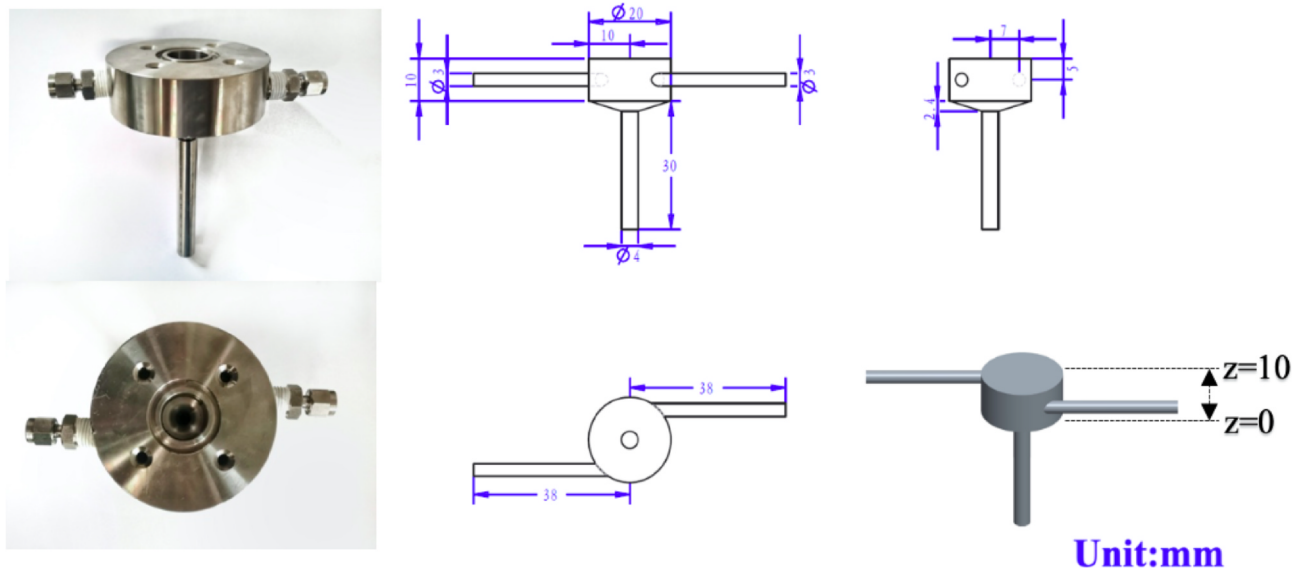


Fig. 2. The experimental rig and dimensions of swirling vortex reactor.

Table 2

Properties of dispersed phase.

Granular viscosity	Gidaspow
Granular bulk viscosity	Lun et al.
Frictional viscosity	Schaeffer
Granular temperature	Algebraic
Solids pressure	Lun et al.
Radial distribution	Lun et al.

12.04  $\mu\text{m}$  with a narrower distribution. This may be attributed to the local mixing behaviour where two swirling streams with different inlet velocities meet and the engulfment is weakened due to the retarding action from the slower stream to the faster stream. Continuous increases in  $R$  leads to larger particle sizes and a broader distribution.

The product before filtration is a colloidal suspension of solid particles in the mixture solution and is small enough to be dominated by the short-range force without consideration of the gravitational forces [24] and these nano-sized particles tends to aggregate in aqueous circumstance as shown in Fig. 4 (a). It can be seen from the TEM images shown in Fig. 4 (b), (c) and (d) that the edge of particles coalesces and overlaps due to aggregation. The sphericity and crystalline microstructure have been magnified under enlargement. Fig. 5 (a) and (b) reveal correlations between the average aggregated particle size and coefficient of variation (CV) as a function of turbulent Reynolds number and ultrasound amplitude. The particles are smallest with the narrowest size distribution ( $d_p/\langle\eta\rangle < 0.36$ ,  $CV < 0.68$ ) produced when ultrasound amplitude applied reaches 50% (600 W) and the Reynolds number, based on the vortex core radius is 7859. In contrast, the largest size particles are synthesised and obtained with a wide size distribution when ultrasound is abandoned at  $Re_V = 7859$  and  $Re_V$  is defined as

$$Re_V = \frac{2\omega R_v^2}{\nu} \quad (22)$$

where  $\omega$  is the angular velocity calculated on basis of flowrate of inlet 1 and vortex characteristic length  $R_v$  is approximately equal to  $(D-2d)/2$ . To examine the relationship between the particle size distribution and the turbulent shear rate and the intensification of ultrasound irradiation, the ratio of particle diameter to the mean Kolmogorov scale,  $d_p/\langle\eta\rangle$  is introduced. In general, the characteristic particle length ratio  $d_p/\langle\eta\rangle$  changes from 0.24 to 0.41 when the ultrasound amplitude increases from 0 to 50% and it varies as Reynolds number  $Re_V$  based on the vortex characteristic length  $R_v$ . Here,  $D$  is the diameter of the reactor and the  $d$

is the diameter of the inlet tube. The local turbulence level can be estimated from the CFD simulation by a turbulent Reynolds number defined as

$$Re_T = \frac{\langle k \rangle}{(\langle \varepsilon \rangle \nu)^{1/2}} \quad (23)$$

where  $\langle k \rangle$  and  $\langle \varepsilon \rangle$  are the volumetric averaged turbulent kinetic energy and turbulent energy dissipation rate, respectively. The correlations of characteristic particle length ratio  $d_p/\langle\eta\rangle$  and CV with  $Re_T$  and the strength of applied ultrasound are found to be well represented by using equations (24) and (25) while the correlations are plotted in Fig. 5 (a) and (b),

$$\frac{d_p}{\langle\eta\rangle} = 0.58 Re_T^{-0.13} P_A^{0.11} \quad (24)$$

$$CV = 0.87 Re_T^{-0.01} P_A^{-0.08} \quad (25)$$

where  $d_p$  is actually obtained from the proportion of particle size  $d_{32}$  of arbitrary samples under the condition of ultrasound amplitude from  $P_A = 0$  to  $P_A = 50\%$  and  $Re_V = 7859$ .  $P_A$  is defined by

$$P_A = \frac{P}{P_s} \quad (26)$$

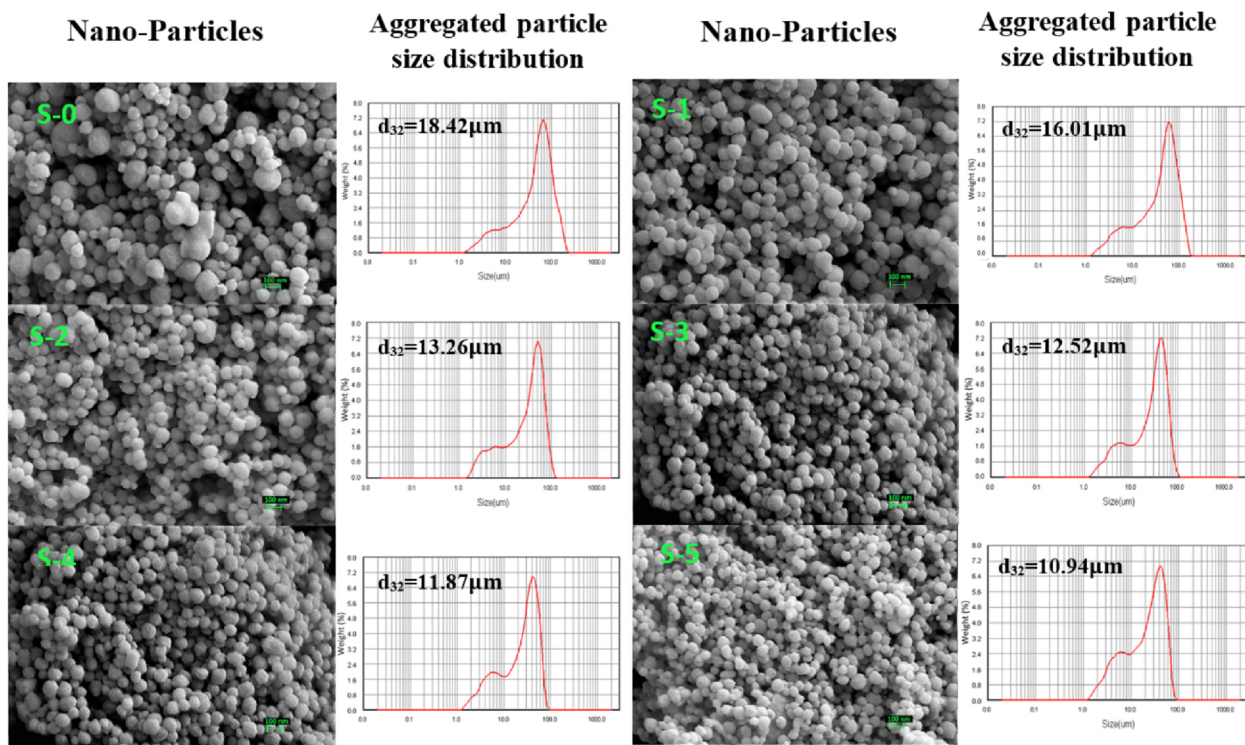
where  $P_s$  is the maximum ultrasound power can be applied (1200 W for ultrasound processor in this case). As the synthesised particle size is highly influenced by the local turbulent eddy shear  $\sqrt{\langle \varepsilon \rangle / \nu}$ , the Reynolds number,  $Re_T$ , which is characterised by  $\langle \varepsilon \rangle$  can be associated with the Reynolds number  $Re_V$ . It can be seen from Fig. 6 that the flow in the SVFR can be well approximated by the turbulent Rankine vortex model with

$$\begin{aligned} u_\theta &= r\omega \leq R_v \\ \frac{\partial u_\theta}{\partial r} &= 0 \text{ or } R_v \end{aligned} \quad (27)$$

The mean turbulent energy dissipation rate  $\langle \varepsilon \rangle$  for the turbulent Rankine vortex is as a function of core radius, i.e.  $\varepsilon = \varepsilon(r)$ . It can be assumed that when the swirling flow in the reactor is turbulent and in dynamic equilibrium, the formed turbulent Rankine vortex is spatially filled with the turbulent eddies with all the scales. Thus,  $\langle \varepsilon \rangle_{exp}$  in experiment can be estimated by the following relation:

$$\langle \varepsilon \rangle_{exp} = 2\nu_{eff} \omega^2 = 2\nu_{eff} \left( \frac{Q_1 + Q_2}{\frac{\pi}{2} d_0^2 R_v} \right)^2 = 2\nu_{eff} \left[ \frac{Q_2(1+R)}{\frac{\pi}{2} d_0^2 R_v} \right]^2 \quad (28)$$

(a)



(b)

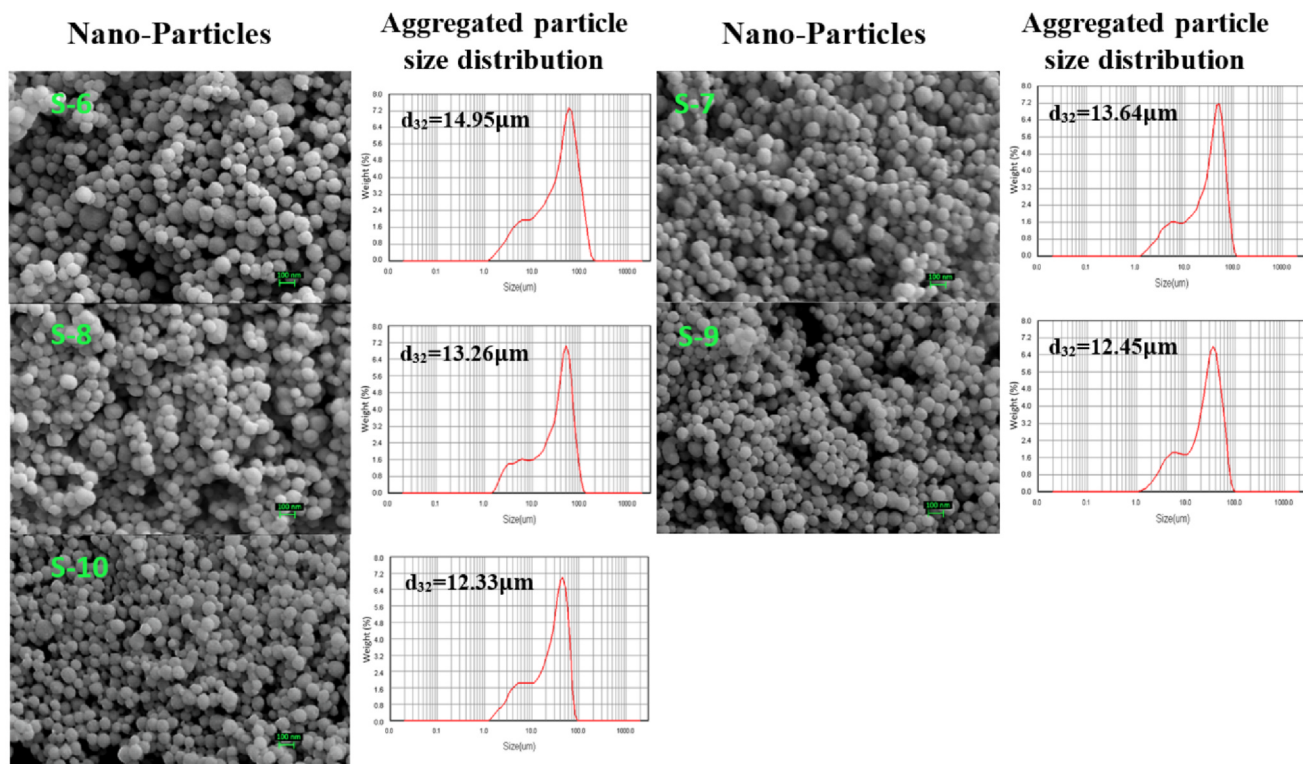


Fig. 3. SEM images and particle size distribution of sample SiO<sub>2</sub> synthesised under different condition of (a) Ultrasound power  $P$  at Reynolds number  $Re_V = 7859$ ; (b) Reynolds number  $Re_V$  under the ultrasound power of 240 W; (c) Volumetric flowrate ratio  $R$  under ultrasound power of 240 W.

(c)

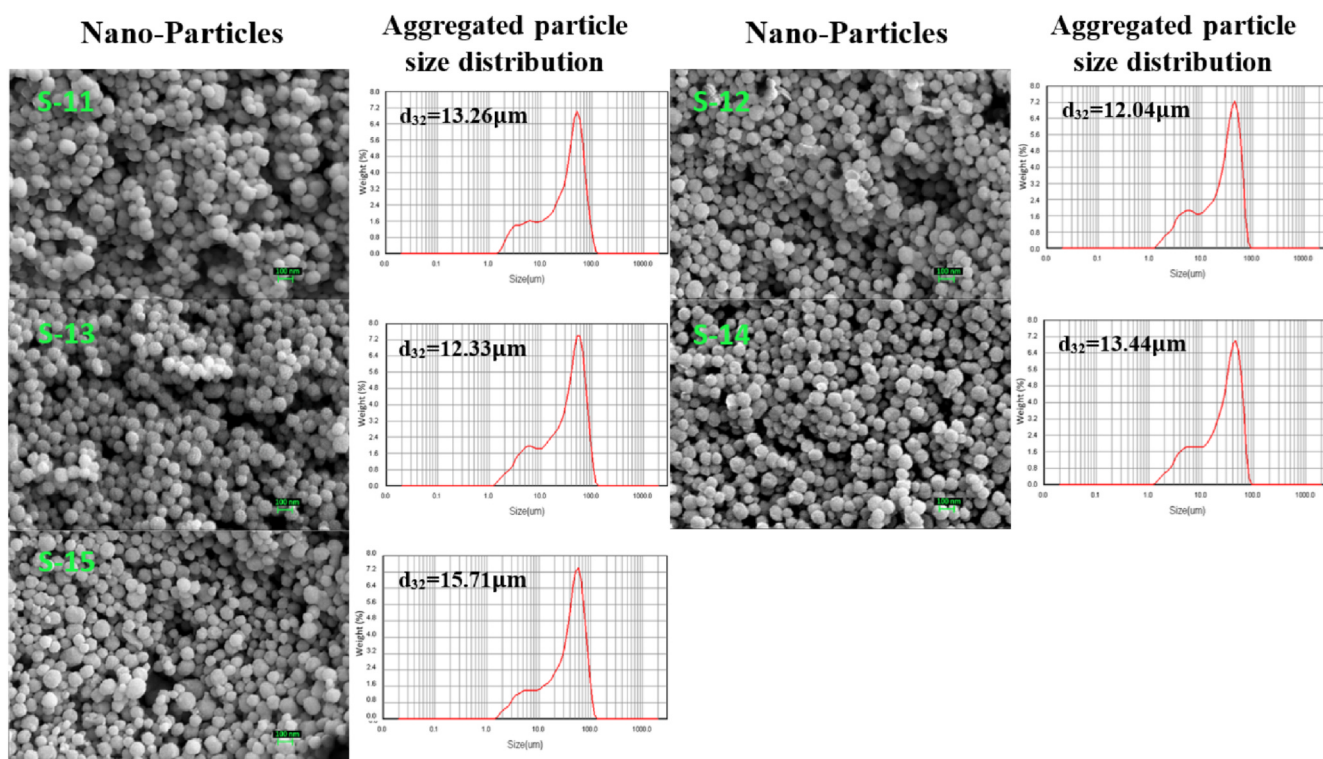


Fig. 3. (continued)

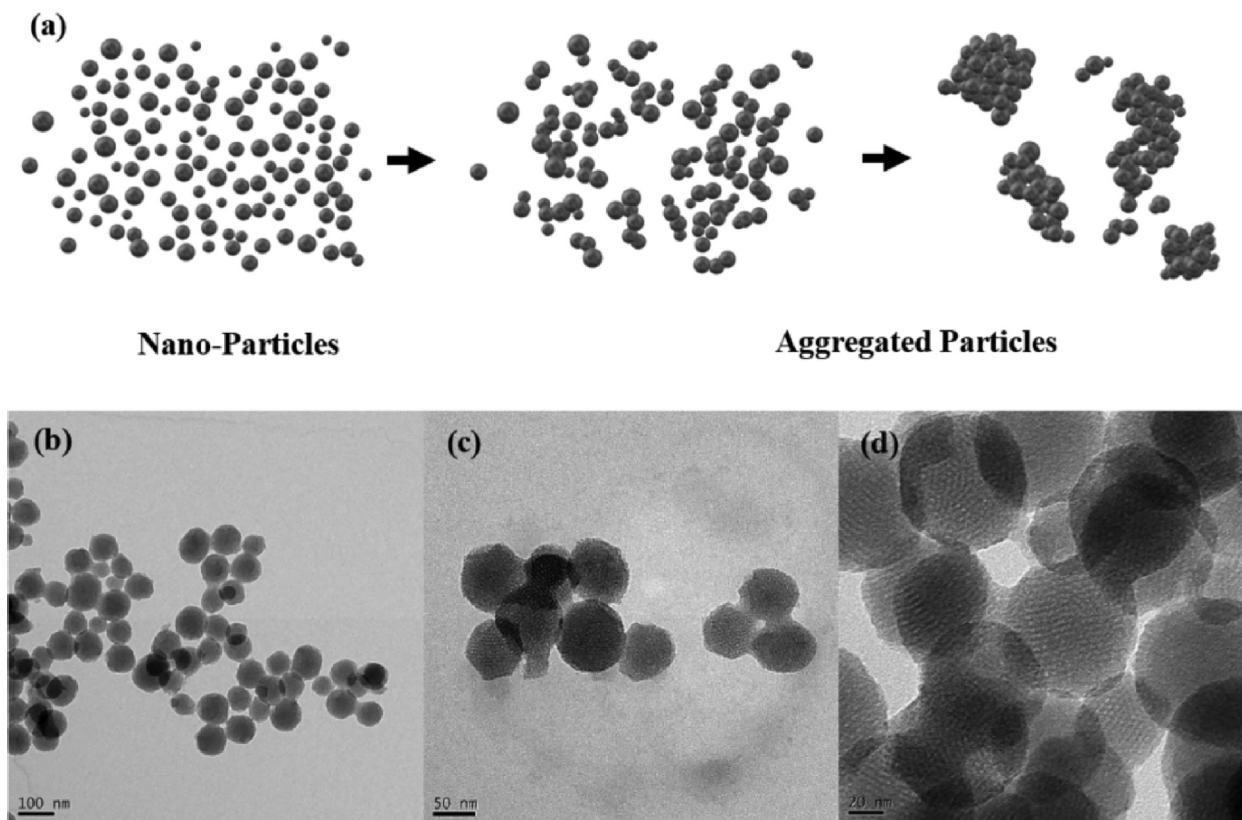


Fig. 4. (a) Schematic diagram of SiO<sub>2</sub> nanoparticles aggregation; TEM images of samples synthesised under the ultrasound power of 600 W at Reynolds number  $Re_V = 7859$  under the proportional scale of (b) 100 nm; (c) 50 nm; (d) 20 nm.

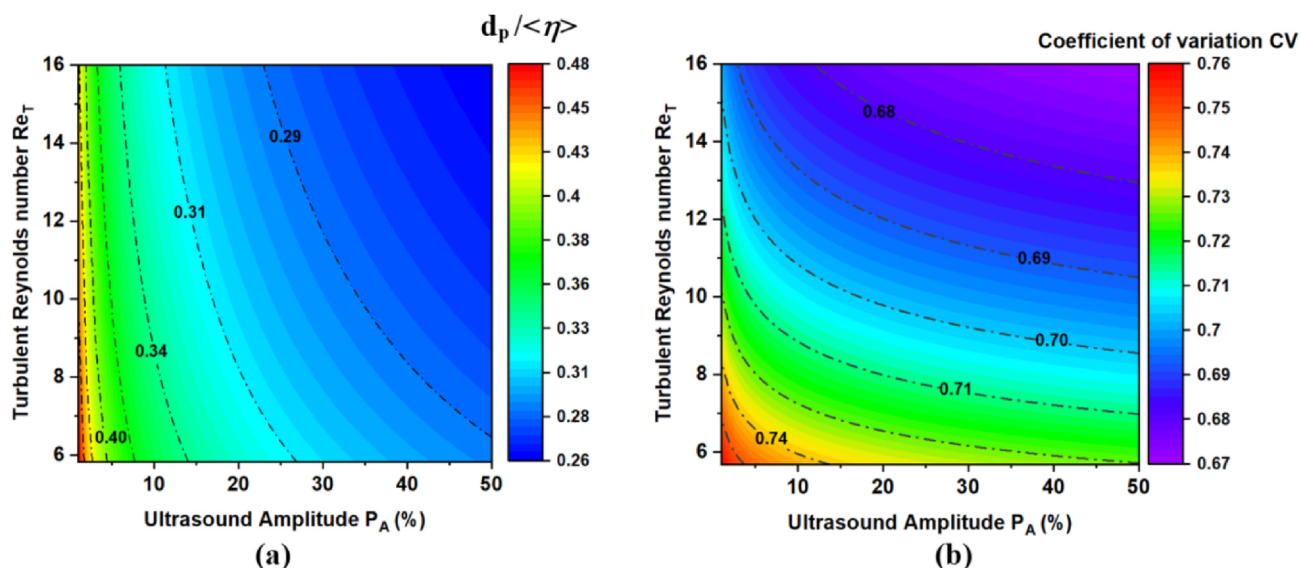


Fig. 5. (a) 2D-contour of characteristic particle length ratio  $d_p/\langle\eta\rangle$  versus ultrasound amplitude  $P_A$  (W) and turbulent Reynolds number  $Re_V$ ; (b) 2D-contour of coefficient of variation (CV) versus ultrasound amplitude  $P_A$  (W) and turbulent Reynolds number  $Re_V$ .

where  $Q_1$  and  $Q_2$  are the volumetric flow rates of faster inlet stream and the slower inlet stream, respectively. The epsilon generated from ultrasound irradiation is estimated from actual ultrasound power  $P_{us}$ .

The nitrogen adsorption/desorption isotherms for  $SiO_2$  samples has been used to characterise the porosity of material by using the Barrett–Joyner–Halenda (BJH) equation. The adsorption average pore

width of samples is shown in Fig. 7. It can be seen from the figure that the application of ultrasound has an impact on particle porosity. When an increase in the ultrasound power was applied, it was observed that the porosity of  $SiO_2$  particles monotonically changes together with the average pore diameter varying from  $65.9 \text{ m}^2/\text{g}$  to  $193.0 \text{ m}^2/\text{g}$  and the corresponding average pore diameter changing from  $8.9 \text{ nm}$  to

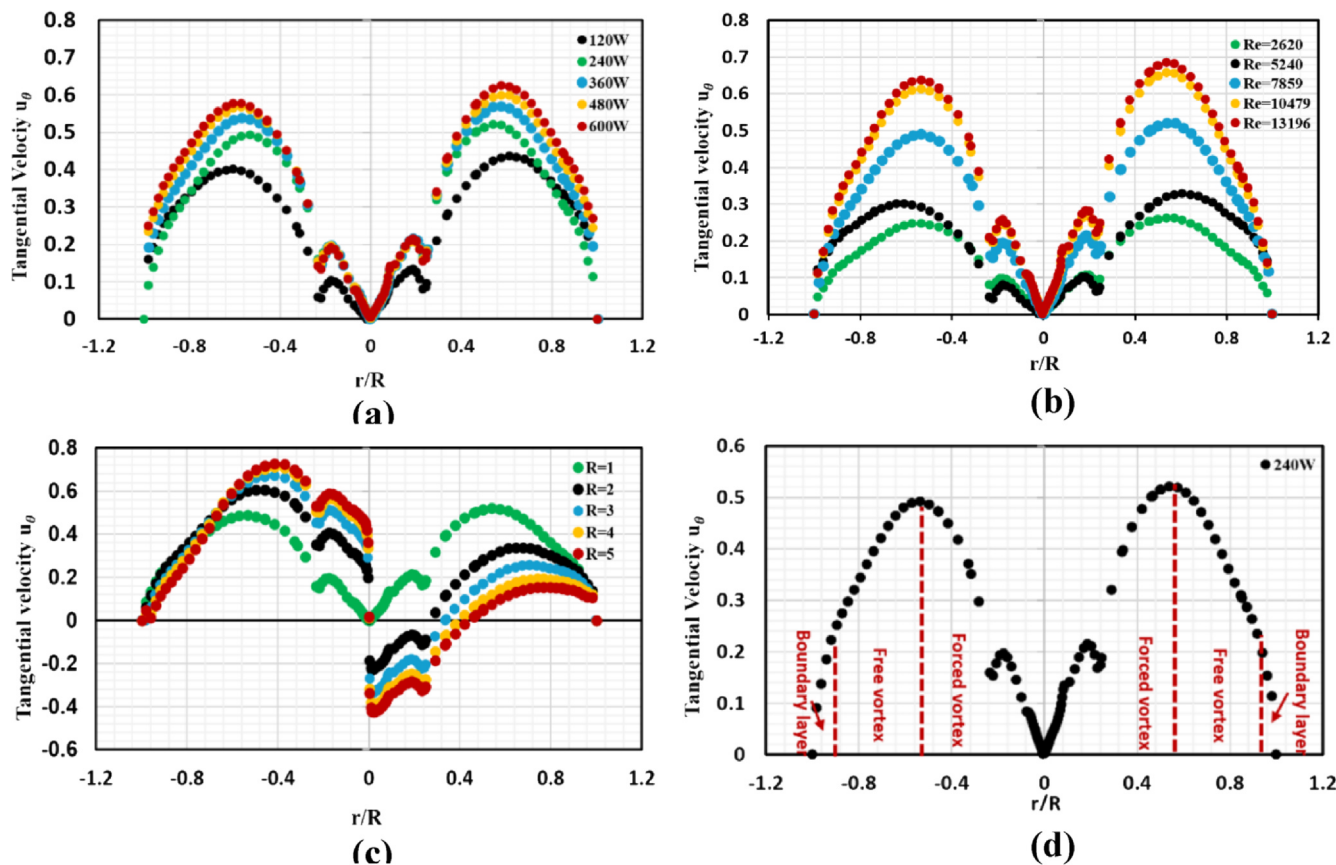


Fig. 6. CFD Predicted tangential velocity  $u_\theta$  (m/s) of continuous phase in the SVFR along radial direction at the surface of  $z = 5 \text{ mm}$  for the cases (a) Effect of variation of ultrasound power  $P$  at Reynolds number  $Re_V = 7859$ ; (b) Effect of Reynolds number  $Re_V$  at ultrasound power of  $240 \text{ W}$ ; (c) Effect of variation of volumetric flowrate ratio  $R$  for the given ultrasound power of  $240 \text{ W}$ ; (d) The tangential velocity distribution in radial direction in the Rankine vortex of the SVFR for Reynolds number  $Re_V = 7859$  and the applied ultrasound power of  $240 \text{ W}$ .

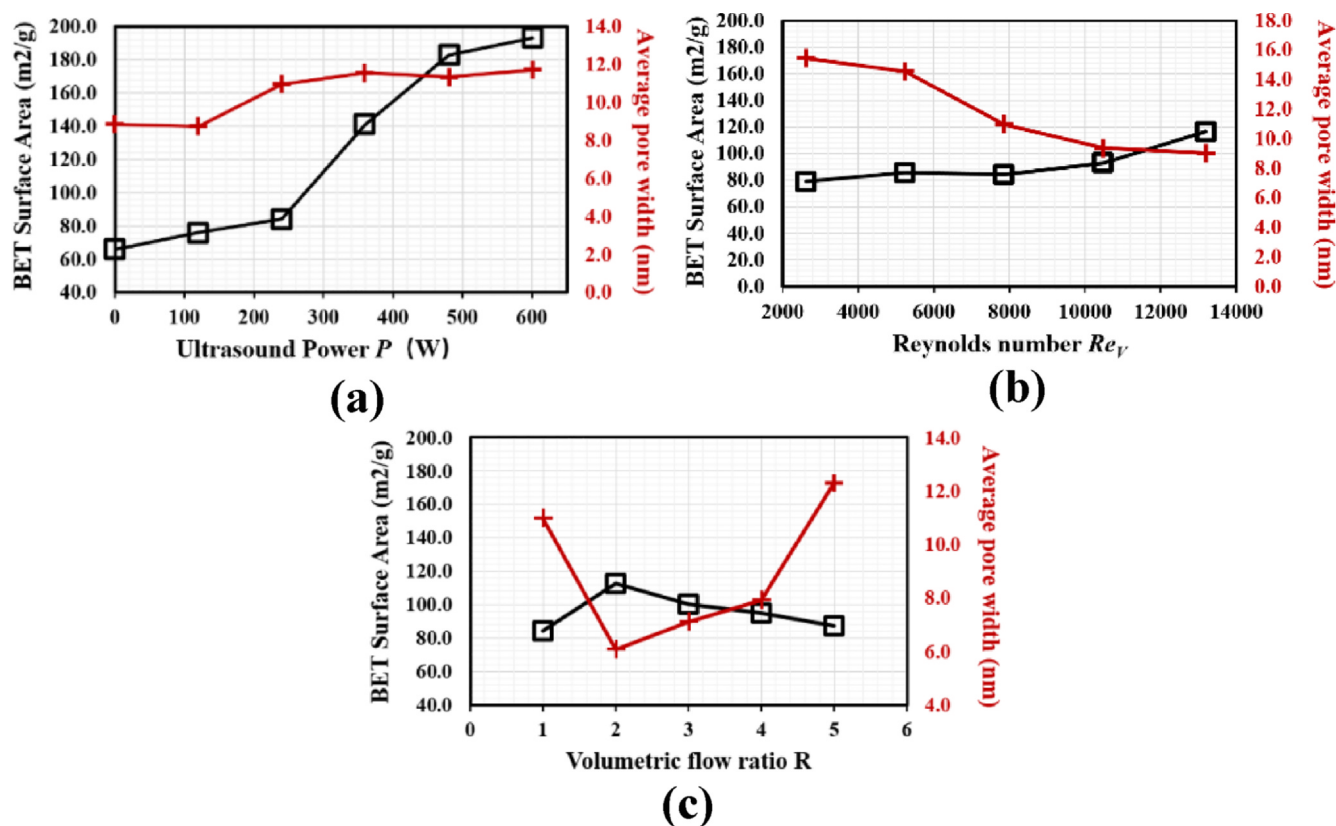


Fig. 7. Brunauer-Emmett-Teller (BET) surface area (m<sup>2</sup>/g) and Average pore width (nm) versus (a) Ultrasound power  $P$  at Reynolds number  $Re_V = 7859$ ; (b) Reynolds number  $Re_V$  under ultrasound power of 240 W; (c) Volumetric flowrate ratio  $R$  under ultrasound power of 240 W.

11.7 nm. When the Reynolds number,  $Re_V$ , is increased from 2620 to 13196, it was found from the tests that the BET surface area gradually increases from 78.9 m<sup>2</sup>/g to 92.9 m<sup>2</sup>/g, then suddenly increases to 116.5 m<sup>2</sup>/g once  $Re_V$  reaches 13,196 with the pore width being significantly reduced from 15.4 nm to 9.0 nm. For the cases of imbalanced inlet velocity, i.e.  $R > 1$ , the BET surface area of particles experiences a significant increase, varying from 84.2 m<sup>2</sup>/g to 112.6 m<sup>2</sup>/g, while the pore width decreases from 10.7 m<sup>2</sup>/g to 6.1 m<sup>2</sup>/g, indicating more pore cavities have formed in the particle. However, when  $R$  increases to 5, this trend is reversed with the corresponding BET surface area of 87.4 m<sup>2</sup>/g and pore width of 12.3 nm. This is likely due to the weak aggregation caused by the reduced local turbulent eddy induced shear.

The synthesised particle characterisation has revealed an important fact that the upturn of Reynolds number  $Re_V$  indicates a reduction in the particle size but with higher porosity. This is strongly associated with the local turbulence. This varies when the volumetric flowrate ratio increases and the small particles with higher porosity are synthesised when  $R$  is around 2–3. However, the effect of ultrasound irradiation on particle size and porosity is conspicuous and consistent. Higher intensity of ultrasound leads to reduced particles sizes with a narrower distribution and higher porosity with larger pore diameters.

#### 4.2. Effect of turbulent intensity and vorticity strength on the synthesis

As can be seen from the previous sub-sections, the synthesis is strongly influenced by the local turbulence level while the turbulence level can be associated with the turbulent intensity in the SVFR. To better quantify the turbulent intensity and structure of “Rankine vortex” inside the SVFR, the following definition for the turbulent intensity is introduced, given by

$$I = \frac{\sqrt{k}}{\omega R_V} \quad (29)$$

The tangential velocity is calculated based on the simulation and is shown in Fig. 6. The overall distribution of tangential velocity can be well fitted and divided into three segments along radial direction [38]. The quasi-forced Rankine vortex core is formed at the centre of the chamber with  $|r/R| \leq 0.6$ , while the quasi-free vortex zone is located at the outer layer of the core ( $0.6 < |r/R| \leq 0.9$ ). A very thin boundary layer zone is found in the vicinity of the wall with  $|r/R| > 0.9$ . The simulated tangential velocity distribution,  $u_\theta$ , of the reactant solution along the radial direction in the SVFR under different ultrasound power levels and Reynolds number are nearly symmetrical due to identical inflow rates. As the ultrasound power level is increased, the gradient of the tangential velocity,  $du_\theta/dr$ , increases with the maximum tangential velocity that takes place at around  $r/R = 0.6$ . When the Reynolds number  $Re_V$  increases, a very similar trend is observed. However, the velocity distribution becomes asymmetrical as the volumetric flowrate ratio  $R$  changes. The inlet stream with fast flow engulfs the weaker one to form a swirling vortex but with the deformed vortex core.

The volumetric average turbulence intensity has been obtained based on the simulation and the results are displayed in Fig. 8. It can be seen that the turbulence intensity has been dramatically intensified by the adoption of ultrasound irradiation of higher power, changing from 120 W to 600 W via adjusting ultrasound amplitude ( $P_A$ ) from 10% to 50%. However, the turbulence intensity with different Reynolds number  $Re_V$  gradually increases from 15.41% to 15.67% for the given ultrasound irradiation condition and turbulence intensity varies in the range of 15.57% to 15.64% for different volumetric flowrate ratio  $R$ . This may suggest that the increase of the applied ultrasound power level is more effective than the increase of the inlet stream flow rate (characterised by the increase in the Reynolds number  $Re_V$ ). This may be attributed to the fact that when increasing the inlet stream speed, the turbulent kinetic energy increases but the turbulent dissipate rate also increases. However, as can be seen from Eq. (28), the increase in  $\langle \varepsilon \rangle$  will be confined by the swirling vortex core.

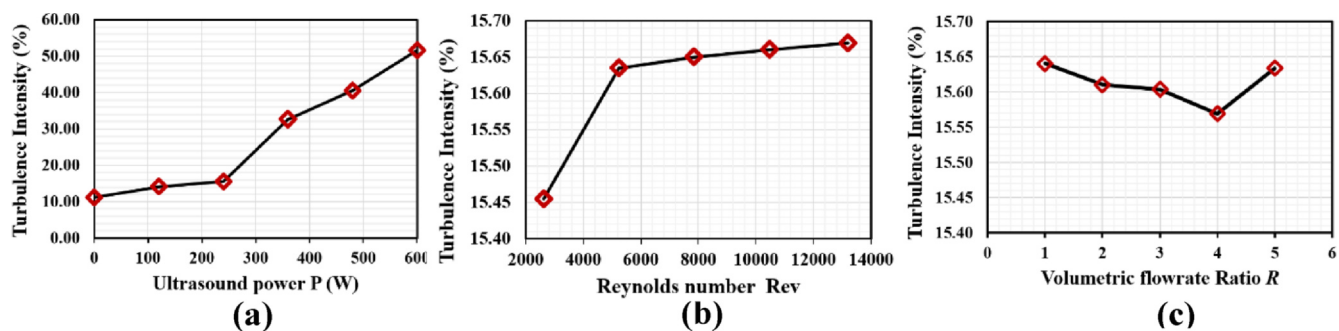


Fig. 8. Turbulence intensity versus (a) Ultrasound power  $P$  at Reynolds number  $Re_V = 7859$ ; (b) Reynolds number  $Re_V$  under ultrasound power of 240 W; (c) Volumetric flowrate ratio  $R$  under ultrasound power of 240 W.

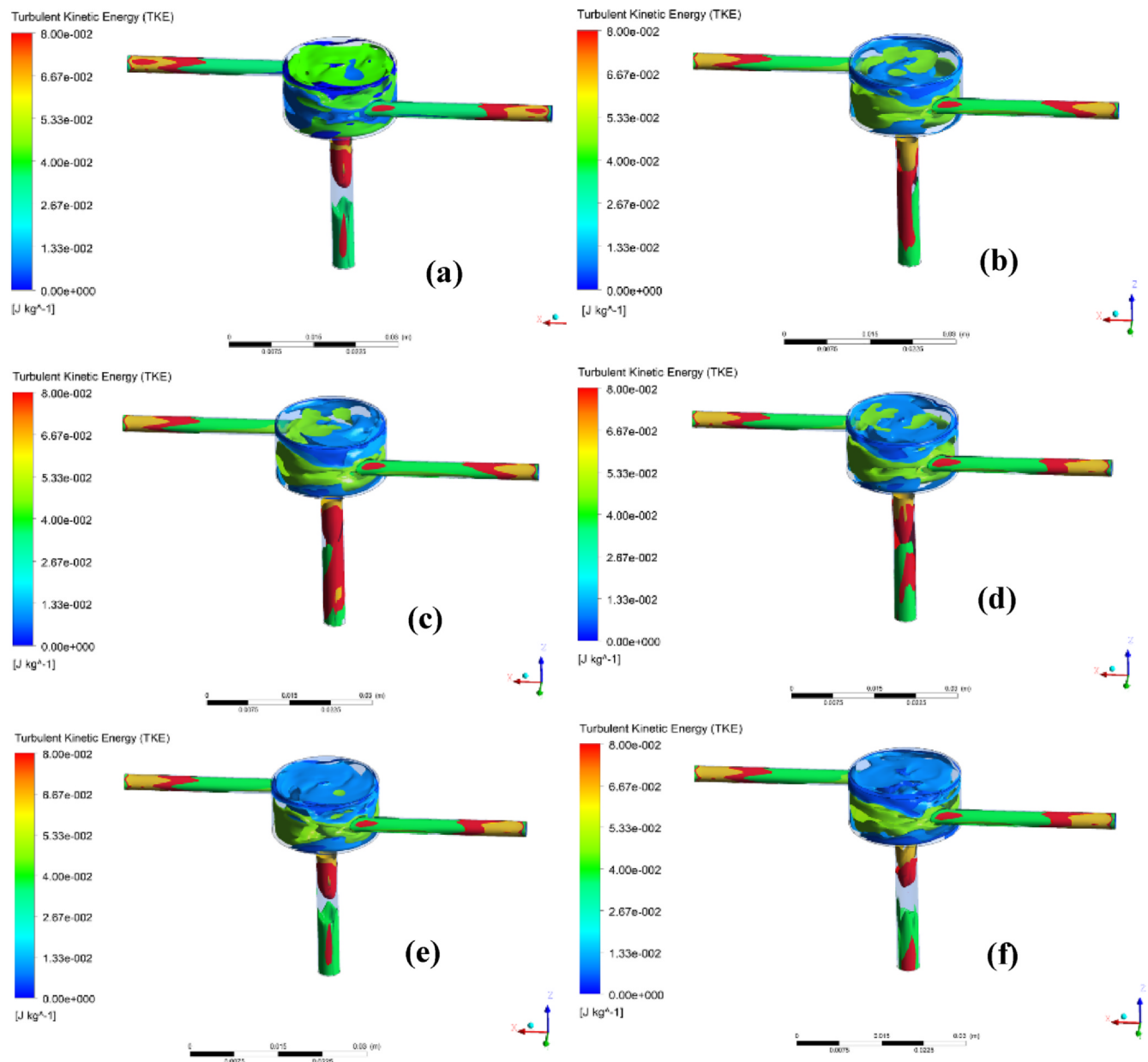


Fig. 9. Turbulent kinetic energy distribution in the reactor chamber under ultrasound power of (a) 0 W (b) 120 W (c) 240 W (d) 360 W (e) 480 W (f) 600 W at Reynolds number  $Re_V = 7859$  at flow time  $t = 2.0$  s.

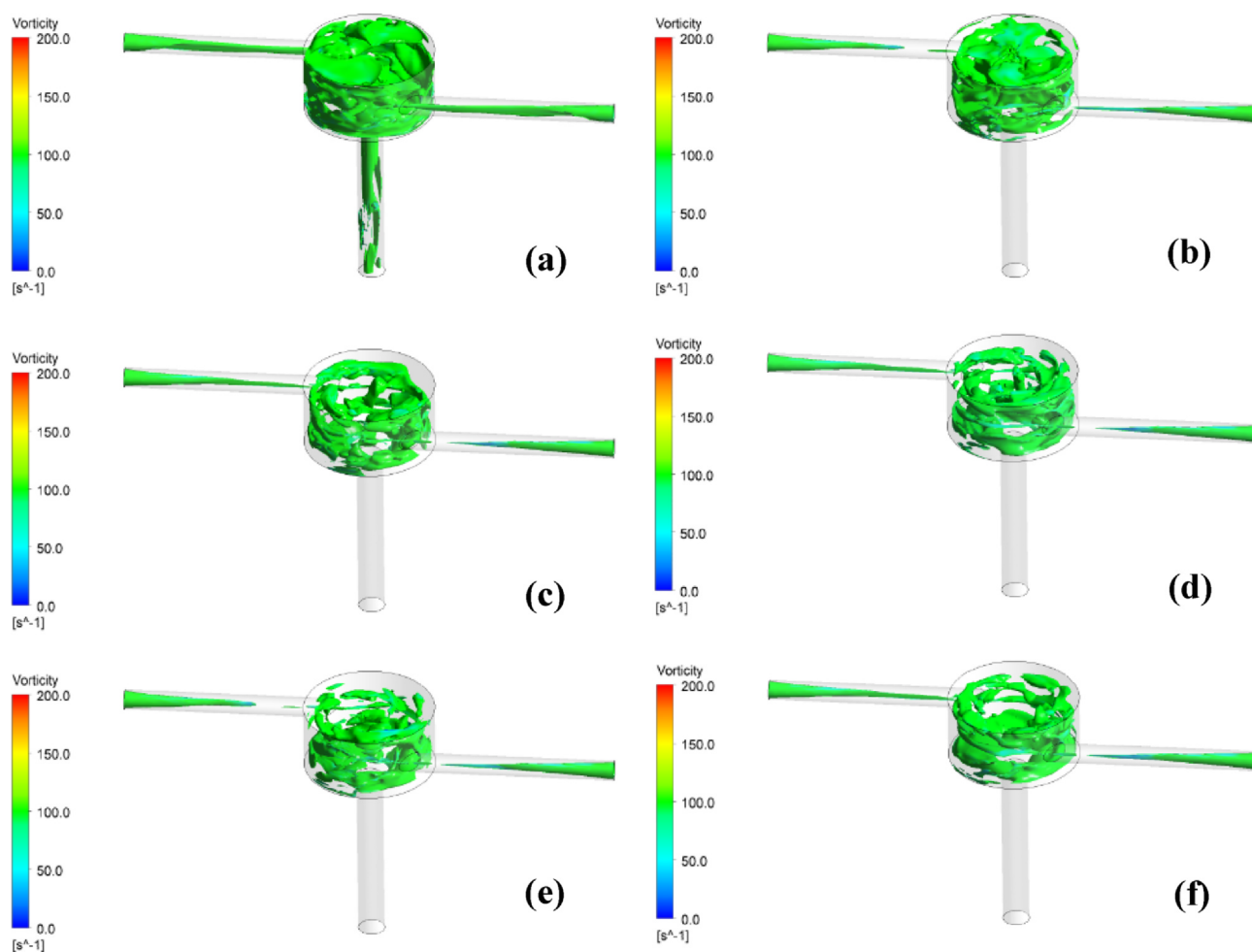


Fig. 10. Iso-surface of vorticity at  $100 \text{ s}^{-1}$  in the reactor chamber under ultrasound power of (a) 0 W (b) 120 W (c) 240 W (d) 360 W (e) 480 W (f) 600 W at Reynolds number  $Re_V = 7859$  at flow time  $t = 2.0 \text{ s}$ .

To further investigate the effect of ultrasound power on turbulence, turbulent kinetic energy distribution in the reactor chamber under different ultrasound power is shown in Fig. 9. As the ultrasound power increases, the turbulent kinetic energy at the upper layer tends to reduce and turbulent kinetic energy tends to increase at lower part in the chamber. This may attribute to acoustic streaming imposing in form of pressure impulsing 'Rankine vortex' towards away from the tip of ultrasound transducer. In addition, as the intensified effect of ultrasound, the strengthened 'Rankine vortex' may centrifuge liquid in upper layer.

Fig. 10 displays the iso-surface contours of vorticity at  $100 \text{ s}^{-1}$  in the reactor chamber when imposing different ultrasound power levels. It can be seen from the figure that with increasing the ultrasound irradiation level, the larger scale vortex structures have been broken into smaller scale vortex structures in the SVFR for the given  $Re_V$ . This is very likely to indicate that the ultrasound waves generate the acoustic streaming in the flow in terms of the local static pressure change while such local static pressure fluctuation may cause the local vortex stretching and deformed so as to break down the original structure with high irregularity, forcing the core of vorticity to a lower position and increasing the overall turbulent dissipation rate in the synthesis process.

#### 4.3. Effects of the interaction between turbulence induced shear and reaction characteristics on the synthesised particles

In addition to the effect of the local turbulence induced shear on the synthesised particles, the interaction between the local turbulence and

the particle nuclei growth dominated by reaction process can be characterised by using the Damköhler number,  $Da$ , as discussed below. The particle synthesis process can be considered to consist of two-step reactions (i) homogenous hydrolysis reaction transforming TEOS to  $\text{Si}(\text{OH})_4$ , and (ii) heterogenous condensation reaction transforming  $\text{Si}(\text{OH})_4$  to  $\text{SiO}_2$ . The hydrolysis reaction is predominant in the present study case. Following [39], the Damköhler number is introduced to characterise the interaction of the local turbulence shear and the chemical reaction, defined as the ratio of the typical turbulent eddy time scale to the chemical reaction time scale, which is expressed as

$$Da = \frac{\tau_t}{\tau_c} = \frac{12 \sqrt{\frac{\nu}{\langle \epsilon \rangle}}}{C' r'} \quad (30)$$

where the Damköhler number,  $Da$ , is volumetric averaged. The estimated  $Da$  as well as mean turbulent energy dissipation rate varying with different Reynolds number  $Re_V$  are displayed in Fig. 11 (a). The chemical reaction time scale  $\tau_c$  is proportional to the reciprocal of reaction constant  $k$  as described in Eq. (1) and mixing time ( $\tau = 12 \sqrt{\frac{\nu}{\langle \epsilon \rangle}}$ ) is proportional to the Kolmogorov time scale is calculated by  $\tau = (\nu/\langle \epsilon \rangle)^{1/2}$  [40]. In consequence,  $Da$  number is found in the order of  $10^{-7}$  to  $10^{-5}$  since the rate of hydrolysis-dominant reaction is comparably slower than the normal precipitation process, slightly decreasing from  $7.77 \times 10^{-7}$  to  $7.73 \times 10^{-7}$  in the range of Reynolds number from 2620 to 13,196 when the ultrasound power level of 240 W was applied as shown in Fig. 11 (b), with respect to turbulent time scale from  $1.80 \times 10^{-5}$  to  $1.79 \times 10^{-5}$ . It is noted that the  $Da$  number has

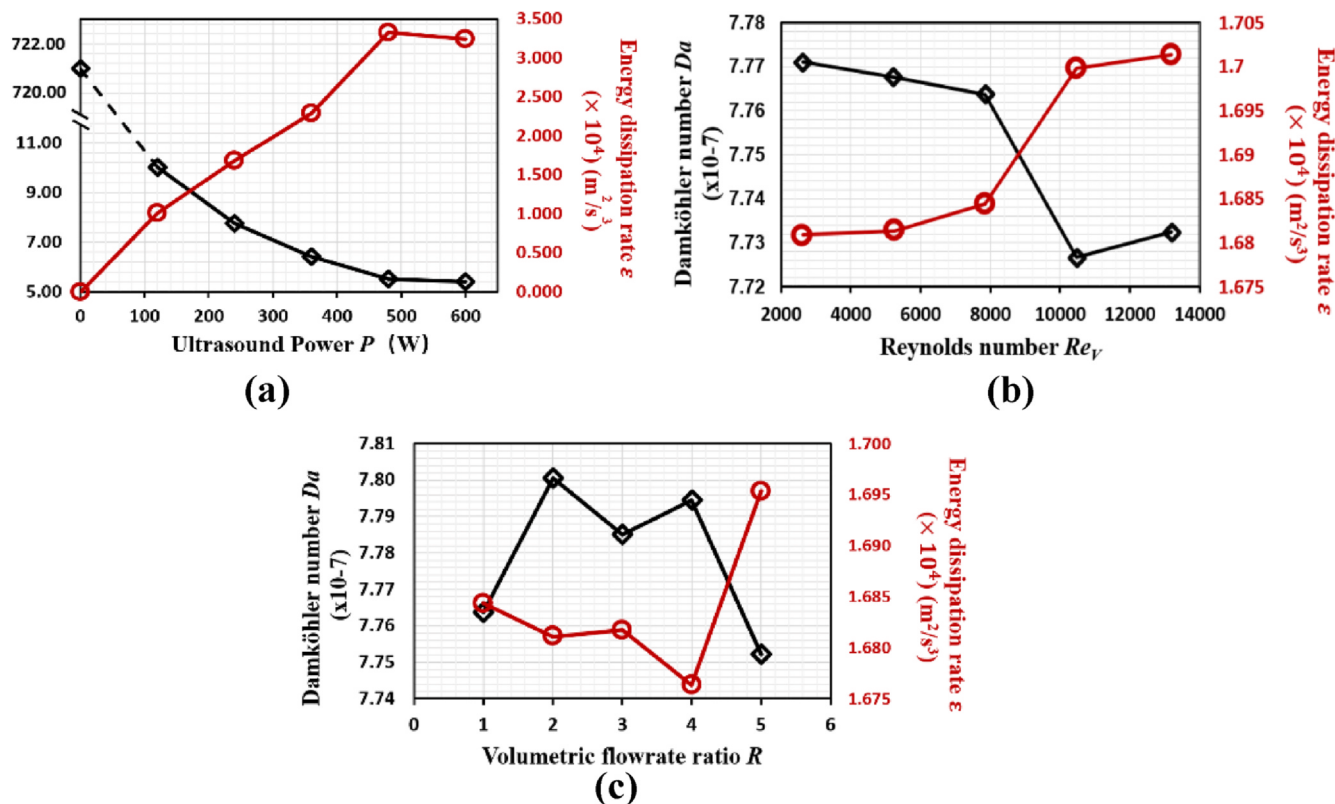


Fig. 11. Damköhler number and mean turbulent energy dissipation rate ( $\epsilon$ ) versus (a) Ultrasound power  $P$  at Reynolds number  $Re_V = 7859$ ; (b) Reynolds number  $Re_V$  under ultrasound power of 240 W; (c) Volumetric flowrate ratio  $R$  under ultrasound power of 240 W.

decreased as the  $Re_V$  number increases from 2620 to 10479, indicating the chemical reaction effect becomes less contributed compared with the effect of the turbulence-induced shear. As continuous increment of  $Re_V$  number from 10,479 to 13,196, the  $Da$  number has slightly increased from  $7.727 \times 10^{-7}$  to  $7.732 \times 10^{-7}$ , indicating that the effect of chemical reaction may be still dominated. An increased  $\epsilon$  value with a greater  $Re_V$  value indicates that the greater local turbulence level is caused by the stronger swirling turbulent vortex flow with the two higher inlet velocity streams. Consequently, this leads to an enhanced turbulent mixing, producing higher local turbulent shear stresses and enhancing the local mass transfer. It can be seen from Fig. 11 (c) that the changes in the volumetric flowrate ratio of two inlet streams  $R$  has an unpredictable impact on the interaction between the turbulence and the synthesis reaction as the  $Da$  number fluctuates in range of  $7.75 \times 10^{-7}$  to  $7.78 \times 10^{-7}$ , with the turbulent eddy time scale from  $1.79 \times 10^{-5}$  to  $1.81 \times 10^{-5}$ . Nevertheless, the adoption of ultrasound has a remarkable influence as the  $Da$  number has reduced significantly from  $7.22 \times 10^{-5}$  to  $5.40 \times 10^{-7}$ . The corresponding turbulent eddy time scale is  $7.52 \times 10^{-4}$  without ultrasound power and it decreases to  $5.63 \times 10^{-6}$  when ultrasound power of 600 W is applied. It is indicated that the mass transfer rate is approximately 200 times larger than the reaction rate when the ultrasound power level reaches 600 W compared with cases without adoption of ultrasound irradiation. As the ultrasound power level increases, the local turbulence is intensified due to the turbulence induced by imposing the ultrasound waves and the acoustic streaming results in the generation of the turbulent eddies that will be superimposed on the existing turbulence shear field, thus leading to the intensified reaction rate.

#### 4.4. Effect of turbulence induced shear on mass transfer rates of the synthesised aggregate particles

As discussed in the previous subsections, the synthesis of aggregated

nano-particles is significantly affected by the local turbulence, implying that the local turbulence has an impact on the mass transfer between the reactant solutions and embedded growing nano-particle aggregates due to the reactions. The Sherwood number ( $Sh$ ) is employed to describe the ratio of the mass transfer to mass diffusion, as defined by Eq. (31):

$$Sh = \frac{k_{sl} d_p}{D_A} \quad (31)$$

The aggregated nano-particle has been assumed to be a sphere with the equivalent diameter of  $d_p$ . In the synthesis, the Sherwood number is a function of the Reynolds number based on the diameter of the aggregate particle,  $Re_p$ , and the Schmidt number,  $Sc$ , based on the correlation described by Armenante and Kirwan [41] and Miller [42], which can be written as

$$Sh = 2.0 + AR e_p^{0.5} Sc^{0.33} \quad (32)$$

where  $Re_p$  and  $Sc$  is given by

$$Re_p = \frac{|\mathbf{u}_l - \mathbf{u}_p| d_p}{\nu} \quad (33)$$

$$Sc = \frac{\nu}{D_A} \quad (34)$$

As the synthesised aggregated nano-particle size is small, typically around  $1.5 \times 10^{-5}$  m from the experimental observation, the corresponding Stokes number,  $St_\eta = \frac{\rho_p d_p^2 \sqrt{\epsilon}}{18\nu^{3/2} \rho_l}$ , based on the volume average turbulent energy dissipation rate and Kolmogorov scale, falls into the range from 0.02 to 2.91 when the ultrasound irradiation power is increased from 0 to 600 W. This clearly indicates that the aggregated particles respond well to the local turbulent eddies with the size down to the Kolmogorov scale and are subject to the shear owing to large swirling turbulent eddies without adoption of the ultrasound

irradiation. However, the size of the turbulent eddies that have a strong interaction with the aggregated particles will reduce when the ultrasound irradiation is imposed, but the particles will be subjected to the shear action contributed from a wide-ranging size of turbulent eddies. In this case, the local particle velocity may be estimated by [40]

$$u_p = 2.0(\varepsilon d_p)^{1/3} \quad (35)$$

Considering the impact of turbulence on mass transfer process, Hiromitsu and Kawaguchi [43] and Al-Sood and Birouk [44] made an attempt on correlating the effect of the freestream turbulence on the mass transfer rate by introducing the turbulence coefficient  $C(I)$ . Introducing a similar modification to take the turbulence intensification into account, Eq. (36) can be modified, expressed as

$$Sh = 2.0 + A'Re_p^{0.5} Sc^{0.33} C(I) \quad (36)$$

Equation (37) can be further rewritten by relating to the Reynolds number  $Re_V$  as

$$Sh = 2.0 + A'Re_V^{0.5} \varphi^{0.5} Sc^{0.33} C(I) \quad (37)$$

where  $\varphi$  represents the aggregated nano-particle size against the Rankine vortex core characteristic length of reactor  $R_v$ , defined by

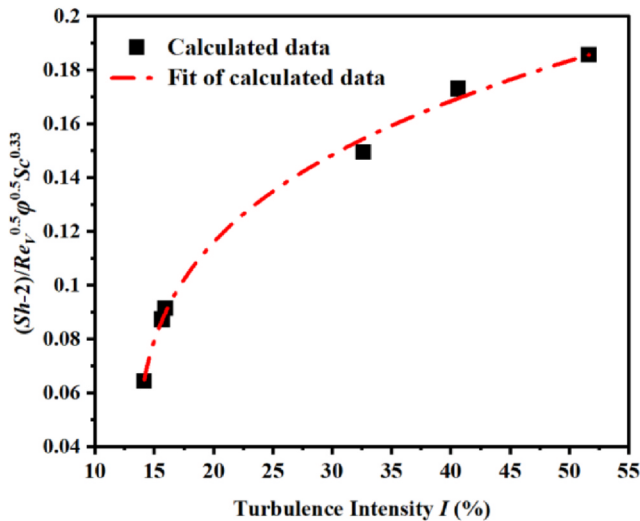
$$\varphi = \frac{|\mathbf{u}_l - \mathbf{u}_p| d_p}{2\omega R_v^2} \quad (38)$$

The coefficient  $A'$  can be obtained by observing the relationship between  $(Sh - 2)/Re_V^{0.5} \varphi^{0.5} Sc^{0.33}$  against turbulence intensity  $I$  based on the experimental data shown in Fig. 12 (a). The product of constant  $A'$  and turbulent coefficient  $C(I)$  is found to be well fitted by the following relationship:

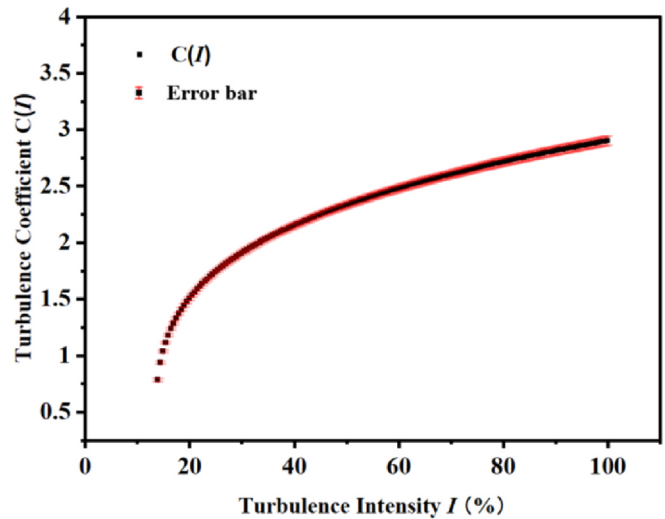
$$A' C(I) = a(I - b)^c \quad (39)$$

where parameters  $a$ ,  $b$ ,  $c$  are found from the fitting of the calculated data to be:  $a = 0.07 \pm 0.0053$ ;  $b = 13.40 \pm 0.32$ ;  $c = 0.27 \pm 0.02$ . In this case, the coefficient of determination  $R^2 = 0.99967$  (perfect fit when  $R^2 = 1$ ). The turbulence coefficient  $C(I)$  as a function of turbulence intensity  $I$  is plotted in Fig. 12 (b) and the deviation is shown as error bars. We thus obtain the Sherwood number for description of the mass transfer in the synthesis of aggregated nano-particle in the SVFR, given by

$$Sh = 2.0 + 0.07 Re_V^{0.5} \varphi^{0.5} Sc^{0.33} (I - 13.4)^{0.27} \quad (40)$$



(a)



(b)

Fig. 12. (a)  $(Sh - 2)/Re_V^{0.5} \varphi^{0.5} Sc^{0.33}$  versus turbulence intensity  $I$  (%) by adoption of ultrasound power from 0 W to 600 W and (b) the plot of turbulence coefficient  $C(I)$  as a function of turbulence intensity  $I$  (%) with the error bar of turbulence coefficient.

Fig. 13 shows the Sherwood number changing as characteristic length ratio  $\varphi$  and turbulence intensity  $I$  at Reynolds number  $Re_V = 7859$ . Higher Sherwood number ( $Sh > 3.5$ ) occurs when  $\varphi$  is larger than  $1 \times 10^{-3}$  where the intensification of ultrasound irradiation enhances the turbulence so that the mass transfer between the particles and the reactant solution is enhanced. In contrast,  $Sh$  number tends to be smaller as the turbulence intensity decreases contributing less to the mass transfer with  $\varphi$  smaller than  $1 \times 10^{-3}$ . To further investigate the correlation between the mass transfer and local turbulent shear in the swirling turbulent flow, a correlation coefficient  $R_{G,Sh}$  between the predicted local reactant consumption rate and the volume average local turbulent shear rate is proposed, which is defined by

$$R_{G,Sh} = \frac{\langle G \rangle_j \langle Sh \rangle_j}{\langle G \rangle_{ref} \langle Sh \rangle_{ref}} \quad (41)$$

where  $\langle G \rangle_j$  is the volume average turbulent shear rate, subscript  $j$  denotes different cases. They are estimated by

$$\langle G \rangle_j = \frac{1}{V} \int_0^V G dV = \frac{1}{V} \int_0^V \sqrt{\frac{\varepsilon}{\nu}} dV \quad (42)$$

$$\langle Sh \rangle_j = \frac{1}{V} \int_0^V Sh dV \quad (43)$$

Fig. 14 shows the correlation coefficient  $R_{G,Sh}$  change in the SVFR on the conditions of adoption of different ultrasound power for the given  $Re_V$  and variation of  $Re_V$  for the given adopted ultrasound irradiation. The change of the correlation coefficient in the SVFR chamber has the following trend. Considering the case without applying ultrasound irradiation as the reference, the correlation  $R_{G,Sh}$  equals one. It increases monotonically when increasing the applied ultrasound power for the given  $Re_V$ , indicating that the mass transfer process is strongly affected by the local turbulence intensification due to the turbulence generation by acoustic streaming. It is postulated that the effect of ultrasound irradiation may significantly enhance the turbulent eddy fluctuations so that the local turbulent shear stresses are increased. When the ultrasound power increases from 0 W to 600 W, the correlation  $R_{G,Sh}$  for the given  $Re_V$  are almost increased up to 2.5 times greater than that without applying the ultrasound irradiation as can be observed from Fig. 14 (a). The consequence of the acoustic streaming of ultrasound irradiation is to intensify the local turbulence, resulting in the enhancement of the mass transfer between the particles and the

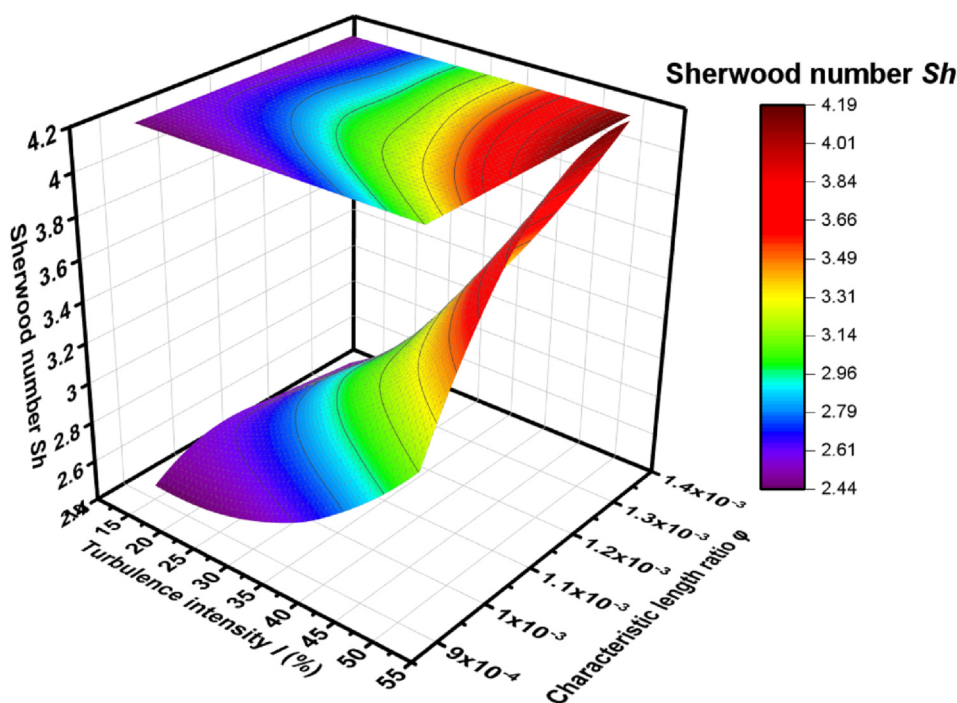


Fig. 13. 3D-plot of Sherwood number  $Sh$  versus characteristic length ratio  $\varphi$  and turbulence intensity  $I$  (%).

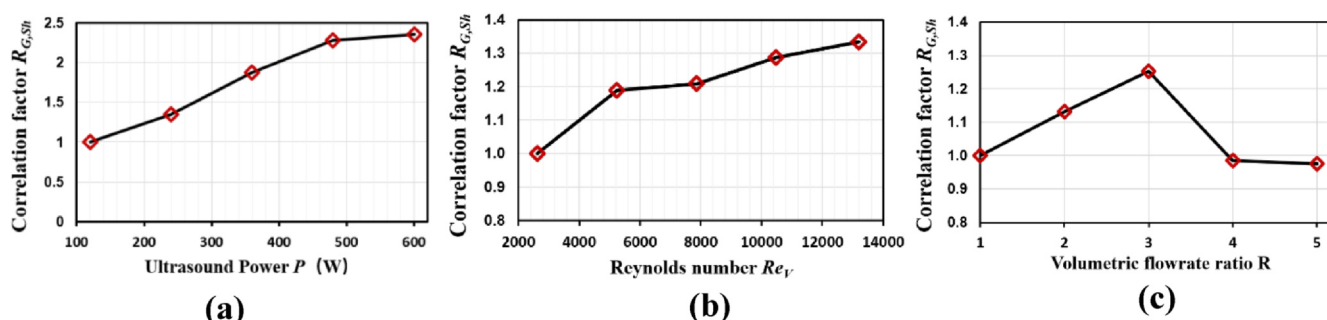


Fig. 14. Correlation factor  $R_{G,Sh}$  between the predicted Sherwood number and local shear rate under (a) Ultrasound power  $P$  at Reynolds number  $Re_V = 7859$ ; (b) Reynolds number  $Re_V$ ; (c) Volumetric flowrate ratio  $R$  under ultrasound power of 240 W.

reactant. It can be seen from Fig. 14 (b) that  $R_{G,Sh}$  also increases up to around 1.4 times with increasing  $Re_V$  for the given ultrasound irradiation of 240 W. It is noted here that as  $\langle \varepsilon \rangle = 2\nu\omega^2$ , an increase in  $Re_V$  means the increase in the rotational angular velocity or vorticity in the Rankine vortex core, thus giving out an increase in the local turbulent shear. As the  $Re_V$  increases, higher dissipation takes place, which results in the improved mass transfer and reactant consumption for the particle growth. However, the Sherwood number and the shear rate are highly correlated when volumetric flowrate ratio  $R = 2-3$ , it has an unpredictable correlation as volumetric flowrate ratio increases.

## 5. Conclusions

Shear turbulence controllable synthesis of nano-sized particles using a swirling vortex flow reactor assisted by ultrasound irradiation has been investigated using both CFD modelling and experimental validation. The effects of the intensification of turbulence by applying ultrasound irradiation and turbulence level in the Rankine vortex core characterised by using the Reynolds number  $Re_T$  on particle synthesis are studied. Characterisation of the synthesised particle morphology, porosity and size distribution are correlated with the local turbulence generated in the SVFR. The conclusions derived from the present study can be summarised as follows:

- (1) It was found that when the Reynolds number  $Re_V$  and the adopted ultrasound power increase, the average synthesised  $\text{SiO}_2$  particle size is reduced, accompanied by a narrower particle size distribution and higher porosity. When increasing the inlet reactant solution volumetric flowrate ratio  $R$ , smaller size  $\text{SiO}_2$  particles with higher porosity are obtained only when  $R$  is around 2 to 3. The effect of change in the volumetric flowrate ratio on the synthesised  $\text{SiO}_2$  particle characteristics is weak due to the enhancement of the turbulence shear stresses acting on the particles being restricted by the variation of the turbulent Rankine vortex formed in the SVFR.
- (2) It has been affirmed that increasing the Reynolds number  $Re_V$  and the adopted ultrasound power leads to the reduction of  $Da$  number, indicating that the effect of turbulence induced shear on the synthesised particles increases compared with the effect of hydrolysis in the synthesis process. The adoption of ultrasound irradiation can significantly enhance the intensity of turbulence embedded in the turbulent Rankine vortex formed in the SVFR and change the local turbulent energy dissipation rate as characterised by the local turbulent shear  $\sqrt{\frac{\varepsilon}{\nu}}$ .
- (3) By introducing the modified Sherwood number, the correlation of the mass transfer in the interface of the aggregated nanoparticles and the reactants with the local turbulent shear stresses has been demonstrated. It has been proved that the intensification of ultrasound will enhance the local turbulence and turbulent shear

stresses. As a result, the mass transfer has been enhanced. Such spatial correlation can be used to predict the mass transfer for the particles in the synthesis process.

### Declaration of Competing Interest

The authors declare that they have no known competing financial interests or personal relationships that could have appeared to influence the work reported in this paper.

### Acknowledgements

This work was financially supported by the National Natural Science Foundation of China (Grant Nos. 21576141, 21761132026, 21908195). Yanqing Guo would also like to acknowledge the PhD scholarship of the International Doctoral Innovation Centre (IDIC) of the University of Nottingham Ningbo China and the support of EPSRC (Grant no. EP/G037345/1).

### References

- [1] S. Usune, M. Kubo, T. Tsukada, O. Koike, R. Tatsumi, M. Fujita, S. Takami, T. Adschiri, Numerical simulations of dispersion and aggregation behavior of surface-modified nanoparticles under shear flow, *Powder Technol.* 343 (2019) 113–121.
- [2] E. Shoukry, L.W. Shemilt, Mass transfer enhancement in swirling annular pipe flow, *Ind. Eng. Chem. Process Des. Dev.* 24 (1) (1985) 53–56.
- [3] Kockmann, N., Föll, C., and Woias, P., Flow regimes and mass transfer characteristics in static micromixers. *Micromachining and Microfabrication*. Vol. 4982. 2003: SPIE.PWM.
- [4] A. Mariotti, C. Galletti, M.V. Salvetti, E. Brunazzi, Unsteady flow regimes in a T-shaped micromixer: mixing and characteristic frequencies, *Ind. Eng. Chem. Res.* 58 (29) (2019) 13340–13356.
- [5] E. Shoukry, L. Shemilt, Mass transfer enhancement in swirling annular pipe flow, *Ind. Eng. Chem. Process Des. Dev.* 24 (1985).
- [6] P. Legentilhomme, H. Aouabed, J. Legrand, Developing mass transfer for annular swirling decaying flow induced by means of a tangential inlet, *Chem. Eng. J.* 52 (3) (1993) 137–147.
- [7] C.C. Contigiani, O. González Pérez, J.M. Bisang, Local mass-transfer study in a decaying swirling flow electrochemical reactor under single-phase and two-phase (gas-liquid) flow, *Chem. Eng. J.* 350 (2018) 233–239.
- [8] J. Zhang, S.-F. Liu, C. Cheng, W.-F. Li, X.-L. Xu, H.-F. Liu, F.-C. Wang, Investigation of three-dimensional flow regime and mixing characteristic in T-jet reactor, *Chem. Eng. J.* 358 (2018).
- [9] B. Sajjadi, A.R. Abdul Aziz, S. Ibrahim, Mechanistic analysis of cavitation assisted transferification on biodiesel characteristics, *Ultrason. Sonochem.* 22 (2015) 463–473.
- [10] T. Hielscher, *Ultrasonic Production of Nano-Size Dispersions and Emulsions*. European Nano Systems 2005, Paris, France, 14–16 December 2005, 2007.
- [11] B. Sajjadi, S. Asgharzadehahmadi, P. Asaithambi, A.A.A. Raman, R. Parthasarathy, Investigation of mass transfer intensification under power ultrasound irradiation using 3D computational simulation: a comparative analysis, *Ultrason. Sonochem.* 34 (2017) 504–518.
- [12] B. Zhang, J. Li, Q. Chen, G. Chen, Precipitation of Al(OH)<sub>3</sub> crystals from supersaturated sodium aluminate solution irradiated with ultrasonic sound, *Minerals En.* 22 (9–10) (2009) 853–858.
- [13] P. Jeevanandam, Y. Koltypin, A. Gedanken, Synthesis of nanosized  $\alpha$ -nickel hydroxide by a sonochemical method, *Nano Lett.* 1 (5) (2001) 263–266.
- [14] J. Jordens, N. De Coker, B. Gielen, T. Van Gerven, L. Braeken, Ultrasound precipitation of manganese carbonate: the effect of power and frequency on particle properties, *Ultrason. Sonochem.* 26 (2015) 64–72.
- [15] M. Rahimi, B. Aghel, B. Hatamifar, M. Akbari, A. Alsairafi, CFD modeling of mixing intensification assisted with ultrasound wave in a T-type microreactor, *Chem. Eng. Process. Process Intensif.* 86 (2014) 36–46.
- [16] Y. Dai, R. Lv, J. Fan, H. Peng, Z. Zhang, X. Cao, Y. Liu, Highly ordered macroporous silica dioxide framework embedded with supramolecular as robust recognition agent for removal of cesium, *J. Hazard. Mater.* 121467 (2019).
- [17] H. Wang, Z. Chen, D. Chen, Q. Yu, W. Yang, J. Zhou, S. Wu, Facile, template-free synthesis of macroporous SiO<sub>2</sub> as catalyst support towards highly enhanced catalytic performance for soot combustion, *Chem. Eng. J.* 375 (2019) 121958.
- [18] A. Hafizi, M.R. Rahimpour, M. Heravi, Experimental investigation of improved calcium-based CO<sub>2</sub> sorbent and Co<sub>3</sub>O<sub>4</sub>/SiO<sub>2</sub> oxygen carrier for clean production of hydrogen in sorption-enhanced chemical looping reforming, *Int. J. Hydrogen Energy* 44 (33) (2019) 17863–17877.
- [19] S. Tian, W. Gao, Y. Liu, W. Kang, H. Yang, Effects of surface modification Nano-SiO<sub>2</sub> and its combination with surfactant on interfacial tension and emulsion stability, *Colloids Surf., A* 595 (2020) 124682.
- [20] S. Morita, M. Iijima, J. Tatami, SiO<sub>2</sub> nanoparticles surface modified with polyethyleneimine-oleic acid complex as stabilizers of Ni fine particles in dense non-aqueous suspensions, *Adv. Powder Technol.* 28 (1) (2017) 30–36.
- [21] K. Keyvanloo, W.C. Hecker, B.F. Woodfield, C.H. Bartholomew, Highly active and stable supported iron Fischer-Tropsch catalysts: Effects of support properties and SiO<sub>2</sub> stabilizer on catalyst performance, *J. Catal.* 319 (2014) 220–231.
- [22] R. Gobinath, G. Raja, E. Prasath, G. Shyamala, A. Vilorio, N. Varela, Studies on strength characteristics of black cotton soil by using novel SiO<sub>2</sub> combination as a stabilizing agent, *Mater. Today: Proc.* (2020).
- [23] D. Harpaz, B. Koh, R.C.S. Seet, I. Abdulhalim, A.I.Y. Tok, Functionalized silicon dioxide self-referenced plasmonic chip as point-of-care biosensor for stroke biomarkers NT-proBNP and S100 $\beta$ , *Talanta* 212 (2020) 120792.
- [24] C.J. Brinker, G.W. Scherer, *Sol-Gel Science: The Physics and Chemistry of Sol-Gel Processing*, Academic Press, 2013.
- [25] J. Yu, L. Zhao, B. Cheng, Preparation of monodispersed microporous SiO<sub>2</sub> microspheres with high specific surface area using dodecylamine as a hydrolysis catalyst, *J. Solid State Chem.* 179 (1) (2006) 226–232.
- [26] K. Yano, Y. Fukushima, Particle size control of mono-dispersed super-microporous silica spheres, *J. Mater. Chem.* 13 (10) (2003) 2577–2581.
- [27] J.L. Gurav, A.V. Rao, A.P. Rao, D. Nadargi, S. Bhagat, Physical properties of sodium silicate based silica aerogels prepared by single step sol-gel process dried at ambient pressure, *J. Alloy. Compd.* 476 (1–2) (2009) 397–402.
- [28] K.-S. Kim, J.-K. Kim, W.-S. Kim, Influence of reaction conditions on sol-precipitation process producing silicon oxide particles, *Ceram. Int.* 28 (2) (2002) 187–194.
- [29] G. De, B. Karmakar, D. Ganguli, Hydrolysis–condensation reactions of TEOS in the presence of acetic acid leading to the generation of glass-like silica microspheres in solution at room temperature, *J. Mater. Chem.* 10 (10) (2000) 2289–2293.
- [30] R. Zhao, P. Dong, Kinetics of TEOS hydrolysis in the preparation of monodisperse SiO<sub>2</sub> system, *Acta Phys. Chim. Sin.* 11 (1995) 612–616.
- [31] S. Elghobashi, T. Abou-arab, A two-equation turbulence model for two-phase flows, *Phys. Fluids* 26 (1983) 931–938.
- [32] X. Zhou, Y. Ma, M. Liu, Y. Zhang, CFD-PBM simulations on hydrodynamics and gas-liquid mass transfer in a gas-liquid-solid circulating fluidized bed, *Powder Technol.* 362 (2020) 57–74.
- [33] E.Y. Bong, N. Eshtiaghi, J. Wu, R. Parthasarathy, Optimum solids concentration for solids suspension and solid-liquid mass transfer in agitated vessels, *Chem. Eng. Res. Des.* 100 (2015) 148–156.
- [34] Y. Kato, S. Hiraoka, Y. Tada, T. Nomura, Solid–liquid mass transfer in a shaking vessel for a bioreactor with “current pole”, *Canad. J. Chem. Eng.* 76 (3) (1998) 441–445.
- [35] D.M. Levins, J.R. Glastonbury, Particle-liquid hydrodynamics and mass transfer in a stirred vessel Part I-Particle-liquid motion, *Trans. Inst. Chem. Engrs* 50 (1972) 32.
- [36] R. Roohi, E. Abedi, S.M.B. Hashemi, K. Marszalek, J.M. Lorenzo, F.J. Barba, Ultrasound-assisted bleaching: Mathematical and 3D computational fluid dynamics simulation of ultrasound parameters on microbubble formation and cavitation structures, *Innov. Food Sci. Emerg. Technol.* 55 (2019) 66–79.
- [37] B. Sajjadi, A.A.A. Raman, S. Ibrahim, Influence of ultrasound power on acoustic streaming and micro-bubbles formations in a low frequency sono-reactor: Mathematical and 3D computational simulation, *Ultrason. Sonochem.* 24 (2015) 193–203.
- [38] J.-P. Wu, Y.-H. Zhang, H.-L. Wang, Numerical study on tangential velocity indicator of free vortex in the cyclone, *Sep. Purif. Technol.* 132 (2014) 541–551.
- [39] J. Bakladya, W. Podgorska, R. Pohorecki, Mixing-precipitation model with application to double feed semibatch precipitation, *Chem. Eng. Sci.* 50 (8) (1995) 1281–1300.
- [40] S.B. Pope, *Turbulent Flows*, Cambridge University Press, Cambridge, 2000.
- [41] P.M. Armentante, D.J. Kirwan, Mass transfer to microparticles in agitated systems, *Chem. Eng. Sci.* 44 (12) (1989) 2781–2796.
- [42] D.N. Miller, Scale-Up of agitated vessels. Mass transfer from suspended solute particles, *Ind. Eng. Chem. Process Des. Dev.* 10 (3) (1971) 365–375.
- [43] N. Hiromitsu, O. Kawaguchi, Influence of flow turbulence on the evaporation rate of a suspended droplet in a hot air flow, *Heat Transfer Japanese Res.* 24 (8) (1995) 689–700.
- [44] M.A. Al-Sood, M. Birouk, A numerical study of the effect of turbulence on mass transfer from a single fuel droplet evaporating in a hot convective flow, *Int. J. Therm. Sci.* 46 (8) (2007) 779–789.



# CFD modelling of the effects of local turbulence intensification on synthesis of LiFePO<sub>4</sub> particles in an impinging jet reactor

Luming Chen<sup>a,b</sup>, Bing Dong<sup>a,c</sup>, Yanqing Guo<sup>a</sup>, Xiaogang Yang<sup>a,\*</sup>, Guang Li<sup>a</sup>

<sup>a</sup> Department of Mechanical, Materials and Manufacturing Engineering, The University of Nottingham Ningbo China, University Park, Ningbo 315100, China

<sup>b</sup> Institute of Process Equipment and Control Engineering, Zhejiang University of Technology, Hangzhou 310014, China

<sup>c</sup> Department of Pharmaceutical Engineering, School of Engineering, China Pharmaceutical University, Nanjing 210009, China

## ARTICLE INFO

### Keywords:

Impinging stream intensified microreactor  
Reynolds number  
Laminar flow  
Transitional flow  
FePO<sub>4</sub>  
LiFePO<sub>4</sub>  
Nanoparticles

## ABSTRACT

LiFePO<sub>4</sub> particles has been widely recognised as a promising positive electrode material for rechargeable lithium-ion batteries due to its excellent properties. Confined impinging jet reactor was recently proposed to replace the stirring reactor for synthesising LiFePO<sub>4</sub> nanoparticles. It has been recognised that the use of impinging jet reactor can provide higher mixing intensity and shorter residence time for the reaction so as to improve the synthesis efficiency. The present work conducts CFD simulations to gain a better understanding of the mechanism of LiFePO<sub>4</sub> synthesis in an impinging jet reactor, focusing on the effects of local turbulent kinetic energy and turbulence dissipation rate distributions in the impinging core region on the mixing of two reactant streams and reaction kinetics. Compared with the experimental results, it is revealed that larger turbulent kinetic energy in the impinging centre region can effectively promote the mixing of reactant streams but the reaction completeness will be reduced due to shortening of reaction time if a large turbulence dissipation rate occurs in the impinging core region. It is also indicated from the simulations that the reaction completeness of LiFePO<sub>4</sub> synthesis significantly depends on the turbulent mixing and turbulent kinetic energy distribution but less on reaction kinetics.

## 1. INTRODUCTION

Mixing of reactants plays an important role in the chemical process. Usually the mixing, based on the scales, can be classified into micro-, meso- and macro mixing while micro-mixing usually determines the selectivity and quality of the final products in the chemical process especially when a rapid reaction process is concerned, for example, precipitation and crystallisation [1–4]. The adoption of confined impinging jet reactor (CIJR) has attracted more and more attentions in the nanoparticle production as it can provide a better micro-mixing of the reactants with higher feed rate than stirred tanks for the mixing-sensitive reactions [5,6] where continuous production and high product quality of particles are required. Within an impinging jet reactor, a high turbulent-energy dissipation region is generated by two head-on impinging coaxial jets, intensifying the mixing of two reactant flows dramatically. However, the residence time in CIJR is quite short due to the high feed velocities and small reactor volume.

Schwarzer and Peukert [7] experimentally and numerically studied the sulfate nanoparticle precipitation and successfully predicted the mean particle size of the precipitated nanoparticles by CFD simulations

where the precipitation model has been coupled with the global mixing model. It was found particle size distributions was underestimated and that considering the effects of back-flow zones and large eddies on the resident time could significantly improve the predictions of particle size distributions by this model. Marchisio et al. [8] investigated the effects of turbulent precipitation on the nanoparticle production in CIJRs and found the turbulent mixing played an important role in the reactor scale up based on the results of CFD and precipitation models and that the characteristic time scales for mixing and reaction extracted from CFD simulations could provide more reliable and accurate supports for the reactor scale-up than those from simple algebraic correlations. Norbert et al. [9] examined the convective micro-mixing in different micro-channels at high Reynolds numbers and revealed that under the condition of relatively high Reynolds number, the mixing performance in the micro-structures can be enhanced and a better mixing than the use of stirred vessels can be obtained. Siddiqui et al. [6] investigated the characterisations of CIJR through the evaluation of energy dissipation rate, micro-mixing efficiency of a homogeneous reaction and particle size of a heterogeneous precipitation reaction. It was found that the energy dissipation in CIJR could reach 100 times greater than that in

\* Corresponding author.

E-mail address: [Xiaogang.Yang@nottingham.edu.cn](mailto:Xiaogang.Yang@nottingham.edu.cn) (X. Yang).

<https://doi.org/10.1016/j.cep.2020.108065>

Received 19 February 2020; Received in revised form 6 July 2020; Accepted 26 July 2020

Available online 30 July 2020

0255-2701/ © 2020 Elsevier B.V. All rights reserved.

**Nomenclature**

$C_p$ [Mol/m <sup>3</sup> ]	Concentration of species p
$D_a$ [-]	Damköhler number
$D_m$ [m <sup>2</sup> /s]	Diffusion coefficient for species p in the mixture
$G$ [m/s <sup>2</sup> ]	Acceleration due to gravity
$G_k$ [kg/(ms <sup>3</sup> )]	Generation of turbulent kinetic energy
$I$ [-]	Unit tensor
$J_p$ [kg/m <sup>2</sup> ]	Diffusive mass flux
$k_s$ [m <sup>3</sup> /(kmol · s)]	Reaction rate constant
$m_{FePO_4}$ [kg/m <sup>3</sup> ]	Mass concentration of FePO <sub>4</sub>
$m_{FePO_4,0}$ [kg/m <sup>3</sup> ]	Theoretical mass concentration of FePO <sub>4</sub>
$Re$ [-]	Reynolds number
$R_{he}$ [kmol/m <sup>3</sup> s]	Reaction rate
$Sc_t$ [-]	Turbulent Schmidt number
$T_i$ [-]	Turbulent intensity
$u$ [m/s]	Instantaneous velocity

$X$ [-]	Completeness of the reaction
$Y_p$ [-]	Mass fraction of species p

*Special characters*

$\kappa$ [m <sup>2</sup> /s <sup>2</sup> ]	Turbulent kinetic energy
$\varepsilon$ [m <sup>2</sup> /s <sup>3</sup> ]	Turbulent dissipation rate
$\rho$ [kg/m <sup>3</sup> ]	Density
$\rho_m$ [mol/m <sup>3</sup> ]	Molar density of the particle
$\mu$ [N.s/m <sup>2</sup> ]	Dynamic viscosity
$\mu_l$ [N.s/m <sup>2</sup> ]	liquid phase dynamic viscosity for laminar flow
$\mu_t$ [N.s/m <sup>2</sup> ]	Eddy viscosity
$\nu$ [m <sup>2</sup> /s]	Kinematic viscosity
$\tau$ [N/m <sup>2</sup> ]	Stress tensor
$\tau_c$ [s]	Characteristic time scale of chemical reaction
$\tau_t$ [s]	Characteristic time scale of eddy engulfment

traditional stirred tanks and that the mixing performance of the CIJR was more sensitive to the concentration than the inlet flow rate. These authors indicated that CIJR presents higher sensitivity to the mixing conditions at high concentrations compared to the stirred tank. Florian et al. [10] have studied the behaviours of CIJR at a low Reynolds number using direct numerical simulation (DNS), revealing that a stable vortex exists in the main mixing duct and dominates the flow. In addition, a monomodal probability density function (PDF) is obtained in the main impinging zone while a bimodal PDF is identified in the cross sections downstream the impinging zone. Jiang et al. [11] investigated the effects of jet velocity on crystal size distribution of pharmaceutical ingredients with a dual impinging jet mixer. They obtained the drug products with smaller sizes and aspect ratios comparing with the case of applying traditional batch process. Meanwhile, it was revealed that the particle size and the distribution width as well as the distribution modality highly depend on the inlet jet velocity. Tari et al. [12] employed CIJR to investigate the anti-solvent crystallisation of glycine and found the particle size obtained in the CIJR was an order of magnitude smaller than that obtained by employing the conventional crystallisation approach.

As one of the promising positive electrode material of rechargeable lithium-ion batteries, LiFePO<sub>4</sub> has excellent characteristics such as nontoxicity, high structural stability at high temperature, relatively cost-effective price of raw material and high theoretical specific capacity [13,14]. It has been recognised that the adoption of traditional stirring reactor for synthesising LiFePO<sub>4</sub> particles may be an ineffective approach where the poor mixing and mass transfer performance dramatically limits the production of LiFePO<sub>4</sub> particles [5,15]. In order to provide a more rapid and better micromixing of feeding streams during the production of LiFePO<sub>4</sub>, the adoption of CIJR is very likely more favourable option than the use of stirring reactor. Compared with the traditional stirred tank, the CIJR can realise the mixing intensity several orders of magnitude higher than the stirring tank though having a shortening residence time with steady feeding streams due to its fixed and confined volume [16,17]. To best knowledge of the authors, only few studies on the preparation of LiFePO<sub>4</sub> in CIJR have been documented. Thus, the main purpose of this paper aims to reveal the effects of turbulent mixing behaviours on the preparation process of LiFePO<sub>4</sub> in the CIJR, gaining a better understanding for facilitating the process optimisation. To provide instantaneous variations of local velocity field and local concentrations of chemical species, CFD modelling coupled with the relevant chemical reaction kinetics has been conducted, focusing on the effects of turbulence intensification due to the impingement of the streams in CIJR on the synthesis of LiFePO<sub>4</sub> particles. In the meantime, the experimental results are used to validate the CFD modelling.

**2. MATHEMATICAL MODELLING***2.1. Governing equations*

The governing equations for CFD modelling in this study can be expressed by a set of continuity, momentum and species transport equations. The energy equation has been ignored as the temperature variation during the chemical reaction in the synthesis of LiFePO<sub>4</sub> is not significant and has less impact on chemical kinetics involved. The liquid solution flow is also assumed to be incompressible and k-ε two equation model is employed for modelling the turbulence in the CIJR reactor following its successful applications to the cases of similar studies [18–20]. Equations (1) and (2) present the continuity and momentum equations, respectively. Species transport equation coupled with 'Direct Quadrature Method of Moments-Interaction by Exchange with the Mean Model' (DAMOM-IEM) (Equations (9)–(12)) is used to model the micro-mixing behaviour of the impinging flow. The reaction kinetics is modelled by an empirical equation based on the experimental results.

*2.2. Continuity Equation*

$$\frac{\partial \rho}{\partial t} + \nabla \cdot (\rho \mathbf{u}) \quad (1)$$

*2.3. Momentum Balance Equation*

$$\frac{\partial}{\partial t} (\rho \mathbf{u}) + \nabla \cdot (\rho \mathbf{u} \mathbf{u}) = -\nabla p + \nabla \cdot \tau + \rho \mathbf{g} \quad (2)$$

where  $\rho$ ,  $\mathbf{u}$ , are the density and instantaneous velocity respectively.  $\mathbf{g}$  denotes the gravity and  $p$  stands for the pressure. Constitutive closure model for shear stresses is adopted for closing equation (2).

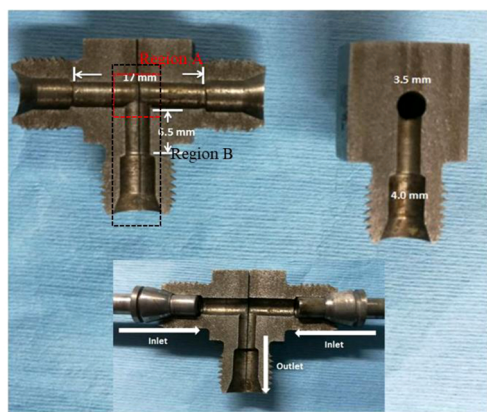
$$\tau_g = \mu ((\nabla \mathbf{u} + (\nabla \mathbf{u})^T) - \frac{2}{3} (\nabla \cdot \mathbf{u}) \mathbf{I}) \quad (3)$$

where  $\mu$  is the dynamic viscosity and  $\mathbf{I}$  is the unit tensor.

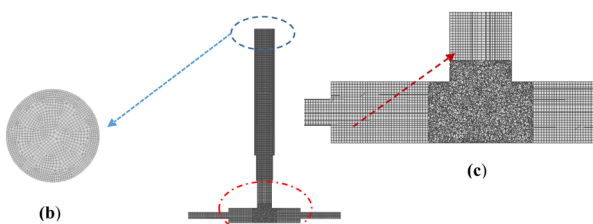
To account for the effect of turbulence, the liquid phase viscosity is expressed as

$$\mu = \mu_l + \mu_t \quad (4)$$

where  $\mu_l$  is the liquid phase dynamic viscosity for laminar flow and  $\mu_t$  is the eddy viscosity which is modelled by a standard k-ε turbulence model as briefly discussed below.



(a)

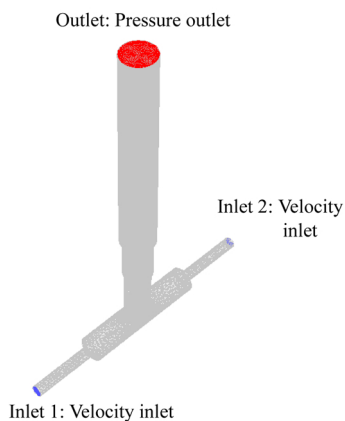


(b)

(c)



(d)



(e)

Fig. 1. The experimental rig of the impinging jet reactor and mesh setup for CFD modelling. (a) The snapshot of the impinging jet reactor internal structure; (b) Grid setup of the cross section of the vertical channel of the reactor outlet; (c) Grid setup of the cutting plane of the impinging jet reactor; (d) Grid setup of cross sectional cutting plane of the impinging jet reactor at the level of the impinging stream centre; (e) Computational domain with boundary conditions.

2.4. Standard  $k-\epsilon$  turbulence model

In order to evaluate the eddy viscosity of liquid phase  $\mu_t$  in Equation (4), the standard  $k-\epsilon$  turbulence model has been used in the CFD modelling in this study. The turbulence kinetic energy  $k$  and its dissipation rate  $\epsilon$  in the CIJR are estimated by Equations (6) and (7), respectively. The eddy viscosity is then estimated in terms of  $k$  and  $\epsilon$  using equation (5)

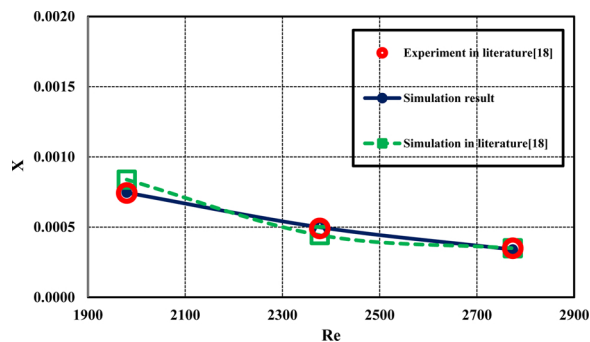


Fig. 2. Validation of the model conducted through predicting  $X$  at different Reynolds number [18].

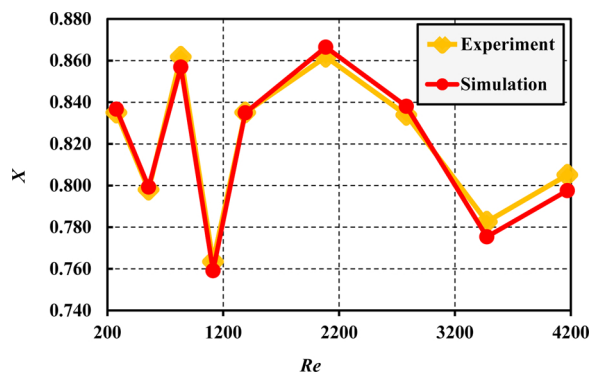


Fig. 3. Comparison between experimental and predicted  $X$  at the outlet of the reactor.

Table 1

Experimental and simulation results at different cases.

Re	Experimental results (X)	Simulation results (X)	Errors	$k_s$	Damkohler number (volume average)
278.059	0.835	0.837	0.204%	10	0.119
556.119	0.798	0.799	0.159%	13.5	0.135
834.016	0.862	0.857	0.572%	30	0.070
1112.076	0.763	0.759	0.564%	20	0.128
1390.135	0.835	0.835	0.019%	40	0.065
2085.203	0.862	0.866	0.541%	76.5	0.037
2780.271	0.834	0.838	0.495%	80	0.038
3475.338	0.783	0.775	0.921%	66	0.049
4170.406	0.805	0.798	0.934%	90	0.035

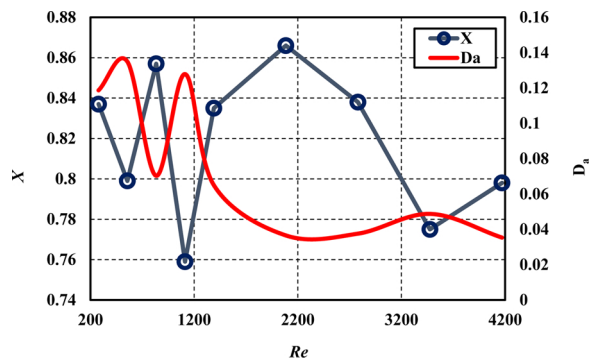


Fig. 4. Variation of Damköhler number with the Reynolds number and predicted  $X$  at the impinging zone of the impinging jet reactor.

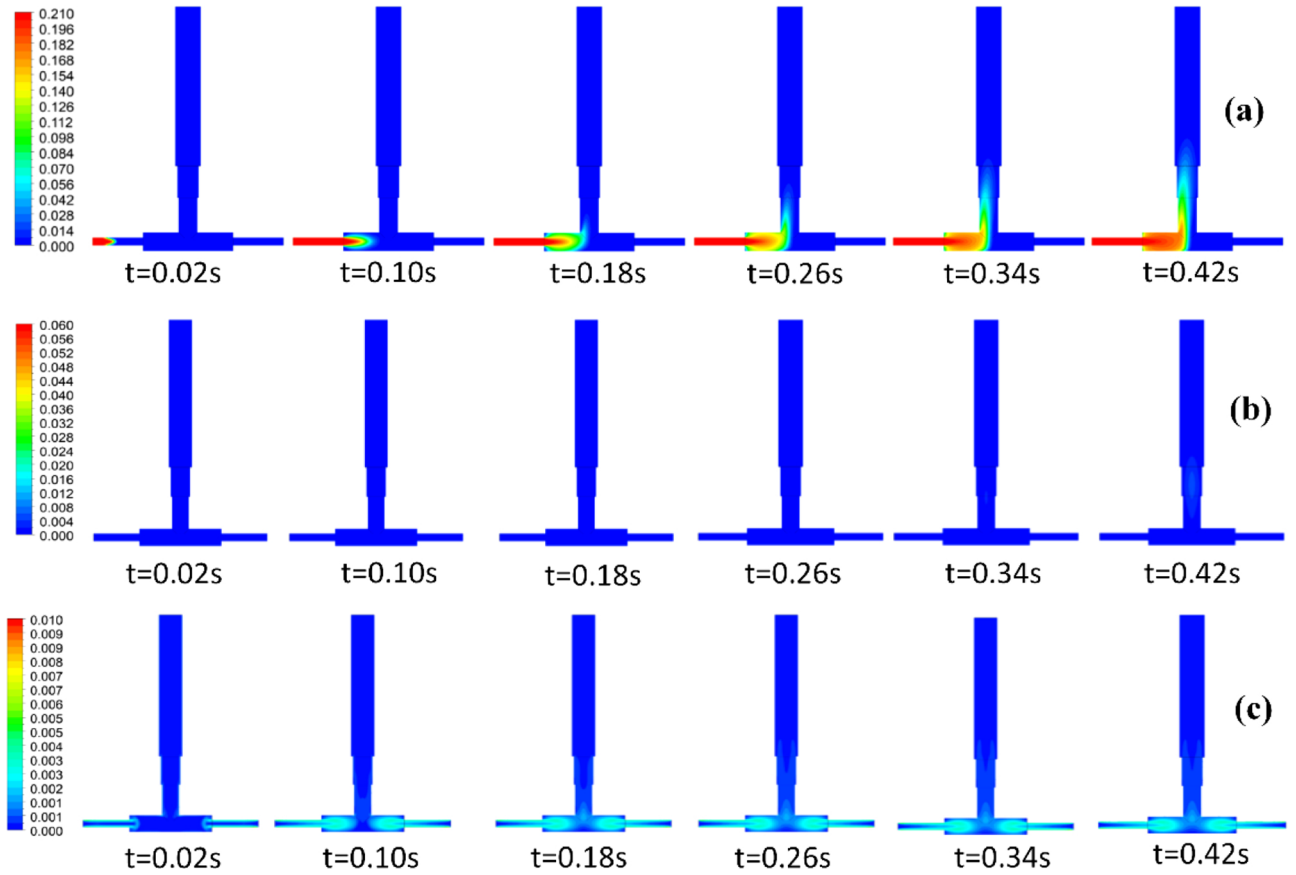


Fig. 5. Time evolution of the concentrations of (a)  $\text{FeNO}_3$  and (b)  $\text{FePO}_4$ ; and (c) Turbulent kinetic energy in the cutting plane (x-y) of the impinging jet reactor at Reynolds number  $\text{Re} = 278$ .

$$\mu_t = \frac{C_\mu \rho k^2}{\varepsilon} \quad (5)$$

$$\frac{\partial}{\partial t}(\rho k) + \nabla \cdot (\rho u k) = \nabla \cdot \left( \frac{\mu_t}{\sigma_k} \nabla k \right) + G_k - \rho_g \varepsilon \quad (6)$$

$$\frac{\partial}{\partial t}(\rho \varepsilon) + \nabla \cdot (\rho u \varepsilon) = \nabla \cdot \left( \frac{\mu_t}{\sigma_\varepsilon} \nabla \varepsilon \right) + \frac{\varepsilon}{k} [C_1 G_k - C_2 \rho \varepsilon] \quad (7)$$

$$G_k = \mu_t (\nabla u + (\nabla u)^T) : \nabla u \quad (8)$$

$G_k$  is the generation of turbulent kinetic energy in equation (8). The constants involved in Equations (5)–(8) are:  $C_\mu = 0.09$ ,  $C_1 = 1.44$ ,  $C_2 = 1.91$ ,  $\sigma_k = 1.0$  and  $\sigma_\varepsilon = 1.0$  [18]. We cautiously note here that as the local turbulence dissipation rate in the CIJR strongly affects the local shear and local micro-mixing, the estimation of turbulence dissipation rate becomes crucial. Compared with the other turbulence model, k- $\varepsilon$  turbulence model has the feature of being reliable and simple for application. For CIJR, the typical length scale of turbulence can be well defined.

## 2.5. Species transport

The synthesis of  $\text{LiFePO}_4$  particles can be described by the transport of species, which is given by

$$\frac{\partial}{\partial t}(\rho Y_p) + \nabla \cdot (\rho u Y_p) = -\nabla \cdot (\mathbf{J}_p) + R_{he} \quad (9)$$

where  $Y_p$  denotes the mass fraction of species  $p$ ,  $\mathbf{J}_p$  for the diffusive mass flux and  $R_{he}$   $R_{he}$  for the reaction rate.  $\mathbf{J}_p$  can be expressed as:

$$\mathbf{J}_p = -\left( \rho D_m + \frac{\mu_t}{Sc_t} \right) \nabla Y_i \quad (10)$$

where  $D_m$   $D_m$  is the diffusion coefficient for species  $p$  in the mixture.  $Sc_t$  is the turbulent Schmidt number with the value in the range of 0.7–1.0 and it is estimated by

$$Sc_t = \frac{\mu_t}{\rho_g D_t} \quad (11)$$

where  $D_t$  is the turbulent diffusivity. In the present study, the joint-composition Probability Density Function (PDF) is solved by a presumed PDF method ‘Direct Quadrature Method of Moments-Interaction by Exchange with the Mean Model’ (DAMOM-IEM) to close equation (9) [21].

The DQMON-IEM employs the summation of multidimensional  $N_e$  delta functions to represent the joint-composition PDF as expressed in equation (12)[18].

$$f_\varphi(\psi; x, t) = \sum_{n=1}^{N_e} p_n(x, t) \prod_{a=1}^N \delta[\psi_a - \varphi_{a,n}] \quad (12)$$

where  $p_n$  represents the probability in each  $N_e$  delta function (or mode).  $\varphi_{a,n}$  denotes the conditional mean composition of  $a$  in the  $n^{\text{th}}$  mode while  $\psi_a$  for the composition space variable of species  $a$ .  $\delta$  is the delta function.

## 2.6. Experimental description

Fig. 1a represents the meshed geometry. The dimensions of the reactor are also indicated in the figure. In order to interpret the results more clearly, Regions A and B which are highlighted by red and black dash lines are named as impinging core and impinging region. In the

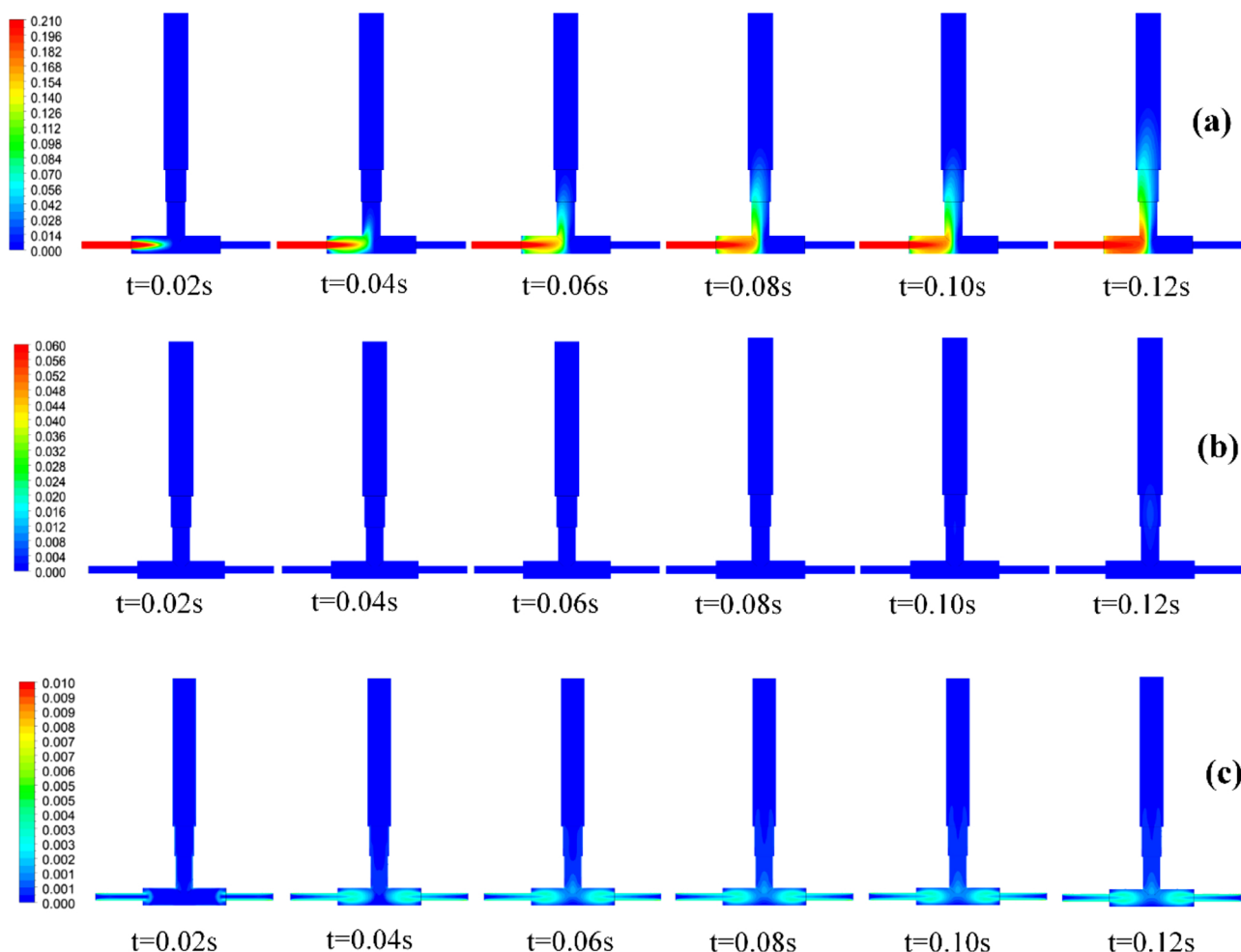


Fig. 6. Time evolution of the concentrations of (a)  $\text{FeNO}_3$  and (b)  $\text{FePO}_4$ ; and (c) Turbulent kinetic energy in the cutting plane (x-y) of the impinging jet reactor at Reynolds number  $Re = 1390$ .

experiment,  $\text{Fe}(\text{NO}_3)_3$  and  $(\text{NH}_4)_2\text{HPO}_4$  solutions were, respectively, pumped into two inlets, marked as Streams A and B. The main chemical reaction involved in the impinging stream reactor can be described by equation (15). It should be noticed that side reactions exist during the synthesis of  $\text{FePO}_4$ , whose reaction rates are quite low compared with the synthesis reaction. For simplicity, the side reactions were ignored. Equation (16) is employed to model the chemical kinetics as defined by equation (15).

In the preparation of the materials for the experiment, 408.1 g  $\text{Fe}(\text{NO}_3)_3 \cdot 9\text{H}_2\text{O}$  (Sinopharm Chemical Reagent Co., Ltd, 99%) was dissolved in DI water, and the volume of mixed solution contained  $\text{Fe}(\text{NO}_3)_3 \cdot 9\text{H}_2\text{O}$  and DI water was adjusted to 1.0 L. As the molar weight of  $\text{Fe}(\text{NO}_3)_3 \cdot 9\text{H}_2\text{O}$  is 404.0 g/mol, the concentration of  $\text{Fe}(\text{NO}_3)_3$  solution is:

$$C_{\text{Fe}(\text{NO}_3)_3} = \frac{408.1 \text{ g} \times 99\%}{404 \text{ g/mol} \times 1.0 \text{ L}} = 1.0 \text{ mol/L} \quad (13)$$

Similarly, 133.4 g  $(\text{NH}_4)_2\text{HPO}_4$  (Sinopharm Chemical Reagent Co., Ltd, 99%) was dissolved in DI water, and adjusted the total solution volume to 1.0 L by adding DI water. As the molar weight of  $(\text{NH}_4)_2\text{HPO}_4$  is 132 g/mol, the concentration of  $(\text{NH}_4)_2\text{HPO}_4$  solution is:

$$C_{(\text{NH}_4)_2\text{PO}_4} = \frac{133.4 \text{ g} \times 99\%}{132 \text{ g/mol} \times 1.0 \text{ L}} = 1.0 \text{ mol/L} \quad (14)$$

The atom ratios between Fe ion and P ion (nFe/nP) of synthesized  $\text{FePO}_4$  product prepared via impinging jet reactor, and the concentration of  $\text{Fe}^{3+}$  and  $\text{PO}_4^{3-}$  at the outlet are measured by plasma mass

spectrometry (ICP-MS). Based on the measurement results, the nFe/nP is 0.997, indicating that  $\text{FePO}_4$  sample prepared in this work has high purity. Therefore, the side reaction can be disregarded accordingly. The details of experimental setup and reaction mechanism have been reported in Dong et al. [22]. The suspension density of the aqueous solution after reaction was measured to be  $1144.4 \text{ kg/m}^3$  with a viscosity of  $0.001005 \text{ Pa}\cdot\text{s}$ .



$$R_{\text{he}} = k_s [\text{Fe}^{3+}] [\text{PO}_4^{3-}] \quad (16)$$

where  $R_{\text{he}}$  denotes the reaction rate, while  $k_s$  for the reaction rate constant of Equation (16)  $[\text{Fe}^{3+}]$  and  $[\text{PO}_4^{3-}]$  represent the molar concentration of  $\text{Fe}^{3+}$  and  $\text{PO}_4^{3-}$ , respectively.

## 2.7. Numerical Modelling

In this study, 3D CFD simulations were conducted with the same configuration and size as the experimental reactor. The mono particle loaded impinging flow is assumed to be regarded as a single-phase flow for convenience since both the mass fraction and volume fraction of  $\text{LiFePO}_4$  nanoparticles in the flow are too small to affect its properties and hydrodynamics. Fig. 1b, 1c and 1d presents the grid imposed in the simulation for the impinging reactor. A grid independence check with different mesh numbers was conducted and a model consisting of 0.6 million mesh cells was eventually selected. Velocity inlet and pressure outlet boundary conditions were applied to the inlets and outlet, where

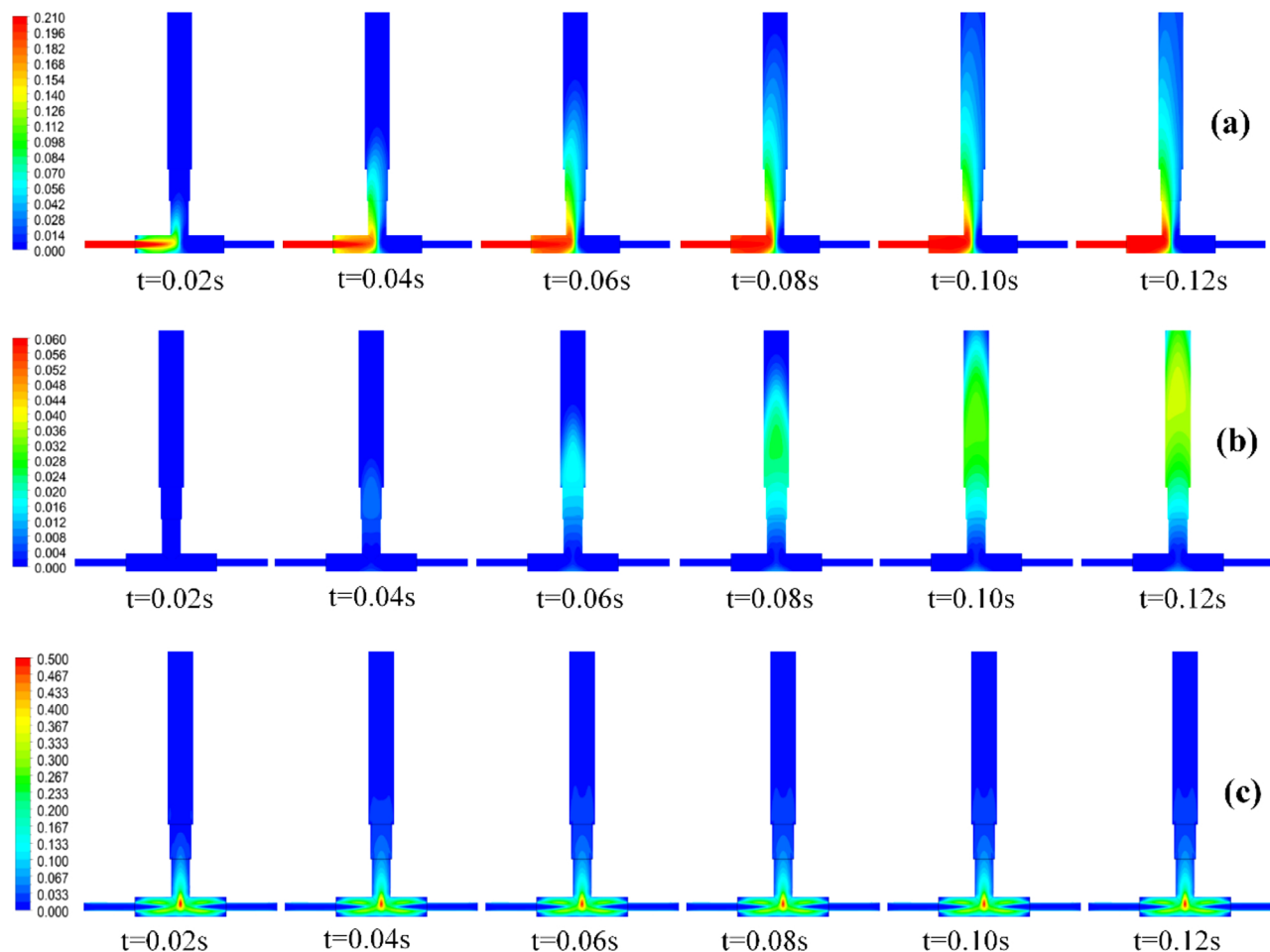


Fig. 7. Time evolution of the concentrations of (a)  $\text{FeNO}_3$  and (b)  $\text{FePO}_4$ ; and (c) Turbulent kinetic energy in the cutting plane (x-y) of the impinging jet reactor at Reynolds number  $\text{Re} = 3475$ .

Streams A and B were introduced from two inlets, respectively. The mass fraction of  $\text{FePO}_4$  was measured at the outlet to determine the value of  $X$ . The inlet velocities of Streams A and B varied in the range of 0.16 to 2.44 m/s with the corresponding inlet Reynolds number from 278 to 4175. The inlet Reynolds number is calculated by  $\frac{\rho_{\text{inlet}} d_{\text{inlet}}}{\mu}$  with the diameter of the inlet port as the characteristic length. No slip wall boundary condition was adopted on the wall of the reactor.

Transient RANS simulations were conducted using the commercial CFD software ANSYS FLUENT 17.0 in the double precision model. The reacting flow was assumed as the single-phase flow of an incompressible fluid. The second order scheme was employed for calculation of those convective terms while the pressure-velocity coupling was achieved by PRESTO scheme. The time step employed in the simulations was set 0.0002 s.

### 3. RESULTS AND DISCUSSION

The study of Liu et al. [18] was used as a benchmark to validate the CFD modelling. The Villermaux-Dushman parallel competing reaction system in the impinging stream reactor was modelled by CFD simulations based on the models described in Section 2. The predictions of the segregation index  $X_s$  at different Reynolds numbers are shown in Fig. 2. It is clear that compared to the experimental results as reported in the literature the CFD modelling conducted in this study is well to predict the reaction kinetics with a maximum error of 2.7%.

#### 3.1. Effects of local turbulent kinetic energy and dissipation rate distribution on the reaction kinetics

A factor  $X$  which represents the ratio of the actual production of  $\text{FePO}_4$  to the theoretical one is defined to indicate the completeness of synthesis reaction, given by equation (17):

$$X = \frac{m_{\text{FePO}_4}}{m_{\text{FePO}_4,0}} \quad (17)$$

The value of  $X$  measures the completeness of the synthesis of  $\text{FePO}_4$  with  $0 < X < 1$ .  $m_{\text{FePO}_4}$  and  $m_{\text{FePO}_4,0}$  are the actual mass concentration and theoretical mass concentration of  $\text{FePO}_4$  at the outlet.  $X = 1.0$  indicates that the production of  $\text{FePO}_4$  reaches theoretical upper limit. The experimental observations and results have illustrated that the reaction rate can be affected by many factors such as the micro-mixing time, turbulent intensity in the reactor, velocities of the feeding streams plus side reactions. Fig. 3 shows the comparisons of the experimental and numerical simulation results of factor  $X$  at the outlet. It can be seen from Fig. 3 that reasonable predictions have been achieved for  $X$  with an appropriate coefficient  $k_s$  as listed in Table 1. The simulation results have a maximum deviation smaller than 1% as compared with the experimental results. In order to characterise the interaction between the synthesis reaction kinetics and turbulence generated in the reactor, Damköhler number is introduced as defined by

$$D_a = \frac{\tau_t}{\tau_c} = \frac{12 \sqrt{\frac{\nu}{\varepsilon}}}{c} \quad (18)$$

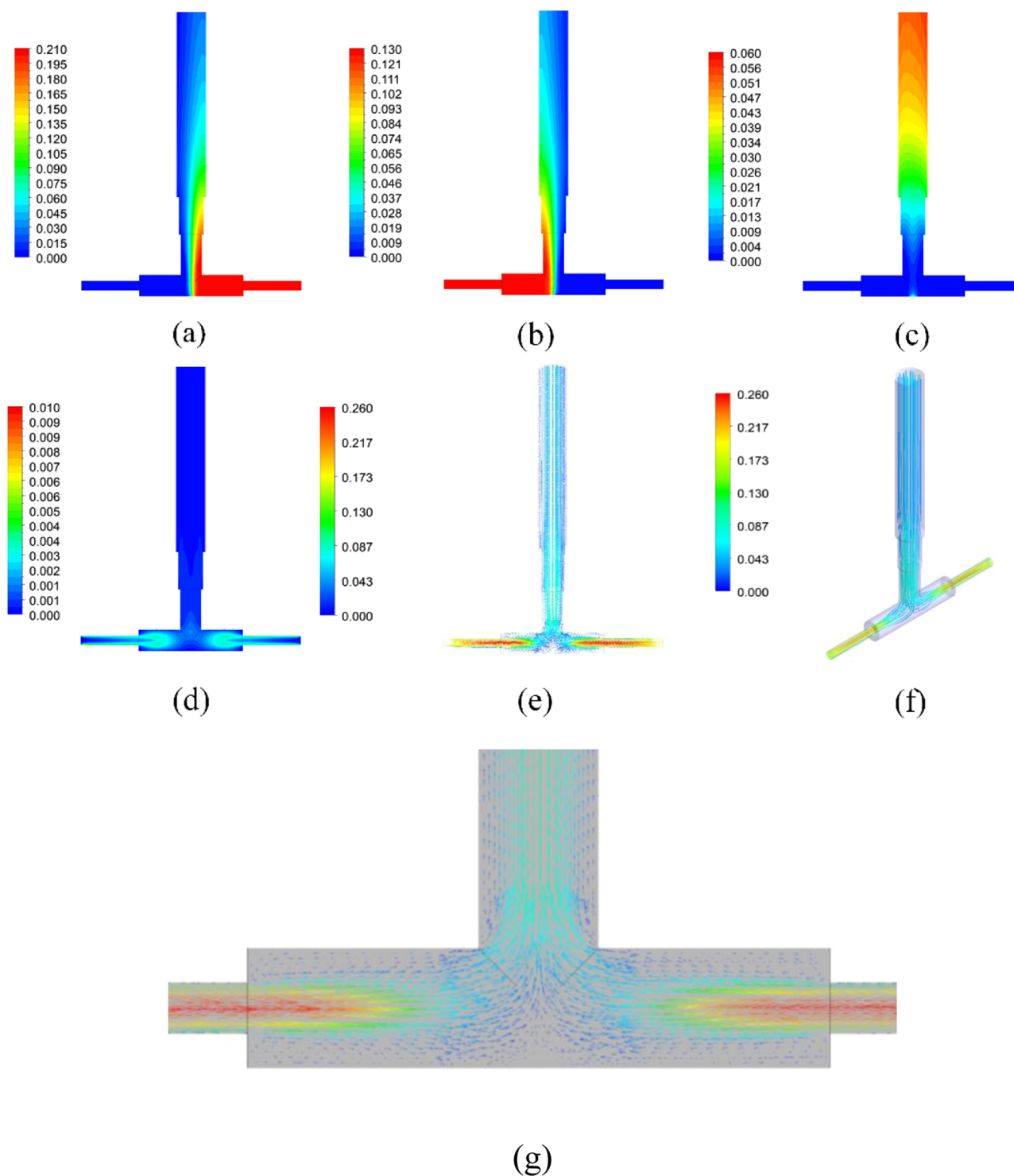


**Fig. 8.** The contours of predicted mass fractions of the reactants and products. (a) Mass fraction of FeNO<sub>3</sub>; (b) Mass fraction of NH<sub>4</sub>HPO<sub>4</sub>; and (c) Mass fraction of FePO<sub>4</sub>. The contours of prediction for (d) Turbulent kinetic energy; (e) Velocity vector; (f) Velocity Streamline and (g) Magnified velocity vector at the impinging centre on the cutting plane (x-y) at Reynolds number  $Re = 278$ .

where  $D_a$  is the Damköhler number,  $\varepsilon$  is the turbulent dissipation rate and  $C$  the molar concentration of the product. The stretching process of the turbulent eddies is strongly related to the incorporation or engulfment of the reactants into the turbulent eddies. Following Baldyga et al. [18], it has been assumed the characteristic time scale for micro-mixing by such eddy engulfment can be estimated based on  $\tau_i \cong 12 \sqrt{\frac{\nu}{\varepsilon}}$ .

Fig. 4 shows the variations of  $D_a$  and  $X$  against different Reynolds numbers. It can be seen from the figure that the trend of variation of

volume-averaged Damköhler number in the impinging reactor is totally opposite to that of  $X$ . A decrease in  $D_a$  indicates an enhanced effect of diffusive mass transport rate caused by turbulent mixing on the synthesis reaction kinetics. Thus, it can be extrapolated that the overall performance of the synthesis reaction will significantly affected by the turbulence generated due to the impinging streams. It also indicates that micro-mixing have significant effects on the selectivity and quality of the final products.

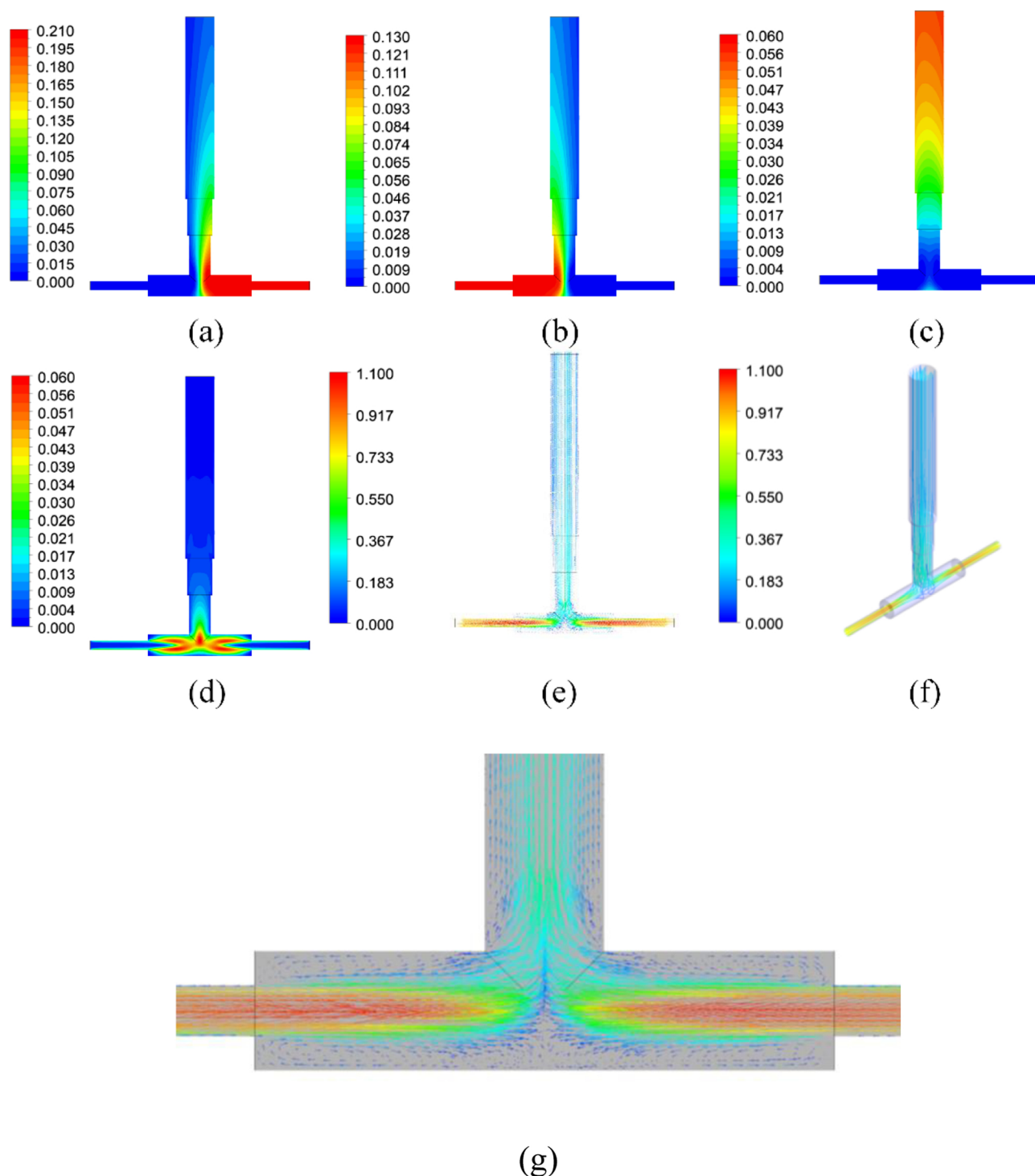


**Fig. 9.** The contours of predicted mass fractions of the reactants and products. (a) Mass fraction of  $\text{FeNO}_3$ ; (b) Mass fraction of  $\text{NH}_4\text{HPO}_4$ ; and (c) Mass fraction of  $\text{FePO}_4$ . The contours of prediction for (d) Turbulent kinetic energy; (e) Velocity vector; (f) Velocity Streamline and (g) Magnified velocity vector at the impinging centre on the cutting plane (x-y) at Reynolds number  $\text{Re} = 1390$ .

### 3.2. Qualitative descriptions of $\text{FePO}_4$ synthesis kinetics under the condition of different Reynolds numbers

Figs. 5–7 show the time evolution of the mass fraction of  $\text{Fe}(\text{NO}_3)_3$  and  $\text{FePO}_4$  and turbulent kinetic energy obtained on the x-y cross section plane at three different Reynolds numbers,  $\text{Re} = 278$ , 1390 and 3475. Their contours at pseudo-steady state are plotted in Figs. 8–10. It can be seen from Figs. 5–7, the product  $\text{FePO}_4$  is firstly generated in the region just below the impingement centre and then extended to the

region with ‘V’ shape above the impingement zone rather than the region where two incoming streams impinge against each other with the highest turbulent kinetic energy. One likely reason is that the intensive turbulent mixing immediately transport the reaction species downstream. In addition to the impinging centre, high turbulent kinetic energy was also observed to take place surrounding the walls of the enlargement section of the horizontal channel. Four eddies can be seen clearly near the walls of horizontal channel in the reactor centre zone as shown in Figs. 8g, 9 g and 10 g. The formation of ‘V’ shape region

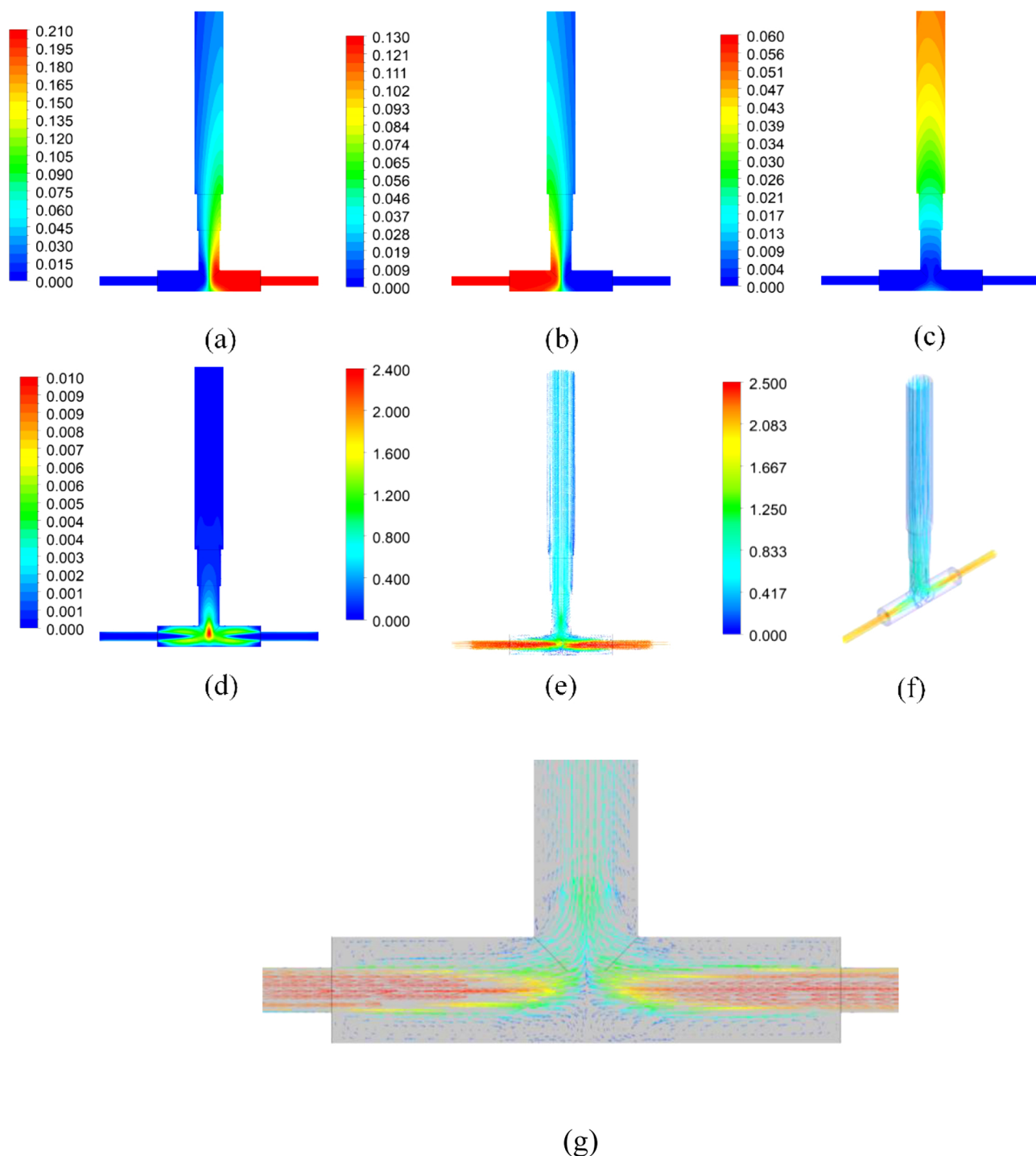


**Fig. 10.** The contours of predicted mass fractions of the reactants and products. (a) Mass fraction of  $\text{FeNO}_3$ ; (b) Mass fraction of  $\text{NH}_4\text{HPO}_4$ ; and (c) Mass fraction of  $\text{FePO}_4$ . The contours of prediction for (d) Turbulent kinetic energy; (e) Velocity vector; (f) Velocity Streamline and (g) Magnified velocity vector at the impinging centre on the cutting plane (x-y) at Reynolds number  $\text{Re} = 3475$ .

results from the interactions of two eddies near the upper wall region of the horizontal channel where sufficient reaction between  $\text{Fe}(\text{NO}_3)_3$  and  $\text{NH}_4(\text{HPO}_4)_2$  occurs as evidenced by existence of high  $\text{FePO}_4$  mass fraction. By comparing the contours of turbulent kinetic energy and the mass fraction of  $\text{FePO}_4$  as shown in Figs. 8–10, it can be found that the size of ‘V’ shape region depends much on the strength of the corresponding eddies. The strength of these eddies is also affected by the impinging streams which is characterised by the Reynolds number based on the length scale of the inlet tubes of the reactor. It is interestingly noted that as can be seen from Figs. 8d, Fig.9d and Fig.10d, the

relative turbulent kinetic energy carried by these eddies decreases with the increase of Reynolds number when comparing the relative turbulence strength in the impinging centre.

### 3.3. Effect of turbulence generated by impinging jets on the synthesis

As discussed in the previous section, the impinging centre and the downward flowing channel are the most important regions that have dominated the synthesis kinetics of  $\text{FePO}_4$  where the turbulence strength due to the collision of two impinging streams is found to be

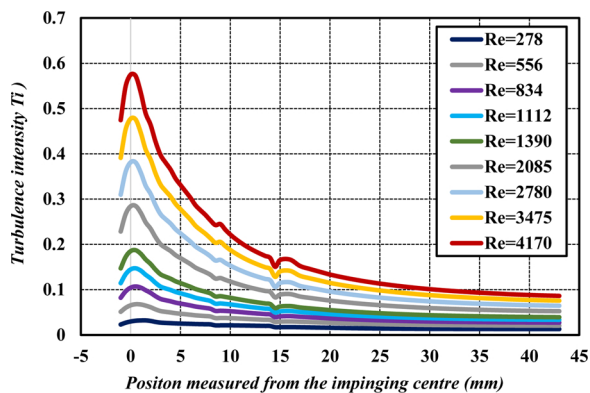


Fig. 11. The cross-sectional area-averaged turbulence intensity variation along the vertical channel of the impinging jet reactor.

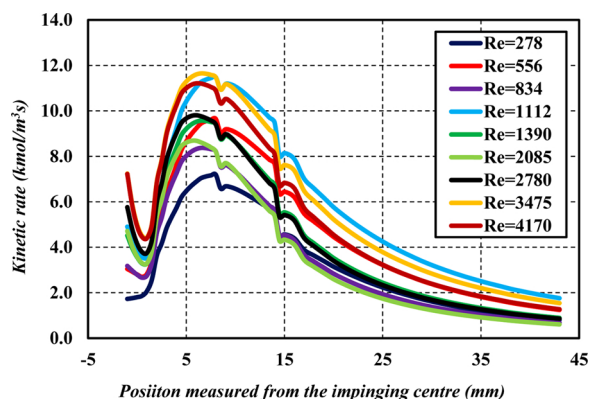


Fig. 12. The cross-sectional area-averaged synthesis reaction rate along the vertical channel of the impinging jet reactor.

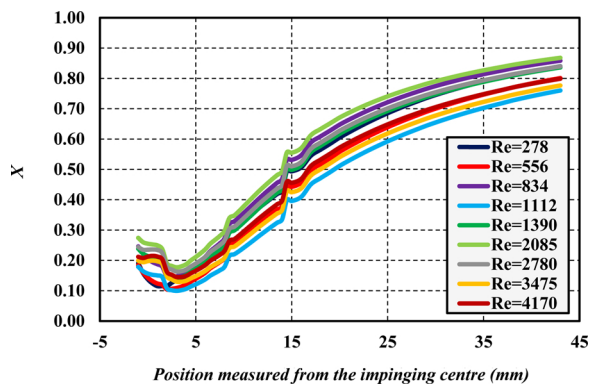


Fig. 13. The cross-sectional area-averaged synthesis reaction completeness  $X$  along the vertical channel of the reactor in the impinging region.

much higher than the other regions. It has been manifested that the turbulence has significantly affected the synthesis reaction. Fig. 11 shows the area-averaged turbulence intensity at different cross-sections along the downward flowing channel of the reactor. The turbulence intensity is the normalised turbulent velocity fluctuations defined by

$$T_i(t) = \frac{1}{\frac{\pi}{4}d_E^2} \int_0^{RE} \sqrt{\frac{2x}{3}} 2\pi r dr \quad (19)$$

where  $T_i$  is the cross-sectional area-averaged turbulence intensity.

It can be seen clearly from Fig. 11 that the turbulence intensity increases with increase in Re but it decreases along with the downward stream towards the outlet. However, it is noticed that compared with surrounding regions, the impinging centre has lower reaction rate as

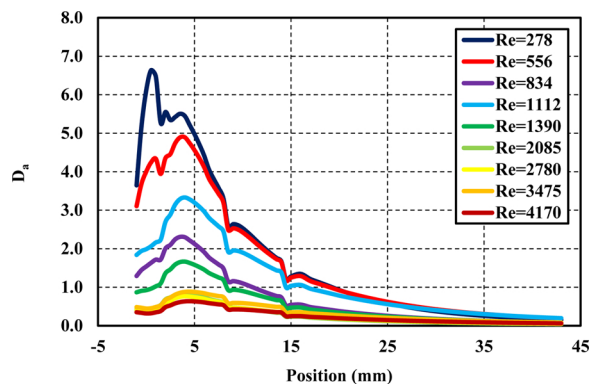


Fig. 14. The cross-sectional area-averaged Damköhler number variation along the vertical channel of the impinging jet reactor.

can be seen from Fig. 12. This may be attributed to the strong turbulence transport which results in the reaction between two impinging reactant streams to take place slightly downstream of the impinging centre. By contrasting Figs. 11 and 12, it can be extrapolated that the turbulence due to the impingement provides an environment that is very rich in the mixture of the reactants in the region just below the impinging centre where the highest reaction rate in the reactor is achieved. Although a great reaction rate occurs along for the condition of a large Re as shown in Fig. 12, it doesn't imply that a good reaction performance has been obtained. Fig. 13 shows the reaction performance, characterised by parameter  $X$ , along the downward flowing channel. It is noted that the largest  $X$  in the reactor occurs at Re = 2085 other than 4750, especially in the impinging centre region. The possible reason is that the reaction performance is determined by both the reaction rate and the mixture residence time. For case of Re = 4750, the turbulence transports so quickly that the residence time is not long enough for those turbulent eddies that carry the reactant mixtures to complete the reaction in the reactor. By contrasting Figs. 12 and 13, it is found that a high  $X$  with low reaction rate takes place in the lower portion of the downward flowing channel, resulted from the accumulation of  $\text{FePO}_4$  from the upper portion of the reactor. Fig. 14 presents the area-averaged Damköhler number along the downward flowing channel in impinging region at different Re. The highest value is observed in the impinging centre region for case of Re = 278 and  $Da$  gradually decreases with the increase in Re. This is clearly indicated that high turbulent strength can be beneficial to the synthesis reaction process. The effect of sudden expansion of the downstream flowing channel of the impinging stream reactor on both turbulence generation and chemical kinetics of synthesis can also be observed as “steeper” and sudden changes in the gradients of the plots in Figs. 12–14.

#### 4. CONCLUSIONS

The effects of the local turbulence due to the impinging streams on the reaction kinetics of  $\text{LiFePO}_4$  synthesis in an impinging jet reactor have been studied. Compared with the experimental results, it has been demonstrated that the CFD modelling is able to provide reasonable predictions on the synthesis reaction kinetics of  $\text{LiFePO}_4$ . Damköhler number was employed to characterise the correlation between reaction kinetics and the local turbulence behaviour. The conclusions reached as the results of the current study are as follows:

- 1 Higher turbulent kinetic energy in the impinging core, corresponding to a higher feeding flux, i.e a larger Re, can effectively promote the mixing of reactant streams in the reactor. Consequently, the reaction kinetic rate in the region just below the impinging core is remarkably enhanced.
- 2 The CFD simulation results suggest that to control the feeding

reactant stream flux with a moderate range of Re can improve the synthesis reaction as too higher turbulent kinetic energy or turbulent dissipation rate in the impinging core may reduce the residence time of the mixing of two reactant streams, leading to a lower reaction completeness.

- 3 The correlation obtained for Damköhler number against the reaction completeness at different Reynolds numbers clearly indicates that the synthesis performance is significantly controlled by the local turbulent kinetic energy and turbulent dissipation rate distribution in the reactor.

#### Declaration of Competing Interest

None.

#### CRediT authorship contribution statement

**Luming Chen:** Investigation, Formal analysis, Software, Writing - original draft. **Bing Dong:** Data curation, Investigation. **Yanqing Guo:** Data curation. **Xiaogang Yang:** Conceptualization, Methodology, Investigation, Supervision, Writing - review & editing. **Guang Li:** Investigation, Validation.

#### Acknowledgement

The authors wish to thank the support from National Natural Science Foundation of China (NSFC) (Grant Nos. 21576141, 91534118, 21908195).

#### References

- [1] H. Hu, Z. Chen, Z. Jiao, Characterization of micro-mixing in a novel impinging streams reactor, *Frontiers of Chemical Engineering in China* 3 (2009) 58–64.
- [2] I. Valente, E. Celasco, D.L. Marchisio, A.A. Barresi, Nanoprecipitation in confined impinging jets mixers: Production, characterization and scale-up of pegylated nanospheres and nanocapsules for pharmaceutical use, *Chemical Engineering Science* 77 (2012) 217–227.
- [3] G. Wu, H. Zhou, S. Zhu, Precipitation of barium sulfate nanoparticles via impinging streams, *Materials Letters* 61 (2007) 168–170.
- [4] Y. Dong, W.K. Ng, S. Shen, S. Kim, R.B. Tan, Controlled antisolvent precipitation of spironolactone nanoparticles by impingement mixing, *International journal of pharmaceuticals* 410 (2011) 175–179.
- [5] S. Bhattacharya, S.M. Kresta, Surface Feed with Minimum by-Product Formation for Competitive Reactions, *Chemical Engineering Research and Design* 82 (2004) 1153–1160.
- [6] S.W. Siddiqui, Y. Zhao, A. Kukukova, S.M. Kresta, Characteristics of a Confined Impinging Jet Reactor Energy Dissipation, Homogeneous and Heterogeneous Reaction Products, and Effect of Unequal Flow, *Ind. Eng. Chem. Res.* 48 (2009) 7945–7958.
- [7] H.-C. Schwarzer, W. Peukert, Combined experimental/numerical study on the precipitation of nanoparticles, *AIChE Journal* 50 (2004) 3234–3247.
- [8] D.L. Marchisio, L. Rivautella, A.A. Barresi, Design and scale-up of chemical reactors for nanoparticle precipitation, *AIChE Journal* 52 (2006) 1877–1887.
- [9] N. Kockmann, T. Kiefer, M. Engler, P. Woias, Convective mixing and chemical reactions in microchannels with high flow rates, *Sensors and Actuators B: Chemical* 117 (2006) 495–508.
- [10] F. Schwertfirm, J. Gradl, H.C. Schwarzer, W. Peukert, M. Manhart, The low Reynolds number turbulent flow and mixing in a confined impinging jet reactor, *International Journal of Heat and Fluid Flow* 28 (2007) 1429–1442.
- [11] M. Jiang, Y.-E.D. Li, H.-H. Tung, R.D. Braatz, Effect of jet velocity on crystal size distribution from antisolvent and cooling crystallizations in a dual impinging jet mixer, *Chemical Engineering and Processing: Process Intensification* 97 (2015) 242–247.
- [12] T. Tari, Z. Fekete, P. Szabo-Revesz, Z. Aigner, Reduction of glycine particle size by impinging jet crystallization, *International journal of pharmaceuticals* 478 (2015) 96–102.
- [13] K.S. Park, J.T. Son, H.T. Chung, S.J. Kim, C.H. Lee, H.G. Kim, Synthesis of LiFePO<sub>4</sub> by co-precipitation and microwave heating, *Electrochemistry Communications* 5 (2003) 839–842.
- [14] Y. Ding, Y. Jiang, F. Xu, J. Yin, H. Ren, Q. Zhuo, Z. Long, P. Zhang, Preparation of nano-structured LiFePO<sub>4</sub>/graphene composites by co-precipitation method, *Electrochemistry Communications* 12 (2010) 10–13.
- [15] J. Baldyga, J.R. Bourne, S.J. Hearn, Interaction between chemical reactions and mixing on various scales, *Chem. Eng. Sci.* 52 (1997) 457–466.
- [16] A. Tamir, *Impinging-Stream Reactors Fundamentals and Applications*, Elsevier Science B.V., Netherlands, 1994.
- [17] T. Panagiotou, S.V. Mesite, R.J. Fisher, Production of Norfloxacin Nanosuspensions Using Microfluidics Reaction Technology through Solvent/Antisolvent Crystallization, *Industrial & Engineering Chemistry Research* 48 (2009) 1761–1771.
- [18] Z. Liu, L. Guo, T. Huang, L. Wen, J. Chen, Experimental and CFD studies on the intensified micromixing performance of micro-impinging stream reactors built from commercial T-junctions, *Chemical Engineering Science* 119 (2014) 124–133.
- [19] Y. Liu, R.O. Fox, CFD predictions for chemical processing in a confined impinging-jets reactor, *AIChE Journal* 52 (2006) 731–744.
- [20] X.Y. Woo, R. Tan, R.D. Braatz, Modelling and Computational Fluid Dynamics-Population Balance Equation-Micromixing Simulation of Impinging Jet Crystallizers, *Crystal growth and design* 9 (2009) 156–164.
- [21] E. Gavi, D.L. Marchisio, A.A. Barresi, CFD modelling and scale-up of Confined Impinging Jet Reactors, *Chemical Engineering Science* 62 (2007) 2228–2241.
- [22] B. Dong, G. Li, X. Yang, L. Chen, G.Z. Chen, Controllable synthesis of (NH<sub>4</sub>)<sub>2</sub>Fe<sub>2</sub>(PO<sub>4</sub>)<sub>2</sub>(OH)·2H<sub>2</sub>O using two-step route: Ultrasonic-intensified impinging stream pre-treatment followed by hydrothermal treatment, *Ultrasonics Sonochemistry* 42 (2018) 452–463.



# Effect of ultrasonic intensification on synthesis of nano-sized particles with an impinging jet reactor

Yanqing Guo, Xiaogang Yang\*, Guang Li, Bin Dong, Luming Chen

Department of Mechanical, Materials and Manufacturing Engineering, University of Nottingham Ningbo, China

## ARTICLE INFO

### Article history:

Received 3 December 2018

Received in revised form 12 March 2019

Accepted 24 May 2019

Available online 29 May 2019

### Keywords:

Impinging jet

Ultrasound

Micromixing

Nanoparticles

Vortices

## ABSTRACT

The preparation of nanoparticles can be conducted in a fast way by intensifying the micromixing due to the enhanced turbulence in an impinging jet Reactor (IJR) where the two linear liquid jets collide with high velocity to diminish the segregation. However, the micromixing is significantly affected by the occurrence of the stagnant region which may partially choke the reaction chamber. By imposing the ultrasound to the IJR, micro-scale turbulent eddies generated as the result of collapse of ultrasonically generated micro cavitation bubbles may generate a strong local shear. Such micro-scale turbulent vortices exert shear on the interface between the particles and surrounding fluid, resulting in uniform particle morphology and high surface area for chemical reaction. The paper aims to optimize the ultrasonic intensification effect on synthesis of nano-sized particles with desired homogeneity, reveal the governing mechanisms and present a kinetic model to describe the multiphase flow dynamics in the IJR. Except for the experimental method, numerical method was also used to demonstrate the impact of fluid dynamics on particle synthesis.

© 2019 Elsevier B.V. All rights reserved.

## 1. Introduction

The mixing performance of different reacting components can be promoted by using hybrid reactor systems. Among these reactors, impinging jet reactor (IJR) provides a facile and direct way of process intensification for microscale chemical precipitation reactions and nanoparticles synthesis [1]. IJR consisted of two linear liquid jets collides with relatively high velocity each other in the impingement zone, which can achieve better micromixing performance by means of diminishing the segregation and improving mass transfer rate [2,3]. It has been reported that the use of IJR provides a homogeneous local environment for the formation of nanoparticles with high supersaturation in milliseconds or less time [4,5]. Due to the violent collision of two streams in the IJR, high dissipation of kinetic energy of the jets in a confined volume leads to local strong shear due to generation of the localized turbulent eddies. However, the mixing performance can be significantly affected by the existence of a stable separated regime and a stagnant region. Foute et al. [6] have shown that the imbalance of branch jet always have negative effects on mixing quality and the mixing efficiency in an IJR mainly depends on the scale of small eddy engulfment but not the amount of energy dissipation of the system.

Due to the particular geometry of IJR, the reaction chamber might be partially choked as a consequence of precipitation process [7]. In order to overcome this drawback and promote the mixing efficiency,

ultrasound intensification was imposed to improve the mixing performance due to strong acoustic impact as the result of micro-bubble collapse characterized by occurrence of micro-streaming, shock waves and micro-scale turbulent eddies. The maximum volume fraction of cavitation bubbles takes up to 0.016% of the total sonoreactor and micro-bubble collapse may lead to intensive local heat (~5000 K), high pressure (~1000 atm), high-speed jet streams (~400 km/h) and strong local shear [5,8,9]. Such energy transfer from acoustic streaming within the fluid at a localized scale exerts a shear force on the interface between the particles and surrounding fluid, resulting in narrower particle size distribution and high surface area for particle synthesis [10]. It has been recognized that acoustic cavitation affects nuclei growth in a liquid media under low-pressure cycles and contributes to micro-bubble collapse under high-pressure cycle, which may be responsible for mass transfer rates enhancement [9].

Most of the previous studies focus on the effect of ultrasonic energy dissipation while overlook the influence of flow dynamics caused by acoustic streaming and mixing zone [11]. In CFD modelling, this was compensated by either superposing the pressure field change or introducing a boundary vibration that is resonant to the ultrasonic field imposed. Based on the existing numerical studies on ultrasound, the acoustic streaming contributes to both the mass transfer and heat transfer improvement of reaction at low viscosity [12–14] and to the enhancement of segregation index up to 20% with low ultrasound intensity [15]. The numerical simulation initially conducted by Rayleigh and Nyborg [16] has demonstrated that the second-order nonlinear ultrasound wave propagation is responsible for acoustic streaming and

\* Corresponding author.

E-mail address: [Xiaogang.Yang@nottingham.edu.cn](mailto:Xiaogang.Yang@nottingham.edu.cn) (X. Yang).

the inertia term can be neglected in the simulation. However, Lighthill [17] argued that the elimination of the inertia term is acceptable only when the flow is in the regime of low Reynolds number ( $Re < 1$ ), known as “creeping motion”. Considering the inertial effect, Wijngaarden [18] proposed a more complex model to reproduce the transient shock waves in a bubbly mixture. Based on Wijngaarden's model, both Jamshidi et al. [19] and Lebon et al. [20] introduced acoustic cavitation into the fluid as a source term for the momentum transfer because micro-bubbles have impact on wave propagation and bulk properties. Whereas, Sajjadi et al. [9] investigated ultrasound effect in liquid bulk by introducing it as a boundary condition in terms of pressure profile change. In addition, to investigate the ultrasound effect on mass transfer coefficient, Jiao et al. [21] came up with a computational model to predict the ultrasonic enhancement on mass transfer coefficient and considered the effect of the extrinsic factors such as temperature, the transducer geometry and the distance between the transducer and ultrasound source. Xu et al. [22] also quantitatively determined the flow field in a sonochemical reactor and found that average stream velocity increased with acoustic power increment. In addition, Niazi et al. [23] have investigated the pressure and temperature distribution of liquid bulk in a sonoreactor and the collapse pressure and temperature of acoustic bubbles were predicted around 3040 bar and 3200 K.

This paper aims at investigating the intensified effects of low-frequency ultrasonic irradiation (20 kHz) on nano-sized  $\text{FePO}_4$  (FP) powder synthesis using a IJR system with the downstream sudden expansion chamber. Both experimental and computational analysis were conducted to explore the effect of ultrasound on synthesized Nano-sized FP particles that can be used as precursor contributing to  $\text{LiFePO}_4$  (LFP) cathode materials with excellent electrochemical performance for rechargeable lithium-ion batteries [24,25].

## 2. Experimental

### 2.1. Experimental setup and product characterization

The experimental setup is shown in Fig. 1. Solution A ( $1 \text{ mol L}^{-1} \text{ Fe}(\text{NO}_3)_3$ , Sinopharm Chemical Reagent Co., Ltd., 99%) and solution B ( $1 \text{ mol L}^{-1} (\text{NH}_4)_2\text{HPO}_4$ , Sinopharm Chemical Reagent Co., Ltd., 99%) were introduced into two separated inlets of the IJR by peristaltic pumps with a flow rate of  $85.74 \text{ ml min}^{-1}$ . In order to stabilize the circumstance and keep a constant pH value at 1.7, aqueous ammonia ( $1.5 \text{ mol L}^{-1}$ ) was simultaneously pumped from the third inlet with automatic pH controller. In the mixing process, the IJR system was irradiated by ultrasound with a power of 360, 480, 600, 720 and 960 W,

respectively. The mixing was also carried out in the same system without imposing ultrasound for purpose of comparison. The samples prepared under different ultrasound intensities were analyzed (herein, referred to as FP-ultrasound power). FP precipitation was washed by deionized water (DI), filtrated and dried in air at  $100^\circ \text{C}$  for 12 h. Then the sample was calcined in the air at  $600^\circ \text{C}$  for 10 h to obtain anhydrous crystalline  $\text{FePO}_4$ .

The structures of synthesized FP powder were identified by X-ray diffraction (XRD, D8 ADVANCE DAVINCI, BRUKE) with  $\text{Cu K}\alpha$  radiation source ( $\lambda = 1.5406 \text{ \AA}$ ) and the scanning angle is ranged from  $10^\circ$  to  $90^\circ$ . The morphology and microstructure were obtained using scanning electron microscope (SEM, sigma VP, ZEISS, Germany). The Brunauer-Emmett-Teller (BET) surface area was determined using ASAP 2020 (Micrometrics, U.S.A). Thermal gravimetric was conducted by thermal analyzer (TG, NETZSCH STA 449 F3 Jupiter, Germany).

### 2.2. LFP/C preparation and electrochemical properties test

The electrochemical properties of the LFP/C synthesized from prepared FP at different ultrasound power were investigated by galvanostatic method using LFP/C half-cells. Anhydrous FP samples were mixed with  $\text{Li}_2\text{CO}_3$  (Sinopharm Chemical Reagent Co., Ltd., 99%) and glucose (Sinopharm Chemical Reagent Co., Ltd., 99%) by ball-milled method of 500 rpm for 5 h. Then the mixture was calcined in nitrogen atmosphere at  $650^\circ \text{C}$  for 10 h.

Electrochemical measurements were performed using CR2032 coin-type cell assembled in an argon-filled glove box. Cathode electrodes were fabricated from the synthesized LFP/C, polyvinylidene fluoride (PVDF) binder and the acetylene black at a weight ratio of 80:10:10 and pasted on pure aluminum foil. Pure lithium foil was used as the counter electrode. The electrolyte is consisted of a solution of 1 M  $\text{LiPF}_6$  in ethylene carbonate and diethyl carbonate (EC + DMC, 1:1 volume ratio). The charge/discharge tests were carried out using a LAND Cell test CT2001A (Wuhan LAND Electronic Co.Ltd., China) between the voltage of 2.5 and 4.2 V.

### 2.3. Description on synthesis reaction

On exposing to ultrasound irradiation, sonolysis of the water is realised through sonochemical reductants such as  $\text{H}\cdot$  radicals. Furthermore, these produced radicals are added to produce secondary radical species that may promote the reduction rate [28]. In the present work,

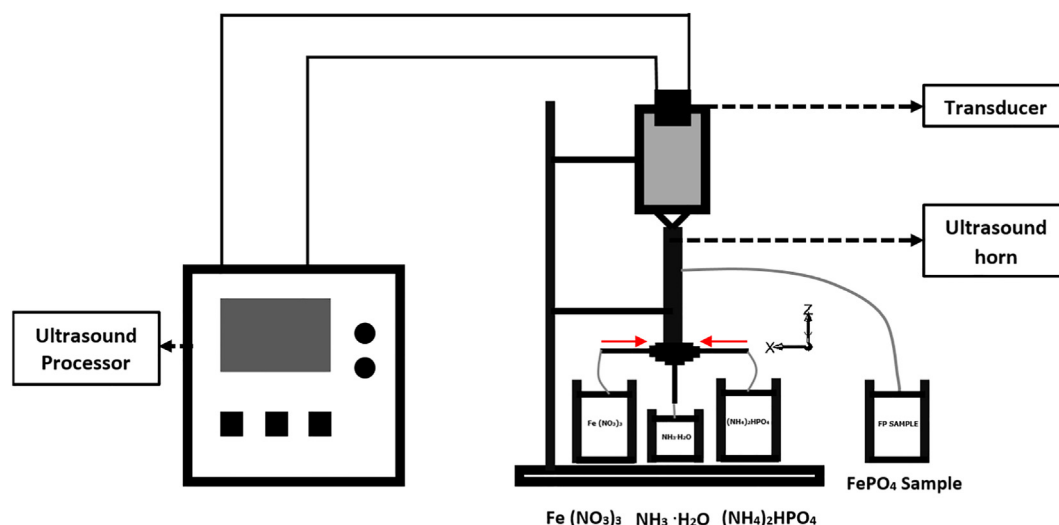


Fig. 1. Schematic diagram of the experimental setup.

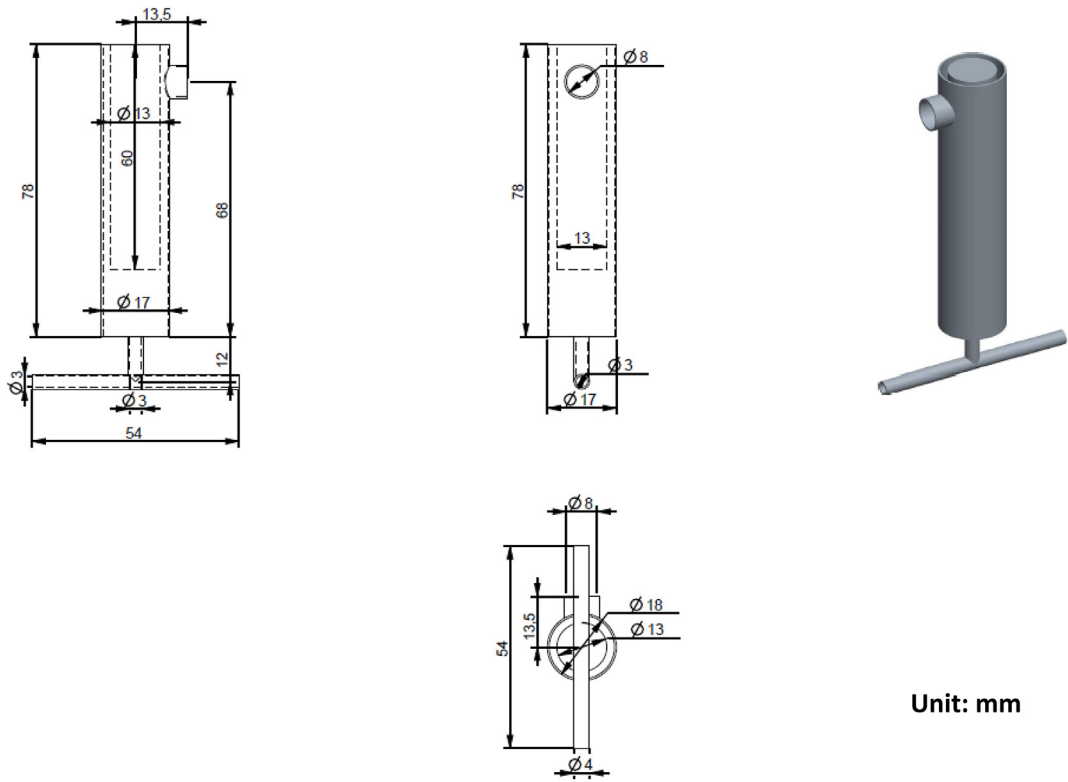


Fig. 2. Configuration of impinging jet reactor with ultrasound transducer.

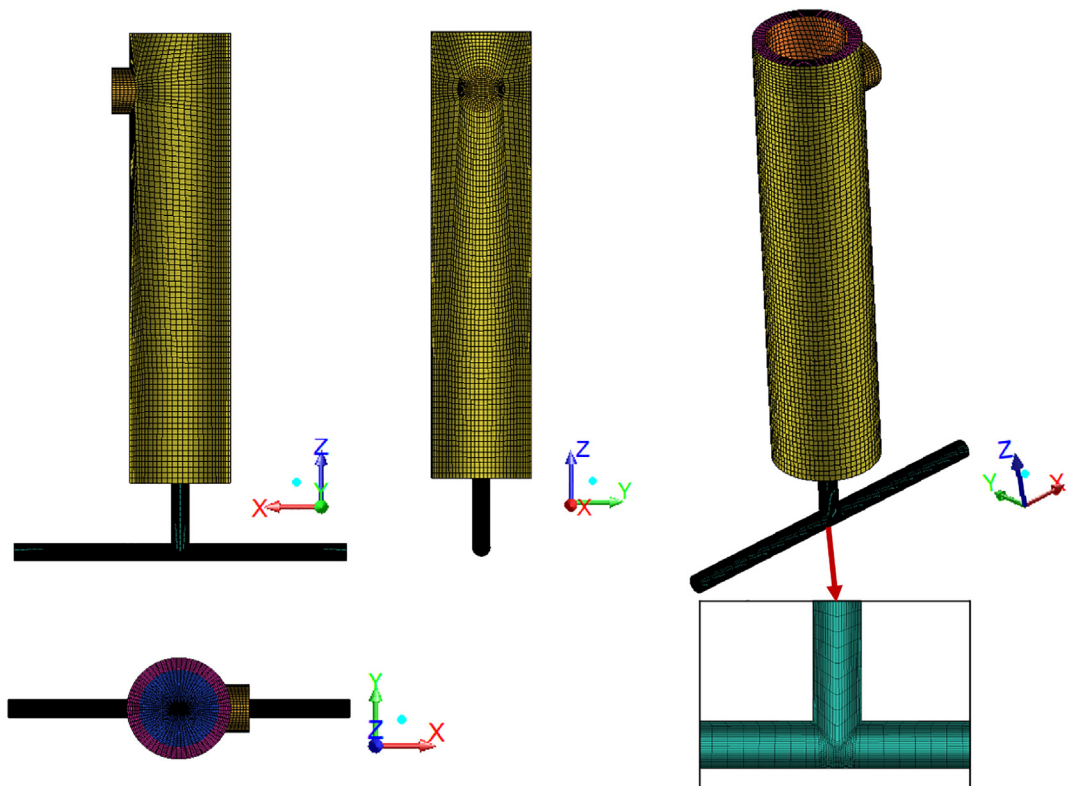


Fig. 3. 3D view of the computational domain and mesh structure.

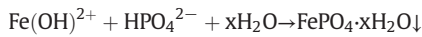
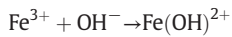
**Table 1**  
Samples with different ultrasound power and intensity.

Samples	Ultrasound power input (W)	Ultrasound intensity $\times 10^6$ (W/m <sup>2</sup> )
FP-0	0	0
FP-360	360	2.713
FP-480	480	3.617
FP-600	600	4.521
FP-720	720	5.426
FP-960	960	7.234

the sonolysis of the water can be characterized by [29]:



$\text{Fe}(\text{NO}_3)_3$  and  $(\text{NH}_4)_2\text{HPO}_4$  were used to synthesise  $\text{FePO}_4$  precursor through the hydrolysis reaction of  $\text{Fe}^{3+}$  and  $\text{HPO}_4^{2-}$  and the main reactions can be described by



In addition, side reaction can be identified as:



Both  $\text{FePO}_4 \cdot x\text{H}_2\text{O}$  and  $\text{Fe}(\text{OH})_3$  are produced in precipitation and they are considered as a parallel-competing reactions. In order to promote the main reactions, the mixing is intensified via the impinge jets to increase the likelihood of ion collision between  $\text{Fe}^{3+}$  and  $\text{PO}_4^{3-}$ . Adoption of acoustic streaming produced by ultrasound wave propagation helps to accelerate the particle migration, resulting in a higher ratio of  $n(\text{Fe}^{3+})/n(\text{PO}_4^{3-})$  in the solution [30]. Although the solubility product constant of  $\text{FePO}_4$  is greater than that of  $\text{Fe}(\text{OH})_3$  ( $K_{\text{sp}}(\text{FePO}_4) = 1.3 \times 10^{-22}$ ,  $K_{\text{sp}}(\text{Fe}(\text{OH})_3) = 2.8 \times 10^{-38}$ ), the side reaction may be ignored as the reaction circumstance is acidic. It should be noted here that with more  $\text{Fe}^{3+}$  ions being engaged into the complex reaction, the solution tends to be acidic due to  $\text{Fe}^{3+}$  hydrolysis and the precipitation dissolves. To keep the pH value around 1.7 with less induced-impurities, ammonia aqueous solution was added after the mixing process of  $\text{Fe}^{3+}$  and  $\text{PO}_4^{3-}$  was fully realised."

### 3. Numerical simulation

#### 3.1. Mathematical modelling

The impinge jet flow together with the flow in the expansion chamber with and without the action of ultrasound was analyzed with the conditions of the frequency of 20 kHz and power ranging from 0 to 960 W. Numerical study helps to analyse the intensified effect of ultrasound on this solid-liquid system. The gas phase in this case is neglected as the volume fraction of cavitation bubbles induced by ultrasound is  $< 1\%$ . The governing equation for continuity, momentum and energy can be solved by the simplified model. The  $Re$  for the confined impinge jet reactor is defined by

$$Re_j = \frac{\rho u d}{\mu}$$

where  $u$  is the mean velocity in the inlet of the T-shape junction and  $d$  is the hydraulic diameter of the circular tube inlet. The mean velocity is 0.2022 m/s based on the feed flow rate, corresponding to  $Re_j$  of 606. However, it should be pointed out that it may be inappropriate to consider the flow to be laminar as the intensive mixing in the chamber of the confined impinge jet will generate small turbulent eddies and the flow will become highly turbulent although the Reynolds number is  $< 2000$ . The ultrasound waves may lead to a sharp localized pressure reduction and the formation of local cavitation due to acoustic streaming [15]. This will give rise up the local turbulence with huge amounts of micro-cavitated bubble collapse in an extremely short time and in a very small volume. To describe the flow in the impinge jet system with a sudden expansion chamber, the following governing equations were employed. The general mass conservation equation for incompressible fluid takes following form

$$\nabla \cdot \vec{u} = 0 \quad (1)$$

where  $\vec{u}$  is the mass-average velocity and the momentum conservation equation in 3-D dimension is given by,

x-Momentum equation,

$$\frac{\partial}{\partial t}(\rho u) + \nabla \cdot (\rho u \vec{u}) = -\frac{\partial p}{\partial x} + \mu \nabla^2 u - \left[ \frac{\partial(\rho \overline{u^2})}{\partial x} + \frac{\partial(\rho \overline{u'v'})}{\partial y} + \frac{\partial(\rho \overline{u'w'})}{\partial z} \right] + S_u \quad (2)$$

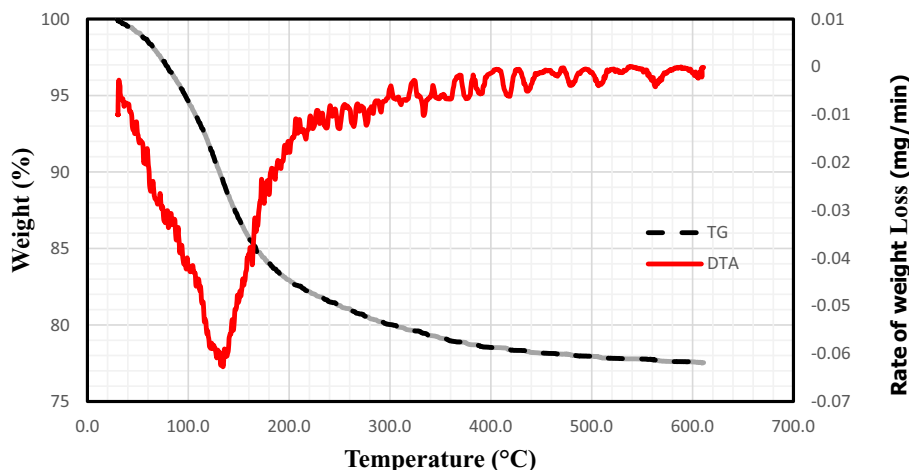


**Fig. 4.** TG-DTA curves of sample FP-600 before calcination at a heating rate of  $10^\circ\text{C min}^{-1}$  in air.

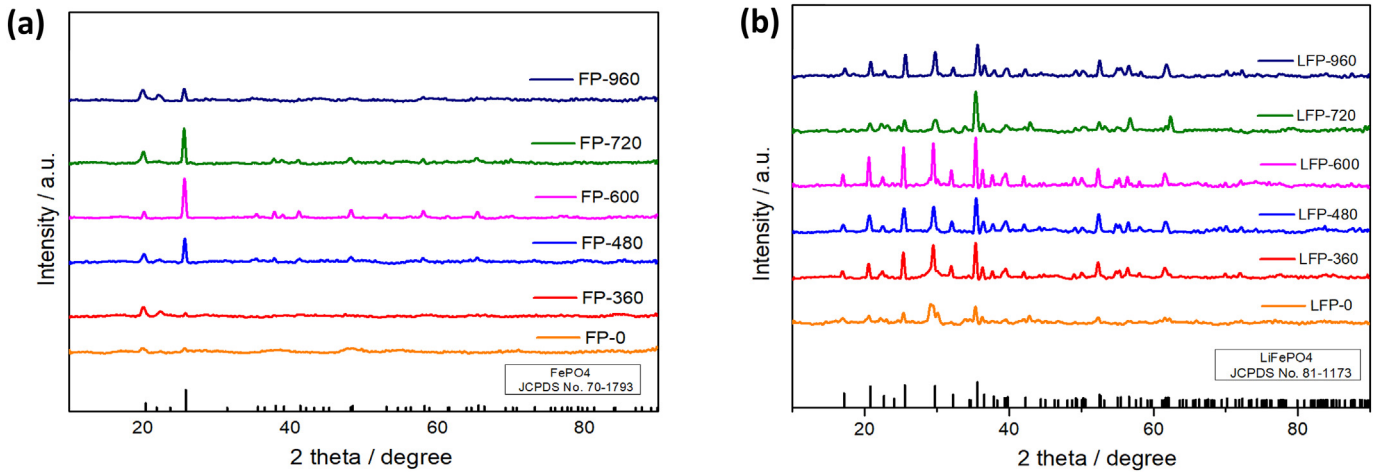


Fig. 5. XRD patterns of (a)  $\text{FePO}_4$  and (b)  $\text{LiFePO}_4$ .

y-Momentum equation,

$$\frac{\partial}{\partial t}(\rho v) + \nabla \cdot (\rho v \vec{u}) = -\frac{\partial p}{\partial y} + \mu \nabla^2 u - \left[ \frac{\partial(\rho \overline{v' u'})}{\partial x} + \frac{\partial(\rho \overline{v' v'^2})}{\partial y} + \frac{\partial(\rho \overline{v' w'})}{\partial z} \right] + S_v \quad (3)$$

z-Momentum equation,

$$\frac{\partial}{\partial t}(\rho w) + \nabla \cdot (\rho w \vec{u}) = -\frac{\partial p}{\partial z} + \mu \nabla^2 w - \left[ \frac{\partial(\rho \overline{w' u'})}{\partial x} + \frac{\partial(\rho \overline{w' v'})}{\partial y} + \frac{\partial(\rho \overline{w' w'^2})}{\partial z} \right] + S_w \quad (4)$$

where  $\rho$  is the fluid density,  $\vec{u}$  is the velocity vector,  $\mu$  is the dynamic viscosity,  $p$  is the pressure and  $S_u, S_v, S_w$  represent the source terms of momentum conservation equation induced by the ultrasound. The standard k- $\epsilon$  model is employed for liquid phase and it is proved to be appropriate to simulate the flow in the imping jet based on Gavi's work as following [31].

$$\frac{\partial(\rho k)}{\partial t} + \nabla \cdot (\rho k \vec{u}) = \nabla \cdot \left[ \left( \mu + \frac{\mu_t}{\sigma_k} \right) \Delta k \right] + G_k - \rho \epsilon \quad (5)$$

$$\frac{\partial(\rho \epsilon)}{\partial t} + \nabla \cdot (\rho \epsilon \vec{u}) = \nabla \cdot \left[ \left( \mu + \frac{\mu_t}{\sigma_\epsilon} \right) \Delta \epsilon \right] + C_1 \frac{\epsilon}{k} G_k - C_2 \rho \frac{\epsilon^2}{k} \quad (6)$$

where  $G_k$  is the generation of turbulence kinetic energy due to the mean

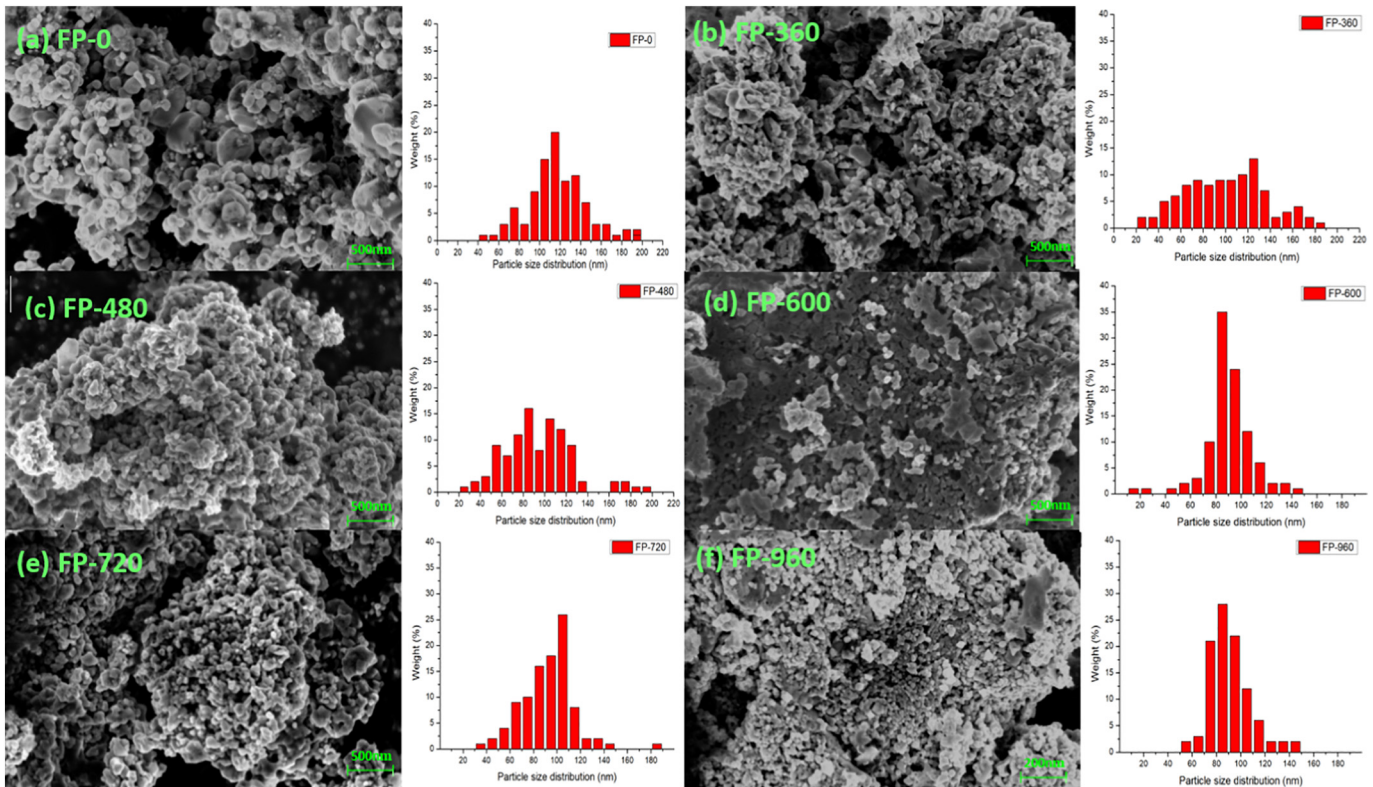


Fig. 6. The SEM images of  $\text{FePO}_4$  synthesized under the conditions of applying different ultrasound powers and corresponding size distribution of  $\text{FePO}_4$  samples synthesized under the conditions of applying different ultrasound powers.

**Table 2**

The average crystallite size of samples under different conditions.

Sample	FP-0	FP-360	FP-480	FP-600	FP-720	FP-960
Average crystallite size L (nm)	191	184	149	107	121	134

velocity gradients as shown in Eq. (7),  $\mu_t$  is the turbulent dynamic viscosity and the coefficients used in this standard k- $\epsilon$  model take the following values  $C_\mu=0.09$ ,  $C_1=1.42$ ,  $C_2=1.92$ ,  $\sigma_k=1.0$  and  $\sigma_\epsilon=1.3$ .

$$G_k = \mu_t \left\{ 2 * \left[ \left( \frac{\partial u}{\partial x} \right)^2 + \left( \frac{\partial v}{\partial y} \right)^2 + \left( \frac{\partial w}{\partial z} \right)^2 \right] + \left( \frac{\partial u}{\partial y} + \frac{\partial v}{\partial x} \right)^2 + \left( \frac{\partial u}{\partial z} + \frac{\partial w}{\partial x} \right)^2 + \left( \frac{\partial v}{\partial z} + \frac{\partial w}{\partial y} \right)^2 \right\} \quad (7)$$

Considering the chemical reaction, species transport equations is shown in eq. (8) without considering the energy equation due to the constant value of kinetic constant  $k$  in the temperature range of 293 to 308 K [32].

$$\frac{\partial(\rho C_i)}{\partial t} + \nabla \cdot (\rho \vec{u} C_i) = \nabla \cdot [(\Gamma_i + \Gamma_t) \Delta C_i] - \left[ \frac{\partial(\rho \overline{u' C_i'})}{\partial x} + \frac{\partial(\rho \overline{v' C_i'})}{\partial y} + \frac{\partial(\rho \overline{w' C_i'})}{\partial z} \right] + S_i \quad (8)$$

In Eq. (8),  $c_i$  represents the concentration of species  $i$ ,  $\Gamma_i$  is the diffusion coefficient of the species  $i$  and  $\Gamma_t$  is the turbulent diffusion coefficient and  $S_i$  is the formation rate the species  $i$ . However, the species transport equation can be solved only if the Probability Density Function (PDF) is known.

3.2. Numerical simulation

The geometry and computational domain are schematically shown in Figs. 2 and 3D CFD simulation was conducted using the commercial code FLUENT 15.0. The computation domain contains a T-shaped impinging jet reactor with an ultrasonic transducer installed in the downstream

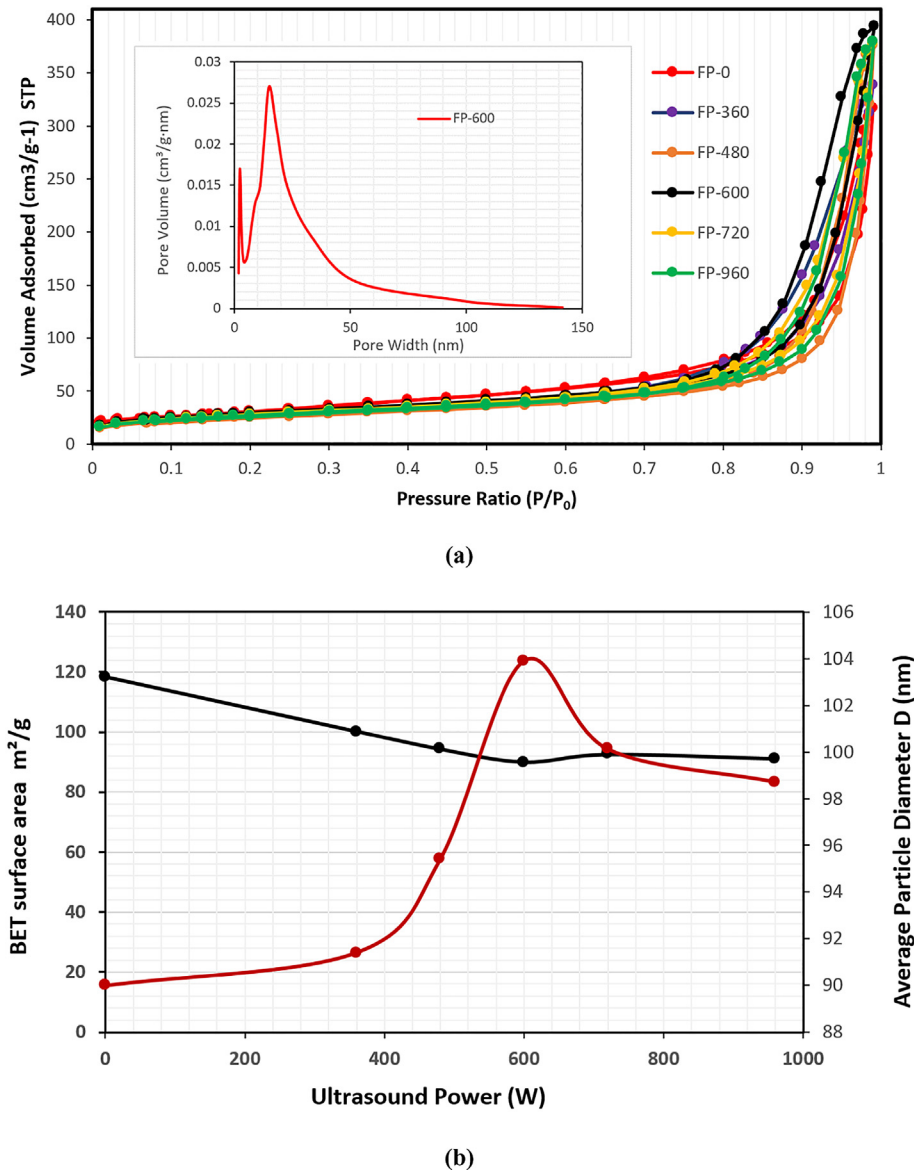


**Fig. 7.** (a) N<sub>2</sub> adsorption–desorption isotherm at 77 K and pore size distribution (the inset) calculated by the BJH method from the desorption branch of FePO<sub>4</sub>; (b) Average particles size and BET surface area of the sample prepared under different ultrasound power.

sudden expansion chamber. The inner diameter of the inlet and the outlet are 3 and 8 mm, respectively. The ultrasonic wave is generated and propagates from the tip of the ultrasonic transducer which has the length of 60 mm and the diameter of 13 mm. The location of boundary condition was at the tip of the ultrasonic transducer marked as blue in Fig. 10, which is 18 mm from the bottom of expanded chamber. The mesh shown in Fig. 3 was generated by using ANSYS ICEM with the feature of grid being orthogonal. The trial simulations were conducted and it was found that when the number of the meshes is  $>160,000$ , there is not noticeable changes observed in the time averaged concentration distributions in the IJR system. As such, all the simulations were conducted using this mesh setup throughout the present work.

In CFD modelling of the hydrodynamics in the confined impinge jet reactor, the pressure–velocity coupling was realised by SIMPLE algorithm with the second-order upwind discretisation scheme [15]. Standard  $k-\varepsilon$  model was employed as the mixing in the core of the confined impinge jet reactor could be highly turbulent although the calculated Reynolds number at the reactor inlet is smaller than 2000. Velocity inlet boundary condition has been imposed for both IJR inlets while the pressure outlet boundary condition was specified for the outlet of the IJR where the synthesized product was collected. The tip of the ultrasonic transducer was set as pressure inlet. No-slip boundary condition was applied to all the walls. Numerical simulations were performed with and without ultrasound exposure.

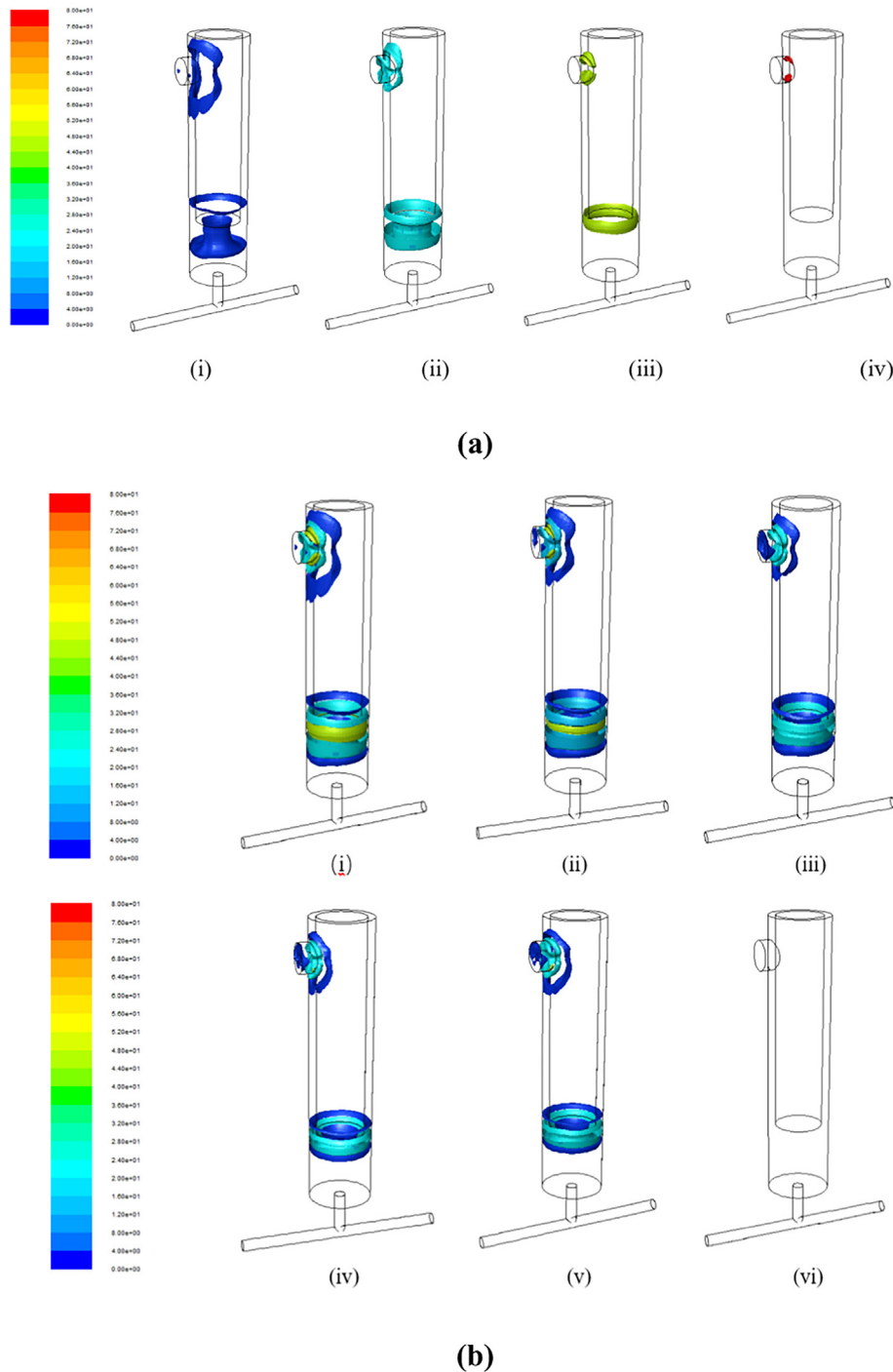


**Fig. 8.** (a) Iso-surface distribution of turbulent kinetic energy ( $k$ ) in IJR under the ultrasound power of 960 W at 0.0023 s. (i)  $5 \text{ m}^2/\text{s}^2$ , (ii)  $20 \text{ m}^2/\text{s}^2$ , (iii)  $50 \text{ m}^2/\text{s}^2$  and (iv)  $80 \text{ m}^2/\text{s}^2$  (b) Turbulence Kinetic Energy ( $k$ ) distribution of IJR under different power of ultrasound at 0.0023 s. (i) 960 W, (ii) 720 W, (iii) 600 W, (iv) 480 W, (v) 360 W and (vi) 0 W.

Ultrasound of different amplitudes was imposed with a fixed ultrasound frequency of 20 kHz. The solutions were treated as being converged when the normalized residuals of all the variables are smaller than  $1 \times 10^{-7}$  since the time step used for CFD modelling to capture the ultrasound wave fluctuation should be at least smaller than a period of the ultrasound wave. The numbers of max iterations per time step is set to be 100 to ensure the convergence." When considering the effect of ultrasound on the bulk flow, the cyclic sound pressure equation of ultrasound wave was induced to describe the distribution of sound field according to the following equation [33].

$$p_u = p_a \cos(2\pi ft) + \frac{1}{2}\rho v^2 \quad (9)$$

where  $p_a$  is the amplitude of the sound pressure (pa),  $f$  is the frequency (Hz),  $t$  is the time (s),  $\rho$  is the average density of liquid bulk ( $\text{kg}/\text{m}^3$ ) and  $v$  is the velocity (m/s).

$$p_a = \sqrt{2I\rho C} \quad (10)$$

$$I = \frac{P_{us}}{A} \quad (11)$$

where  $I$  is the sound intensity ( $\text{W}/\text{m}^2$ ),  $p_{us}$  is the ultrasonic power (W),  $A$  is the tip area of the ultrasonic transducer ( $\text{m}^2$ ) and  $C$  is the sound speed in the water (m/s). In the present work, synthesis were proceeded under different conditions by changing the input power of the ultrasound as listed in Table 1.

## 4. Result and discussion

### 4.1. Effect of ultrasound power intensity on crystallinity and morphology of FP precursors

Thermal gravimetric analysis (TG) and Differential Thermal Analysis (DTA) technologies was used to confirm the thermal properties of FP precursors and Fig. 4 shows TG-DTA curves of sample FP-600 at a heating rate of  $10 \text{ }^\circ\text{C min}^{-1}$  in the air TG curves indicating the mass loss of samples. The absorbed water begin to lose at  $100^\circ\text{C}$  and the there is a strong endothermic peak near  $120^\circ\text{C}$  indicating the loss of crystallized where  $\text{FePO}_4 \cdot x\text{H}_2\text{O}$  transformed to anhydrous hexagonal  $\text{FePO}_4$  crystal residues. Therefore,  $x$  is calculated in the range of 0.73 to 2.50. In addition, the gradual weight loss from  $200$  to  $600^\circ\text{C}$  is ascribed to the decay of hydroxide and thus  $600^\circ\text{C}$  is considered to be the

minimum temperature needed for the calcinations process to obtain product with high purity [26].

The crystallinity and phase of FP specimens prepared under different ultrasound intensities were detected by XRD as shown in Fig. 5. The morphology and size of FP nano-particles were detected by SEM image as shown in Fig. 6. It can be seen from the figure that the relative intensity of sample peaks is well consistent with that of hexagonal  $\text{FePO}_4$  crystal (JCPDS No.70-1793), which indicates its high purity and crystallinity. The intensity of diffraction peaks became noticeably stronger when imposing ultrasound wave. A similar trend can be observed in Fig. 5 (b), implying ultrasound waves strengthen the crystal structure of  $\text{LiFePO}_4$  crystal (JCPDS No.81-1173). It is noticed that when ultrasound power is as high as 960 W, the intensity of peaks for both FP and LFP specimens becomes smaller. From XRD patterns, the average crystallite size  $L$  can be calculated through Scherrer equation [27,34].

$$L = \frac{K\lambda}{\beta \cos\theta} \quad (12)$$

where  $K$  is the crystallite shape factor or denoted as Scherrer's constant equals to 0.9,  $\lambda$  is the wavelength of X-ray taken as  $0.145056 \text{ nm}$ ,  $\beta$  is the peak width of the diffraction peak profile at half maximum height and  $\theta$  is the degree. The average crystallite size in nanometres of different samples are listed in Table 2. Sample prepared without applying ultrasound exposure has the largest average crystallite size of  $191 \text{ nm}$  while that prepared under ultrasound power of  $600 \text{ W}$  has the smallest diameter of  $107 \text{ nm}$ . A similar appearance was also observed in a series of SEM images of FP samples as shown in Fig. 6, indicating that higher intensity of the ultrasound may cause smaller particles size and uniform microstructure.

### 4.2. Effect of ultrasound power on particle size and porosity of FP precursors

Except for crystallinity and morphology, ultrasound has impact on particle size and porosity as well. The particle size distribution of FP precursors under different conditions are shown in Fig. 6. It shows that the main peaks of particle size distribution of FP samples have fallen into the range of  $90\text{--}130 \text{ nm}$ . FP samples prepared without applying ultrasound present a broader size distribution and  $<47\%$  of particles are in the range of  $90\text{--}130 \text{ nm}$ . In contrast, samples for cases of FP-600 and FP-720 exhibit a narrower particle size distribution, corresponding to the percentage up to  $77\%$  and  $68\%$  of the particles falling into this size range. The broader size distribution contributes non-uniform products that is consistent to the average crystallite size of samples shown in Table 2. In

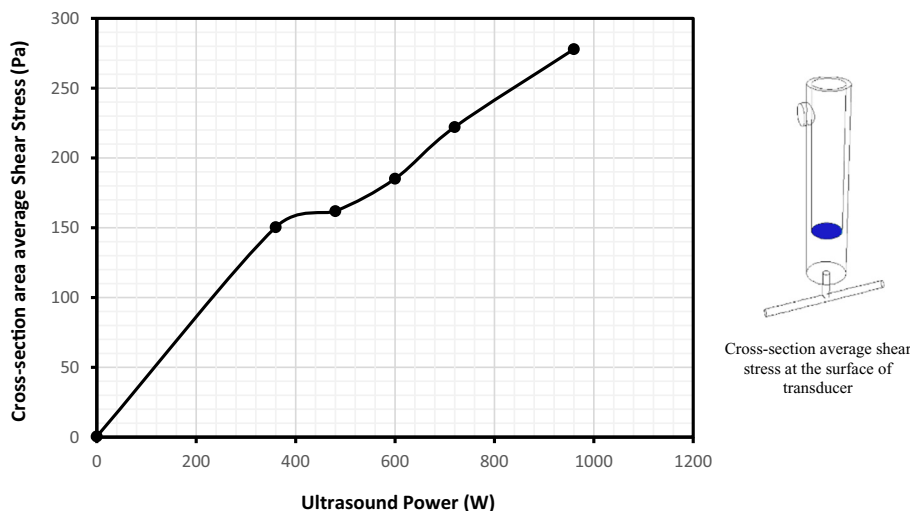
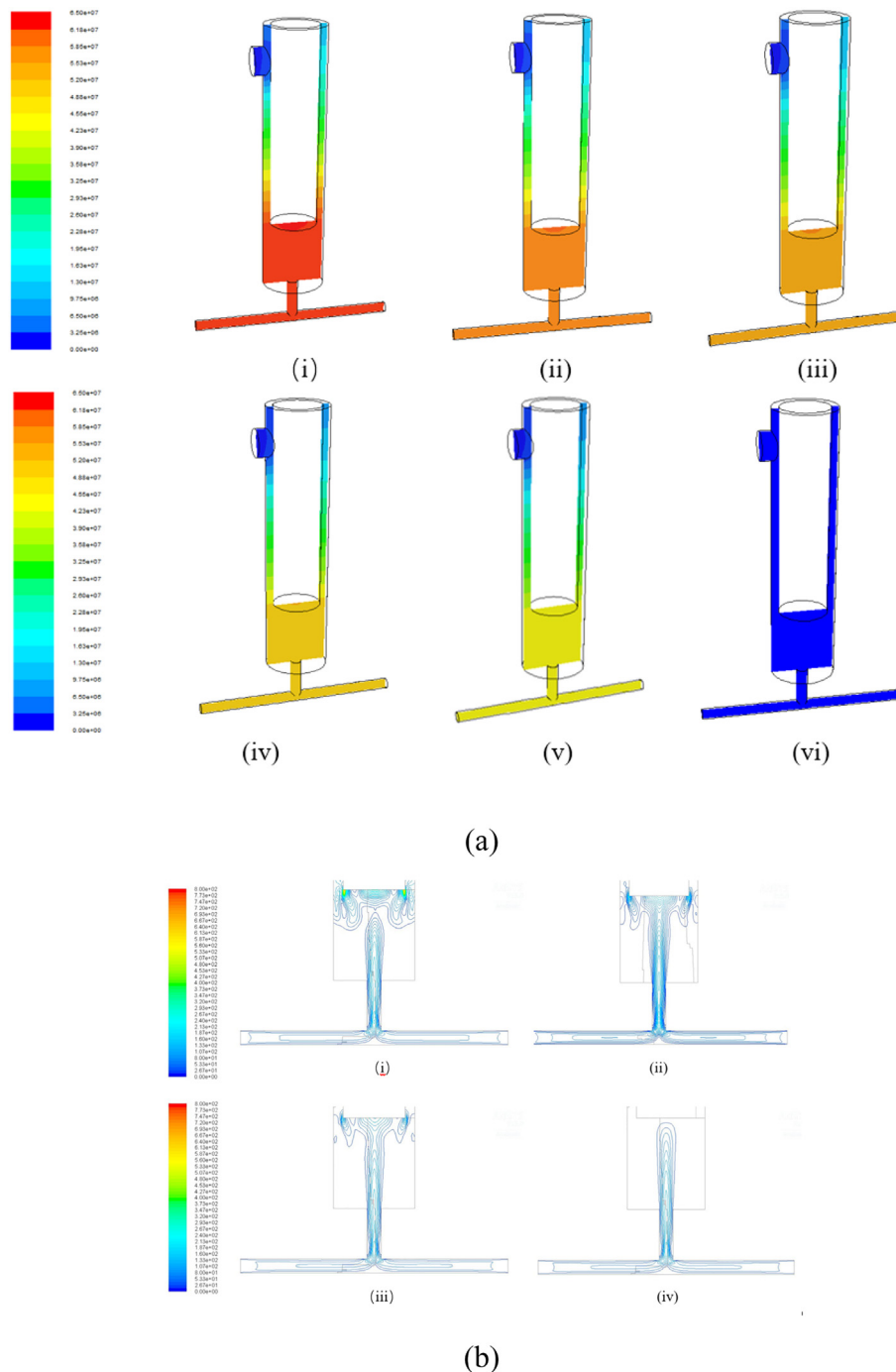


Fig. 9. Cross-section averaged shear stress at the transducer surface under the conditions of applying different ultrasound powers.

addition, samples FP-600 and FP-720 give narrow particle size distribution but that of FP-960 is boarder. The impact of ultrasound intensity on particle size and porosity can be also reflected by BET test as shown in Fig. 7, verifying that the product with smaller particle size in the presence of ultrasound irradiation can be obtained. It can be postulated that the ultrasound waves in the process of particle formation may cause porosity increment as shown in Fig. 7. This may be ascribed to micro-bubble collapse in an extremely short time to generate the porous structures.

The ultrasound irradiation intensifies the reactant mixing and encourages rapid reaction to form the nuclei of  $\text{FePO}_4$  with smaller size, which can be also evidenced from the experimental results. The

turbulent eddies induced by acoustic streaming may exert strong shear force on the nanoparticles to diminish and smooth its ragged surface. This can be interpreted as the fact that the synthesized micro-particles that entrained by the turbulent eddies experience the local shear so that the particle size may be reduced due to the surface rip-off. This can be also supported by turbulent kinetic energy ( $k$ ) distribution in the IJR system as shown in Fig. 8. Fig. 8 (a) shows the isosurface distribution of turbulent kinetic energy ( $k$ ) under the ultrasound power of 960 W in the IJR while Fig. 8 (b) shows the turbulent kinetic energy ( $k$ ) distribution under diverse ultrasound power. It can be seen from Fig. 9 that enhancement of the turbulent kinetic energy  $k$  in the vicinity of the tip of ultrasound transducer and the reactor outlet



**Fig. 10.** (a) Total pressure distribution ( $P$ ) of  $x$ - $z$  plane of IJR under different power of ultrasound at 0.0023 s. (i) 960 W, (ii) 720 W, (iii) 600 W, (iv) 480 W, (v) 360 W and (vi) 0 W. (b) Dynamic pressure distribution ( $P$ ) of  $x$ - $z$  plane of IJR under different power of ultrasound at 0.0023 s. (i) 960 W, (ii) 600 W, (iii) 360 W, (iv) 0 W.

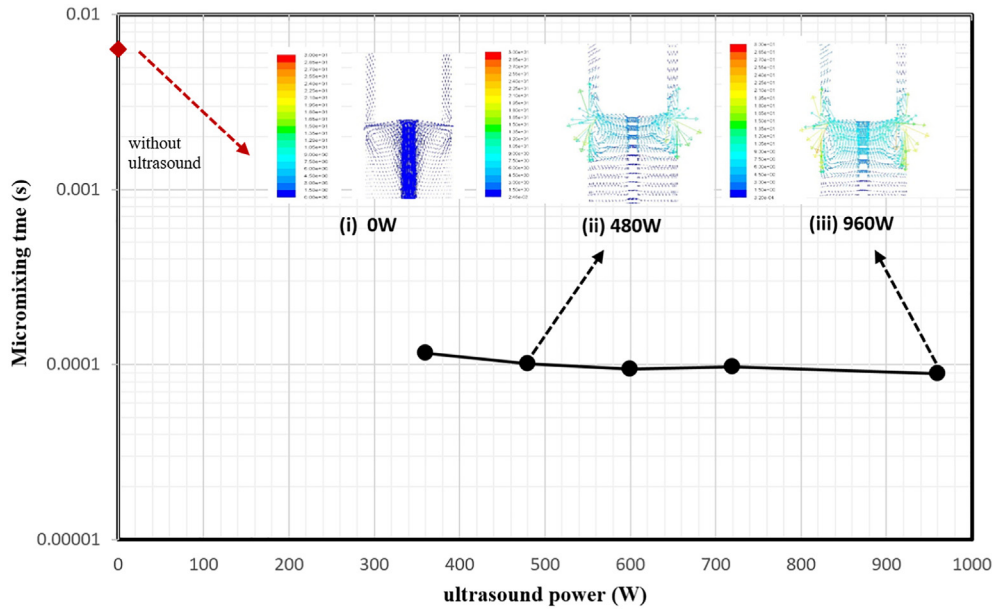


Fig. 11. Micromixing time  $t_m$  as a function of ultrasound power  $P$  and velocity Magnitude (m/s) of  $x-z$  plane of IJR under different power of ultrasound at 0.0023 s.

is observed as the acoustic streaming is introduced at 0.0023 s of 46 period. As the effect of ultrasound intensification on the pressure change will give rise to the change in the velocity field, such velocity fluctuation will have an impact on the turbulent kinetic energy  $k$  due to the periodical fluctuation of acoustic wave of applied ultrasound. Consequently, it can be reasonably assumed that the application of ultrasound can strengthen the local turbulent shear as more small length scale turbulent eddies could be generated, which will enhance turbulent kinetic energy  $k$  (see Fig. 9).

When the ultrasound power used is higher than its threshold, aggregate of particles becomes prevalent and leads to larger particle size as can be seen from Fig. 8 (b). An explanation is that small particles tend to agglomerate to diminish the high surface energy induced by ultrasound and regress to steady state [35]. Another reason responsible for aggregation is the temperature impact. Larger ultrasound energy causes higher temperature change and this enlarges the enthalpy change with negative value when it cools down. At the room temperature, however, entropy enhancement owing to the release of water from the hydrophobic part drives

aggregation process [36]. In this way, temperature increment is the result of turbulence energy dissipation which  $\varepsilon$  can be estimated by the following equation [37],

$$\varepsilon = \frac{\Delta PQ}{\rho V} \tag{13}$$

Flow in ultrasound-assisted IJR is pressure-driven since solution is pumped in to IJR and the effect of ultrasound wave can be expressed in terms of pressure. From the numerical works, the total pressure distribution varies under different power of ultrasound as shown in Fig. 10 (a). The pressure from inlet is predominant and pressure drops as with flow upwards. From eq. (13), large pressure drop is responsible for high-energy dissipation rate leading to intense temperature increase. Under the impact of ultrasound waves, the dynamic pressure profile was predicted theoretically to be sectorial shape and was acoustically generated from a fictitious “orifice” as shown in the Fig. 10 (b).

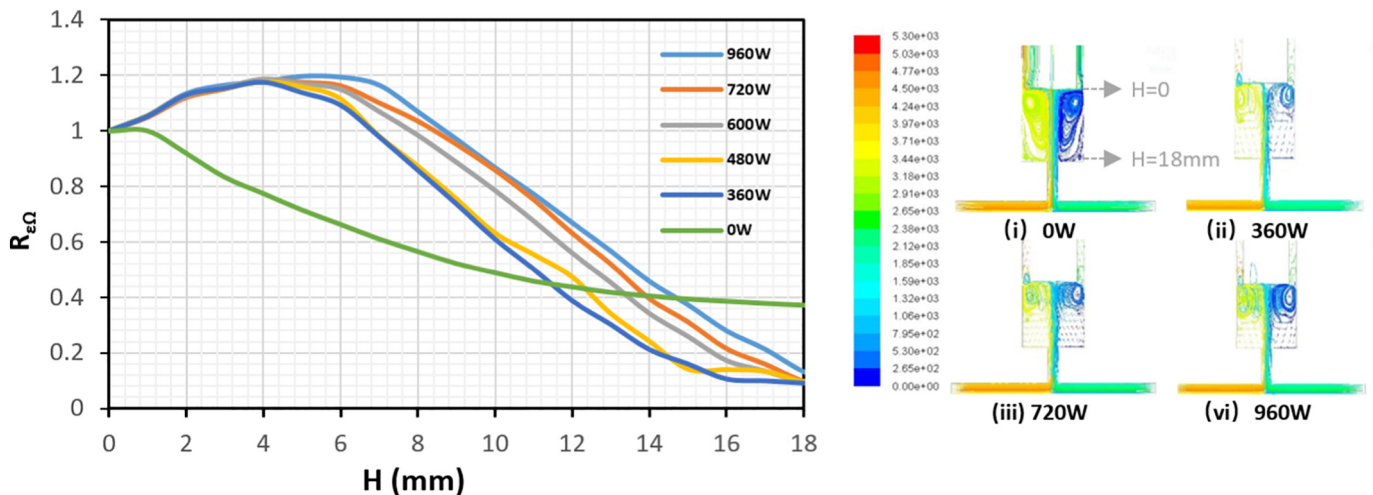


Fig. 12. Spatial correlation  $R_{\epsilon, \Omega}$  along the reaction chamber from the tip of the ultrasound transducer ( $H = 0$ ) to the bottom of expansion ( $H = 18$  mm) under different power of ultrasound at 0.0023 s.

#### 4.3. Effect of adoption of different ultrasound power intensities on the mixing

There are two scales used to describe mixing performance, macro-mixing for blending and micro-mixing for turbulent mixing. In this case, acoustic streaming helps to intensify micro-mixing as a result of ultrasound wave propagation and mixing parameter  $\gamma$  is used to define the micromixing time as,

$$t_m = \frac{1}{2\gamma} \quad (14)$$

$$\gamma = \frac{C_\phi \varepsilon}{2k} \quad (15)$$

Where  $C_\phi$  is a function of local turbulent Reynolds number  $Re_t$  in eq. (26),  $k$  and  $\varepsilon$  are the turbulent kinetic energy and the turbulent dissipation rate that can be derived from numerical works.

$$Re_t = \frac{k}{(\varepsilon\nu)^{1/2}} \quad (16)$$

In this case,  $C_\phi \approx 2$  is used for turbulent flow and it is overestimated for this case [33]. The mixing time shown in Fig. 11 reveals that the adoption of ultrasound can noticeably reduce the mixing time up to 98.6%. In the presence of ultrasound, the mixing performance is intensified and it was found an empirical relationship between  $\varepsilon$  and  $t_m$  based on power law relation as following,

$$t_m = 0.0005\varepsilon^{-0.164} \quad (17)$$

From the velocity magnitude in Fig. 11, the ultrasound waves lead to an “active” zone near the tip of ultrasound transducer where eddies are induced. This turbulence-like micro-streams entrain the particles to convey with these eddies. The intensity of the vortices changes along with the amplitude of the ultrasound waves. In order to illustrate the effect of ultrasound on the mixing behaviour in the IJR, especially for the zone just downstream of the impinge jet, a special correlation between cross-section area average turbulent dissipation rate and cross-section area average vorticity is proposed. The results of such correlation are shown in Fig. 12. The  $R_{\varepsilon, \Omega}$  represents the correlation factor and it can

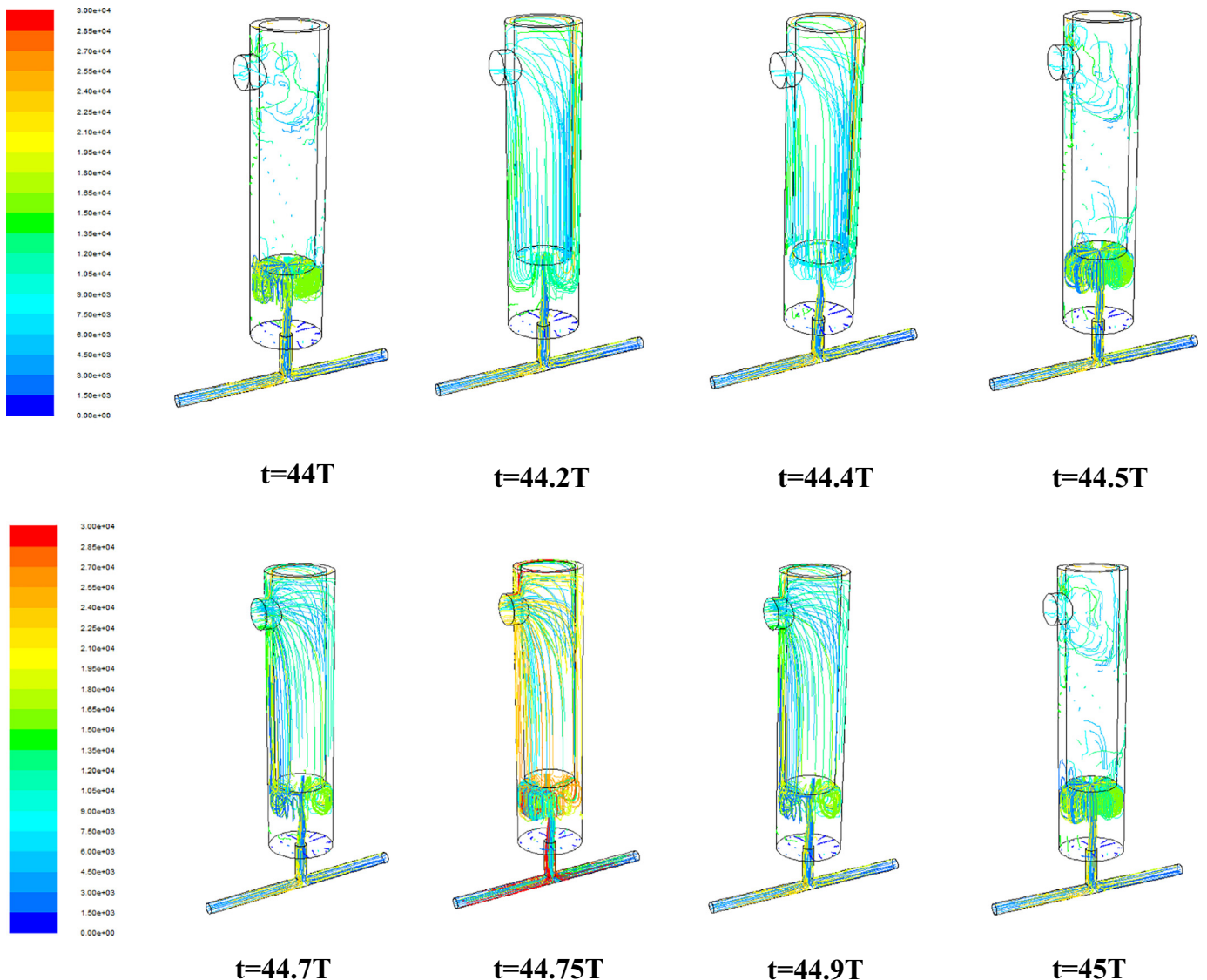


Fig. 13. The streamline flow of the fluid in the time period from 44 to 45 T.

be calculated by eq. (18) as given

$$R_{\varepsilon, \Omega} = \frac{\varepsilon(h, t) |\Omega(h + \Delta h, t)|}{\sqrt{\varepsilon(h, t)^2} \sqrt{\Omega(h, t)^2}} \quad (18)$$

$$\varepsilon(h, t) = \frac{1}{A} \int_0^A \varepsilon dA \quad (19)$$

$$\Omega(h, t) = \frac{1}{A} \int_0^A |\Omega| dA \quad (20)$$

where  $\varepsilon$  is the cross section area-weighted average turbulent dissipation rate and  $\Omega$  is the cross section average area-weighted vorticity. In the case without applying ultrasound (0 W), the coefficient gradually decreases from the position corresponding to the tip of ultrasound transducer to the bottom of the expansion. With being exposure to the ultrasound, the correlation significantly increases around the position of toroidal vortices underneath the tip of ultrasonic sensor, accompanying by the turbulent energy dissipation rate enhancement. The impact of the ultrasound on the flow just downstream of the expansion causes a reduction in vorticity strength, indicated by the correlation  $R_{\varepsilon, \Omega}$  being smaller than the case of 0 W. This may need further investigation but the phenomenon is very likely caused by cancelation between the toroidal vortex generated just at the bottom of the expansion and those turbulent eddies generated as the result of microbubble collapse. As the ultrasound power increases, the spatial correlation factor increases in the expansion chamber, indicating an enhanced impact of ultrasound on flow patterns.

High correlation factor indicates the great contribution to intensify turbulence thus expected mixing performance by inducing ultrasound waves. Simultaneously, intensified eddies may exert a strong shear force to shape the particles or carry the particles in circulation. Such correlation not only interprets mixing performance can be intensified as the ultrasound power increases but also helps to optimize the conditions for particle preparation. Whereas, fluid near the ultrasound transducer has diverse pathway due to the impact of ultrasound period as shown in Fig. 13. It shows the streamline flow of the fluid in the period from 44 to 45 T and this verifies the vortices changes near the ultrasound transducer.

## 5. Conclusion

In this work, impinging jet reactor with a downstream sudden expansion chamber that is equipped with ultrasound transducer was employed to assess the effect of intensification of ultrasound on synthesis of FP particles. It was found that  $\text{FePO}_4$  particles could be obtained with higher crystallinity and uniformity, higher porosity and smaller size with ultrasound intensification. However, adoption of excess high ultrasound intensity may induce free radicals and generate the other compounds due to the local high temperature and pressures, leading to unpredictable changes in physical and chemical properties and excessive energy waste [38]. With caution, the application of ultrasound can be still considered as an effective means for synthesis of FP nanoparticles if the threshold of the applied ultrasound intensity is suitable. It has been clearly indicated that the ultrasound-assisted impinging jet reactor system can effectively intensify the micro-mixing as the result of enhancement on the local turbulent dissipation rate. The increase of the local turbulent dissipation rate gives rise to an increase of the local shear which can assist the controllable synthesis of nanoparticles with desired characteristics. It has been demonstrated from the experiments that better behaviour of LFP/C electrode material can be obtained as the consequence of increase in the ultrasound power applied, which has reaffirmed that with ultrasonic intensification, the synthesized particles tend to aggregate due to the locally

enhanced shear strain due to the occurrence of high turbulent kinetic energy dissipation.

## Nomenclature

A	cross section area of the reactor chamber ( $m^2$ )
C	the sound speed in the water (m/s)
$C_\phi$	a function of the local turbulent Reynolds number
$G_k$	the generation of turbulence kinetic energy (J)
K	crystallite shape factor or Scherrer's constant
L	average crystallite size L (nm)
P	pressure drop (Pa)
Q	volumetric flow rate ( $m^3/s$ )
V	volume ( $m^3$ )
$c_1$	empirical constant
$c_2$	empirical constant
$c_i$	the concentration of species i (mol/L)
f	frequency of the ultrasound wave (Hz)
h	distance from the bottom the IJR (m)
k	turbulent kinetic energy ( $m^2/s^2$ )
I	sound intensity ( $W/m^2$ )
$\rho$	average density of liquid bulk ( $kg/m^3$ )
$p_{us}$	ultrasonic power (W)
p	pressure (pa)
$p_u$	pressure induced by sound field (pa)
$p_a$	amplitude of the sound pressure (pa)
R	Space correlation factor
$Re_t$	local turbulent Reynolds number $Re_t$
S	Source term in the momentum equation ( $kg/m^2 \cdot s^2$ )
t	time (s)
$\mu_t$	turbulence viscosity ( $kg/m \cdot s$ )
u	liquid velocity (m/s)
v	inlet velocity (m/s)

## Greek letters

$\beta$	peak width of the diffraction peak profile at half maximum height
$\varepsilon$	turbulence dissipation rate
$\sigma_k$	empirical constant
$\sigma_\varepsilon$	empirical constant
$\theta$	degree in XRD diffraction (degree)
$\nu$	dynamic viscosity ( $N \cdot s/m^2$ )
$\lambda$	the wavelength of X-ray (nm)
$\gamma$	mixing parameter
$\Gamma$	turbulent diffusion coefficient
$\Omega$	cross section average vorticity ( $S^{-1}$ )

## Subscripts

i	continuous or dispersed phase
t	turbulent flow
m	mixing
us	ultrasound

## Operators

In the three-dimensional coordinates (x, y, z) with the unit vectors (i, j, k), the operators can be defined as follows,

$$\nabla = \mathbf{i} \frac{\partial}{\partial x} + \mathbf{j} \frac{\partial}{\partial y} + \mathbf{k} \frac{\partial}{\partial z}$$

$$\Delta = \nabla^2 = \frac{\partial^2}{\partial x^2} + \frac{\partial^2}{\partial y^2} + \frac{\partial^2}{\partial z^2}$$

## Acknowledgements

This work was financially supported by the National Natural Science Foundation of China (Grant No. 21576141). Yanqing Guo and Bin Dong would also like to acknowledge the PhD scholarship of the International Doctoral Innovation Centre (IDIC) of the University of

Nottingham Ningbo China and the support of EPSRC (Grant no. EP/G037345/1).

## Appendix A. Supplementary data

Supplementary data to this article can be found online at <https://doi.org/10.1016/j.powtec.2019.05.066>.

## References

- [1] R. Abiev, O. Almyasheva, S. Izotova, V. Gusarov, Synthesis of cobalt ferrite nanoparticles by means of confined impinging-jets reactors, *J. Chem. Technol. Appl.* 1 (1) (2017) 7–13.
- [2] A. Nie, Z. Gao, L. Xue, Z. Cai, G.M. Evans, A. Eaglesham, Micromixing performance and the modeling of a confined impinging jet reactor/high speed disperser, *Chem. Eng. Sci.* 184 (2018) 14–24.
- [3] Y. Ying, G. Chen, Y. Zhao, S. Li, Q. Yuan, A high throughput methodology for continuous preparation of monodispersed nanocrystals in microfluidic reactors, *Chem. Eng. J.* 135 (3) (2008) 209–215.
- [4] X. Liu, P. Yan, Y. Xie, H. Yang, X. Shen, Z. Ma, Synthesis of superior fast charging-discharging nano-LiFePO<sub>4</sub>/C from nano-FePO<sub>4</sub> generated using a confined area impinging jet reactor approach, *Chem. Commun.* 49 (47) (2013) 5396–5398.
- [5] A.J. Mahajan, D.J. Kirwan, Micromixing effects in a two-impinging-jets precipitator, *AIChE J.* 42 (7) (1996) 1801–1814.
- [6] C.P. Fonte, M.A. Sultan, R.J. Santos, M.M. Dias, J.C.B. Lopes, Flow imbalance and Reynolds number impact on mixing in confined impinging jets, *Chem. Eng. J.* 260 (2015) 316–330.
- [7] T. Guo, B. Ruan, Z. Liu, M.A. Jamal, L. Wen, J. Chen, Numerical and experimental investigations of liquid mixing in two-stage micro-impinging stream reactors, *Chin. J. Chem. Eng.* 25 (4) (2017) 391–400.
- [8] T. Hielscher, Ultrasonic production of nano-size dispersions and emulsions, Dans European Nano Systems Workshop-ENS, 2005, Paris, France <https://arxiv.org/ftp/arxiv/papers/0708/0708.1831.pdf>.
- [9] B. Sajjadi, S. Asgharzadehahmadi, P. Asaithambi, A.A.A. Raman, R. Parthasarathy, Investigation of mass transfer intensification under power ultrasound irradiation using 3D computational simulation: a comparative analysis, *Ultrason. Sonochem.* 34 (2017) 504–518.
- [10] M.R. Jamei, M.R. Khosravi, B. Anvaripour, Investigation of ultrasonic effect on synthesis of nano zero valent iron particles and comparison with conventional method, *Asia Pac. J. Chem. Eng.* 8 (5) (2013) 767–774.
- [11] Y. Zhao, G. Chen, Q. Yuan, Liquid-liquid two-phase mass transfer in the T-junction microchannels, *AIChE J.* 53 (12) (2007) 3042–3053.
- [12] F. Laugier, C. Andriantsiferana, A.M. Wilhelm, H. Delmas, Ultrasound in gas-liquid systems: effects on solubility and mass transfer, *Ultrason. Sonochem.* 15 (6) (2008) 965–972.
- [13] H. Monnier, A. Wilhelm, H. Delmas, Effects of ultrasound on micromixing in flow cell, *Chem. Eng. Sci.* 55 (19) (2000) 4009–4020.
- [14] M. Abolhasani, M. Rahimi, M. Dehbani, S.R. Shabanian, CFD modeling of low, medium and high frequency ultrasound waves propagation inside a liquid medium, 4rd National Conference on CFD Applications in Chemical & Petroleum Industries, Ahwaz, Iran, 2012.
- [15] M. Rahimi, B. Aghel, B. Hatamifar, M. Akbari, A. Alsairafi, CFD modeling of mixing intensification assisted with ultrasound wave in a T-type microreactor, *Chem. Eng. Process. Process Intensif.* 86 (2014) 36–46.
- [16] W.L. Nyborg, Acoustic streaming due to attenuated plane waves, *J. Acoust. Soc. Am.* 25 (1) (1953) 68–75.
- [17] M.J. Lighthill, On sound generated aerodynamically II. Turbulence as a source of sound, *R. Soc. 222* (1148) (1954) 1–32.
- [18] L.V. Wijngaarden, On the equations of motion for mixtures of liquid and gas bubbles, *J. Fluid Mech.* 33 (3) (1968) 465–474.
- [19] R. Jamshidi, B. Pohl, U.A. Peucker, G. Brenner, Numerical investigation of sonochemical reactors considering the effect of inhomogeneous bubble clouds on ultrasonic wave propagation, *Chem. Eng. J.* 189–190 (2012) 364–375.
- [20] G.B. Lebon, I. Tzanakis, G. Djambazov, K. Pericleous, D. Eskin, Numerical modelling of ultrasonic waves in a bubbly Newtonian liquid using a high-order acoustic cavitation model, *Ultrason. Sonochem.* 37 (2017) 660–668.
- [21] Q. Jiao, X. Tan Bayanheshig, J. Zhu, Numerical simulation of ultrasonic enhancement on mass transfer in liquid-solid reaction by a new computational model, *Ultrason. Sonochem.* 21 (2) (2014) 535–541.
- [22] Z. Xu, K. Yasuda, S. Koda, Numerical simulation of liquid velocity distribution in a sonochemical reactor, *Ultrason. Sonochem.* 20 (1) (2013) 452–459.
- [23] S. Niazi, S.H. Hashemabadi, M.M. Razi, CFD simulation of acoustic cavitation in a crude oil upgrading sonoreactor and prediction of collapse temperature and pressure of a cavitation bubble, *Chem. Eng. Res. Des.* 92 (1) (2014) 166–173.
- [24] M.D. Luque de Castro, F. Priego-Capote, Ultrasound-assisted crystallization (sonocrystallization), *Ultrason. Sonochem.* 14 (6) (2007) 717–724.
- [25] F. Croce, A. D'Epifanio, P. Reale, L. Settimi, B. Scrosati, Ruthenium oxide-added quartz iron phosphate as a new intercalation electrode in rechargeable lithium cells, *J. Electrochem. Soc.* 150 (5) (2003) A576–A581.
- [26] X.-m. Liu, P. Yan, Y.-Y. Xie, H. Yang, X.-d. Shen, Z.-F. Ma, Synthesis of superior fast charging-discharging nano-LiFePO<sub>4</sub>/C from nano-FePO<sub>4</sub> generated using a confined area impinging jet reactor approach, *Chem. Commun.* 49 (47) (2013) 5396–5398.
- [27] U. Holzwarth, N. Gibson, The Scherrer equation versus the 'Debye-Scherrer equation', *Nat. Nanotechnol.* 6 (2011) 534.
- [28] J.H. Bang, K.S. Suslick, Applications of ultrasound to the synthesis of nanostructured materials, *Adv. Mater.* 22 (10) (2010) 1039–1059.
- [29] M. Kohno, T. Mokudai, T. Ozawa, Y. Niwano, Free radical formation from sonolysis of water in the presence of different gases, *J. Clin. Biochem. Nutr.* 49 (2) (2011) 96–101.
- [30] B. Dong, X. Huang, X. Yang, G. Li, L. Xia, G. Chen, Rapid preparation of high electrochemical performance LiFePO<sub>4</sub>/C composite cathode material with an ultrasonic-intensified micro-impinging jetting reactor, *Ultrason. Sonochem.* 39 (2017) 816–826.
- [31] E. Gavi, D.L. Marchisio, A.A. Barresi, CFD modelling and scale-up of confined impinging jet reactors, *Chem. Eng. Sci.* 62 (8) (2007) 2228–2241.
- [32] P. Guichardon, L. Falk, J. Villermaux, Characterisation of micromixing efficiency by the iodide-iodate reaction system. Part II: kinetic study, *Chem. Eng. Sci.* 55 (19) (2000) 4245–4253.
- [33] J. Cai, X. Huai, R. Yan, Y. Cheng, Numerical simulation on enhancement of natural convection heat transfer by acoustic cavitation in a square enclosure, *Appl. Therm. Eng.* 29 (10) (2009) 1973–1982.
- [34] Y. Liu, R.O. Fox, CFD predictions for chemical processing in a confined impinging-jets reactor, *AIChE J.* 52 (2) (2006) 731–744.
- [35] D. Vollath, F.D. Fischer, D. Holec, Surface energy of nanoparticles—influence of particle size and structure, *Beilstein J. Nanotechnol.* 9 (1) (2018) 2265–2276.
- [36] J.A. Yu, S.H. Oh, Y.R. Park, J.S. Kim, Enthalpy-Entropy Compensation in Aggregation of Poly (styrene-co-sodium methacrylate) Ionomers in Aqueous Solution, *Macromolecular Symposia*, Wiley Online Library, 2007.
- [37] A.W. Burton, K. Ong, T. Rea, I.Y. Chan, On the estimation of average crystallite size of zeolites from the Scherrer equation: a critical evaluation of its application to zeolites with one-dimensional pore systems, *Microporous Mesoporous Mater.* 117 (1–2) (2009) 75–90.
- [38] A.R. Jambrak, T.J. Mason, V. Lelas, L. Paniwnyk, Z. Herceg, Effect of ultrasound treatment on particle size and molecular weight of whey proteins, *J. Food Eng.* 121 (2014) 15–23.